PROGRESS IN RESEARCH

April 1, 2013 - March 31, 2014

CYCLOTRON INSTITUTE

Texas A&M University

College Station, Texas

PROGRESS IN RESEARCH

APRIL 1, 2013- MARCH 31, 2014

Prepared By

The Cyclotron Institute Staff

Texas A&M University

College Station, TX 77843-3366

Phone: (979) 845-1411
Fax: (979) 845-1899

Web: http://cyclotron.tamu.edu

June 2014

TABLE OF CONTENTS

SECTION II: HEAVY ION REACTIONS

SECTION III: NUCLEAR THEORY

SECTION IV: SUPERCONDUCTING CYCLOTRON, INSTRUMENTATION AND RIB UPGRADE

Introduction
April 1, 2013 – March 31, 2014

Progress in research and operations at the Texas A&M Cyclotron Institute is summarized in this report for the period April, 1, 2013 through March 31, 2014. The format follows that of previous years. Sections I through III contain reports from individual research projects. Operation and technical developments are given in Section IV. Section V lists the publications with Cyclotron Institute authors and outside users and the Appendix gives additional information including talks presented by members of the Institute during the past year. Once again, the full volume of this year's Progress in Research is available only on our web site (http://cyclotron.tamu.edu). *Since most of the contributions presented here are truly reports on progress in research, results and conclusions should not be quoted from the report without the consent of the authors.*

This year we have seen important changes in our faculty. Dr. Grigory Rogachev has joined us as a Professor of Physics. Dr. Robert Tribble has begun an 80% appointment as the Assistant Scientific Director at BNL. Dr. Tribble remains in charge of the Upgrade Project and supervising his research program. Dr. Joseph Natowitz, a long time member of the Institute faculty, retired from the chemistry department, but retains a 25% appointment and a very active research program at the Cyclotron Institute. Additionally, this year Dr. Dan Melconian was tenured and promoted to Associate Professor of Physics. On March 1st I was appointed Director of the Cyclotron Institute.

We were pleased that the construction on the new floor of offices was successfully completed this year and all Institute personnel have moved back in to the building.

We have now completed 9 ½ years of the Upgrade Project, which when finished will give us accelerated radioactive beams at intermediate energies. During this reporting period the K150 cyclotron provided 2,038 hours of beams including strip extracted protons, ^{12}C, ^{16}O beams for the development of the light-ion guide system, and high intensity ^{40}Ar beams at various energies to work towards reaching the final milestone of the project. Over 1,500 hours of beams from the K150 cyclotron were provided during simultaneous operation with the K500 cyclotron. This demonstrates that once the ion guides are fully functional, the laboratory is operationally ready for radioactive beam production. The commissioning work on the light-ion guide via $^{nat}Zn(p,n)^{64}Ga$ at 15 MeV showed very high production efficiency from the gas cell. The final step of transporting the radioactive ions from the gas cell to charge breeding ECR ion source using the helium-jet method is in progress. The LN_2 cryopanel was installed and tested with ^{40}Ar beams and yielded an intensity improvement of ~25%. An even larger gain is expected when the cryopanel is cooled by LHe or cold He gas. Improvements to ECR2 including plasma chamber water chilling, increasing the output power of the 14.4 GHz transmitter and a better biased plate design yielded a record production of 46 μA of $^{40}Ar^{13+}$. Despite all the improvements made, about a factor of 2 in either ECR output or throughput efficiency is still needed to reach the project milestone of 0.9 pμA of $^{40}Ar^{13+}$ at 13.7 MeV/u. Also the heavy-ion guide system and its many components are now being installed in the ion-guide cave.

As in previous reports, I include here some highlights of work carried out over the past year.

- The energies of the giant monopole resonance in mass 92 nuclei and in some Ca isotopes are not reproduced in mean field calculations, suggesting nuclear structure is significantly affecting the position of the GMR in these nuclei.
- A nucleation-time moderated chemical equilibrium model has been developed and used to probe the clusterization in the low-density neck region of a ternary fissioning nuclei.
- Measurements of transverse single-spin asymmetries, A_N, for forward multi-photon, jet-like events in $\sqrt{s}$ = 500 GeV *pp* collisions indicate the large A_N that has been observed for forward inclusive hadron production at RHIC does not arise from conventional parton fragmentation to jets.
- The measured cross sections of ^{45}Sc and ^{50}Ti projectiles reacting with lanthanide targets are substantially smaller than those for ^{48}Ca-induced reactions, suggesting that discovering new elements using ^{45}Sc or ^{50}Ti projectiles could be very difficult.
- Analysis of the first-ever measurement of the beta asymmetry parameter, A_β, using laser-cooled atoms at TRIUMF is nearing completion, with an expected total uncertainty of 2%. We have upgraded our system and taken data with much higher statistics and expect to reach 0.3% sensitivity.
- We have measured the lifetime and are analyzing the data from a branching ratio measurement of the beta decay of ^{37}K. Once completed, the *ft* value of this isobaric analogue decay will be the best known among the T=1/2 mirror transitions.
- A pair of mirror superallowed transitions – ^{38}Ca $\rightarrow ^{38}$K^{m} and ^{38}K^{m} $\rightarrow ^{38}$Ar – has been fully characterized for the first time. The ratio of their *ft* values has been measured with 0.2% precision and the result provides a first step in constraining the isospin-symmetry-breaking corrections used to extract the value of V_{ud} from superallowed nuclear decays.
- Work aimed at understanding stellar reaction rates for proton capture around A~28 has continued with the neutron transfer experiment ^{13}C(^{27}Al,^{28}Al)^{12}C. Using charge symmetry, this provides information for the ^{27}Si(p,γ)^{28}P reaction.
- A method for determining the mean-field directly from data on single particle matter density has been developed and applied to the case of the charge density difference between the isotones ^{206}Pb – ^{205}Tl, associated with the proton $3S_{1/2}$ single particle orbit.
- Calculations of isoscalar dipole (ISD) strength distributions in nuclei, within the Hartree-Fock based random phase approximation, demonstrate that the ISD in neutron-rich nuclei provides substantial contribution to the nuclear Schiff moment which is central to the measurement of time reversal violation in an atom.
- Including both partonic and hadronic mean fields in a multiphase transport model, we have found that the relative elliptic flow differences between protons and antiprotons as well as between positively and negatively charged kaons in the STAR data at RHIC can be reproduced if the ratio of the partonic vector to scalar coupling is appreciable, which is expected to have significant implications in understanding the QCD phase structure at finite baryon chemical potential.
- A theory of the deuteron stripping populating bound states and resonances based on the surface-integral formalism using ADWA (adiabatic distorted wave approach) and CDCC (continuum

discretized coupled channels) has been developed. To test the theory first experiments $^{14}C(d,p)^{15}C$ were performed at 23.4 and 60 MeV.

- A link between dilepton data and chiral symmetry restoration in high-energy heavy-ion collisions has been established by evaluating QCD and Weinberg sum rules. Based on the in-medium ρ spectral function that describes dilepton spectra, and in-medium condensates from lattice QCD, an in-medium a_1 spectral function has been found that gradually degenerates with the ρ channel.
- The calculation of the ω(782) width in nuclear matter using existing in-medium ρ and π propagators yields results consistent with what is observed in ω photoproduction off nuclei. This corroborates the hadronic many-body approach as a suitable framework to study hadron properties in matter.
- In preparation for accelerated radioactive beams, significant upgrades are being made to improve the isotopic resolution of the MDM focal-plane detector.
- Construction of a prototype of a general purpose active target detector (Texas Active Target Prototype, TexAT-P) for wide variety of experiments with rare isotope beams at the Cyclotron Institute has been initiated.
- The Quadrupole Triplet Spectrometer beam line to focus heavy residues for time of flight measurements has been commissioned. The QTS is designed to be run in conjunction with the FAUST array.
- The FAUST detector array has been upgraded with position sensitive detectors (the Dual-Axis Dual-Lateral "DADL" detectors).
- A gas stopper for a future online chemistry program has been commissioned. The data shows that the device can be operated in either a fast extraction or a maximum efficiency mode.
- Received the first irradiated sample for a new nuclear forensics program. The first destructive analyses were conducted shortly after the cutoff date of this publication.

Institute scientists remain active in a number of collaborative research efforts around the world. Major programs include: mass measurements using the Penning Trap at the University of Jyväskylä; continued work with the STAR collaboration at RHIC; measurements of beta decays with the TRINAT collaboration at TRIUMF; ANASEN at MSU; and participation in the SAMURAI collaboration at RIBF in Tokyo, Japan.

I am indebted to Dr. Y.-W. Lui for assembling this report.

S. J. Yennello
June 3, 2014

SECTION I

NUCLEAR STRUCTURE, FUNDAMENTAL INTERACTIONS AND ASTROPHYSICS

Anomalous behavior of the giant monopole resonance

D. H. Youngblood, Y. -W. Lui, J. Button, Y. Xu, M. Anders, and S. Shlomo

The energy of the giant monopole resonance (GMR) in ^{48}Ca is higher than in ^{40}Ca, which is not reproducible with self-consistent mean field calculations[1], and the GMR's in both ^{92}Zr and ^{92}Mo are much higher in energy than predicted with mean field calculations that reproduce the energies of the GMR in the other Zr and Mo isotopes.[2] Moreover the GMR's in all Zr and Mo isotopes studied are split into two components separated by several MeV. In the past year we have studied the GMR in ^{44}Ca and ^{94}Mo to further explore these issues.

Fig. 1 shows a plot of the energy of the GMRs in ^{40,44,48}Ca vs A ,and the ^{44}Ca energy falls between the ^{40}Ca and ^{48}Ca energies. Also plotted are calculations using the Leptodermous expansion.

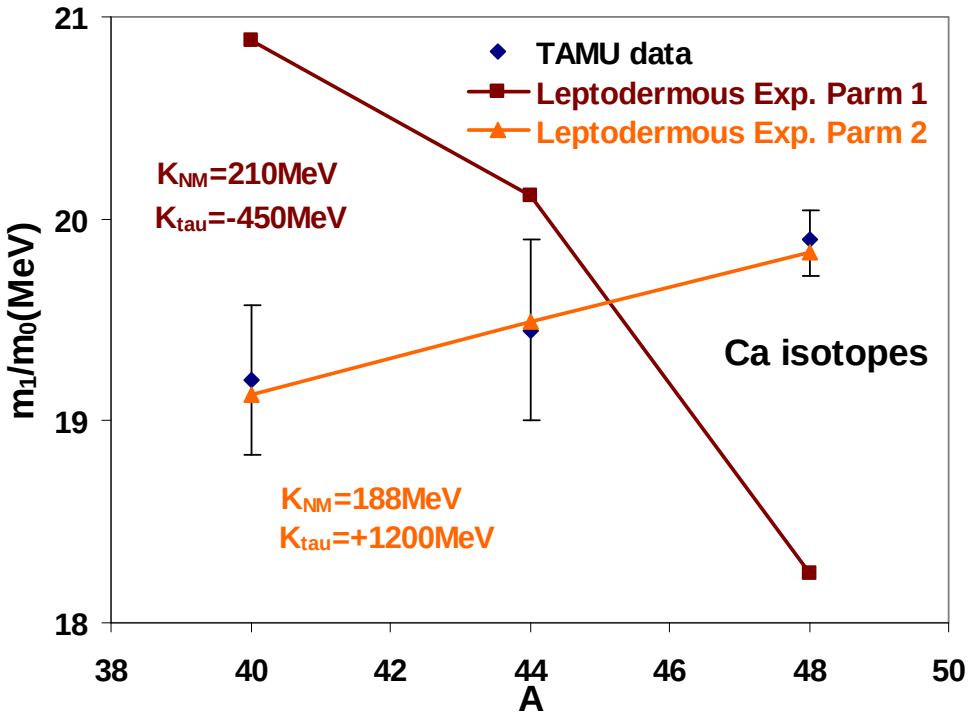

FIG. 1. GMR energy vs A for Ca isotopes. Two calculations using the Leptodermous expansion are shown.

The brown squares were calculated using values for K_{NM} and $K\tau$ obtained in a study of the Sn isotopes [3] , and the A dependence of the GMR energy is opposite that of the data, with the GMR in ^{40}Ca well above that in ^{44}Ca, and the GMR in ^{48}Ca well below that in ^{44}Ca. Varying K_{NM} and K_τ to fit the data (orange triangles) results in K_{NM}=188 MeV and K_τ=+1200 MeV . K_τ is generally accepted to be negative and roughly ~-500MeV, so the +1200MeV necessary to fit the ^{40,44,48}Ca results is badly in disagreement. Fig. 2 shows a comparison of the Ca experimental results with three mean field calculations. The two calculations [4-5] that give an energy for ^{44}Ca agree with the experimental results

for ^{44}Ca, and the Anders et al. calculation [4] shows the GMR energy in ^{48}Ca above that for ^{44}Ca in agreement with the data though it shows the ^{40}Ca energy much higher than either ^{44}Ca or ^{48}Ca The HF_QRPA calculation with pairing by Vesely *et al.* [5] shows the energy systematically decreasing as A increases, in contrast to the data. The RMF calculation by Sharma [6] shows the GMR in ^{48}Ca below that in ^{40}Ca.

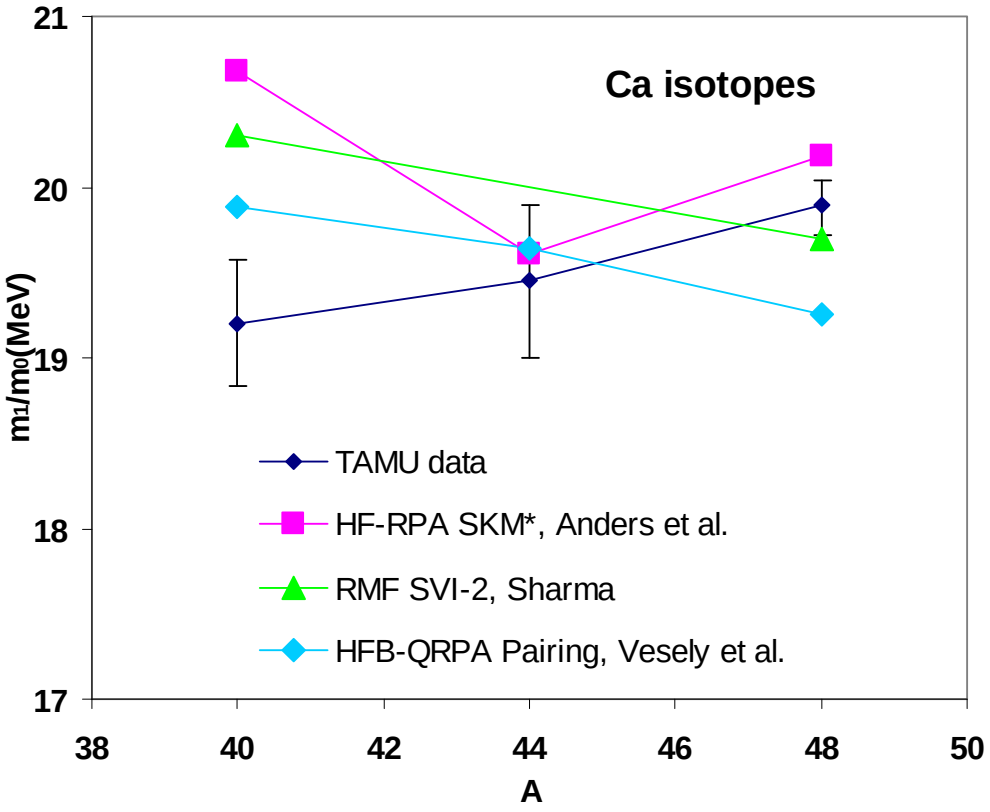

FIG. 2. Experimental GMR energies and three theoretical calculations of the GMR energy vs A for Ca isotopes.

We also studied ^{94}Mo to complement our previous study [2] of ^{92,96,98,100}Mo and ^{90,92,94}Zr. The E0 strength distribution obtained (Fig. 3) is similar to those for ^{96,98,100}Mo and ^{90,94}Zr with a lower energy peak at E_x~16.9MeV containing most of the strength and ~ 20% of the strength in a peak at E_x~ 24MeV. The total E0 strength seen is 108% of the E0 EWSR. The anomalous behavior of the centroid of the GMR is described in ref. [2], with those of both ^{92}Mo and ^{92}Zr well above values expected from mean field or Leptodermous expansion calculations. The GMR in ^{94}Mo is well reproduced by the mean field calculations. In Figs. 4 & 5 we plot the energies of the low and high peaks separately vs A. The energies of the lower peaks have a smooth behavior for both Zr and Mo isotopes and those for Mo are well reproduced by a Leptodermous expansion calculation with K_{NM}=210MeV and K_τ=-750MeV. The Zr data would require a slightly more negative K_τ. The high energy peaks in the Mo isotopes are within errors at

the same energy whereas the high energy peak in ^{92}Zr is over an MeV higher than in ^{94}Zr and about 0.5 MeV higher than in ^{90}Zr.

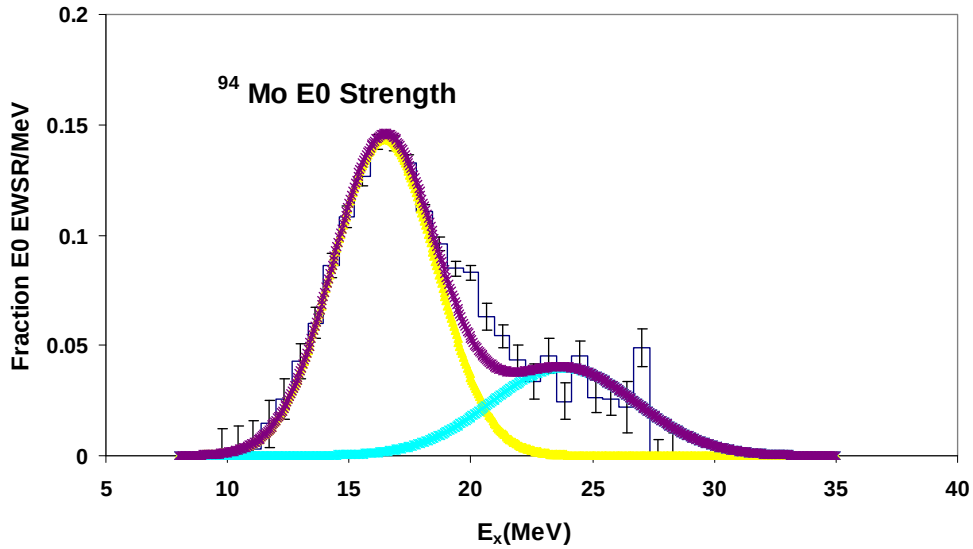

FIG. 3. E0 strength distribution for ^{94}Mo plotted vs excitation energy.

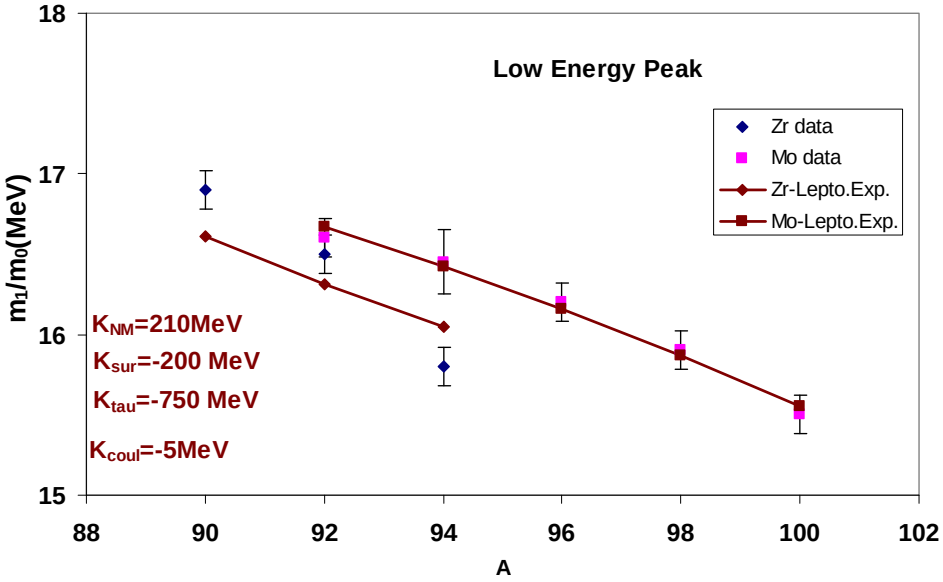

FIG. 4. Plot of energy of the low energy E0 peaks in the Mo and Zr isotopes vs A. The uncertainties are indicated by the error bars. Also shown are Leptodermous calculations using the parameters indicated in the figure.

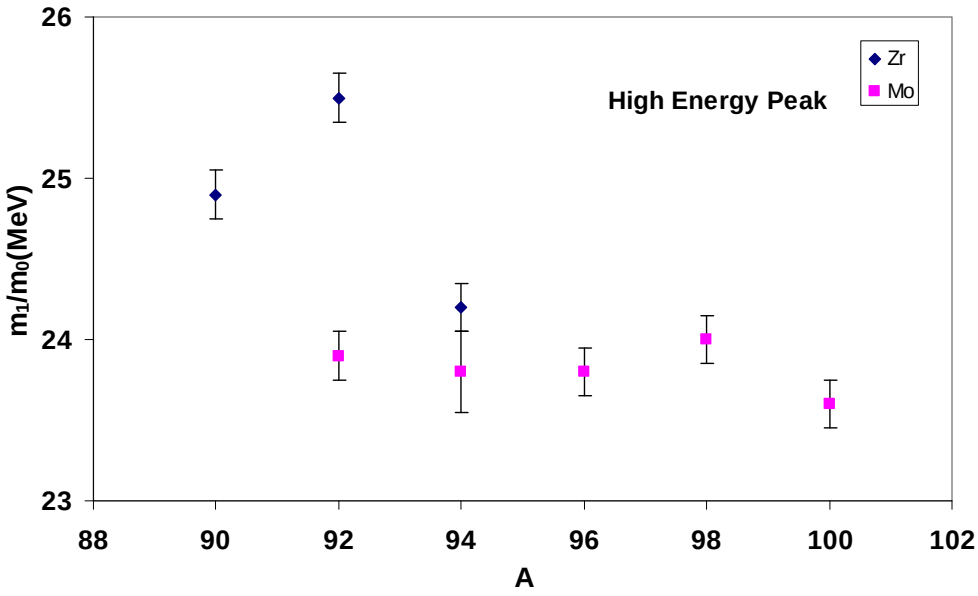

FIG. 5. Plot of energy of the high energy E0 peaks in the Mo and Zr isotopes vs A.

1. Y.-W. Lui, D.H. Youngblood, S. Shlomo, X. Chen, Y. Tokimoto, Krishichayan, M.R. Anders, and J. Button, Phys. Rev. C **83**, 044327 (2011).
2. D.H. Youngblood, Y.-W. Lui, Krishichayan, J. Button, M.R. Anders, M.L. Gorelik, M.H. Urin, and S. Shlomo, Phes. Rev. C **88**, 021301(R) (2013).
3. T. Li *et al.*, Phys. Rev. C **81**, 034309 (2010).
4. M.R. Anders, S. Shlomo, Tapas Sil, D.H. Youngblood, Y.-W. Lui, and Krishichayan, Phys. Rev. C **87**, 024303 (2013), private communitcation.
5. P. Veselý *et al*,. Phys. Rev. C **86**, 024303 (2012).
6. M.M. Sharma, Nucl. Phys. **A816**, 65 (2009).

Double folding optical parameters for 240 MeV ^{6}Li beam -revisited

Y. Xu, J. Button, Y. -W. Lui, and D. H. Youngblood

I. Nuclear density distribution

We collect 4 kinds of 6Li nuclear density distributions for constructing the nuclear double folding potentials between ^{6}Li projectile and seven target nuclei (^{24}Mg, ^{28}Si, ^{40}Ca, ^{48}Ca, ^{58}Ni, ^{90}Zr, and ^{116}Sn). These nuclear density distributions are the theoretical results from *ab initio* [1], COSMA [2], and HFB [3], as well as the experimental results by electron scattering [4]. Fig. 1 shows the comparison of these 4 kinds of nuclear density distributions for ^{6}Li. We finally choose the adopted experimental results [4] as the ^{6}Li projectile density distributions for the construction of nuclear double folding potential.

On the other hand, we employ the calculated results by HFB theory [3] as the density distributions of the 7 target nuclei for the construction of nuclear double folding potential.

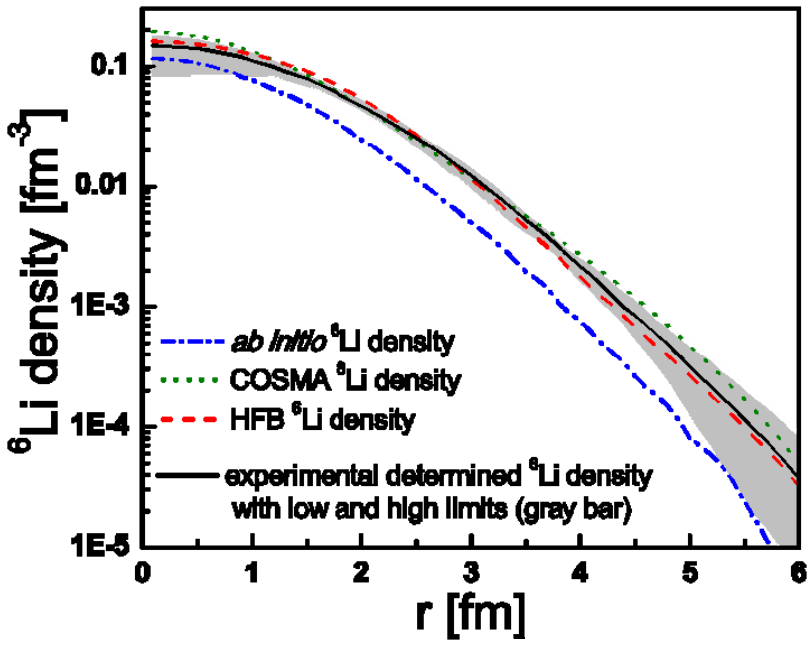

FIG. 1. Comparison of the different nuclear density distributions for ^{6}Li.

II. Nuclear DDM3Y double folding potential

By folding the nuclear densities (both projectile and target) and nucleon-nucleon interaction, we obtained the DDM3Y double folding potentials between ^{6}Li and these 7 target nuclei. The detail folding

method could be found in Refs. [5, 6]. Fig. 2 shows such DDM3Y double folding potential between ^{6}Li and ^{116}Sn as the example, where the 4 kinds of ^{6}Li density distributions are all presented.

We finally choose the DDM3Y double folding potential, deduced by ^{6}Li experimental density distribution, as the real part of nuclear potential in the further fitting of elastic data.

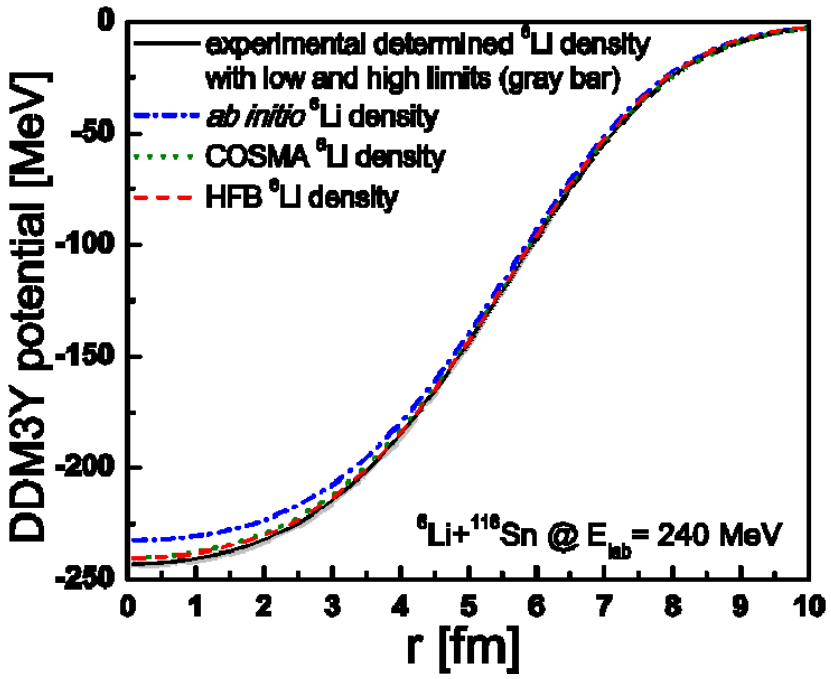

FIG. 2. DDM3Y double folding potential between 6Li and 116Sn. The 4 kinds of 6Li density distributions are all presented.

III. Elastic scattering fitting

By using the ECIS06 code, we fit the experimental data (angular distributions) of ^{6}Li elastic scattering on these 7 target nuclei at $E_{c.m.}$=240MeV. During the fitting, the DDM3Y double folding potential (as described in Part II) is adopted as the real part, while the Wood-Saxon potential is adopted as the imaginary part. Such choice is similar to those in Refs [5, 6]. To obtain the best fitting, a normalized factor and a scaling factor are introduced for the DDM3Y double folding potential. For the elastic scattering between 6Li and these 7 target nuclei, Fig. 3 shows the fitting results and Table I lists the corresponding potential parameters and χ^2 for Fig. 1.

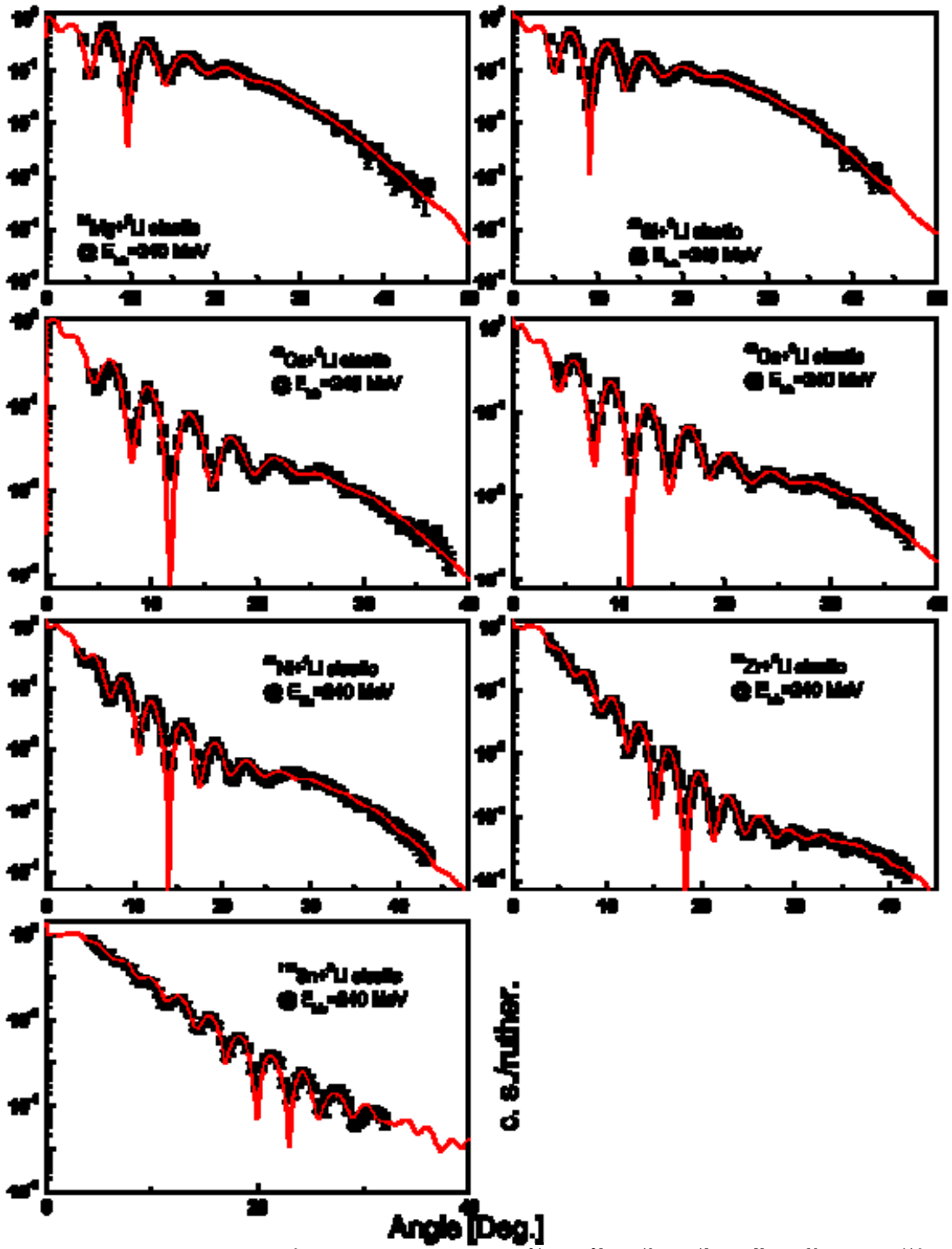

FIG. 3. The fitting results of ^{6}Li elastic scattering on ^{24}Mg, ^{28}Si, ^{40}Ca, ^{48}Ca, ^{58}Ni, ^{90}Zr, and ^{116}Sn at $E_{c.m.}$=240MeV.

Table I. The parameters for DDM3Y potential and Wood-Saxon potential and χ^2 for Fig. 1.

Z	N	A	Nuclei	Normalized	Scaling factors	V	r	a	X^2	previous X^2
				DDM3Y real part		Wood-Saxon imaginary part				for comparison
12	12	24	24Mg	0.852	1.0587	50.28739	4.00815	1.07187	1.101	1.039
14	14	28	28Si	0.8598	1.0512	42.69501	4.4028	1.04332	1.343	1.461
20	20	40	40Ca	0.8672	1.0717	44.45008	4.86415	1.09883	1.637	1.7
20	28	48	48Ca	0.8823	1.0653	32.99495	5.74968	0.90051	1.134	1.2
28	30	58	58Ni	0.8496	1.0608	39.60765	5.67734	1.08959	1.222	0.9
40	50	90	90Zr	0.8566	1.0561	35.07076	6.87215	0.98615	0.905	1.1
50	66	116	116Sr	0.8502	1.0658	59.11377	6.68749	1.04347	1.396	1.19

Furthermore, we also fit the obtained 7 sets of normalized factors and the scaling factors against the nuclear mass number, which are shown in Fig. 4. It is expected to predict these (normalized and scaling factors) parameters for ^{6}Li elastic scattering on other target nuclei.

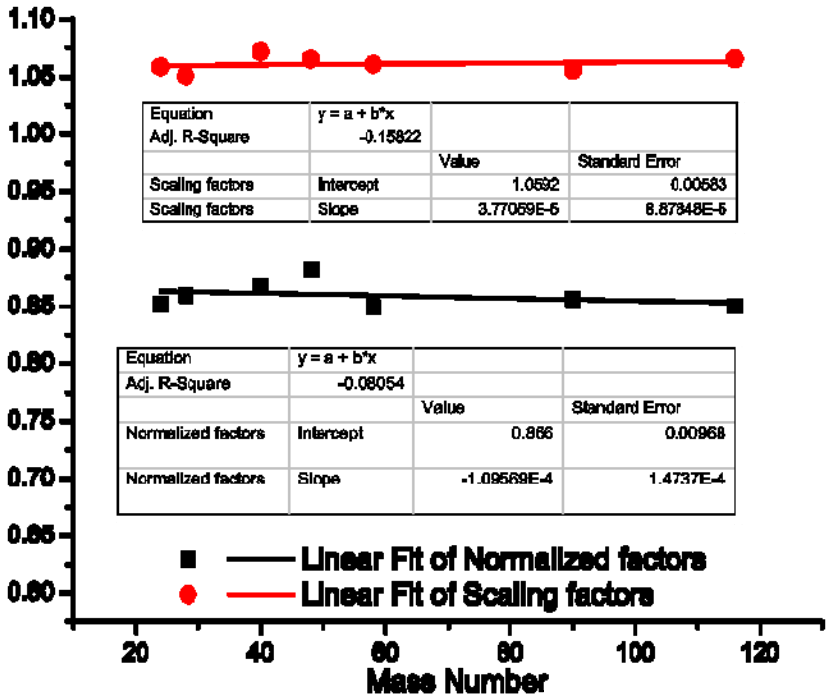

FIG. 4. The fitting results of obtained normalized factors and the scaling factors against the nuclear mass number for the 7 sets of elastic scattering.

IV. Inelastic scattering calculation

According to the nuclear potential (DDM3Y real part and Wood-Saxon imaginary part) obtained by elastic scattering fitting, we calculate the angular distributions of the differential cross sections for 6Li inelastic scattering to the low-lying excited states of these 7 target nuclei. Here, the results for ^{24}Mg (2^+ state at E*=1.369MeV), ^{28}Si (2^+ state at E*=1.779MeV and 3^- state at E*=6.888MeV) and ^{116}Sn (2^+ state at E*=1.29MeV and 3^- state at E*=2.27MeV) are shown in Fig. 5.

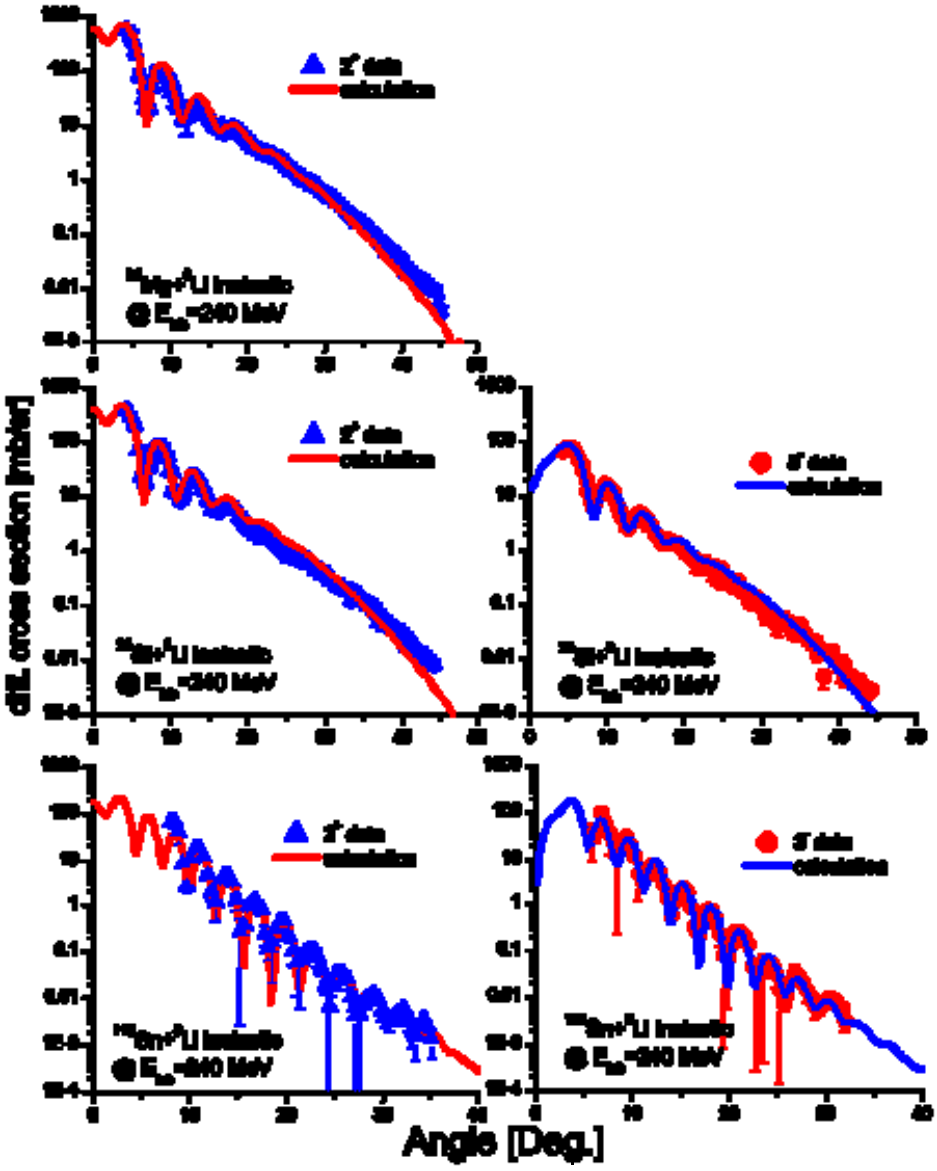

FIG. 5. The angular distributions of ^{6}Li inelastic scattering to the low-lying excited states of ^{24}Mg, ^{28}Si and ^{116}Sn

During the calculations, the transfer potentials to low-lying excited states [5, 7] are taken into account, thus the reduced transition possibilities, namely the B(E2) and B(E3) values, are deduced. The procedure of extracting the B(EL) value is described in Refs. [5,7,8]. Here, we obtained that B(E2) =0.0451 for 2^+ state of ^{24}Mg (E*=1.369MeV), B(E2) =0.0317 for 2^+ state of ^{28}Si (E*=1.779MeV), B(E3)=0.00305 for 3^- state of ^{28}Si (E*=6.888MeV), B(E2) =2.30 for 2^+ state of ^{116}Sn (E*=1.29MeV), and B(E3)=1.28 for 3^- state of ^{116}Sn (E*=2.27MeV). The results for other 4 nuclei are still on studying.

[1] C. Cockrell *et al.*, Phys. Rev. C **86**, 034325 (2012).

[2] A.A. Korsheninnikov *et al.*, Nucl. Phys. **A617**, 45 (1997).

[3] Y. Xu *et al.*, Astron. Astrophys. **549**, A106 (2013), and S. Goriely, private communication

[4] A.V. Dobrovolsky *et al.*, Nucl. Phys. **A766**, 1 (2006).

[5] X. Chen *et al.*, Phys. Rev. C **76**, 054606 (2007).

[6] X. Chen *et al.*, Phys. Rev. C **80**, 014312 (2009).

[7] X. Chen et al., Phys. Rev. C **79**, 024320 (2009).

[8] H.L. Clark *et al.*, Phys. Rev. C **57**, 2887 (1998).

Superallowed beta decay

J. C. Hardy, I. S. Towner, V. E. Iacob, H. I. Park, L. Chen, V. Horvat, N. Nica,
M. Bencomo and R. E. Tribble

Superallowed $0^+ \rightarrow 0^+$ beta decay between T=1 analogue states has been a subject of continuous and often intense study for five decades. The *ft* values of such transitions are nearly independent of nuclear-structure ambiguities and depend uniquely on the vector part of the weak interaction. Their measurement gives us access to clean tests of some of the fundamental precepts of weak-interaction theory, and, over the years, this strong motivation has led to very high precision being achieved in both the experiments and the theory used to interpret them. We have a major program at the Cyclotron Institute to study superallowed beta decay.

To obtain the *ft* value for any transition, three quantities must be measured: the half life of the parent, the Q_{EC} value for the transition of interest, and the branching ratio for that transition. Our most recent complete survey of existing data on these superallowed decays, published in 2009 [1], provided a critical evaluation of all the experimental data and obtained final *ft* values from the averaged results, to which improved radiative and isospin-symmetry-breaking corrections [2] were applied in order to derive a final set of "corrected ft values", denoted $\mathcal{Ft}$ (see Fig. 1). One of the new features added at that time was that we calculated the radial-overlap correction, δ_{C2}, with Hartree-Fock radial wave functions as well as the Saxon-Woods wave functions we have used before. The differences in the results from these two methods are used as a measure of the systematic uncertainty to be applied to the theoretical corrections. These differences also offer the possibility that measured *ft* values with the highest precision could actually distinguish between the two methods and thereby reduce the systematic uncertainty.

With the updated world data and improved corrections the $\mathcal{Ft}$ values were seen to be completely consistent with one another, thus demonstrating the constancy of G_V to 1.3 parts in 10^4. Not only is this an important confirmation of the Conserved Vector Current (CVC) hypothesis but it sets the stage for using the average value of G_V to test a fundamental principle of the electroweak standard model: the unitarity of the Cabibbo-Kobayashi-Maskawa (CKM) matrix. The up-down quark mixing element of that matrix, V_{ud}, is given by $V_{ud} = G_V / G_F$, where G_F is the weak interaction constant for the purely leptonic muon decay. The value of V_{ud} is a key component of the most demanding test available for the unitarity of the CKM matrix, the sum of squares of its top-row elements [1]. As elaborated in our 2010 review article on the evaluation of V_{ud} [3], superallowed nuclear beta decays provide by far the most precise and reliable value for V_{ud} and, in fact, that element is also the most precisely known one in the CKM matrix – by an order of magnitude! Its current value [1,3,4] is 0.97425(22), a result that yields the most up-to-date CKM unitarity sum of 1.0008(56) [4], in full agreement with the standard-model expectation, and carrying the smallest uncertainty yet obtained.

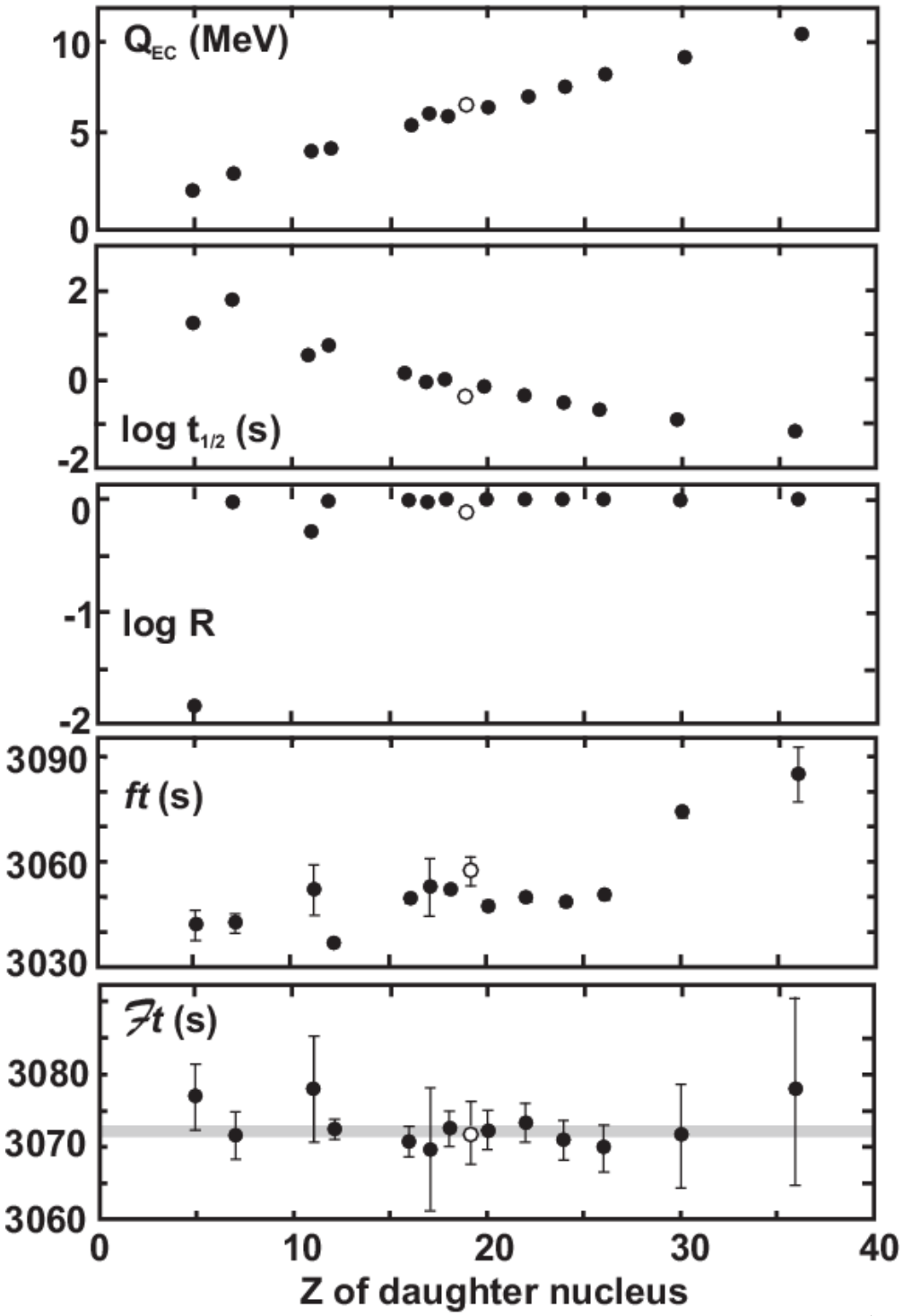

FIG. 1. Results from the most recent survey of 13 precisely measured superallowed $0^+ \rightarrow 0^+$ β transitions appear as solid black circles. The parents of these transitions, from left to right, are ^{10}C, ^{14}O, ^{22}Mg, ^{26}Al^m, ^{34}Cl, ^{34}Ar, ^{38}K^m, ^{42}Sc, ^{46}V, ^{50}Mn, ^{54}Co, ^{62}Ga and ^{74}Rb. The top three panels present the average of measured Q_{EC}, log $t_{1/2}$ and log R values for each transition. The bottom two panels give the corresponding *ft* and $\mathcal{F}t$ values. The shaded horizontal line in the bottom panel represents the overall average $\mathcal{F}t$ value for all transitions. All error bars are shown: in the cases where none are visible, they are smaller than the data point. Recent results for ^{38}Ca are shown as open circles.

This result is not only a significant verification of the standard model but the uncertainty quoted on the sum provides a tight limit on any possible new physics beyond the standard model, such as right-hand currents, extra *Z* bosons or supersymmetric models. In short, superallowed $0^+ \rightarrow 0^+$ beta decay provides a high-profile application of nuclear-physics measurements to the study of fundamental symmetries, a subject of vital interest to both nuclear and particle physicists. Although much has already been achieved in this field by nuclear physicists, improvements are still possible. Reducing the uncertainty on the unitarity sum – and, with it, the scope for new physics – remains the primary goal of our research program.

Our approach follows from the observation [1,3,4] that the second largest contributor to the uncertainty in V_{ud} is the theoretical uncertainty in the nuclear-structure-dependent corrections, δ_{NS} and δ_C, used in the derivation of the $\mathcal{Ft}$ values. Though these corrections are only of order 1%, their effect is very significant: The bottom two panels of Fig. 1 show the result of applying δ_{NS} and δ_C (together with δ'_R, which is nearly independent of *Z*). Obviously they act very well to remove the considerable "scatter" in *ft* values apparent in the second panel from the bottom, replacing it with the consistent set of corrected $\mathcal{Ft}$ values appearing in the bottom panel. Since these corrections were determined [2] completely independently of the superallowed decay data, this consistency in $\mathcal{Ft}$ values is already a powerful validation of these calculated corrections, but obviously the remaining uncertainty still influences the final result for V_{ud}.

Even though the 2009 survey [1] included more than 145 individual measurements relating to 13 precisely known *ft* values, it is still possible for well selected experiments to make real improvements in the validation tests of the nuclear-structure-dependent correction terms. At TAMU we are currently focusing on adding to the *ft*-value list new superallowed transitions, selected from amongst those with *large* calculated corrections. If the *ft* values measured for cases with large calculated corrections also turn into corrected $\mathcal{Ft}$ values that are consistent with the others, then this must verify the calculations' reliability for the existing cases, which have smaller corrections. We are studying decays from $T_z = -1$ parent nuclei, which consistently have higher predicted structure-dependent correction terms than the well known $T_z = 0$ cases.

Of particular importance are the four $T_z = -1$ parent nuclei – ^{26}Si, ^{34}Ar, ^{38}Ca and ^{42}Ti – whose decays are mirrors to well-known superallowed decays from $T_z = 0$ parents. Specifically, the mirror-decay pairs are $^{26}\text{Si} \rightarrow ^{26}\text{Al}^m \rightarrow ^{26}\text{Mg}$, $^{34}\text{Ar} \rightarrow ^{34}\text{Cl} \rightarrow ^{34}\text{S}$, $^{38}\text{Ca} \rightarrow ^{38}\text{K}^m \rightarrow ^{38}\text{Ar}$ and $^{42}\text{Ti} \rightarrow ^{42}\text{Sc} \rightarrow ^{42}\text{Ca}$. Their importance stems from our observation that the ratio of mirror *ft* values for such cases is very sensitive to the model used to calculate the small isospin-symmetry-breaking corrections δ_{NS} and δ_C. The details are described elsewhere in this Progress Report [5]. Until very recently, none of the $T_z = -1$ parent decays was known precisely enough to provide a statistically significant constraint on the correction terms via the ratio of mirror *ft* values, but we are now well on our way to rectifying this situation.

After a long period of incremental upgrades to our experimental techniques, we have succeeded in pushing our precision in branching ratio measurements close to ±0.1%, our ultimate goal. This is crucial for the characterization of $T_z = -1$ parent decays, which – unlike $T_Z = 0$ decays – exhibit a number of strong Gamow-Teller branches that compete with the superallowed Fermi branch. A demonstration of our success in this endeavor is our very recent determination of the superallowed branching ratio for the

decay of ^{38}Ca ($t_{1/2}$ = 444 ms) to a precision of ±0.2%, where that precision was actually limited by counting statistics, not systematics. This experiment, the results of which were published recently in Physical Review Letters [6], is described briefly elsewhere in this report [7].

To our knowledge, this is the most precise direct branching-ratio measurement ever made for short-lived beta emitter. It also provides the first mirror pair of $0^+ \rightarrow 0^+$ superallowed emitters (^{38}Ca and ^{38}K^m) that is precise enough to distinguish meaningfully between the Saxon-Woods-based radial-overlap correction, δ_{C2}, and the one based on Hartree-Fock radial wave functions. It favors the former over the latter, but we must await results from the other mirror pairs before we can be confident of the verdict. We are now well embarked on the measurement of the remaining three accessible pairs. We have already made a measurement of the branching ratio for the superallowed decay of ^{34}Ar, the data from which are currently being analyzed [8]; we have had a successful test experiment on ^{42}Ti [9]; and we have a run to measure the branching ratio from ^{26}Si scheduled for August 2014

We are also endeavoring to improve our data acquisition techniques for half-life measurements by a variety of means, including a new TDC-based data-acquisition system, which allows us to determine half-lives by time-interval analysis [10], and a digital-pulse-analysis system for the signals from our 4p proportional gas counter. We have just completed an experiment to measure the half-life of another T_z = -1 superallowed emitter, ^{30}S, in which we have used three different methods for taking data from the proportional gas counter: our standard analog technique, the new TDC-based approach, and the digital-pulse-analysis system. The results will determine whether we can improve our half-life precision in future and, if so, by which path. It will also yield the first precise study of this previously neglected superallowed emitter.

[1] J.C. Hardy and I.S. Towner, Phys. Rev. C **79**, 055502 (2009).

[2] I.S. Towner and J.C. Hardy, Phys. Rev. C **77**, 025501 (2008).

[3] I.S. Towner and J.C. Hardy, Rep. Prog. Phys. **73**, 046301 (2010).

[4] J.C. Hardy and I.S. Towner, Ann. Phys. **525**, 443 (2013).

[5] I.S. Towner and J.C. Hardy, *Progress in Research,* Cyclotron Institute, Texas A&M University (2013-2014), p. III-10.

[6] H.I. Park, J.C. Hardy, V.E. Iacob, M. Bencomo, L. Chan, V. Horvat, N. Nica, B.T. Roeder, E. Simmons, R.E. Tribble and I.S. Towner, Phys. Rev. Lett. **112**, 102502 (2014).

[7] H.I. Park, J.C. Hardy, V.E. Iacob, M. Bencomo, L. Chan, V. Horvat, N. Nica, B.T. Roeder, E. Simmons, R.E. Tribble and I.S. Towner, *Progress in Research,* Cyclotron Institute, Texas A&M University (2013-2014), p. I-16.

[8] V.E. Iacob, J.C. Hardy, H.I. Park, M. Bencomo, L. Chan, V. Horvat, N. Nica, B.T. Roeder and I.S. Towner, *Progress in Research,* Cyclotron Institute, Texas A&M University (2013-2014), p. I-20.

[9] H.I. Park, L. Chan, J.C. Hardy, M. Bencomo, V. Horvat, V.E. Iacob, N. Nica, B.T. Roeder, A. Saastamoinen and R.E. Tribble, *Progress in Research,* Cyclotron Institute, Texas A&M University (2013-2014), p. I-23.

[10] V. Horvat and J.C. Hardy, *Progress in Research,* Cyclotron Institute, Texas A&M University (2013-2014), p. IV-22.

The β decay of ^{38}Ca: Sensitive test of isospin symmetry-breaking corrections from mirror superallowed $0^+ \rightarrow 0^+$ transitions

H. I. Park, J. C. Hardy, V. E. Iacob, M. Bencomo, L. Chen, V. Horvat, N. Nica, B. T. Roeder, E. Simmons, R. E. Tribble, and I. S. Towner

We have measured for the first time precise branching ratios for the β decay of ^{38}Ca (see Fig. 1), which includes a superallowed $0^+ \rightarrow 0^+$ branch not previously characterized. Our result sets a new benchmark for such measurements: ±0.35% systematic experimental uncertainty. With the corresponding Q_{EC} value and half-life [1] already known, the transition's *ft* value can now be determined to ±0.2%. This is the first addition to the set of well-known superallowed transitions in nearly a decade and, being from a T_Z = -1 parent nucleus, it provides the opportunity to make a high-precision comparison of the *ft* values from a pair of mirror superallowed decays, ^{38}Ca $\rightarrow ^{38}$K^m and ^{38}K$^m \rightarrow ^{38}$Ar. The ratio of mirror *ft* values is very sensitive to the model used to calculate the small isospin symmetry-breaking corrections that are required to extract V_{ud} from the data. Since the uncertainty in these corrections contributes significantly to the uncertainty both on V_{ud} and on the unitarity sum, experimental constraints imposed by mirror *ft*-value ratios can serve to reduce those uncertainties by up to 10%.

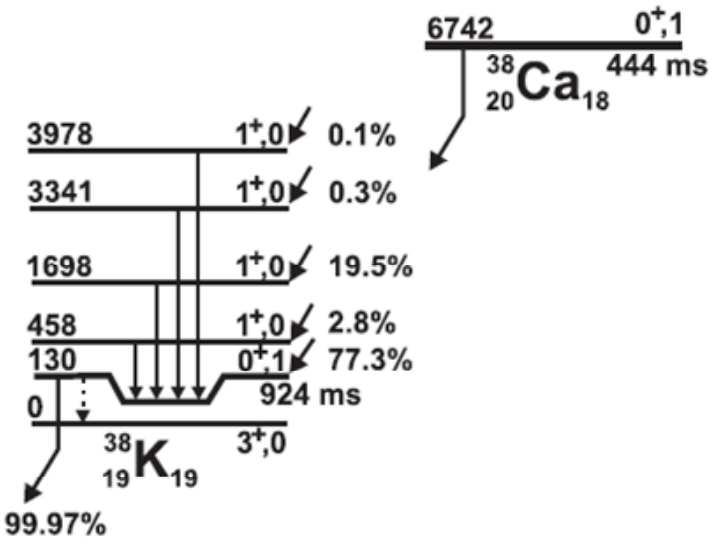

FIG. 1. Beta-decay scheme of ^{38}Ca showing the most intense branches, For each level, its (J^π,*T*) is given as well as its energy expressed in keV relative to the ^{38}K ground state. Branching percentages come from this measurement.

We produced 444-ms ^{38}Ca using a 30*A*-MeV ^{39}K primary beam from the K500 superconducting cyclotron to initiate the ^{1}H(^{39}K, 2n)^{38}Ca reaction on a LN_2-cooled hydrogen gas target. The fully stripped

ejectiles were separated by their charge-to-mass ratio in the MARS recoil separator, producing a ^{38}Ca beam at the focal plane, where the beam composition was monitored by the periodic insertion of a position-sensitive silicon detector. With the detector removed, the ^{38}Ca beam exited the vacuum system through a 50-μm-thick Kapton window, passed successively through a 0.3-mm-thick BC-404 scintillator and a stack of aluminum degraders, finally stopping in the 76-μm-thick aluminized Mylar tape of our fast tape-transport system. The combination of *q/m* selectivity in MARS and range separation in the degraders provided implanted samples that were 99.7% pure ^{38}Ca, with the main surviving trace contaminants being ^{34}Ar, ^{35}Ar and ^{36}K. Approximately 24,000 atoms/s of ^{38}Ca were implanted in the tape.

During the measurement, each ^{38}Ca sample was accumulated in the tape for 1.6 s, with its rate of accumulation being measured by the scintillation detector located ahead of the degrader stack. Then the beam was turned off and the tape moved the sample in 200 ms to a shielded counting location 90 cm away, where data were collected for 1.54 s, after which the cycle was repeated. This computer-controlled sequence was repeated continuously for nearly 5 days.

At the counting location, the sample was positioned precisely between a 1-mm-thick BC-404 scintillator to detect β^+ particles, and our specially calibrated 70% HPGe detector for γ rays. The former was located 3 mm from one side of the tape, while the latter was 15.1 cm away on the other side. We saved β-γ coincidences event-by-event, recording the energy of each β and γ ray, the time difference between their arrival, and the time that the event itself occurred after the beginning of the counting period. For each cycle we also recorded the rate of accumulation of ^{38}Ca ions in the tape as a function of time, the total number of β- and γ-ray singles, and the output from a laser ranging device that recorded the distance

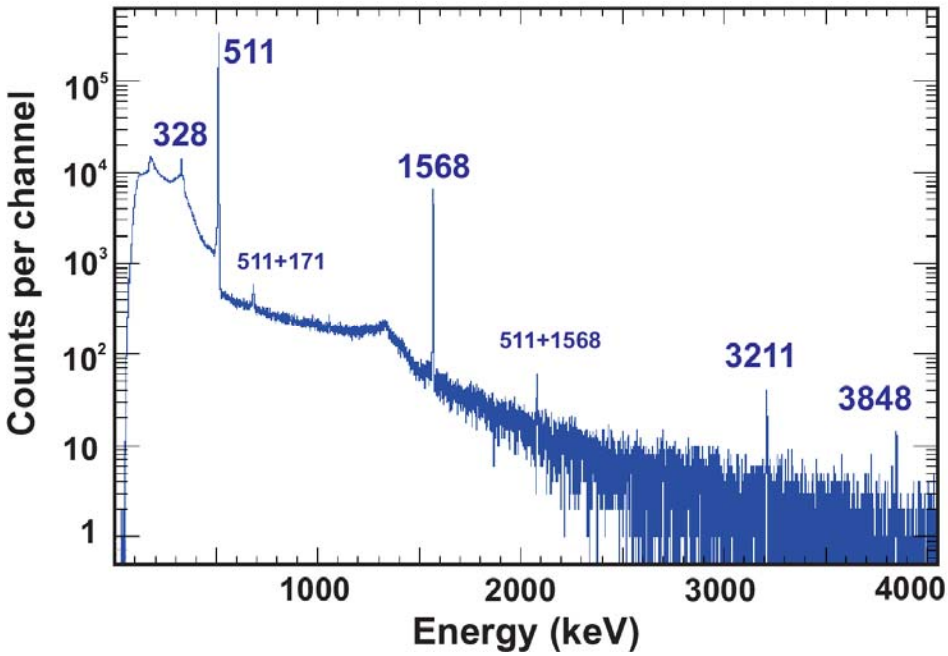

FIG. 2. Spectrum of γ rays observed in prompt coincidence with positrons from the decay of ^{38}Ca. The small peak labeled ``511+171" is caused by positron annihilation, from which one 511-keV γ ray sums with a back-scattered γ ray from the second 511-keV γ ray. The ``511+1568" peak is the result of coincidence summing between a 1568-keV γ ray and annihilation radiation from the positron decay that preceded it.

of the stopped tape from the HPGe detector. From cycle to cycle that distance could change by a few tenths of a millimeter, enough to require a small adjustment to the HPGe detector efficiency. Our recorded spectrum of β-coincident γ rays appears in Fig. 2.

It can be seen from Fig. 1 that all β transitions from ^{38}Ca populate prompt γ-emitting levels in ^{38}K, except for the superallowed branch. To obtain the superallowed branching ratio, our approach is first to determine the number of 1568-keV γ rays relative to the total number of positrons emitted from ^{38}Ca. This establishes the β-branching ratio to the 1^+ state in ^{38}K at 1698 keV. Next, from the relative intensities of all the other (weaker) observed γ-ray peaks, we determine the total Gamow-Teller β-branching to all 1^+ states. Finally, by subtracting this total from 100%, we arrive at the branching ratio for the superallowed transition.

More specifically, if the γ ray de-exciting state *i* in ^{38}K is denoted by γ_i, then the β-branching ratio, R_i, for the β-transition populating that state can be written:

$$R_i = \frac{N_{\beta\gamma i}}{N_\beta \varepsilon_{\gamma i}} \frac{\varepsilon_\beta}{\varepsilon_{\beta i}} \qquad (1)$$

where $N_{\beta\gamma i}$ is the total number of β-γ coincidences in the γ_i peak; N_β is the total number of beta singles corresponding to ^{38}Ca β decay; $\varepsilon_{\gamma i}$ is the efficiency of the HPGe detector for detecting γ_i; $\varepsilon_{\beta i}$ is the efficiency of the plastic scintillator for detecting the betas that populate state *i*; and ε_β is the average efficiency for detecting the betas from all ^{38}Ca transitions.

After correction for dead time, pile-up and other small factors [2], we found the branching ratio for the β transition to the 1698-keV state in ^{38}K to be 0.1949(13). Then, by analyzing the full γ-ray spectrum of Fig.2 and making provision for weak $1^+ \rightarrow 1^+$ γ transitions, we obtained the total of all Gamow-Teller branches relative to this transition. Our final result for the total Gamow-Teller branching from ^{38}Ca is 0.2272(16), and this leads to a superallowed branching ratio of $0.7728 \pm 0.0014_{stat} \pm 0.0009_{syst}$ or, with the uncertainties combined in quadrature, 0.7728±0.0016.

The half-life of ^{38}Ca is 443.77(35) ms [3,4] and the Q_{EC} value for its superallowed branch is 6612.12(7) keV [5]. Taking these results with our new value for the branching ratio and correcting for electron capture, we arrive at an *ft* value for the ^{38}Ca superallowed branch of ft^a = 3062.3(68) s. The *ft* value for the mirror transition from ^{38}K^m is ft^b = 3051.5(9) s, a value that comes from our 2009 survey [1] updated for a more recent Q_{EC} measurement reported by Eronen *et al.* [6]. The ratio of the two, ft^a/ft^b = 1.0036(22), appears in Fig. 3, where it can be compared with the calculated results, which appears in Table I of the Progress Report by I.S. Towner and J.C. Hardy [7].

Although our experimental result favors the Woods-Saxon (WS) calculation of δ_C (see [7]), it is not yet definitive. Nevertheless, it clearly points the way to a potential reduction of the uncertainty on V_{ud} through the elimination of alternatives to the WS-calculated corrections currently used. The lack of precise branching-ratio measurements has so far prevented the T_Z = -1 decays of ^{26}Si, ^{34}Ar, ^{38}Ca and ^{42}Ti from being fully characterized with high precision. Now that we have demonstrated the capability to make such a measurement on ^{38}Ca, the other three cases should not be far behind. Together, if all four

convey a consistent message, they can have a major impact by sensitively discriminating among the models used to calculate the isospin-symmetry-breaking corrections.

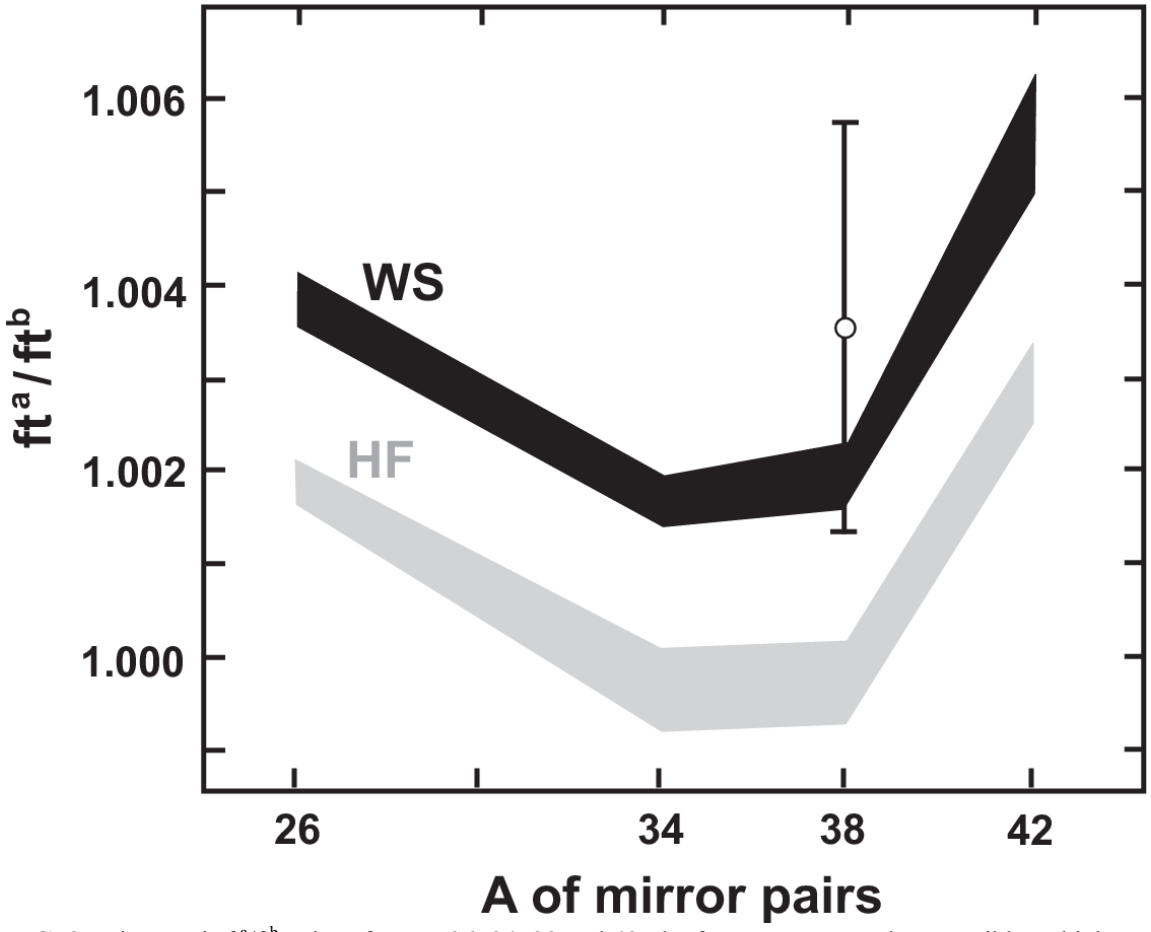

FIG. 3. Mirror-pair ft^a/ft^b values for A = 26, 34, 38 and 42, the four cases currently accessible to high-precision experiment. The black and grey bands connect calculated results that utilize Woods-Saxon (WS) and Hartree-Fock (HF) radial wave functions, respectively (see [7]). Our measured result for the A=38 mirror pair is shown as the open circle with error bars.

[1] J.C. Hardy and I.S. Towner, Phys. Rev. C **79**, 055502 (2009).

[2] H.I. Park, J.C. Hardy, V.E. Iacob, M. Bencomo, L. Chen, V. Horvat, N. Nica, B.T. Roeder, E. Simmons, R.E. Tribble and I.S. Towner, Phys. Rev. Lett. **112**, 102502 (2014).

[3] B. Blank *et al.*, Eur. Phys. J. A **44**, 363 (2010).

[4] H.I. Park *et al.*, Phys. Rev. C **84**, 065502 (2011).

[5] T. Eronen *et al.*, Phys. Rev. C **83**, 055501 (2011).

[6] T. Eronen *et al.*, Phys. Rev. Lett. **103**, 252501 (2009).

[7] I.S. Towner and J.C. Hardy, *Progress in Research,* Cyclotron Institute, Texas A&M University (2013-2014), p. III-10.

The superallowed β-decay branching ratio in the decay of ^{34}Ar

V. E. Iacob, J. C. Hardy, H. I. Park, M. Bencomo, L. Chen, V. Horvat, N. Nica, and B. T. Roeder

Precise *ft* values for superallowed $0^+ \rightarrow 0^+$ β^+-decays contribute to the most demanding unitarity test of the Cabibbo-Kobayashi-Maskawa matrix. The decay from a $T_z = -1$ nucleus like ^{34}Ar is particularly valuable because it completes a mirror pair of superallowed decays and can thus constrain the isospin symmetry-breaking corrections that must be applied to the measured *ft*-values [1,2] before they can be used to extract V_{ud} for the unitarity test. The experimental *ft* values require three ingredients: the Q_{EC}-value of the decay, the half-life of the parent, and the branching ratio of the superallowed branch. If an *ft* value is to be relevant for the unitarity test or a mirror comparison, it needs to be determined to a precision of ~0.1% or better. For the case of ^{34}Ar, its only branching-ratio measurement was made four decades ago [3] and does not currently meet this criterion. Based on the significant improvement to the performance of our acquisition system for the measurement of branching ratios [4] we have repeated the measurement of the ^{34}Ar decay aiming at a precision exceeding 0.1%.

We produced a pure ^{34}Ar beam (>99%) at the exit of the MARS recoil separator using a 30*A* MeV ^{35}Cl beam from the K500 cyclotron to bombard a hydrogen gas target kept at a pressure of ~2 atm and at liquid-N_2 temperature. The ^{34}Ar beam was extracted into air, degraded and implanted in the center of the 75-μm-thick Mylar tape of our fast transport system. In repeated cycles, ^{34}Ar samples were collected for 2 s and then moved in 160 ms to the center of a well-shielded β-γ counting station, where β singles, γ singles (scaled only), and β-γ coincidences were recorded for 2 s. The β's were detected in a 1-mm-thick plastic scintillator, located 2.5 mm from one side of the tape. The γ's were detected in our precisely efficiency-calibrated HPGe detector located 151 mm away on the other side of the tape. The beam was checked daily for stability and purity to ensure maximum consistency in the acquired data.

More than 3 billion ^{34}Ar nuclei were implanted during a week-long experiment. A total of 22×10^6 β-γ coincidences (distributed over about 74×10^3 cycles) were recorded. Fig. 1 presents the spectrum of γ rays coincident with positrons from the decay of ^{34}Ar. Only γ rays associated to this decay are observed: full-energy γ-ray peaks at 461, 666, 2580 and 3129 keV; the annihilation peak at 511 keV and the single- and double-escape peaks for hard gammas.

As discussed in [4], we read the tape-to-HPGe distance with a laser sensor to a precision better than 0.1 mm. This distance is recorded for each cycle. The tape-to-HPGe is an important ingredient in the analysis of the experiment: A deviation of 0.1 mm from the nominal position translates in a change of 0.11% in the absolute detection efficiency of the HPGe detector. Fig. 2 presents the distribution of the distance as observed in this experiment. The histogram shows good consistency in the tape positioning, with a full-width-at-half-maximum of 0.4 mm (the central red region). Although the individual positions do not meet the accuracy requirement for the most precise superallowed beta decays, our knowledge of the exact value in each cycle overcomes this obstacle.

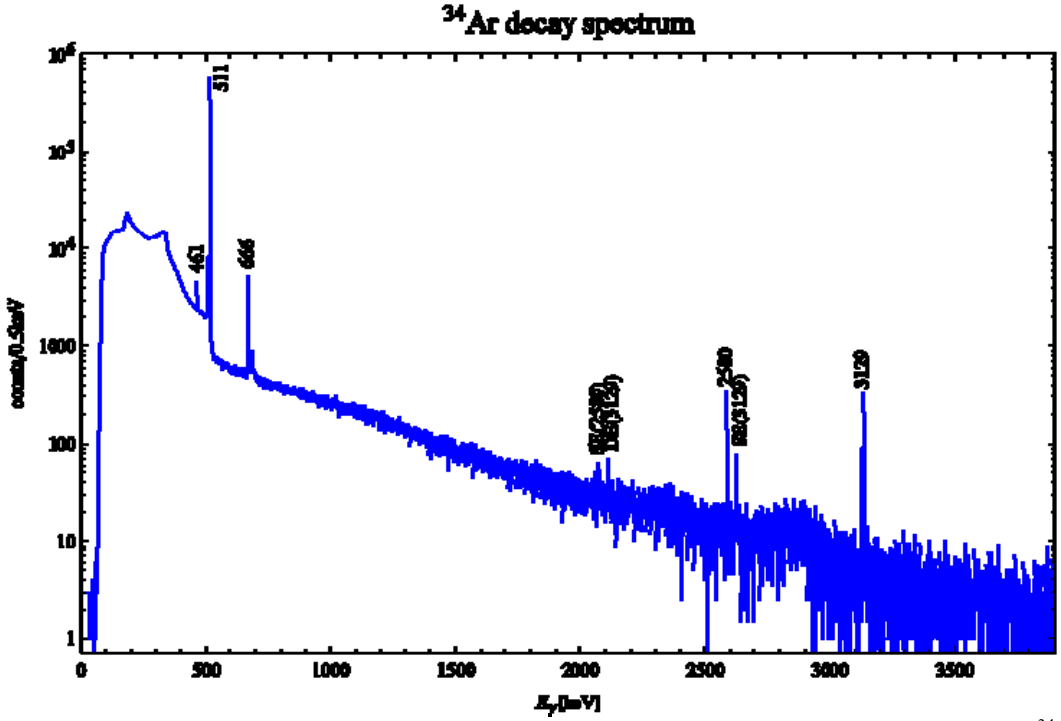

FIG. 1. Spectrum of γ rays observed in prompt coincidence with positrons from the decay of ^{34}Ar. The peaks are labeled with their energy and, in a few cases, their designation as single-escape (SE) or double-escape (DE) peaks. The structure just to the right of the 666-keV peak is the result of coincidence summing between one 511-keV γ ray from an annihilation pair with the back-scattered γ ray (171 keV) from the second 511-keV γ ray.

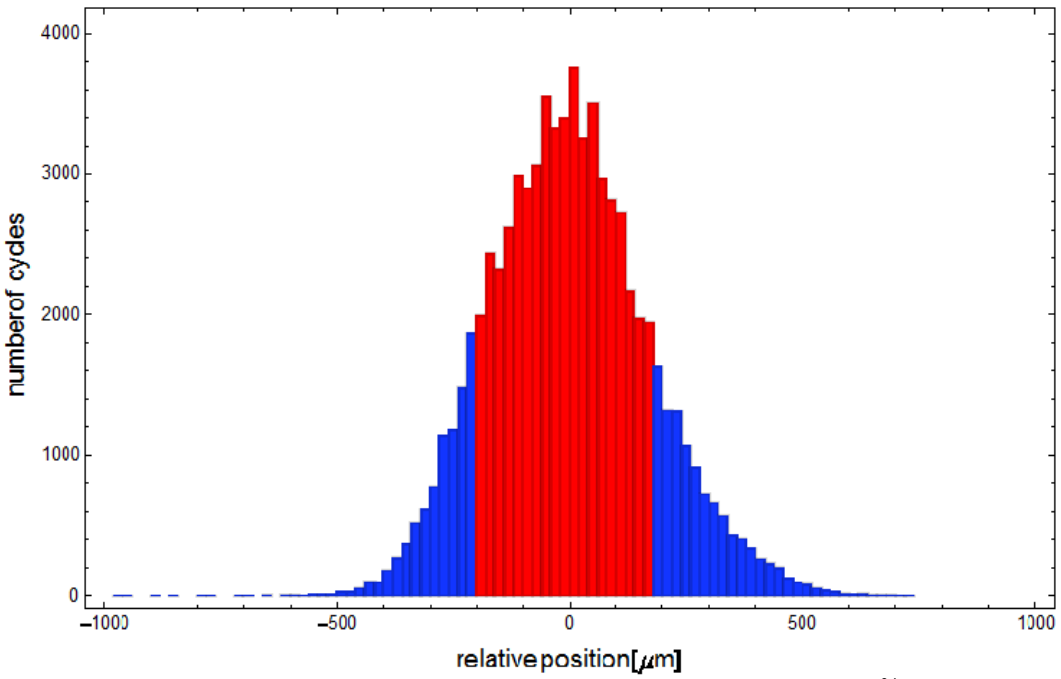

FIG. 2. Distribution of the tape-to-HPGe distance as recorded during the ^{34}Ar branching-ratio measurement. Zero on the position scale corresponds to the nominal distance of 151 mm. The FWHM of the distribution (in red) is less than 0.4 mm.

The experiment is still being analyzed but a very preliminary analysis yielded an *ft*-value consistent with the other superallowed emitters. The compete and detailed analysis is expected to produce a value with the accuracy and precision required to make a statistically-significant comparison with the mirror decay of ^{34}Cl, and from that to make a meaningful test of the isospin-symmetry-breaking corrections. The ultimate goal, of course, is to reduce the uncertainty on the CKM unitarity test.

[1] I.S. Towner and J.C. Hardy, *Progress in Research,* Cyclotron Institute, Texas A&M University (2013-2014), p. III-10.

[2] H.I. Park *et al.*, *Progress in Research,* Cyclotron Institute, Texas A&M University (2013-2014), p. I-16.

[3] J.C. Hardy, H. Schmeing, J.S. Geiger and R.L. Graham, Nucl. Phys **A223**, 157 (1974).

[4] V.E. Iacob, J.C. Hardy, and H.I. Park, *Progress in Research,* Cyclotron Institute, Texas A&M University (2011-2012), p. V-21; V.E. Iacob, H.I. Park, and J.C. Hardy, *Progress in Research,* Cyclotron Institute, Texas A&M University (2012-2013), p. IV-43.

Exploratory measurement of the ^{42}Ti half-life

H. I. Park, L. Chen, J. C. Hardy, M. Bencomo, V. Horvat, V. E. Iacob, N. Nica, B. T. Roeder, A. Saastamoinen, and R. E. Tribble

In our program to study superallowed beta decay, we are currently focused on completing the four mirror pairs with A ≤ 42 because they have the potential to distinguish clearly between competing calculations of the isospin-symmetry-breaking corrections required to extract V_{ud} from the experimental *ft* values [1,2]. What is required is precise measurements of the superallowed decays from the T_Z = -1 parent nuclei, ^{26}Si, ^{34}Ar, ^{38}Ca and ^{42}Ti. (The corresponding decays of ^{26}Al^m, ^{34}Cl, ^{38}K^m and ^{42}Sc are all well known.) We have recently published branching-ratio results for ^{38}Ca [3], are well advanced on ^{34}Ar [4] and plan a measurement on ^{26}Si in the summer of 2014. We report here our first exploratory measurement on ^{42}Ti ($t_{1/2}$ = 199 ms). To date, its branching ratio is known to ±2% and its half-life to ±0.2% [5], both being of insufficient precision to contribute meaningfully to the determination of V_{ud}.

For our study, we used our 4π proportional gas counter and digitizer-based data-acquisition system [6] to measure the half-life of ^{42}Ti. The advantages of this experimental set-up are that it has nearly 100% overall efficiency for the detection of decay positrons and it allows us to record the maximum information, including waveforms from the detector, for later off-line analysis.

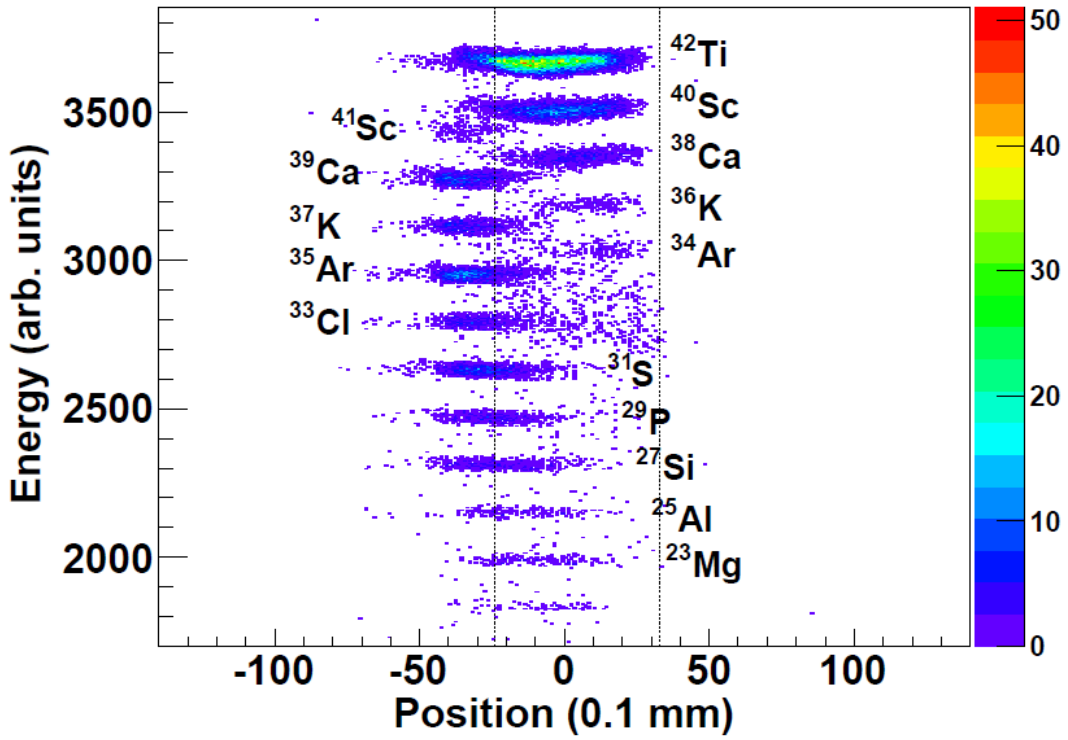

FIG. 1. The deposited energy versus position as obtained with the PSSD in the MARS focal plane when the reaction was ^{4}He(^{40}Ca, 2n)^{42}Ti. The spectrometer had already been optimized for ^{42}Ti production. Dashed lines show the position of the extraction slits in MARS, which we used during these measurements. Impurities are all identified.

We tried two reactions, ^{4}He(^{40}Ca, 2n)^{42}Ti and ^{3}He(^{40}Ca, n)^{42}Ti, in inverse kinematics at different primary ^{40}Ca beam energies to test the production of ^{42}Ti with MARS. A position-sensitive silicon detector (PSSD) was inserted at the MARS focal plane to identify the nearby reaction products and to optimize the separation of ^{42}Ti. From the results obtained with this detector, we concluded that the ^{4}He(^{40}Ca,2n)^{42}Ti reaction produces fewer strong impurities and is thus more suitable for future measurements of ^{42}Ti. This reaction can provide approximately 2000 particles/s of ^{42}Ti with 300 nA of ^{40}Ca at 32*A*-MeV. More details about the production of ^{42}Ti are described elsewhere in this report [7].

With this beam, the spectrum of products shown in Fig. 1 was recorded in the MARS focal plane once the spectrometer had been tuned for ^{42}Ti. With the extraction slits set as indicated in the figure, our primary concerns among the remaining impurities were ^{40}Sc ($t_{1/2}$ = 182 ms), ^{41}Sc ($t_{1/2}$ = 596 ms), ^{38}Ca ($t_{1/2}$ = 444 ms) and ^{39}Ca ($t_{1/2}$ = 860 ms). To investigate the effect of impurities on the decay of ^{42}Ti, we varied the thickness of the aluminum degrader in front of our collection tape from 1.00 to 4.00 mils in six steps, and measured the decay spectra at each.

Fig. 2 presents the calculated implantation profiles of ^{42}Ti and the identified impurities in and beyond the collection tape under two conditions, 1.00 mil of Al degrader (see Figure 2(a)) and 2.75 mils of Al degrader (see Figure 2(b)). It is evident that the former is expected to be nearly free of impurities while the latter should be overwhelmed by impurities. Decay data were analyzed for the three thinnest degrader settings – 1.00, 1.25 and 1.50 mils – and processed in the manner described in Ref [5]. Then a least-squares fit was performed for each case with a fit function that included, in addition to ^{42}Ti and its daughter ^{42}Sc, contributions from impurities as determined from the calculated implantation profiles. The ^{42}Ti half-life results from these three measurements were consistent with the result in Ref. [5], which was obtained with a trap system. This gives us confidence that by using a 1.00-mil degrader and running the left extraction slit at -1.5 mm instead of -2.5 mm (see Fig. 1) we should have a very nearly pure ^{42}Ti beam. The prospects for high-precision measurements of the half-life and branching ratio of ^{42}Ti appear very promising.

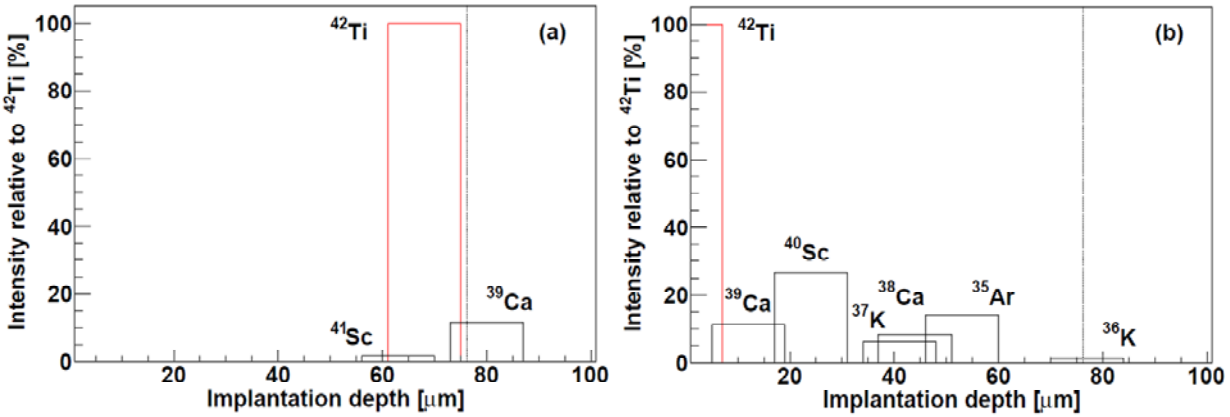

FIG. 2. The calculated implantation profiles of ^{42}Ti (red) and identified impurities (black) in and beyond the collection tape, under two different conditions: (a) 1.00 mil of Al degrader and (b) 2.75 mils of Al degrader. The calculations incorporate the measured momentum spread of MARS. In both cases the beams enter from the left, with the dashed line indicating the back of our 76-μm-thick collection tape. All ions left of the dashed line are collected in our sample; all others are not.

[1] I.S. Towner and J.C. Hardy, *Progress in Research*, Cyclotron Institute, Texas A&M University (2013-2014), p.III-10.
[2] J.C. Hardy *et al*., *Progress in Research*, Cyclotron Institute, Texas A&M University (2013-2014), p. I-11.
[3] H.I. Park *et al*., Phys. Rev. Lett. **112**, 102502 (2014).
[4] V.E. Iacob *et al.*, *Progress in Research*, Cyclotron Institute, Texas A&M University (2013-2014), p. I-20.
[5] T. Kurtukian Nieto *et al*.,Phys. Rev. C **80**, 035502 (2009).
[6] L. Chen *et al*., Nucl, Instrum. Methods Phys. Res. **A728** , 81 (2013).
[7] B.T. Roeder *et al.*, *Progress in Research*, Cyclotron Institute, Texas A&M University (2013-2014), p.I-48.

Tests of internal-conversion theory with precise y- and x-ray spectroscopy: The case of ^{127m}Te

N. Nica, K. Brandenburg, J. C. Hardy, V. E. Iacob, H. I. Park, and M. B. Trzhaskovskaya[1]
[1]*Petersburg Nuclear Physics Institute, Gatchina RU-188300, Russia*

Internal conversion is an important component of most nuclear decay schemes. In order to balance decay schemes correctly, one needs to know the internal conversion contribution to each transition as expressed by its internal conversion coefficient (ICC). Nevertheless, ICCs are only rarely measured; instead they are taken from tabulations. As a result, calculated ICCs are essential input to every decay scheme, except those for the lightest nuclei. Unfortunately, over the decades, tabulated ICC values have differed significantly from one calculation to another by a few percent. Although for many applications such differences can be tolerated, transitions used in critical calibrations require very precise and accurate ICC values, precision that has simply been impossible to guarantee at the one-percent level or below.

In order to correct for this deficiency one can only seek guidance from measured ICCs that have sufficient precision to distinguish among the various calculations. However, as recently as about a decade ago, when a survey of measured ICCs was made by Raman et al. [1], there were only five published ICC values with precision of the order of ±1%, not enough to make any definitive conclusion possible. At that time, one aspect of the ICC calculations remained a particular concern. The final-state electron wave function must be calculated in a field that adequately represents the remaining atom. But should that representation include the atomic vacancy created by the conversion process? Some calculations included it and some did not.

Thus the problem of measuring ICCs at the ±1% precision level became critical and, with our very precisely efficiency-calibrated HPGe detector [2], we found ourselves in a position to be able to address it. Consequently, over the past decade we have been measuring a series of ICCs [3,4] covering a wide range of atomic numbers, $50 \le Z \le 78$. So far, all these results have indicated that the atomic vacancy should be taken into account in the calculations. With $Z = 52$, the new case reported here – an 88.2-keV $M4$ transition in ^{127}Te – lies in the lower end of that range.

As can be seen from Fig. 1, the 88.2-keV $M4$ transition in ^{127}Te is an isolated transition that converts in the atomic K shell. For such a transition, the observation of a K x ray is a signal that an electron conversion has taken place; whereas a γ ray indicates that no conversion has taken place. If both x rays and γ rays are recorded in a measurement, then the value of α_K is given by

$$\alpha_K \omega_K = \frac{N_K}{N_\gamma} \cdot \frac{\varepsilon_\gamma}{\varepsilon_K} \quad , \qquad (1)$$

where ω_K is the fluorescence yield, which we take from Ref. [5]; N_K and N_γ are the respective peak areas of the K x rays and the γ ray; and ε_K and ε_γ are the corresponding detector efficiencies. As described in Ref. [2], the ε_γ for an 88.2-keV γ ray in our detector is known to ±0.15% relative precision; however a special investigation was required in order to get a precise value for ε_K at the ~28-keV energy of the Te K x rays.

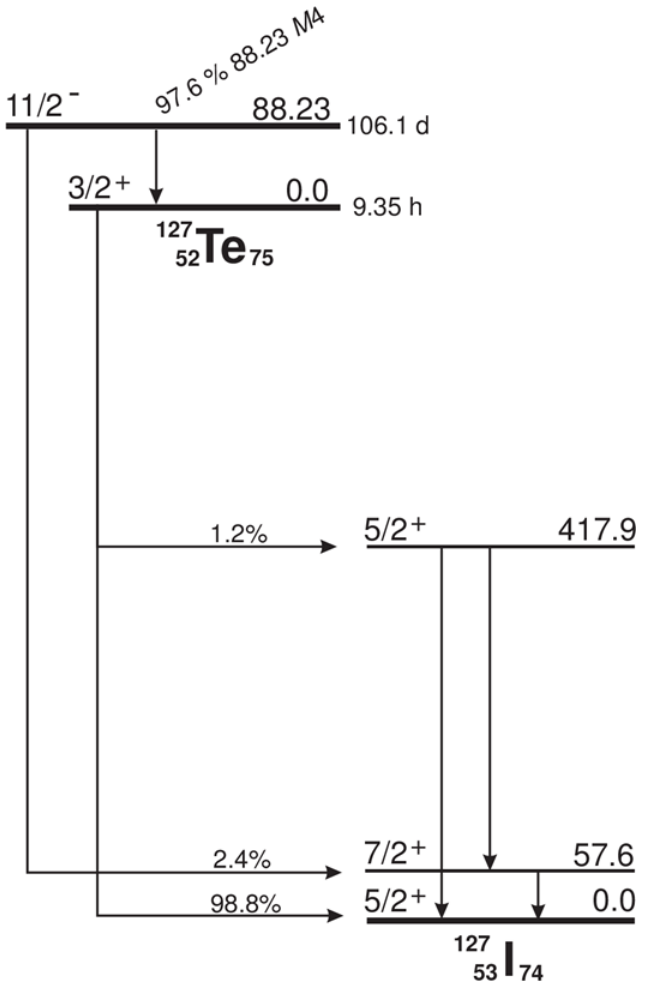

FIG. 1. Decay scheme of the ground and isomeric state in ^{127}Te. Very weak beta branches have been left out for clarity.

We produced a source of ^{127m}Te by neutron activation of ^{126}Te. Tellurium is an element with eight stable isotopes: ^{120}Te (0.09%), ^{122}Te (2.55%), ^{123}Te (0.89%), ^{124}Te (4.74%), ^{125}Te (7.07%), ^{126}Te (18.84%), ^{128}Te (31.74%), and ^{130}Te (34.08%). Even though ^{126}Te is one of the more abundant isotopes, we could not use natural tellurium for activation since the other tellurium isotopes produce radiation, particularly x rays, which interfere with those emitted by ^{127m}Te itself. For this reason we procured ^{126}Te, 98.8% enriched, from Trace Sciences International. Nevertheless, even the small concentrations of other tellurium isotopes that remained produced some interference in the K x ray region of the spectrum.

As delivered, our ^{126}Te material was in the form of metal powder with a grain size of 25±5 microns. We ground this powder until its grain size was less than 1 micron, as determined by our observing the grains with a microscope. A 12-micron tungsten wire placed in the visual field was used for reference. An amount of about 1.3 mg of this powder was spread uniformly in a 10-mm-diameter layer, about 2 microns thick, held between two thin Mylar films. This sample was activated for 24 h at the Texas A&M Nuclear Science Center TRIGA reactor, in a thermal neutron flux of 7.5×10^{12} neutron/(cm^{2}s). An identical "blank" sample (only Mylar with no ^{126}Te) was also activated together with the real sample, so as to establish the impurities that come from the activation of Mylar.

After the activation was completed the sources were kept for one month to allow the short-lived impurities to decay. This was especially necessary to remove the 2.7-d activity from ^{122}Sb, which is strongly present in activated Mylar. When we prepared the ^{127m}Te source for measurement with the HPGe detector we found that it was no longer flat, but was curled into a small rolled cylinder. Because the Mylar had become brittle after activation, the sample cracked as we unrolled it and about one quarter of the tellurium powder was lost. The partially unrolled source was then sealed between two additional thin Mylar foils. After this repair the source was twice as thick as the unbroken initial one. The extra thickness was accounted for when we later calculated the relative attenuation of the K x rays and γ rays in the sample.

The repaired source was placed at our standard distance of 151 mm from the face of our well-calibrated HPGe detector and a spectrum was recorded continuously for about one month. A 24-h spectrum was also acquired from the blank Mylar source. The only remaining impurity we observed coming from Mylar was ^{124}Sb, which β^--decays to ^{124}Te and, through subsequent internally-converted transitions, leads to the emission of Te x rays. These had to be corrected for in our analysis of the ^{127m}Te decay.

As shown in Fig. 1, the 88.2-keV, 106.1-d metastable state in ^{127}Te decays 97.6% by the *M*4 transition we are interested in here. The remaining 2.4% of the state's decay is via β^--decay to ^{127}I. Furthermore, the ^{127}Te, 9.4-h ground state, which is populated by the *M*4 transition, also decays by β^- to ^{127}I. Both these decay branches produce, through subsequent internally-converted transitions in ^{127}I, iodine K x rays, which overlap the tellurium x rays of interest. The contributions that these two decays made to the tellurium x-ray energy region were: 3.5(6)% from the metastable state decay and 0.226(15)% from the ground-state decay. The other sources of impurity contributing to the same energy region were: ^{125m}Te 2.63(6)%, ^{129m}Te 0.309(12)%, ^{129}Te 0.12(5)%, ^{123m}Te 0.104(3)%, ^{131}I 0.0374(9)%, ^{121}Te 0.0171(12)%, ^{124}Sb 0.0144(3)% and ^{110m}Ag 0.000487(11)%. Thus, the total contribution to the K x-ray energy region from activities other than the *M*4 decay of ^{127m}Te amounted to about 7%. A small 0.081(3)% impurity (coming from the 88.5-keV γ ray from ^{123m}Te) affected the 88.2-keV γ ray.

Some of the photons from a radioactive source scatter from nearby materials - including air - in the vicinity of the detector setup and, entering the detector, they form a continuum in the energy spectrum extending to lower energy from the peak created by unscattered photons. For photons above ~50 keV this continuum is rather flat and extends to energies well below the corresponding peak so, by extrapolation, its contribution to the area of the peak can easily be determined and removed. However, for peaks with energies as low as 27.4 keV and 31.1 keV, the energies of the tellurium K_α and K_β x rays respectively, the

continuum is more like a shelf that extends only 2-3 keV below the peak energy. At our energy resolution of ~1 keV in this region, an important part of the continuum gets "hidden" in, and potentially counted together with, the peak itself. The number of counts in the "hidden" continuum is very dependent not only on the source-detector geometry, but also on the details of its neighborhood. For this reason it is impossible to define a universal efficiency calibration with useful precision below ~50 keV. Rather, one must examine each geometry as a special case, which must be calibrated based on its specific properties.

For our previously measured α_K case in ^{119m}Sn [4] we followed two different approaches to this part of the analysis. In the first, described fully in our paper on ^{134}Cs and ^{137}Ba [3], we employed Monte Carlo calculations with the CYLTRAN code - the same code used in our calibration procedures [2] - to simulate the scattering "shelf"; then we scaled up the result to match the small component of the shelf visible in the data; and finally used that scaled-up result to determine the component of the shelf contained within the peak.

Our second approach in Ref. [4] was to measure a calibration source, ^{109}Cd, which decays by electron capture to ^{109}Ag followed by the emission of a unique 88.0-keV M4 γ transition. The K x rays of silver, following both the electron capture decay and the electron conversion of the 88.0-keV transition, form prominent x-ray groups situated at 22.1 keV (K_α) and 25.0 keV (K_β). The K x-rays together with the 88.0 keV γ ray can be used with a formula similar to eq. (1) to deduce ε_K at silver K x-ray energies if we use calculated α_K values for the 88.0-keV transition in ^{109}Ag. By taking the mean value of calculated 'vacancy' and 'no vacancy' α_K values with an uncertainty encompassing both, we obtain an α_K value that is independent of the treatment of the atomic vacancy. Then by a short interpolation from silver K x-ray energies to tellurium K x-ray energies, we can arrive at ε_K values for tellurium with a total uncertainty of about ±1%.

For ^{119m}Sn, the result obtained by this method was in very good agreement (within 0.3%) with the CYLTRAN-based value, giving us confidence in this methodology to correct for scattering effects. We have used the same procedure in the case of ^{127m}Te.

The preliminary result we report here for the 88.2-keV, *M*4 transition from ^{127m}Te is $\alpha_K = 489(7)$ which compares well with the with the 'hole' calculation in the "frozen orbital" approximation (486.4), and disagrees with the 'no hole' calculation (468.6). Our new result confirms and strengthens our conclusion that the atomic vacancy created by the internal conversion process must be taken into account when calculating ICCs.

[1] S. Raman *et al.*, Phys. Rev. C **66**, 044312 (2002).

[2] J.C. Hardy *et al.*, Appl. Radiat. Isot. **56**, 65 (2002) ; R.G. Helmer *et al.*, Nucl. Instrum. Methods Phys. Res. **A511**, 360 (2003); R.G. Helmer *et al.*, Appl. Radiat. Isot. **60**, 173 (2004).

[3] N. Nica *et al.*, Phys. Rev. C **70**, 054305 (2004); Phys. Rev. C **71**, 054320 (2005); N. Nica *et al.*, Phys. Rev. C **75**, 024308 (2007); Phys. Rev. C **77**, 034306 (2008) ; Phys. Rev. C **80**, 064314 (2009).

[4] N. Nica *et al.*, Phys. Rev. C **89**, 014303 (2014); J.C. Hardy *et al.*, Appl. Radiat. Isot. 87, **87** (2014).

[5] E. Schönfeld and H. Janssen, Nucl. Instrum. Methods Phys. Res. **A369,** 527 (1996).

United States nuclear structure data program (USNDP) and evaluated nudear structure data file (ENSDF) at Texas A&M University

N. Nica,[1] and J. C. Hardy

[1] *Under contract with Brookhaven National Laboratory*

Since 2005 we have been an important partner in the nationwide United States Nuclear Data Program (USNDP), which is part of the Nuclear Structure and Decay Data (NSDD) international nuclear data evaluation network. USNDP is in fact the backbone of the NSDD network, making the greatest effort in completion of the goals of the nuclear-structure data-evaluation communities. Nuclear data evaluation is a national-interest activity financed by DOE, through which relevant nuclear-science results in virtually all world publications are retrieved and put together in a large Evaluated Nuclear Structure Data File (ENSDF) database according to *general polices,* a set of rules that make possible a standard approach through which the data are uniformly evaluated.

This activity is carried by a relatively small group of professionals located mostly in national institutes but also hosted by a few universities. The nuclear data network is the nodal point for the wide dissemination of nuclear knowledge to many users, from those in basic science to those engaged in commercial applications in American and international businesses. The output is published in the Nuclear Data Sheets, an Elsevier publication, and also is disseminated by different on-line databases, which can be retrieved at the NNDC site (http://www.nndc.bnl.gov), IAEA Vienna's site (http://www-nds.iaea.org) and several other locations.

For nine years now at Texas A&M we have covered mass chains from essentially all the regions of the periodic table. Up to the past year we have published in Nuclear Data Sheets the superheavy A=252 mass chain [1]; the very data-rich mid-mass chains, A=140 [2], A=147 [3] and A=148 [4]; the relatively lighter chains, A=97 [5] and A=84 [6]; and, in collaboration with B. Singh and a group of authors from McMaster University, Canada, we also published the A=77 [7], A=37 [8], A=36 [9], and A=34 [10] chains. Another mid-mass mass chain, A=141, was also completed and is now in the final correction process after peer review. Since nuclear-data evaluation depends critically on the experience of the evaluator, with a veteran evaluator typically completing only a couple of mass chains per year, coverage of such a wide range of A chains in a short time at a contracted effort of 0.67 FTE per year is a considerable accomplishment.

During the past year we covered another mass chain, A=158, a report of which has been submitted and pre-reviewed. We have also started the evaluation of A=157, by considering all world publications after January 2004, the cut-off date of the previous full evaluation of this mass chain. The chain includes Nd, Pm, Sm, Eu, Gd, Tb, Dy, Ho, Er, Tm, Yb, Lu, Hf, Ta, and W, a total of 15 isobars. More than 130 relevant papers have been published during this interval. This work is in progress.

[1] N. Nica, Nucl. Data Sheets **106,** 813 (2005).
[2] N. Nica, Nucl. Data Sheets **108,** 1287 (2007).
[3] N.Nica, Nucl. Data Sheets **110,** 749 (2009).

[4] N. Nica, Nucl. Data Sheets **117,** 1 (2014).
[5] N. Nica, Nucl. Data Sheets **111,** 525 (2010).
[6] D. Abriola *et al*., Nucl. Data Sheets **110,** 2815 (2009).
[7] B. Singh, N. Nica, Nucl. Data Sheets **113,** 1115 (2012).
[8] J. Cameron, J. Chen, B. Singh, and N. Nica, Nucl. Data Sheets **113,** 365 (2012).
[9] N. Nica, J. Cameron, and B. Singh, Nucl. Data Sheets **113,** 1 (2012).
[10] N. Nica and B. Singh, Nucl. Data Sheets **113,** 1563 (2012).

The half-life of ^{27}P

E. Simmons, H. I. Park, J. C. Hardy, V. E. Iacob, R. Chyzh, M. Dag, T. Davinson,[1] D. Doherty,[1] M. McCleskey, R. G. Pizzone,[2] B. Roeder, A. Spiridon, L. Trache, R. E. Tribble, and J. Wallace[1]

[1]*School of Physics, University of Edinburgh, Edinburgh, United Kingdom*

[2]*INFN-Laboratori Nazionali del Sud, Catania, Italy*

The motivation to study the lifetime of ^{27}P arose from an experiment done earlier, the β-delayed proton and gamma study of ^{27}P, which led to the observation of previously unobserved beta-delayed gamma rays and levels in the ^{27}Si daughter. In order to produce useful log *ft* calculations for these new beta transitions, a value for the ^{27}P half-life is required that is more precise than the current value of 260 (80) ms [1], which is uncertain to ±30%. Ours was a quick experiment, without sufficient statistics for a true 0.1% precision result of the type normally done with this experimental setup. However, we acquired enough data to greatly improve the current half-life value.

A primary beam of ^{28}Si at 40 MeV/u from the K500 superconducting cyclotron at TAMU impinged upon a hydrogen gas target kept at liquid nitrogen temperature (77 K) and a pressure of 2 atm. The desired ^{27}P was then separated out with the MARS spectrometer, producing a beam at the focal plane with a rate of 7.63 evts/nC (191pps) and about 93 % purity. Fig. 1 shows the optimal production results achieved with the coffin slits at ±1.0 cm (a momentum spread of about ±0.7%).

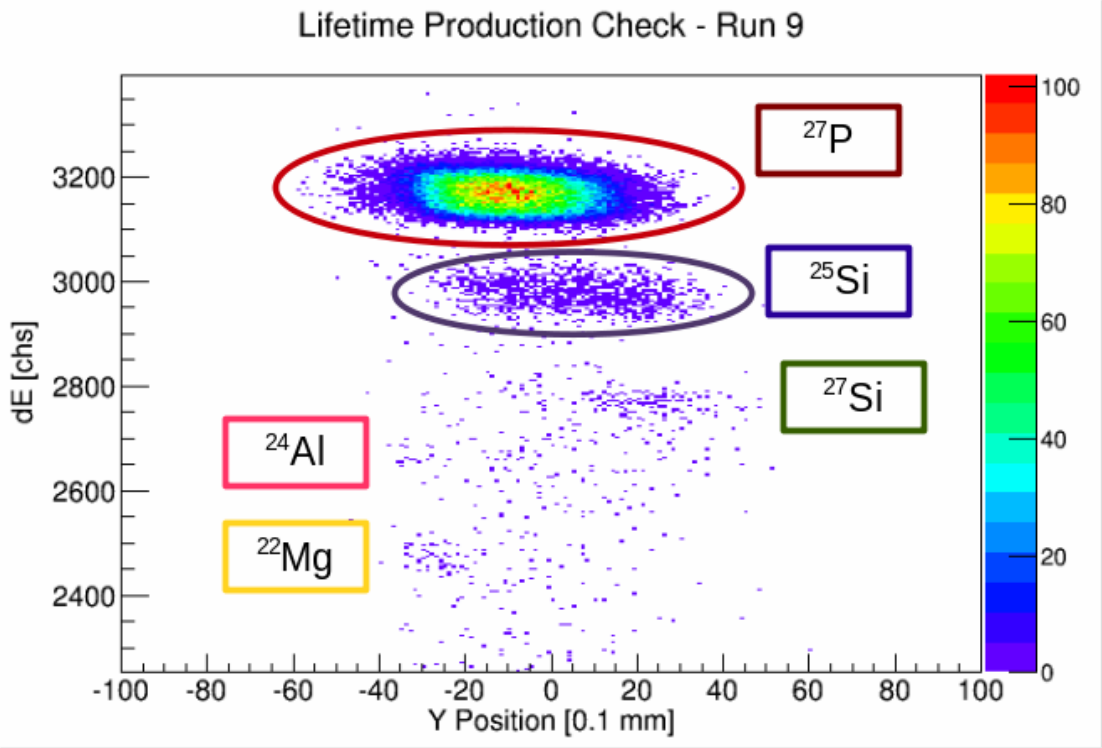

FIG. 1. Production check done with a position-sensitive silicon detector at the focal plane of MARS, recorded at the end of the lifetime experiment.

The measurement was done using the Precision On-Line Decay Facility, which is located at the end of the MARS beam line [2, 3]. A 50.8-μm-thick Kapton widow allowed the separated beam to pass out of the chamber, into air and through a 300 μm BC-404 plastic scintillator (to count the heavy ions), through a 17.25 mil Al degrader and one "dummy" tape (76.2 μm aluminized Mylar) before being implanted into the movable 76.2-μm aluminized Mylar tape. After a collection time of 0.52 sec, the beam was turned off and the tape was quickly moved (normally in 68 ms) to a position between two halves of a 4π proportional gas counter, where the β-particles were detected and recorded during a 3 second time period. This collect-move-record cycle was repeated until sufficient statistics had been accumulated.

Fig. 2 shows the setup at the back end of MARS. Note that the gas counter was moved as close as possible to the exit window to accommodate the short half-life involved in this study; this was also the reason for using a short continuous loop of tape instead of the usual reel-to-reel configuration. In separate runs, the gas counter was operated at three different biases (2600, 2700 and 2800 V), which were all within the detector's proportional region, and with three different discriminator voltages (150, 200 and 250 mV). These parameter changes are routinely done with this equipment to test that there is no systematic dependence on these parameters.

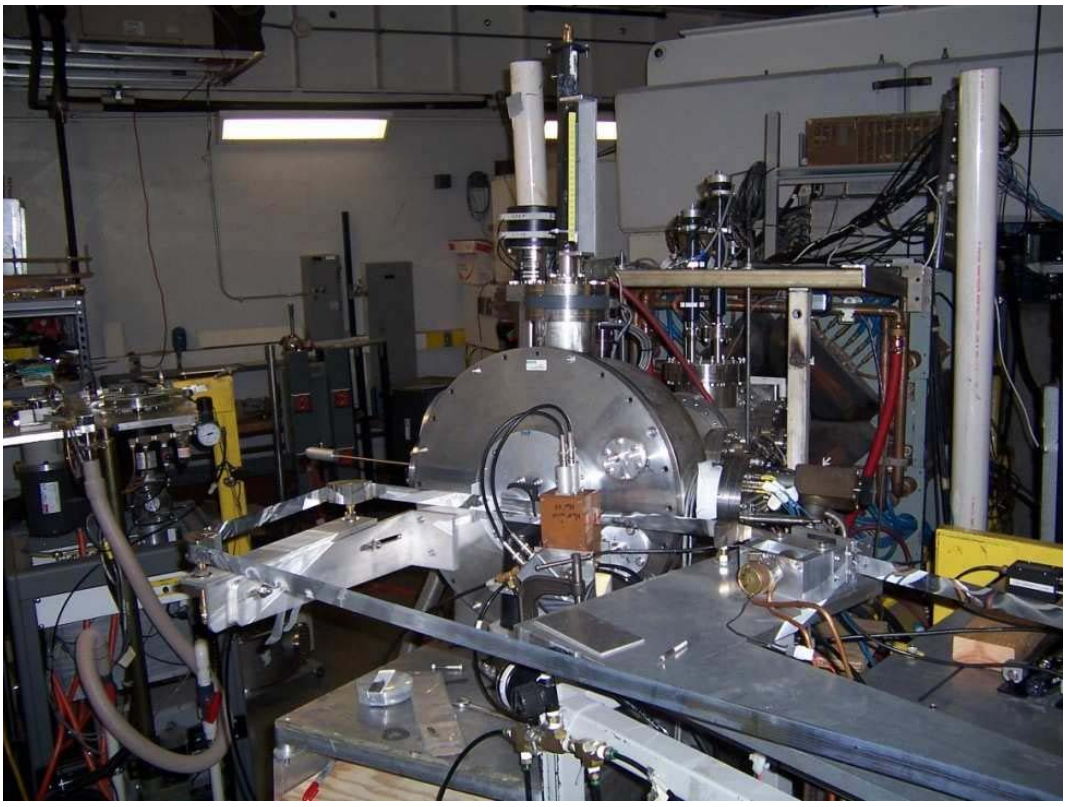

FIG. 2. The tape transport system setup at the back end of MARS.

SRIM ion-range calculations [4] together with the beam composition measured at the focal plane of MARS (see Fig. 1) were used to determine the composition of the sample actually collected on the tape. Of the four impurity beams identified in Fig. 1, only ^{24}Al [$t_{1/2}$ = 2.053 (4) s] is collected on the tape

and it constitutes a mere 0.2 % of the total sample. ^{25}Si and ^{22}Mg both punch through the tape, and ^{27}Si is stopped in the degraders and never reaches the tape.

The first step in the analysis process has been to check that all data files are consistent with one another and that each event's header numbers are an accurate representation of the data listed. Three output files were obtained for each run; the heavy ion event file, the MCA event file and the MCB event file. The MBA and MCB files contain the same primary data but recorded with different pre-selected dead times. Within each of the 22 runs, any cycle that displayed significant variations between the three files was discarded. This resulted in less than 0.15% of the collected data being thrown out. Fig. 3 shows a preliminary representation of the total data recorded, on which we have placed a calculated decay spectrum for ^{27}P and the growth-and-decay spectrum for its daughter, ^{27}Si. The analysis is still in progress.

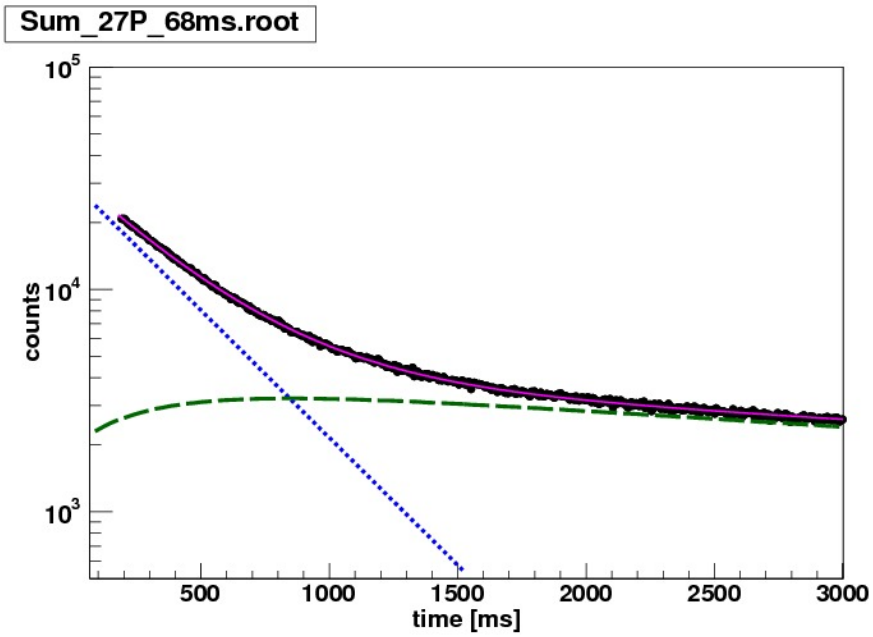

FIG. 3. Preliminary data from the measurement are shown in black. The calculated contributions from the parent (blue line) and daughter (green line) are also shown. No impurities have been taken into account at this point.

[1] T.J. Ognibene *et al.*, Phys. Rev C **54**, 1098 (1996)

[2] V.E. Iacob *et al.*, Phys. Rev. C, **74**, 055502 (2006)

[3] H.I. Park *et al.*, Phys. Rev. C, **85**, 035501 (2012)

[4] J.F. Ziegler *et al.*, SRIM: The Stopping and Range of Ions in Matter (2008), www.srim.org.

[5] V.T. Koslowsky *et al.*, Nucl. Instrum. Methods Phys. Res. **A401,** 289 (1997).

Progress on the analysis of the beta-delayed proton and gamma decay study of ^{27}P

E. Simmons, A. Banu, T. Davinson,[1] D. Doherty,[1] G. J. Lotay,[1] M. McCleskey, B. Roeder, A. Saastamoinen,[2] A. Spiridon, L. Trache, R. E. Tribble, J. Wallace,[1] and P. J. Woods[1]

[1]*School of Physics, University of Edinburgh, Edinburgh, United Kingdom*

[2]*Department of Physics, University of Jyvaskyla, Finland*

The first observation in the interstellar medium of the 1.809 MeV gamma-ray line originating from the β-decay of ^{26}Al [1] was an important discovery in the history of Nuclear Astrophysics. Due to its (relatively speaking) short half-life of 7.2 x 10^5 years, its observation in the galactic environment was indicative of ongoing nucleosynthesis. The destruction of ^{26}Al can be accomplished by proton capture on either the ground state or the metastable-state. Therefore, understanding all processes involved is key to pinpointing the currently unknown stellar creation and destruction sites. The purpose of this experiment was to look into the ^{26}Al^{m}(p,γ) reaction.

The very nature of stars make this reaction very difficult to study directly because of the extremely low cross section involved (due to tunneling through the Coulomb barrier) and the presence of electrical noise and natural background in the lab environment, which can be minimized but never entirely eliminated. Thus, an indirect method was employed to gain the required information, the β-delayed proton decay of ^{27}P. This method was chosen because the selection rules involved populated the same states of interest in the indirect as well as the direct approach, summarized below in Fig. 1. The states of interest, resonances in the direct proton capture process, are located above the proton threshold (E* > Sp + E(0+) = 7.463 + 0.228 = 7.691 MeV), so that they can then decay by proton emission to the metastable-state in ^{26}Al.

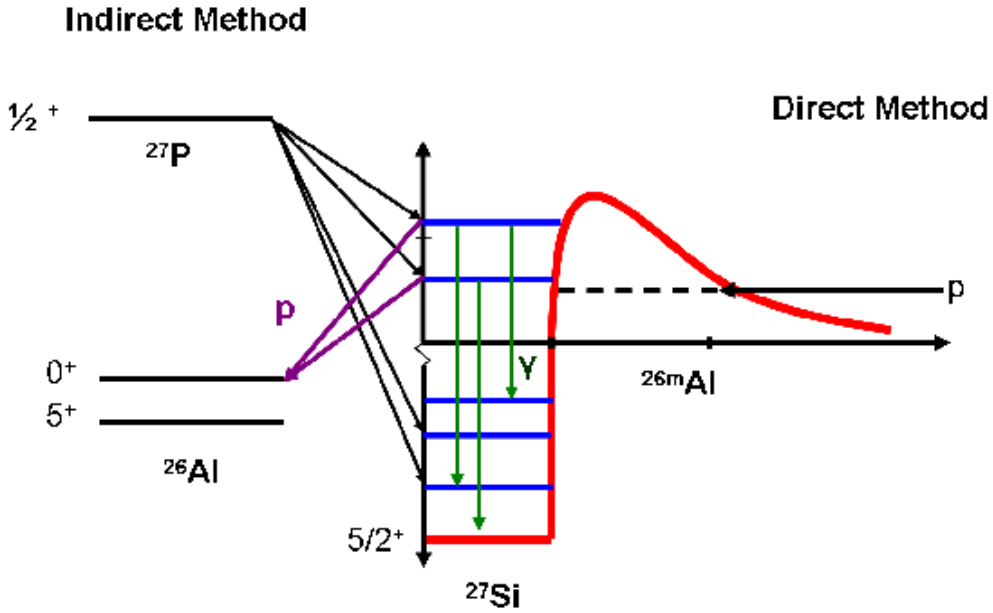

FIG. 1. Comparison between direct and indirect processes.

The general experimental setup was covered in detail by [2,3], however, significant changes were made to the implantation and decay station placed at the end of MARS for this experiment. The main goal of the re-design was to move the HPGe detectors in as close as possible to the point of implantation in the thin silicon detector. This involved a total re-location of all internal parts such as the water cooling pipes and the detector holder itself, as well as the external parts such as the electrical feedthrough components. The efficiency was greatly increased, especially in the low energy region, as desired, but it should be noted that this increased efficiency also increased the presence of sum peaks in the gamma-ray spectra, requiring careful peak identification.

The protons observed by the Berkeley group [4], whom were the first to study the β-delayed proton decay of ^{27}P, were also identified in this experiment. However, in the region of interest (~200 keV), only background was observed despite the fact that this experiment reduced the noise level significantly from earlier experiments of the same type. This was due to the extremely low proton branching ratio involved (estimated originally at 0.07%). Attempts to subtract out this background resulted in a 'bulge' remaining, as shown below in Fig. 2 [5]. With an upper and lower estimate on the β-background included, the total proton branching ratio was found to be 0.155(3)% – 0.163(3)%. A detector that is less sensitive to β-particles while retaining good energy resolution, efficiency and linearity would be ideal to improve upon the conclusions reached with this experiment.

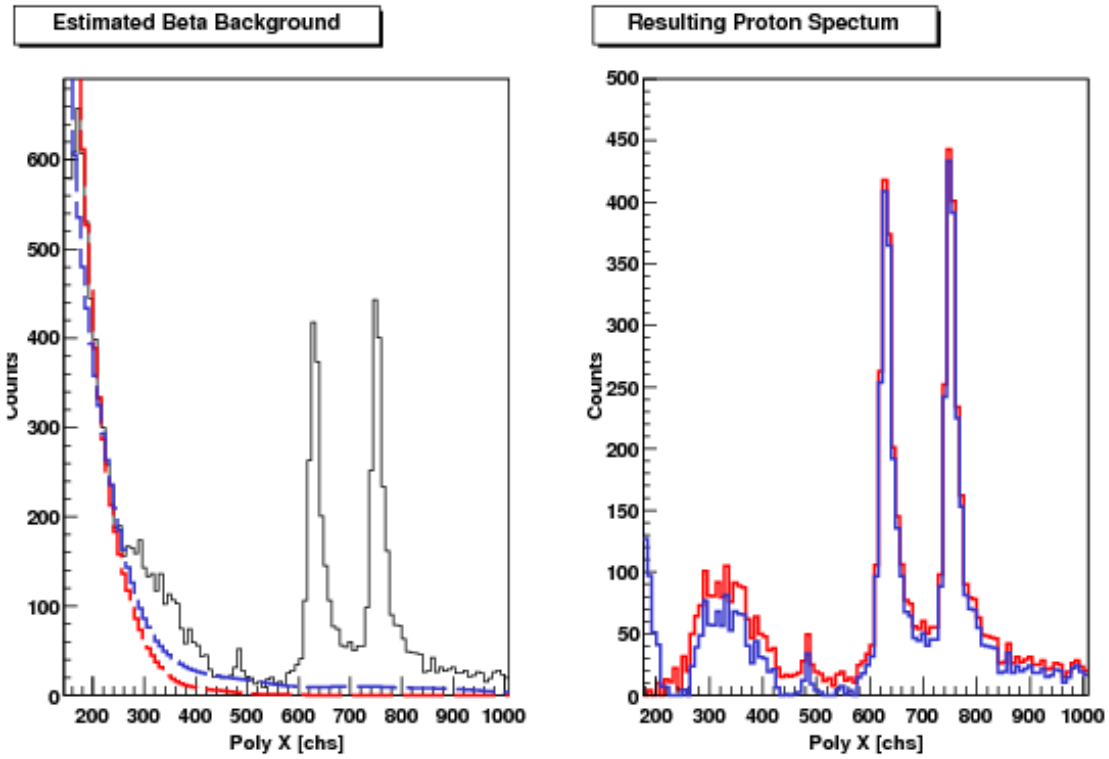

FIG. 2. Upper and lower estimates for the β-background from the 22P decay measurement. The right panel shows the β -delayed proton spectrum after the β -background are subtracted.

Never before has a study been done on the population of states in ^{27}Si from the β-decay of ^{27}P. Thus, several gamma-rays that were predicted but never seen due to selection rules [6, 7] have been confirmed, as well as the identification of gamma-rays never before observed. With the aid of a better half-life value (soon to be published) the log *ft* values for each level identified were calculated and the spin and parity were assigned based on selection rules. Most importantly, the isobaric analog state was found to lie at 6638 (1) keV, differing significantly from previous values [8, 9]. Currently work is being done on improving all calibrations and final numbers in preparation for publication. A Geant4 simulation is being created to estimate the efficiency of the silicon detector setup and to help understand the overall results.

[1] W.A. Mahoney *et al*., Astrophys. J. **262**, 742 (1982).
[2] A. Saastamoinen *et al*., Phys. Rev. C **83**, 045808 (2011).
[3] M. McCleskey *et al*., Nucl. Instrum. Methods Phys. Res. **A700**, 124 (2013).
[4] T.J. Ognibene *et al*., Phys. Rev C **54**, 1098 (1996).
[5] E. Simmons, Ph.D. Thesis, Texas A&M University, 2013.
[6] G. Lotay *et al.*, Phys. Rev. C **80**, 055802, (2009).
[7] G. Lotay *et al.*, Phys. Rev. C **84**, 035802, (2011).
[8] W. Benenson *et al.*, Phys. Rev. C **15**, 1187 (1977).
[9] P. Schmalbrock *et al.*, Nucl. Phys. **A457**, 182 (1986).

Elastic scattering of ^{13}C at 12 MeV/n on ^{27}Al

A. Spiridon, R. Chyzh, M. Dag, V. Z. Goldberg, E. McCleskey, M. McCleskey, B. T. Roeder, A. Saastamoinen, and R. E. Tribble

X-ray bursts are the most frequent thermonuclear explosion occurring in the universe and represent one type of phenomena responsible for heavier element nucleosynthesis. For this reason and others, a number of powerful X-ray observatories have been used to take large amounts of data on these bursts. The interpretation of these observations, however, is problematic due to the lack of a complete understanding of the nuclear physics at the base of these phenomena [1].

Among the various processes occurring in X-ray bursts, the most important is the rp-process. It is dominated by (p, γ), (α, p) reactions and β-decays. Critical nuclear data is needed related to these processes such as: nuclear masses, β-decay rates and reaction rates. There have been major strides made for the first two parameters. However, as most of the nuclei participating in the rp-process do not exist as stable nuclei, most of the reaction rates, so far, have only been estimated based on theory [2].

As with any nuclear reaction network, some reactions are more important than others. Several have been suggested for X-Ray bursts following different model calculations. One such reaction that we chose to research is the radiative proton-capture reaction ^{27}Si(p, γ)^{28}P. The goal is to determine its rate using a re-accelarated radioactive beam of ^{27}Si from the Cyclotron Institute T-Rex upgrade and the MDM spectrometer.

However, until such a beam is available we intend to study the mirror reaction ^{27}Al(n, γ)^{28}Al with the purpose of using the properties of the mirror nucleus ^{28}Al in the estimation of the reaction rate. A secondary motivation is to look for new structure information on ^{27}Al and ^{28}Al. The asymptotic normalization coefficients will be obtained from the DWBA analysis of the measured angular distributions of the transfer reaction ^{27}Al(^{13}C,^{12}C)^{28}Al. For that we need to know the optical potential parameters for the elastic scattering channel.

For that purpose, in the last year we have done two experiments. Both times, we used a beam of ^{13}C at 12 MeV/u on targets of ^{27}Al of different thicknesses (100 μg/cm^2, 270 μg/cm^2 and 800 μg/cm^2) and measured the elastic and inelastic scattering at a total angular range of 4 to 42 degrees in the laboratory system. The primary beam was accelerated by the K150 cyclotron at Texas A&M University. Then the reaction products were separated using the Multipole-Dipole-Multipole (MDM) spectrometer and were observed with the Oxford focal plane detector.

Preliminary results can be seen in the figures below. Fig. 1 shows the angular distribution of the cross-section in the lab system for the elastic scattering. Fig. 2 shows a comparison between the previous data and the distributions for two inelastic states where you can see the expected phase relationship. However, analysis is still ongoing as we are having issues resolving the peaks corresponding to the various excited states at larger angles where we sacrificed resolution for higher production rate by using a thicker target.

The measurement of the transfer reaction is planned for the second half of 2014.

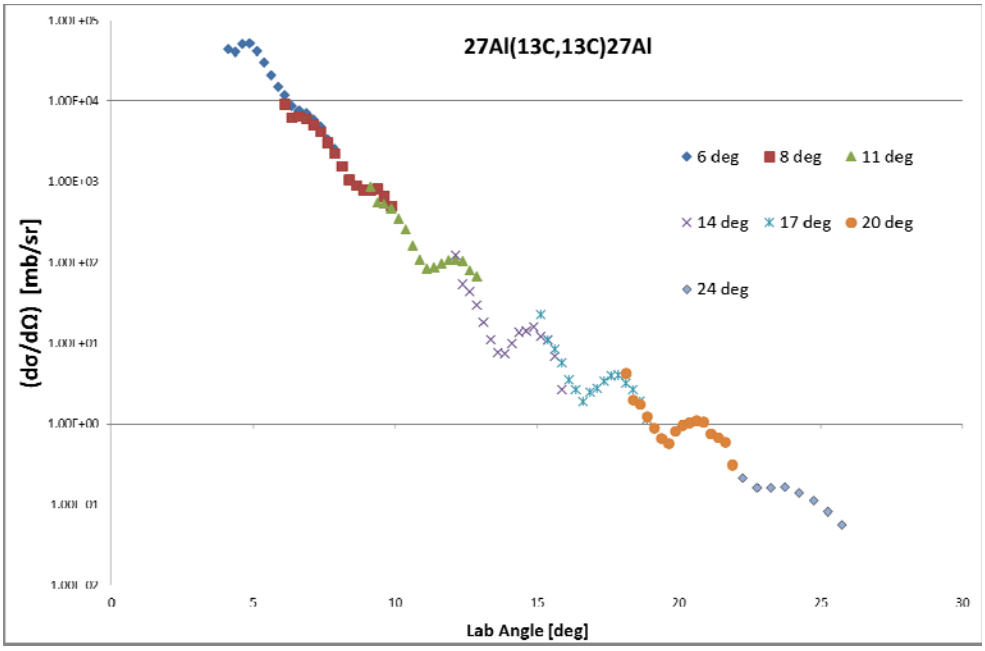

FIG. 1. Measured angular distribution of the elastic scattering cross section.

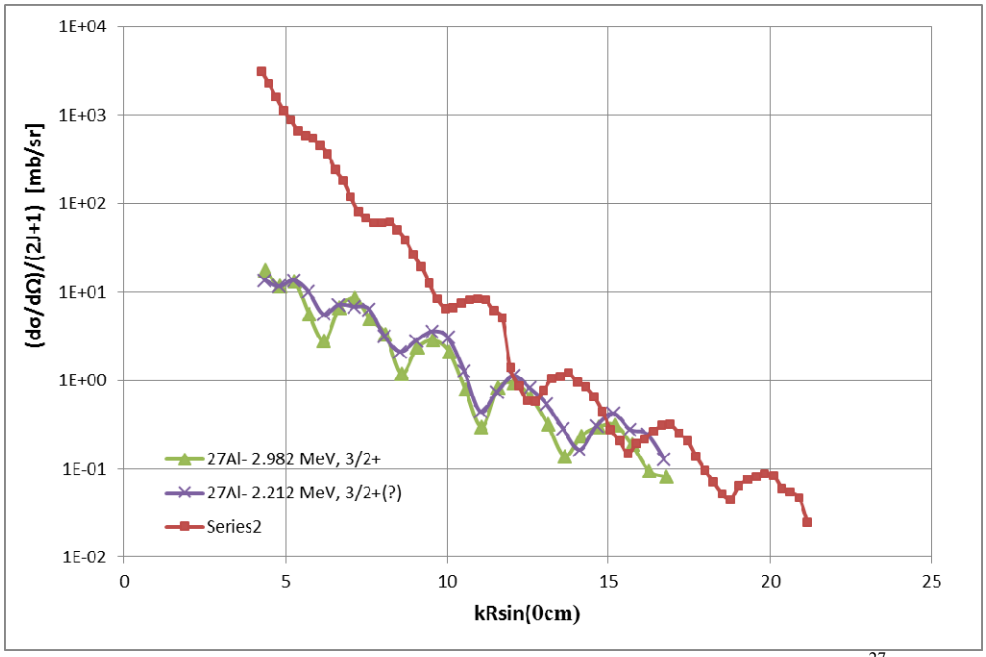

FIG. 2. Measured angular distributions for the elastic and inelastic scattering on ^{27}Al in the CM system.

[1] H. Schatz, Prog. Part. Nucl. Phys. **66**, 277 (2011).

[2] H. Schatz and K.E. Rehm, Nucl. Phys. **A777**, 601 (2006).

Determination of optical model parameters for the elastic scattering of ^{26}Mg on ^{13}C

M. Dag, M. McCleskey, R. Chyzh, V. Z. Goldberg, B. Roeder, A. Saastamoinen, E. Simmons, A. Spiridon, and R. E. Tribble

In an experiment carried out at the Cyclotron Institute, a ^{26}Mg beam at 12 MeV/u impinged on a ^{13}C target and the elastic scattering and transfer reaction angular distributions were measured at several spectrometer angles as shown below in Fig 1. The elastic scattering has been used to extract the parameters of the optical model potentials that were needed for DWBA calculations to determine the ANC for the ^{26}Mg + n → ^{27}Mg systems from the ^{13}C(^{26}Mg,^{27}Mg)^{12}C reaction. See Ref. [1] for more details.

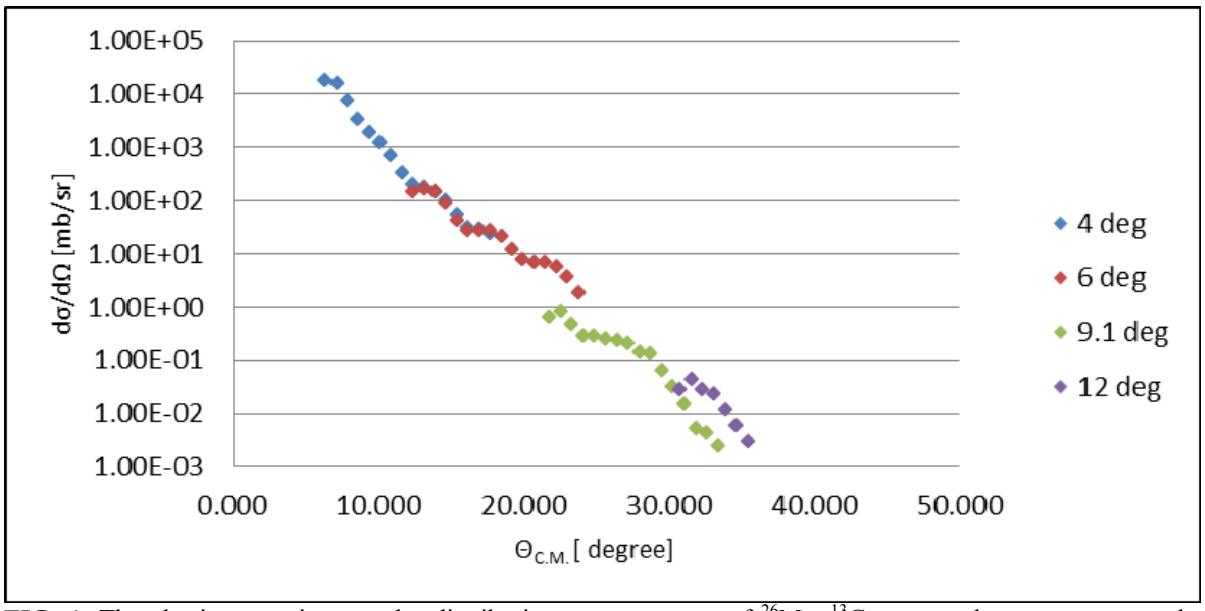

FIG. 1. The elastic scattering angular distribution measurements of ^{26}Mg+^{13}C at several spectrometer angles. Due to consistency checks of the data at all angles, overlapping measurements were performed.

Due to the difficulties in particle identification and the uncertainty of the separation of ^{26}Mg$_{(g.s)}$ from impurities while analyzing the elastic scattering measurements at 9.1^{o} and 12^{o}, those angles were excluded from the calculation of optical model parameters to eliminate an inconsistency in angular distribution measurement of ^{26}Mg on ^{13}C and to minimize the complexity of fitting procedure. Upgrading the existing setup of the Oxford Detector to have better resolution in particle identification at higher masses A≥26 is now in progress. A detailed description can be found in Ref. [2]. New measurements will be carried out after these upgrades.

In order to determine the ANC from the ^{13}C(^{26}Mg ,^{27}Mg)^{12}C transfer reaction, a good and reliable optical potential is needed. The Woods-Saxon optical-model parameterization of the elastic scattering data therefore was performed with the computer code PTOLEMY [4]. A Woods-Saxon optical potential of form [3]

$$U(r) = -V_0\left\{\frac{1}{\left(1+e^{r-\frac{R_V}{a_V}}\right)}\right\} - iW_0\left\{\frac{1}{\left(1+e^{r-\frac{R_W}{a_W}}\right)}\right\} + Vc(r) \qquad , \quad R = r\left(A_t^{\frac{1}{3}} + A_p^{\frac{1}{3}}\right)$$

where ***a*** determines the surface diffuseness, ***R*** is the nuclear radius, ***V*** and ***W*** are related to the real and the imaginary well-depth of the potential and an additional Coulomb potential ($V_c(r)$) for charged particles.

$$V_c(r) = \begin{cases} \frac{Z_t Z_p e^2}{2R_c}\left(3 - \frac{r^2}{R_c^2}\right), & r \le R_c \\ \frac{Z_t Z_p e^2}{r}, & r > R_c \end{cases} \qquad , \quad R_c = r_{CO}\left(A_t^{\frac{1}{3}} + A_p^{\frac{1}{3}}\right)$$

was used. The imaginary surface and spin-orbit interactions were neglected to decrease the number of parameters and complication of the fitting procedure.

The Woods-Saxon optical-model parameter set which best described each set of elastic scattering data was determined according to the following procedure. A grid search was performed, stepped in 1 MeV increments, over a range from 1 to 300 MeV in ***V*** and ***W***, the depth of real and imaginary potential respectively, and then a complete search on all six parameters was run to determine the best fit. All the sets of parameters are shown in Table I.

Table I. The best fit parameters of the Woods-Saxon optical model potential obtained from the analysis of the elastic scattering data for $^{26}Mg+^{13}C$.

Pot.	V [MeV]	r_v [fm]	r_w [fm]	W [MeV]	a_v [fm]	a_w [fm]	$\chi 2$	Jv [MeV fm3]	Jw [MeV fm3]	Rv [fm]	Rw [fm]
1	21.96	0.84	1.42	5.61	1.48	0.41	0.58	51	31	6.50	6.04
2	41.17	0.69	1.90	3.58	1.10	0.43	0.76	48	46	4.98	7.97
3	301.40	0.30	1.35	11.30	1.32	0.49	0.99	134	54	5.02	5.83

In the Table, r_v (r_w) and a_v (a_w) are the real (imaginary) nuclear radius parameter and the surface diffuseness respectively. The Coulomb radius parameter is fixed to r_{CO} = 1 fm. χ^2 is given by

$$\chi^2 = \frac{1}{N-f}\sum_i \frac{(\sigma_{exp}(\theta_i) - \sigma_{th}(\theta_i))^2}{(\Delta\sigma_{exp}(\theta_i))^2}$$

where N is the number of data points, f is the number of free parameters. J_v and J_w are the volume integral per interacting nucleon pair of the real and imaginary part, respectively.

$$J = J_V + J_W = -\left(\frac{1}{A_T A_P}\right)4\pi\int_0^\infty (V(r) + iW(r))r^2 dr$$

The root mean square radius of the real and imaginary potentials are respectively given by

$$< R_v^2 > = \int_0^\infty V(r) r^4 dr \Big/ \int_0^\infty V(r) r^2 dr \qquad < R_w^2 > = \int_0^\infty W(r) r^4 dr \Big/ \int_0^\infty W(r) r^2 dr$$

As shown in Fig. 2, all calculated optical model potentials fit quite well up to the point at which data ended. Due to the limited experimental data available, this experiment will be repeated in the near future to obtain additional data at larger angles to avoid the ambiguity in determination of optical potential that were needed for DWBA calculations. Also, repeating the experiment will allow us to accurately determine the ANC for the ^{26}Mg + n → ^{27}Mg systems.

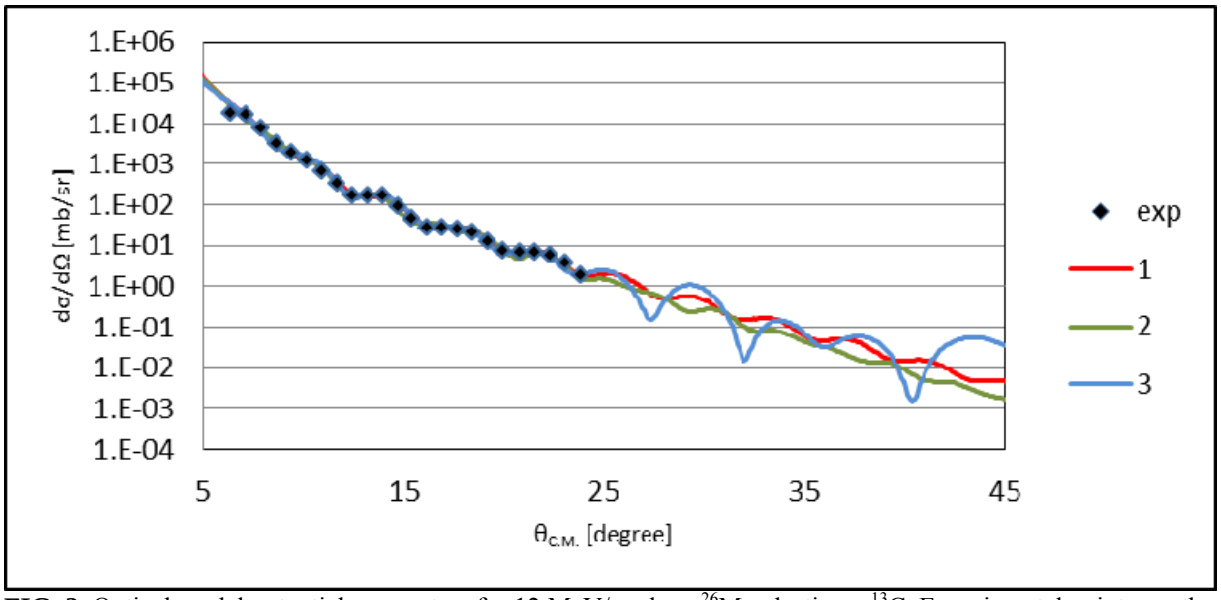

FIG. 2. Optical model potential parameters for 12 MeV/nucleon ^{26}Mg elastic on ^{13}C. Experimental points are the black dots.

In addition to the analysis with Woods-Saxon type potentials, the data have been analyzed using double folding potentials with the computer code OPTIMINIX [5]. In this model, the potential is obtained by considering the effective NN(nucleon-nucleon) interaction between the matter distributions of the colliding particles.

$$V_{fold}(r) = \iint d\vec{r}_1 d\vec{r}_2 \rho_1(r_1) \rho_2(r_2) v_{eff}(\vec{r}_1 + \vec{r} - \vec{r}_2).$$

The Hartree-Fock procedure was followed to calculate the nuclear density distributions, then the Jeukenne, Lejeune and Mahaux (JLM) effective interaction was used for the nucleon-nucleon interaction potential (V_{eff}). The resulting double folding potential is

$$U(r) = N_v V_{fold}(r) + iN_w W_{fold}(r)$$

The fitting procedure started with the average values N_v=0.37, N_w=1.0 for the renormalizations, and the standard range parameters t_v=1.2 fm and t_w=1.75 fm. The elastic scattering data is fitted by adjusting four parameters. The best fit to the data was obtained with N_v=0.4, N_w=1.0, t_v=1.2 and t_w=1.75 and is shown in Fig. 3.

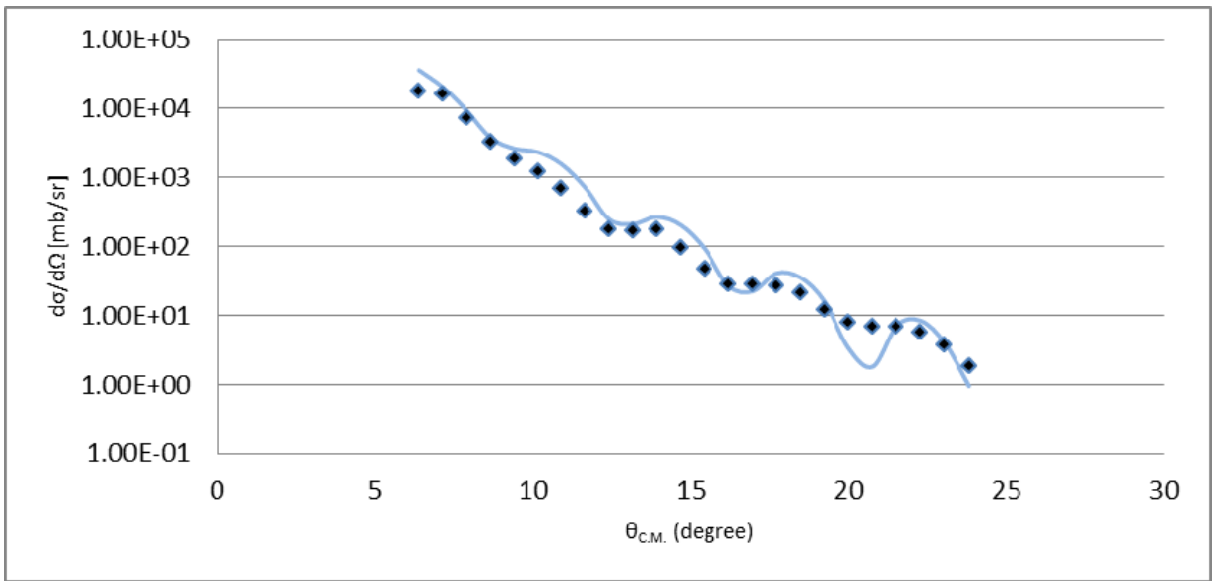

FIG. 3. The blue line is the optical model calculations obtained with the double folding procedure. Experimental points are the black dots.

[1] M. McCleskey et al., *Progress in Research*, Cyclotron Institute, Texas A&M University (2009-2010) p. I-31.

[2] A. Spiridon, R. Chyzh, M. Dag, M. McCleskey, and R.E. Tribble, *Progress in Research*, Cyclotron Institute, Texas A&M University (2012-2013) p.IV-50

[3] L. Trache, A. Azhari, H.L. Clark, C.A. Gagliardi, Y.-W.Lui, A.M. Mukhamedzhanov, and R.E. Tribble, Phys. Rev. C **61**, 024612 (2000).

[4] M.H. Macfarlane, S.C. Piper, and M. Macfarlane, computer code PTOLEMY, Argonne National Lab Report ANL-76-11-rev-1 (1978).

[5] F. Carstoiu, computer code OPTIMINIX (unpublished), Institute of Physics and Nuclear Engineering, Bucharest, Romania (1996).

Study of the lowest states in ^{9}He as a test of unusual nuclear structure beyond the neutron dripline

R. Chyzh, A. Saastamoinen, M. McCleskey, V. Z. Goldberg, G. V. Rogachev, Y. Koshchiy,
E. Simmons, A. Spiridon, M. Dag, and R. E. Tribble

Examining nuclear matter under extreme conditions makes the most demanding test of our understanding of nuclear structure. A well known opportunity is provided by the study of nuclei which are far from the valley of stability. Indeed, it looks like we encounter cases of very light neutron rich nuclei: ^{9}He, ^{10}He, and ^{7}H, which challenge our current knowledge of nuclear structure. A controversy between different experimental results and predictions for ^{7}H and ^{10}He is broadly discussed (see [1, 2] and references therein). However, the most evident contradiction between the theoretical predictions and experimental results is for ^{9}He.

The structure of ^{9}He, with its 2 protons and 7 neutrons could be expected to be simple: two protons fill the *s* shell, while six neutrons fill the p3/2 sub shell and the extra neutron should be in the $p_{1/2}$ shell. The most sophysticated modern calculations ([3,4] and references therein) support this "naive" view on the ^{9}He structure. This means that the reduced neutron decay width for the $1/2^{-}$ state should be close to the Wigner limit and the state should be rather broad (all calculations predict the ^{9}He to be unstable to a neutron decay to ^{8}He). However several high resolution measurements of spectra of products of complicated binary or quasi binary reactions induced by heavy ions by a group in the Hahn-Meitner Institute [5, 6] brought interesting data with rather small uncertainties. They found the $1/2^{-}$ state of ^{9}He at 1.27 ± 0.10 MeV above the ^{8}He + n threshold with $\Gamma = 0.10 \pm 0.06$ MeV. The width appeared to be more than ten times smaller than could be expected [4]. The narrow width of the $½^{-}$ state could be considered as a direct evidence for its complicated, non shell model structure, and also could be a sign of an unusual structure appearing at the neutron dripline. Several groups tried to obtain detailed information on the lowest states in ^{9}He (including using the ^{8}He(d,p) reaction[7]), but low counting statistics or unadequate energy resolution did not give a possibility to test results [5,6].

We began an experimental study of the lowest states in ^{9}He using the ^{9}Be(^{18}O,^{18}Ne)^{9}He reaction. In contrast to other similar investigations we used coincidence between ^{18}Ne and the products of the ^{9}He decay, ^{8}He and ^{6}He. This should provide for the assignment of the correct excitation energy to the reaction products because there are excited states in ^{18}Ne which are stable to a nucleon decay, and improve the signal/background ratio. The experiment was made using ^{18}O beam of 12 MeV/A from the K150 cyclotron. Heavy ions were detected using MDM spectrometer [8] in the angular interval $5^{\circ} \pm 2^{\circ}$. The detection system of the MDM spectrometer [8] provided for the needed angular ($\pm 0.3^{\circ}$) and energy resolution (~200 keV). The charged products of ^{9}He decay: ^{8}He, ^{6}He or ^{4}He were detected by Si detectors placed in the scattering chamber of the MDM spectrometer (a scheme of the setup is given in Fig.1). The identification of the mass of He isotopes was made using the reaction kinematics and by time of flight between heavy ions detected by MDM and the products of ^{9}He decay. As tests of the setup and the experimental parameters we used reactions of the ^{18}O+^{9}Be elastic scattering and the ^{9}Be(^{18}O,^{19}Ne)^{8}He reaction. In particular, the test reactions provided for spread of times of flight of ions of different

energies through the MDM. This spread of ions covered the whole interval of the energy interval of the ^{18}O ions appeared to be less than 2ns.

The results of the test experiment are currently under analyzed.

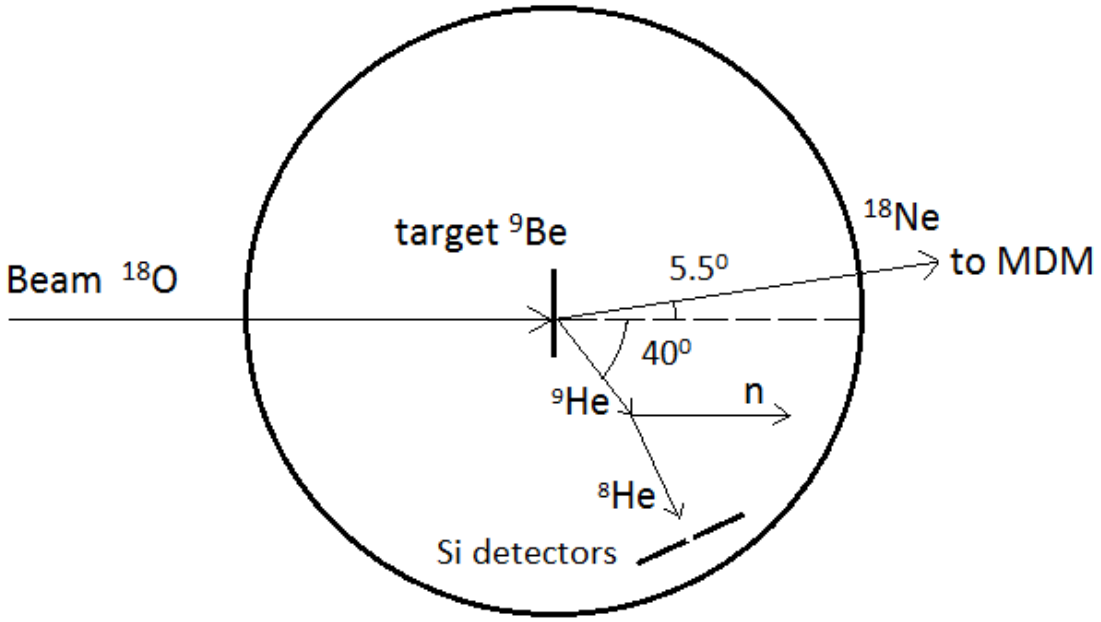

FIG. 1. Scheme of setup of the experiment.

[1] Z. Kohley *et al*., Phys.Rev.Lett. **109**, 232501 (2012).

[2] E.Yu. Nikolskii *et al.*, Phys. Rev. C **81**, 064606 (2010).

[3] B.R. Barrett, Prog. Part. Nucl. Phys. **67**, 521 (2012).

[4] K.M. Nollett, Phys. Rev. C **86**, 044330 (2012).

[5] H.G. Bohlen *et al.*, Prog. Part. Nucl. Phys. **42**, 17 (1999).

[6] W. von Oertzen *et al.*, Nucl. Phys. **A588,** 129c (1995).

[7] T. Al Kalanee, Phys. Rev. C **88**, 034301 (2013).

[8] D.M. Pringle *et al.*, Nucl. Instrum. Methods Phys. Rev **A245**, 230 (1986).

Study of low energy resonances in $^{13}C+^{4}He$ interaction

V. Z. Goldberg, G. V. Rogachev, R. E. Tribble, N. A. Mynbayev,[1] A. K. Nurmukhanbetova,[1]
M. S. Golovkov,[2] V. N. Dzybin,[1] M. V. Koloberdyn,[3] and I. Ivanov[3]
[1]*Nazarbayev University Research and Innovation System, Astana, Kazakhstan*
[2]*Flerov Laboratory of Nuclear Reactions, JINR Dubna, Russia*
[3]*L. N. Gumylov Eurasian National University, Astana, Kazakhstan*

About half of all elements heavier than iron are produced in a stellar environment through the *s* process, which involves a series of subsequent neutron captures and α decays. The reaction $^{13}C(\alpha,n)^{16}O$ is considered to be the main source of neutrons for the *s* process at low temperatures in low mass stars in the asymptotic giant branch (AGB) [1]. Two factors determine the efficiency of this reaction: the abundance of ^{13}C and the rate of the $^{13}C(\alpha,n)^{16}O$ reaction (see [2], and references therein). The rate of the $^{13}C(\alpha,n)^{16}O$ reaction at temperatures of ~10^8 K is uncertain by ~300% [3] due to the prohibitively small reaction cross section at energies below 300 keV. α clustering may generally play a role in helium burning in astrophysical systems. Indeed, even if astrophysical reactions involving helium do not proceed through strong α-cluster states (because of high excitation energy), these states can provide an α width to the states that are closer to the region of astrophysical interest through configuration mixing [4].

The available data on the α-cluster states in neutron rich nuclei are scarce [5–9], but they give indications for the developed cluster structures with very large moments of inertia. The study of non-self-conjugate nuclei has an advantage in that one now can investigate isobaric analog states in mirror systems, using r/a beams. Comparison of the results for both systems can bring new spectroscopic information and shed light on such properties as the radii of the cluster states.

There are old measurements of low energy resonances in the $\alpha+^{13}C$ elastic scattering using a target with ~50% enrichment of ^{13}C. The data were obtained only at four angles, and the analysis was mainly qualitative (see [10] and references therein). Recently much more complete measurements were made by the Notre Dame group [11] However all previous measurements were made using forward kinematics when a tandem beam of α particles strikes a target of ^{13}C.

We made a study of the resonance $\alpha+^{13}C$ elastic scattering using the Thick Target Inverse Kinematics method (TTIK) (see [12] and references therein) at the DC-60 cyclotron at Astana. The advantage of the TTIK method is that an excitation function can be measured in a large interval using a "single" beam energy. It provides also a possibility to make measurements at zero degrees (180º cms) where the resonance cross section is the largest and the potential one is minimal. It is important that the TTIK method provides for an easier access to the low energy of interaction because of the kinematic increase of the energy of light recoils.

The measurements were made at initial energy of ^{13}C of 1.75 MeV/A. The data on the $\alpha+^{13}C$ elastic scattering excitation function were obtained using 16 Si detectors covering laboratory angles in the interval 0-30^0. The 180^0 cms (0^0 in the lab. system) is shown in Fig.1. It is seen in Fig.1 that there is a structure at low energies (less than 2 MeV) which has not been observed before. Additional measurements were made to find background contribution. It was found that the background is negligible

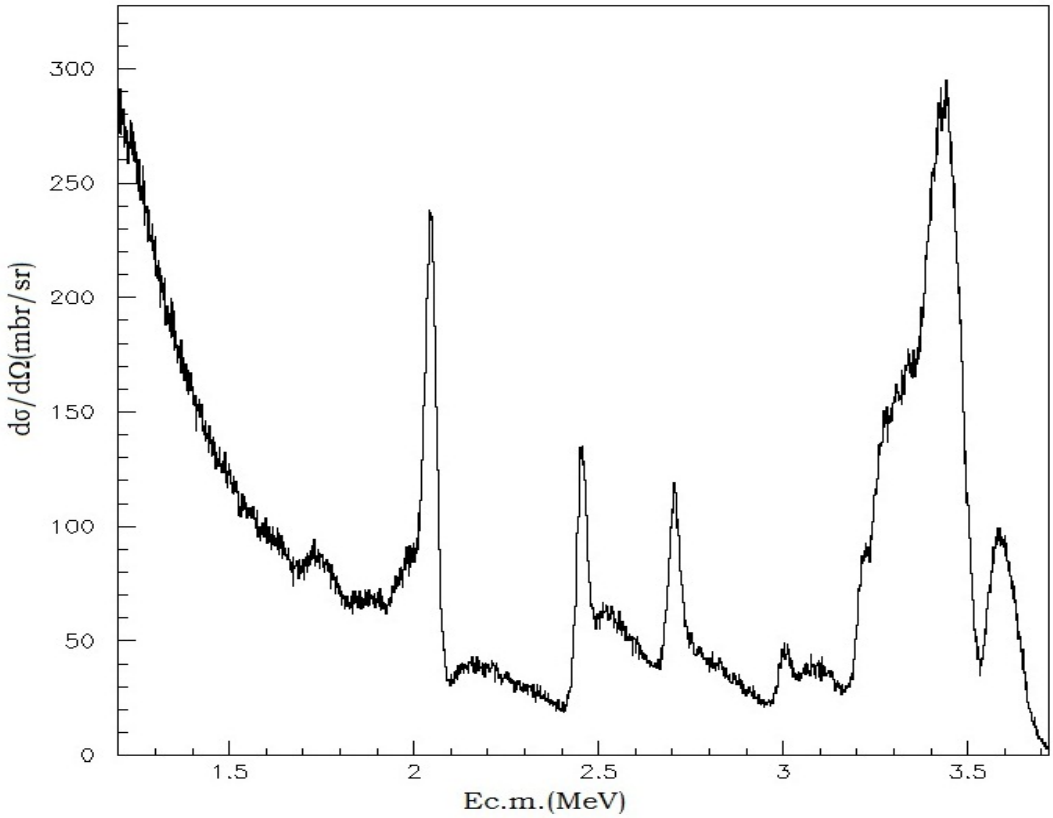

FIG. 1. Excitation function for the $\alpha+^{13}C$ elastic scattering at 180^0 degrees.

(also important was the absence of the reactions with ^{12}C which are always present in the conventional setup when ^{13}C target is used)

The complete multilevel *R*-matrix analysis of the data is in progress. It is worthwhile to note that it was the first nuclear physics experiment at the Astana cyclotron.

[1] I. Iben, Astrophys. J. **196**, 525 (1975).
[2] S. Goriely and L. Siess, Astron. Astrophys. **378**, L25 (2001).
[3] C. Angulo *et al.*, Nucl. Phys. **A656**, 3 (1999).
[4] X.D. Tang, *et al.*, Phys. Rev. Lett. **99**, 052502 (2007).
[5] M. Freer, *et al.*, Phys. Rev. Lett. **96**, 042501 (2006).
[6] A.A. Korsheninnikov *et al.*, Phys. Lett. **B343**, 53 (1995).
[7] V.Z. Goldberg *et al.*, Phys. Rev. C **69**, 024602 (2004).
[8] L. Buchmann, *et al.*, Phys. Rev. C **75**, 012804(R) (2007)
[9] E. Johnson *et al.*, Eur. Phys. J. A **42**, 135 (2009)
[10] G.W. Kerr, J.M. Morris, and J.R. Risser. Nucl. Phys. **A110**, 637 (1968).
[11] M. Heil *et al.*, Phys. Rev. C 78, 025803 (2008).
[12] V.Z. Goldberg *et al.*, Phys. Lett. B **692**, 307 (2010).

Production of new radioactive beams ^{42}Ti, ^{35}K, ^{9}C, ^{8}B, and ^{20}O with MARS

B. T. Roeder, A. Saastamoinen, M. McCleskey, E. McCleskey, A. Spiridon, E. Koshchiy,
G. Rogachev, H. I. Park, and R. E. Tribble

This year we produced and separated several new radioactive beams for the physics program at the Cyclotron Institute at Texas A&M University with the Momentum Achromat Recoil Separator (MARS) [1]. While the production tests for ^{35}K, ^{9}C, and ^{8}B were more or less straightforward, the production tests of the new ^{42}Ti and ^{20}O beams were challenging. Details about the production and separation of each of these beams are provided in this report. All of the beams in this report will be used in experiments in the coming year.

I. Production of ^{42}Ti secondary beam

In November 2013, we studied the production and separation of ^{42}Ti with MARS for the group of Prof. J.C. Hardy. ^{42}Ti is needed as part of his research group's continuing study of the lifetime and branching ratios for superallowed β-decays.

The nuclei for the superallowed β-decay studies are usually produced with the fusion-evaporation reaction (p,2n) in inverse kinematics with primary beam energies around 30 MeV/u. However, this reaction is not available in the case of ^{42}Ti because it is too far from the valley of stability in this region of the nuclear chart (A > 40). If a ^{45}Sc primary beam is used with the hydrogen gas target, the reaction p(^{45}Sc,^{42}Ti)4n requires much higher primary beam energy (> 50 MeV/u) and would produce ^{42}Ti at energies too high to be stopped efficiently inside the tape-transport system used for studying the superallowed β-decays. Further, ^{45}Sc primary beam is known have a relatively weak intensity, in particular when a high charge state is needed to produce this beam at this energy with the K500 cyclotron. Another possible method to produce ^{42}Ti beam would be to employ a high energy beam such as ^{50}Cr at 50 MeV/u with a thick ^{9}Be target and produce ^{42}Ti with the projectile fragmentation reaction mechanism. However, this method, in addition to the high energies and weak beam intensities mentioned in the previous case, is also not a good choice because additional contamination from nuclei close to the ^{42}Ti would be produced with similar or higher intensities than the ^{42}Ti.

Thus, with the above considerations in mind, we decided to attempt to produce ^{42}Ti with ^{40}Ca primary beam and gas targets of ^{3}He and ^{4}He. ^{40}Ca beam is available with high intensity at beam energies from 5-40 MeV/u. Simulations of the ^{40}Ca+^{3}He and ^{40}Ca+^{4}He reactions were conducted with the LISE++ program [2] prior to the production test. These simulations suggested that ^{42}Ti would be produced with the most intensity at low beam energies (~10-15 MeV/u) with the fusion-evaporation reaction mechanism, but also that it would still be possible to produce ^{42}Ti with reasonable intensity at higher primary beam energies with the direct-transfer reaction mechanism. Given that a primary beam of at least 30 MeV/u is needed to implant the ^{42}Ti secondary beam into the tape-transport system, a primary beam energy of 32 MeV/u was chosen for the production test.

The results of the production tests for ^{4}He(^{40}Ca,^{42}Ti)2n and ^{3}He(^{40}Ca,^{42}Ti)n at 32 MeV/u are shown in Fig 1. ^{42}Ti was produced and separated with MARS in both reactions. For the ^{40}Ca+^{4}He case,

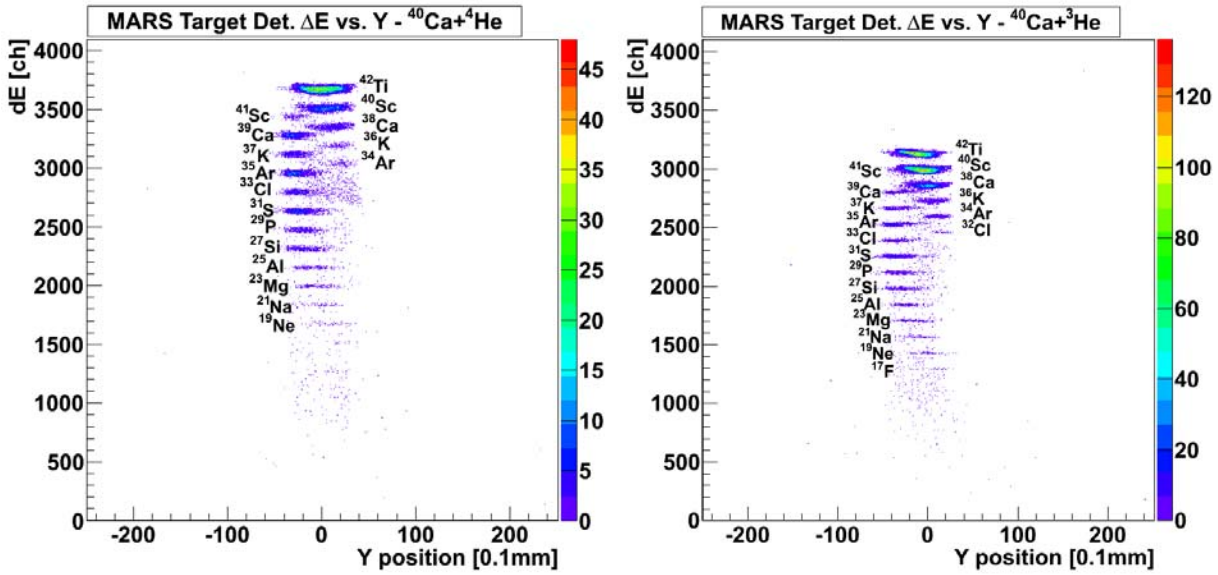

FIG. 1. (left panel) Results of the ^{42}Ti production test with the ^{40}Ca+^{4}He reaction. Impurities in the secondary beam are also labeled. (right panel) Results of the ^{42}Ti production test with the ^{40}Ca+^{3}He reaction. In the latter case, the impurities were found to be more intense.

with 2 atm of ^{4}He gas at a temperature of 77 K in the MARS gas cell target, ^{42}Ti was produced at a rate of 7 events/nC. In that case, about 50% of the total secondary beam was made up of impurities, with the most intense contribution coming from ^{40}Sc produced at ~30% of the rate of the ^{42}Ti. For the ^{40}Ca+^{3}He case, with 1 atm of ^{3}He gas at a temperature of 77 K in the MARS gas target, ^{42}Ti was produced at a rate of 6.3 events/nC. This implies that the production rate with the ^{3}He gas target could be higher than the ^{4}He case if 2 atm of ^{3}He gas were to be used. However, in the ^{3}He target case, impurities in the secondary beam made up 63% of the total secondary beam intensity. Also, ^{40}Sc was produced in this case at a slightly higher rate (~7% higher) than the ^{42}Ti. Therefore, the ^{4}He(^{40}Ca,^{42}Ti)2n production reaction was favored by Prof. Hardy's research group as it produced ^{42}Ti at an acceptable rate of ~1400 particles/sec (assuming ~200 nA of ^{40}Ca primary beam) and with less impurities in the secondary beam.

Prof. Hardy's research group made a preliminary measurement of the ^{42}Ti lifetime during this production test. The details of that measurement are given in a separate report [3].

II. Production of ^{35}K secondary beam

In March 2014, we produced and separated ^{35}K with MARS. ^{35}K is needed by the group of Prof. R.E. Tribble for the latest experiment in the series of measurements of β-delayed proton decay of proton-rich nuclei [4]. The ^{35}K was produced with the fusion-evaporation reaction (p,2n) in inverse kinematics with ^{36}Ar primary beam at 35 MeV/u. Hydrogen gas at a pressure of 2 atm and at a temperature of 77K was used in the MAS gas cell target.

In the planned experiment, the ^{35}K secondary beam will be slowed down and implanted into a thin silicon strip detector that is only ~45 μm thick. Thus, the ^{35}K secondary beam must have a small momentum spread such that all the nuclei produced are implanted into the detector. For the ^{35}K production test, we set the MARS momentum slits (the "coffin slits") to ± 0.5 cm, which corresponds to a momentum spread of the secondary beam of $\Delta P/P \approx \pm 0.3\%$. With this momentum slit setting, we produced ^{35}K at a rate of 3.5 events/nC. This should give a production rate of between 350 and 1000 particles/sec of the ^{35}K, depending on how much primary beam will be available for the future experiment.

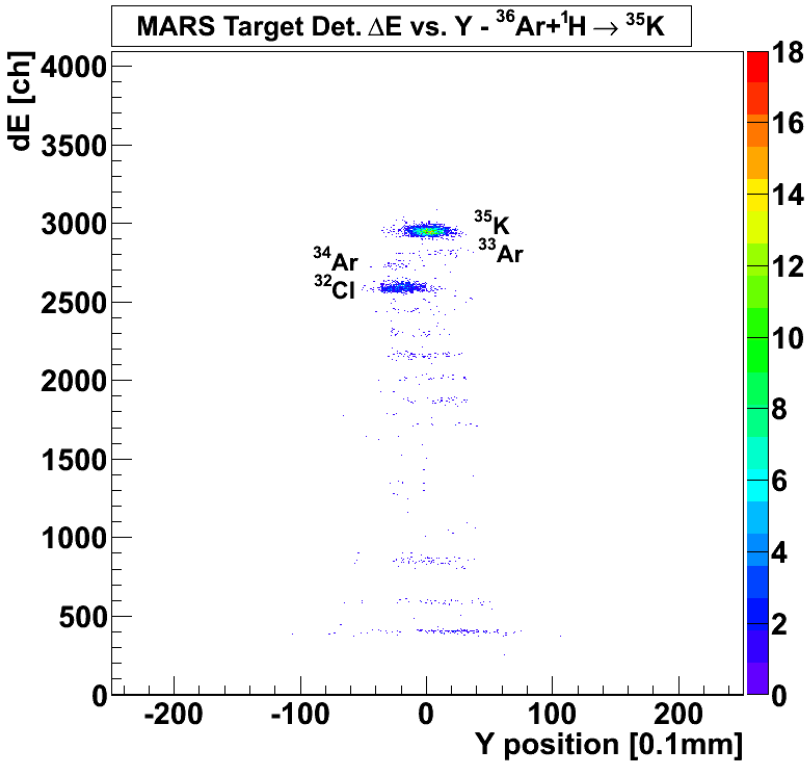

FIG. 2. Results of the ^{35}K production test.

The MARS target detector spectrum showing the final tune of the ^{35}K secondary beam is shown in Fig 2. While the ^{35}K is the most intense species shown in the secondary beam, about 45% of the secondary beam is from impurities. The most intense impurity is from the "tail" of the ^{32}Cl distribution. It was found that reducing the MARS gas cell pressure down to 1.5 atm of H_2 gas reduced the ^{35}K production rate down to 2.7 events/nC, but it also reduced the impurity ratio in the secondary beam to 34%. If the reduction of impurities will be important for the measurement, lower gas cell pressure seems to be one possible way of reducing the secondary beam impurities. It should be noted that most of the secondary beam impurities will not stop in the thin silicon strip detector or have low β-delayed proton or α-particle decay branching ratios relative to the ^{35}K. Thus, these impurities are not expected to cause problems in the future measurement.

The ^{35}K β-delayed proton decay measurement is planned for June 2014.

III. Production of ^{9}C and ^{8}B secondary beams

Also in March 2014, we produced and separated ^{9}C and ^{8}B with MARS. ^{9}C and ^{8}B are needed by the group of Prof. G. Rogachev for their upcoming experiments with resonant elastic proton scattering using the Thick Target Inverse Kinematics (TTIK) method. These experiments will be similar to those that have been conducted in the past by V. Goldberg at TAMU [5]. The ^{9}C secondary beam will be employed to study the unbound ^{10}N nucleus and the ^{8}B secondary beam will be used to study resonances in the ^{9}C nucleus. Both experiments are expected to be conducted later this year.

For the ^{9}C production test, a ^{10}B primary beam at 30 MeV/u bombarded the MARS gas cell target. The gas cell target was filled with 2 atm of hydrogen gas at a temperature of 77K. The ^{9}C was produced with the fusion-evaporation reaction (p,2n) in inverse kinematics. The Q-value for the p(^{10}B,^{9}C)2n reaction is -25.7 MeV. Thus, 30 MeV/u was chosen for the primary beam energy as a compromise between the production rate for ^{9}C, which is better at higher primary beam energies, and the desire to have the ^{9}C at the lowest possible energy. The optimum setting for the ^{9}C production was found at the MARS D1 dipole setting of 443 A, which corresponds to a ^{9}C beam energy of 23.2 MeV/u. For the planned experiment, this energy will be reduced to ~10 MeV/u with degraders.

The optimized production rate for the ^{9}C secondary beam was 4.1 events/nC, which will give ~10^{3} particles/sec with 250 nA of ^{10}B beam on target. The ^{9}C secondary beam was relatively pure, although there is some contamination in the beam from α-particles and ^{3}He. Some of this contamination will be removed in the future experiment by closing the slits of MARS.

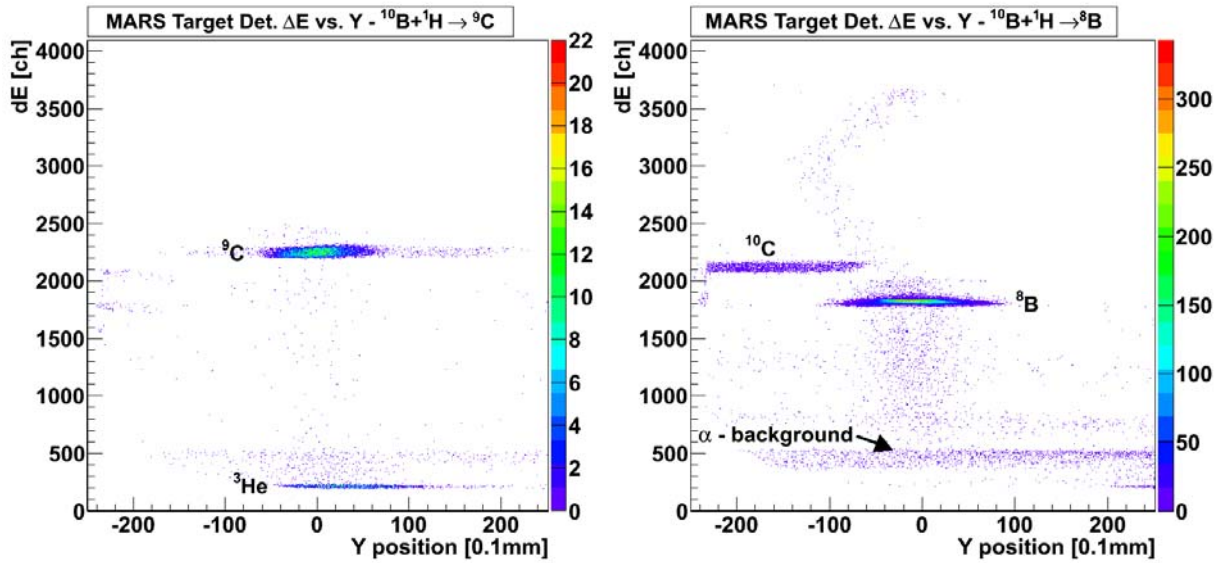

FIG. 3. (left panel) Results of the ^{9}C production test. The main contaminant of the secondary beam is from ^{3}He. (right panel) Results of the ^{8}B production test. The contributions from the ^{10}C and other backgrounds will be reduced by the MARS slits for the planned experiments.

For the ^{8}B production test, a ^{10}B primary beam at 24 MeV/u bombarded the MARS gas cell target. The gas cell target was filled with 2 atm of hydrogen gas at a temperature of 77K. The ^{8}B was produced with the (p,t) reaction in inverse kinematics. The Q-value for the p(^{10}B,^{8}B)t reaction is -18.5 MeV. Thus, 24 MeV/u was chosen for the primary beam energy to have a good production rate for ^{8}B, while still producing it at a reasonable energy. The optimum setting for the ^{8}B production in case was found at the MARS D1 dipole setting of 451 A, which corresponds to a ^{8}B beam energy of 21.1 MeV/u. For the planned experiment, this energy will also be reduced to ~10 MeV/u with degraders.

The optimized production rate for the ^{8}B secondary beam was 130 events/nC, which will give ~3*10^{4} particles/sec with 250 nA of ^{10}B beam on target. The ^{8}B secondary beam was relatively pure, although there is some contamination in the beam from α-particles. Some of this contamination will be removed in the future experiment by closing the slits of MARS and focusing the beam better with the quadrupole magnets of MARS.

The MARS target detector spectra for the ^{9}C and ^{8}B secondary beams are shown in Fig. 3.

IV. Production of ^{20}O secondary beam

The final production tests for this year were to produce and separate ^{20}O secondary beam with MARS at two energies. ^{20}O secondary beam was requested by group of Prof. Rogachev and by a group from Washington University in St. Louis (WUSTL) for separate experiments planned for later this year.

In the first production test, an ^{18}O primary beam at 15 MeV/u bombarded the MARS gas cell target. The gas cell was filled with ^{4}He gas at a pressure of 2 atm and a temperature of 77K. The reaction of ^{18}O+^{4}He had been employed previously to produce ^{20}O with MARS in 2007 [6]. In the previous measurement, it was noted that in addition to ^{20}O, this reaction produced other secondary beams in charge states with the same charge-to-mass (q/m) ratio, and in some cases, the same mass as the ^{20}O^{+8}. To properly identify these contaminants in the secondary beam, a 143 μm thick position sensitive silicon detector was employed as the ΔE detector in the MARS focal plane and a 500 μm thick silicon detector was used behind it. Thus the particle identification could be verified with both the ΔE vs. Y-position and ΔE vs. E techniques.

The result of the ^{20}O production test with the ^{18}O+^{4}He reaction is shown in Fig. 4, left panel. The secondary beam contained 6 species, ^{20}Ne^{+8}, ^{20}F^{+8}, ^{20}O^{+8}, ^{15}N^{+6}, ^{15}C^{+6} and ^{10}Be^{+4}. These other species cannot be separated from the ^{20}O^{+8} by MARS because they all have q/m = 0.4. Of particular note is the ^{20}F^{+8}, which is produced at 2 times the rate of the ^{20}O^{+8}. The best production rate of ^{20}O^{+8} obtained was 9.8 eV/nC at the MARS D1 dipole setting of 450 A. This corresponds to a secondary beam energy of 8.7 MeV/u for the ^{20}O^{+8}. With about 115 nA of ^{18}O beam on target, ^{20}O^{+8} rates of ~10^{3} particles/sec are possible.

In the second production test, a ^{22}Ne primary beam at 31 MeV/u bombarded the MARS gas cell target. This time, the gas cell was filled with ^{2}H gas at a pressure of 2 atm and a temperature of 77K. The reaction of ^{22}Ne+^{2}H was employed because LISE++ simulations [2] predicted that it would have would less contamination in the secondary beam from ^{20}F^{+8}. Further, the simulation also predicted that ^{22}Ne+^{2}H would have a better cross section for ^{20}O at the higher beam energy requested by the WUSTL group. To

identify the reaction products, the same 143 μm thick position sensitive silicon detector was employed as the ΔE detector in the MARS focal plane and a 500 μm thick silicon detector was used behind it.

The result of the ^{20}O production test with the ^{22}Ne+^{2}H reaction is shown in Fig. 4, right panel. The secondary beam again contained 6 species, ^{20}Ne^{+8}, ^{20}F^{+8}, ^{20}O^{+8}, ^{15}N^{+6}, ^{15}C^{+6} and ^{10}Be^{+4}. These other species cannot be separated from the ^{20}O^{+8} by MARS again because they all have q/m = 0.4. The best production rate of ^{20}O^{+8} obtained was 10.1 eV/nC at the MARS D1 dipole setting of 818 A. This corresponds to a secondary beam energy of 25.0 MeV/u for the ^{20}O^{+8}. With about 100 nA of ^{22}Ne beam on target, ^{20}O^{+8} rates of 10^3 particles/sec again are possible, which is similar to the lower energy case. However, with the ^{22}Ne+^{2}H reaction, ^{20}O^{+8} is the most intense species in the secondary beam and is more than 2 times as intense as the ^{20}F^{+8}. This result is consistent with what was predicted by the LISE++ simulation.

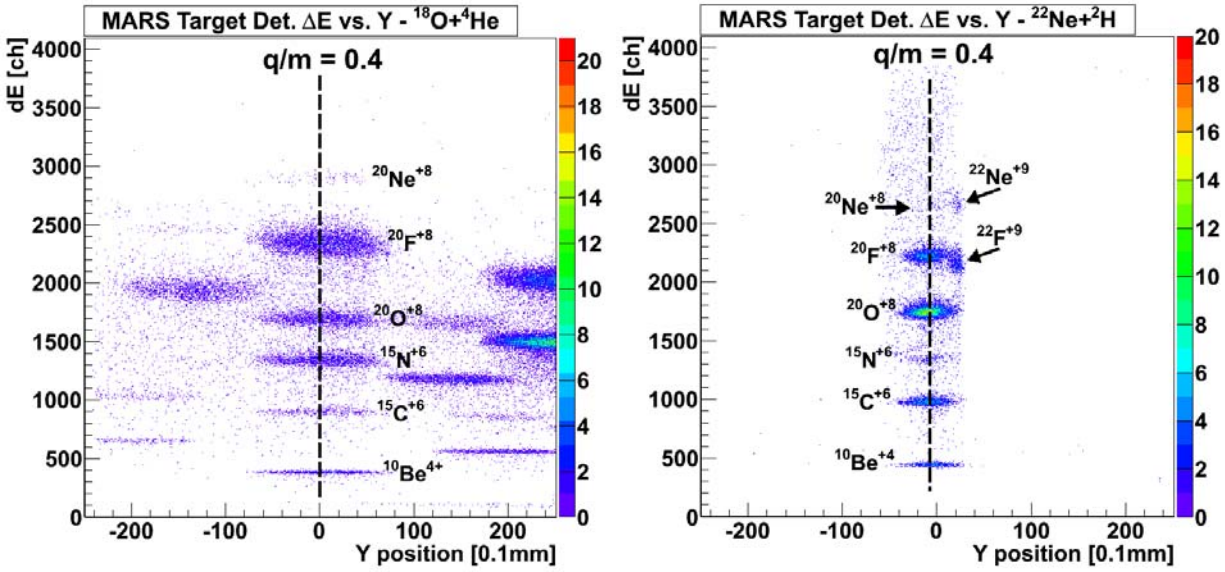

FIG. 4. (left panel) Results of the ^{20}O production test with the ^{18}O+^{4}He reaction at 15 MeV/u. Components of the secondary beam with q/m=0.4 can not be separated from the ^{20}O. The final slits of MARS were left open in this experimental run. (right panel) Results of the ^{20}O production test with the ^{22}Ne+^{2}H reaction at 31 MeV/u. The results are similar to the lower energy case, except that the ^{20}O in this case is the most intense component of the nuclei with q/m = 0.4. The final slits of MARS were also closed around the ^{20}O in this experimental run.

The contamination in the ^{20}O secondary beams will require event-by-event tracking of the secondary beam. The planned experiments will take this consideration into account.

[1] R.E. Tribble, R.H. Burch and C.A. Gagliardi, Nucl. Instrum. Methods Phys. Res. **A285**, 441 (1989).

[2] O.B. Tarasov and D. Bazin, Nucl. Instrum. Methods Phys. Res. **B266**, 4657 (2008).

[3] H.I. Park *et al.*, *Progress in Research*, Cyclotron Institute, Texas A&M University (2013-2014).

[4] L. Trache *et al.*, *Progress in Research*, Cyclotron Institute, Texas A&M University (2007-2008), p.I-29; http://cyclotron.tamu.edu/2007 Progress Report/index.html.

[5] V. Goldberg *et al.*, *Progress in Research*, Cyclotron Institute, Texas A&M University (2008-2009), p.I-21; http://cyclotron.tamu.edu/2009 Progress Report/index.html.
[6] C. Fu *et al.*, *Progress in Research*, Cyclotron Institute, Texas A&M University (2007-2008), p.I-38; http://cyclotron.tamu.edu/2007 Progress Report/index.html.

Investigation of the structure of nuclear cluster states at the University of São Paulo, Brazil

B. T. Roeder, M. R. D. Rodrigues,[1] T. Borello-Lewin,[1] L. B. Horodynski-Matsushigue,[1] J. L. M. Duarte,[1] C. L. Rodrigues,[1] H. Miyake,[1] X. X. Zhang,[1] and G. M. Ukita[2]

[1]*Instituto de Física, Universidade de São Paulo, São Paulo-SP, Brasil*

[2]*Faculdade de Psicologia, Universidade de Santo Amaro, São Paulo-SP, Brasil*

This year, we have started a collaboration with the Light-Ion Spectroscopy group at the University of São Paulo in Brazil. For many years, the Light-Ion Spectroscopy group has been measuring transfer reactions with the Pelletron-Enge-Split-Pole facility at the University of São Paulo. Recently, this group has become interested in measuring α-particle transfer reactions, such as the (^{6}Li,d) reaction, in order to investigate the cluster structure in highly-excited states of light nuclei [1]. Their experimental setup has several advantages for making these measurements. First, the beam produced by their Tandem Van de Graff Accelerator (Pelletron) has high energy resolution and be tuned to an extremely small beam spot size. Second, the Enge Split-Pole spectrograph [2] can select and separate specific reaction products and focus them at the exit of the spectrograph. Finally, the particles are detected with the nuclear emulsion technique which allowed them to obtain an excellent detection resolution of 15 keV in their most recent measurement of the ^{12}C(^{6}Li,d)^{16}O reaction [3].

In the near future, the Light-Ion Spectroscopy group is planning to build a new focal plane detector for the Enge Split-Pole spectrograph in collaboration with the University of Orsay, France and the Laboratori Nazionali del Sud in Catania, Italy that will allow for coincidence measurements and the measurement of heavier ions with the spectrograph. In preparation for this new detector, a simulation of the Enge Split-Pole spectrograph has been developed with the GEANT4 toolkit [4]. A diagram of the Enge Split-Pole spectrograph and a figure showing the GEANT4 simulation are shown in Fig. 1. The

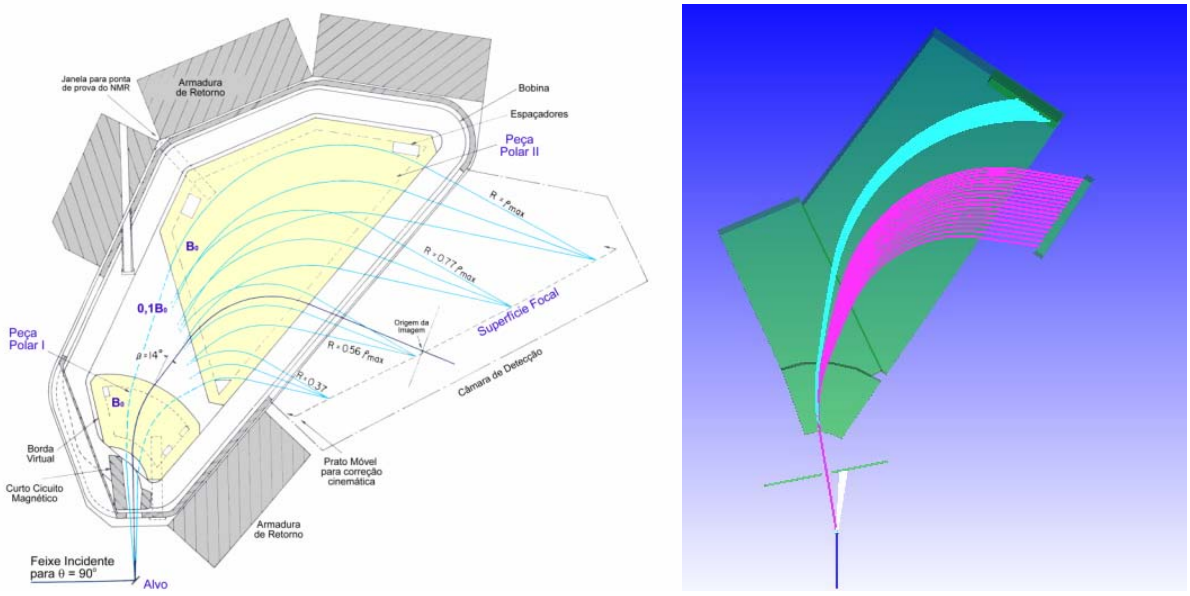

FIG. 1. (Left) Schematic representation of the Enge split-pole magnetic spectrograph with lines showing the paths of particles with different magnetic rigidities. (Right) GEANT4 simulation of the Enge split-pole magnetic spectrograph showing the separation between protons (magenta tracks) and deuterons (light-blue tracks) from different reactions.

reactions $^{12}C(^{6}Li,d)^{16}O$ and $^{12}C(^{6}Li,p)^{17}O$ are simulated with the magnetic field of the spectrograph set for the protons. In the simulation, the particles from the two reactions are well-separated.

In order to test the capabilities of the Enge Split-Pole spectrograph, as well as to obtain new data for ^{17}O at high excitation energies, we have proposed an experiment to measure the $^{12}C(^{6}Li,p)^{17}O$ reaction with a ^{6}Li beam energy of 28.4 MeV. This reaction, along with the similar reaction $^{12}C(^{7}Li,d)^{17}O$, was measured previously by Crisp *et al.* [5]. While differential cross sections were obtained in that work for levels in ^{17}O up to 12.5 MeV excitation, in the spectrum from the detector (see Fig. 2) they show that they were able to populate states up to 13.5 MeV excitation and beyond. More recently, Milin et al. [6] measured the $^{13}C + {}^{9}Be \rightarrow {}^{13}C+2\alpha+n$ reaction and were able to reconstruct ^{17}O states with $^{13}C+\alpha$ coincidences. While their detection resolution was relatively poor, they were able to populate ^{17}O levels up to 19 MeV excitation. Clearly, a high-resolution measurement of ^{17}O at these high-excitation energies would help to reveal the structure of ^{17}O in this region, and perhaps indicate the presence of new cluster states.

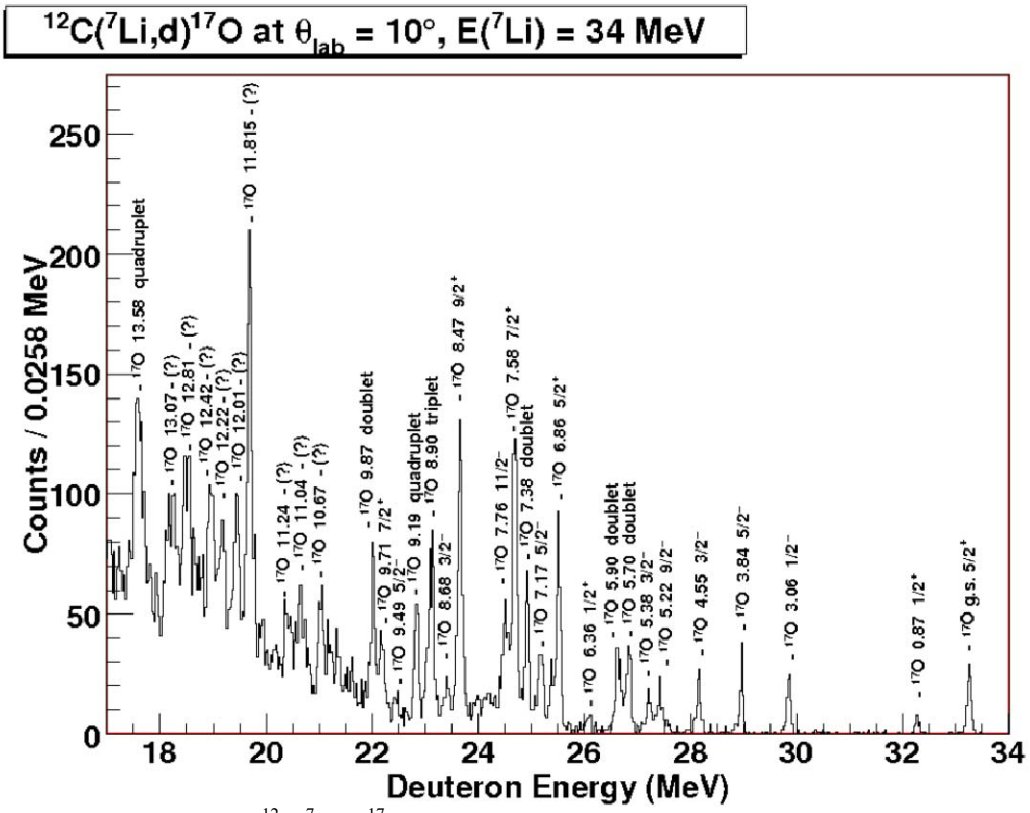

FIG. 2. Spectrum of the $^{12}C(^{7}Li,d)^{17}O$ reaction from Crisp *et al.* [5]. Several strongly-populated states from ^{17}O are shown above 11 MeV excitation.

The $^{12}C(^{6}Li,p)^{17}O$ measurement will be conducted at the Pelletron-Enge-Split-Pole facility at the University of São Paulo this July. The proton tracks, shown in magenta in the simulation of Fig. 1, show that ^{17}O states from 11 MeV to 20 MeV excitation can be measured in the focal plane of the spectrograph with a single magnetic field setting. Assuming that the $^{12}C(^{6}Li,p)^{17}O$ measurement is successful, the

$^{12}C(^{7}Li,d)^{17}O$ might be measured in the future for comparison. However, the $^{12}C(^{7}Li,d)^{17}O$ reaction may require the use of silicon detector telescopes in the focal plane, or perhaps the new focal plane detector, in order to properly identify the deuteron reaction products.

[1] M. Freer, Rep. Prog. Phys. **70**, 2149 (2007).
[2] J.E. Spencer and H.A. Enge, Nucl. Instrum. and Meth. **49** 181 (1967).
[3] M.R.D. Rodrigues *et al.*, Phys. Rev. C **89**, 024306 (2014).
[4] S. Agostinelli *et al.*, Nucl. Instrum. Methods Phys. Res. **A506**, 250 (2003).
[5] A.M. Crisp *et al.*, Phys. Rev. C **77**, 044315 (2008).
[6] M. Milin *et al.*, Eur. Phys. J. A **41**, 335 (2009).

Production of proton-rich *T*=2 superallowed β-decaying nuclei

R. S. Behling, B. Fenker, M. Mehlman, D. Melconian, and P. D. Shidling

Part of our recent efforts have been directed in investigating in detail the production and separation of radioactive ion beams in the energy range expected from the K150 cyclotron. Low energy secondary beams for the TAMUTRAP facility will be delivered by the Cyclotron Institute's T-REX upgrade project. In short, a large-bore 7T superconducting solenoid will act as a separator following the production target, and the high-energy RIB will be slowed and collected as a low-energy (15 keV) beam using the ANL-type heavy-ion gas catcher.

We will employ the in-flight method for producing nuclei of our interest. Our recent measurement and calculations indicate that the application of fusion evaporation or projectile fragmentation reactions seems to be a very efficient way to produce proton rich nuclei at the K150 energies. Calculations for nuclei of our interest were carried out using LISE [1] for fusion evaporation and EPAX [2] for projectile fragmentation. In Table I we tabulate proposed target and projectile combination for producing nuclei of our interest via fusion evaporation reaction in inverse kinematic mode. Secondary beams in this mode will be more forward directed with a relative small emittance.

Table I. Calculated production rates of the *T*=2 superallowed proton emitting nuclei that may be measured at TAMUTRAP. All reactions use a ^{3}He gas target cooled to 77K.

RIB	Primary Beam	Calculated Cross-section [$\times 10^{-3}$mb]	Estimated production rate [$\times 10^{5}$ pps]
^{20}Mg	^{20}Ne @ 24 MeV/u	16.2	14.0
^{24}Si	^{24}Mg @ 23 MeV/u	15.5	6.5
^{28}S	^{28}S @ 23 MeV/u	4.5	1.5
^{32}Ar	^{32}S @ 23 MeV/u	7.3	1.4
^{36}Ca	^{36}Ar @ 23 MeV/u	6.3	2.5
^{40}Ti	^{40}Ca @ 23 MeV/u	1.7	0.7

We have recently performed a ^{32}Ar production experiment using the K500 Cyclotron in combination with the MARS spectrometer to: (1) verify that the proposed reaction is able to produce ^{32}Ar; (2) estimate the total isobaric yields (A=32); and (3) determine the experimental production cross section of ^{32}Ar and compare it with the theoretical prediction.

^{32}Ar was produced in an inverse kinematics reaction by bombarding a primary beam of ^{32}S at 23 MeV/u on a 1 atm. ^{3}He gas target cooled to liquid nitrogen temperature. Reaction products were analyzed using MARS with a total momentum acceptance of $\Delta p/p$ = 1.92% . Reaction products were identified using position sensitive strip detector in the focal plane of MARS. Fig. 1 shows the energy loss versus the vertical *Y*-position in the strip detector. The yield of different isotopes/products and isobars produced in this reaction were determined by recording the 2D spectrum for different rigidity settings of MARS. The preliminary conclusion of this measurement is that the proton rich nuclei of our interest can be produced using a fusion evaporation reaction. We are currently working on determining the experimental cross

section of ^{32}Ar. In the coming year on the experimental front, we will be performing ^{24}Si production experiment via fusion evaporation reaction, and production of ^{32}Ar via projectile fragmentation. On the theoretical front, we will be estimating the production cross section of proton rich nuclei of our interest using TALYS code [3].

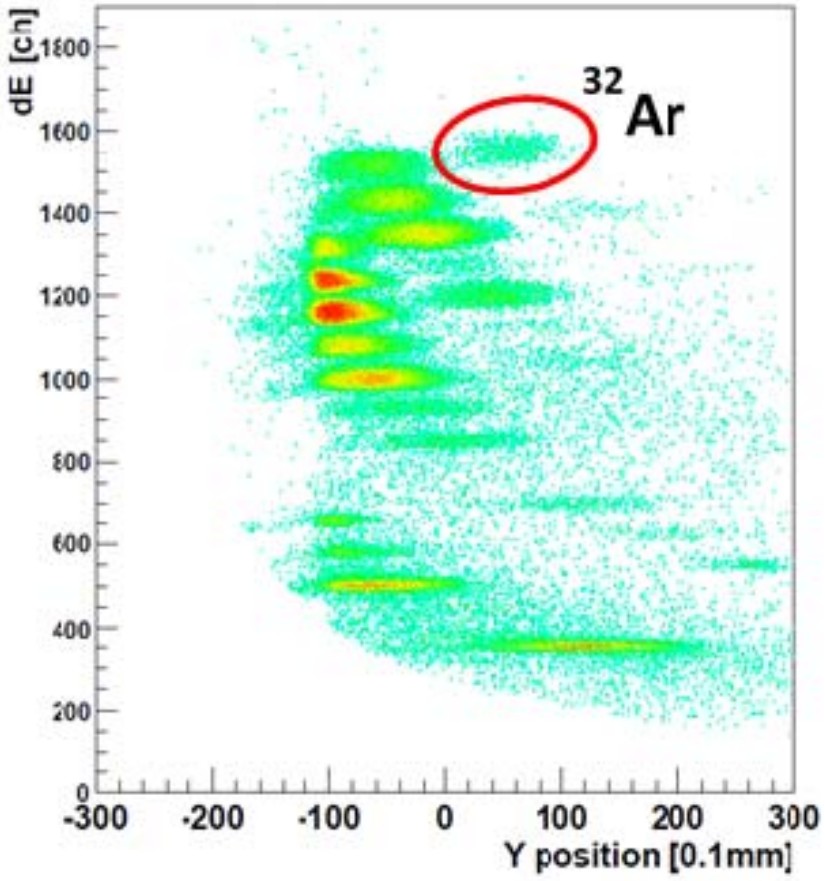

FIG. 1. Results of ^{32}Ar production run. The 2D plot of the energy loss versus Y position in the strip detector separates the different reaction products; the isotope of interest, ^{32}Ar, is clearly resolved.

[1] O. Tarasov, D. Bazin, M. Lewitowicz and O. Sorlin, Nucl. Phys. **A701**, 661 (2002).

[2] K. Suemmerer and B. Blank, Phys. Rev. C **61** (2000) 034607.

[3] http://www.talys.eu/

First-ever measurement of the β-asymmetry parameter from Laser-Cooled atoms: Status of the ^{37}K experiment at TRIUMF

R. S. Behling, B. Fenker, M. Mehlman, D. Melconian, and P. D. Shidling

Recently the TRINAT collaboration made up of members from the Texas A&M University Cyclotron Institute and TRIUMF in Vancouver BC undertook an experiment to measure for the first time the β-asymmetry of ^{37}K. The analysis of the data is nearing a conclusion and the publication of the physics result is forthcoming.

There have been a number of major analysis task that have been completed in the last year. First a major bug was found in the readout of the detector data stream. The effect of this was that the silicon detector signals and the signals from the scintillator detectors were read out into different events. This lead to unexpected results when imposing coincidences between detectors. The bug has subsequently been patched and coincidence conditions using the strip detectors are now reliable.

The correction of the previously mentioned software bug enabled the completion of the calibration of all of the scintillators and all of the 160 channels from the silicon detectors. Using this calibration has allowed us to develop our analysis of the asymmetry as a function of β energy in addition to what we originally looked at which was the asymmetry as a function of the optical pumping time. Additionally the asymmetry as a function of cos(θ) was investigated, but with small detectors and low statistics it is difficult to make meaningful bins in cos(θ).

In this experiment we had very few ^{37}K atoms in the trap for a number of reasons that were enumerated in our report from 2013. One of the consequences of this is that the previously used technique of measuring the polarization by counting photo-ions was not available. We have subsequently decided to use an offline measurement of the polarization made with ^{41}K. It can be shown that the uncertainty that would arise from the change in isotopes is small because the hyperfine structures are extremely similar and the isotope shift is well measured. Reproducing the experimental conditions of the run turns out to be the largest source of uncertainty in using such a measurement. Examples of the types of systematic effects that we considered were the temperature of the liquid crystal variable retarders, the power in the laser sidebands, and long timescale drifts of the power supplies. Our final number for the polarization of the ^{37}K in the December 2012 run and the largest systematic error in the experiment is 99±1%.

The analysis of the data is ongoing and we expect to publish the results shortly. We are continuing to quantify some systematic errors such as the effect of cloud movement and uncertainties in the energy calibrations of the detectors. These effects are small in comparison to the statistical uncertainty which is ~1% and the uncertainty in the polarization. Currently at TRIUMF setup is underway for a follow up experiment that will collect ~x20 more data and will have better tools to determine the polarization such as a position sensitive electron MCP that will provide complementary information to what is currently provided by the ion MCP. Additionally each of these detectors has been optimized to increase the signal to noise ratio for better background suppression.

α ANCs of the near α-threshold states in ^{16}O, ^{17}O and ^{20}Ne

G. V. Rogachev, E. Koshchiy, M. L. Avila,[1] L. Baby,[1] and D. Santiago-Gonzales[1]
[1]*Department of Physics, Florida State University, Tallahassee, Florida*

The ^{12}C(α,γ) and ^{13}C(α,n) are two very important reactions for nuclear astrophysics. The first one is considered the "Holy Grail" of nuclear astrophysics. During the helium burning process in a massive star the ^{12}C to ^{16}O ratio determines the subsequent nucleosynthesis of heavier elements. This ratio is set by the ^{12}C(α,γ) reaction rate. The relative carbon/oxygen abundance in the Universe also hinges on the rate for this reaction. The ^{13}C(α,n) reaction is an important source of neutrons for the s-process, slow neutron capture that is believed to be responsible for the production of half of all chemical elements in the Universe that are heavier than Iron. Direct measurements of these astrophysically important reaction rates cannot be done due to very small cross sections at energies of interest. This is because at low energies, relevant for stellar nucleosynthesis, the cross section of the reactions that involve charged particles is strongly suppressed due to the Coulomb barrier. Therefore, one has to rely on extrapolation made from the direct measurements at higher energies down to the energy of interest. However, near α-threshold resonances with unknown properties may affect these extrapolation for the ^{12}C(α,γ) and ^{13}C(α,n) reactions. The goal of this work was to measure the α-particle Asymptotic Normalization Coefficients (ANC) for the excited states in ^{16}O and ^{17}O. This is done by measuring the cross section for the (^{6}Li,d) α-transfer reaction at sub-Coulomb energy. This technique was first suggested in Ref. [1] and was further developed in [2,3]. The main advantage of the method is substantial and quantifiable reduction of the dependence of the final result on specifics of theoretical analysis. The only unknown value for the relevant resonances in ^{16}O and ^{17}O is the corresponding α-ANC. Once it is known, the contribution of the specific state to the reaction rate can be evaluated. In spite of the fact that the method of sub-Coulomb α-transfer reaction was used previously, no direct verification of the accuracy of this method was reported.

We performed the verification of the sub-Coulomb α-transfer technique by measuring the ANC of the 1^- state at 5.8 MeV in ^{20}Ne using the ^{16}O(^{6}Li,d) reaction. All experiments discussed in this report were carried out at the John D. Fox superconducting linear accelerator facility at Florida State University. The partial α-width of the 1^- state (same as the total width) is known from direct measurements (28±0.3 eV). It can also be calculated from the measured ANC using formulation suggested in [4]. This gives the value of 29±6 eV. The 6 eV uncertainty includes statistical and systematic experimental uncertainties and also uncertainty related to the theoretical analysis. The agreement with the known value is excellent.

The excited states in ^{16}O that influence the ^{12}C(α,γ) reaction rate the most are the 1^- at 7.12 MeV and 2^+ at 6.92 MeV. ANCs for these states were measured previously in [1], and the ANC values determined in this work are in good agreement with the previous measurements. However, the 0^+ state at 6.05 MeV can also contribute through the direct α-capture. The α ANC for this state have not been measured before. We measured the ^{12}C(^{6}Li,d) reaction cross section at several beam energies. The reaction was performed in inverse kinematics (^{12}C beam, E_{12C} = 5, 7 and 9 MeV). Recoil deuterons were detected at the forward angle (backward angle in c.m.) by a telescope detector. The telescope consisted of position sensitive propositional counter, backed by an array of silicon pin-diode detectors. Pure ^{6}Li target

was used. Spectrum of deuterons is shown in Fig. 1. All three states relevant for the α-capture reaction rate are populated. Angular distributions for the 0^+ state measured at three beam energies (5, 7 and 9 MeV) are shown in Fig. 2. Curves are the corresponding DWBA fits. It is clear from the shape of angular

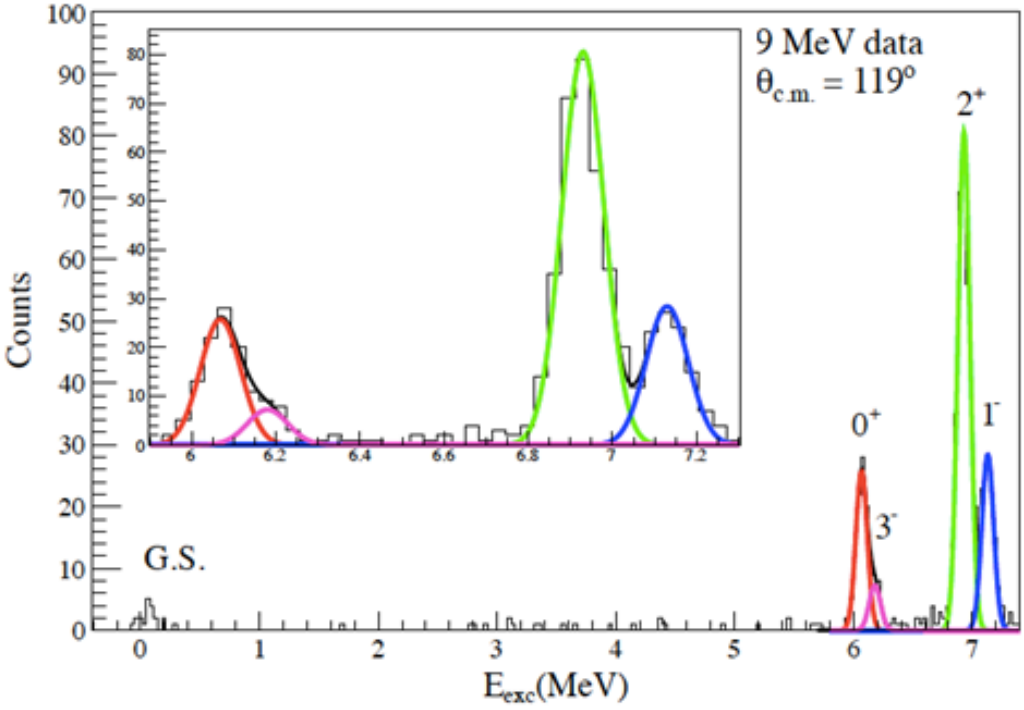

FIG. 1. Spectrum of deuterons from the ^{6}Li(^{12}C,d) reaction at E_{12C} = 9 MeV. The astrophysically relevant 1^-, 2^+ and 0^+ excited states in ^{16}O are populated.

distributions that reaction becomes sub-Coulomb at 5 MeV (the cross section is peaked at 180° c.m.). The ANC of the 0^+ state at 6.05 MeV was determined to be 2.25 ± 0.82 x 10^6 fm^{-1}. The contribution of this state to the astrophysical S-factor determined from the measured ANC at the energies relevant for astrophysics is 2-3 keV b. All of it is due to a direct E2 transition (E1 and E0 are negligible). This is only about 2% of the total s-factor value for the ^{12}C(α,γ) at 300 keV [1]. Although small, this value is at the level of the desired uncertainly for the S-factor for this reaction. Our result eliminates the uncertainty that was associated with contribution of the 0^+ state to the ^{12}C(α,γ) reaction rate.

The ANC for the $1/2^+$ state at 6.356 MeV in ^{17}O was determined using the ^{13}C(^{6}Li,d) reaction. Previously the SF_α and ANC for this state were measured [5,2,6,7,8], but results were not consistent. We remeasured the ANC for this state to constrain its contribution to the ^{13}C(α,n) reaction rate. The coulomb-modified ANC determined in this work is 3.4+/-0.5 fm^{-1}. It is the most precise measurement and it is consistent with [6,7] but not consistent with [5,2,8]. We used the same sub-Coulomb α-transfer reaction (^{6}Li,d) that was used in [2]. We believe that disagreement with [2] is caused by the fact that the target thickness was not controlled during the run in Ref. [2], and the effective beam energy in the middle of the target was changing due to target deterioration. This beam energy shift caused the lower (wrong) value of the ANC in [2]. The analysis in [5] appears to be wrong (as shown in [9]). The Trojan Horse Method

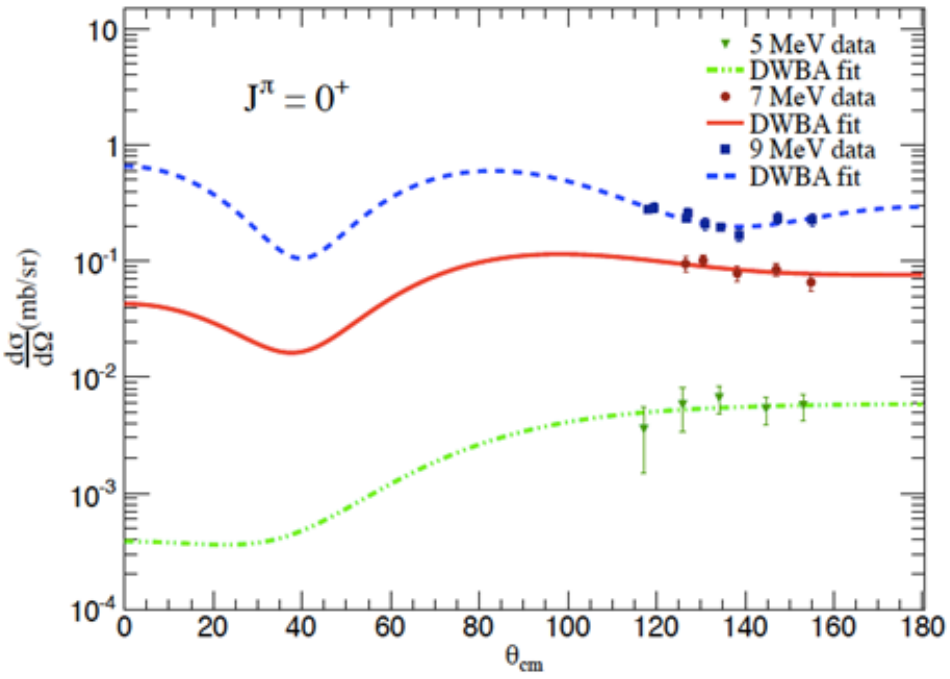

FIG. 2. Angular distribution of deuterons for the ^{6}Li(^{12}C,d) reaction measured at three beam energies (5, 7 and 9 MeV) and the corresponding DWBA fits.

(THM) was used to determine ANC in [8] and it has the largest value of all previous measurements, $6.7^{+0.9}_{-0.6}$ fm^{-1}. We do not have a good explanation what can cause the difference of the ANC values determined from the α-transfer reactions ([6,7] and this work) and the THM measurements [8].

In summary, the sub-Coulomb α-transfer reaction is a very useful tool to determine ANCs for the near α-threshold states that can then be used to constrain the astrophysical reaction rate. The method was verified using the 1^- state at 5.8 MeV in ^{20}Ne with the known partial α-width. The ANCs for the 0^+ state at 6.05 MeV in ^{16}O and $1/2^+$ state at 6.356 MeV in ^{17}O, that contribute to the astrophsically important ^{12}C(α,γ) and ^{13}C(α,n) reaction rates, were measured. The contribution of these states to the astrophysical S-factor were evaluated.

[1] C.R. Brune, W.H. Geist, R.W. Kavanagh, and K.D. Veal, Phys. Rev. Lett. **83**, 4025 (1999).

[2] E.D. Johnson, G.V. Rogachev *et al.*, Phys. Rev. Lett. **97**, 192701 (2006).

[3] E.D. Johnson, G.V. Rogachev *et al.*, Phys. Rev. C **80**, 045805 (2009).

[4] A. Mukhamedzhanov and R.E. Tribble, Phys. Rev. C **59**, 3418 (1999).

[5] S. Kubono *et al.*, Phys. Rev. Lett. **90**, 062501 (2003).

[6] M.G. Pellegriti *et al.*, Phys. Rev. C **77**, 042801 (2008).

[7] B. Guo *et al.*, Astrophys. J. **756**, 193 (2012).

[8] M. La Cognata *et al.*, Phys. Rev. Lett. **109**, 232701 (2012).

[9] N. Keeley, K. Kemper, and D.T. Khoa, Nucl. Phys. **A726**, 159 (2003).

α-cluster structure of ^{18}O

G. V. Rogachev, V. Z. Goldberg, M. L. Avila,[1] E. D. Johnson,[1] K. W. Kemper,[1] D. Robson,[1]
Yu. M. Tchuvilśky,[2] and A. Volya[1]
[1]*Department of Physics, Florida State University, Tallahassee, Florida*
[2]*Lomonosov Moscow State University, 119992 Moscow, Russia*

The concept of α-clustering has been successfully applied to explain multiple features in nuclear spectrum. In particular, a number of known structure peculiarities in light N=Z, 4N nuclei, such as ^{8}Be, ^{12}C, ^{16}O, and ^{20}Ne is associated with clustering. The most striking are the twin α-cluster, inversion doublet, quasi-rotational bands. All members of these bands that have excitation energies above the α-decay threshold have α-reduced widths close to the single particle limit, indicating their extreme α-cluster character. Extensive experimental and theoretical studies ([1] and references therein) lead to understanding of these bands as well developed α+core structures.

It proved to be far more difficult to study clustering phenomena in non-self-conjugate nuclei. Clustering might manifest itself in a much more complex way in these nuclei. This is because the ``extra'' nucleons introduce additional degrees of freedom which may modify: enhance or destroy cluster structures. In addition to that there are difficulties of the experimental studies, which require a more complicated analysis due to the presence of low-lying nucleon decay channels and higher level density. On the other hand, the investigation in this region seems very promising because the structure and decay information about states in non-self-conjugate nuclei allows one to explore the interplay between the single nucleon and cluster degrees of freedom. An ^{18}O nucleus represents an attractive target for such investigation, it is a non-self-conjugate nucleus that is in close proximity to the ^{16}O and ^{20}Ne, nuclei with well developed and extensively studied cluster structure.

The cluster structure of ^{18}O was studied using detailed R-matrix analysis of the α+^{14}C elastic scattering excitation functions. Measurements were performed at the John D. Fox Superconducting Linear accelerator facility at the Florida State University using Thick Target Inverse Kinematics technique. The complete excitation function for 180^{o} in c.m. for the entire energy range measured in this experiment is shown in Fig. 1.

We have performed detailed R-matrix analysis. Spin-parity assignments, excitation energies and partial widths were determined for 54 excited states in ^{18}O. Detailed description of the 18O level structure will be published in [2]. The ^{14}C(α,α) elastic scattering is particularly sensitive to the states that have α+^{14}C(g.s.) configuration and completeness of experimental data complemented by the detailed R-matrix analysis allows for most accurate assessment of α-clustering phenomena in ^{18}O.

Search for α-cluster inversion doublet rotational bands in ^{18}O has been a subject of many experimental and theoretical studies [3-7], but corresponding assignments remained controversial. Based on the results of this work we conclude that unlike for N=Z, ^{16}O and ^{20}Ne nuclei, the α-strength is split about evenly between two or more states for each spin-parity and it is not possible to define an inversion doublet rotational bands in the same sense as for ^{16}O and ^{20}Ne nuclei. This splitting is likely the result of configuration mixing. The Cluster-Nucleon Configuration Interaction Model (CNCIM) [8] calculations

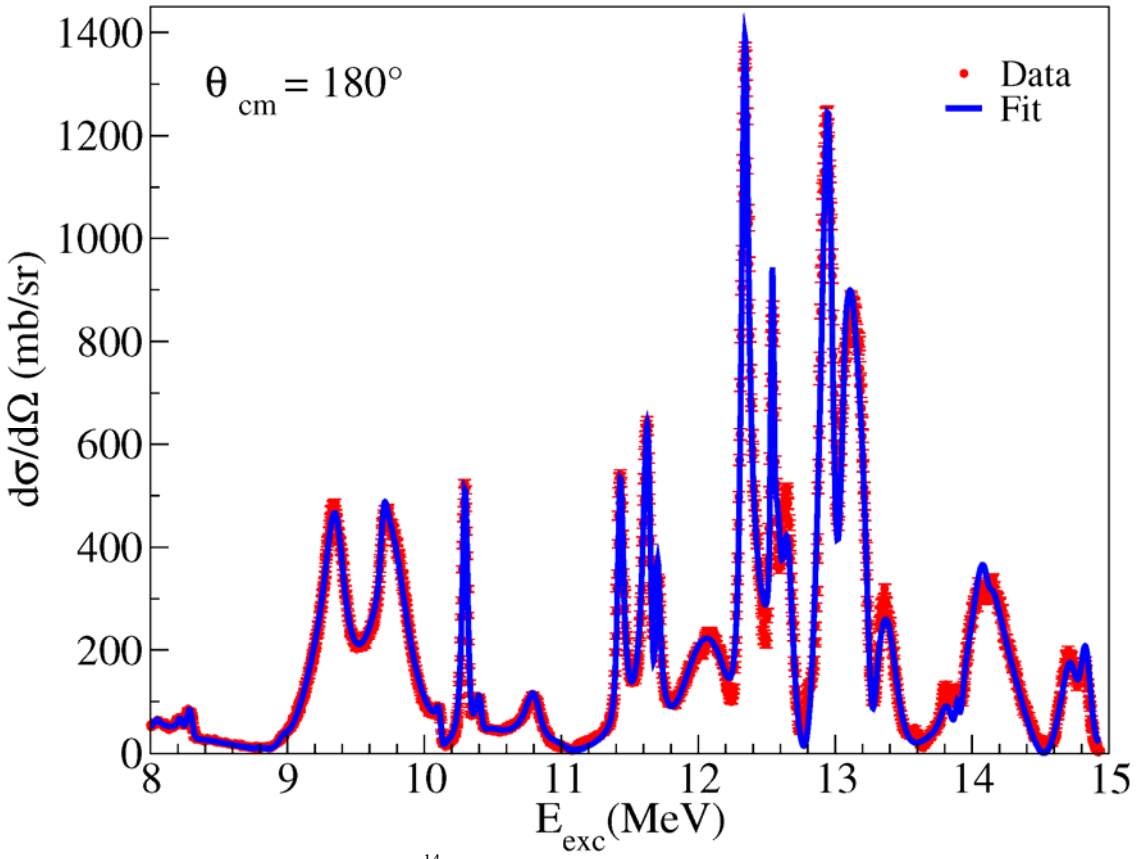

FIG. 1. The excitation function for $\alpha+^{14}C$ elastic scattering at 180◦ in c.m. for the entire energy range measured in this experiment. The solid curve is the best R-matrix fit.

performed for 18O in this work indicate that splitting of α-strength for the positive parity band is the result of $(1s0d)^4$, and $(0p)^2(1s0d)^2$, configuration mixing. For the negative parity states the (1p0f) shell (not included in the CNCIM) probably play an important role. These findings highlight importance of considering the nucleon and cluster degrees of freedom on an equal footing for the non-self-conjugate nuclei.

Assignment of the α-cluster rotational bands without knowledge of partial α-width is dangerous. The most striking example is the assignment of a 0^- inversion doublet rotational band in [3], where authors did the best they could without this crucial information. It turns out that all states in the 0^- rotational band suggested in [3] have α-strength that is at least a factor of 10 smaller than the α-strength of the strongest cluster state with the corresponding spin-parity. This obviously excludes them from being the members of the 0^- inversion doublet rotational band.

The broad, purely α-cluster 0^+ and 2^+ states at 9.9 MeV and 12.9 MeV were observed in ^{18}O. Most likely these states have similar nature (and configuration) as the well known 0^+ and 2^+ broad states in ^{20}Ne at 8.7 and 8.9 MeV [9].

[1] M. Freer, Rep. Prog. Phys. **70**, 2149 (2007).
[2] M. Avila *et al.*, Phys. Rev. C (submitted).

[3] W. von Oertzen *et al.*, Eur. Phys. J **43**, 17 (2010).
[4] A. Cunsolo *et al.*, Phys. Rev. C **24**, 476 (1981).
[5] A. Cunsolo *et al.*, Phys. Lett. B **112**, 121 (1982).
[6] P. Descouvemont and D. Baye, Phys. Rev. C **31**, 2274 (1985).
[7] N. Furutachi *et al.*, Prog. Theor. Phys. **119**, 403 (2008).
[8] A. Volya and Y. Tchuvilśky, IASEN2013 Conference Proceedings, World Scientific (2014).
[9] D. Tilley, H. Weller, C. Cheves, and R. Chasteler, Nucl. Phys. **A595**, 1 (1995).

Clustering in ^{10}Be

G. V. Rogachev, E. Koshchiy, V. Z. Goldberg, A. Kuchera,[1] M. L. Avila,[1] L. Baby,[1] J. Blackmon,[2] K. Macon,[2] D. Santiago-Gonzales,[1] and I. Wiedenhover[1]

[1]*Department of Physics, Florida State University, Tallahassee, Florida*

[2]*Department of Physics and Astronomy, Louisiana State University, Louisiana*

Clustering phenomena clearly manifest themselves in light nuclei. It is well established that the low-lying states in ^{8}Be can be described as a two-center structure [1]. Recent *ab initio* GFMC calculations explicitly show how this structure emerges naturally for the ^{8}Be ground state [2]. The suggestion that this two-center structure may survive when "valence nucleons" are added to the system has been made in the early 1970s [1]. A semiquantitative discussion of this subject can be found in [3] where the two-center molecular states in ^{9}B, ^{9}Be, ^{10}Be, and ^{10}B nuclei were considered in the framework of a two-center shell model. An AMD plus Hartree-Fock (AMD+HF) approach was proposed in [4] as a theoretical tool to study the structure of low-lying levels in ^{9,10,11}Be isotopes. Deformation (distance between the two α's) for several low-lying states in Be isotopes has been calculated. Very large deformation (~0.8) for the 6.179 MeV 0^+ state in ^{10}Be was suggested, which corresponds to an α-α inter-distance of 3.55 fm. This is 1.8 times more than the corresponding value for the ^{10}Be ground state. A similar result was obtained in [5] where the spectrum of ^{10}Be was reasonably well reproduced using a Molecular Orbital model. The second 0^+ state in ^{10}Be has an enlarged α-α distance and the highly deformed rotational band with large moment of inertia built on that configuration emerges according to these calculations. The 0^+ at 6.179 MeV and the 2^+ at 7.542 MeV in ^{10}Be are believed to be associated with this rotational band. The 4^+ member was suggested at 10.2 MeV. However, contradicting spin-parity assignments (3- in [6] and 4^+ in [7,8]) have been made for this state. No experimental information on the possible next member of this band, the 6+ state, (predicted, for example, in [9]) is available. The goal of this study was observation of the state at 10.2 MeV and determination of its spin-parity, and search for the next, 6+, member of this highly deformed rotational band.

The excitation function for ^{6}He+α elastic scattering was measured using Array for Nuclear Astrophysics and Structure with Exotic Nuclei (ANASEN). Experiment was carried out using RESOLUT rare isotope beam facility at the John D. Fox superconducting linear accelerator facility at the Florida State University. ANASEN is an active target detector. Helium gas with 5% admixture of CO_2 was used as an active volume. ANASEN consist of an array of silicon double sided strip detectors and an array of position sensitive proportional counters that allow for reconstruction of the recoil tracks. The angle integrated (75^o-135^o) excitation function is shown in Fig. 1. The strong peak at 2.78 MeV c.m. energy corresponds to the 10.2 MeV excited state in ^{10}Be. The R-matrix fit to angular distributions in the area of the 10.2 MeV state were used to determine the spin-parity of this state unambiguously as 4^+. The angular distribution for 2.72 MeV excitation energy is shown in Fig. 2. The solid curve on Fig. 2 is an R-matrix fit with the 4^+ state at 2.78 MeV. No other spin-parity assignment is consistent with the data. This assignment is consistent with the results of earlier ^{6}He+α measurements [7,10].

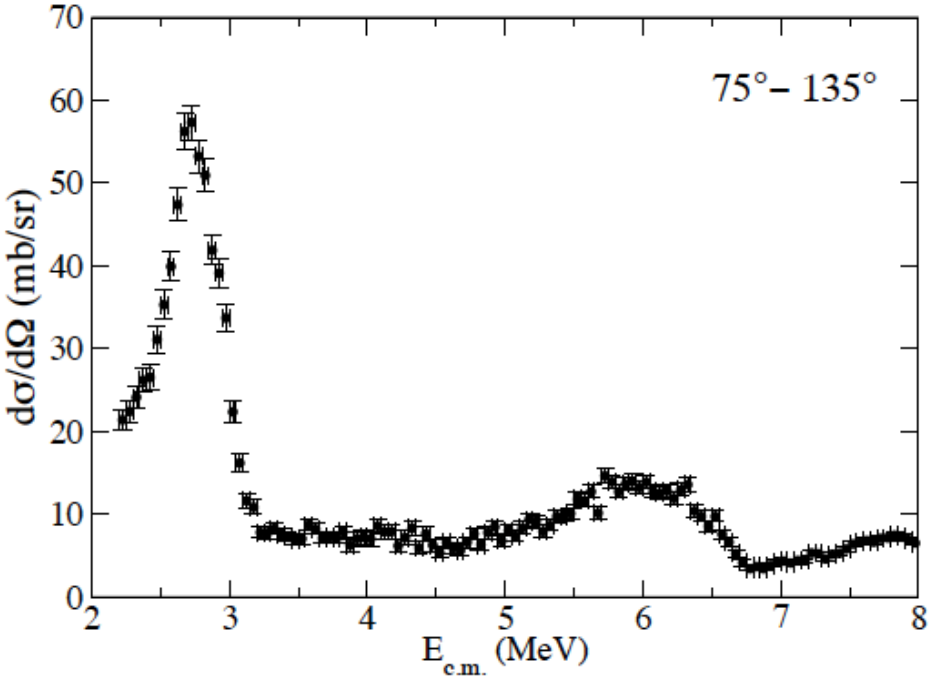

FIG. 1. Angle integrated (75° - 135°) excitation function for the ^{6}He+α elastic scattering measured using the Array for Nuclear Astrophysics and Structure with Exotic Nuclei (ANASEN).

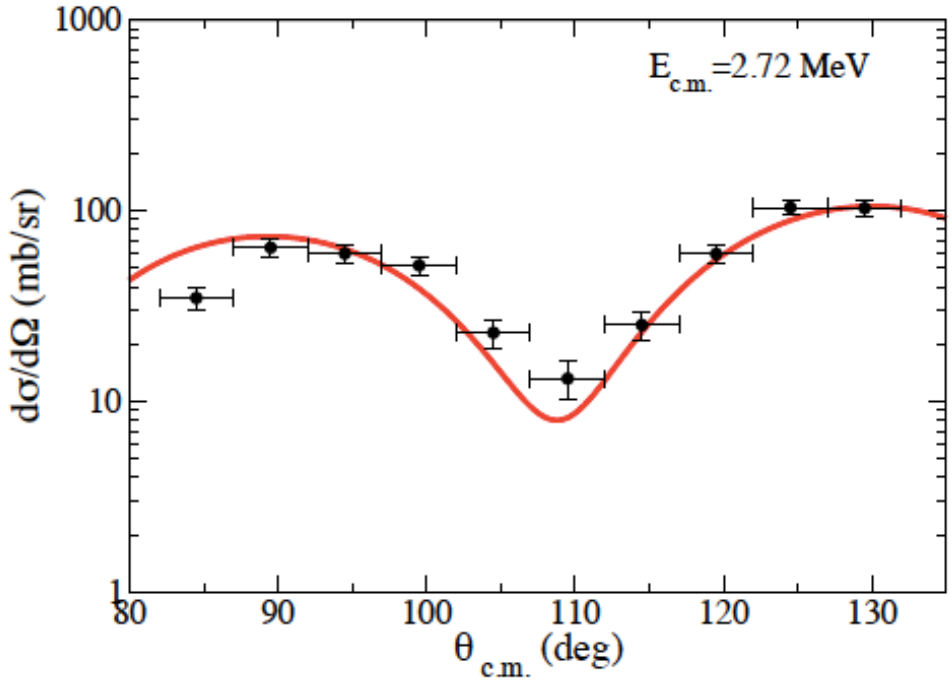

FIG. 2. Angular distribution for the ^{6}He+α elastic scattering at 2.72 MeV c.m. energy. The red solid curve is an R-matrix fit with a 4^{+} state at 2.78 MeV.

Another interesting feature of the measured ^{6}He+α excitation function is a broad peak at 6 MeV c.m. energy (13 MeV excitation energy of ^{10}Be). It is clearly visible in the 90°+/-5° excitation function (see Fig. 3), but it is not obvious at any other angle. This may indicate a high spin, positive parity state. The R-matrix fit to the 90° excitation function shown in Fig. 3 includes a highly clustered 6^+ state at 6.0 MeV. It is a good candidate for next, 6^+, member of the highly deformed rotational band mentioned above. However, the angular distribution over the wider angular range differ from the R-matrix prediction for the 6^+. This is probably due to the fact that lower orbital angular moment partial waves contribute (0^+ and 2^+, predominantly) and it is difficult to fix the corresponding phase shifts for this largely flat excitation function using only limited set of angles. Future measurement of the ^{6}He+α excitation function at angles close to 180° (where the 6^+ state has a strong maximum) is essential to decide if the peak at 6 MeV is indeed a 6^+.

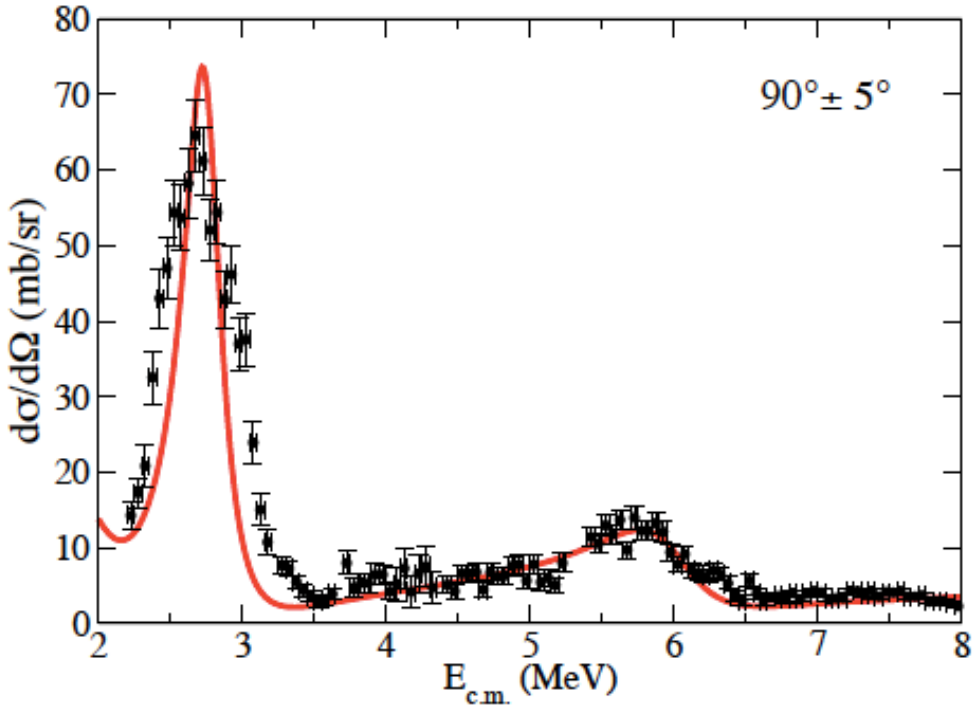

FIG. 3. Excitation function for the ^{6}He+α elastic scattering at 90° in c.m. Solid curve is an R-matrix fit with 4^+ and 6^+ states at 2.78 MeV and 6.0 MeV respectively.

In summary, the excitation function for ^{6}He+α was measured in the broad energy range from 2.0 to 8.0 MeV and angular range of 75° to 135°. The strong state at 10.2 MeV is observed. We confirm the results of the previous ^{6}He+α measurements [7,10] that indicate that the state at 10.2 MeV is a highly clustered 4^+ state. The dimensionless reduced α-width for this state is ~1.5. We observed a peak at 6.0 MeV that may be assigned spin-parity 6^+, but this assignment is tentative. If this state is indeed 6+ then it has dimensionless reduced α-width close to unity and can be assigned to the highly deformed cluster band

in ^{10}Be, that has a 0^+ band head at 6.18 MeV, 2^+ member at 7.54 MeV, 4^+ at 10.2 MeV and a tentative 6^+ at 13.5 MeV. This band has moment of inertia that is a factor of three larger than the moment of inertia of the ground state band.

[1] J. Hiura and R. Tamagaki, Prog. Theor. Phys. Suppl. **52**, 25 (1972).
[2] R.B. Wiringa *et al.*, Phys. Rev. C **62**, 014001 (2000).
[3] W. Oertzen, Z. Phys. A **354**, 37 (1996).
[4] A. Doté, H. Horiuchi, and Y. Kanada-Enýo, Phys. Rev. C **56**, 1844 (1997).
[5] N. Itagaki and S. Okabe, Phys. Rev. C **61**, 044306 (2000).
[6] N. Curtis *et al.*, Phys. Rev. C **64**, 044604 (2001).
[7] M. Freer *et al.*, Phys. Rev. Lett. **96**, 042501 (2006).
[8] M. Milin *et al.*, Phys. At. Nucl. **69**, 1360 (2006).
[9] R. Wolsky *et al.*, Phys. At. Nucl. **73**, 1405 (2010).
[10] D. Suzuki *et al.*, Phys. Rev. C **87**, 054301 (2013).

Exploring gluon polarization with NNPDF and STAR

A. B. Cudd, P. Djawotho, C. A. Gagliardi, and the STAR Collaboration

The NNPDF group uses neutral networks to obtain parton distribution functions (PDFs). The use of neutral nets allows them to make no assumptions regarding the Bjorken-*x* dependence of the PDFs at their input scale, in contrast to other groups performing PDF fitting. Recently, they published their first polarized PDF set, NNPDFpol1.0 [1], which they obtained from a global analysis of polarized deep-inelastic electron and muon scattering measurements. In addition to their best fit, NNPDF has posted 100 "replica" PDF sets, each of which they consider to be equally probable given their input data.

The NNPDF group has developed a reweighting method [2,3] to include new experimental data into an existing PDF set without the need to repeat the entire fitting process. The method involves calculating weighted averages over the 100 replicas, with the weight for each replica derived from the χ^2 probability for the replica to describe the new data. We have implemented this method to produce a modified NNPDF fit that includes the 2006 and 2009 STAR inclusive jet A_{LL} results. When calculating the χ^2 probabilities for the jet asymmetries, we included both the statistical and systematic uncertainties and their correlations.

We find that the jet data have a negligible impact on the polarized quark and anti-quark distributions, but a significant impact on the polarized gluon distribution. Fig. 1 shows the original NNPDF polarized gluon distribution as a function of *x* at $Q^2 = 10$ GeV^2, as well as the modified fit that

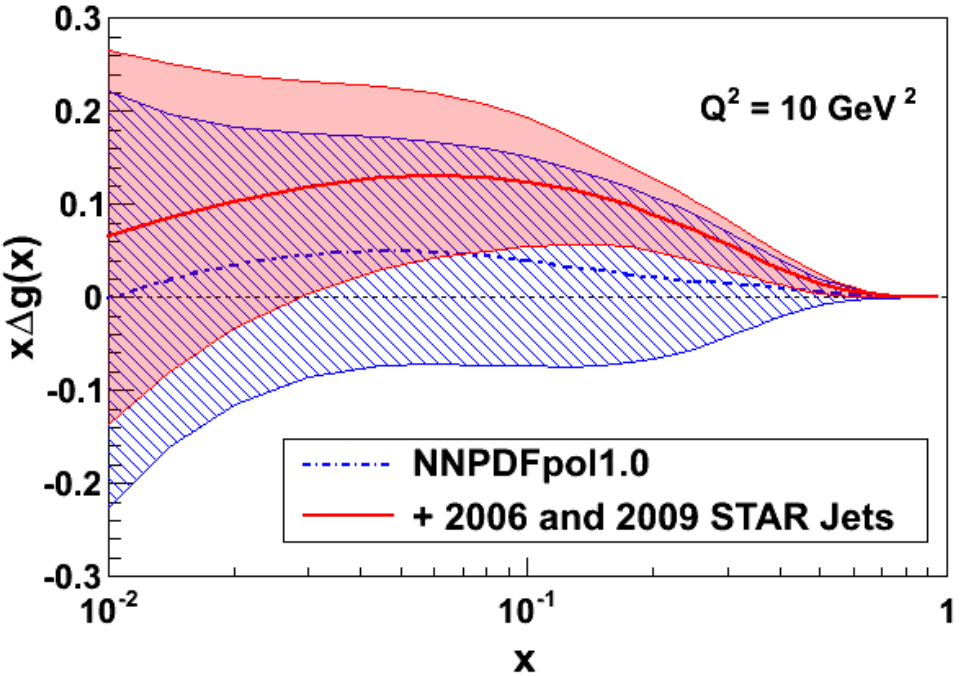

FIG. 1. Gluon polarizations from NNPDF (blue dot-dashed curve, hatched uncertainty band) [1], and from a modified version of NNPDF that we obtain when including the 2006 and 2009 STAR inclusive jet A_{LL} results through reweighting (red solid curve and uncertainty band).

includes the 2006 and 2009 STAR data. The integral of $\Delta g(x,Q^2=10\ \mathrm{GeV}^2)$ over the range $0.05 < x < 0.5$ is 0.06 ± 0.18 for the original NNPDF fit and 0.21 ± 0.10 when the fit is reweighted using the STAR jet data. The inclusion of the STAR jet data results in a substantial reduction in the uncertainty for the gluon polarization in the region $x > 0.05$ and indicates a preference for the gluon helicity contribution to be positive in the RHIC kinematic range.

[1] R.D. Ball *et al*. (NNPDF Collaboration), Nucl. Phys. **B874**, 36 (2013).

[2] R.D. Ball *et al*. (NNPDF Collaboration), Nucl. Phys. **B849**, 112 (2011). [*Errata*: **B854**, 926 (2012); **B855**, 927 (2012).]

[3] R.D. Ball *et al*. (NNPDF Collaboration), Nucl. Phys. **B855**, 608 (2012).

Spin physics with STAR at RHIC

Z. Chang, P. Djawotho, C. A. Gagliardi, M. M. Mondal, R. E. Tribble,
and the STAR Collaboration

Our group continues to play major roles in STAR investigations of both longitudinal and transverse spin phenomena in polarized *pp* collisions at RHIC. During the past year, we made substantial progress toward the determination of A_{LL} for inclusive jet production at mid-rapidity in 510 GeV *pp* collisions with data that STAR recorded during 2012, and obtained preliminary results for the transverse single-spin asymmetry, A_N, for jet-like events at forward rapidity using data that STAR recorded during 2011.

One of the primary goals of the RHIC spin program is to determine the gluon contribution to the proton spin. At RHIC energies, jet production at mid-rapidity is dominated by *gg* and *qg* scattering. This makes A_{LL} for inclusive jet production a sensitive probe of gluon polarization. The 2009 STAR inclusive jet A_{LL} results for 200 GeV *pp* collisions [1] provide the first indication of non-zero gluon polarization in the region $x > 0.05$ [2]. Inclusive jet measurements at mid-rapidity in 510 GeV *pp* collisions provide the opportunity to extend the gluon polarization sensitivity down to $x > 0.02$.

STAR recorded a large inclusive jet data set in 510 GeV *pp* collisions during the 2012 RHIC run. Mr. Z. Chang is using the 2012 STAR data to determine A_{LL} for inclusive jet production for his dissertation research. A_{LL} values of only 0.001~0.002 are expected for the low-p_T jet bins that provide information regarding gluon polarization at the lowest x values. Thus, it's essential to minimize the systematic uncertainties in the analysis. The two dominant systematics are expected to involve the relative luminosity measurement and trigger and reconstruction bias. Last year, Mr. Chang performed a detailed analysis of the scaler data for three different STAR subsystems – the Beam-Beam Counter (BBC), the Vertex Position Detector (VPD), and the Zero-Degree Calorimeter (ZDC). He found that the VPD provides the best measure of the relative luminosities for the 2012 STAR data. The present estimate is that the relative luminosity determination will contribute a systematic uncertainty to A_{LL} of ±0.0004. Since then, Mr. Chang has performed a detailed QA of the 2012 jet data, identifying those runs where the detector response is best understood in order to minimize the trigger and reconstruction bias. Recently, Mr. Chang has identified anomalies in the trigger response associated with energy depositions in a small subset of the calorimeter front-end electronics modules. Once these are resolved, he will be ready to generate the large Monte Carlo simulation that is necessary to estimate the trigger and reconstruction bias systematics. Mr. Chang expects to have preliminary results for inclusive jet A_{LL} at 510 GeV during the coming year.

Another major goal of the RHIC spin program is to unravel the origin of the large transverse single-spin asymmetries for inclusive π^0 production that have been seen at forward rapidities at RHIC [3,4]. The asymmetries have been attributed to the Sivers effect, a correlation between the spin of the incident proton and the transverse momentum of the quark or gluon that experiences the hard scattering, the Collins effect, which arises from the spin-dependent fragmentation of polarized scattered quarks, or a combination of the two. The Sivers effect provides a window into parton orbital motion because it

requires interference between amplitudes involving partons with different orbital angular momenta. The Collins effect provides a means to explore quark transversity, the third collinear, leading-twist parton distribution function. (The other two are the unpolarized distribution and the helicity distribution, which is explored in longitudinally polarized collisions as discussed above.)

We have developed the ability to reconstruct photon and multi-photon jet-like events with the STAR Forward Meson Spectrometer (FMS) in order to gain more insight into the dynamics that lead to the observed large transverse single-spin asymmetries. The FMS provides electromagnetic calorimetry over the full azimuth for the range $2.5 < \eta < 4$. We use the anti-k_T algorithm with resolution parameter R=0.7 to construct jets from the photons observed by the FMS. We then measure A_N for the highest energy jet that satisfies $2.8 < \eta < 4$ and $p_T > 2$ GeV/c. We find that the transverse spin asymmetry depends strongly on the number of photons in the reconstructed jet-like event. Fig. 1 shows the measured

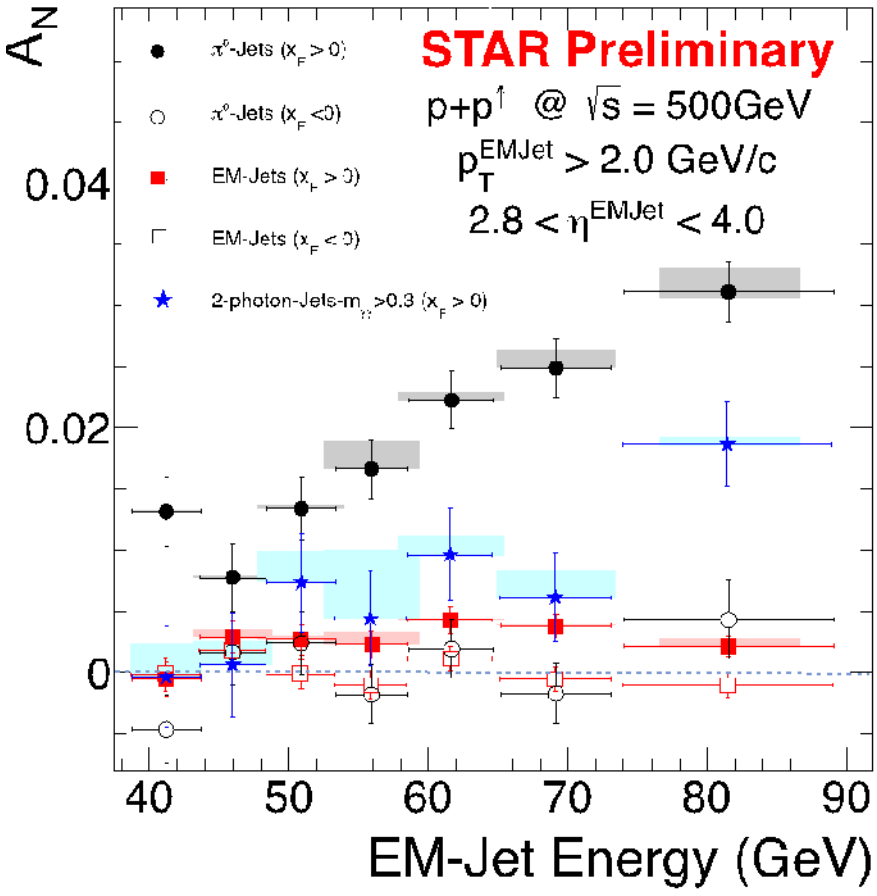

FIG. 1. A_N vs. EM-Jet Energy for three different classes of jet-like events detected with the STAR FMS. See text for a description of the three event classes. The error bars indicate statistical uncertainties, and the shaded bands show the systematic uncertainties.

asymmetry vs. EM-jet energy for three different event classes. Isolated π^0s, or "π^0-jets", represent jets that contain exactly two photons with effective mass $m_{\gamma\gamma} < 0.3$ GeV and energy sharing $|E_1-E_2|/(E_1+E_2) < 0.8$. Their asymmetry is large and increasing with energy. In contrast, EM-jets with three or more

photons have a very small asymmetry. The asymmetry for 2-photon EM-jets with mass $m_{\gamma\gamma} > 0.3$ GeV, which arise from the photon combinatorial continuum together with a small contribution from the η meson, falls in between these two limits.

To further explore the dependence of A_N on the event class, we've examined it as a function of EM-jet energy, p_T, and number of photons. The results are shown in Fig. 2. One-photon events, which include a large π^0 contribution in this analysis, are similar to 2-photon events. Three-photon jet-like events have a clear non-zero asymmetry, but it's substantially smaller than that for isolated π^0. A_N then decreases as the event complexity, i.e., the "jettiness", increases. These results indicate that the π^0s that produce the large observed forward transverse spin asymmetry do not arise from the conventional parton fragmentation to jets.

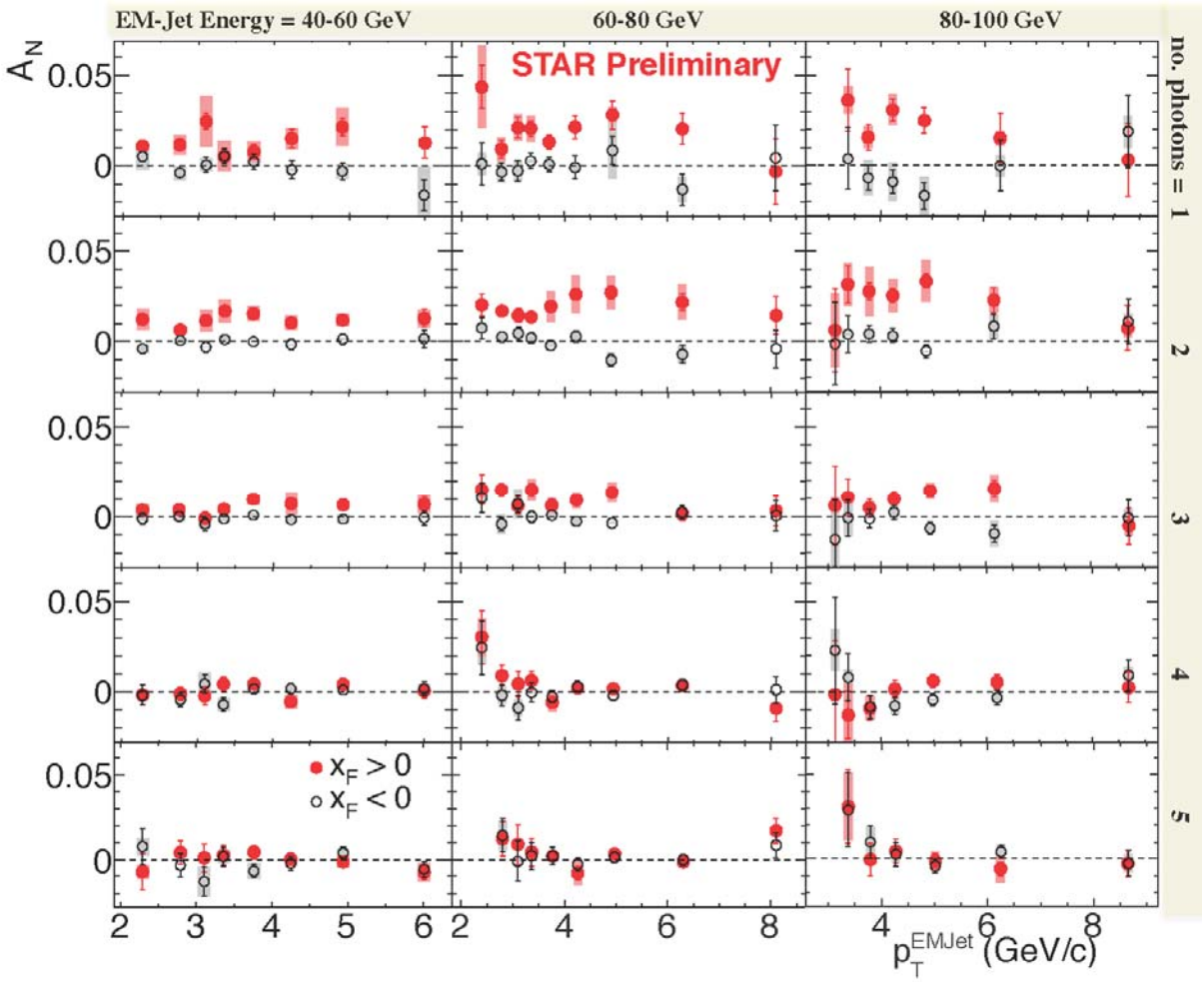

FIG. 2. A_N as a function of EM-jet energy, p_T, and number of photons. We also find that A_N for jet-like events with more than 5 photons (not shown) is similar to that for N_γ=5. The error bars are statistical, and the shaded bands show the systematic uncertainties.

At present, work is underway to explore the sensitivity of the forward transverse asymmetries to the presence or absence of an away-side jet at mid-rapidity.

During the past year, group members served as chair of the god-parent committee for one paper [5], and members of the god-parent committee for two other papers.

[1] P. Djawotho, for the STAR Collaboration, arXiv:1106.5769.
[2] E.C. Aschenauer *et al*. (RHIC Spin Collaboration), arXiv:1304.0079.
[3] B.I. Abelev *et al*. (STAR Collaboration), Phys. Rev. Lett. **101**, 222001 (2008).
[4] L. Adamczyk *et al*. (STAR Collaboration), Phys. Rev. D **86**, 051101(R) (2012).
[5] L. Adamczyk *et al*. (STAR Collaboration), arXiv:1302.6184.

SECTION II

HEAVY ION REACTIONS

Recent results of ^{45}Sc-induced fusion evaporation reactions on ^{158,160}Gd

T. A. Werke, D. A. Mayorov, M. C. Alfonso, M. M. Frey, and C. M. Folden III

Recent superheavy element discoveries have benefitted from ^{48}Ca projectiles bombarding actinide targets. The possibilities for making new elements (Z > 118) in ^{48}Ca reactions have been exhausted and projectiles with higher Z such as ^{45}Sc, ^{50}Ti, etc. must be used instead.

Cross sections have been measured for the *4n* exit channel of the ^{45}Sc + $^{158,\ 160}$Gd reactions. These complement previous bombardments of the lanthanide targets ^{159}Tb and ^{162}Dy with ^{45}Sc projectiles [1]. These systems allow for the study of projectile/target effects and the effects of the relative neutron content in the compound system on the *4n* cross sections. The evaporation residues (EVRs) were produced using beam from the K500 cyclotron. Unreacted beam and undesired reaction products were filtered using the spectrometer MARS [2]. The general experimental details are described in Ref. [3]. All data presented here are preliminary. The *4n* and *p3n* cross sections for the reactions of ^{45}Sc + ^{158,160}Gd, ^{159}Tb are plotted in Fig. 1 and Fig. 2, respectively. For the ^{45}Sc + ^{159}Tb reaction, the *p3n* exit channel cross section is significantly larger than the *4n* cross section. For the ^{45}Sc + ^{158,160}Gd reactions, sensitivity to the *p3n* product is limited by small alpha branches (~1-3%).

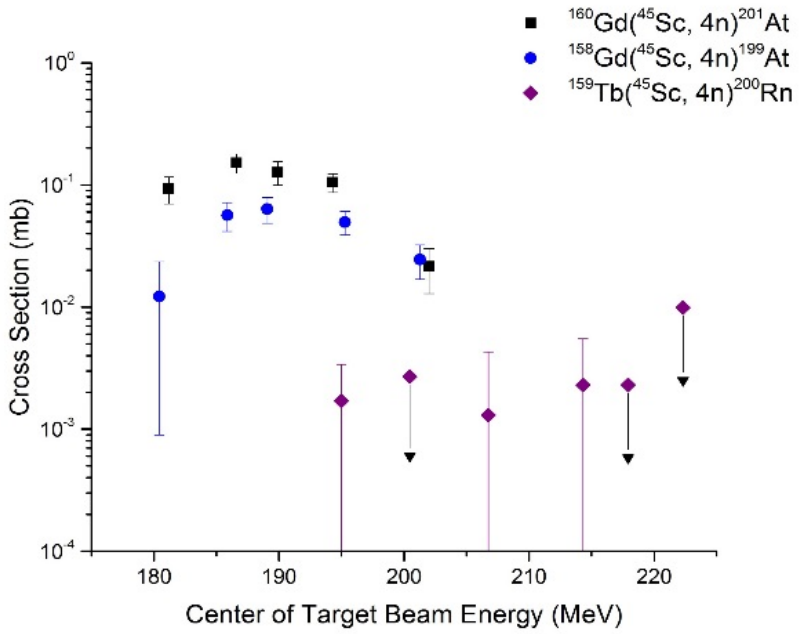

FIG. 1. Cross sections for the *4n* channels in the ^{45}Sc + ^{158,160}Gd (blue circles and black squares) and ^{45}Sc + ^{159}Tb (purple diamonds) reactions.

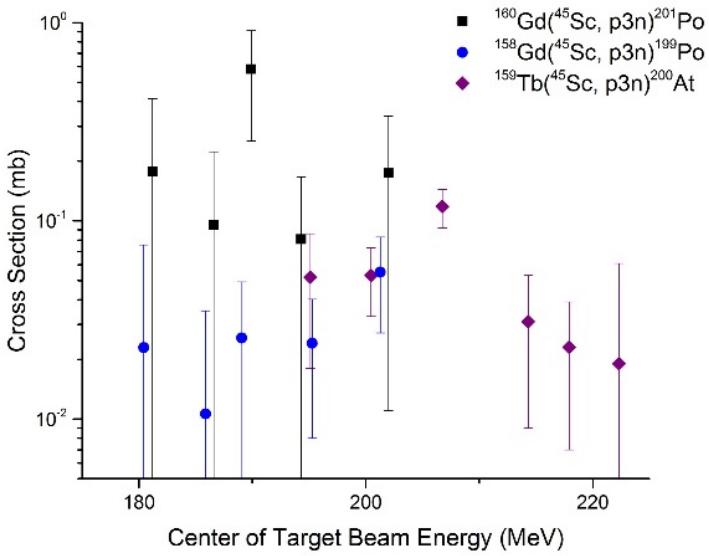

FIG. 2. Cross sections for the *p3n* channels in the ^{45}Sc + ^{158,160}Gd (blue circles and black squares) and ^{45}Sc + ^{159}Tb (purple diamonds) reactions.

These data were analyzed within a simple, three-step model of fusion evaporation reactions:

$$\sigma_{EVR} = \sigma_{capt} P_{CN} W_{sur},$$

where the fusion cross sections, σ_{capt}, were calculated using the coupled-channel code CCFULL[4]; compound nucleus formation probabilities, P_{CN} , were estimated using the functional form of the Fusion-by Diffusion [5] approach that is presented in Ref. [6], and survival probabilities, W_{sur}, were calculated using the standard transition state theory approach presented in Ref. [7]. The calculation of survival cannot be reduced to the well-known Vandenbosch and Huizenga formula [8] due to the large contribution of proton emission from the compound nucleus. The survival probabilities are shown to be the main force in driving down the *4n* cross sections in the ^{45}Sc + ^{159}Tb reaction. Calculations are still in progress and final results will be published in a future work.

[1] C.M. Folden III *et al.*, J. Phys. Conf. Ser. **420** 012007 (2013).
[2] R.E. Tribble *et al.*, Nucl. Instrum. Methods Phys. Res. A**285**, 441 (1989).
[3] C.M. Folden III *et al.*, Nucl. Instrum. Methods Phys. Res. A**678**, 1 (2012).
[4] K. Hagino *et al.*, Comp. Phys. Commun. **123**, 143 (1999).
[5] W.J. Świątecki *et al.*, Phys. Rev. C **71**, 014602 (2005).
[6] D. Mayorov *et al.*, Phys. Rev. C (submitted).
[7] K. Siwek-Wilczyńska *et al.*, Phys. Rev. C **72**, 034605 (2005).
[8] R. Vandenbosch and J.R. Huizenga, *Nuclear Fission* (Academic, New York, 1973), p. 232.

Production cross sections of residues in ^{50}Ti-induced reactions

D. A. Mayorov, T. A. Werke, M. C. Alfonso, M. M. Frey, E. E. Tereshatov, and C. M. Folden III

Excitation functions for the synthesis of *xn* evaporation residues were measured in ^{50}Ti-induced reactions with ^{159}Tb, ^{160}Gd, and ^{162}Dy targets. These data complement the data previously collected for ^{48}Ca-induced reactions with ^{159}Tb and ^{162}Dy, where ^{48}Ca + ^{162}Dy forms the same compound nucleus (CN) as ^{50}Ti + ^{160}Gd. Collectively, the measured excitation functions permit a systematic evaluation of the influence of nuclear properties of the projectile, target, and product nuclei on the evaporation channel production cross section. Such information may be of interest in the field of superheavy elements, where constraints on available targets makes a switch from ^{48}Ca to ^{50}Ti a necessary step to reach elements with $Z > 118$ [1].

The data were collected at the Texas A&M University Cyclotron Institute. A ^{50}Ti beam with an energy of 5.0 MeV/u was delivered by the K500 cyclotron to the MARS spectrometer [2], prepared by sputtering an enriched metal sample. The beam energy was varied with ^{nat}Al degraders positioned upstream of the targets. Particle separation relied on differences in magnetic rigidity and velocity of recoiling nuclei. The transmitted reaction products were detected at the focal plane of the spectrometer by a 16-strip position-sensitive silicon detector. An MCP detector located upstream served to discriminate implantation events from α-decay events occurring in the silicon detector.

Preliminary excitation functions for the 4*n* evaporation channel (having highest product yield) measured in reactions of ^{50}Ti with ^{159}Tb, ^{160}Gd, and ^{162}Dy are shown in Fig. 1 as red squares. These are compared to complementary reactions of ^{48}Ca with the same targets, shown in the figure as black circles.

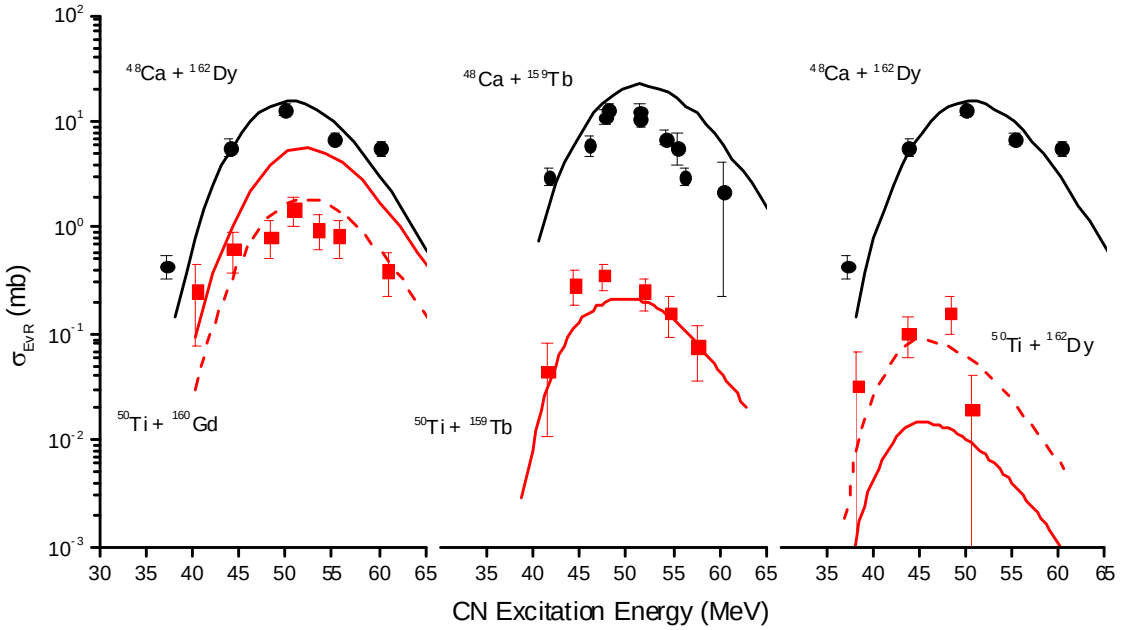

FIG. 1. Excitation functions for the 4*n* evaporation channel in reactions of ^{48}Ca and ^{50}Ti with ^{160}Gd, ^{159}Tb, and ^{162}Dy targets. The identical CN is produced in reactions in the left panel. The center and right panels show reactions on identical targets. The curves are theoretical predictions (see main text). The compound nucleus excitation energy is given for the center-of-target projectile energy.

The solid curves represent theoretical predictions and are largely based on the framework discussed in [3]. The dashed curves are obtained by uniformly scaling the solid curves down by a factor of 3 for the ^{50}Ti + ^{160}Gd reaction and up by a factor of 6 for the ^{50}Ti + ^{162}Dy reaction. The scaling shows the rough magnitude of over- or under-prediction of the model, while also demonstrating very satisfactory predictions for the shape and the peak of each excitation function. The agreement between theory and data is generally good for all reactions, considering the inherent uncertainties entering the calculation. Theoretically, the production cross section is given by the product of the capture cross section, amalgamation probability (P_{CN}) leading to a CN, and survival probability against fission. The greatest uncertainty is associated with the calculation of P_{CN} as it is the least well-understood stage of the mechanism. A phenomenological expression was used for P_{CN} [4], where for the ^{48}Ca reactions the estimates were constrained by pertinent literature data [5]. This information was extended to the ^{50}Ti reactions, for which no applicable literature data is available and where the greater Coulomb interaction of the projectile-target pair should further reduce P_{CN}. A major uncertainty in the survival probability comes from lack of experimental data on fission barrier heights, B_f, relevant to the present reactions. A 0.5 MeV change in B_f can reflect as up to an order-of-magnitude change in the calculated cross section (especially true for excited nuclei with similar neutron emission and fission decay widths) [6].

The analysis of the ^{50}Ti data is presently ongoing. These preliminary results show a moderate decrease in production cross section for the ^{50}Ti reactions relative to the ^{48}Ca reactions. Naturally, the properties of the CN, not just the projectile, determine the cross section. However, the present results indicate that even in synthesizing the same CN, that the increased symmetry of the ^{50}Ti reaction significantly suppresses the residue production cross section.

[1] J. Khuyagbaatar *et al.*, GSI Scientific Report 2012, No. PHN-ENNA-EXP-01, edited by K. Große, p. 131.

[2] R.E. Tribble *et al.*, Nucl. Instrum. Methods Phys. Res. **A285**, 441 (1989).

[3] K. Siwek-Wilczyńska *et al.*, Phys. Rev. C **72**, 034605 (2005).

[4] K. Siwek-Wilczyńska *et al.*, Int. J. Mod. Phys. E **17**, 12 (2008).

[5] G.N. Knyazheva *et al.*, Phys. Rev. C **75**, 064602 (2007).

[6] V.I. Zagrebaev *et al.*, Phys. Rev. C **65**, 014607 (2001).

Development of nuclear forensics program at Texas A&M University

T. K. Bhardwaj,[1] J. R. Allred, K. F. Jones, P. M. Mendoza, R. L. Du, C. M. Folden III, and S. S. Chirayath

[1]*Cyclotron Institute and Nuclear Security Science and Policy Institute*
Texas A&M University, College Station, Texas

Nuclear proliferation is a growing concern worldwide due to the increased availability of nuclear materials, knowledge of sensitive technologies, and the possibility of diverting nuclear materials such as uranium and plutonium away from peaceful uses. Due to this increasing risk of nuclear threats, we are developing nuclear forensics capabilities at Texas A&M University with sponsorship from the Department of Homeland Security. Our objective is to determine the differences in fission products and actinides characteristics for uranium samples irradiated in different type of nuclear reactors (thermal and fast reactors).

The experimental equipment used in this research is shown in Fig. 1, The uranium samples for this project were irradiated at the High Flux Isotope Reactor (HFIR) at Oak Ridge National Laboratory. For the chemical processing of the irradiated uranium samples, a glovebox was installed in a radiochemistry lab. The glovebox provides a controlled environment, with both the H_2O and O_2 levels below 100 ppm. It also houses a lead-shielded workstation to handle the radioactive samples while

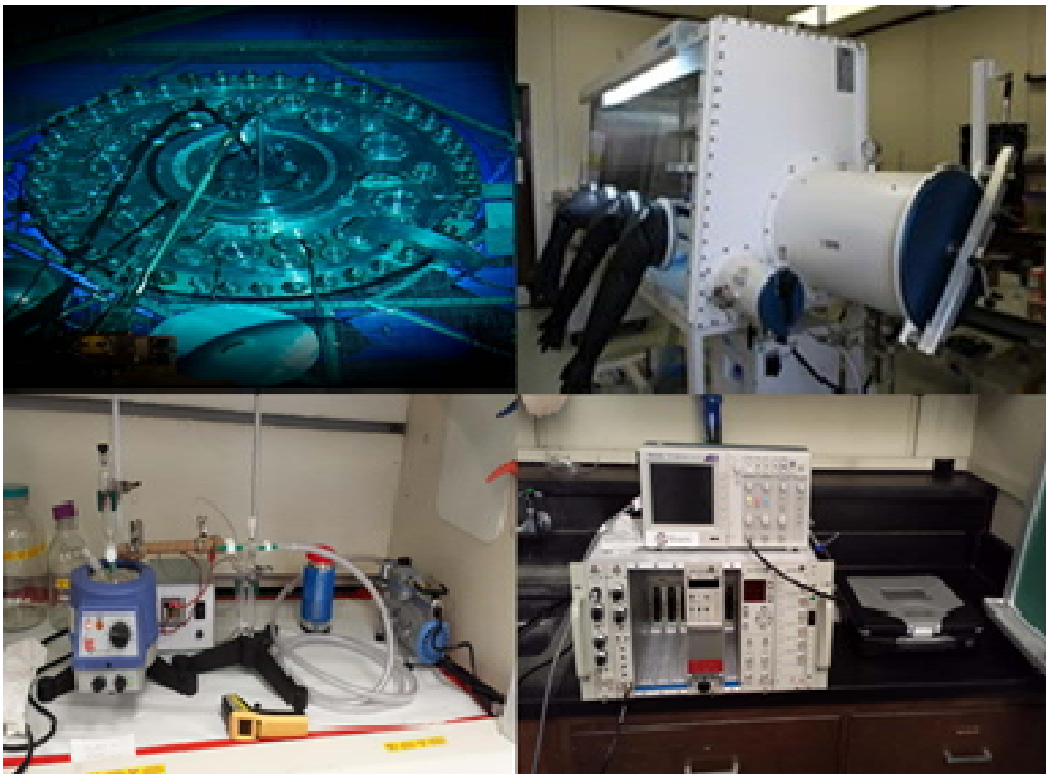

FIG. 1. Clockwise from top left: HFIR at ORNL, glovebox, alpha spectrometer, and dissolution setup at TAMU.

preventing radioactive material from escaping to the atmosphere. A CANBERRA alpha spectrometer was installed to analyze Pu samples. In addition, an experimental setup was designed and developed to dissolve the irradiated UO_2 pellet.

To test the method, experiments were conducted with unirradiated UO_2. Approximately 25 mg of $^{dep}UO_2$ was dissolved in 10 ml of 4 M HNO_3. Ce was added to the dissolved uranium and then the uranium was separated from the mixture by a solvent extraction method. The samples were analyzed by ICP-MS and the results were within the uncertainties of the analytical procedure. During the next stage of the project, the experimental setup was moved to a heavily shielded glovebox at the Nuclear Science Center (NSC) where the actual irradiated $^{dep}UO_2$ pellet will be dissolved. Several test runs were conducted at the NSC to analyze the risk factors and ensure the safety of the dissolution procedure. Additionally, a lead coffin was designed, developed, tested, and moved separately to the NSC to store a flask containing the fission product gases evolved during the dissolution process. All chemicals and equipment have been procured, and flowsheets have been prepared for the quantitative separation and analysis of ^{239}Pu, ^{240}Pu, ^{134}Cs, ^{137}Cs and ^{144}Ce. The first destructive analyses of the irradiated sample will be conducted in May 2014.

Exploring the structure of ^{12}C using the thick target inverse kinematics technique

M. Barbui, E. -J. Kim, V. Z. Goldberg, K. Hagel, H. Zheng, G. Giuliani, G. G. Rapisarda, S. Wuenschel, X. Liu,[1] and J. B. Natowitz

[1]*Institute of Modern Physics, Chinese Academy of Sciences, Lanzhou, China*

The reaction ^{20}Ne on α was studied using the Thick Target Inverse Kinematics (TTIK) technique [1]. This technique allows the exploration of a large range of incident energies in the same experiment. Moreover, in inverse kinematics, the reaction products are focused at forward angles and can be detected with detectors covering a relatively small portion of the solid angle in the forward direction.

A ^{20}Ne beam of energy 11 AMeV was delivered by the K150 cyclotron at Texas A&M University. The effective beam energy after the entrance window was 9.7 AMeV. The reaction chamber was filled with ^{4}He gas at a pressure sufficient to stop the beam at few centimeters from the detectors (3800 mbar). In this way we could detect light particles emitted at zero degrees. The energy of the light reaction products was measured by three silicon detector telescopes placed at a radial distance of 48 cm from the entrance window. Each telescope consisted of two 5x5 cm^2 Micron Semiconductors DC quadrant detectors (Design G). The time of flight of the detected particles was also measured relative to the cyclotron radiofrequency. A monitor detector was used to measure the intensity of the incident beam. The details of the experimental setup are given in [2].

According to the Ikeda picture [3] ^{24}Mg can be described as ^{20}Ne + α, ^{16}O + 2α, ^{12}C + 3α or a cluster of 6 α particles. Each configuration is expected to be observable at excitation energies around the corresponding threshold values. The preliminary results from the analysis of the events with alpha multiplicity one and two are shown in [2]. Here we focus on the analysis of the events with alpha multiplicity three. Alpha multiplicity one and two events show interesting resonant structures when looking at events where the alpha particles are emitted at angles near zero degrees. Therefore, considering the events with alpha multiplicity three, first we analyzed the events where three alpha particles are detected in the telescope centered at 1.5 degrees.

The left panel of Fig. 1 shows the sum of the energies of the three alpha particles detected in the

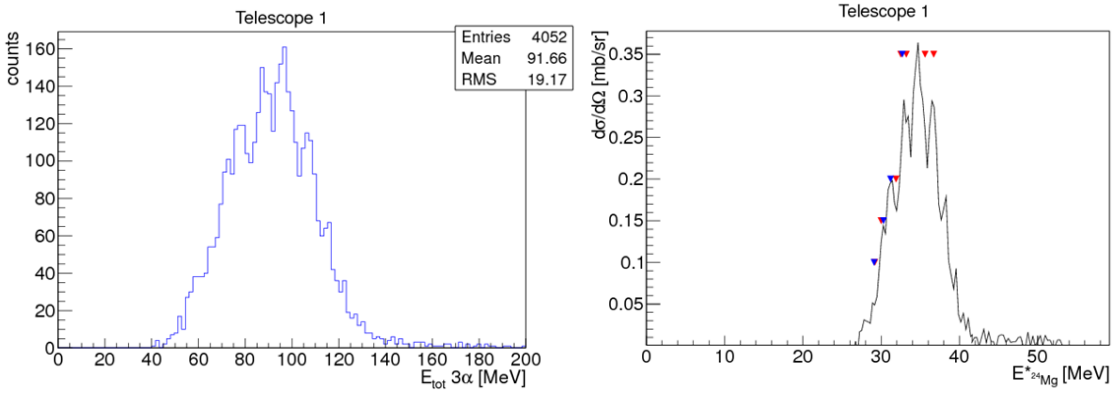

FIG. 1. Left panel: Sum of the energy of the 3 alpha particles with subtraction of the uncorrelated event spectrum obtained summing the energies of three alpha particles form different events. Right panel: Reconstructed excitation energy of ^{24}Mg assuming that the excited magnesium is decaying into two carbons one in the ground state, the other with enough excitation energy to split in three alphas. The blue and red triangles show the excitation energies of ^{24}Mg decaying into two ^{12}C as found in refs. [4,5] respectively.

central telescope, after subtraction of the uncorrelated events. This spectrum is obtained from the measured energies without any energy loss correction. It is interesting to note that the total energy spectrum shows a series of peaks. We can interpret those peaks as resonant states in ^{24}Mg decaying into two ^{12}C, one in the ground state, the other with enough excitation energy to split in three alphas. With this assumption we can reconstruct the interaction point position using the reaction kinematics and the energy and momentum conservation in a recursive procedure. The result is shown in the right panel of Fig. 1 and compared with the data in refs [4, 5]. The excitation energy of the ^{12}C splitting into 3 alpha particles is obtained from the sum of the kinetic energies of the 3 alpha particles in the center of mass of the ^{12}C and the Q value. The result is shown in the left panel of Fig. 2, together with the spectrum of the uncorrelated events obtained by randomly mixing three alpha particle energies form different events. The spectra in Fig. 2 show two peaks one at 7.65 MeV corresponding to the energy of the Hoyle state and one at 9.64 MeV corresponding to a (3$^-$) state. In order to determine if the decay is proceeding through the

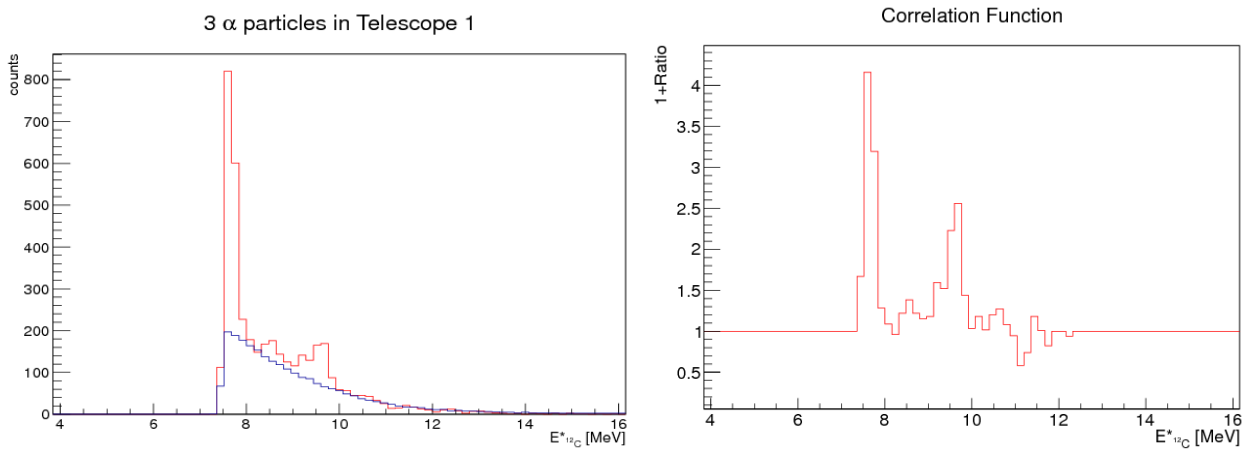

FIG. 2. Left panel: (Red line) excitation energy of ^{12}C splitting into 3 alpha particles, (Blue line) spectrum of uncorrelated events obtained by mixing three alpha particles from different events. Right panel: Correlation function obtained by dividing the two spectra in the right panel.

ground state of ^{8}Be we calculated event by event the relative energy of the three possible couples of alpha particle. The minimum two alphas relative energy spectrum is shown in Fig.3 for the Hoyle state and the (3$^-$) state. The two spectra in Fig.3 show a clear peak around 100 keV, corresponding to the separation

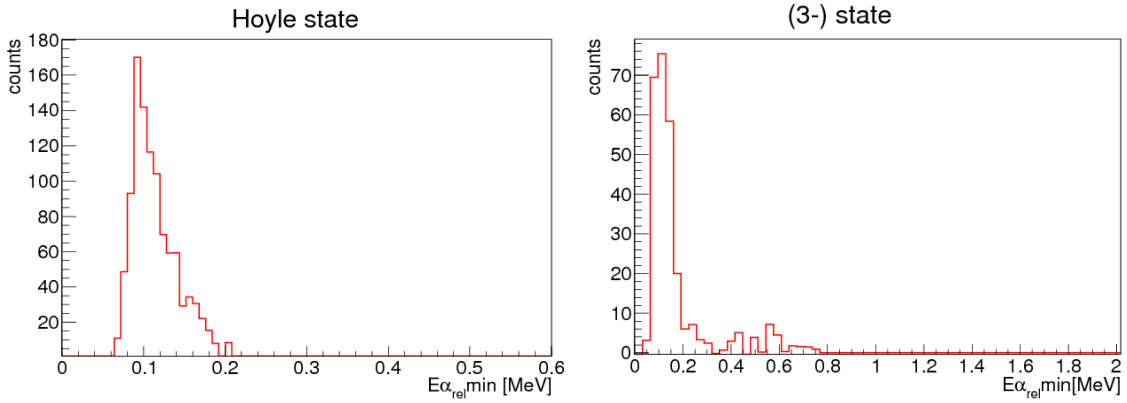

FIG. 3. Left panel: minimum relative energy of two alpha particles for the Hoyle state, with subtraction of the uncorrelated events. Right panel: minimum relative energy of two alpha particles for the (3-) state, with subtraction of the uncorrelated events.

energy of ^{8}Be. The Dalitz plots for the Hoyle state and the (3^{-}) state are also presented in Fig.4. Those plots confirm the decay of the two states through the ^{8}Be ground state.

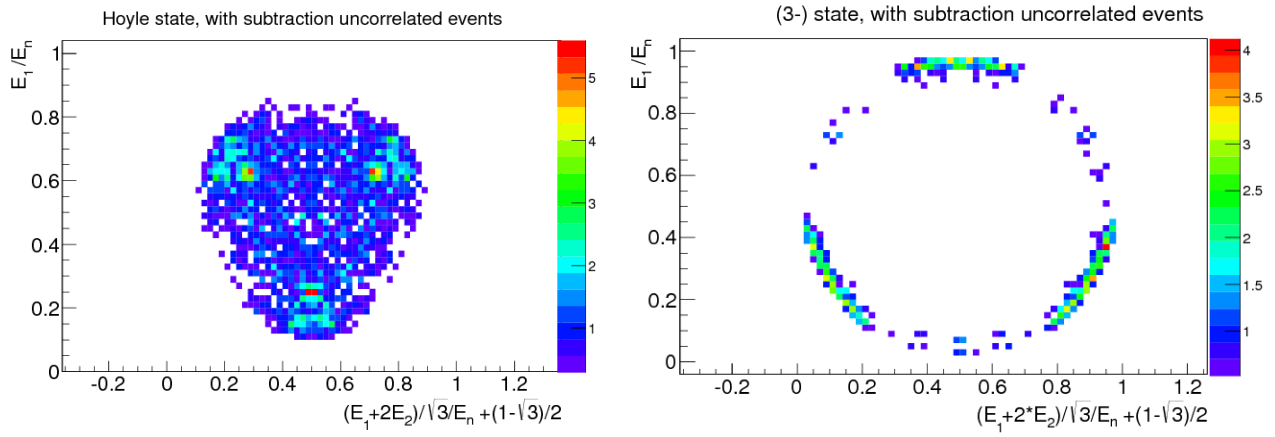

FIG. 4. Dalitz plots of the Hoyle state (left panel) and (3^{-}) state (right panel). The uncorrelated events are subtracted.

From the data in Figs. 3 and 4 we can conclude that the Hoyle state almost completely decays through the ground state of ^{8}Be, and upper limit of less than 1% can be set for the direct decay into three alpha particles; the (3^{-}) state mostly decays through the ^{8}Be ground state, a few percent of the events are not decaying through the ^{8}Be ground state, as known from the literature.

During this run we did not observe any direct decay of ^{24}Mg into six alpha particles. We are planning a new experiment with an improved experimental setup with larger granularity and better efficiency to investigate the decay of self-conjugate nuclei in n-alpha particles.

[1] K. Artemov *et al.*, Sov. J. Nucl. Phys. **52**, 406 (1990).

[2] M. Barbui *et al.*, Eur. Phys. J. Web of Conferences **66**, 03005 (2014).

[3] K. Ikeda, N. Takigawa, and H. Horiuchi, Prog. Theor, Phys. Suppl. Extra Number, 464 (1968).

[4] M. Freer *et al.*, Phys. Rev C **57**, 1277 (1998).

[5] M. Freer *et al.*, Phys. Rev C **63**, 034317 (2001).

Pastina formation in low density nucleonic matter – a mechanism for ternary fission

S. Wuenschel, H. Zheng. K. Hagel, B. Meyer, M. Barbui, E. -J. Kim, G. Roepke, and J. B. Natowitz

Approximately 0.3 % of binary fission decays observed in the spontaneous or thermal neutron induced fission of a heavy nucleus are accompanied by emission of an energetic light particle or fragment in a direction perpendicular to the axis defined by the separating massive fragments. Considerable theoretical and experimental effort has been directed towards understanding this type of ternary fission. Generally, statistical or dynamical only models have had limited success and have been unable to explain such key experimental results as the high yield of scission tritons relative to scission protons and the non-observation of ^{3}He. Recently, Lestone proposed a model in which a statistical evaporation of the ternary particle is moderated by time dependent emission barriers that evolve as the fissioning nucleus approaches the scission point [1]. Parameterizing the neck radius, the range of the nuclear force, temperature, time, and emission barrier height provided a good reproduction of isotopic yields for $Z \leq 6$ and reasonable predictions for $Z > 6$.

The experimental results of Koester et al. provide the most comprehensive data available for ternary fission yields [2]. For this study we focus on the data for the ^{241}Pu(n_{th},f) reaction [2]. These experimental data include measured yields per fission event for 42 isotopes. In addition, 17 upper limits are also reported for yields of other isotopes.

For our initial approach to modeling the yield data we employed the stellar nucleo-synthesis statistical equilibrium calculation (NSEC) of Meyer et al [3] to determine the relative yields of the constituent species. The key assumption of nuclear statistical equilibrium is that the chemical potential $\mu(Z, A)$ is governed by the equation

$$\mu(Z,A)=Z\mu_p +(A-Z)\mu_n \qquad (1)$$

where μ_p and μ_n are the proton and neutron chemical potentials, respectively. The yields follow from the relationship given in Eq 2.

$$\mu(Z,A) = m(Z,A)c^2 + kT \ln\left(\frac{\rho N_A Y(Z,A)}{G(Z,A)} \left[\frac{h^2}{2\pi m(Z,A) kT} \right]^{3/2} \right) \qquad (2)$$

In this equation, m(Z,A) the mass, k is Boltzmann's constant, T is Temperature, ρ is the density, N_A is Avogadro's number, Y(Z,A) is the yield and G(Z,A) is the nuclear partition function. The partition function for a given nuclear species incorporates excited states as multiples of the ground state. For nuclei above Z =7 the modified partition functions of Rauscher et al [4], determined for temperatures up to 1.4 MeV, have been employed. Experimental binding energies were obtained from the JINA astrophysical database [5]. The input parameters of the NSEC calculation are temperature, density, and proton fraction.

After surveying results for a wide variety of temperature, density and proton fraction, values we adopted a multi-parameter minimization technique in an attempt to simultaneously fit the available experimental data. The fit metric used is that of Lestone [1], defined by

$$M^2 = \sum_j \{\ln[P_{TF}^{\exp}(Z_j, A_j)] - \ln[P_{TF}(Z_j, A_j)]\}^2 / n, \qquad (3)$$

where P_{TF} are the calculated ternary fission probabilities, P_{TF}^{exp} are the corresponding experimental emission probabilities, and n is the number of fitted experimental data points. The exponential of M is a measure of the typical relative difference between the model calculations and the experimental data. For M ~1 the average relative discrepancy between model and experiment would be a factor of ~3.

While this approach produced reasonable fits for the lighter isotope yields A≤15, it greatly overestimated the yields for heavier isotopes. The results of one such calculation are presented in Fig. 1a. The choice of parameters used there, indicated in the figure caption, is based on extensions of the fitting model described below and plotted in Fig. 1b. To visually separate yields for different elements and isotopes we have plotted

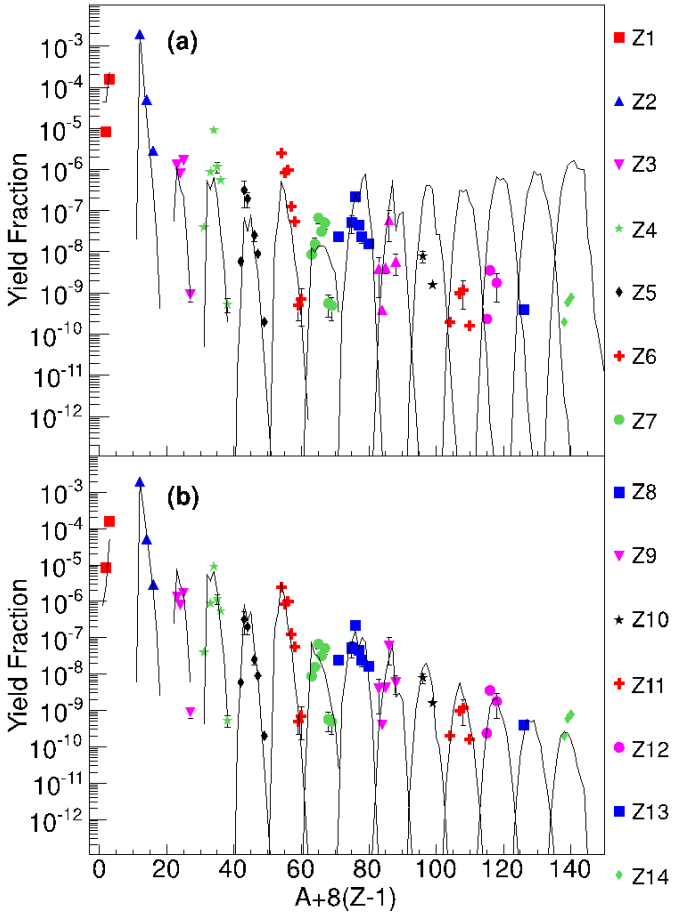

FIG. 1. Yield fraction as a function of mass(A) and charge(Z) of products. Solid points represent ^{241}Pu(n,f) experimental yeilds from Koster et al[2]. Lines are theoretical predictions from NSE calculation [7]. NSE parameters are T= 1.4 MeV, ρ= 4E-4 fm-3, and Yp= 0.34. Top) NSE calculation only. M^2 fit metric = 4.28. Bottom) NSE calculation with nucleation. Nucleation parameters are time = 6400 fm/c and Ac = 5.4. Fit metric = 1.18.

the yields as a function of the parameter 8(Z-1) +A suggested by Lestone [1]. Here Z is atomic number and A is mass number.

For application to nucleation in nuclear matter Demo and Kozisek have proposed a single component nucleation model [6] which allows derivation of a relatively simple analytical expression for the yield distribution as a function of normalized time $\tau = \frac{3.967\rho}{A_c^{2/3}\sqrt{T}}t$, where ρ is density, Ac is the critical cluster size, T is temperature, and t is time [6]. That expression is

$$Y(A,\tau) = \frac{1}{2}\rho \exp\left[-\frac{G(A)}{T}\right] erfc\left[B(T,\sigma)\frac{\left(\sqrt[3]{A/A_c}-1\right)+\left(1-A_c^{-1/3}\right)\exp(-\tau)}{\sqrt{1-\exp(-2\tau)}}\right] \qquad (4)$$

Where, the term representing the equilibrium concentration of the species of mass A is modulated by a complementary error function term which depends upon the parameters B(T,σ) and A_c where

$$B(T,\sigma) = 2R_0\left(\frac{\pi\sigma}{T}\right)^{1/2} A_c^{1/3} \qquad (5)$$

R_0 is the range of the effective nucleon potential taken as 1.4 fm and σ is the droplet surface tension. A temperature dependent formula for σ is given in [6]. However, for the relatively low temperatures in this study, it can be treated as a constant 1.12 MeV fm^{-2}. In nucleation theory Ac , the critical cluster size, is viewed as the size below which clusters break down and above which clusters grow. In our application of this approach we treat both τ and Ac as free parameters.

Fig. 1b shows results of the multi-parameter minimization fit in which the addition of the time dependence of the nucleation prevents the yields of heavier isotopes from achieving the NSE equilibrium values. The temperature, density and proton fraction fit parameters derived here are the ones used for Figure 1a. We see that the fits provide a much better representation of the experimental yields. The fit metric, M^2= 1.18 over the entire range of isotopes. For a fitting range Z≤ 6, that employed by Lestone in his paper, M^2= 1.19.

The assumption of a nucleation-modulated approach to nuclear statistical equilibrium, with reasonable parameters, provides a rather good fit to the ternary fission data. The success suggests that the process is dominated by cluster formation in low temperature low-density nucleonic matter. Naturally there is some interplay among the parameters and slight variations in one may be compensated for by changes in another.

The present approach is useful in understanding some of the main features of the ternary fission data. For example the yield trend for Z=1 and Z=2 yields is well reproduced and the absence of ^{3}He can now be understood as reflecting the very large yield difference for the mirror nuclei ^{3}H and ^{3}He.

Since the nucleation model we have employed makes no distinction between protons and neutrons, it is useful to ask whether fits to the isotope mass distributions make any significant change in the quality of the model fits. We tested a fit to the experimental mass distributions and obtained M^2 = 0.561 over the entire range of isotopes. This fit is significantly better that of the fit to the isotopes

presented in Figure 1b. This suggests that a binary system nucleation approach, treating neutrons and protons separately, might offer some improvement in modeling the isotope yields and this should be investigated in future work. Additional details of this work can be found in reference [7].

[1] J.P. Lestone, Intl. J. Mod. Phys. E, **V17**, 323 (2008).
[2] U. Koester *et al.*, Nucl. Phys. **A652**, 371 (1999).
[3] http://sourceforge.net/p/libnuceq
[4] T. Rauscher, Astrophys. J. Supp. **147**, 403 (2003).
[5] http://www.jinaweb.org
[6] P. Demo and Z. Kozisek, J. Phys. G **23**, 971 (1997).
[7] S. Wuenschel *et al.*, arXiv:1404.4303 (2014)

Progress on campaign surveying deep inelastic multi-nucleon transfer for creation of super- and hyper-heavy elements

S. Wuenschel, J. B. Natowitz, K. Hagel, M. Barbui, G. Giuliani, E. -J. Kim, N. Blando, H. Zheng, S. Kowalski, K. Schmidt, Z. Majka, Z. Sosin, and A. Wieloch

In recent years, we have investigated the deep-inelastic transfer method for creating new super- and possibly hyper-heavy nuclei. As of our last report [1], we were in the process of constructing an improved ionization chamber based design for detection of alpha particles emitted from the reaction products. An approximate schematic of the detection set up is provided in Fig. 1.

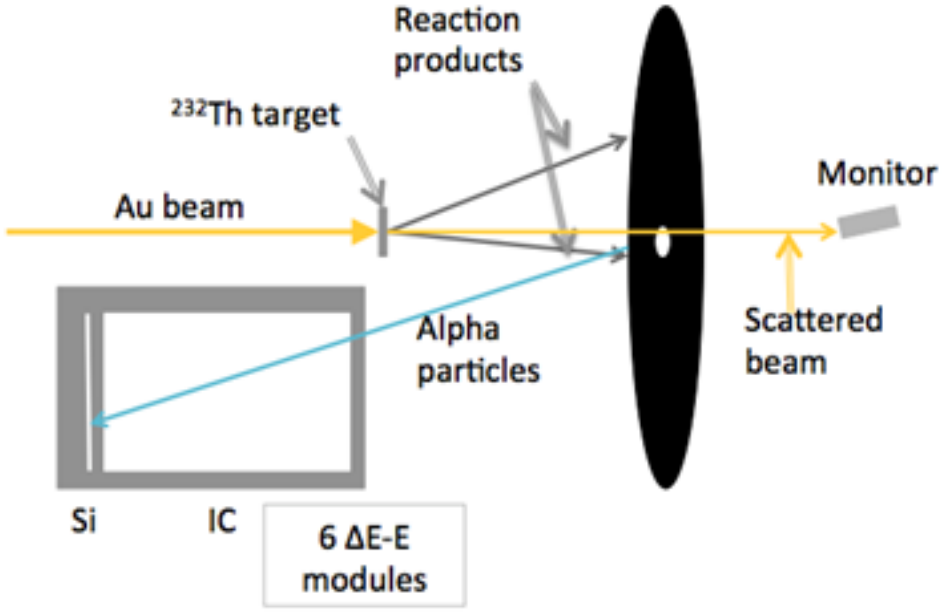

FIG. 1. Schematic arrangement of detectors versus target, catcher foil, and monitor for experiments.

The ionization chambers were constructed as described in [1], with the following modifications: PPACs were not included, and the 16 strip detectors were omitted.

Three experiments were carried out in the last year utilizing these ionization chambers to observe 7.5MeV/A ^{197}Au+^{232}Th reactions. During the first experiment, a variety of beam pulsing times were surveyed. These beam on/off scenarios provided alpha energy dependent growth and decay curves. Example curves are provided in Fig. 2 for the 100ms on/off beam pulsing. It is clear from these data, that as the alpha energy increases the particles observed are emitted from nuclei with increasingly short half-lives.

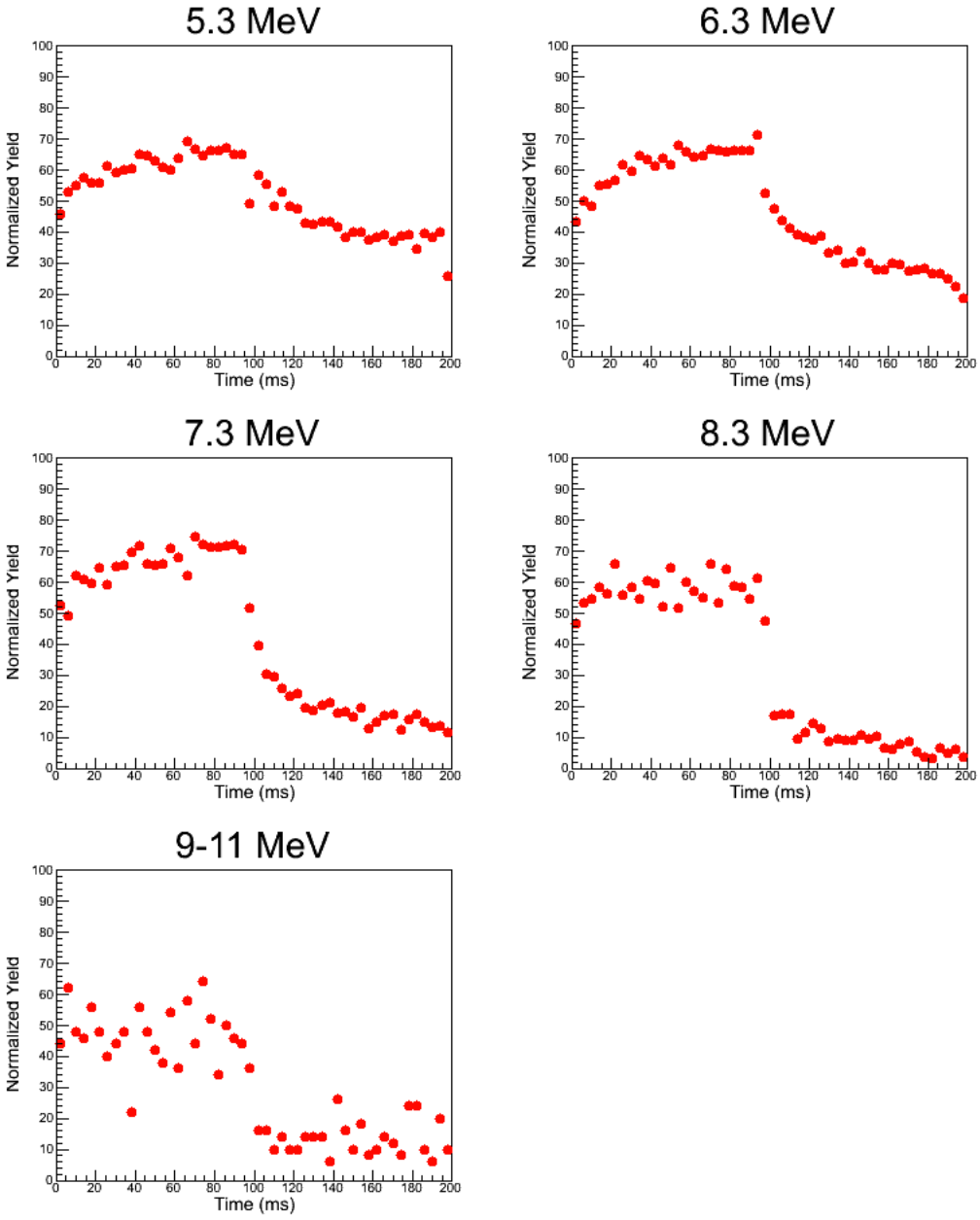

FIG. 2. Yield versus time curves divided into energy windows. Data was obtained with 100ms on/off beam pulsing.

A collective plot of all beam on/off events is provided in Fig. 3. Here we must point out difference in relative intensity between beam on/off events as well as the evolution of distribution shape with alpha energy. The evolution of distribution shape has been shown to be dependent upon the choice of beam on/off interval. The ratio of beam on/off events reaches as high as a factor of 80 in the 9-10 MeV region.

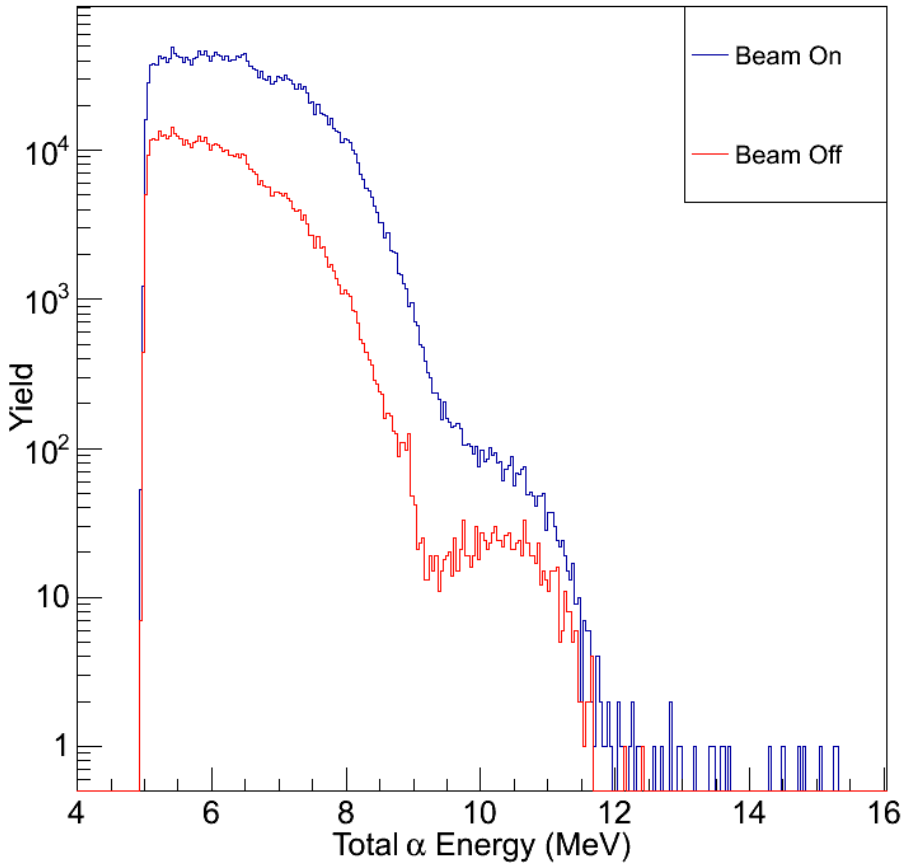

FIG. 3. Yield of detected alpha particles versus total energy lost in the ΔE-E detectors and windows. The top curve (blue) reflects alphas arriving during the beam on period and the lower curve (red) alphas arriving while the beam was turned off.

It must be noted that the 'total' alpha energy, plotted in Fig. 3, does not include any energy lost prior to entering the ionization chamber. Two-body kinematics calculations [2] estimate that interesting super-heavy events may implant as much as 40 μm into the polypropylene catcher foil. This implantation depth was explored during the second experiment of last year. Three thicknesses of catcher foil: 1ply, 2ply, and 4ply (each ~20 μm thick) were tested. After normalizing to total incident beam, the alpha yield distributions indicated that the alpha-emitting reaction products implanted within the first two layers of polypropylene. Calculations utilizing the energy loss code of Barbui *et al.* [3] and SRIM indicate that the observed alpha energies shown in Figure 3 may be 0.5-3 MeV lower than their true values.

The major challenge moving forward will be to correlate detected alphas into decay chains. To do so, we are designing and building an active catcher array to replace the polypropylene foil. This array will consist of ~96 modules of fast plastic read by phototubes. In addition to determining correlations, the active catcher array will provide the capability to identify and/or eliminate ternary alpha emission as a source of high-energy alphas. Prototype modules from the active catcher array were tested during the third heavy element experiment of last year. These modules provided good timing resolution but may not

be sufficiently radiation hard. We are investigating including diamond detectors for active catcher angles at which scattered beam is most damaging.

[1] S. Wuenschel *et al.*, *Progress in Research*, Cyclotron Institute, Texas A&M University (2012-2013), p. II-15.
[2] http://nrv.jinr.ru/nrv/webnrv/kinematics/two_body.php
[3] M. Barbui *et al.,* Nucl. Insrum. Methods Phys. Res. **B268**, 2377 (2010).

The clusterization of alpha-conjugate nuclei

K. Schmidt, E. -J. Kim, M. Barbui, S. Wuenschel, J. B. Natowitz, H. Zheng, N. Blando, K. Hagel, A. Bonasera, G. Giuliani, M. Rodrigues, R. Wada, M. Huang, C. Botosso, G. Liu, G. Viesti, S. Moretto, G. Prete, S. Pesente, D. Fabris, Y. El Masri, T. Keutgen, S. Kowalski, Z. Kohley, and A. Kumar

We reported in several previous years on a study probing the clusterization of alpha conjugate nuclei [1,2]. As noted, data was taken with NIMROD on a number of systems that are composed of alpha conjugate nuclei. Two experiments were performed, one with a Ca beam at 35, 25 and 10 MeV/u and the other with at Si beam at 35 and 15 MeV/u. Data were collected with each of the beams using Ca, Si, C and Ta targets. The previous reports focused on the analysis of the 35 MeV/u Ca + Ca system.

We have extended the study by progressing in the analysis of the 35 MeV/u Ca + C, Ca + C, Ca + Ta, Si + C, Si + Si, Si + Ta systems. This extension of the analysis allows a systematic comparison of the breakup of alpha-conjugate nuclei for different projectile/target comparisons. In all of these systems, we observe a strong propensity of the system to break up into nuclei that are alpha-like in nature. We also observe a strong enhancement of emission from a defined neck-like region in the systems where the target is an alpha-conjugate nucleus. This enhancement is absent in the systems with the Ta target.

Fig. 1 shows how the various systems have a significant probability to break up into

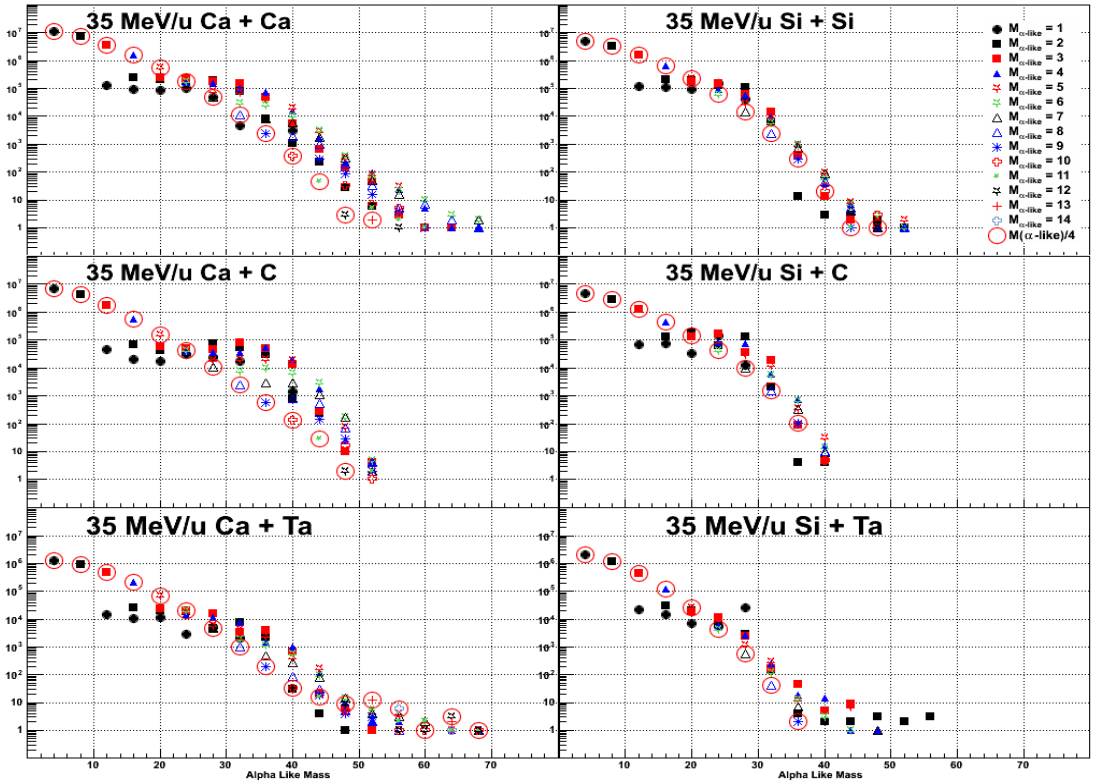

FIG. 1. Probability distributions of various breakup channels for the different systems studied. The x axis shows the alpha like mass and the y axis shows the probability of the breakup into different channels as depicted by the various symbols. The open circles indicate the probability the total alpha like mass being contained in alpha particles.

predominantly alpha like masses. The x axis shows the value of the total mass contained in alpha like nuclei (alpha-like-mass) and the y axis shows the probability of the various decay channels into alpha like nuclei. The open circles indicate the probability that all of the alpha like mass is contained in alpha particles. We see on all of these plots that there is a significant probability of breakup of a large fraction of the complete system into alpha like mass. We note that this occurs on all of the studied systems.

In Ref. [1], we showed a strong neck like origin of the alpha particles as well as fragments having an alpha like mass. Fig. 2 shows invariant velocity plots of the products that originate from events selected to have a total detected alpha-like mass of 40. We show the emission patterns for the various

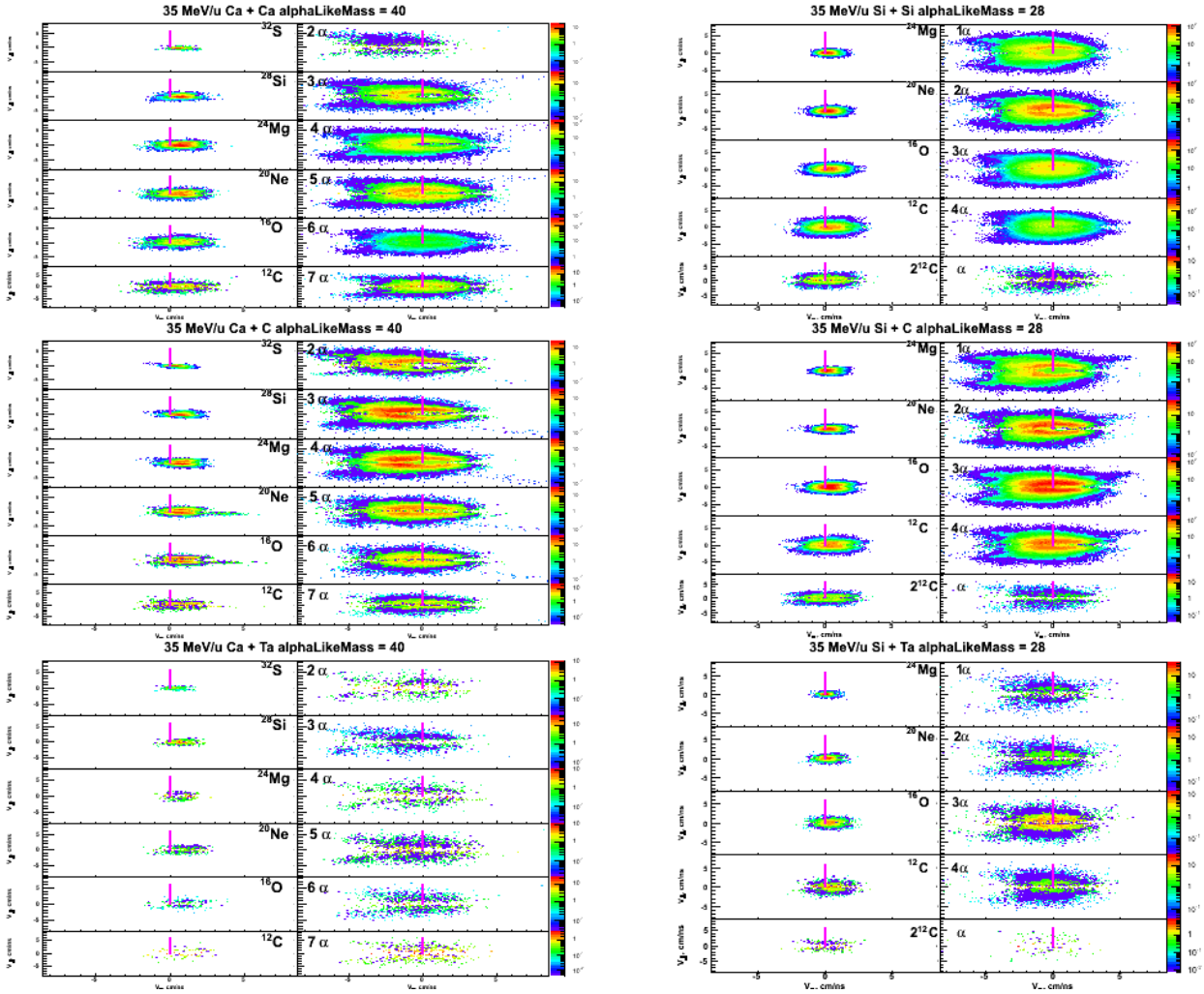

FIG. 2. Invariant velocity distributions of products resulting from the various decays channels of a decaying source reconstructed in events having a detected alpha like mass of 40 for the Ca beams and 28 for the Si beams. The vertical lines indicate vz=0, the frame of the reconstructed source.

decay channels that lead to an alpha-like mass of 40 for all of the systems that were studied. The left side of the frame of each system shows the velocity distributions of the heavier alpha like fragments and the right side shows the velocity distributions of the alpha particles associated with those heavier fragments. The vertical lines indicate the location vz=0 which is the frame of the reconstructed decaying system. This distribution shows that the neck like origin of the alpha particles is present in the reactions where the

complete system is composed of alpha-like nuclei. We note that the majority of the alpha-particles are at velocities less than that of the emitting source in the defined neck region. It is also shown that the heavy partner is found at a velocity larger than that of the reconstructed source.

We note, however, that the alpha-like heavier fragments and the alpha-particles themselves do not exhibit such behavior in the reactions with the Ta target for both the Ca and Si beams. The emission of fragments and alpha particles are more or less symmetric around the velocity of the reconstructed source suggesting different dynamics when the nucleus is not an alpha conjugate nucleus.

Since the data from these systems are calibrated, we are now in a position extract systematics from the various projectile/target combinations and expect to make significant progress on the analysis in the coming months. We have the, Ca+Si and Si+Ca systems where the calibrations are in the early stages. The calibrations of the data at 25 and 10 MeV/u for both beams are also in the initial stages. We hope to make progress on these calibrations in the coming year.

[1] K. Schmidt *et al., Progress in Research*, Cyclotron Institute, Texas A&M University (2012-2013), p. II-20.

[2] K. Schmidt *et al., Progress in Research*, Cyclotron Institute, Texas A&M University (2011-2012), p. II-9.

Transverse momentum of ionized atoms and diatomic molecules acquired in collisions with fast highly-charged heavy ion

V. Horvat and R. L. Watson

The momenta of ions and electrons emerging from collisions between charged projectiles and neutral target atoms or molecules have been topics of interest over the past few decades. However, precise simultaneous measurements of all three individual vector components of momentum for charged recoil ions produced in the collisions became possible more recently, following the development of recoil-ion momentum spectrometers (RIMS) that incorporated fast timing and simultaneous two-dimensional position determination capabilities. The high resolution, high efficiency, and reliability of RIMS's is accomplished by combining large-area microchannel plate detectors with delay-line anodes, high-precision time digitizers, and advanced signal-reconstruction algorithms [1].

So far, it has been established [2-6] that ionizing collisions involving fast highly-charged heavy ions and neutral atoms having more than two electrons occur predominantly at large impact parameters and may result in single, double, or multiple ionization of the target atoms, thus turning them into charged recoil ions. Ionization of the target atoms is predominantly due to pure ionization, in which the projectile charge does not change. The resulting recoil-ion charge distribution is a steep monotonically decreasing function of charge [7], while the recoil-ion transverse momentum $q_\perp$ (perpendicular to the momentum of the incoming projectile) is relatively small for low-charged recoil ions (*i.e.* no more than a few atomic units), but increases rapidly as a function of recoil-ion charge [2-6]. This increase is a consequence of the fact that Coulomb interaction between the projectile and the recoil ion (after its formation) is stronger when the recoil-ion charge is higher and when the impact parameter is smaller. These two causes are related, since recoil ions with higher charge are generally produced in collisions characterized by smaller impact parameters.

The production of very high recoil-ion charge states at very small impact parameters is increasingly due to ionization accompanied by single, double or multiple electron transfer from the target to the projectile or single, double, or multiple projectile electron loss. The recoil-ion charge distributions resulting from these processes are generally bell-shaped [7].

However, there are no known reports of measured $q_\perp$ distributions in strong-interaction collisions between fast highly-charged heavy ions and molecules having more than two electrons. Presumably, the transverse momentum of molecular ions emerging from the collisions should have a distribution similar to that expected for ionized atomic targets having comparable charge-to-mass ratio, as long as the size of the molecule is much smaller than the impact parameter. However, this may not hold true for small-impact-parameter collisions that result in double or multiple target ionization, which in turn leads to the dissociation of molecules, predominantly into positively charged fragments.

In our experiment a RIMS system was used to detect recoil ions created by bombardment of Ne, Ar, CO, N_2, and O_2 gas targets by a beam of 2.5 MeV/u Xe^{13+} ions [8]. Regardless of the target used, the outgoing beam was found to consist of about 98 % Xe^{13+}, 1.3 % Xe^{12+}, and 0.3 % Xe^{14+}. The $q_\perp$ resolution was estimated as being better than 5 a.u..

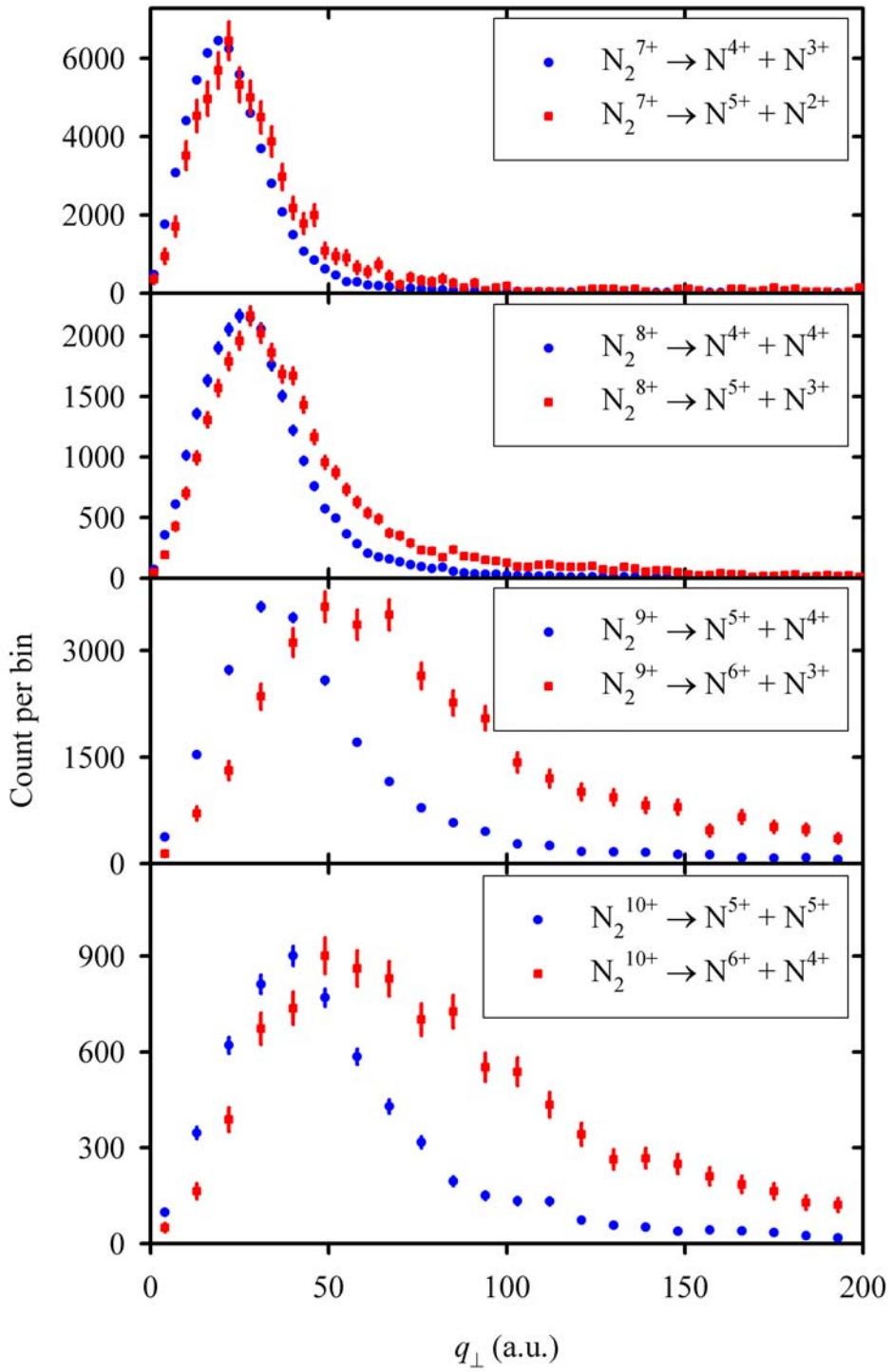

FIG. 1. Comparison of the $q_\perp$ distributions for dissociation channels corresponding to the same N_2 parent molecular ion, which is assumed to have charge number equal to the combined fragment charge numbers. In each plot, the number of counts per bin as indicated on the vertical axis scale applies to the dominant dissociation channel (*i.e.*, one that is listed first in the legend). Distributions for the remaining dissociation channels in each plot were scaled so that their maximum values match that of the corresponding dominant dissociation channel. The bin size is 3 a.u. for N_2^{7+} and N_2^{8+} and 9 a.u. for N_2^{9+} and N_2^{10+} parent molecular ions. The error bars shown are purely statistical.

Since in the strong interaction regime the duration of a collision (on the order of 10^{-17} s in the present case) is typically much shorter than the target relaxation time (on a time scale of 10^{-14} s in this work), it can be expected that target relaxation is virtually unaffected by the projectile. Consequently, in the case of ionization of a diatomic molecule by a fast projectile, followed by the molecular dissociation into two positively charged fragments having charge numbers Q_1 and Q_2, it is expected that the $q_\perp$ distributions are essentially the same for all dissociation channels corresponding to the same combined fragment charge number $Q = Q_1 + Q_2$. An upward shift (*Q-shift*) of the distributions as Q increases is expected due to the fact that a parent molecular ion with a higher value of Q is more likely to be produced in a collision at a smaller impact parameter, which in turn is more likely to result in a larger transverse momentum of the target core due to the increased Coulomb interaction between these two collision partners.

Both of these expectations were confirmed to be true for values of $Q < 7$ for all three molecular targets used. However, for $Q \geq 7$, it was found that a more asymmetric dissociation channel (*i.e.*, one corresponding to a larger value of $| Q_1 - Q_2 |$) has a larger Q-shift compared to a less asymmetric dissociation channel (*i.e.*, one corresponding to a smaller value of $| Q_1 - Q_2 |$). The absolute difference between these Q-shifts was found to increase as Q increases. This is demonstrated in Fig. 1 for the case of N_2 molecular dissociation. This effect will be referred to as the *ΔQ-split* in the text that follows.

Moreover, Fig. 1 also shows that for $Q = 9$ and 10, the ΔQ-splits are much larger than those observed for $Q = 7$ and 8. Considering that the two more asymmetric dissociation channels for $Q = 9$ and 10 include a hydrogen-like N^{6+} ion, this effect is presumably due to the fact that in order to remove a tightly-bound nitrogen *K*-shell electron in addition to other more loosely-bound electrons, a significant increase in the ionization potential must be overcome, for which the average impact parameter must decrease more drastically than is required for the removal of a less tightly bound electron. The same argument also helps explain why the less asymmetric dissociation channel is the dominant one.

For $Q = 9$ and 10, the $q_\perp$ distributions for the dissociation channels involving an N^{6+} ion, compared to the other two distributions, also have significantly longer tails, well beyond what could be expected based on the overall upward shift of the distributions (the ΔQ-split), which includes the upward shift of the distributions' peak values. This additional has a different character than that of the ΔQ-split and will be referred to as the *tail effect* in the text that follows. The onset of the tail effect at $Q = 8$ is most likely related to the increased importance of a different ionization mechanism involving target-to-projectile electron transfer, which is known to become increasingly important for the production of highly charged recoils [7] and also for the removal of tightly-bound target electrons. Therefore, the tail effect could be explained by the difference between the impact parameter *distribution* of pure ionization (which in the present case is dominant for $Q \leq 7$) and that of ionization accompanied by electron transfer from the target to the projectile (which in the present case becomes apparent at $Q \geq 8$ when the target starts losing its tightly-bound electrons).

The $q_\perp$ distributions for N_2 and CO molecular ions dissociating into positively charged fragments, as a function of the combined fragment charge number $Q \leq 7$, are compared in Fig. 2, in which contributions from dissociation channels corresponding to the given combined charge are added together. Apparently, there is hardly any significant difference between any two distributions shown in

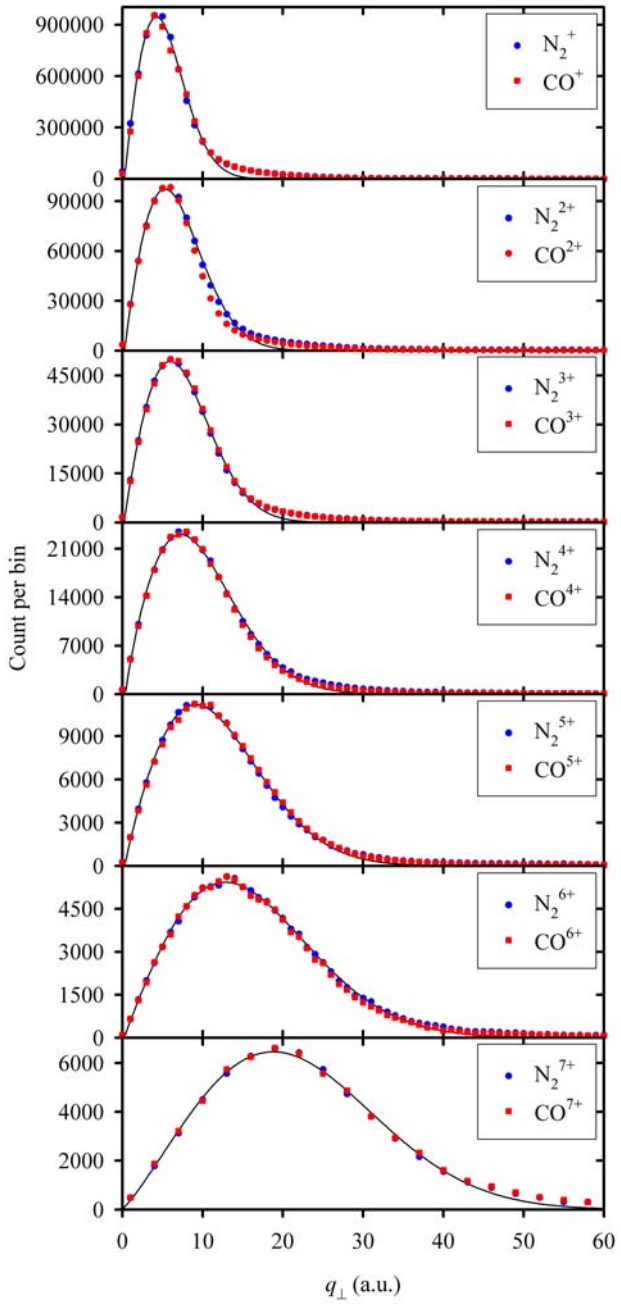

FIG. 2. Comparison of the $q\perp$ distributions for N_2 and CO molecular ions dissociating into positively charged fragments, as a function of the combined fragment charge number. Contributions from the dissociation channels corresponding to the given combined charge were added together. In each plot, the number of counts per bin as indicated on the vertical axis scale applies to the case of N_2. The distribution corresponding to CO in each plot was scaled so that the two maximum values match. The bin size is 3 a.u. for CO^{7+} and N_2^{7+} and 1 a.u. for the remaining parent molecular ions. The statistical error bars are not visible because they are smaller than the symbol size. The parent molecular ion's charge state listed in the legend is assigned the value equal to the combined fragment charge number. For completeness, also included is a plot showing the $q\perp$ distributions for non-dissociated N_2^+ and CO^+ molecular ions. The solid lines represent the overall fit of the distributions for N_2^{Q+} (parent) molecular ions ($Q \leq 7$) using Weibull functions.

the same plot. This can be expected based on the fact that the two molecules have the same combined atomic mass number and the same combined atomic number. However, N_2 and CO also have significantly different distributions of their excited states, which is evidenced by the significantly different kinetic-energy release (KER) spectra for doubly and triply charged molecular ions, as shown in Figs. 3 and 5 of Ref. [8]. This implies that, as long as tightly-bound electrons are not removed, or as long as pure ionization is the dominant mechanism for electron removal, the electronic or molecular structure of the target does not significantly affect the $q_\perp$ distribution.

Also included in Fig. 2 is a plot showing the $q_\perp$ distributions for non-dissociated N_2^+ and CO^+ molecular ions, which shows that the transverse momentum resolution in the present work is about 5 a.u. or better, as expected considering that a skimmer-collimated effusive gas jet was used [3].

All of the measured $q_\perp$ distributions were fitted with a four-parameter Weibull function. The results for N_2^{Q+} (parent) molecular ions ($Q \leq 7$) are shown by the solid lines in Fig. 2. Apparently, Weibull functions represent the shapes of the $q_\perp$ distributions very well, with only minor discrepancies at the tail for $Q \leq 3$. A similar quality of fit was obtained for all the other $q_\perp$ distributions. By restricting the region of fit to the area around the peak of the distribution (typically the region covered by the full width at half maximum), best estimates of the peak positions $q_\perp^0$ could be determined precisely and in a consistent way.

Since periods of rotation for the diatomic molecules used in this work are on the order of 10^{-12} s, while molecular fragmentation resulting from Coulomb explosions of the multi-charged molecular ions occurs on a much shorter time scale (of 10^{-14} s), it may be assumed that the orientation of the molecular axis remains unchanged between the time just prior to the collision and the end of the dissociation process. Therefore, it also may be assumed that orientation of the target molecule at the time of collision is defined by the momentum vector of its charged fragments during dissociation.

It is expected that orientation of the target molecule at the time of collision does not affect $q_\perp$ as long as the impact parameter is significantly larger than the size of the molecule. This condition is fulfilled for the majority of collisions that result in the removal of only a small number (or fraction) of electrons from the target. On the other hand, most close collisions result in the removal of a large fraction of electrons from the target and the process might be expected to have some dependence on the molecular orientation. Specifically, if the target molecule is initially oriented in the longitudinal direction, the impact parameters for two atomic centers are similar and the collision is expected to result in a symmetric or nearly-symmetric charge distribution between the atomic centers of the molecule. On the other hand, if the target molecule is initially oriented in the transverse direction, the impact parameters for two atomic centers are significantly different and the collision is expected to result in a highly asymmetric charge distribution. Therefore, the dissociation channels characterized by highly asymmetric charge distributions between the atomic centers are expected to have angular distributions that are enhanced in the transverse direction, while the dissociation channels characterized by symmetric or nearly-symmetric charge distributions are expected to have angular distributions that are suppressed in the transverse direction.

As expected, no conclusive evidence was found of anisotropy in the distributions of fragment pairs from low-charged molecular ions. However, for the symmetric and the nearly-symmetric dissociation channels (*i.e.*, those corresponding to $|Q_1 - Q_2| \leq 1$), the fragments with combined charge

number Q exceeding 9 for N_2 and 10 for O_2 were found to be distributed with a reduced probability at angles α close to 90° relative to the beam direction, as illustrated in Fig. 3. Furthermore, the effect was found to become more significant as Q increases. Interestingly, the magnitude of the effect seems to

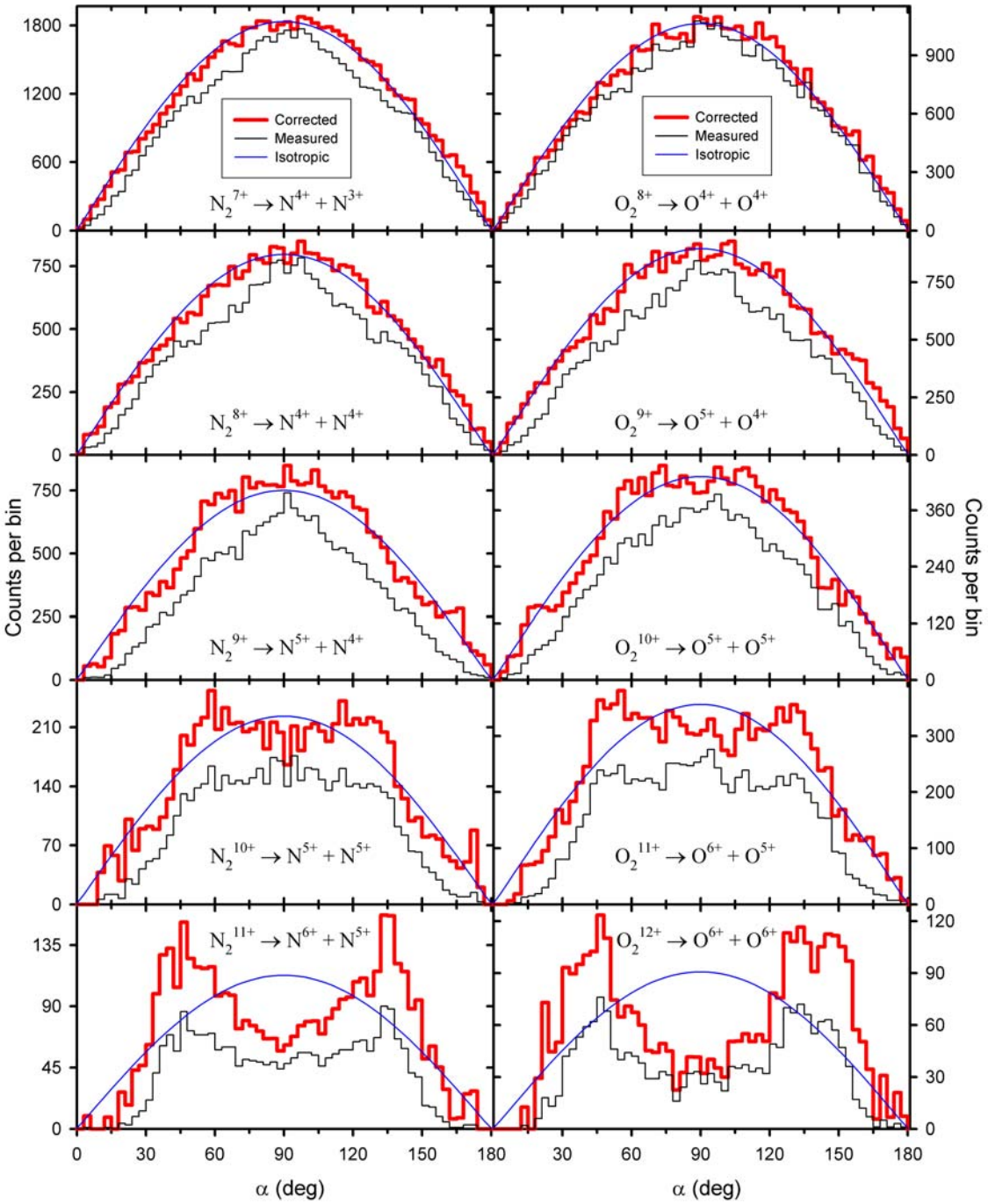

FIG. 3. Distributions of the numbers of correlated charged N_2 and O_2 molecular fragment pairs for the dissociation channels as indicated by the labels, shown as a function of angle α between the molecular axis at the time of collision and the beam direction. The thin (black) line represents the histogram of raw data, while the histogram shown with the thick (red) line is obtained by correcting the raw data for efficiency and fragment-pair acceptance of the apparatus, as described in detail in Ref.[8]. The smooth thin (blue) line shows the ideal isotropic distribution for the corrected total number of events. The N_2 and O_2 molecular ions in each row have the same value of Δn.

depend on Δn, the number of electrons removed *in addition* to one half of the number of available electrons ($\Delta n = Q - Z$). Consequently, the plots shown in Fig. 3 are selected and arranged so that each row corresponds to a given number $Q - Z$, where Z is the atomic number of nitrogen (in the first column) or oxygen (in the second column).

For highly asymmetric dissociation channels (*i.e.*, those corresponding to $|Q_1 - Q_2| \geq 2$) usable experimental results (selectively shown in Fig. 4) are limited to the cases with $Q < 11$, due to the fact that

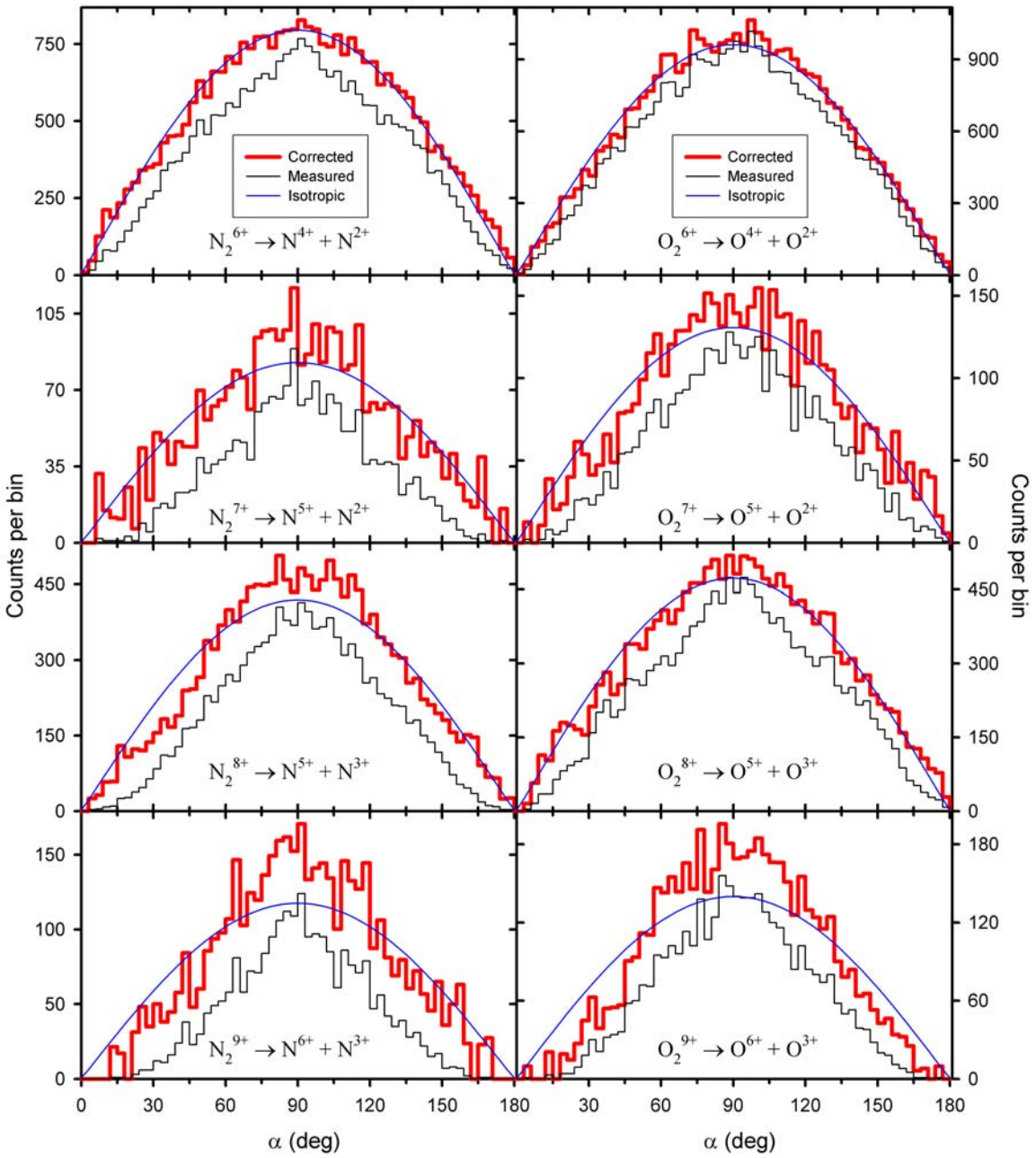

FIG. 4. Caption identical to that of Fig. 3 applies.

the production cross section decreases as Q increases and the fact that the predominant dissociation channels are symmetric or nearly symmetric. Also, the highest observed fragment charge number was 6. A

higher fragment charge would require *K*-shell ionization of oxygen or double *K*-shell ionization of nitrogen, for which the cross section is relatively low due to the relatively high binding energy of the *K* electrons. Nevertheless, the angular distributions shown in Fig. 4 for $Q = 9$ are slightly different than those shown in Fig. 3 for the same value of Q, indicating that the fragments of highly-charged molecular ions may be distributed with an *enhanced* probability at angles α close to 90^o relative to the beam direction.

The onset of the observed angular anisotropy may also be affected by the charge redistribution between the molecular fragments that may occur during dissociation and by autoionization, which is more likely to affect the fragment having lower charge (*i.e.*, more electrons). Both effects are likely to lead to charge equalization, which in effect makes an event from a more asymmetric dissociation channel appear in a less asymmetric (and more prominent) dissociation channel. Due to the apparent complementary properties of the angular distributions for these two dissociation channels (as described above), such events could make the angular distribution of the latter dissociation channel appear less anisotropic, thus shifting the onset of the observed anisotropy to higher values of Q.

As Q becomes large, autoionization becomes less likely because of the smaller number of available electrons and higher electronic binding energies, while charge redistribution may require tunneling of the electrons through the potential barrier between the atomic centers, which occurs with a drastically reduced probability. It can be estimated that the potential barrier of an electron transferring from N^{3+} to N^{6+} (about 80 eV) is only slightly higher than the ionization potential of N^{3+} (about 77 eV), which would imply that charge redistribution is unlikely for $Q > 9$. The reduced probability of charge equalization for $Q > 9$ coincides with the seeming onset of the deviations from an isotropic distribution, as shown in Figs. 3 and 4.

The effect of molecular orientation on $q_\perp$ distributions was found to be small. Consequently, the angular scale was reduced to only two bins; one covering $60^o \leq \alpha \leq 120^o$ and the other covering the remainder of the angular range, so that $|\cos\alpha| \leq 0.5$ in the former case and $|\cos\alpha| > 0.5$ in the latter case. For an isotropic angular distribution the two cases are expected to correspond to the same number of events. The results for the symmetric and nearly-symmetric dissociation channels are shown in Fig. 5. Apparently, the molecular orientation at the time of collision does have an effect on the $q_\perp$ distributions for $Q - Z > 0$ and its magnitude seems to depend on $Q - Z$. This effect was not present for the observed highly asymmetric dissociation channels.

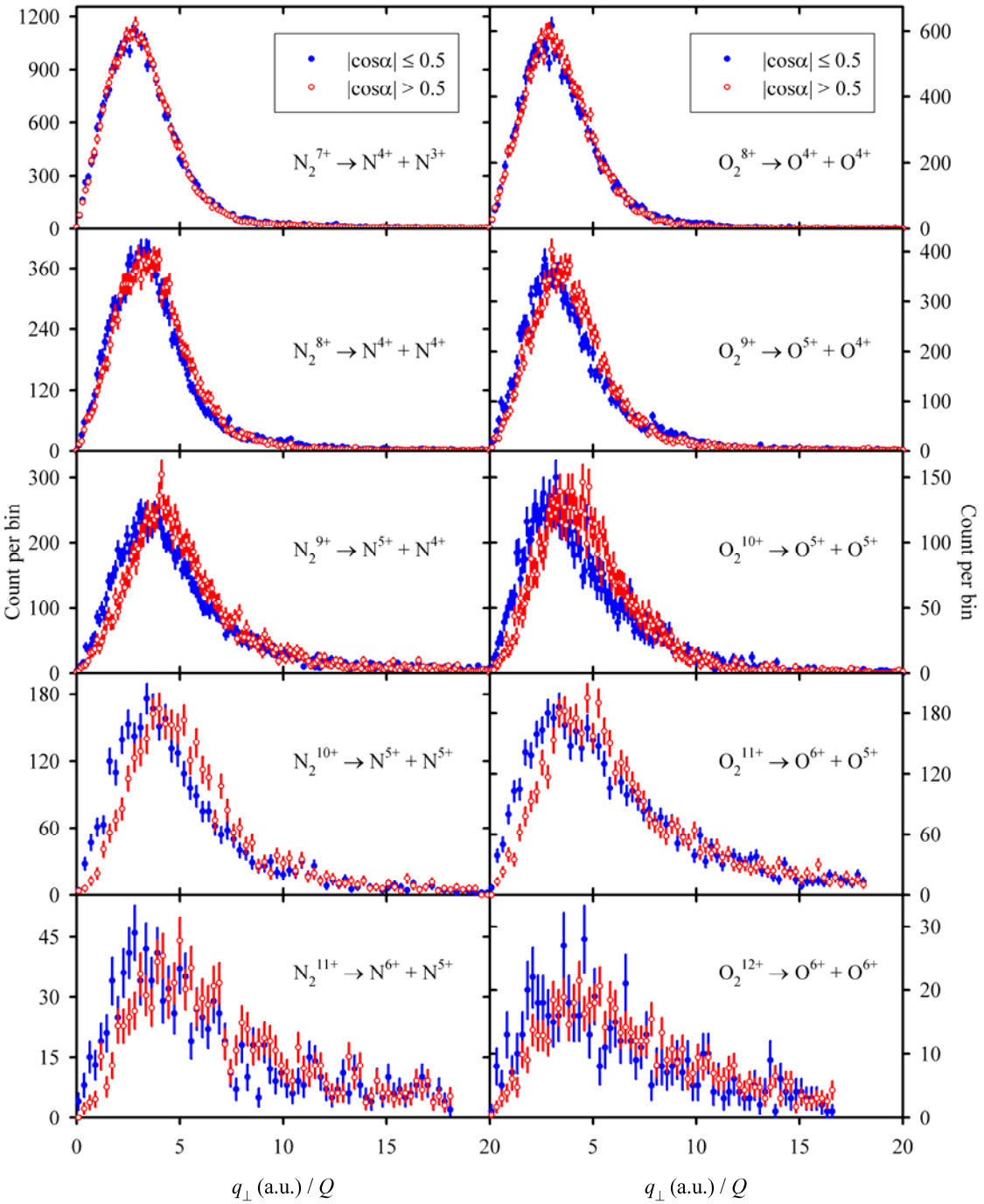

FIG. 5. Measured $q_{\perp}$ distributions for the selected N_2 and O_2 dissociation channels (as indicated by the labels) for angles $60^{o} \leq \alpha \leq 120^{o}$ ($|\cos\alpha| \leq 0.5$) and for the remainder of the angular range ($|\cos\alpha| > 0.5$), as indicated by the legend. The latter distribution was normalized to the total number of events of the former distribution and the scaling on the horizontal axis (*i.e.*, division by Q) was applied to enhance the details.

[1] http://www.roentdek.com.
[2] C.L. Cocke and R.E. Olson, Phys. Rep. **205**,153 (1991).
[3] J. Ullrich, R. Moshammer, R. Dörner, O. Jagutzki, V. Mergel, H. Schmidt-Böcking, and L. Spielberger, J. Phys. B **30**, 2917 (1997).
[4] R. Dörner, V. Mergel, O. Jagutzki, L. Spielberger, J. Ullrich, R. Moshammer, and H. Schmidt-Böcking, Phys. Rep. **330**, 95 (2000).
[5] J. Ullrich, R. Moshammer, A. Dorn, R. Dörner, L.Ph.H. Schmidt, and H. Schmidt-Böcking, Rep. Prog. Phys. **66**, 1463 (2003).
[6] M. Schulz and D.H. Madison, International J. Mod. Phys. A **21**, 3649 (2006).
[7] T.J. Gray, C.L. Cocke, and E. Justiniano, Phys. Rev. A **22**, 849 (1980); Phys. Rev. A **53**, 2407 (1996).
[8] V. Horvat and R.L. Watson, Nucl. Instrum. Methods Phys. Res. **B269**, 2584 (2011).

Equation of state effects on nucleon transport

L. W. May, P. Cammarata, L. Heilborn, J. Mabiala, A. McIntosh, M. Youngs,
A. Zarrella, and S. J. Yennello

The nuclear equation-of-state (EoS) has been well studied for symmetric nuclear matter at nuclear saturation densities. However, there are not strong constraints on the density dependence of the symmetry energy at sub-saturation densities. Nucleon transport, which includes isospin drift and diffusion, describes the interaction and movement of nucleons between projectile and target in a nuclear reaction. Isospin diffusion, the transport of nucleons due to differences in isospin content, can be used to further constrain the density dependence of the symmetry energy [1,2].

Experimental data was collected for the systems of 35 MeV/nucleon ^{70}Zn, ^{64}Ni+^{64}Zn and ^{64}Zn+^{70}Zn, ^{64}Ni in order to supplement the 35 MeV/nucleon ^{70}Zn+^{70}Zn, ^{64}Zn+^{64}Zn, and ^{64}Ni+^{64}Ni data collected by Z. Kohley [3]. All experimental data were measured using the NIMROD-ISiS array, briefly described below. With the addition of the previously acquired systems, a complete data set of 7 reaction systems will be formed and used to perform the isospin equilibration and nucleon transport analysis.

The NIMROD-ISiS array is a 4π charged particle array that consists of 228 detector telescopes covering the complete solid-angle in φ and 3.6°-167° in θ. Each telescope is composed of a silicon detector (150 or 300 μm thickness) followed by a CsI(Tl) crystal connected to a photomultiplier tube [4]. This Si-CsI combination allows for the identification of charged particles by energy deposited in the detectors via ΔE-E plots. A linearization is performed where lines are drawn to match the curves seen in the ΔE-E. These lines are then straightened and projected on the x-axis to give mass distributions of the particles detected allowing for isotopic particle identification up to Z=20. Fast vs. Slow pulse-shape discrimination in the CsI crystals allows for high-resolution identification of light charged particles, up to ^{6}Li.

Identification of particle charge and mass and energy calibrations have been completed throughout the array. Silicon detectors are calibrated using the known threshold-corrected punch-through points (energy at which a particle passes through the Si detector but does not have enough energy to penetrate the CsI crystal) for specific isotopes. These punch-through points are then fit and compared to elastic scattering peaks from known calibration beams in order to get a linear calibration fit (Fig. 1a). The CsI crystals are calibrated by using elastic peaks from calibration beams and the use of a modified fitting function based on the Birks equation for light output of a CsI crystal [5,6]. A CsI calibration plot showing the results of this fit to the calibration points is shown in Fig. 1b. A preliminary calibration was completed previously allowing the examination of the resulting preliminary physics tapes. Figure 1c shows the Z=1 charged particle calibrated kinetic energy spectra for each ring of the NIMROD-ISiS array. Such plots are used to examine the energy calibration at each step through the process so that the quality of the calibration can be checked and assured. Complete energy calibrations will be finished in May 2014.

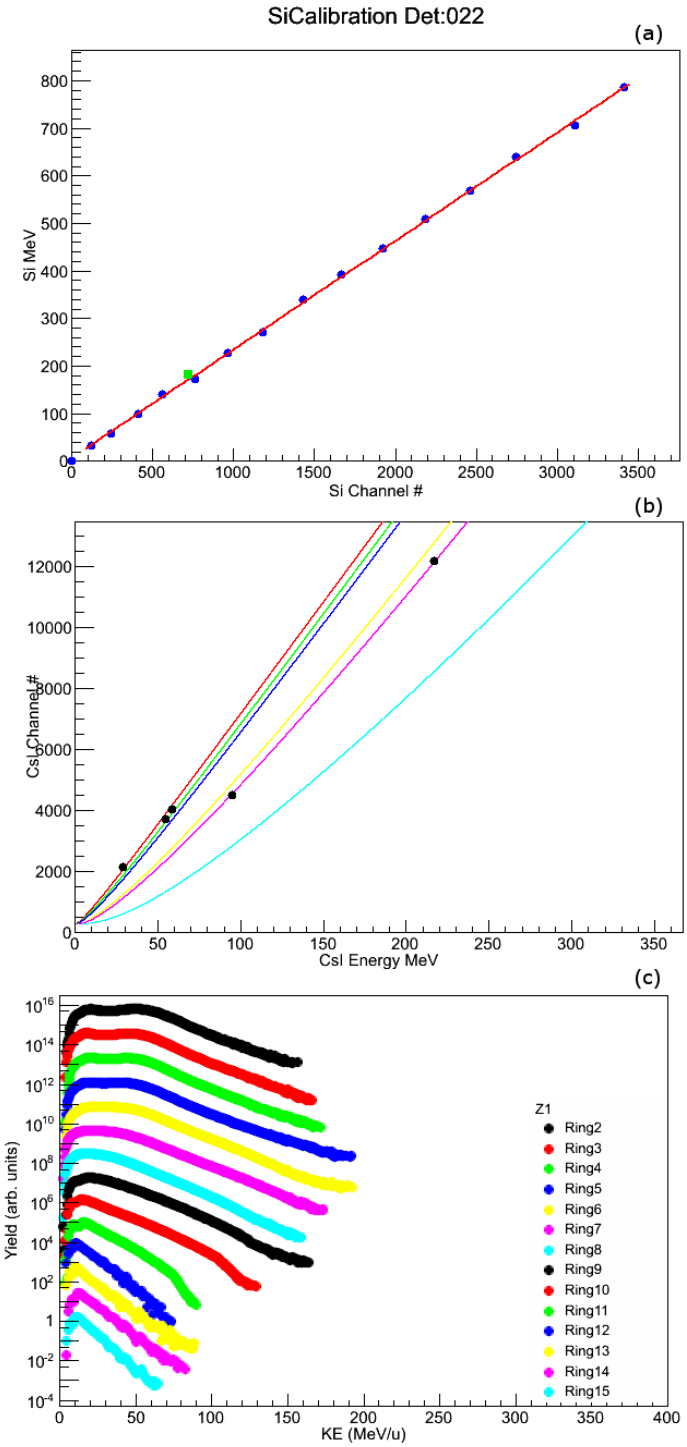

FIG. 1. (a)Si detector calibration plot: blue dots correspond to punch-through points, green dots are calibration beam points and red line is best-fit line used to extract calibration parameters. (b) CsI detector calibration plot: dots correspond to calibration beam points while colored lines are best-fit calibration parameters corresponding different isotopes (p,d,t,^{3}He,^{4}He,^{6}Li). c) Z=1 charged particle kinetic energy spectra as a function of theta (ring number) in NIMROD-ISiS array. Yield is given in arbitrary units and scaled so that curves are separated.

[1] A.L. Keksis *et al.*, Phys. Rev C **81**, 054602 (2010).
[2] M.B. Tsang *et al.*, Phys. Rev. Lett. **92**, 062701 (2004).
[3] Z. Kohley *et al.*, Phys. Rev. C **81**, 064601 (2010).
[4] S. Wuenschel *et al.*, Nucl. Instrum, Methods Phys. Res. **A604**, 578 (2009).
[5] G.F. Knoll, Radiaton Detection and Measurement (John Wiley & Sons, Ann Arbor, 2000).
[6] W.R. Leo, Techniques for Nuclear and Particle Physics Experiments. (Spring-Verlag, New York, 1994).

Coulomb corrections to experimental temperatures and densities in Fermi-energy heavy-ion collisions

J. Mabiala, H. Zheng, A. Bonasera, P. Cammarata, K. Hagel, L. Heilborn, Z. Kohley,* L. W. May, A. B. McIntosh, M. D. Youngs, A. Zarrella, and S. J. Yennello

Understanding the behavior of nuclear matter at various densities and temperatures is one of the main goals of the study of heavy-ion reactions. The determination of nuclear parameters (temperature, density, pressure, free energy, etc) that characterize the nuclear equation of state (NEOS), essential in understanding a number of important issues in astrophysics, remains a difficult task despite a wide body of available experimental data. A number of methods can be found in the literature that have been developed and applied to the study of thermodynamic properties of highly excited nuclear systems. These include the slope thermometer from kinetic energy distributions of emitted particles [1–4], the population of excited states thermometer [5–7] and the double isotopic yield ratio method [3, 4, 7–9] to extract the density and temperature of the system. All these methods were derived from a classical approach. However, a coalescence approach was also developed to estimate the density [9, 10]. The densities obtained using a coalescence approach were found to be higher than those from a double ratio densitometer. This is undoubtedly due to the coalescence parameter that might mimic important quantum effects [11] resulting in relatively high densities.

Another method for measuring temperatures was proposed by Wuenschel *et al.* [12] based on quadrupole momentum fluctuations of fragments using a classical Maxwell-Boltzmann distribution. Within the same framework but for a Fermi-Dirac distribution or a Bose-Einstein distribution, a new method for extracting simultaneously both density and temperature of the system was suggested in Refs. [13–15]. A proper treatment of the quantum statistical nature of particles produced during heavy-ion reactions is taken into account in this newly proposed method. In such an approach, particle multiplicity fluctuation is used in addition to quadrupole momentum fluctuation to infer a temperature and density of the system. Also, important quantum effects, such as Fermion Quenching or Bose-Einstein Condensation (BEC) [16–19], can be traced when fermions and bosons are treated differently. In subsequent works [20–22], this method has been further modified by taking explicitly into account Coulomb corrections.

In the present study, we extend our previous analysis [23–25] which used protons as the probe particle. We provide additional results from the same experimental data set by Coulomb correcting the density and temperature. The experiment was performed at the K-500 superconducting cyclotron facility at Texas A&M University. ^{64,70}Zn and ^{64}Ni beams were used to respectively irradiate ^{64,70}Zn and ^{64}Ni targets at 35 MeV/nucleon. Charged particles and free neutrons were detected with the NIMROD-ISiS 4π detector array [26]. Further details of the experiment may be found in Refs. [27, 28]. The excellent energy resolution achieved allowed isotopic resolution of charged particles up to Z=17 and elemental resolution up to the charge of the beam. The quasi-projectile (QP), the large, excited, primary fragment of the projectile following a non-central collision with the target, was reconstructed from events in which all charged particles were isotopically identified. The Neutron Ball [29] provided event-by-event

* Present address: National Superconducting Cyclotron Laboratory, Michigan State University, East Lansing, Michigan 48824

experimental information on the free neutrons emitted during a reaction. The number of free neutrons emitted by the QP was deduced from the total measured number of neutrons, background and efficiencies for measuring neutrons produced from QP and quasi-target sources [12]. The excitation energy was deduced using the transverse kinetic energy of the charged particles, the neutron multiplicity and the energy needed for the breakup (Q-value). This method of reconstruction has previously been fully described in Refs. [12, 30]. Using the three reaction systems, we selected a QP mass range not too far from the projectile mass ($54 \leq A \leq 64$) and a span in neutron-proton asymmetry (m_s) with sufficient statistics.

The temperatures of reconstructed QPs and nucleon densities are obtained with the quadrupole momentum and multiplicity fluctuation method fully reported in Refs [13–15, 20]. Protons have been used as the probe particle. In Refs. [20, 21], Zheng *et al.* addressed the issue of correcting for Coulomb effects in the determination of densities and temperatures of hot sources produced in heavy-ion collisions. This method borrowed from electron scattering was adopted and applied to classical as well as to quantum systems. The Coulomb field is taken to be the Fourier transform of the Coulomb potential of the source. In this way, the equations of quadrupole momentum fluctuation, the average multiplicity, as well as the multiplicity fluctuation containing the Coulomb field term, were numerically solved to derive the temperature (T), the density (ρ) and the volume of the system (V). Using model calculations, the authors of Refs. [20, 21] showed that derived temperatures of protons and neutrons are very similar whereas densities are largely not affected by Coulomb effects. The same behavior was also observed for composite fermions in the classical case. We have applied the same procedure to our experimental data.

In Fig. 1 (top panels), we present QP temperatures as a function of the excitation energy per nucleon using protons as the probe particle. These caloric curves show a monotonic rising behavior for both cases (without and with Coulomb corrections). A weak dependence on m_s is observed for temperatures extracted without and with Coulomb correction. It is also observed that Coulomb corrections lower the temperature value by almost 2 MeV.

The densities of QP regions probed by protons versus the excitation energy per nucleon are shown in bottom panels of Fig. 1. The left and right panels correspond to results without and with Coulomb corrections, respectively. As protons refer to the gas component (low-density) region of the system in the liquid/gas-type phase transition, we observe that the density rises as the excitation energy increases. In fact, as the excitation energy increases more protons leave the liquid phase and enter the gas phase thus creating a larger density of protons in the gas phase. A clear dependence on m_s is seen in each panel for the four density curves: the larger the asymmetry, the lower the density. In our previous studies [25, 31, 32], a strong dependence of temperatures on m_s has been shown within a classical treatment. However, in the present treatment where we extract simultaneously both temperature and density, the dependence on m_s is rather strongly exhibited in the density. We also note that Coulomb corrections have, in general, a small effect on the derived densities as was shown for model calculations reported in Refs. [20, 21].

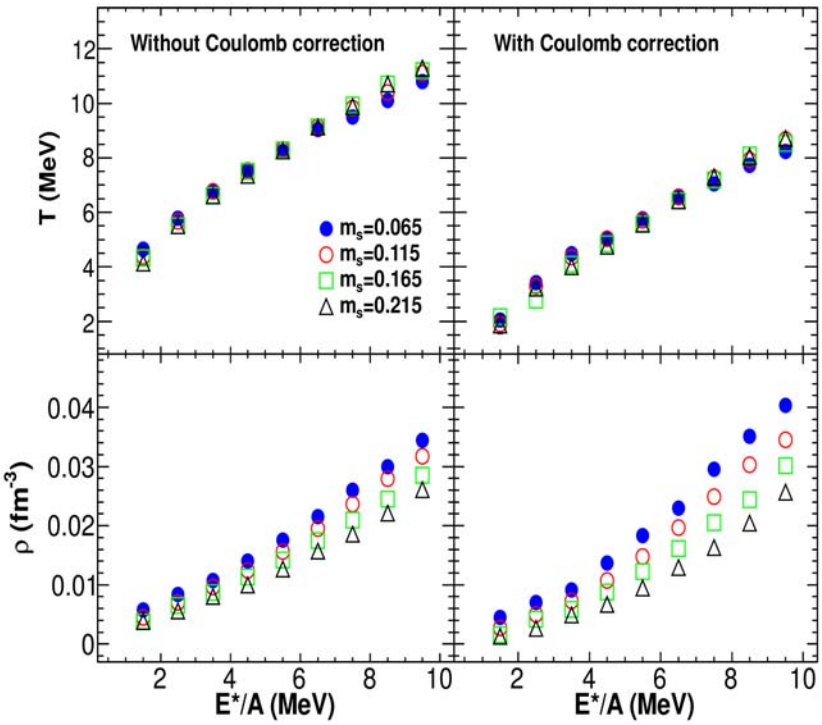

FIG. 1. Temperatures (top panels) and densities (bottom panels) of the gas phase for QPs that differ in neutron-proton asymmetry (m_s) as a function of the excitation energy per nucleon. Protons are used as the probe particle. Left and right panels correspond respectively to results without and with Coulomb correction. Statistical errors are smaller than the symbols.

The correlation between the density and the temperature, as probed by protons, is presented in the left panel of Fig. 2 for the four different source asymmetries. All curves display a rising behavior. It is also interesting to notice that as the system temperature increases, the spacing between the proton density values for different asymmetries increases. These features may be attributed to the competing roles of symmetry and Coulomb energies. From the values of density and excitation energy, we examine in the right panel of Fig. 2 the energy density $\varepsilon=(E^*/A)\rho$ against the temperature. It is observed that ε monotonically increases as T increases and the differences between curves seen in the left panel of Fig. 2 are less noticeable.

To summarize, we have presented and discussed temperatures and densities of hot sources produced in heavy-ion collisions near Fermi energies determined with the very recently established quantum fluctuation method. Coulomb corrections applied to derived temperatures and densities using protons as the probe particle have shown to lower temperature values by almost 2 MeV compared to non-corrected results while little effect is shown on derived densities. The results of energy density versus temperature have shown a small dependence on the neutron-proton asymmetry of the system.

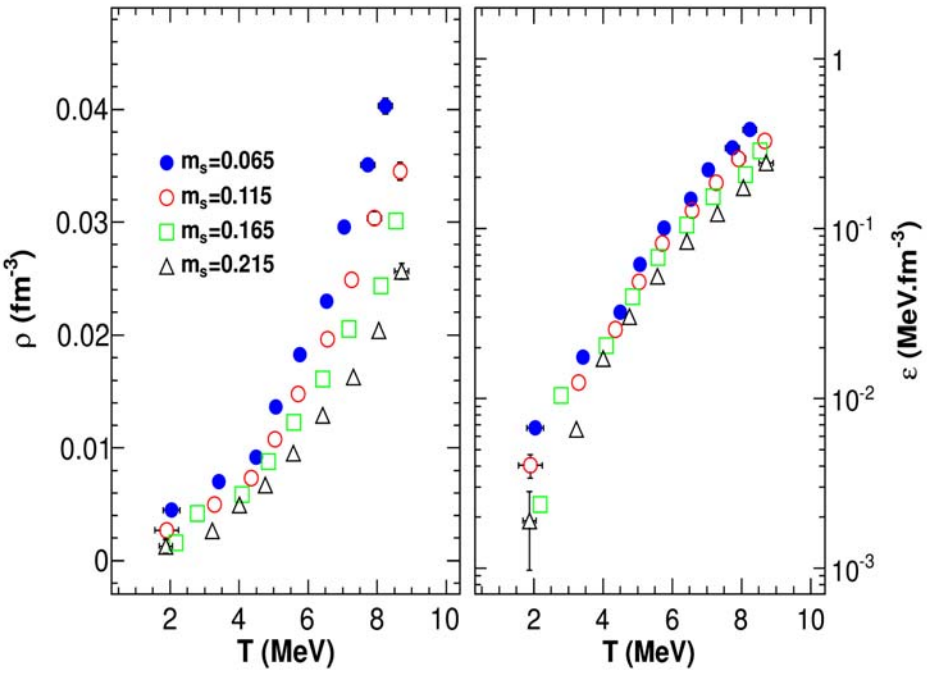

FIG. 2. Left panel: Correlation between the density and the temperature of the system as probed by protons. Right panel: Energy density versus temperature. All quantities are corrected for Coulomb. Statistical errors are shown by the bars and are not shown when smaller than the symbols.

[1] G. Westfall *et al.*, Phys. Lett. B **116**, 118 (1982).

[2] B.V. Jacak *et al.*, Phys. Rev. Lett. **51**, 1846 (1983).

[3] J.B. Natowitz *et al.*, Phys. Rev. C **65**, 034618 (2002).

[4] A. Bonasera *et al.*, La Rivista Del Nuovo Cimento **23**, 1 (2000).

[5] D. Morrissey *et al.*, Phys. Lett. B **148**, 423 (1984).

[6] J. Pochodzalla *et al.*, Phys. Rev. Lett. **55**, 177 (1985).

[7] M.B. Tsang *et al.*, Phys. Rev. C **53**, R1057 (1996).

[8] S. Albergo *et al.*, Il Nuovo Cimento A Series 11 89, 1 (1985).

[9] L. Qin *et al.*, Phys. Rev. Lett. **108**, 172701 (2012).

[10] A. Mekjian, Phys. Rev. Lett. **38**, 640 (1977).

[11] G. Röpke *et al.*, Phys. Rev. C **88**, 024609 (2013).

[12] S. Wuenschel *et al.*, Nucl. Phys. **A843**, 1 (2010).

[13] H. Zheng and A. Bonasera, Phys. Lett. B **696**, 178 (2011).

[14] H. Zheng and A. Bonasera, Phys. Rev. C **86**, 027602 (2012).

[15] H. Zheng, G. Giuliani, and A. Bonasera, Nucl. Phys. **A892**, 43 (2012).

[16] T. Müller *et al.*, Phys. Rev. Lett. **105**, 040401 (2010).

[17] C. Sanner *et al.*, Phys. Rev. Lett. **105**, 040402 (2010).
[18] B.C. Stein *et al.*, J. Phys. G **41**, 025108 (2014).
[19] J. Esteve *et al.*, Phys. Rev. Lett. **96**, 130403 (2006).
[20] H. Zheng, G. Giuliani, and A. Bonasera, Phys. Rev. C **88**, 024607 (2013).
[21] H. Zheng, G. Giuliani, and A. Bonasera, J. Phys. G **41**, 055109 (2014).
[22] G. Giuliani, H. Zheng, and A. Bonasera, Prog. Part. Nucl. Phys. **76**, 116 (2014).
[23] J. Mabiala *et al.*, J. Phys. : Conf. Ser. **420**, 012110 (2013).
[24] J. Mabiala *et al.*, Int. J. Mod. Phys. E **22**, 1350090 (2013).
[25] A. McIntosh *et al.*, Eur. Phys. J. A **50**, 1 (2014).
[26] S. Wuenschel *et al.*, Nucl. Instrum. Methods Phys. Res. **A604**, 578 (2009).
[27] Z. Kohley, Ph.D. Thesis, Texas A&M University (2010).
[28] Z. Kohley *et al.*, Phys. Rev. C **86**, 044605 (2012).
[29] R. Schmitt *et al.*, Nucl. Instrum. Methods Phys. Res. **A354**, 487 (1995).
[30] S. Wuenschel, Ph.D. Thesis, Texas A&M University (2009).
[31] A.B. McIntosh *et al.*, Phys. Rev. C **87**, 034617 (2013).
[32] A.B. McIntosh *et al.*, Phys.Lett. B **719**, 337 (2013).

Using transport simulations in comparison to experimental data in order to constrain the nuclear equation of state and nucleon effective mass splitting

M. Youngs, S. J. Yennello, A. Bonasera, P. Cammarata, L. Heilborn, Z. Kohley, L. W. May, J. Mabiala, A. B. McIntosh, and A. Zarrella

The nuclear equation of state (EoS) near saturation density has been constrained for some time, however the behavior at significantly sub- and super-saturation densities is still poorly constrained. Numerous simulations suggest that the ratio of the kinetic energy spectra of neutrons and protons would be sensitive to both the symmetry energy as well as the nucleon effective mass splitting, should any exist. This ratio is defined as $SR\left(\frac{n}{p}\right) = \frac{Y(n)}{Y(p)}$ where $Y(X)$ is the kinetic energy spectrum of particle X. This yield can also be represented by the double differential $\frac{dM}{d\Omega d(E/A)}$. In the case of a stronger symmetry energy, neutrons would be accelerated away from a neutron rich source while protons would be attracted towards the same source. In a similar fashion, if $m_n^* < m_p^*$ the neutrons would feel a stronger force than the protons and be accelerated to larger energies. By making comparisons it should be possible to constrain these quantities.

One difficulty with the n/p ratio is the difficulty of accurately measuring both the neutron detection efficiency as well as the effects due to Coulomb acceleration from the source. There are three primary options that can be used in order to minimize these effects. The first is the independent particle ratio, $IPR(X) = \frac{Y_{\delta_2}(X)}{Y_{\delta_1}(X)}$ where $\delta = \frac{N-Z}{A}$ of the initial system. In this case δ_1 is defined as a system, typically symmetric or as close as possible while still being stable enough to use as a target, and δ_2 a more neutron rich system. This ratio can minimize the effects of detection efficiency as well as some Coulomb effects. This ratio also has a potential downfall because it does not compare particles of different isospin. The next option is to use the double ratio, defined as $DR\left(\frac{n}{p}\right) = \frac{IPR(n)}{IPR(p)} = \frac{SR_{\delta_2}(n/p)}{SR_{\delta_1}(n/p)}$. This takes advantage of the effects of the IPR while still comparing particles of different isospin.

The final option is to use different particles to measure each of these ratios. In particular the particles that have been suggested are mirror nuclei including the A =3, 7, 11, 15 and 19 pairs. There has been some debate over whether or not these mirror nuclei should be sensitive to the symmetry energy and nucleon effective mass splitting.

Recent experimental evidence implies an answer to this debate with the following derivation. For this treatment, a central collision resulting in a single expanding source is used. This collision results in a high density neutron rich environment. As the system expands the density will decrease to a point where clusters can begin to coalesce and bind together. This density was experimentally measured to exist in a region of densities $\rho < \rho_0/10$ [1]. The symmetry energy and the effects of the effective mass splitting at these densities should be negligible in comparison to the effects that existed in the high density regions.

In the Awes model of clustering [2], the spectra at the point of emission of a cluster with Z protons and N neutrons can be directly compared to the spectra at emission of protons ($Y(p)$) and neutrons ($Y(n)$) using the following form,

$$Y(Z,A) = Y(p)^Z Y(n)^N f(Z,A)$$

where $f(Z,A)$ is an energy dependent scaling factor. This scaling factor can be thought of as a coalescence volume in momentum space. In principle it is possible for the scaling factor to be different from one collision system to another, however for the systems of interest in this work the scaling factor will be assumed to be the same due to the relatively small differences between the systems. This indicates that the IPR for deuterons, the simplest cluster, would be

$$IPR(d) = \frac{Y_{\delta_2}(d)}{Y_{\delta_1}(d)} = IPR(n)IPR(p)$$

Since one would not expect the symmetry energy to affect symmetric particles like deuterons and alphas, it would be predicted that $IPR(d) = IPR(\alpha) = 1$ from which the result that $IPR(n) = 1/IPR(p)$ would naturally follow. Using this result and investigating the $A = 3$ clusters, the predicted value for those particle ratios provides

$$IPR(t) = IPR(p)IPR(n)^2 = IPR(n)$$
$$IPR(h) = IPR(p)^2 IPR(n) = IPR(p)$$

This method can continue upwards in cluster size indicating that for every isotope with $N - Z = 1(-1)$ that isotope's independent particle ratio should be equivalent to that of neutrons(protons). As a consequence, it also suggests that $DR(n/p) = IPR(n)^2$. There exists experimental evidence supporting these assumptions for clusters up through alpha particles in Ref [3].

This result has two significant impacts. This result suggests that the double ratio of any mirror nuclei that differ by a single neutron should be equally as sensitive to the symmetry energy and nucleon effective mass splitting as the n/p ratio. If this holds true, then it indicates that measuring the kinetic energy of neutrons, a notoriously difficult task, is not necessary to constrain either quantity so long as a sufficient measurement of charged particles is obtained. To date this treatment has been applied to systems that specifically measured light clusters (up through$A \leq 4$) but were not applied to larger clusters.

In order to test the validity of this theory for larger clusters the experimental data obtained by Kohley *et al.* and described in Ref [4] will be used. While research on this project is ongoing several comparisons can be made with initial existing data. A test of the validity of this cluster model can be immediately made by investigating the IPR of different particles. In order to attempt to constrain the symmetry energy, comparisons can be made between the spectra and ratios from ^{64}Zn+^{64}Zn and ^{70}Zn+^{70}Zn both at 35 MeV/A to simulations using the AMD [5] and CoMD [6,7] transport codes. In both simulations, the results are passed through an experimental filter in order to directly compare the number of counts per event between the simulated and experimental results. In all cases, only particles emitted in the range of $70 \leq \theta_{CM} \leq 110$ are considered so that effects from secondary breakup and decay are

minimized. In addition, the events considered are those deemed most violent, which at this time are assumed to be the most central collisions.

The first comparisons involve the IPR of different particles in the system to test the validity of the coalescence. The IPR for several pairs of mirror nuclei as well as symmetric particles are provided in Fig. 1. These ratios are generated by taking the raw counts per event for each system. This is a very raw measurement with future considerations needed such as compensation for detector losses, multiple hit probabilities and changes in geometric acceptances between the two systems; however even with this raw measurement some interesting observations can be made. In the "proton-like" plot (left panel), the three lightest clusters, ^{1}H, ^{3}He and ^{7}Be, show very good agreement. The three larger clusters have a different value but display the same flat behavior. The "deuteron-like", or symmetric particles (middle panel), all agree quite well up through 40 MeV, at which point the alpha particles deviate significantly for an as yet not understood reason. The "deuteron-like" ratio is approximately 1.1, however efficiency corrections have not yet been applied. Finally, the "neutron-like" particles (right panel) show one of the largest ranges of results, however, with the exception of the tritons all behave quite similarly. This collection of results which is admittedly still very raw provides some evidence to support the coalescence predictions and encourages further pursuit.

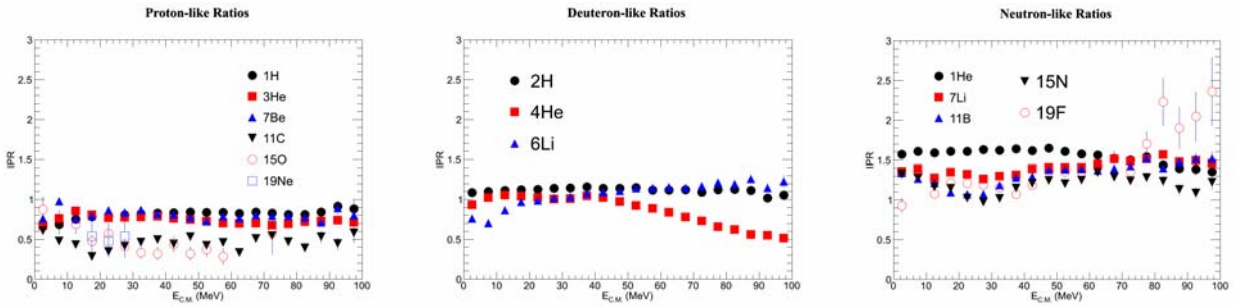

FIG. 1. The "proton-like", "deuteron-like" and "neutron-like" particle ratios are shown in order from left to right.

The ultimate goal of this analysis is to attempt to constrain the symmetry energy and/or the nucleon effective mass splitting by comparing the results to transport calculations. Since neutron energy spectra was not measured in this experiment, the most basic comparison would be made using the t/h double ratio. The spectra of tritons (left) and helions (right) from the ^{64}Zn+^{64}Zn collision that are used in constructing both the double ratio and the independent particle ratio are provided in Fig. 2. In both cases they are compared to a CoMD simulation using a roughly linear form for the symmetry energy and an AMD simulation using the GognyAS parameterization. For both simulations, an experimental filter has been applied in an attempt to recreate experimental conditions and is compared to the raw counts per event from the experimental results. It is immediately obvious that the simulated spectra provide a distinctly different shape that the experimental results.

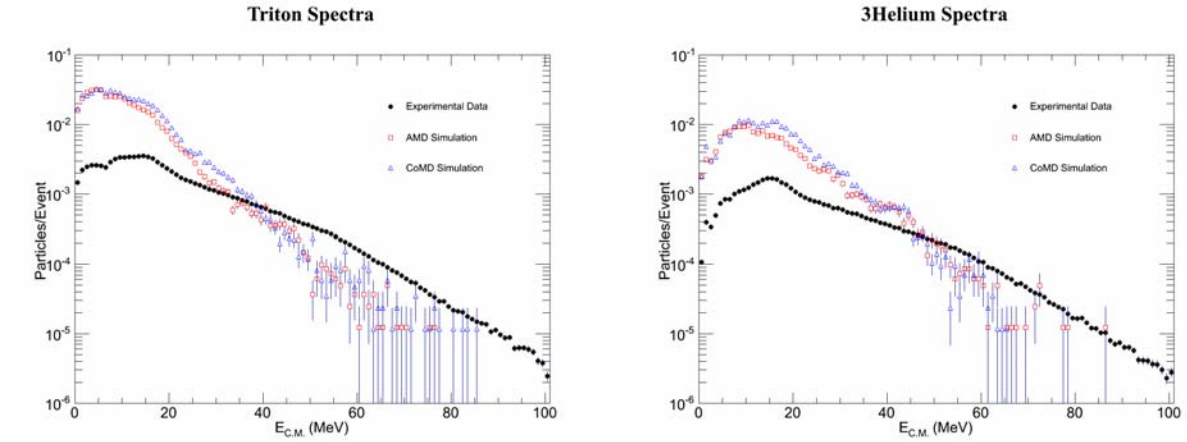

FIG. 2. The spectra of measured tritons (left) and helions (right) in comparison to simulated AMD and CoMD predictions.

This is a potentially dangerous result as it is tempting to use the double ratio to constrain the symmetry energy since it is possible to provide reasonable comparisons between theoretical and experimental results despite being built from spectra that are unreasonable in comparison. Any attempt to extract constraints on the symmetry energy from the double ratio or independent particle ratios need to be tempered until the discrepancy between the simulated and measured kinetic energy spectra can be understood.

[1] K. Hagel *et al.*, Phys. Rev. Lett. **108**, 062702 (2012).
[2] T. Awes *et al.*, Phys. Rev. C **24**, 89 (1981).
[3] M. Youngs, Ph.D. Thesis, Michigan State University (2013).
[4] Z. Kohley, Ph.D. Thesis, Texas A&M University (2010).
[5] A. Ono *et al.*, Prog. Part. Nucl. Phys. **53**, 501 (2004).
[6] M. Papa *et al.*, Phys. Rev. C **64**, 024612 (2001).
[7] M. Papa *et al.*, J. Comp. Phys. **208**, 403 (2005).

Theoretical feasibility of using machine learning to determine experimental observables sensitive to the asymmetry energy

P. Cammarata, A. Bonasera, M. Colonna,[1] Z. Kohley, A. B. McIntosh, M. B. Chapman, L. A. Heilborn, J. Mabiala, L. W. May, A. Raphelt, A. Zarrella, and S. J. Yennello

[1]*Laboratori Nazionali del Sud-INFN, via Santa Sofia 62, 95123 Catania, Italy*

Heavy-ion collisions provide an important probe of the nuclear equation-of-state (EoS). However, the dependence of different observables on the underlying interaction is not always clearly defined. A multidimensional analysis technique has been used to discriminate the observables sensitive to the asymmetry energy based on the results from the interaction of $^{124}Sn+^{64}Ni$ at 15 MeV/nucleon simulated from within Constrained Molecular Dynamics (CoMD) [1] and a Stochastic Mean Field (SMF) model [2, 3]. This multidimensional technique can be used to enhance our analysis of experimental observables and, thus, improve our ability to constrain the nuclear equation of state.

As experimental data sets in physics become larger and more complicated, there is an increasing need for data analysis methods that can treat the data efficiently and in an unbiased manner. This is most apparent as we refine our understanding, and focus our attention on finer details. In such cases, examining several observables simultaneously can lead to a consistent physical picture, where examining a single observable leaves room for uncertainty. The community has recognized this issue of the need to consider multiple variables simultaneously instead of treating them one-by-one. The approach is based on a modern version of a classical approach [4] to multi-variate statistical analysis, namely using the Sliced Inverse Regression algorithm [5, 6] within the R statistical environment[7]. The Sliced Inverse Regression Method (SIR) offers the ability to efficiently and, in an unbiased way, perform such analysis. We have demonstrated how the SIR method may be applied to a currently relevant topic in nuclear physics, namely constraining the asymmetry energy in the nuclear equation of state.

Approximately 3,000 events were simulated with SMF to train the SIR algorithm in identifying the way observables behave relative to a change in E_{sym}. The output of SMF (flat impact parameter distribution from 6 to 8 fm) was then treated with a coalescence code[8] to identify the free nucleons and clusters that appear in the exit channel based on the locations and proximity of the test particles relative to each other in phase space. The coalescence code output was then filtered in order to select only on the projectile-like fragment (PLF) at t=450 fm/c. The data was then filtered with a geometric software filter for the Forward Array Using Silicon Technology (FAUST)[9]. This was done to examine the ability of the SIR method to find observables that may be reasonable through experimental techniques for detection.

The observables selected for use in the SIR method were determined from those proposed by theory to be sensitive to the EoS [3, 10–15]. These observables include the mass (A), charge (Z), excitation energy ($E*$), spin (J), center of mass momentum vector components (p_x, p_y, p_z), position in the center of mass frame (x, y, z), distance from the center of the fragment to the center of mass frame ($r2$), and the quadrupole ($Quad_{mom}$) and octupole (Oct_{mom}) moments, all of the PLF. Fig. 1

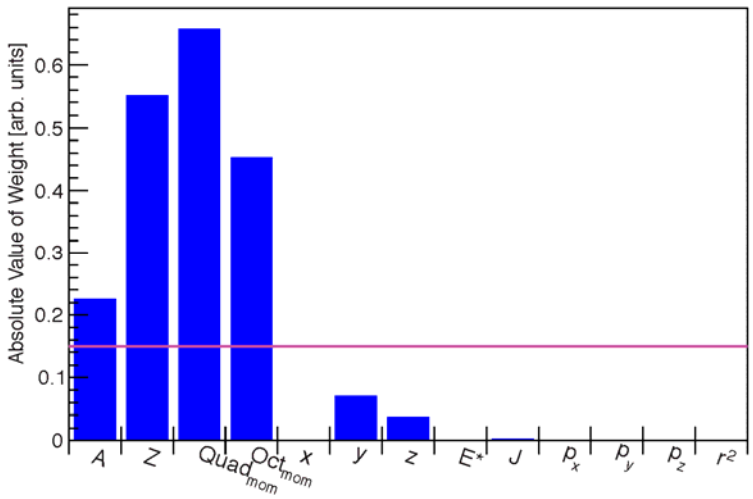

FIG. 1. Absolute values of the observable weights as determined by SIR for the case of 2 E*sym* at an impact parameter of 6 fm using SMF. The solid pink line, equivalent to an observable weight of 0.15, indicates the cut-off used to determine the most important observables. This value is arbitrarily defined and may vary depending on the analysis.

shows the absolute value of the weighted coefficients for each of the 13 observables. The most important observables were chosen to be those that had a weight greater than 0.15, represented by the solid red line. This value is arbitrarily defined and may vary depending on the analysis. In this regard, the mass, charge and deformation in momentum space of the PLF (quadrupole and octupole moments) were the most significant terms. By looking at the distributions of the observables for the PLFs individually, it is difficult to make a clear determination as to how they are affected by the asymmetry energy. In Fig. 2, both stiff and soft forms of E_{sym} are overlaid for each observable from SMF that was determined to be significant. A close inspection shows there is clearly no real separation in the mean value of each observable for the PLFs using the stiff and soft asymmetry energy from SMF.

Re-analysis of the same data this time using only the principal observables as determined previously by SIR (shown above the red line in Fig. 1 as A, Z, $Quad_{mom}$ and Oct_{mom}) provided a clear separation between the mean SIR_{value} for the stiff and soft forms of E_{sym} in SMF, as shown in Fig. 3. This emphasizes that analyzing multiple observables together yields a better understanding and more complete picture of the effect of the asymmetry energy on the observables. The analysis, using only the principal observables, yields the function

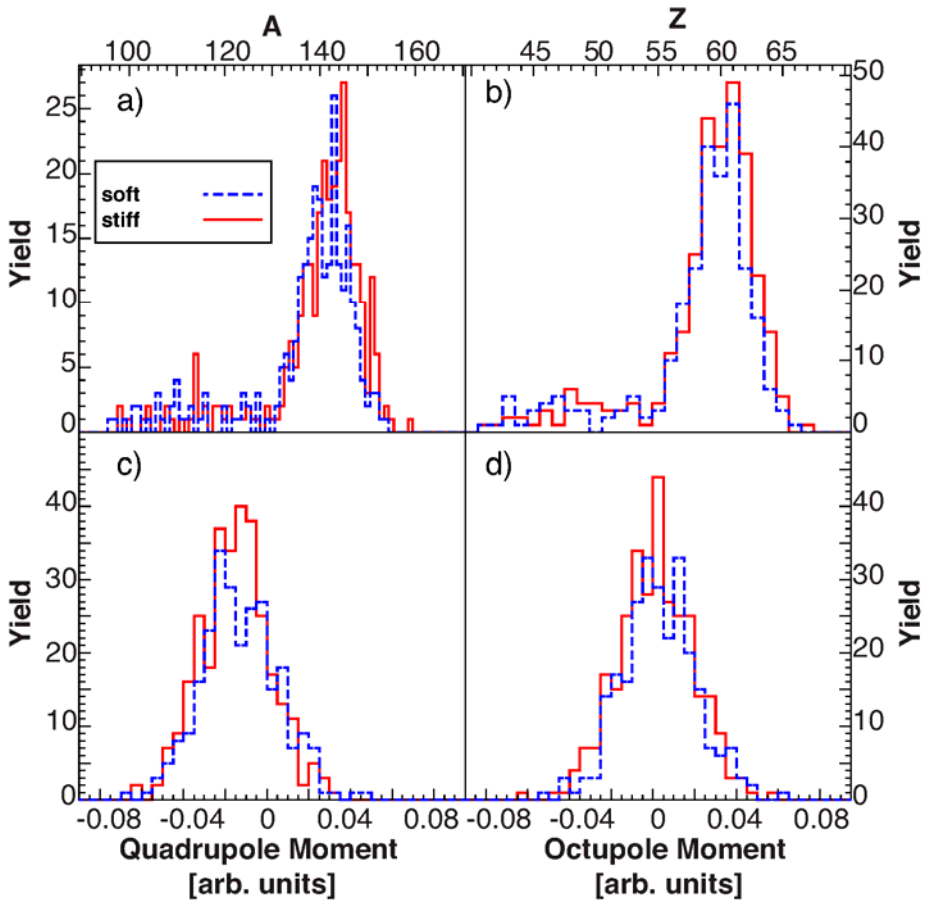

FIG. 2. Mass (a), Charge (b), (c) Quadrupole Moment and (d) Octupole Moment for stiff (solid red) and soft (dashed blue) E_{sym} at an impact parameter of 6fm. All data shown is for PLFs resulting from a 2-body (binary) breakup of the system at t=450 fm/c using the SMF model.

$$SIR_{value} = -0.7338A + 0.17392Z + 0.97921Quad_{mom} - 0.07429Oct_{mom} + constan \quad (1)$$

where the SIR_{value} is a value based on the linear combination of the weighted observables in arbitrary units. The same methodology was applied to similar observables in CoMD with similar results [16].

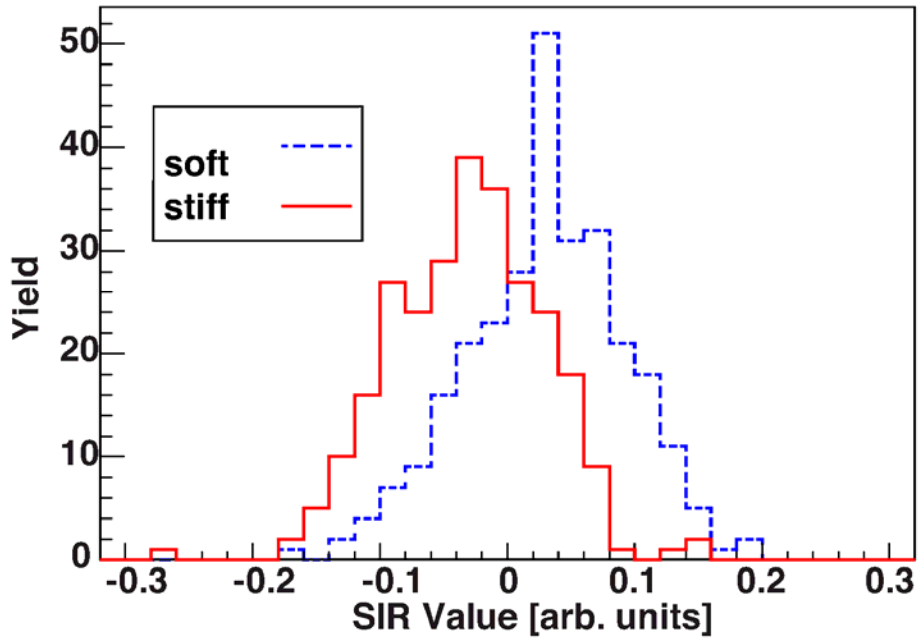

FIG. 3. Separation of the asymmetry energy via SIR for the projectile-like fragment from SMF. The dashed blue line represents the soft and the solid red line represents the stiff E*sym* at an impact parameter of 6 fm.

[1] M. Papa *et al.*, J. Comput. Phys. **208**, 403 (2005).

[2] V. Greco *et al.*, Phys. Rev. C **59**, 810 (1999).

[3] L. Shvedov *et al.*, Phys. Rev. C **81**, 054605 (2010).

[4] R. Fisher, Annals of Eugenics **7**, 179 (1936).

[5] K. Li, J. Amer. Statist. Assoc. **86**, 316 (1991).

[6] S. Weisberg, J. Statistical Software **7**, 1 (2002).

[7] *R: A Language and Environment for Statistical Computing* (R Foundation for Statistical Computing, Vienna, Austria, 2013).

[8] M. Colonna *et al.*, Phys. Rev. C **82**, 054613 (2010).

[9] F. Gimeno-Nogues *et al.*, Nucl. Instrum. Methods Phys. Res. **A399**, 94 (1997).

[10] V. Baran *et al.*, Nucl. Phys. **A703**, 603 (2002).

[11] R. Lionti *et al.*, Phys. Lett. B **625**, 33 (2005).

[12] M. Colonna, J. Phys.: Conf. Ser. **168**, 012006 (2009).

[13] V. Baran *et al.*, Nucl. Phys. **A730**, 329 (2004).

[14] C. Rizzo *et al.*, Phys. Rev. C **83**, 014604 (2011).

[15] M. Di Toro *et al.*, Nucl. Phys. **A787**, 585 (2007).

[16] P. Cammarata *et al.*, Nucl. Instrum. Methods Phys. Res. A (submitted).

Toward understanding relativistic heavy-ion collisions with the STAR detector at RHIC

M. Cervantes, S. Mioduszewski, N. Sahoo, and the STAR Collaboration

RHIC at Brookhaven National Laboratory has been providing high energy heavy-ion collisions since the year 2000, with the current program capitalizing on the high luminosity through measurements of rare probes. Two of these are direct photon correlations and heavy-quarkonium production.

Measurement of γ-Jet at lower z_T and higher trigger p_T

A measurement of hadrons correlated with a high-p_T direct photon is an ideal means to investigate the path-length dependence of partonic energy loss in the dense matter created at RHIC. With increased sensitivity to the path-length dependence expected at low $z_T=p_{T,assoc}/p_{T,trig}$ (less than 0.4), our current efforts focus on extending the published measurement down to z_T = 0.2. In the last year, we have reproduced the Run-6 published results with the same cuts in Run-9 p+p data, we applied the higher trigger p_T cut necessary to extend the measurement to lower z_T. Fig. 1 shows the new result from Run 9 compared to the published result from Run 6. The left panel has the trigger p_T cut at 8-16 GeV/c, which was used in the publication, showing that we can reproduce previous results. The right panel has the 15 GeV/c cut applied in the Run-9 data, extending the z_T range down to 0.2.

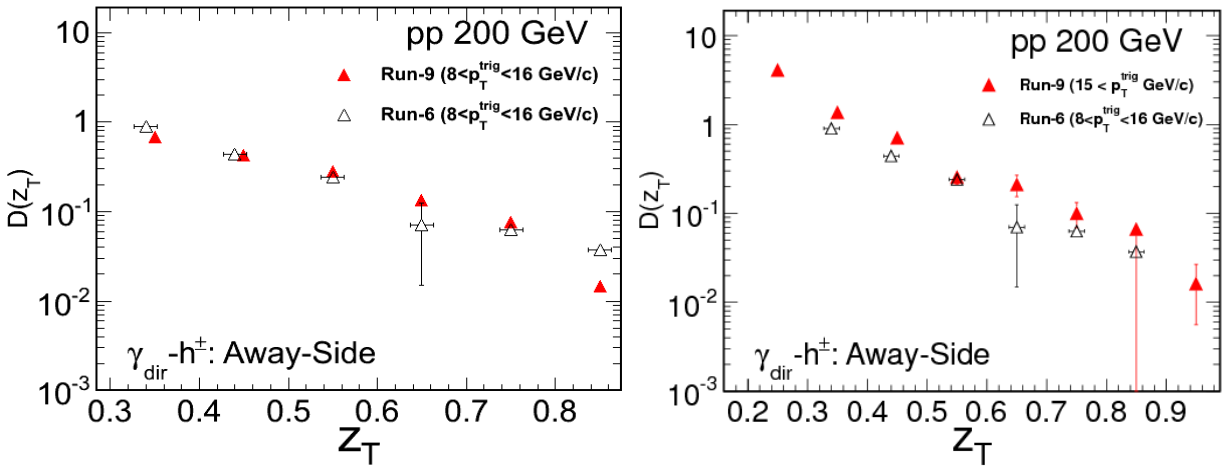

FIG. 1. (Left) Run-9 vs. Run-6 (from STAR publication) direct-photon-triggered yields on recoil side of the direct photon. The p_T trigger cuts, for this comparison, are the same in both data sets. (Right) Run-9 data with a higher p_T trigger cut, compared to the published result, extending the measured range to lower z_T.

We are currently working on the Run-11 Au+Au data, which will provide the numerator in our I_{AA} measurement extended to lower z_T.

Direct-γ v_2 (dependence of γ yields on direction with respect to the reaction plane)

At large transverse momentum, where collective flow is no longer operative, the azimuthal anisotropy (v_2) measured for particles, i.e. the dependence of particle yields on the direction of the particles emitted with respect to the reaction plane, is considered to be a measure of the path-length dependence of energy loss, due to the asymmetric overlap region in Au+Au collisions. The measurement was performed with our former postdoc, Dr. Hamed, and is shown in Fig. 2. The left panel is a result using Run-7 Au+Au data and the full TPC for the reaction-plane determination, while the right panel is a new result from the Run-11 Au+Au data using the forward TPC (FTPC). Using a detector at more forward rapidity should decrease the likelihood of jet particles entering into the reaction-plane determination, which can bias the reaction-plane determination.

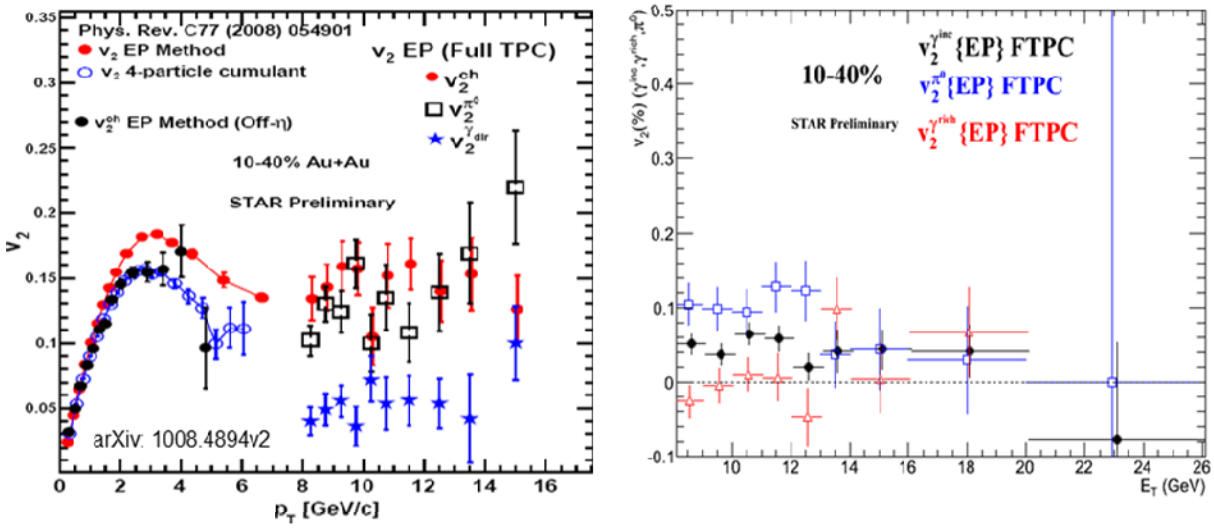

FIG. 2. Azimuthal anisotropy (v_2) measured as a function of particle p_T. For p_T<7 GeV/c, the results are shown for charged particles from minimum-bias triggered events using 3 different methods, the Event-Plane Method (EP) using the full TPC, a 4-particle cumulant, and the EP Method with a rapidity gap (Off-η). The data shown for p_T>8 GeV/c are from "high-tower" triggered events and show the v_2 of charged particles (red) compared to that of π^0 and direct photons. The left panel uses the TPC to calculate the reaction plane, and the right panel uses the Forward TPC.

The lower p_T (p_T<7 GeV/c) data in the left panel is presented to show that we can reproduce previous results from a STAR publication of v_2 measured for charged particles. The methods, labeled as "4-particle cumulant" and "EP Method (Off-η)", use multiple-particle correlations or a pseudo-rapidity gap in the reaction-plane determination, respectively, in order to reduce the bias due to the presence of jets. Our result is the "EP Method (Off-η)" and agrees with the 4-particle cumulant method. At high p_T, we performed the analysis with neutral clusters (rather than charged particles) from the high-tower-triggered data. We find the v_2 of π^0 is at an approximately constant value of 0.12 using the TPC-determined reaction plane (left panel) and closer to 0.10 using the FTPC-determined reaction plane (right panel). The direct photon v_2 is measured to be approximately 0.04 in the left panel and 0 in the right panel. This indicates that a remaining bias in the TPC-determined reaction-plane (due to the presence of an away-side jet, in the case of direct photons) was eliminated in the FTPC reaction-plane determination. Systematic uncertainties are yet to be finalized.

Upsilon (Υ) Production Mechanism through Spin-Alignment ("Polarization") Measurement

We are interested in studying heavy quarkonium production in p+p collisions. The systematics of prompt production of heavy quarkonium is not fully described by common production models, e.g. the Color Singlet Model (CSM) and the Color Octect Model (COM). A measurement that puts constraints on theoretical models of the production mechanism is the spin-alignment (or "polarization") of the Υ. Here, the angle between the direction of the e^+ momentum is measured in the Υ's rest frame with respect to the Υ's direction of motion, i.e. the "polarization axis". The distribution of Υ as a function of this angle θ is then fit with the function $dN/d\theta = A(1 + \alpha\cos^2\theta)$, where α is the polarization. The value of α can vary from -1 to 1; with -1 corresponding to a fully longitudinal polarization, 0 no polarization, and +1 fully transverse polarization. The current version of our main physics result is shown in Fig. 3, with efforts now focused on better subtraction of the Drell-Yan background.

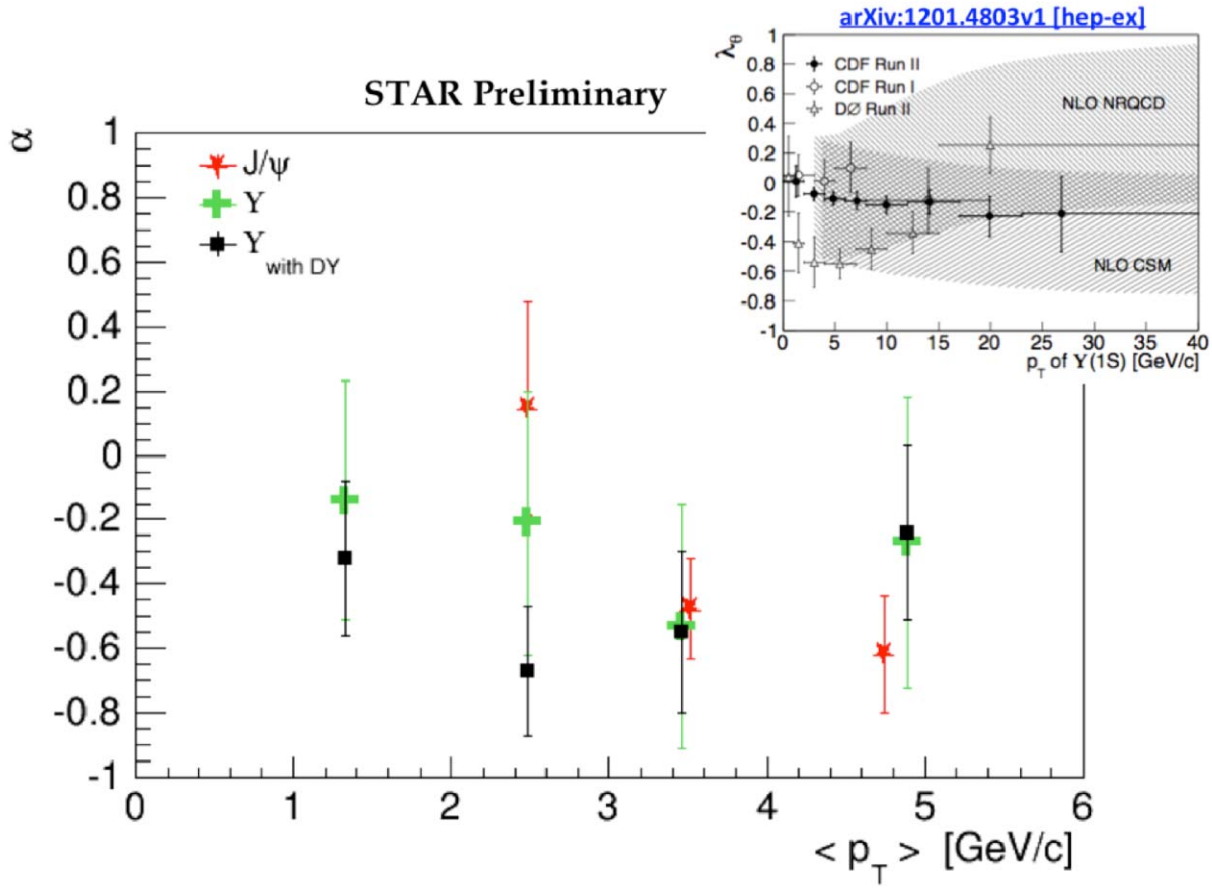

FIG. 3. Polarization parameter α as a function of p_T, measured in Run-11 500-GeV p+p collisions, for Υ particles (our results), compared to J/ψ particle measured in 200-GeV collisions (another STAR group's results currently submitted for publication). The black data points (labeled "$\Upsilon_{\text{with DY}}$") still have ~25% contribution to the Υ measurement from Drell-Yan background, while the green data points are from an analysis in which we attempted to subtract this background as a function of angle θ. The upper right insert shows the measurements of Υ polarization from Fermilab.

Measurements of magnetic moments of low-lying excited states in nuclei beyond the limits of stability: ^{82}Sr, AND ^{90}Sr

N. Benczer-Koller,[1] G. Kumbartzki,[1] and the Rutgers-TAMU- LLNL collaboration
[1]*Dept. of Physics and Astronomy, Rutgers University, Piscataway, New Jersey*

A new experiment was set up at TAMU to carry out magnetic moment measurements. The setup consists of a removable angular correlation table for four clover detectors and a beam line with target chamber, beam diagnostics, and vacuum pump system. A three layer target (C/GdCu) is held between the pole pieces of an electromagnet, which is incorporated in a Displex Cryocooler. The target temperature is kept below 50K. A Si-particle detector at 0 deg. detects emitted charged particles. Gamma rays were recorded in four clover detectors (from the LLNL array at TAMU). Altogether 17 detector output signals were recorded in a Rutgers owned PIXIE-4 digital pulse processing data-acquisition system. A schematic of the setup is shown in Fig.1.

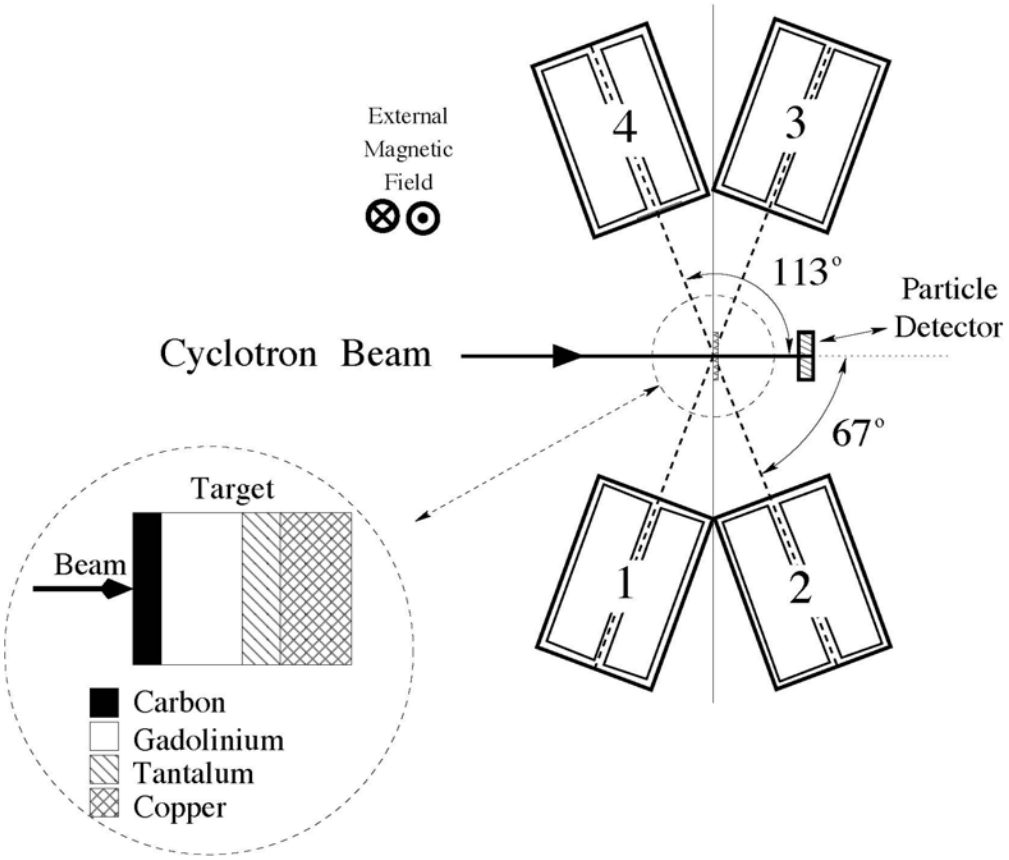

FIG. 1. A schematic of the experimental setup.

Two runs were carried out in the summer and fall of 2013 with beams of ^{78}Kr and ^{86}Kr at 3.0, 3.1 and 3.2 MeV/u. The alpha-transfer reactions from the C layer of the target to a beam of ^{78}Kr of ^{86}Kr ions was used to populating low-lying excited states of the radioactive nuclei ^{82}Sr and ^{90}Sr. The transient field

technique was used to extract the magnetic moment. Simultaneously ^{78}Kr and ^{86}Kr were excited by Coulomb excitation and were used for calibrations as well as for the first measurement of the 4^+ state in ^{86}Kr. A qualitative estimate of the energy dependence of the alpha-capture cross section was obtained.

These experiments were very successful and underscore the high quality of the beams accelerated by the K500 cyclotron, especially their adaptability for magnetic moment measurements. The analysis of these experiments was completed. The structure of ^{82}Sr is clearly that of a collective nucleus while the structure of ^{90}Sr states reflects the dominance of single particles occupying specific shells. Large scale shell model calculations were carried out or ^{90}Sr, ^{86}Kr and ^{92}Zr using a ^{78}Ni core by K. Sieja (Strasbourg). The systematics of the magnetic moments in the region are displayed in Fig. 2 where, in addition, the similarities between Sr and Zr nuclei are highlighted. The newly determined g factors of the first 2^+ and 4^+ in ^{90}Sr together with the same prior measured g factors in ^{92}Zr shed light on the robustness of ^{88}Sr and ^{90}Zr nuclei as closed core nuclei, which are of great interest for shell model calculations.

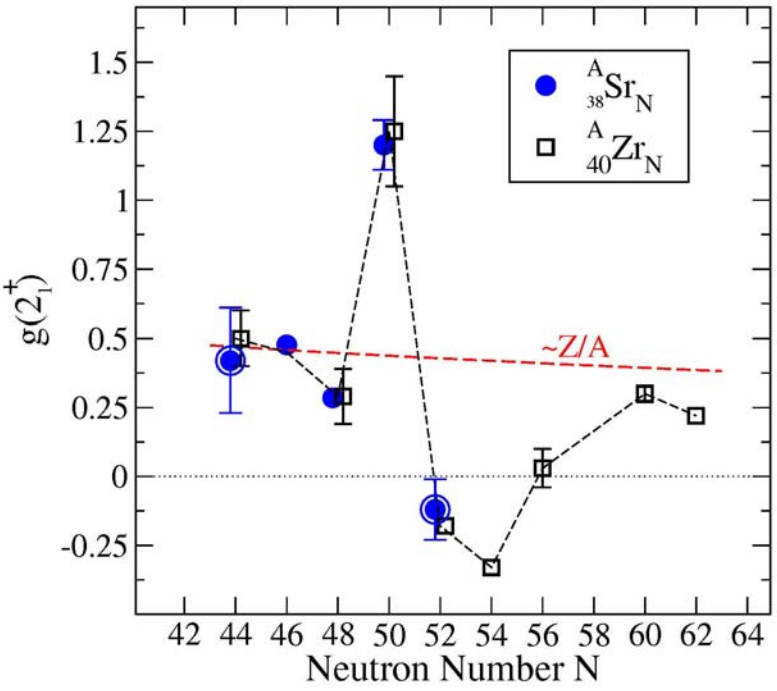

FIG. 2. The systematics of the magnetic moments of Sr and Zr nuclei.

Structure and surrogates from STARS at Texas A&M

C. W. Beausang,[1] A. Simon,[1] P. Humby,[1] J. A. Burke,[2] R. Casperson,[2] J. M. Allmond,[3] T. J. Ross,[4]
M. McCleskey, E. Simmons, A. Saastimoinen, R. Chyzh, and M. Dag
[1]*Physics Department, University of Richmond, Richmond, Virginia*
[2]*Lawrence Livermore National Laboratory, Livermore, California*
[3]*Oak ridge National Laboratory, Oak Ridge, Tennessee*
[4]*University of Kentucky, Lexington, Kentucky*

During the year the Richmond group continued our active involvement at TAMU. Highlights include two weeklong STARLITER experiments, in May and October. These focused on the low/medium spin structures of of shape-transitional rare-earth nuclei, Gd and Sm with N ~ 90, from the ground state up to and well into the bound quasi-continuum, and on a first attempt to investigate the structure of light Cd nuclei of importance to the astrophysical p-process. Our latest surrogate cross section measurement, ^{236,237}Pu(n,f), has been submitted for publication.

The P.I., two postdoctoral fellows, two graduate students (collaborative with the University of Surrey UK) and four Richmond undergraduate students participated in these experiments as well as our collaborators from LLNL, ORNL and the University of Surrey. Visiting and working at the TAMU Cyclotron Facility is an enormously beneficial experience for all of these young scientists but is particularly so for the undergraduates. Preliminary results from these experiments have already been presented at the Annual SSAP Symposium in Washington DC in February and via three talks at the 2013 DNP meeting in Newport News, including one from an undergraduate student. An abstract has been accepted for a poster presentation at Vancouver for Nuclear Structure 2014 in Vancouver BC.

Our workshop apparatus at TAMU is the STARLITER array. STARLITER, developed and commissioned by our LLNL colleagues, consists of a highly segmented Si detector array (STARs, the Silicon Telescope Array for Reaction studies) to detect light charged-particle and fission fragments coupled to the 5-6 Clover-Ge detectors of the LITER (LIvermore TExas Richmond) array. Typical efficiencies are ~20% for light charged particles, ~30% for fission fragments and ~5% (200 keV) and ~1.5% (1.3 MeV) for γ-rays.

Our surrogate reaction program aims to test the efficacy of and to exploit the surrogate reaction technique to extract (n,f) and (n,xnγ) cross sections for unstable nuclei. Direct measurements of such cross sections are difficult or impossible for short-lived species. The surrogate reaction produces the same 'compound' system as the neutron induced reaction but using a stable beam and target combination. A measurement of the decay probabilities and a calculation of the formation probability yields the cross section of interest: assuming the system is equilibrated and that the spin/parity/excitation energy distributions are similar.

Our results for (n,f) cross sections in actinide nuclei show remarkable agreement with the evaluated databases for multiple nuclei and reactions, typically within 5-10% of the accepted values. Our latest results, ^{236,237,238}Pu(n,f) measurements based on a recent TAMU experiment, have been submitted for publication [1]. The result for ^{237,238}Pu(n,f) show good agreement with the database values. However,

the surrogate cross section for ^{236}Pu(n,f) deviates significantly, in both magnitude and trend, from the ENDF values, Fig. 1. It is significant that for ^{236}Pu(n,f) there are essentially no data to guide the database values. We believe that our result is correct and points to an issue with the database.

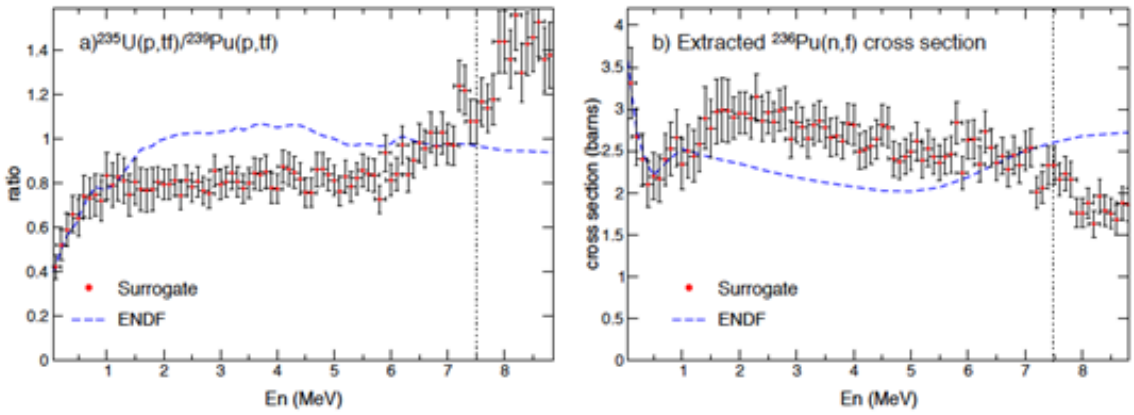

FIG. 1. Left: The data shows the ratio of ^{235}U(p,tf)/^{239}Pu(p,tf) compared to the ENDF value. Right: the extracted surrogate cross section for ^{236}Pu(n,f) compared to the ENDF value. From R.O. Hughes *et al.*, to be published.

Finally, Sm and Gd nuclei with N ~90 are know to undergo a rapid shape change from near spherical (N =88) to well deformed (N = 92) and are an interesting testing ground for a variety of collective models and are also of interest for surrogate (n,γ) measurements. Low / medium spin states in $^{150\text{-}154}$Sm were populated via (p,p'), (p,d) and (p,t) reactions using STARLITER at TAMU.

The data quality is excellent and analysis is well underway. Already we have observed several new levels, have begun to extract entry-spin distributions in the bound quasi-continuum, to work on extracting level densities, to have made an improved lifetime measurement of at least one long lived isomeric state (96 minute), etc. To illustrate the selectivity of the data, Fig. 2 shows our preliminary

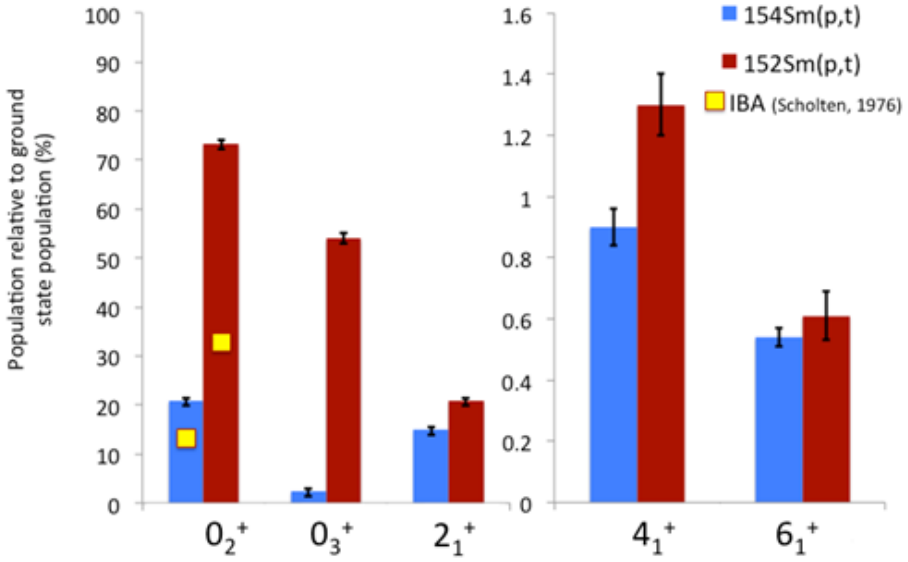

FIG. 2. (Preliminary) Measured population probability, relative to the ground state, for selected levels in ^{152,154}Sm following the (p,t) reaction. Our data are compared to the calculations of Scholten and Iachello, Annals of Physics, **115**, 325 (1978).

measurements of the direct population cross section for just a few states in the yrast band and the first two excited 0^+ states, in ^{152,154}Sm. Note the dramatic difference in the relative population of the 0_3^+ level (factor of ~25) and the relatively poor agreement with calculated values (from 1976). We are working with our theory colleagues from LLNL for improved and expanded calculations for these cross sections.

[1] R.O. Hughes *et al.*, submitted for publication.

SECTION III

NUCLEAR THEORY

Anomalous asymptotics of radial overlap functions for bound systems of three or more particles

L. D. Blokhintsev, A. M. Mukhamedzhanov, and R. Yarmukhamedov

All transfer reactions and radiative capture nuclear-astrophysical reactions at low energies measured so far are analysed using a reaction theory that contains overlap functions between the wave functions of the target and residual nuclei. These overlaps are assumed to have an asymptotic form determined by the separation energy of the transferred (or radiative captured) cluster and such an assumption is incorporated into all reaction codes. We point out that although this asymptotic form is dominant for the majority of the transfer reactions and the nuclear-astrophysical radiative capture reactions, for some cases the overlap function has anomalous asymptotic behavior. This behavior originates from virtual decays of the complex nucleus into intermediate channels and, mathematically, is generated by contributions from the singularities of the triangle Feynman diagram and the generalized triangle diagram containing a loop. In the present work, these contributions are investigated in detail and expressions are derived for the strengths of the anomalous terms taking spin variables and the Coulomb effects into account. We present specific examples of nuclear vertices with anomalous asymptotics and discuss their application for peripheral nuclear processes.

The work was published in Eur. Phys. J. A **49**, 108 (2013).

Astrophysical reaction rate for ^{17}F(p,γ)^{18}Ne from the transfer reaction ^{13}C(^{17}O, ^{18}O)^{12}C

T. Al-Abdullah, F. Carstoiu, X. Chen, H. L. Clark, C. A. Gagliardi, Y. -W. Lui, A. Mukhamedzhanov, G. Tabacaru, Y. Tokimoto, L. Trache, R. E. Tribble, and Y. Zhai

The asymptotic normalization coefficients of the bound states $J^{\pi} = (0_1^+, 2_1^+, 4_1^+, 2_2^+)$ in ^{18}O are extracted from the peripheral neutron transfer reaction $^{13}C(^{17}O, ^{18}O)^{12}C$. They are then converted to their mirror states in ^{18}Ne, which are further used to evaluate the astrophysical S factor for the proton capture reaction $^{17}F(p,\gamma)^{18}Ne$. The elastic-scattering cross sections have been measured in both incoming and outgoing channels in order to extract the optical potentials needed for distorted-wave-Born-approximation calculations. The S- factor is found to be $S_{1-17}(0) = 2.17 \pm 0.35$ keVb. The contribution of the direct capture rate to this reaction is estimated, and its consequences on the production of ^{18}F at stellar energies in ONe novae are discussed. The work has been published in Phys. Rev. C **89**, 025809 (2014).

Big bang nucleosynthesis revisited via Trojan Horse method measurements

R. G. Pizzone, R. Spartá, C. A. Bertulani, C. Spitaleri, M. La Cognata, J. Lalmansingh,
L. Lamia, A. Mukhamedzhanov, and A. Tumino

Nuclear reaction rates are among the most important input for understanding primordial nucleosynthesis and, therefore, for a quantitative description of the early universe. An up-to-date compilation of direct cross-sections of $^{2}H(d,p)^{3}H$, $^{2}H(d,n)^{3}He$, $^{7}Li(p,\alpha)^{4}He$, and $^{3}He(d,p)^{4}He$, reactions is given. These are among the most uncertain cross-sections used and input for big bang nucleosynthesis calculations. Their measurements through the Trojan Horse method are also reviewed and compared with direct data. The reaction rates and the corresponding recommended errors in this work were used as input for primordial nucleosynthesis calculations to evaluate their impact on the ^{2}H, $^{3,4}He$, and ^{7}Li, primordial abundances, which are then compared with observations. The work has been published in Astrophysical Journal **786**, 112 (2014)**.**

Determination of the ANC for $^{14}C+n\rightarrow{}^{15}C$, the $^{14}C(n,\gamma)^{15}C$ reaction rate, and the evaluation of a new method to determine spectroscopic factors

M. McCleskey, A. M. Mukhamedzhanov, L. Trache, R. E. Tribble, A. Banu, V. Eremenko,
V. Z. Goldberg, Y. -W. Lui, E. McCleskey, B. T. Roeder, A. Spiridon,
F. Carstoiu, V. Burjan, Z. Hons, and J. Thompson

The $^{14}C+n\leftrightarrow{}^{15}C$ system has been used as a test case in the evaluation of a new method to determine spectroscopic factors that uses the ANC. The method proved to be unsuccessful for this case. As part of this experimental program, the ANCs for the ^{15}C ground state and first excited state were determined using a heavy ion neutron transfer reaction as well as the inverse kinematics (d,p) reaction, measured at the Texas A&M Cyclotron Institute (TAMU-CI). The values $C^2_{2s1/2} = 1.88 \pm 0.18 \text{fm}^{-1}$ for the ground state and $C^2_{1d5/2} = 4.25 \pm 0.38 \text{fm}^{-1}$ for the first excited state (E_{ex}= 740 keV) were obtained. The ANCs were used to evaluate the astrophysical direct neutron capture rate on ^{14}C, which was then compared with the most recent direct measurement and found to be in good agreement. A study of the ^{15}C SF via its mirror nucleus ^{15}F and a new insight into deuteron stripping theory are also presented. The work has been published in Phys. Rev. C **89**, 044605 (2014).

Electron screening effects in (p,α) reactions induced on boron isotopes studied via the Trojan Horse Method

L. Lamia, C. Spitaleri, N. Carlin, S. Cherubini, M. Gameiro Munhoz, M. Gimenez Del Santo, M. Gulino, G. G. Kiss, V. Kroha, S. Kubono, M. La Cognata, C. Li, A. Mukhamedzhanov, R. G. Pizzone, S. M. R. Puglia, Q. Wen, G. G. Rapisarda, S. Romano, M. L. Sergi, E. Somorjai, F. A. Souza, A. Szanto de Toledo, A. Tumino, Y. Wakabayashi, and H. Yamaguchi

The Trojan Horse Method is a powerful indirect technique allowing one to measure the bare nucleus S(E)-factor and the electron screening potential for astrophysically relevant reactions without the needs of extrapolations. The case of the (p,α) reactions induced on the two boron isotopes $^{10,11}B$ is here discussed in view of the recent Trojan Horse (TH) applications to the quasi-free $^{10,11}B + {}^{2}H$ reactions. The comparison between the TH and the low-energy direct data allowed us to determine the electron screening potential for the ^{11}B(p,α) reaction, while preliminary results on the ^{10}B(p,α) reaction have been extracted. The work published in J. Phys.: Conf. Ser. **436** 012075 (2013).

Indirect techniques in nuclear astrophysics

R. E. Tribble, C. A. Bertulani, M. La Cognata, A. M. Mukhamedzhanov, and C. Spitaler

In this review work we address three different commonly used indirect techniques to obtain the information about astrophysical reactions, the asymptotic normalization coefficient (ANC) method, the Trojan Horse method (THM), and the Coulomb Dissociation (CD) method. The ANC method focuses on determining the normalization of the tail of the overlap function. The ANC for a nuclear level determines the direct capture reaction rate associated with that level. For some reactions, this dominates over resonant capture. In other reactions, direct capture often interferes with resonant capture, which can be very important in determining the overall rate at stellar energies. Including both direct and resonant capture in a consistent framework can be done through an *R*-matrix analysis if the relevant information is available. The THM provides a way to determine the reaction rate for rearrangement reactions by obtaining the cross section for a binary process through the use of a surrogate "Trojan Horse" particle. The CD technique uses the virtual photon flux from the interaction of a high-energy ion with a very heavy target to dissociate the heavy-ion. The dissociation is an inverse process to a capture-gamma reaction that takes place in a stellar environment. Measurements of the dissociation cross section can be used to infer the reaction rate of radiative capture processes at stellar energies. All three of these methods provide information on stellar reaction rates at very low energy without requiring an extrapolation of data from higher energies. These three indirect techniques have in common an underlying connection to nuclear reaction theory. The review paper has been submitted to Journal of Physics G.

New determination of the $^{2}H(d,p)^{3}H$ and $^{2}H(d,n)^{3}He$ reaction rates at astrophysical energies

A. Tumino, R. Spartà, C. Spitaleri, A. M. Mukhamedzhanov, S. Typel, R. G. Pizzone, E. Tognelli, S. Degl'Innocenti, V. Burjan, V. Kroha, Z. Hons, M. La Cognata, L. Lamia, J. Mrazek, S. Piskor, P. G. Prada Moroni, G. G. Rapisarda, S. Romano, and M. L. Sergi

The cross-sections of the $^{2}H(d,p)^{3}H$ and $^{2}H(d,n)^{3}He$ reactions have been measured via the Trojan Horse method applied to the quasi free $^{2}H(^{3}He,p^{3}H)^{1}H$ and $^{2}H(^{3}He,n^{3}He)^{1}H$ processes at 18 MeV off the proton in ^{3}He. For the first time, the bare nucleus S (E) factors have been determined from 1.5 MeV, across the relevant region for standard Big Bang nucleosynthesis, down to the thermal energies of deuterium burning in the pre main sequence (PMS) phase of stellar evolution, as well as of future fusion reactors. Both the energy dependence and the absolute value of the S (E) factors deviate by more than 15% from the available direct data and existing fitting curves, with substantial variations in the electron screening by more than 50%. As a consequence, the reaction rates for astrophysics experience relevant changes, with a maximum increase of up to 20% at the temperatures of the PMS phase. From a recent primordial abundance sensitivity study, it turns out that the $^{2}H(d,n)^{3}He$ reaction is quite influential on ^{7}Li, and the present change in the reaction rate leads to a decrease in its abundance by up to 10%. The present reaction rates have also been included in an updated version of the FRANEC evolutionary code to analyze their influence on the central deuterium abundance in PMS stars with different masses. The largest variation of about 10%–15% pertains to young stars ($\leq$ 1 Myr) with masses $\geq 1M_{\odot}$.

The work has been published in Astrophysical Journal, **785** 96 (2014).

On the measurement of the $^{13}C(\alpha,n)^{16}O$ *S*-factor at negative energies and its influence on the *s*-process

M. La Cognata, C. Spitaleri, O. Trippella, G. G. Kiss, G. V. Rogachev, A. M. Mukhamedzhanov, M. Avila, G. L. Guardo, E. Koshchiy, A. Kuchera, L. Lamia, S. M. R. Puglia, S. Romano, D. Santiago, and R. Spartà

The $^{13}C(\alpha,n)^{16}O$ reaction is the neutron source for the main component of the s -process, responsible for the production of most of the nuclei in the mass range $90 \leq A \leq 208$. This reaction takes place inside the helium burning shell of asymptotic giant branch stars, at temperatures $\leq 10^8$ K, corresponding to an energy interval where the $^{13}C(\alpha,n)^{16}O$ reaction is effective in the range of 140–230 keV. In this regime, the astrophysical S (E)-factor is dominated by the -3 keV sub-threshold resonance due to the 6.356 MeV level in ^{17}O, giving rise to a steep increase in the S -factor. Its contribution is still controversial as extrapolations, e.g., through the R -matrix and indirect techniques such as the asymptotic normalization coefficient (ANC), yield inconsistent results. The discrepancy amounts to a factor of three or more precisely at astrophysical energies. To provide a more accurate S -factor at these energies, we have applied the Trojan horse method (THM) to the $^{13}C(^6Li,n^{16}O)d$ quasi-free reaction. The ANC for the 6.356 MeV level has been deduced through the THM as well as the n -partial width, allowing us to attain unprecedented accuracy for the $^{13}C(\alpha,n)^{16}O$ astrophysical factor. A larger ANC for the 6.356 MeV level is measured with respect to the ones in the literature $(\tilde{C}_{\alpha^{13}C}^{^{17}O(1/2^+)})^2 = 7.7 \pm 0.3_{stat} \pm^{1.6}_{1.5 norm}$ fm^{-1}, yet in agreement with the preliminary result given in our preceding letter, indicating an increase of the $^{13}C(\alpha,n)^{16}O$ reaction rate below about 8×10^7 K if compared with the recommended values. At $\sim 10^8$ K, our reaction rate agrees with most of the results in the literature and the accuracy is greatly enhanced thanks to this innovative approach. The work has been published in Astrophysical Journal, **777,** 143 (2013).

Proton decay of excited states in ^{12}N and ^{13}O and the astrophysical ^{11}C(p,γ)^{12}N reaction rate

L. G. Sobotka, W. W. Buhro, R. J. Charity, J. M. Elson, M. F. Jager, J. Manfredi, M. H. Mahzoon, A. M. Mukhamedzhanov, V. Eremenko, M. McCleskey, R. G. Pizzone, B. T. Roeder, A. Spiridon, E. Simmons, L. Trache, M. Kurokawa, and P. Navrátil

Using a ^{13}O beam, we have observed proton decays of ^{12}N and ^{13}O excited states following proton-knockout and inelastic interactions on a 9Be target. The excited states were determined from detected two- and three-body exit channels using the invariant mass method. The width of the second excited state of ^{12}N was determined to be 55(20) keV, considerably smaller than the value listed in the ENSDF data base. Three new excited states of narrow width (≤50 keV) were observed in ^{13}O from the p+^{12}N and 2p + ^{11}C exit channels. One of these states (E_x= 3.67 MeV) was found to sequentially decay to the second excited of ^{12}N. We again found these data to be inconsistent with the listed decay width. The ramifications for the astrophysically interesting ^{11}C(p,γ)^{12}N reaction are given. The work has been published in Phys. Rev. C **87**, 054329 (2013).

Mirror superallowed beta transitions

I. S. Towner and J. C. Hardy

Of the 20 superallowed $0^+ \rightarrow 0^+$ β decays surveyed in 2009 [1] there are four pairs that are isospin mirrors. These transitions deserve a renewed scrutiny because they have the potential to distinguish clearly between competing calculations of the isospin-symmetry breaking correction. To illustrate this, we start with a few definitions. The measured quantity in a beta transition is the *ft* value. To this is applied two sets of theoretical corrections: a radiative correction, δ_R, and an isospin-symmetry-breaking correction, δ_C, defining in the process a corrected $\mathcal{Ft}$ value

$$\mathcal{Ft} = ft\,(1+\delta_R)(1-\delta_C). \tag{1}$$

The corrected $\mathcal{Ft}$ values have one very important property: for superallowed transitions between isospin $T = 1$ states, the $\mathcal{Ft}$ values are constant, independent of the nucleus under study. This follows from the conserved vector current (CVC) hypothesis. Indeed one of the strongest vindications of the CVC hypothesis is the fact that the superallowed $\mathcal{Ft}$ values in many different nuclei are all consistent with one another. Here, however, we will turn the argument around. We assume the validity of the CVC hypothesis and use the experimental results to test the theoretical isospin-symmetry-breaking corrections. This strategy has already been proposed and implemented by Towner and Hardy [2]. However by focusing on a pair of mirror transitions, a number of systematic uncertainties in the theoretical corrections drop out, sharpening even further the test of the theory.

In discussing a pair of mirror transitions, we will use the superscript *a* for a property of the decay of the proton-rich member of the isospin triplet (the $T_z = -1$ member), and the superscript *b* for its mirror ($T_z = 0$) transition. Then the experimental property we wish to examine is the ratio of *ft* values, ft^a/ft^b. From the CVC hypothesis, this ratio can be written

$$\frac{ft^a}{ft^b} = 1 + \left(\delta_R^b - \delta_R^a\right) - \left(\delta_C^b - \delta_C^a\right). \tag{2}$$

The test therefore is to measure ft^a/ft^b and compare with the theoretical value calculated from the right-hand side of Eq. (2). The expected values are given in Table I. There are many model calculations of the isospin-symmetry breaking correction, but for our illustration here we concentrate on just two: one based on phenomenological Woods-Saxon (WS) eigenfunctions the other based on Hartree-Fock (HF) mean-field eigenfunctions. These two models give quite different predictions for ft^a/ft^b : The Woods – Saxon calculation predicts a larger deviation from one than does the Hartree-Fock calculation. It is anticipated that an experimental measurement of ft^a/ft^b will have sufficient precision to distinguish between these two models. Indeed a first result has just been published [3] for the A = 38 doublet where a result of 1.0036(22) favours the Woods-Saxon calculation.

Table I. Calculated ft^a/ft^b ratios for four doublets with Woods-Saxon(WS) and Hartree-Fock(HF) radial wave functions used to calculate δ_C. The uncertainties due to differences in δ_R and δ_C. are combined in quadrature.

		$(\delta_C^b - \delta_C^a)$ (%)		ft^a/ft^b	
Decay pairs, $a; b$	$(\delta_R^b - \delta_R^a)$ (%)	WS	HF	WS	HF
$^{26}\mathrm{Si} \rightarrow ^{26m}\mathrm{Al}$; $^{26m}\mathrm{Al} \rightarrow ^{26}\mathrm{Mg}$	0.264(20)	−0.125(16)	0.075(16)	1.00389(26)	1.00189(26)
$^{34}\mathrm{Ar} \rightarrow ^{34}\mathrm{Cl}$; $^{34}\mathrm{Cl} \rightarrow ^{34}\mathrm{S}$	0.126(15)	−0.045(21)	0.155(40)	1.00171(26)	0.99971(43)
$^{38}\mathrm{Ca} \rightarrow ^{38m}\mathrm{K}$; $^{38m}\mathrm{K} \rightarrow ^{38}\mathrm{Ar}$	0.101(20)	−0.095(34)	0.125(38)	1.00196(39)	0.99976(43)
$^{42}\mathrm{Ti} \rightarrow ^{42}\mathrm{Sc}$; $^{42}\mathrm{Sc} \rightarrow ^{42}\mathrm{Ca}$	0.296(30)	−0.270(57)	0.000(29)	1.00566(65)	1.00296(42)

[1] J.C. Hardy and I.S. Towner, Phys. Rev. C **79**, 055502 (2009).

[2] I.S. Towner and J.C. Hardy, Phys. Rev. C **82**, 065501 (2010).

[3] H.I. Park, J.C. Hardy, V.E. Iacob, M. Bencomo, L. Chen, V. Horvat, N. Nica, B.T. Roeder, E. Simmons, R.E. Tribble, and I.S. Towner, Phys. Rev. Lett. **112**, 102502 (2014).

Parameterization of the statistical rate function

I. S. Towner and J. C. Hardy

In precision work with superallowed beta decay the integral over the phase space, customarily denoted as *f*, is required to be evaluated with an accuracy of 0.1%. For this, the electron wave function needs to be determined with comparable precision, which is accomplished [1] by solving the Dirac equation, exactly but numerically, for the emerging electron moving in the Coulomb field of the nuclear charge distribution. The full expression for the computation of *f* is

$$f = \xi R(W_0) \int_1^{W_0} pW(W_0 - W)^2 F(Z,W) f_1(W) Q(Z,W) r(Z,W) dW, \quad (1)$$

where W is the electron total energy in electron rest-mass units, W_0 is the maximum value of W, $p = (W^2 - 1)^{1/2}$ is the electron momentum, Z is the charge number of the daughter nucleus (positive for electron emission, negative for positron emission), $F(Z, W)$ is the Fermi function and $f_1(W)$ is the shape-correction function as defined by Holstein [2] (but with kinematic recoil corrections omitted). Further, $Q(Z, W)$ is a screening correction for which we use the analytic prescription of Rose [3] and $r(Z, W)$ is an atomic overlap correction described in [4]. The kinematic recoil correction that Holstein includes in $f_1(W)$ is here written separately as $R(W_0)$:

$$R(W_0) = 1 - \frac{3W_0}{2M_A}, \quad (2)$$

where M_A is the average of the initial and final nuclear masses expressed in electron rest-mass units. Last, for allowed transitions it is customary to remove from f the leading nuclear matrix element contained in the shape-correction function, $f_1(W)$. Thus we have introduced ξ in Eq. (1), where $\xi = 1/|\mathcal{M}_F|^2$ for superallowed Fermi transitions, $\mathcal{M}_F$ being the Fermi matrix element. For pure Gamow-Teller transitions, $\xi = 1/|g_A \mathcal{M}_{GT}|^2$ with $\mathcal{M}_{GT}$ being the Gamow-Teller matrix element and g_A the axial-vector coupling constant.

Our goal is to parameterize f and present tables of the fitting parameters for transitions of interest. For this, we have computed f for 100 values of W_0 taken over a range of ±60 keV around the transition Q-value. Our aim in fitting these 100 values is to achieve an accuracy of 0.01%, a factor of ten more precise than required. It is convenient to factor f into two contributions:

$$f = f_0(1 + \delta_S), \quad (3)$$

$$f_0 = \int_1^{W_0} pW(W_0 - W)^2 F(Z,W) Q(Z,W) r(Z,W) dW, \quad (4)$$

$$\delta_S = (f - f_0)/f_0 \quad (5)$$

The purpose of the factorization is to place the role of the shape-correction function $f_1(W)$ entirely within the correction term δ_S , which is typically of the order of a few percent. The shape-correction function depends on nuclear matrix elements and differs for Fermi and Gamow-Teller transitions. So this piece of the calculation is somewhat less certain, being nuclear-structure dependent, but being small its accuracy is less critical.

For f_0, we choose a fitting function with four parameters, a_0, a_1 , a_2 and a_3, of the same form as would be obtained analytically in the $Z = 0$ limit:

$$f_0 = a_0 W_0^4 p_0 + a_1 W_0^2 p_0 + a_2 p_0 + a_3 W_0 \ln(W_0 + p_0), \tag{6}$$

where $p_0 = (W_0^2 - 1)^{1/2}$. In fitting 100 values of f_0 it was found that four parameters could not be determined with the required accuracy. Thus it was decided to fix the coefficients of the two smallest terms, a_2 and a_3, to their $Z = 0$ values, namely $a_2 = -2/15$ and $a_3 = 1/4$, and use the fitting to determine a_0 and a_1. This procedure yielded the required accuracy.

For the correction δ_S we again choose a four-parameter fitting function:

$$\delta_S = b_0 + b_1 W_0 + \frac{b_2}{W_0} + b_3 W_0^2, \tag{7}$$

where, for a Fermi transition, approximate values of the coefficients can be derived from Holstein's expressions [2] for the shape-correction function $f_1(W)$: namely

$$\begin{aligned} b_0^F &\simeq \tfrac{2}{5} R^2 + \tfrac{61}{630} (\alpha Z)^2, \\ b_1^F &\simeq -\tfrac{6}{7} (\alpha Z) R - \tfrac{3}{2M_A}, \\ b_2^F &\simeq -\tfrac{9}{7} (\alpha Z) R, \\ b_3^F &\simeq -\tfrac{1}{7} R^2, \end{aligned} \tag{8}$$

where R is the nuclear radius in electron Compton-wavelength units. The exactly computed value of δ_S in Eq. (5) is fitted by the expression in Eq. (7) to obtain parameters b_0, b_1 , b_2 and b_3. Again, it was found that four parameters could not be determined with the required accuracy. So coefficients b_2 and b_3 were fixed at the values given in Eq. (8) and the fitting used to determine b_0 and b_1.

For Gamow-Teller transitions, approximate expressions for the fitting parameters were derived in Towner's report for the summer of 2013 [5] and are

$$b_0^{GT} \simeq \frac{2}{15} R^2 + \frac{1}{15} R^2 x + \frac{1}{3} \beta (\alpha Z) \left[\pm 2\bar{b} + \bar{d} \right] + \frac{61}{630} (\alpha Z)^2,$$

$$\begin{aligned} b_1^{GT} &\simeq -\tfrac{26}{35} (\alpha Z) R - \tfrac{1}{35} (\alpha Z) R x + \tfrac{1}{3} R \bar{d} - \tfrac{3}{2M_A}, \\ b_2^{GT} &\simeq -\tfrac{9}{7} (\alpha Z) R - \tfrac{5}{6} R \left[\pm 2\bar{b} + \bar{d} \right], \end{aligned}$$

$$b_3^{GT} \simeq -\frac{11}{105} R^2 \left(1 + \frac{1}{11} x\right), \tag{9}$$

where

$$x = -\sqrt{10}\, \mathcal{M}_{1y} / \mathcal{M}_{\sigma r^2}, \tag{10}$$

$$\bar{b} = \frac{1}{MR} \left[\frac{g_M}{g_A} + \frac{\mathcal{M}_L}{\mathcal{M}_{GT}}\right], \tag{11}$$

$$\bar{d} = \frac{1}{MR} \frac{\mathcal{M}_{\sigma L}}{\mathcal{M}_{GT}}, \tag{12}$$

and $\beta \simeq 6/5$, g_M = 4.706 and M the nucleon mass in electron rest-mass units. The nuclear matrix elements are defined in Eq. (68) of [2]. Schematically, they are written: $\mathcal{M}_{GT} = \langle\sigma\rangle$, $\mathcal{M}_{\sigma r^2} = \langle r^2 \sigma\rangle$, $\mathcal{M}_{1y} = (16\pi/5)^{1/2} \langle r^2 [Y_2 \times \sigma]\rangle$, $\mathcal{M}_L = \langle L\rangle$ and $\mathcal{M}_{\sigma L} = \langle \sigma \times L\rangle$. Note that the matrix element $\mathcal{M}_{\sigma L}$, and hence $\bar{d}$, vanishes in diagonal matrix elements as would occur in a mirror transition between isobaric analogue states.

Again in fitting exact values of δ_S with the expression Eq. (7) parameters b_2 and b_3 were held fixed at values given in Eq. (9) and parameters b_0 and b_1 varied in the fit. Tables of the fitted parameters for the superallowed Fermi transitions and for mixed Fermi and Gamow-Teller transitions that occur in mirror transitions between isospin T = 1/2 analogue states are given in Towner's summer report [5]and will be published.

[1] J.C. Hardy and I.S. Towner, Phys. Rev. C **71**, 055501 (2005).

[2] B.R. Holstein, Rev. Mod. Phys. **46**, 789 (1974); erratum, Rev. Mod. Phys. **48**, 673 (1976).

[3] M.E. Rose, Phys. Rev. **49**, 727 (1936).

[4] J.C. Hardy and I.S. Towner, Phys. Rev. C **79**, 055502 (2009).

[5] I.S. Towner, *Parameterizations useful in nuclear beta decay*, private communication.

Studies of two β-decay correlation coefficients

I. S. Towner and J. C. Hardy

In studies of nuclear beta decay, the two most commonly examined correlation coefficients are the beta-neutrino angular correlation coefficient, a_{ev}, and the beta asymmetry, A_β the correlation between the direction of polarization in the parent nucleus and the direction of the emitted electron. These two correlation coefficients can be written in the form

$$a_{ev}(W) = a^0_{ev} + \Delta a_{ev}(W),$$
$$A_\beta(W) = A^0_\beta + \Delta A_\beta(W), \quad (1)$$

where a^0_{ev} and A^0_β are the major contributions depending on just two parameters, a_1 and c_1, defined as $a_1 = g_V\mathcal{M}_F$ and $c_1 = g_A\mathcal{M}_{GT}$ with $\mathcal{M}_F$ and $\mathcal{M}_{GT}$ being the Fermi and Gamow-Teller matrix elements and g_V and g_A their respective coupling constants:

$$a^0_{ev} = \frac{a_1^2 - \frac{1}{3}c_1^2}{a_1^2 + c_1^2} \quad A^0_\beta = \frac{2\alpha a_1 c_1 \pm \gamma c_1^2}{a_1^2 + c_1^2}. \quad (2)$$

Here α and γ are simple geometric functions of the initial and final nuclear spins, J_i and J_f, and defined as

$$\alpha = (-)^{J_i - J_f} W(J_i J_i 01; 1 J_f) \left[\frac{3J_i(2J_i+1)}{(J_i+1)}\right]^{1/2} = \delta_{J_i J_f} \left[\frac{J_i}{J_i+1}\right]^{1/2}, \quad (3)$$

$$\gamma = (-)^{J_i - J_f + 1} W(J_i J_i 11; 1 J_f) \left[\frac{6J_i(2J_i+1)}{(J_i+1)}\right]^{1/2}, \quad (4)$$

with W(...) being a Racah recoupling coefficient. The upper sign is used for electron emission, the lower sign for positron emission. Added to these major contributions in Eq. (1) are small correction terms Δa_{ev} and ΔA_β, typically of order 1%, that are dependent on the electron energy, W. Our goal here is to study these correction terms firstly by using the exact β-decay formalism of Behrens-Bühring (BB) [1], secondly by finding approximate formulae based on BB obtained by making appropriate expansions of the lepton functions, and thirdly by using approximate formulae given in Holstein [2] and Wilkinson [3]. The formalism associated with this study is given in Towner's summer report [4] and will not be reproduced here.

In what follows we give some numerical results for the beta-neutrino correlation coefficient a_{ev} and the β-asymmetry parameter A_β for the neutron and five examples of mirror transitions in the *s,d*-shell. These five examples were the cases studied by Naviliat-Cuncic and Severijns [5], who used measured values of lifetimes and correlation coefficients to determine the Cabibbo-Kobayashi-Maskawa quark-mixing matrix element, V_{ud}. In their analysis, these authors used the Holstein formulae to apply

corrections $\Delta a_{e\nu}(W)$ and $\Delta A_\beta(W)$ to the measured correlation coefficients, Eq. (1). In this work, we will display the numerical differences between the BB and Holstein formulae for these corrections.

The beta-neutrino and beta-asymmetry correlation coefficients can be cast into the form

$$a(W) = a^0(1 + s_0 + s_1 W + \frac{s_2}{W} + s_3 W^2), \tag{5}$$

where a stands for either the beta-neutrino correlation coefficient $a_{e\nu}$ or the beta-asymmetry parameter A_β and a^0 its Standard-Model value, either $a^0_{e\nu}$ or A^0_β as given in Eq.(2).

Eight nuclear-structure parameters a_1, c_1, x, $\bar{b}$, $\bar{d}$, $\bar{g}$, $\bar{J_2}$ and $\bar{p}$ need to be specified. They are defined as

$$\begin{aligned}
a_1 &= g_V \mathcal{M}_F, \\
c_1 &= g_A \mathcal{M}_{GT}, \\
x &= -\sqrt{10}\,\frac{\mathcal{M}_{1y}}{\mathcal{M}_{\sigma r^2}}, \\
\bar{b} &= \frac{1}{MR}\left[\frac{g_M}{g_A} + \frac{g_V}{g_A}\frac{\mathcal{M}_L}{\mathcal{M}_{GT}}\right], \\
\bar{d} &= \frac{1}{MR}\frac{\mathcal{M}_{\sigma L}}{\mathcal{M}_{GT}}, \\
\bar{g} &= -\frac{4}{3}\sqrt{6}\,\frac{1}{R^2}\, g_V \mathcal{M}_Q, \\
\bar{J_2} &= -2\,\frac{1}{R^2}\, g_A \mathcal{M}_{2y}, \\
\bar{p} &= \frac{1}{(MR)^2}\frac{g_P}{g_A},
\end{aligned} \tag{6}$$

with $g_V = 1$, the vector coupling constant, g_A the axial-vector coupling constant, $g_M = 4.706$ the nucleon isovector magnetic moment, M the nucleon mass in electron rest-mass units and R the nuclear radius in electron Compton wavelength units. The pseudoscalar coupling constant, g_P, is fixed from the PCAC relation at zero momentum transfer: $g_P = -(2M/m_\pi)^2 g_A$, with m_π the pion mass. The required nuclear matrix elements are defined in Eq. (68) of [2]. Schematically they are written: $\mathcal{M}_F = \langle 1 \rangle$, $\mathcal{M}_{GT} = \langle \sigma \rangle$, $\mathcal{M}_{\sigma r^2} = \langle r^2 \sigma \rangle$, $\mathcal{M}_{ky} = (16\pi/5)^{1/2}\langle r^2 [Y_2 \times \sigma]^{(k)} \rangle$, $\mathcal{M}_L = \langle L \rangle$, $\mathcal{M}_{\sigma L} = \langle \sigma \times L \rangle$ and $\mathcal{M}_Q = (4\pi/5)^{1/2}\langle r^2 Y_2 \rangle$. For the present time, we have left out the relativistic matrix elements denoted in [2] as $\mathcal{M}_{r.p}$, $\mathcal{M}_{\{r,p\}}$ and $\mathcal{M}_{\sigma rp}$ and dropped any second-class current terms.

For the neutron and the five mirror transitions in the *s,d*-shell, a_1 is fixed by the CVC hypothesis to be the same in all cases, $a_1 = 1$. The matrix elements, $\mathcal{M}_{\sigma L}$ and $\mathcal{M}_{2y}$ and hence $\bar{d}$ and $\bar{J_2}$, are zero because the expectation values of $\boldsymbol{\sigma} \times \mathbf{L}$ and $[\boldsymbol{\sigma} \times Y_2]^{(2)}$ vanish in diagonal matrix elements. The neutron is considered a pure *S*-state, so $\mathcal{M}_L$, $\mathcal{M}_Q$, $\mathcal{M}_{1y}$, and hence x, are all zero, while the Gamow-Teller matrix element is fixed at $\mathcal{M}_{GT} = \sqrt{3}$. For the *s,d*-shell nuclei, we perform a shell-model calculation using the USD effective interaction [6] to determine the nuclear matrix elements. Their values are given in Table I. Coupling constants g_A and g_M in finite nuclei are customarily treated as effective coupling constants

because they are combined with nuclear matrix elements that have been calculated, inevitably, in a finite model space. Adjusting the coupling constants is one way of compensating for the inadequacy of the shell-model calculation. In practice, we adjust g_A and g_M so that the shell-model calculation yields the experimental value of the partial-decay lifetime and the isovector combination of magnetic moments. Values of g_A^{eff} and g_M^{eff} are given in Table I. We also need to specify the nuclear

Table I. Nuclear matrix elements and related parameters used in the computations of a_{ev} and A_β. For the *s,d*-nuclei, the matrix elements were obtained with the shell model using the USD effective interaction [6]. Coupling constants g_A and g_M are quenched in finite nuclei in order that the shell model reproduces the experimental values for the partial decay lifetimes and the isovector combination of magnetic moments. For these mirror transitions, $\bar{d}$ and $\bar{f}_2$ are identically zero.

Decay Nucleus	$\mathcal{M}_{GT}$	$\mathcal{M}_{\sigma r^2}$ fm^2	$\mathcal{M}_L$	$\mathcal{M}_{1y}$ fm^2	g_A^{eff}	g_M^{eff}	a_1	c_1	x	$\bar{b}$	$\bar{g}$	$\bar{p}$
n	1.732	5.39	0.000	0.00	1.270	4.706	1.00	2.200	0.000	0.700	0.000	−6.456
^{19}Ne	−1.676	−18.22	−0.717	−0.15	0.951	4.237	1.00	−1.593	−0.025	0.275	0.000	−0.569
^{21}Na	0.726	8.09	0.944	0.92	0.969	4.919	1.00	0.703	−0.360	0.351	−0.263	−0.540
^{29}P	0.513	6.21	0.556	4.89	1.015	4.957	1.00	0.521	−2.491	0.315	0.000	−0.506
^{35}Ar	0.328	4.17	−1.493	8.51	0.867	3.806	1.00	0.284	−6.461	−0.042	0.048	−0.418
^{37}K	−0.624	−8.05	1.416	−10.11	0.942	4.220	1.00	−0.587	−3.972	0.100	0.144	−0.425

radius parameter, R. We set $R^2 = \frac{3}{5}\langle r^2\rangle$, where $\langle r^2\rangle$is the mean-square radius of the charge-density distribution of the daughter nucleus in β-decay. This is the charge distribution the emitted β-decay electron encounters and is used in the Dirac equation that is solved to determine the electron wave function.

Our numerical results for the electron-neutrino correlation and beta-asymmetry coefficients are given in Tables II and III. The corrections $\Delta a_{ev}(W)$ and $\Delta A_\beta(W)$ have been averaged over the entire electron spectrum $\overline{a_{ev}}$ and $\overline{A_\beta}$. For the neutron, this average correction is about 3% for a_{ev} and 2% for A_β. The formulae of Holstein [2] slightly underestimate this correction compared to the exact result computed from the formulae of Behrens and Bühring [1]. The results obtained by Wilkinson [3] are derivable from Holstein's formulae on setting $(\alpha Z) \to 0$ and $R^2 \to 0$, but retaining terms linear in R. Only the weak magnetism term in $\bar{b}$ and the kinematic recoil correction are retained by Wilkinson. We see that Wilkinson's results for the neutron are very similar to Holstein's.

For the five examples of mirror transitions in the *s,d*-shell, we see that Holstein's formulae significantly underestimate the correction to a_{ev} in ^{19}Ne, ^{21}Na, ^{29}P and to A_β in ^{21}Na and ^{29}P, while overestimating the correction to A_β in ^{19}Ne. This discrepancy can be traced to the lack of a term in $(\alpha Z)\bar{b}$, an electromagnetic correction in the weak-magnetism form factor. For ^{35}Ar and ^{37}K, the difference between Holstein and BB is somewhat less, but then from Table I one observes the weak-magnetism parameter $\bar{b}$ is somewhat less in these two cases.

Table II. Electron-neutrino correlation coefficient $\boldsymbol{a_{ev}^0}$ from the Standard Model, the correction to it, $\boldsymbol{\Delta a_{ev}(W)}$, averaged over the electron energy spectrum $\boldsymbol{\overline{\Delta a_{ev}}}$ and the final corrected coefficient again averaged over the entire energy spectrum $\boldsymbol{\overline{a_{ev}}}$. Shown are the results obtained with shell-model nuclear matrix elements given in Table I from the approximate formulae of Wilkinson [3], Holstein [2], Behrens-Bühring (BB) [1], and the exactly computed result with the BB formalism. Also given are the parameters of the correction s_0, s_1, s_2 and s_3 as defined in Eq. (5).

Nucleus		$s_0(\%)$	$s_1(\%)$	$s_2(\%)$	$s_3(\%)$	$a_{e\nu}^0$	$\overline{\Delta a_{e\nu}}$	$\overline{a_{e\nu}}$
neutron	Wilkinson	−3.052	3.449	0.141	0.000	−0.1050	−0.0026	−0.1076
	Holstein	−3.043	3.453	0.141	−0.003	−0.1050	−0.0027	−0.1077
	BB-approx	−2.311	3.456	0.142	−0.013	−0.1050	−0.0034	−0.1084
	BB-exact	−2.509	3.510	0.139	−0.013	−0.1050	−0.0033	−0.1083
^{19}Ne	Holstein	−14.85	5.219	−0.163	0.087	0.0435	0.0004	0.0439
	BB-approx	−23.65	5.231	−0.136	0.107	0.0435	−0.0033	0.0402
	BB-exact	−23.11	5.129	−0.096	0.104	0.0435	−0.0032	0.0403
^{21}Na	Holstein	−1.175	0.364	−0.120	0.007	0.5587	0.0000	0.5587
	BB-approx	−2.242	0.363	−0.086	0.007	0.5587	−0.0058	0.5529
	BB-exact	−2.226	0.365	−0.083	0.007	0.5587	−0.0057	0.5530
^{29}P	Holstein	−0.830	0.154	−0.108	0.006	0.7154	−0.0003	0.7151
	BB-approx	−1.595	0.148	−0.058	0.006	0.7154	−0.0058	0.7096
	BB-exact	−1.597	0.154	−0.056	0.006	0.7154	−0.0056	0.7098
^{35}Ar	Holstein	0.131	−0.070	−0.084	0.005	0.9004	−0.0010	0.8995
	BB-approx	0.218	−0.077	−0.015	0.005	0.9004	−0.0004	0.9001
	BB-exact	0.258	−0.073	−0.015	0.005	0.9004	0.0002	0.9006
^{37}K	Holstein	−0.224	−0.021	−0.103	0.008	0.6580	−0.0004	0.6575
	BB-approx	−0.517	−0.038	−0.033	0.009	0.6580	−0.0028	0.6552
	BB-exact	−0.349	−0.035	−0.033	0.009	0.6580	−0.0016	0.6564

Table III. Beta-asymmetry correlation coefficient $\boldsymbol{A_\beta^0}$ from the Standard Model, the correction to it $\Delta A_\beta(W)$ averaged over the electron energy spectrum $\overline{\boldsymbol{\Delta A_\beta}}$ and the final corrected coefficient, again averaged over the entire energy spectrum $\overline{\boldsymbol{A_\beta}}$. Shown are the results obtained with shell-model nuclear matrix elements given in Table I from the approximate formulae of Wilkinson [3], Holstein [2], Behrens-Bühring (BB) [1], and the exactly computed result with the BB formalism. Also given are the parameters of the correction s_0, s_1, s_2 and s_3 as defined in Eq. (5).

Nucleus		$s_0(\%)$	$s_1(\%)$	$s_2(\%)$	$s_3(\%)$	A_β^0	$\overline{\Delta A_\beta}$	$\overline{A_\beta}$
neutron	Wilkinson	−0.874	1.408	0.141	0.000	−0.1175	−0.0017	−0.1192
	Holstein	−0.871	1.409	0.141	−0.001	−0.1175	−0.0017	−0.1192
	BB-approx	−0.050	1.411	0.142	0.001	−0.1175	−0.0027	−0.1202
	BB-exact	−0.048	1.375	0.142	0.001	−0.1175	−0.0026	−0.1201
^{19}Ne	Holstein	−5.14	3.961	−0.163	0.030	−0.0417	−0.0027	−0.0444
	BB-approx	−13.75	3.972	−0.136	0.028	−0.0417	0.0009	−0.0408
	BB-exact	−13.57	4.079	−0.112	0.027	−0.0417	0.0007	−0.0410
^{21}Na	Holstein	0.308	−0.019	−0.120	−0.001	0.8614	0.0017	0.8631
	BB-approx	0.817	−0.029	−0.086	0.000	0.8614	0.0060	0.8674
	BB-exact	0.735	−0.019	−0.086	0.000	0.8614	0.0056	0.8670
^{29}P	Holstein	0.666	−0.098	−0.108	−0.001	0.6154	0.0011	0.6166
	BB-approx	1.650	−0.094	−0.058	0.000	0.6154	0.0075	0.6229
	BB-exact	1.512	−0.091	−0.059	0.000	0.6154	0.0068	0.6222
^{35}Ar	Holstein	−0.309	0.053	−0.084	−0.001	0.4371	−0.0003	0.4368
	BB-approx	−0.762	0.061	−0.015	0.000	0.4371	−0.0019	0.4352
	BB-exact	−1.239	0.073	−0.014	0.000	0.4371	−0.0037	0.4334
^{37}K	Holstein	0.090	0.013	−0.103	0.002	−0.5739	−0.0012	−0.5752
	BB-approx	0.175	0.016	−0.033	0.003	−0.5739	−0.0021	−0.5760
	BB-exact	0.024	0.025	−0.033	0.003	−0.5739	−0.0015	−0.5754

[1] H. Behrens and W. Bühring, *Electron Radial Wave Functions and Nuclear Beta-decay* (Clarendon Press, Oxford,1982); H. Behrens, H. Genz, M. Conze, H. Feldmeir, W. Stock and A. Richter, Ann. of Phys. **115**, 276 (1978).

[2] B.R. Holstein, Rev. Mod. Phys. 46, 789 (1974); erratum, Rev. Mod. Phys. 48}, 673 (1976).

[3] D.H. Wilkinson, Nucl. Phys. **A377**, 474 (1982).

[4] I.S. Towner, *Parameterizations useful in nuclear beta decay*, private communication.

[5] O. Naviliat-Cuncic and N. Severijns, Phys. Rev. Lett. **102**, 142302 (2009).

[6] B.H. Wildenthal, in *Progress in Particle and Nuclear Physics*, ed. D.H. Wilkinson (Pergamon Press, Oxford 1984) Vol. **11**, p. 5.

Coulomb corrections to the extraction of the density and temperature in non-relativistic heavy ion collisions

H. Zheng, G. Giuliani, and A. Bonasera

The properties of the Nuclear Equation of State (NEOS) can be investigated by means of Heavy Ion Collisions. In the microscopic system formed in the collision, non-equilibrium effects could be dominant. As a consequence, the derivation of quantities needed to constrain the NEOS like density, pressure and temperature is not an easy task. To determine densities and temperatures of colliding systems we have recently suggested a method based on fluctuations of quantities such as the light particles multiplicity and quadrupole momentum [1-5]. In particular, in Refs. [2-3] the method takes into account the quantum statistical nature of nuclear particles and clusters obeying to the Fermi-Dirac statistics, while in Ref. [4] the same procedure is applied for Boson clusters like deuterons and alpha particles. The choice of fluctuations, particularly along the perpendicular direction to the beam axis, is motivated by their relation to the temperature as it is stated by the fluctuation-dissipation theorem. We expect fluctuations to give the closest possible determination of the "temperature" of the system, even though it could be chaotic but non-ergodic. In the classical limit [1], Quadrupole momentum Fluctuations (QF) can be easily connected to the temperature. Of course, if the system is classical and ergodic, the temperature determined from QF and, say from the slope of the kinetic distribution of the particles should be the same. In the ergodic case, the temperature determined from isotopic double ratios should also give the same result. This is, however, not always observed, which implies that the system is non-ergodic, or non-classical. We can go beyond the classical approximation. When we are dealing with fermions, in such a case it is not possible to disentangle the 'temperature' from the Fermi energy, thus the density [2-3]. For bosons case, we have similar situation, even more complicated because of the possible Bose-Einstein Condensate (BEC). Because we have two unknowns, we need another observable, which depends on the same physical quantities. In [2-4] we have proposed to look at multiplicity fluctuations (MF) which, similarly to QF, depends on T and ρ of the system in a way typical of fermions [2-3] or bosons, such as alpha particles [4]. The application of these ideas in experiments has produced interesting results such as the sensitivity of the temperature from the symmetry energy [6], fermion quenching [7] and the critical T and ρ in asymmetric matter [8]. Very surprisingly, the method based on quantum fluctuations [8] gives values of T and ρ very similar to those obtained using the double ratio method and coalescence and gives a good determination of the critical exponent β. This stresses the question on why sometimes different methods give different values, including different particles ratios, while in other cases the same values are obtained.

In Ref. [1] the classical temperature derived from QF gave different values for different isotopes. Clearly the Coulomb repulsion of different charged particles can distort the value of the temperature obtained from QF, which depends on kinetic values. Also the obtained values, say of the critical temperature and density, might be influenced by Coulomb as well as by finite size effects. For these reasons, it is highly needed to correct for these effects as best as possible. In Refs. [9, 10] we proposed a method to correct for Coulomb effects in the exit channels related to the emitted charged clusters (Fermions and Bosons respectively). In order to support our findings, we will compare our results to the

neutron case, which is of course independent, at least not directly, from the Coulomb force. Of course, neutron distributions and fluctuations are not easily determined experimentally, thus we will base our considerations on theoretical simulations using the CoMD model.

In Fig. 1, we plot T and ρ versus excitation energy per nucleon respectively. As we can see the derived T of protons are much closer to the neutrons. The good agreement for the obtained temperatures suggests that thermal equilibrium in the transverse direction is nearly reached. The modification to the density due to Coulomb is very small which implies that the MFs are not so much affected by Coulomb.

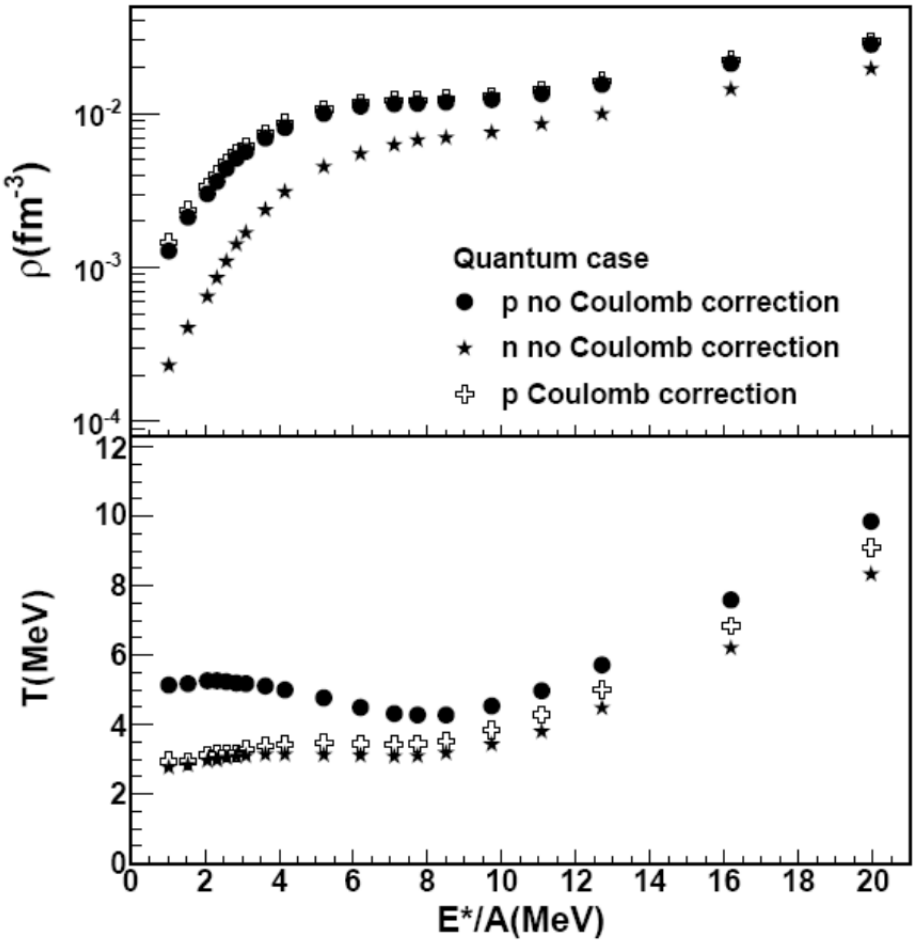

FIG. 1. (Top panel) Densities extracted from CoMD simulated data versus excitation energy per nucleon E*/A. (Bottom panel) Temperatures versus E*/A. Solid circles and solid stars refer to p and n obtained from quantum fluctuations without Coulomb correction respectively; open crosses refer to p-case obtained from quantum fluctuations with Coulomb correction.

In Fig. 2, we plot reduced density $\tilde{\rho} = \rho/\rho_0$ where ρ_0 is the nuclear ground state density and T vs excitation energy respectively obtained from CoMD simulations. The neutron case is also included. As we see the densities derived from d and alpha observables with Coulomb correction are very close to each other and to those derived from the neutron observables. There is a large difference between the cases

with Coulomb correction and without Coulomb correction which demonstrates the crucial role of adding the Coulomb repulsion between bosons. For completeness we also include the results for bosons from Landau's O (m^6) approach [4] which is close to the results without Coulomb corrections. The derived T of d and alpha with Coulomb correction are also much closer to the neutron values. The good agreement for the obtained temperatures and densities suggests that thermal equilibrium is nearly reached for particles emitted in the transverse direction, similar to the fermions case.

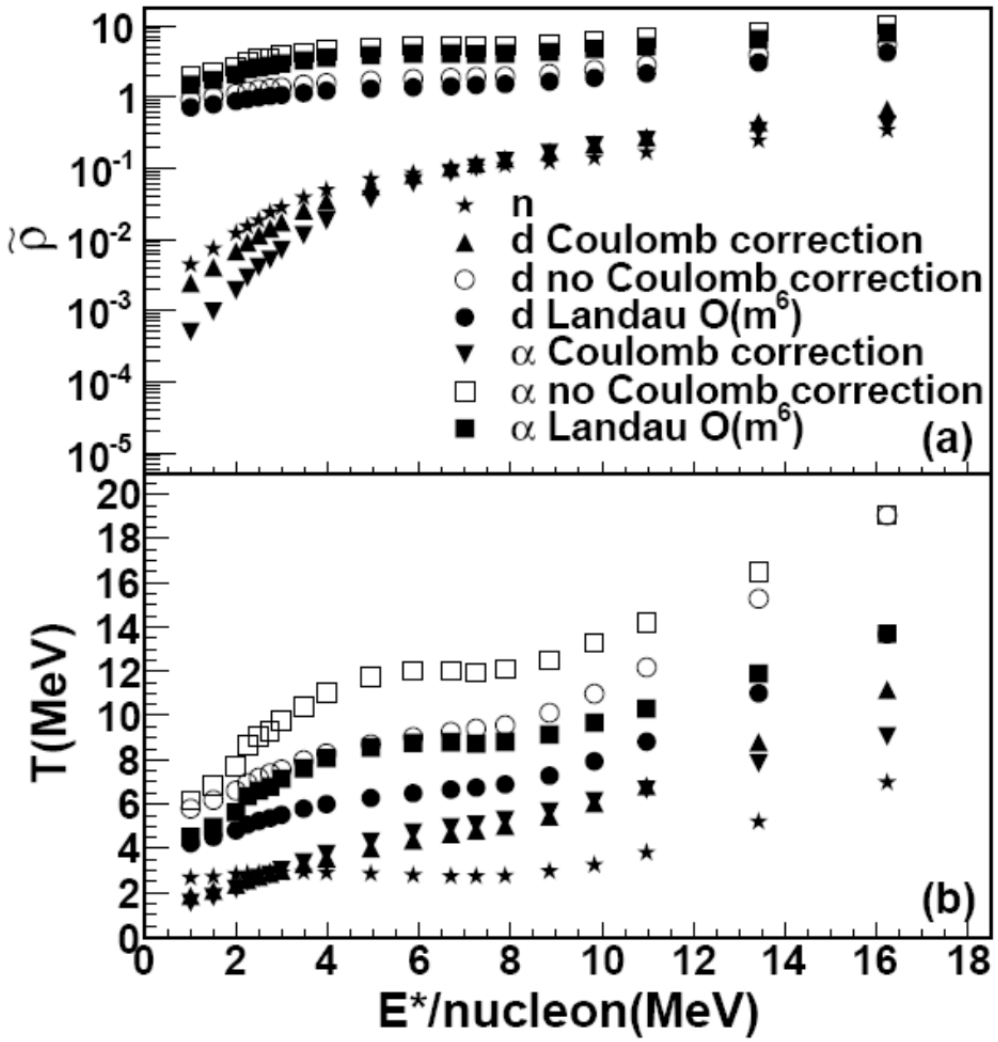

FIG. 2. The reduced density (a) and temperature (b) versus E*/nucleon of d and alpha from CoMD simulations. Three methods, with Coulomb correction, without Coulomb correction and Landau's O(m^6) theory, are used to calculate the density and temperature. The corresponding results for neutrons are also included as a reference.

[1] S. Wuenschel *et al.*, Nucl. Phys. **A843**, 1 (2010).

[2] H. Zheng and A. Bonasera, Phys. Lett. B **696**, 178 (2011).

[3] H. Zheng and A. Bonasera, Phys. Rev. C **86**, 027602 (2012).

[4] H. Zheng , G. Giuliani, and A. Bonasera, Nucl. Phys. **A892**, 43 (2012).

[5] G. Giuliani, H. Zheng and A. Bonasera, Prog. Part. Nucl. Phys. **76**, 116 (2014).
[6] A.B. McIntosh *et al.*, Phys. Lett. B 719, 337 (2013); A.B. McIntosh *et al.*, Phys. Rev. C **87**, 034617 (2013).
[7] B.C. Stein *et al.*, J. Phys. G **41**, 025108 (2014).
[8] J. Mabiala *et al.*, Int. J. Mod. Phys. E **22**, 1350090 (2013).
[9] H. Zheng, G. Giuliani, and A. Bonasera, Phys. Rev. C 88, 024607 (2013).
[10] H. Zheng , G. Giuliani, and A. Bonasera, J. Phys. G **41**, 055109 (2014).

The many facets of the (non-relativistic) nuclear equation of state

H. Zheng, G. Giuliani, and A. Bonasera

A nucleus is a quantum many body system made of strongly interacting Fermions, protons and neutrons (nucleons). This produces a rich Nuclear Equation of State whose knowledge is crucial to our understanding of the composition and evolution of celestial objects. The nuclear equation of state displays many different features; first neutrons and protons might be treated as identical particles or nucleons, but when the differences between protons and neutrons are spelled out, we can have completely different scenarios, just by changing slightly their interactions. At zero temperature and for neutron rich matter, a quantum liquid gas phase transition at low densities or a quark-gluon plasma at high densities might occur. Furthermore, the large binding energy of the α particle, a Boson, might also open the possibility of studying a system made of a mixture of Bosons and Fermions, which adds to the open problems of the nuclear equation of state.

Many aspects of the Nuclear Equation of State (NEOS) have been studied in large detail in the past years. Finite nuclei resemble classical liquid drops, the crucial difference is that the nucleus in its ground state, or zero temperature, does not `solidify' similarly to a drop at low temperatures. This is due to the quantum nature of the nucleus: more specifically its constituents, neutrons (n) and protons (p), are Fermions. They obey the Pauli principle which forbids two equal Fermions, two protons with the same spin or two neutrons with the same spin (either both up or both down), to occupy the same quantum state. Thus at zero temperature, two or more Fermions cannot be at rest (a solid) when confined in a finite volume. In order to constrain the NEOS, we need to use the thermodynamic concepts, therefore we need to create in laboratory equilibrated systems at temperature T and density ρ.

In this review paper [1], the starting point of the NEOS is the understanding of the nucleus in its ground state. The paradigm of the nuclei is the liquid drop model and the Weizsäcker mass formula. Using a simple Fermi gas formula which takes into account finite sizes and neutron-proton asymmetries, we discussed the finite effects and symmetry energy. Then we review the approach to extract symmetry energies with isobaric analog states. After this, we proposed a Skyrme type NEOS at zero temperature assuming the interaction is local and there is a second order phase transition from nuclear matter to quark gluon plasma. We study the physical quantities, S (symmetry energy), L (slope of symmetry energy) and Ksym (curvature of symmetry energy) with different assumptions. We demonstrate that these quantities are coupled. We also review the NEOS with momentum dependence and effective mass of nucleons at zero temperature. Then we extend our NEOS at zero temperature to temperature dependence assuming the nucleons system is in Fermi case or classical case. The results show we need to be careful for both cases since the behavior of nuclear matter might seem reasonable in a given region but not so in another. Then we review the finite size effects of one of temperature dependence NEOS and compare the results with ones from experiments and percolation model. The knowledge of the NEOS is necessary to explain observed celestial objects and events. We briefly review the relevance of NEOS in case of neutron stars. We test our NEOS and 150 Skyrme NEOS with the mass and radius relation of neutron stars. A good correlation between the mass and radius with Ksym has been shown. The simulation models have played

an important role helping us understand what happened in heavy ion collisions. We recall some features and differences of the popular simulation models. Boltzmann-Nordheim-Vlasov (BNV) and Constraint Molecular Dynamics (CoMD) models have been used to study the neutron skin and Giant Resonances (GR) with different NEOS. The models's results are compared with the experimental measurements. At the end, we review the different methods which used to extract the temperature and density from heavy ion collisions, eg. the Saha equation, coalescence model and quantum fluctuation method. The comparison of the results extracted with different methods from CoMD has been shown. The popular Fisher model, Landau approach to extract free energy, isoscaling and m scaling are also covered.

[1] G. Giuliani, H. Zheng, and A. Bonasera, Prog. Part. Nucl. Phys. **76**, 116 (2014).

Heavy quark potential at finite temperature

S. H. Lee,[1] K. Morita,[2] T. Song, and C. M. Ko
[1]*Institute of Physics and Applied Physics, Yonsei University, Seoul 120-749, Korea*
[2]*Yukawa Institute for Theoretical Physics, Kyoto University, Kyoto 606-8502, Japan*

Using the QCD sum rule with its operator product expansion reliably estimated from lattice calculations for the pressure and energy density of hot QCD matter [1], we have calculated the strength of the J/ψ wave function at origin [2] and find that it decreases with temperature when the temperature is above the transition temperature as shown in Fig.1. This result is seen to follow exactly that obtained from the solution of the Schroedingier equation for a charm and anticharm quark pair using the free energy from lattice calculations as the potential and is in sharp contrast to that using the deeper potential associated with the internal energy, which shows an enhanced strength of the J/ψ wave function at origin. This conclusion remains unchanged after including in the Schroedinger equation an imaginary potential from the Hard Thermal Loop (HTL) calculations [3,4], which reaches an asymptotic value of order -100 MeV at r >0.5 fm near T_c. Our result thus suggests that the free energy potential from lattice calculations is the appropriate heavy quark potential for analyzing the charmonium spectrum at finite temperature.

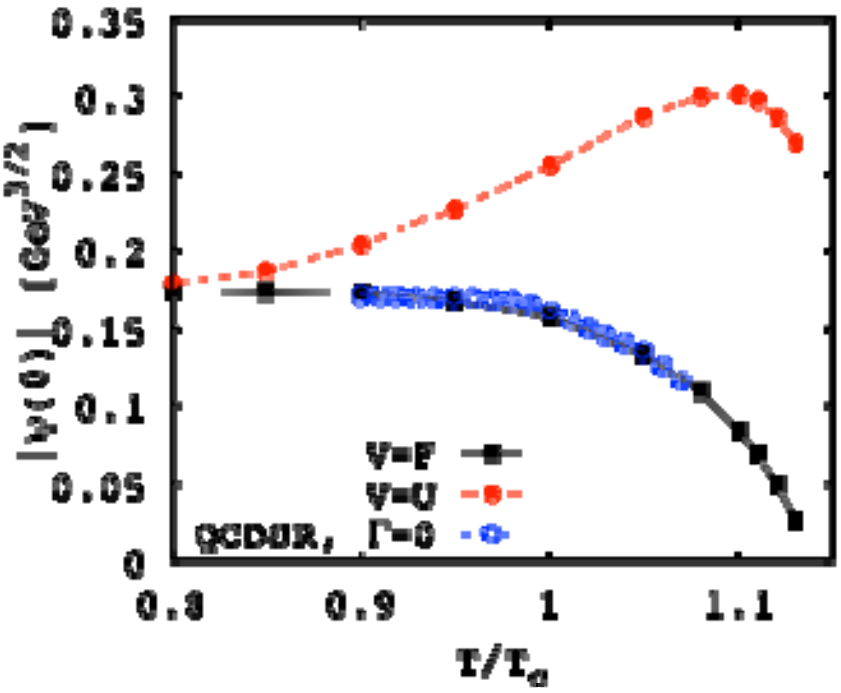

FIG. 1. Temperature dependence of the J/ ψ wave function at origin |ψ(0)| obtained from the free energy (filled squares) and internal energy (filled circles) potentials together with that from the QCD sum rule (open circles).

[1] K. Morita and S.H. Lee, Phys. Rev. D **82**, 054008 (2010); Phys. Rev. C **85**, 044914 (2012).

[2] S.H. Lee, K. Morta, T. Song, and C.M. Ko, Phys. Rev. D, submitted.
[3] M. Laine, O. Philipsen, P. Romatschke and M. Tassler, JHEP **0703**, 054 (2007).
[4] P. Petreczky, C. Miao and A. Mocsy, Nucl. Phys. A 855, 125 (2011).

Gluon dissociation of J/ψ beyond the dipole approximation

J. P. Liu, C. M. Ko, and T. Song

Using a nonrelativistic potential model, we have derived the cross section for the leading-order gluon dissociation of J/ ψ at zero temperature by including the full gluon wave function [1]. In the limit of long gluon wavelength, the usually used cross section based on the dipole approximation [2,3] is recovered. In this process, the gluon can be absorbed by either heavy quarks or by the exchanged gluon between them. Both processes contribute equally in the dipole approximation in the large N_c limit. The cross section is, however, smaller beyond the dipole approximation as shown in Fig. 1, and this is mainly

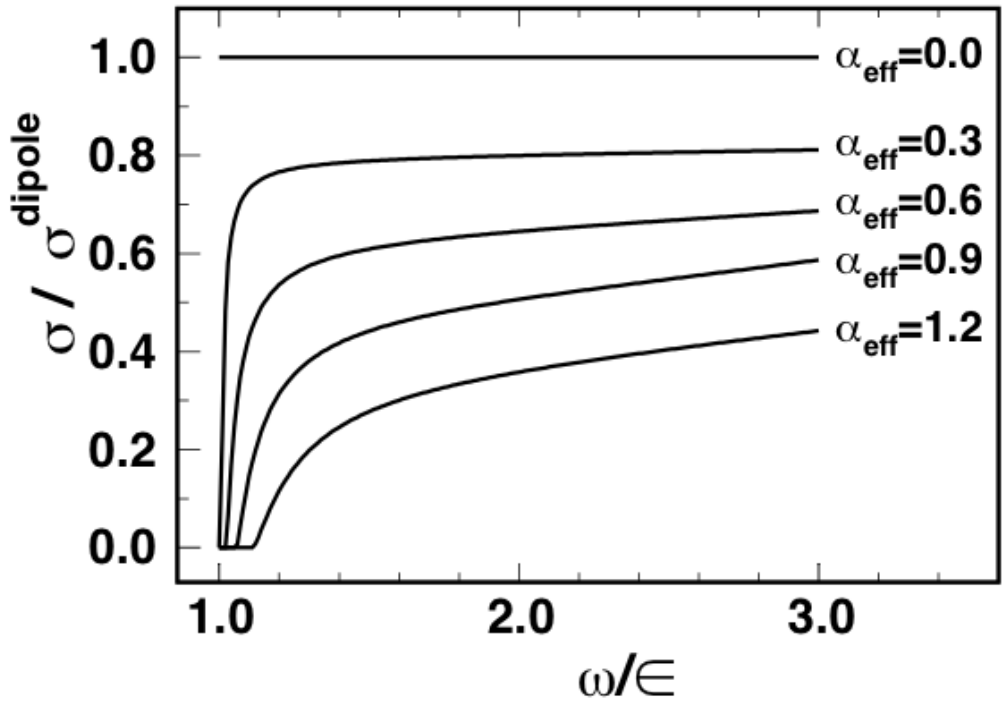

FIG. 1. Ratio of J/ψ dissociation cross section calculated beyond the dipole approximation to that with the dipole approximation as a function of the ratio of the gluon energy in the quarkonium frame and the J/ψ binding energy.

due to the latter process because the momentum of the gluon affects the range of the external gluon induced transition potential. We have also found that the angular distribution of the relative momentum of heavy quarks in the final state is modified with the inclusion of the full gluon wave function, leading to heavy quarks more likely to be scattered close to the momentum of the initial gluon rather than perpendicular to it as in the dipole approximation as shown in Fig. 2. At finite temperature, including the full gluon wave function only slightly modifies the dissociation width of a J/ψ at high temperature whether the charm quark potential is taken to be the internal energy or the free energy from the lattice

calculations, but it significantly reduces the dissociation width at low temperature in the case that the internal energy from the lattice calculations is used as the charm quark potential.

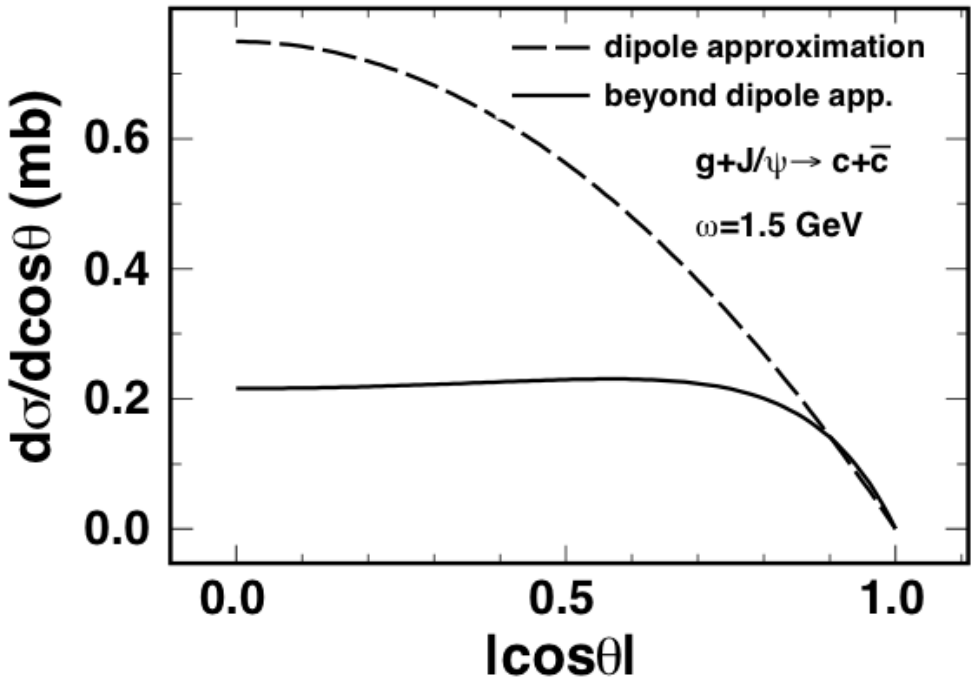

FIG. 2. Differential cross section for the gluon dissociation of J/ψ as a function of |cos θ| for the gluon energy ω = 1.5 GeV in the J/ψ frame, where θ is the angle between the momentum of the gluon and the relative momentum of final charm and anticharm quarks.

[1] Y.P. Liu, C.M. Ko, and T. Song, Phys. Rev. C **88**, 064902 (2013).

[2] M.E. Peskin, Nucl. Phys. **B156**, 365 (1979).

[3] Y. Oh, S. Kim, and S.H. Lee, Phys. Rev. C **65**, 067901 (2002).

Elliptic flow splitting as a probe of the QCD phase structure at finite baryon chemical potential

J. Xu,[1] C. M. Ko, T. Song, and F. Li

[1]*Shanghai Institute of Applied Physics, Chinese Academy of Sciences, Shanghai 201800, China*

We have studied the effects of both the partonic and the hadronic potential on the elliptic flow splitting of particles and their antiparticles in relativistic heavy-ion collisions [1] carried out in the beam energy scan (BES) program at RHIC [2]. With the evolution of the partonic phase described by an NJL transport model, we have obtained a larger elliptic flow for nucleons and K^- than antinucleons and K^+, respectively, right after hadronization [3]. After the hadronic evolution described by a relativistic transport model that includes the empirically determined hadronic potentials for particles and antiparticles [4], the final elliptic flow is larger for nucleons and K^+ than antinucleons and K^-, respectively. The relative elliptic flow differences from the STAR data can be reproduced if the ratio R_V of the vector coupling constant G_V to the scalar coupling constant G in the NJL model is between 0.5 and 1.1, after taking into account the mean-field potential effects in both the partonic and the hadronic phase as shown in Fig. 1. Our results therefore suggest that studying the elliptic flow splitting of particles and their antiparticles in heavy-ion collisions provides the possibility of studying the QCD phase structure at finite baryon chemical potential, thus helping understand the nature of the strong interaction.

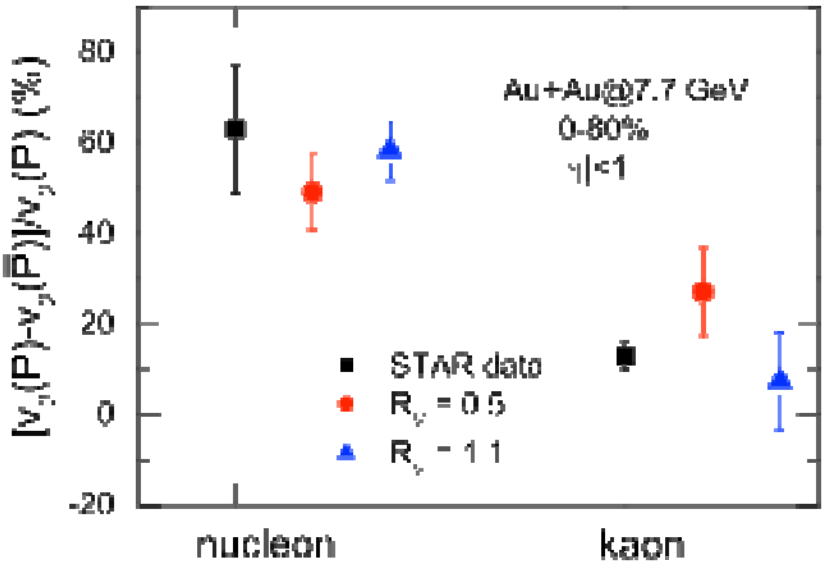

FIG. 1. Relative elliptic flow difference between nucleons and antinucleons as well as kaons and antikaons for different values of $R_V=G_V/G$ in the NJL model compared with the STAR data [5].

[1] J. Xu, T. Song, C.M. Ko, and F. Li, Phys. Rev. Lett. **112**, 012301 (2014).
[2] L. Kumar [STAR Collaboration], J. Phys. G **38**, 124145 (2011).
[3] T. Song, S. Plumari, V. Greco, C.M. Ko, and F. Li, Phys. Lett. B (submitted).
[4] J. Xu, L.W. Chen, C.M. Ko, and Z.W. Lin, Phys. Rev. C **85**, 041901 (2012).
[5] B. Mohanty [STAR Collaboration], J. Phys. G **38**, 124023 (2011).

Energy dependence of pion in-medium effects on π^+/π^- ratio in heavy-ion collisions

J. Xu,[1] L. W. Chen,[2] C. M. Ko, B. A. Li,[3] and Y. G. Ma[1]

[1]*Shanghai Institute of Applied Physics, Chinese Academy of Sciences, Shanghai 201800, China*

[2]*NPAC, Department of Physics and Shanghai Key Laboratory for Particle Physics and Cosmology, Shanghai Jiao Tong University, Shanghai 200240, China*

[3]*Department of Physics and Astronomy, Texas A&M University-Commerce, Commerce, Texas 75429*

Within the framework of a thermal model [1] with its parameters fitted to the results from an isospin-dependent Boltzmann-Uehling-Uhlenbeck (IBUU) transport model [2], we have studied the pion in-medium effect on the charged-pion ratio in heavy-ion collisions at various energies [3]. We have found that despite the cancellation between the pion-nucleon s-wave interaction [4], which reduces the π^-/π^+ ratio, and the p-wave interaction [5], which increases the π^-/π^+ ratio, the π^+/π^- ratio generally decreases after including the pion in-medium effect as shown in Fig.1. Although at lower energies the charged-pion ratio is more sensitive to the symmetry energy, the pion in-medium effect is also larger, especially at collision energies below the pion production threshold. Our results thus indicate that to understand quantitatively the symmetry energy effect on pion production in heavy-ion collisions, it is important to include the isospin-dependent pion in-medium effects.

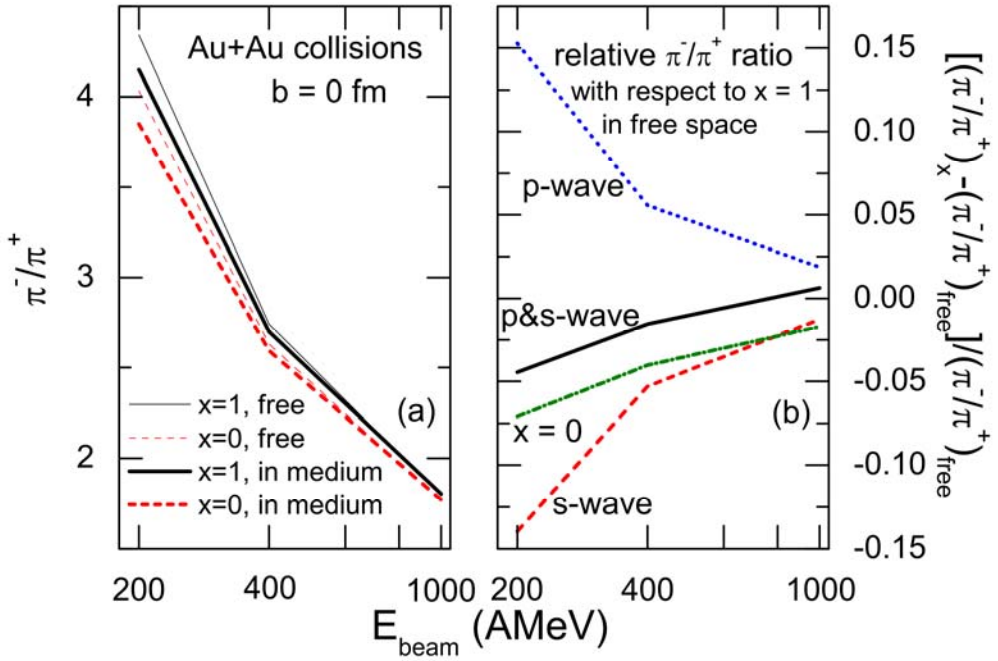

FIG. 1. Collision energy dependence of (a) π^-/π^+ ratios with and without pion in-medium effects and (b) relative π^-/π^+ ratios from pion-nucleon s-wave interaction, p-wave interaction, both p- and s-wave interactions, and x = 0 (stiffer symmetry energy) with respect to that from x = 1 (softer symmetry energy) in free space from the thermal model for central Au + Au collisions at different energies.

[1] J. Xu, C.M. Ko, and Y. Oh, Phys. Rev. C **81**, 024910 (2010).
[2] C.B. Das, S. Das Gupta, C. Gale, and B.A. Li, Phys. Rev. C **67**, 034611 (2003).
[3] J. Xu, L.W. Chen, C.M. Ko, B.A. Li, and Y.G. Ma, Phys. Rev. C **87**, 054902: (2013).
[4] N. Kaiser and W. Weise, Phys. Lett. B **512**, 283 (2001).
[5] G.E. Brown and W. Weise, Phys. Rep. **22**, 279 (1975); E. Oset, H. Toki, and W. Weise, Phys. Rep. **83**, 281 (1982); C.L. Korpa, M.F.M. Lutz, and F. Riek, Phys. Rev. C **80**, 024901 (2009).

Hot medium effects on J/ψ production in p+Pb collisions at $\sqrt{s_{NN}}$ = 5.02 TeV

J. P. Liu, C. M. Ko, and T. Song

Based on a kinetic description of J/ψ dissociation and production in an expanding quark-gluon plasma that is described by a 2+1-dimensional ideal hydrodynamics, we have studied the hot medium effects on J/ψ production in p+Pb collisions at $\sqrt{s_{NN}}$ = 5.02 TeV [1]. Including also the cold nuclear matter effects, we have been able to reproduce recent experimental results on the J/ψ nuclear modification factor measured by the ALICE Collaboration [2] as shown in Fig. 1. Our results indicate that the suppression of J/ψ production due to screening and thermal dissociation is more important than the contribution due to regeneration from the charm and anticharm quarks in the produced QGP, which leads to a smaller J/ψ nuclear modification factor than in the case of including only the cold nuclear matter effects. We have also found that the canonical enhancement effect due to smaller number of produced charm and anticharm quarks is important for the regeneration contribution since it would be negligible otherwise. We have further made predictions for the J/ψ nuclear modification factor and the ratio of the nuclear modification factor of prompt ψ' to that of J/ψ, and found that the J/ψ nuclear modification factor is slightly smaller than that in the minimum bias collisions, and the ratio is significantly less than one at backward rapidity.

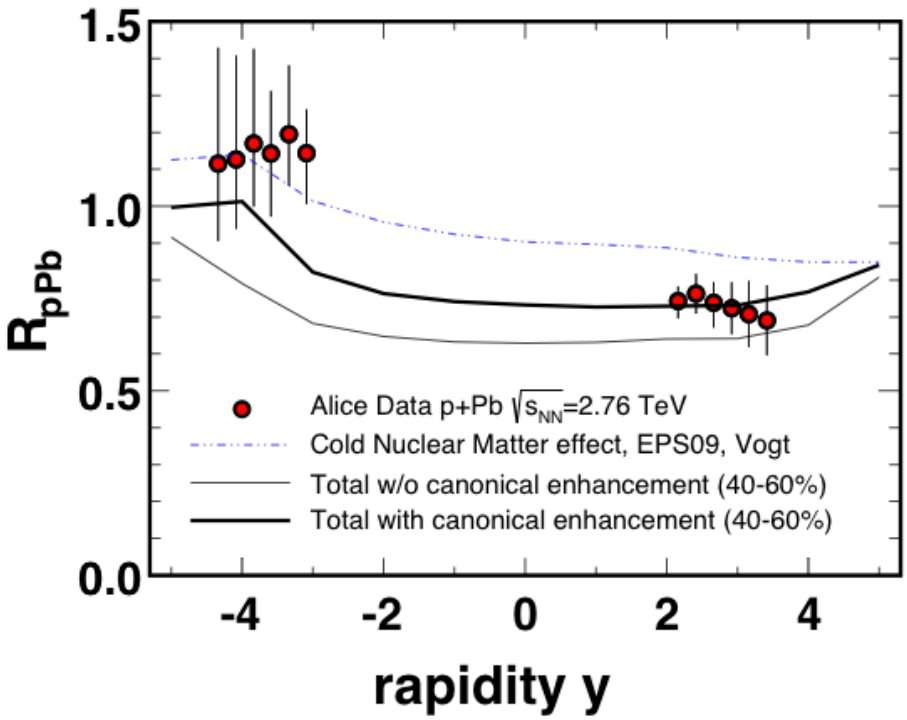

FIG. 1. Nuclear modification factor of J/ψ in the 40-60% centrality bin of p+Pb collisions as a function of rapidity. The (blue) dash-double-dotted line is for results with only cold nuclear matter effects [2]. The (black) thin solid line and (black) thick solid line are the total nuclear modification factor without and with the canonical enhancement, respectively. Experimental data are for minimum bias collisions from the ALICE Collaboration [3].

[1] Y.P. Liu, C.M. Ko, and T. Song, Phys. Lett. B **728**, 437 (2013).
[2] J.L. Albacete *et al.*, Int. J. Mod. Phys. E **22**, 1330007 (2013).
[3] L. Manceau, ALICE Collaboration, Quarkonium measurements in Pb–Pb and *p*–Pb collisions with ALICE at the LHC, 2013.

ψ' production and B decay in heavy ion collisions at LHC

B. Chen,[1] J. P. Liu, K. Zhou,[1] and P. Zhuang[1]
[1]*Physics Department, Tsinghua University, Beijing 100084, China*

Based on a transport approach, we have calculated the ratio of nuclear modification factors of inclusive ψ' and ψ in heavy ion collisions at LHC energy [1]. We have found that after experiencing the hot medium created in the early stage of the collisions, a part of the promptly produced J/ψs still survive and dominate the final state J/ψ distributions, but most of the prompt ψ's are dissociated in the hot medium, and the finally observed ψ's are mainly from the B-hadron decay. Therefore, the ratio of nuclear modification factors of inclusive ψ' and ψ in semi-central and central heavy ion collisions is controlled by the B decay. Our transport approach calculations agree reasonably well with the LHC data [2,3] in most transverse momentum and rapidity regions, but fail to explain the data in the region of $3<p_t<30$ GeV/c and $1.6<y<2.4$ as shown in Fig. 1. The big difference between the theory and the data needs further theoretical study and precise experimental measurement.

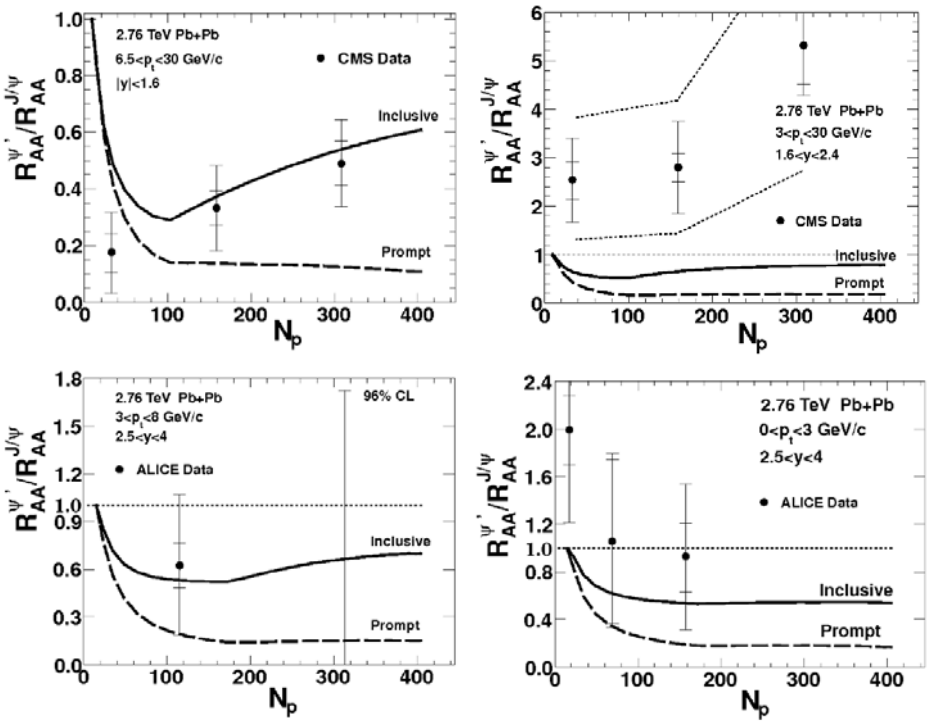

FIG. 1. Ratio of ψ' and ψ nuclear modification factors as a function of number of participants N_p. The data are from the CMS [1] (top windows) and ALICE (bottom windows) [2] collaborations, and the solid and dashed lines are, respectively, the transport model calculations with and without considering the B decay contribution.

[1] B. Chen, Y. Liu, K. Zhou, and P. Zhuang, Phys. Lett. B **726**, 725 (2013).
[2] D. Moon, [for the CMS Collaboration], arXiv:1209.1084v2[hep-ex].
[3] E. Scomparin, [for the ALICE Collaboration], arXiv:1211.1623[nucl-ex].

Effects of initial fluctuations on jet-energy loss

H. Zhang,[1] T. Song, and C. M. Ko

[1]*Institute of Particle Physics and Key Laboratory of quark & Lepton Physics, Central China Normal University, Wuhan, 430079, China*

Based on the 2+1-dimensional ideal hydrodynamics, we have studied the effect of initial fluctuations on jet-energy loss in relativistic heavy ion collisions within the description of the NLO perturbative QCD [1]. Our results show that fluctuating initial conditions lead to slightly more energy loss than smooth initial conditions as shown in Fig. 1. In general, the jet-energy loss increases with time due to its path-length dependence. This increase is, however, reduced by the decreasing medium density

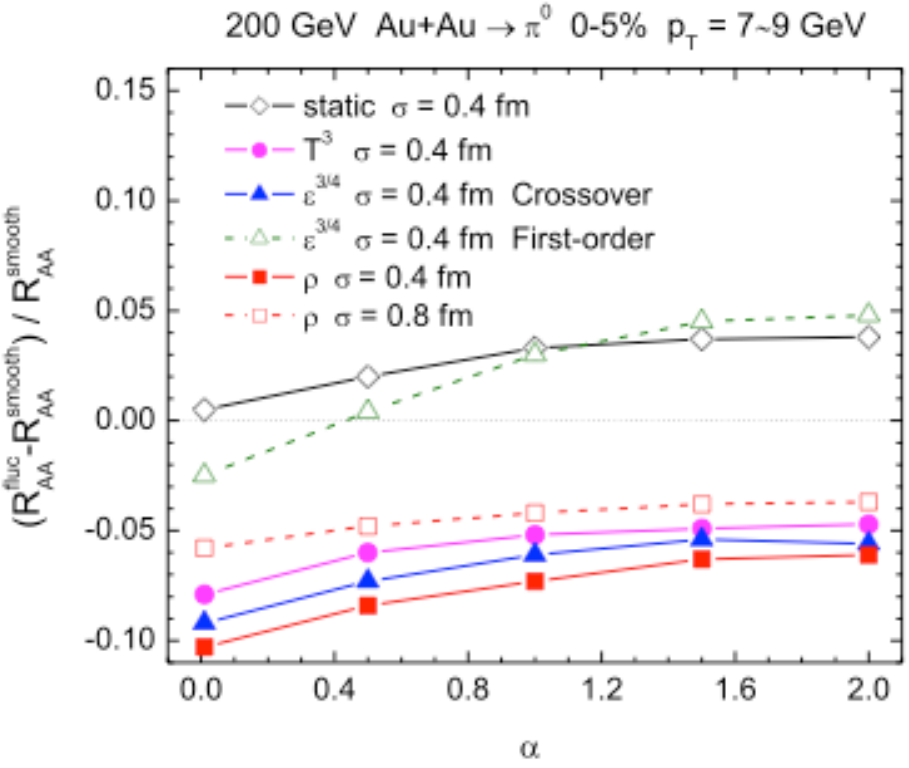

FIG. 1. Relative difference between the nuclear modification factor of p_T = 7-9 GeV hadrons as a function of the path-length dependence parameter α for different medium dependence in central Au+Au collisions.

with time. Where the total energy loss mainly takes place along the jet path is determined by the competition between the path-length dependence of jet-energy loss and the time dependence of the medium density. For fluctuating initial conditions, our results for the rate of the average energy loss difference between the two cases of fluctuating and smooth initial conditions show that the correlation between the fluctuation in the production probability of initial parton jets and the fluctuation in the local medium density is positive during the early times along the jet path and negative during the later times.

Consequently, the net effect of initial fluctuations on jet-energy loss is determined by whether the energy loss mainly takes place when this correlation is positive or negative. The total energy loss in the fluctuation conditions is then larger than that in the smooth case if most energy loss takes place when the correlation is positive, while it is smaller if it takes place when the correlation is negative. Our results further show that the initial positive correlation dominates the fluctuation effect for linear and quadratic path-length dependence of jet-energy loss in central as well as in noncentral A + A collisions. However, because this dominance is stronger in non-central collisions than in central collisions, the difference between the nuclear modification factors calculated with fluctuating initial conditions and smooth initial conditions in non-central A + A collisions is greater than that in central A + A collisions. Similarly, the jet-energy loss for the linear (α =1) path-length dependence is more affected by the fluctuation effect than that for the quadratic (α =2) path-length dependence. Our results are opposite to those found in Ref. [2] for a static medium and also those in Ref. [3] using a 2 + 1 ideal hydrodynamics and with the jet-energy loss depending on the local energy density, which show a reduced jet-energy loss in the QGP for the fluctuating initial conditions.

[1] H. Zhang, T. Song, and C.M. Ko, Phys. Rev. C **87**, 054902 (2013).
[2] R. Rodriguez, R.J. Fries, and E. Ramirez, Phys. Lett. B **693**, 108 (2010).
[3] T. Renk, H. Jolopainen, J. Auvinen, and K.J. Eskola, Phys. Rev. C **85**, 044915 (2012).

Effects of medium modification of pion production threshold in heavy ion collisions and the nuclear symmetry energy

T. Song[1] and C. M. Ko

[1]*Frankfurt Institut for Advanced Studies and Institute for Theoretical Physics, Johann Wolfgang Goethe Universitat, Frankfurt am Main, Germany*

Using the relativistic Vlasov--Uehling-Uhlenbeck equation based on the nonlinear relativistic mean-field models [1-3], we have studied the covariant threshold effect on the pion yield and the π^-/π^+ ratio in Au+Au collisions [4]. We have found that besides enhancing the pion yield and the π^-/π^+ ratio, the threshold effect also reverses the effect of nuclear symmetry energy on the π^-/π^+ ratio as shown in the left two panels of Fig. 1. Although including the threshold effect leads to a better description of the measured π^-/π^+ ratio from the FOPI Collaboration [5], it gives too large a total pion yield compared to the experimental data. Introducing a density dependence in the Delta resonance production cross section, we have been able to describe both the pion yield and the π^-/π^+ ratio measured in experiments as shown in the right two panels of Fig. 1. The large errors in the experimentally measured π^-/π^+ ratio prevent, however, the distinction between the predictions from the NLρ and NLρδ models [6], which correspond to the soft and stiff nuclear symmetry energies, respectively. Since the in-medium threshold effect has an opposite effect on the π^-/π^+ ratio in heavy ion collisions from the effect due to the stiffness of nuclear symmetry energy at high density, it is important to include this effect in extracting the high-density behavior of nuclear symmetry energy from experimentally measured π^-/π^+ ratio.

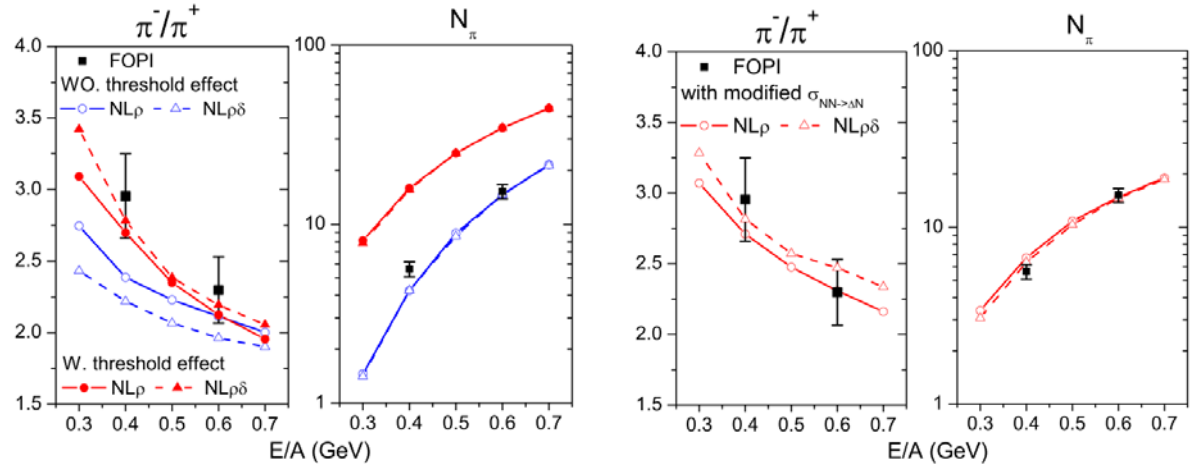

FIG. 1. The π^-/π^+ ratio and pion yield as functions of collision energy with and without the threshold effect in Au+Au collisions at impact parameter of 1 fm from the NLρ and NLρδ models for the case of free (left two panels) and density-dependent (right two panels) Delta resonance production cross section. Experimental data are from the FOPI Collaboration [5].

[1] C.M. Ko, Q. Li and R.-C. Wang, Phys. Rev. Lett. **59**, 1084 (1987).

[2] C.M. Ko and Q. Li, Phys. Rev. C **37**, 2270 (1988).

[3] C.M. Ko and G.-Q. Li, J. Phys. G **22**, 1673 (1996).
[4] T. Song and C.M. Ko, Phys. Rev. C (submitted).
[5] W. Reisdorf *et al.* [FOPI Collaboration], Nucl. Phys. **A781**, 459 (2007).
[6] B. Liu, V. Greco, V. Baran, M. Colonna and M. Di Toro, Phys. Rev. C **65**, 045201 (2002).

Spin asymmetry of J/ψ in peripheral Pb+Pb collisions at LHC

J. P. Liu, C. Greiner,[1] and C. M. Ko

[1]*Institut fur Theoretische Physik, Johann Wolfgang Goethe-Universitat Frankfurt, Max-von-Laue-Str. 1, D-60438 Frankfurt am Main, Germany*

By generalizing the statistical hadronization model [1,2] to the spin degree of freedom, we have calculated the influence of the magnetic field existing in the early stage of peripheral heavy ion collisions on the spin asymmetry of produced J/ψ at the LHC energy [3]. The fraction of J/ψs with spin in the direction of the magnetic field (J_y = 0) is found to be above 1/3 and to increase in peripheral Pb+Pb collisions with the transverse momentum in the color singlet model (CSM) [4] scenario, while it is 1/3 in the color octet model (COM) [5] scenario as shown in Fig. 1. In the absence of vanishing J/ψ spin flipping cross section (ε=0), the fraction can be as large as 0.42 for J/ψ of transverse momentum p_T around 10 GeV. Even if the J/ψ flipping cross section is the same as the dissociation cross section (ε=1), the fraction can still be above 0.39 at p_T = 10 GeV. For a more realistic value of J/ψ spin flipping cross section, which would be strongly model dependent, the spin fraction is expected to lie between these two extreme cases. Our finding thus indicates that studying the spin asymmetry of J/ψ produced in relativistic heavy ion collisions provides the information on how the J/ψ is produced in initial hard collisions.

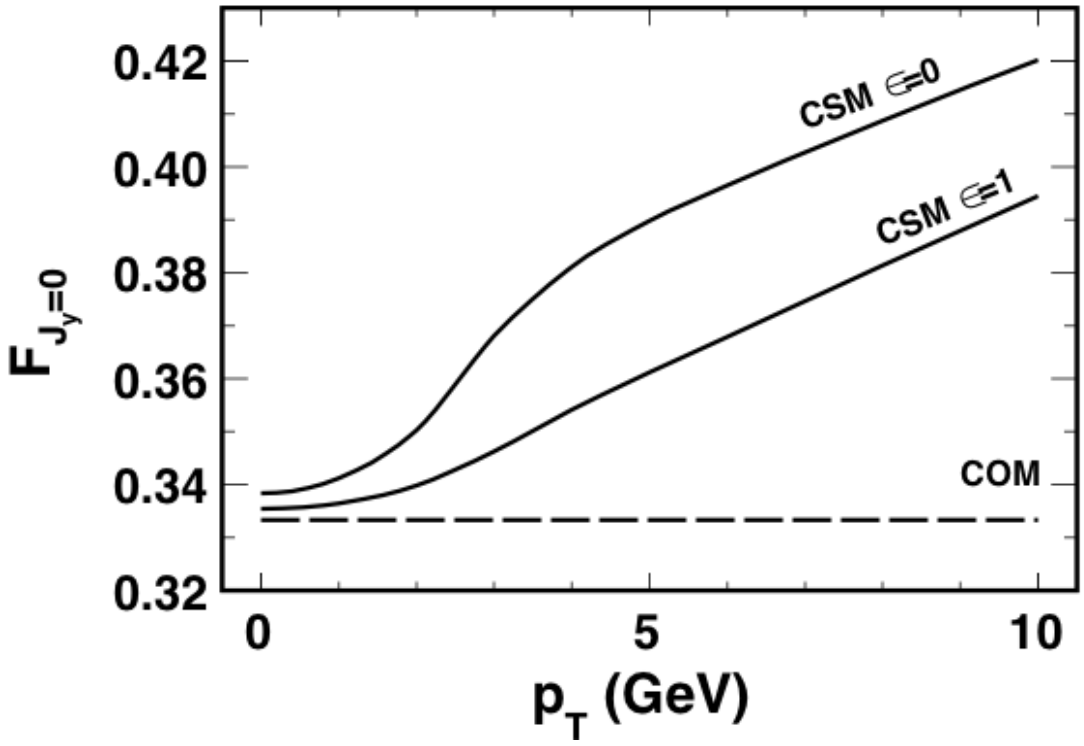

FIG. 1. Transverse momentum dependence of the fraction of J/ψs with spin along the direction of the magnetic field in peripheral Pb+Pb collisions at impact parameter b = 10.5 fm at $\sqrt{s_{NN}}$ = 2.76 TeV for different values of the ratio ε between the average spin flipping cross section to the average dissociation cross section of J/ψ in the CSM scenario (solid) compared with that in the COM scenario (dashed).

[1] A. Andronic, P. Braun-Munzinger, and J. Stachel, Phys. Lett. B **673**, 142 (2009).
[2] P. Braun-Munzinger and J. Stachel, Phys. Lett. B **490**, 196 (2000).
[3] Y.P. Liu, C.M. Ko, and C. Greiner, Phys. Rev. C (submitted).
[4] C.-H. Chang, Nucl. Phys. **B172**, 425 (1980).
[5] G.T. Bodwin, E. Braaten, and G.P. Lepage, Phys. Rev. D **51**, 1125 (1995).

Shear viscosity of neutron-rich nucleonic matter near liquid-gas phase transition

J. Xu,[1] L. W. Chen,[2] C. M. Ko, B. A. Li,[3] and Y. G. Ma[1]

[1]*Shanghai Institute of Applied Physics, Chinese Academy of Sciences, Shanghai 201800, China*

[2]*NPAC, Department of Physics and Shanghai Key Laboratory for Particle Physics and Cosmology, Shanghai Jiao Tong University, Shanghai 200240, China*

[3]*Department of Physics and Astronomy, Texas A&M University-Commerce, Commerce, Texas 75429*

Within a relaxation time approach using free nucleon–nucleon cross sections modified by the in-medium nucleon masses that are determined from an isospin- and momentum-dependent effective nucleon– nucleon interaction [1,2], we have investigated the specific shear viscosity (η/s) of neutron-rich nucleonic matter near its liquid–gas phase transition [3]. We have found that as the nucleonic matter is heated at fixed pressure or compressed at fixed temperature, its specific shear viscosity shows a valley shape in the temperature or density dependence, with the minimum located at the boundary of the phase transition as shown in Fig. 1. Moreover, the value of η/s drops suddenly at the first-order liquid–gas phase transition temperature, reaching as low as 4–5 times the KSS bound [4]. However, it varies smoothly for the second-order liquid–gas phase transition. We have further found that the density dependence of the symmetry energy affects the value of the specific shear viscosity of nucleonic matter in the mixed phase region, although it has little effects on the location of its minimum. Our results are expected to be useful for investigating the nature and signatures of the liquid–gas phase transition in neutron-rich matter using intermediate-energy heavy-ion collisions induced by rare isotopes.

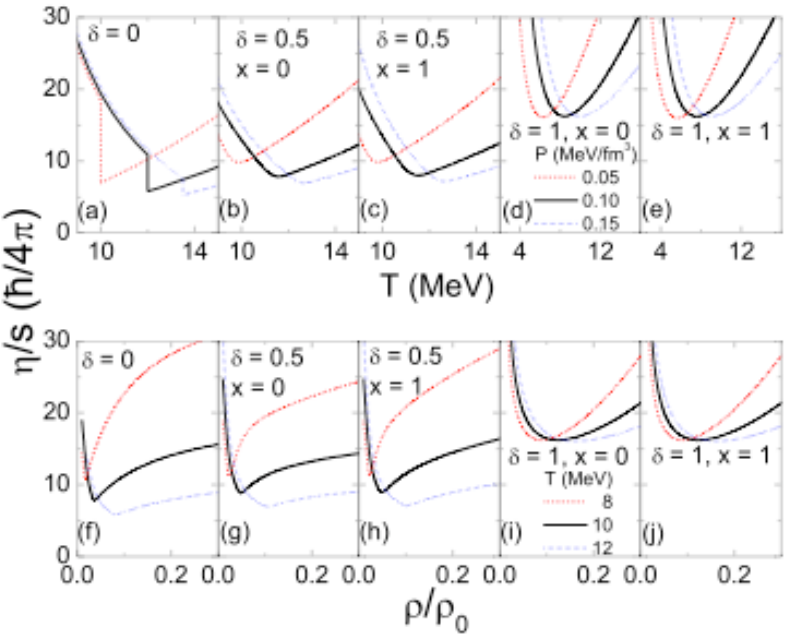

FIG. 1. Temperature (upper panels) and density (lower panels) dependence of the specific shear viscosity at different fixed pressures and temperatures, respectively, in isospin symmetric matter ($\delta = 0$), neutron-rich matter ($\delta = 0.5$), and pure neutron matter ($\delta = 1$) for both a stiffer (x=0) and a softer (x=1) symmetry energy.

[1] C.B. Das, S. Das Gupta, C. Gale, and B.A. Li, Phys. Rev. C **67**, 034611 (2003).
[2] L.W. Chen, C.M. Ko, and B.A. Li, Phys. Rev. Lett. **94**, 032701 (2005).
[3] J. Xu, L.W. Chen, C.M. Ko, B.A. Li, and Y.G. Ma, Phys. Lett. B **727**, 244-248 (2013).
[4] P.K. Kovtun, D.T. Son, A.O. Starinets, Phys. Rev. Lett. **94**, 111601 (2005).

Relativistic Langevin dynamics

R. J. Fries, R. Rapp, and Collaborators

The approach of heavy-quark (charm, bottom) distributions to thermal equilibrium is one of the outstanding theoretical questions in heavy-ion collisions. While it has been established experimentally that light quarks and gluons thermalize early in the collision, heavy-quark thermalization times are believed to be suppressed by their large masses, implying incomplete thermalization during the lifetime of the fireball. However, measurements of heavy-flavor observables in heavy-ion collisions at RHIC and LHC show a remarkable degree of thermalization, allowing us to study heavy-quark interactions with hot nuclear matter in detail.

On the theoretical side the thermalization process of heavy quarks can be described by the Fokker-Planck (FP) equation which can be obtained from the Boltzmann equation. The drag and diffusion coefficients in the FP equation can therefore be strictly derived from the theory underlying the Boltzmann equation. The commonly used numerical implementation of the Brownian motion is given by the Langevin equation, representing a stochastic realization of the FP equation. Different realizations of the Langevin algorithm exist (post-point, pre-point, etc.) which require special care in how to implement the noise. This is known as the Ito-Stratonovich dilemma which, in the relativistic case has, has posed considerable challenges [1,2]. This rather general problem in transport theory also applies to heavy-quark thermalization in quark gluon plasma.

Starting from the assumptions that the transport coefficients in the Fokker-Planck equation are fixed by the underlying microscopic theory, and that the correct equilibrium distributions are reached in the long-time limit, we have shown that there are unique relations between the drag coefficient Γ in each Langevin implementation and the transport coefficients A and D of the Fokker-Planck equation [3]. If those relations are taken into account the different Langevin implementations give the same result and converge to the correct equilibrium distributions. We have given explicit formulas which set up the correct algorithm for the Langevin equations in pre-point and post-point formulation for non-homogeneous, relativistic background media.

We have furthermore explicitly checked our results numerically with test particles diffusing in a relativistic medium, confirming that the correct equilibrium (Boltzmann-Jüttner) distributions are obtained. Fig. 1 shows the results of Langevin calculations for heavy quarks in a flowing background medium in the pre-point algorithm, using the appropriate relation between the drag coefficient Γ and the diffusion coefficient D (circles and triangles) which lead to the known equilibrium (Boltzmann-Jüttner) distribution (red solid line), while a Langevin calculation violating the relation we found (squares) leads to an incorrect equilibrium distribution (green dotted line). These results have been used in our previously reported calculations of heavy-flavor observables in heavy-ion collisions.

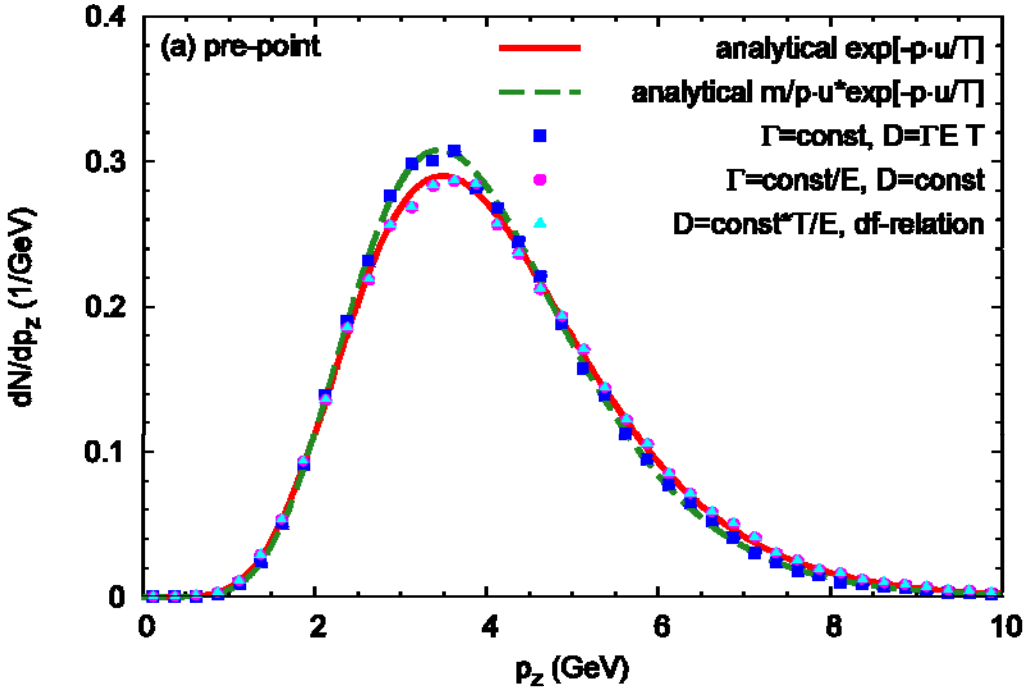

FIG. 1. Langevin simulations in the pre-point scheme for heavy quarks of mass 1.5 GeV in a medium with temperature of T=180 MeV and homogeneous velocity v=0.9 in z-direction. Only simulations with the correct relation between Γ and *D* (circles and triangles) converge to the equilibrium distribution (red solid line).

[1] J. Dunkel and P. Hänggi, Phys. Rep. **471**, 1 (2009).

[2] T. Koide and T. Kodama, Phys. Rev. E **83**, 061111 (2011).

[3] M. He, H. van Hees, P.B. Gossiaux, R.J. Fries and R. Rapp, Phys. Rev. E **88**, 032138 (2013).

The rapidity profile of the initial energy density in high energy nuclear collisions

R. J. Fries and Collaborators

Color Glass Condensate has been identified as the asymptotic limit of quantum chromodynamics (QCD) at very large energies. In this limit hadrons and nuclei can be described as Lorentz-contracted sheets of color charges (in the simplest picture the charges are the valence quarks inside the hadrons) generating a quasi-classical gluon field. There are hints from experimental measurements that large nuclei colliding at RHIC and LHC have reached this asymptotic regime.

Using Color Glass as an effective theory of QCD one can calculate the gluon distribution function of a high energy nucleus. One can then proceed to compute the initial energy density deposited between two such nuclei once they collide. The latter result can serve as the starting point of a calculation describing the evolution of these classical fields toward a thermalized quark gluon plasma. Some work in this direction has been described in previous reports.

However, one basic shortcoming of virtually all Color Glass-based calculations is that they are carried out at the asymptotic point, i.e. for nuclei moving strictly on the light-cone, or in other words with infinite kinetic energy. At RHIC and LHC nuclei are indeed ultra-relativistic (the Lorentz γ-factor is $\approx$100 at top RHIC energies and even larger at LHC). Therefore the asymptotic limit allows for a large number of observables in nuclear collisions to be calculated as long as the rapidity y of the particles involved is much smaller than the rapidity of the colliding nuclei (the beam rapidity). At larger rapidity observables receive corrections if one takes into account that the nuclei are slightly off the light-cone. The corrections grow with $|y|$, and any calculation assuming the asymptotic limit will be unreliable if $|y|$ grows close to the beam rapidity. As an example the initial energy density ε calculated in the asymptotic limit is completely independent of the space-time rapidity η, because the nuclei on the light cone exhibit boost-invariance as a symmetry. But of course causality dictates that ε has to go to zero if $|\eta|$ is larger than the beam rapidity.

In our work we used gluon distribution functions calculated by Lam and Mahlon [1] for nuclei slightly off the light cone in the Color Glass formalism to estimate the rapidity dependence of ε. Our calculation is valid as long as the passing time of the two nuclei $\sim R/\gamma$ is much smaller than the internal time scale of the color glass $\sim 1/Q_s$ where Q_s is also known as the saturation scale. Our results (see Fig. 1 for an example at LHC energies) exhibit approximate boost-invariance around $\eta = 0$ but then predicts a rapid fall off toward beam rapidity. The final result can be conveniently parameterized in terms of Woods-Saxon functions. The parameters for parameterizations are given for Au+Au collisions at RHIC energies and Pb+Pb collisions at LHC energies in our publication [2]. Our result can be used as a starting point for 3+1-dimensional hydrodynamic studies of high energy nuclear collisions.

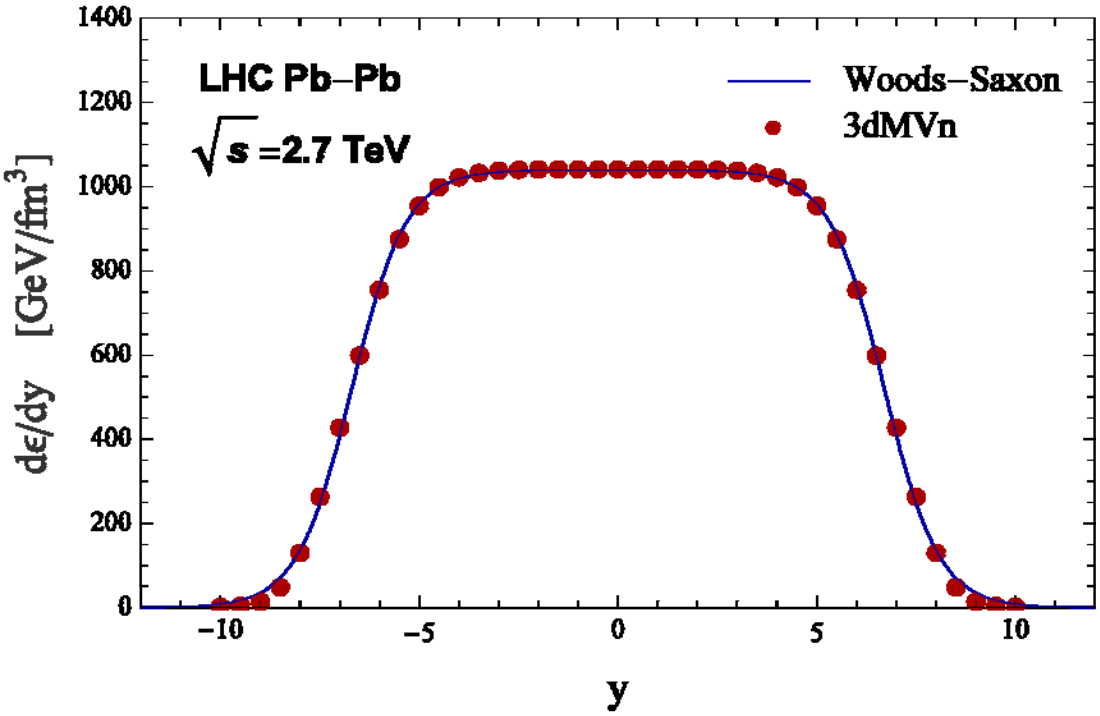

FIG. 1. Initial energy density in the collision of two lead nuclei at LHC as a function of space-time rapidity. The results of the calculation (red circles) can be parameterized by a Woods-Saxon function (blue solid line).

[1] C.S. Lam and G. Mahlon, Phys. Rev. D **62**, 114023 (2000).

[2] S. Ozonder and R.J. Fries, Phys. Rev. C **89**, 034902 (2014).

Is ρ-meson melting compatible with chiral restoration?

P. M. Hohler and R. Rapp

The QCD vacuum spontaneously breaks chiral symmetry at low temperatures and chemical potentials through the formation of the quark condensate. At higher temperatures, this condensate melts across a region around a pseudo-critical temperature, T_{pc}~160MeV, thus restoring the symmetry [1, 2]. How this restoration is imprinted on the observable hadronic states has been a long standing question. One way to study this is through the in-medium spectral functions of chiral partners, e.g. the ρ and a_1 (vector and axial-vector) mesons. The vector channel can be experimentally accessed through dilepton spectra in ultra-relativistic heavy ion collisions [3-5]. Theoretical calculations from a microscopic hadronic effective field theory [6] turn out to agree with experimental data, implying that the in-medium ρ spectral function melts through spectral peak broadening without a significant mass shift [7]. To relate this melting to chiral symmetry restoration requires knowledge about the axial-vector channel. However, to date, the latter remains experimentally elusive. Therefore, progress can only be made through theoretical techniques which inherently connect the vector and axial-vector channels. A rigorous method are sum rules, in particular QCD [8] and Weinberg-type sum rules [9-11] which relate the vector and axial-vector spectral function to each other and to ground-state condensates. Here, our strategy is to provide inputs to the sum rules in terms of the in-medium vector spectral function (as tested in experiment) and condensates from lattice QCD, to search for possible solutions for the axial-vector spectral function to satisfy the sum rules.

In the current work [12], we build on our earlier sum rule investigation [13] of the vacuum vector and axial-vector spectral functions and extend it to finite temperature. In medium, the sum rules translate the temperature dependence of the QCD condensates to medium modifications of the spectral functions. For our analysis, there are four important inputs. The first is the in-medium ρ spectral function for which we use the results of Ref. [6]; thus a direct connection to the dilepton data and the melting scenario is made. The second is the temperature dependence of the condensates. For this we use a hadron resonance gas approach with guidance from lattice QCD calculations. The resulting temperature dependencies of the quark and 4-quark condensates are depicted in Fig. 1. Third, we specify the temperature dependence of the excited vector and axial-vector meson states through chiral mixing with a mixing parameter derived from both thermal pions as well as the pion cloud of other hadrons [14, 15]. In this way, the effect of the hadron resonance gas is incorporated into this mixing. This constraint facilitates to focus our study on the contribution from the axial-vector ground state. Lastly, we stipulate that the chirally invariant vacuum continuum in both vector and axial-vector spectral functions is temperature independent. The medium modifications of the a_1 spectral function are represented by four parameters: one for the mass, two for the width, and one for the coupling strength to the current. These parameters are determined at each temperature by requiring that both the axial-vector QCD sum rule and the Weinberg sum rules are satisfied. It is the combination of *both* sets of sum rules which is critical in constraining possible spectral functions. With these ansaetze, we were able to show that 1) the vector QCD sum rule can be satisfied better than the 0.67% level with a small (order 5%) modification of the vector dominance coupling, and

2) an axial-vector spectral function can be determined which satisfies the axial-vector QCD sum rule better than 0.59% and the first two Weinberg sum rules better than 0.004%.

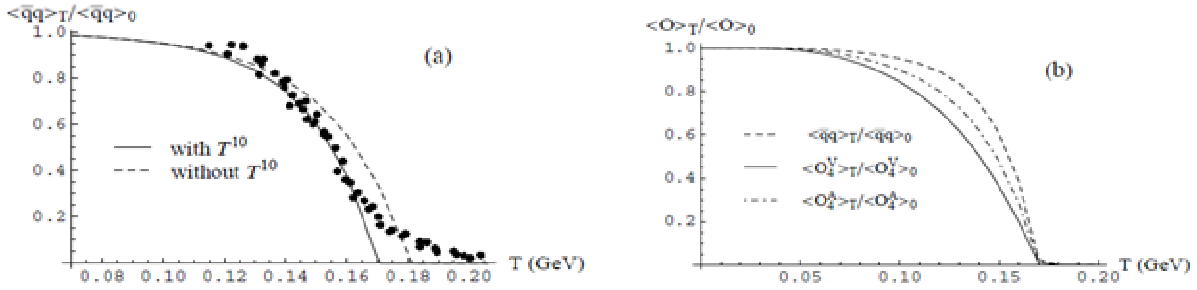

FIG. 1. Temperature dependence of: (a) the quark condensate relative to its vacuum value, compared to thermal lattice-QCD data [1]; (b) axial-/vector 4-quark condensates relative to their vacuum values, compared to the quark condensate.

The resulting spectral functions are shown in Fig. 2. By being able to satisfy the sum rules at each temperature, the manner in which restoration is achieved can be studied through the temperature progression of the spectral functions. One notices that with increasing temperature, the a_1 spectral peak broadens and shifts its mass to lower energies, ultimately merging with the vector channel at the highest temperature. The mass shift in the axial-vector channel can be thought of as the burning off the chirally breaking ρ-a_1 mass difference. This study thus demonstrates that the ρ-melting scenario is consistent with chiral restoration.

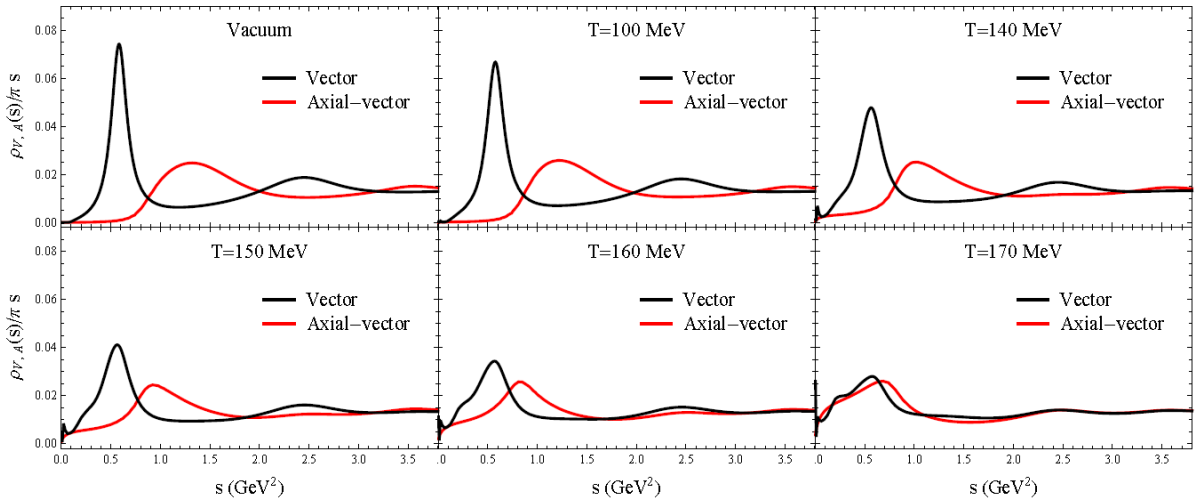

FIG. 2. Finite- temperature vector (black/darker curve) and axial-vector (red/lighter curve) spectral functions.

[1] S. Borsanyi *et al.* [Wuppertal-Budapest Collaboration], JHEP **1009**, 073 (2010).

[2] A. Bazavov *et al.*, Phys. Rev. D **85**, 054503 (2012).

[3] R. Arnaldi *et al.* [NA60 Collaboration], Eur. Phys. J. C **61**, 711 (2009).

[4] D. Adamova *et al.* [CERES/NA45 Collaboration], Phys. Lett. B **666**, 425 (2008).

[5] F. Geurts *et al.* [STAR Collaboration], Nucl. Phys. A **904-905**, 217c (2013).

[6] R. Rapp and J. Wambach, Eur. Phys. J. A **6**, 415 (1999).
[7] R. Rapp, PoS CPOD **2013**, 008 (2013).
[8] M.A. Shifman, A.I. Vainshtein, and V.I. Zakharov, Nucl. Phys. B **147**, 385 (1979); ibid. 448.
[9] S. Weinberg, Phys. Rev. Lett. **18**, 507 (1967).
[10] T. Das, V.S. Mathur, and S. Okubo, Phys Rev. Lett. **19**, 859 (1967).
[11] J.I. Kapusta and E.V. Shuryak, Phys. Rev. D **49**, 4694 (1994).
[12] P.M. Hohler and R. Rapp, Phys. Lett. B **731**, 103 (2014).
[13] P.M. Hohler and R. Rapp, Nucl. Phys. **A892**, 58 (2012).
[14] G. Chanfray, J. Delorme, and M. Ericson, Nucl. Phys. **A637**, 421 (1998).
[15] B. Krippa, Phys. Lett. B **427**, 13 (1998).

The πρ cloud contribution to the ω width in nuclear matter

D. Cabrera and R. Rapp

Medium modifications of hadrons at finite temperature and density are key to the understanding of the phase structure of QCD matter. Dilepton measurements in heavy-ion collisions have established that the ρ meson undergoes a strong broadening that ultimately melts its resonance structure close to the QCD phase transition temperature, as predicted by many-body theory in hot/dense hadronic matter [1]. For the ω meson, indirect measurements of its absorptive width in photo-induced production experiments off nuclei also indicate a large broadening in nuclear matter, by about 150 MeV or so over its vacuum value of only ~8 MeV [2,3]. This large effect has been difficult to understand theoretically, especially when working to linear order in density using the so-called T-ρ approximation.

In the present work [4], we have evaluated the ω width in nuclear matter by calculating the modifications to its selfenergy due to in-medium decays into a pion and ρ-meson, schematically given by

$$\Pi_\omega = \int v_{\pi\rho\omega}\, D_\rho\, D_\pi\, v_{\pi\rho\omega}\,,$$

where $v_{\pi\rho\omega}$ is the πρω vertex function. The key point here is the use of in-medium π and ρ propagators, $D_{\pi,\rho}$, taken from our previous work on in-medium ρ-mesons [5]. It turns out that the resulting ω width in nuclear matter reaches values of about 150-200 MeV at nuclear saturation density, see left panel of Fig. 1. These values, along with the 3-momentum dependence displayed in the right panel of Fig. 1, are in approximate agreement with the experimentally extracted values. The largest theoretical uncertainty is

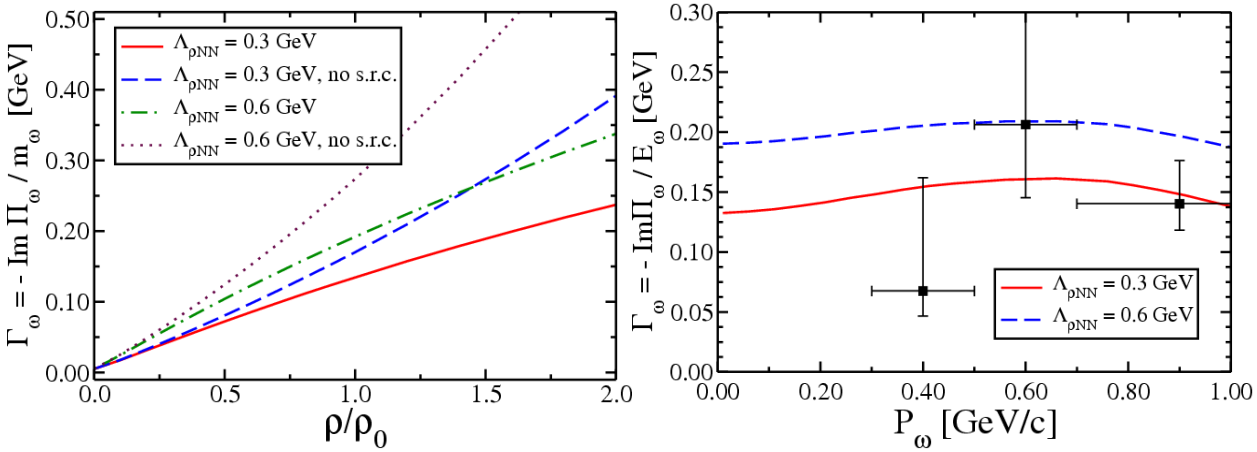

FIG. 1. The on-shell width of the ω(782) meson in cold nuclear matter as a function of nuclear density at vanishing 3-momentum (left), and as a function of 3-momentum at nuclear saturation density, ρ_0=0.16fm^{-3} (right). The various curves illustrate the uncertainty due to different parameters in the ρNN^{-1} selfenergy. The experimental data in the left panel are extracted from absorption measurements of w photoproduction off nuclei [2]

associated with the thus far not well constrained parameters of the ρNN interaction vertex, which correspond to t-channel ρ exchange processes in ωN → πN scattering. The resulting large ω width in

nuclear matter based on existing in-medium π and ρ properties is encouraging and further corroborates the quantum-many body approach as a suitable tool to evaluate hadron properties in medium.

[1] R. Rapp, J. Wambach and H. van Hees, in *Relativistic Heavy-Ion Physis (R. Stock, ed.)*, Landolt-Börnstein (Springer), New Series, vol. **I/23A** (2010) 4-1; e-print arXiv:0901.3289 [hep-ph].
[2] M. Kotulla *et al.* [CBELSA/TAPS Collaboration], Phys. Rev. Lett. **100**, 192302 (2008).
[3] M.H. Wood *et al.* [CLAS Collaboration], Phys. Rev. Lett. **105**, 112301 (2010).
[4] D. Cabrera and R. Rapp, Phys. Lett. **B 729**, 67 (2014).
[5] R. Rapp and J. Wambach, Eur. Phys. J. A **6**, 415 (1999).

Direct determination of mean-field from data on matter density

M. R. Anders, S. Shlomo, and I. Talmi[1]
[1]*Weizmann Institute of Science, Rehovot, Israel*

In this work we consider the single particle Schrodinger equation and develop a method for determining the single particle potential *V* from a given single particle wave function $\Psi(\vec{r})$ or matter density, assuming it is known for all $\vec{r}$. In particular, we consider the case of spherical symmetry. The results of this work are very important for investigation of the validity of the shell model and for the development of a modern EDF which provides enhanced predictive power for properties of nuclei and the equation of state (EOS) of nuclear matter (NM).

For the single particle Schrodinger equation,

$$-\frac{\hbar^2}{2m}\Delta\Psi + V\Psi = E\Psi\,, \tag{1}$$

we have that for a given single particle wave function $\Psi(\vec{r})$, known for all $\vec{r}$, the corresponding single particle potential *V* is uniquely determined [1] from

$$V(\vec{r}) = E + \frac{\hbar^2}{2m}\frac{\Delta\Psi(\vec{r})}{\Psi(\vec{r})}\,. \tag{2}$$

Note that for a nonsingular *V*, $\Delta\Psi(\vec{r}) = 0$ when $\Psi(\vec{r}) = 0$. In the spherical case we have for the centroid potential

$$V_{cen}(r) = E + \frac{\hbar^2}{2m}\frac{d^2R_{nlj}}{dr^2}\frac{1}{R_{nlj}(r)} - \frac{\hbar^2}{2m}\frac{l(l+1)}{r} - \frac{1}{2}(1-\tau_z)V_{coul}(r) - c_{ls}\,V_{s.o.}(r)\,. \tag{3}$$

Here, $V_{cen}(r), \vec{s}\cdot\vec{l}\,V_{s.o.}(r)\ and\ \frac{1}{2}(1-\tau_z)V_{coul}(r)$, are the central, spin-orbit and coulomb potentials, respectively, and τ_z=1 for a neutron and -1 for a proton.

We consider, in particular, the charge density difference, $\Delta\rho_c(r)$, between the isotones ^{206}Pb – ^{205}Tl, associated with the proton $3S_{1/2}$ single particle orbit, and determine the corresponding single particle potential. The experimental data for the charge densities, $\rho_c(r)$, of the isotones ^{206}Pb and ^{205}Tl, obtained from accurate elastic electron scattering experiments, are taken from Ref. [1]. In Fig. 1a we present the experimental data for the charge density difference, $\Delta\rho_c(r)$, between the isotones ^{206}Pb – ^{205}Tl, shown by the dashed line. It is normalized to a total charge of one proton (Z=1). The dotted lines indicate the experimental uncertainty. Note that the two nodes associated with the proton $3S_{1/2}$ orbit are clearly seen in the figure. To extract the corresponding single particle potential we need the point proton distribution, $\Delta\rho_p(r)$. This is obtained by determining the point proton form factor, $F_p(q)$, and then extracting $\Delta\rho_p(r)$. The results are shown in Fig. 1b. Note that $\Delta\rho_p(r)$ (dashed line) is slightly negative at the first node (at

~2.6 fm) and above zero at the second node (r~4.9 fm). Using these results we determine the corresponding mean field associated with the $3S_{1/2}$ orbit in ^{206}Pb [2].

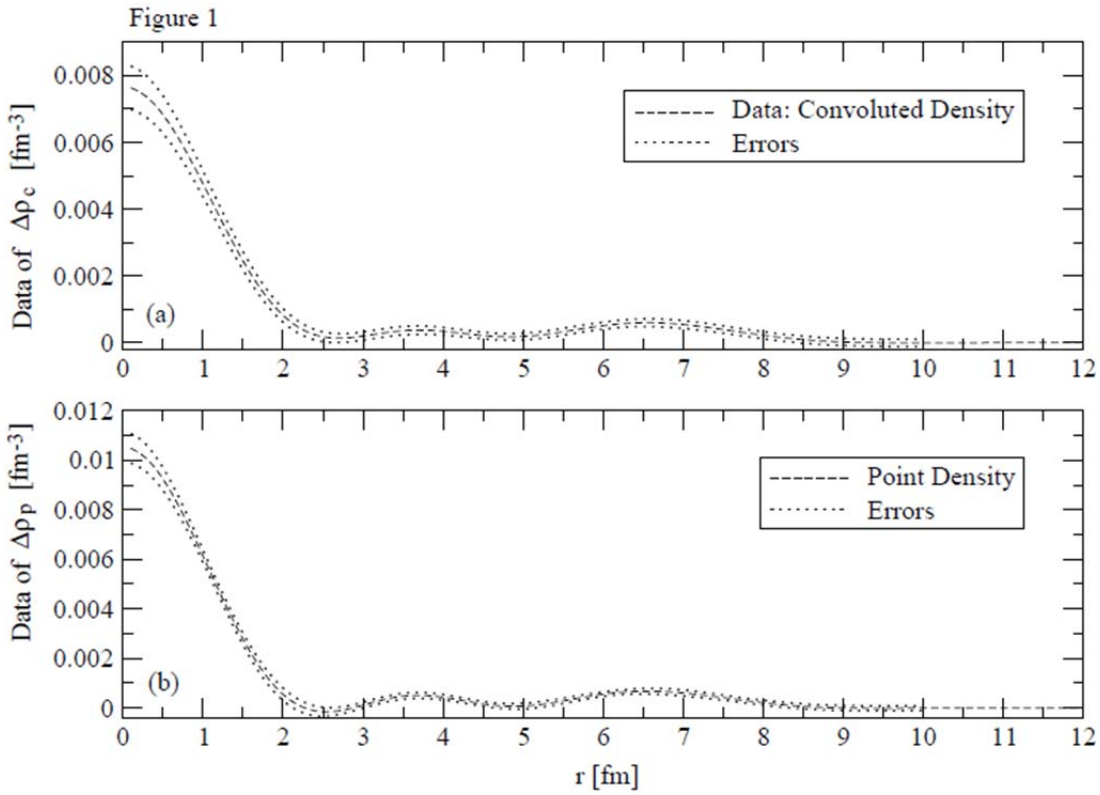

FIG. 1. Charge density (a) and point density (b) for the $3_{S1/2}$ orbit in ^{206}Pb.

[1] J.M. Cavedon *et al.*, Phys. Rev. Lett. **49**, 978 (1982).

[2] M.R. Anders, S. Shlomo and I. Talmi, in preparation.

Isoscalar dipole strength distributions in nuclei and the Schiff moment

N. Auerbach,[1] Ch. Stoyanov,[2] M. R. Anders, and S. Shlomo
[1]*School of Physics and Astronomy, Tel Aviv University, Tel Aviv 69978, Israel,*
and Department of Physics and Astronomy, Michigan State Univ., East Lansing, Michigan
[2]*Inst. for Nuclear Research and Nuclear Energy, Bulgarian Academy of Science, Sofia Bulgaria*

In a recent paper [1] it was pointed out that the isoscalar dipole (ISD) resonance could have a substantial contribution to the nuclear Schiff moment whose operator is the same as the operator commonly used in the study of the ISD strength distribution. The value of the Schiff moment is central to the measurement of time reversal violation in an atom. The mechanism considered in Ref. [1] finds that the Schiff moment in odd-even nuclei *is proportional to the inverse energy weighted sum (IEWS) of the ISD strength distribution* in the even-even core and therefore the Schiff moment is quite large when the contribution of the ISD is included. The odd nucleon couples to the 0^+ ground state and to the 1^- dipole strength. States with the same angular momentum, J, but opposite parity, mix via an assumed time reversal and parity violating interaction. As a result one finds a non-zero Schiff moment. That Schiff moment induces in the atom parity and time reversal mixing which in turn produces a static electric dipole moment of the atom which is measured in experiment.

The commonly used operator for the ISD is defined as [1]:

$$D = \sum_i (r_i^2 - \frac{5}{3} < r^2 >) \mathrm{r}_i, \tag{1}$$

while *the isoscalar* part of the Schiff operator is defined as [1]:

$$S = \frac{1}{10} \sum_i (r_i^2 - \frac{5}{3} < r^2 >) \mathrm{r}_i, \tag{2}$$

Thus the two operators, apart from normalization, are the same. The Schiff moment is the ground state expectation value of the Schiff operator in an odd-even nucleus in the presence of a time reversal violating interaction [1]. The Schiff strength distribution we are discussing in this work is related to the even-even nucleus. The Schiff moment that is relevant to the measurement of the static atomic dipole moment is the one that is present in the odd-even nucleus

We have carried out fully self-consistent HF-RPA calculations, using 18 commonly employed Skyrme type interactions [2], for the strength functions and corresponding inverse energy moments of the isocalar dipole (ISD) for various nuclei using a probing operator which is the same as the Schiff operator up to a normalization.

In Fig. 1 we display the HF-based RPA results for the strength function divided by the energy, S(E)/E, of the ISD, in ^{90}Zr, ^{104}Zr, ^{144}Sm, and ^{208}Pb calculated [2] using the KDE0v1 Skyrme interaction.

Note the relatively large contribution to moment m_{-1} from the low energy region, in particular in the case of neutron rich nuclei.

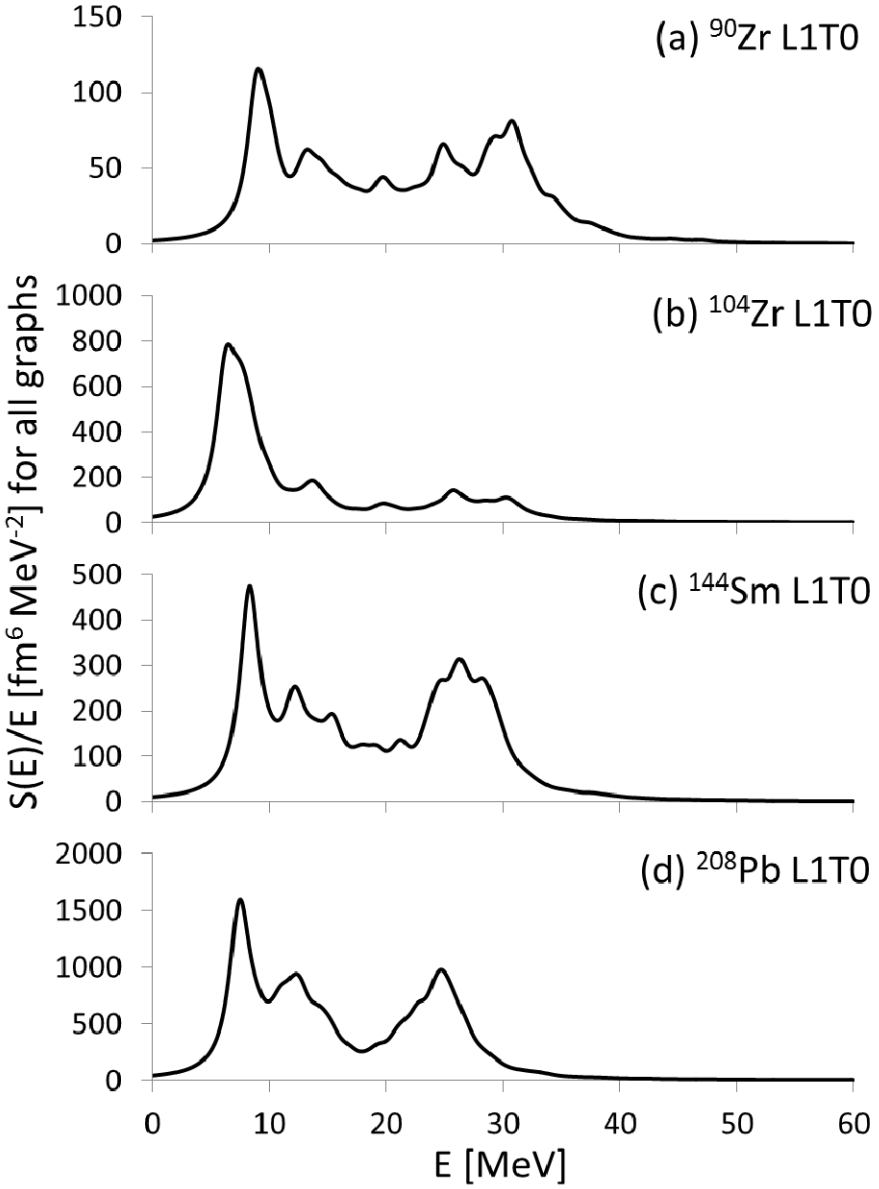

FIG. 1. Self-consistent HF-based RPA results for the distribution of the strength function divided by the energy, S(E)/E, of the isoscalar dipole, obtained for the ^{90}Zr, ^{104}Zr, ^{144}Sm, and ^{208}Pb nuclei, calculated [2] using the KDE0v1 Skyrme interaction. An excitation energy range of 0-60 MeV and Lorenzian smearing of a 2 MeV width were used in the calculation

[1] N. Auerbach and V. Zelevinsky, Phys. Rev. C **86**, 045501 (2012).

[2] N. Auerbach, Ch. Stoyanov, M.R. Anders and S. Shlomo, Phys. Rev. C **89**, 014335 (2014).

Isovector giant resonances in ^{208}Pb and the symmetry energy

M. R. Anders and S. Shlomo

It is well-known that accurate knowledge of the dependence of the symmetry energy, $E_{sym}(\rho)$, on the matter density ρ, commonly parameterized in terms of the quantities J, L and K_{sym}, is needed for better description of nuclei away from the valley of stability and for the EOS of asymmetric nuclear matter (NM), the needed ingredient in the study of astrophysical phenomena. There have been many attempts to determine $E_{sym}(\rho)$ by considering physical quantities sensitive to $E_{sym}(\rho)$, such as the energy of the isovector giant dipole resonance (IVGDR), since the restoring force for the IVGDR oscillation is due to the n-p interaction.

To study the sensitivity of the isovector giant resonances to the symmetry energy density we carried out fully self-consistent HF-based RPA calculations of the strength functions and centroid energies of the isovector giant monopole resonance (IVGMR), IVGDR, first overtone of the IVGDR (IVGDR2), isovector giant quadrupole resonance (IVGQR) and the isovector giant octupole resonance (IVGOR) in ^{208}Pb, using 34 commonly employed Skyrme type effective nucleon-nucleon interactions. Fig. 1 shows the results [1] of HF-based RPA calculations (full circles), for the centroid energies E_{CEN} of the IVGMR, IVGDR, IVGDR2, IVGQR and IVGOR in ^{208}Pb as functions of the symmetry energy coefficient J, in the range of J = 26.80 –36.7 MeV. The dashed lines show the regions of the experimental data. An agreement with experimental data is obtained for several interactions. However, a very weak correlation is obtained between the centroid energies and J. Similar results were also obtained when using instead of J, the quantities L and K_{sym} [1]. These results, which contradict statements in the literature, can be understood by noting that the strength distributions of giant resonances also depend on other nuclear matter (NM) quantities, such as K and m*/m, which have different values for different interactions used in the calculations.

[1] M.R. Anders and S. Shlomo, in preparation.

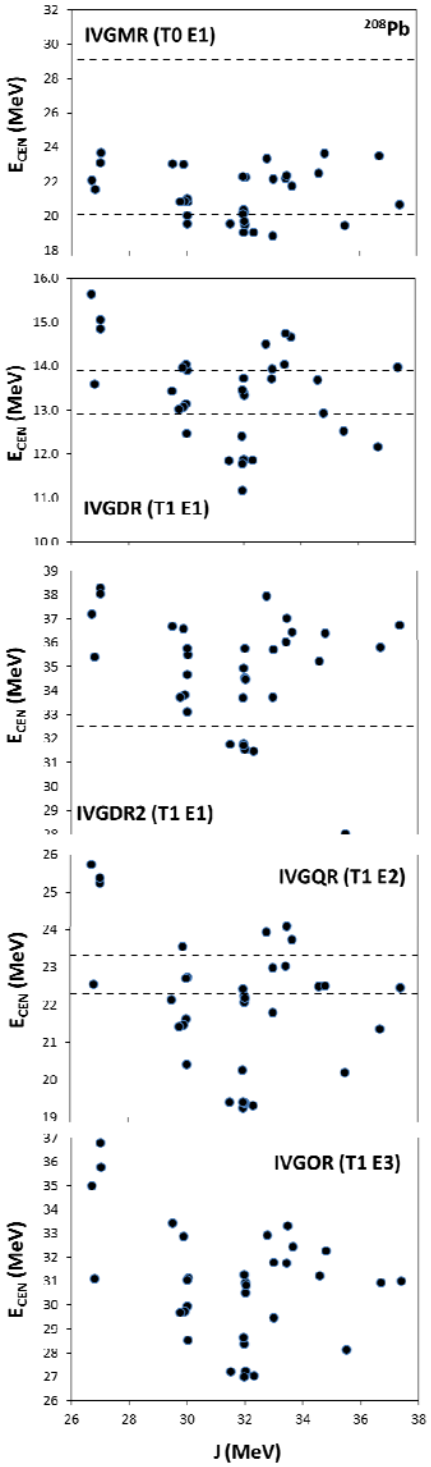

FIG. 1. The centroid energies, E_{CEN}, of the IVGMR, IVGDR, IVGDR2, IVGQR and IVGOR in ^{208}Pb, as functions of the symmetry energy coefficient J. The experimental data are shown as the region between the dashed lines. The results of fully self-consistent HF-based RPA calculation using 34 commonly employed Skyrme interactions [1] are shown as solid points.

The isovector giant dipole resonance and the neutron skin in ^{208}Pb

M. R. Anders and S. Shlomo

A recent high-resolution measurement [1] of the isovector giant dipole resonance (IVGDR) strength distribution in ^{208}Pb leads to an accurate value for the electric dipole polarizability α_D, which is directly related to the inverse energy moment m_{-1} of the strength function of the IVGDR. The value of α_D in ^{208}Pb was then used in this work to determine the magnitude of the neutron skin thickness, the difference $r_n - r_p$ between the root mean square (rms) radii of the neutron and proton density distributions in this nucleus, resulting in the value of $r_n - r_p = 0.156$ (.025) fm. However, the analysis in this work was based on only one form of energy density functional (EDF), associated with a specific parameterization of the Skyrme interaction. To examine the conclusion of the work of Ref. [1], HF calculations of the neutron skin thickness, $r_n - r_p$, and fully self-consistent HF-based RPA calculations of the electric dipole polarizability of ^{208}Pb were carried out [2] using 34 commonly employed Skyrme type interactions. Fig. 1 shows the predictions of the 34 Skyrme interactions for the polarizability α_D as a function of the neutron skin, $r_n - r_p$, in ^{208}Pb. The experimental data [1] on α_D is shown as the region between the dashed lines. Also shown is the Pearson correlation coefficient $C_{AB} = 0.54$, which indicates a weak correlation between α_D and $r_n - r_p$. One thus concludes that EDFs associated with theoretical predictions of values of $r_n - r_p$ in

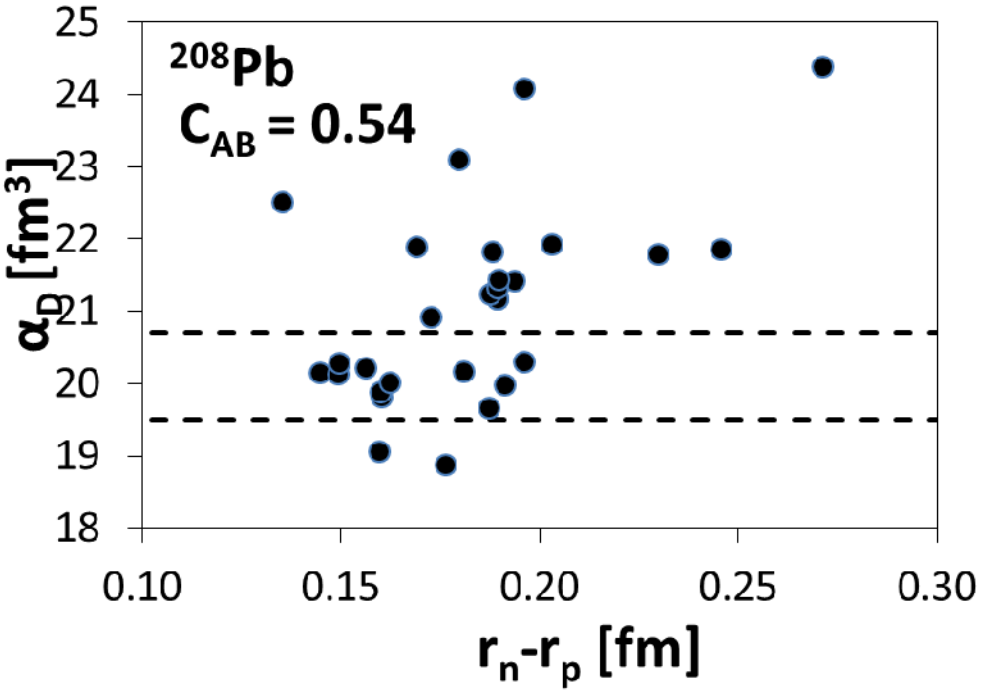

FIG. 1. The IVGDR polarizability α_D as a function of $r_n - r_p$ in ^{208}Pb. The experimental data on α_D [1] are shown as the region between the dashed lines. The results of fully self-consistent HF-based RPA calculation of 34 commonly used Skyrme interactions [2] are shown as solid points. Also shown is the Pearson correlation coefficient C_{AB}.

the range of 0.14 to 0.20 fm are all consistent with the experimental data on α_D.

[1] A. Tamii *et al.*, Phys. Rev. Lett. **107**, 062502 (2011).
[2] M.R. Anders *et al.*, in preparation.

SECTION IV

SUPERCONDUCTING CYCLOTRON, INSTRUMENTATION AND RIB UPGRADE

K500 operations and development

D. P. May, G. J. Kim, B. T. Roeder, H. L. Clark, and F. P. Abegglen

Introduction

During the 2013-2014 reporting period a total of 28 different beams, including 13 newly developed beams, were used for experiments, and there were a total of 34 beam tunings for these experiments. The SEE program and the charge-breeding effort are treated separately in this progress report.

Ion Sources

During the shutdown ECR1 was opened for examination, and it was found that there had been no further deterioration in the damaged spot that had developed over a plasma flute on the aluminum wall.

Cyclotron Beams

New beams of ^{10}B at 24 AMeV, ^{12}C at 22.9 AMeV, ^{32}S at 23 AMeV, ^{36}Ar at 35 AMeV, ^{48}Ca at 4.7 AMeV, ^{78}Kr at 3.2 AMeV, ^{86}Kr at 3.0, 3.1 and 3.2 AMeV, ^{124}Sn at 15 AMeV, ^{124}Xe at 15 AMeV and ^{136}Xe at 15 AMeV were developed for experiments. In addition, a beam of ^{107}Ag at 24.8 AMeV was developed to be used with the SEE program.

Operations

For the period April 1, 2013 through March 31, 2014, the operational time is summarized in Table I, while Table II lists how the scheduled time was divided. The bulk of unscheduled maintenance time involved the repair of a dee-stem water leak in May. Scheduled maintenance occurred mainly in the January-February shut-down.

Table I. 2013-2014 operational time.

Time	Hrs.	%Time
Beam on target	5953	68.0
Beam development	640	7.3
Scheduled maint.	1366	15.6
Unscheduled maint.	801	9.1
Total	**8760**	**100.0**

Table II. 2012-2013 Scheduled Beam Time.

Time	Hrs.	%Time
Nuclear physics	717	10.9
Nuclear chemistry	2238	33.9
Outside collaboration	385	5.8
Outside users	2613	39.6
Beam development	640	9.7
Total	**6593**	**100.0**

Axially-mounted, high-temperature oven for ECR2

F. P. Abegglen, H. Peeler, and D. P. May

In order to satisfy the demand for K150 beams that are most easily produced using a high-temperature oven with the ECR2 ion source, an axially-mounted oven was designed, constructed and tested off-line. It was decided to mount the oven axially because of the limited space available for radial insertion. Axial insertion limits the source to only one microwave injection port, and so the old single-frequency injection flange was modified to accommodate the new oven (Fig. 1). Unfortunately, this means that two-frequency injection cannot be used with the oven mounted and that the axial steel plug must be removed when the oven is mounted or dismounted.

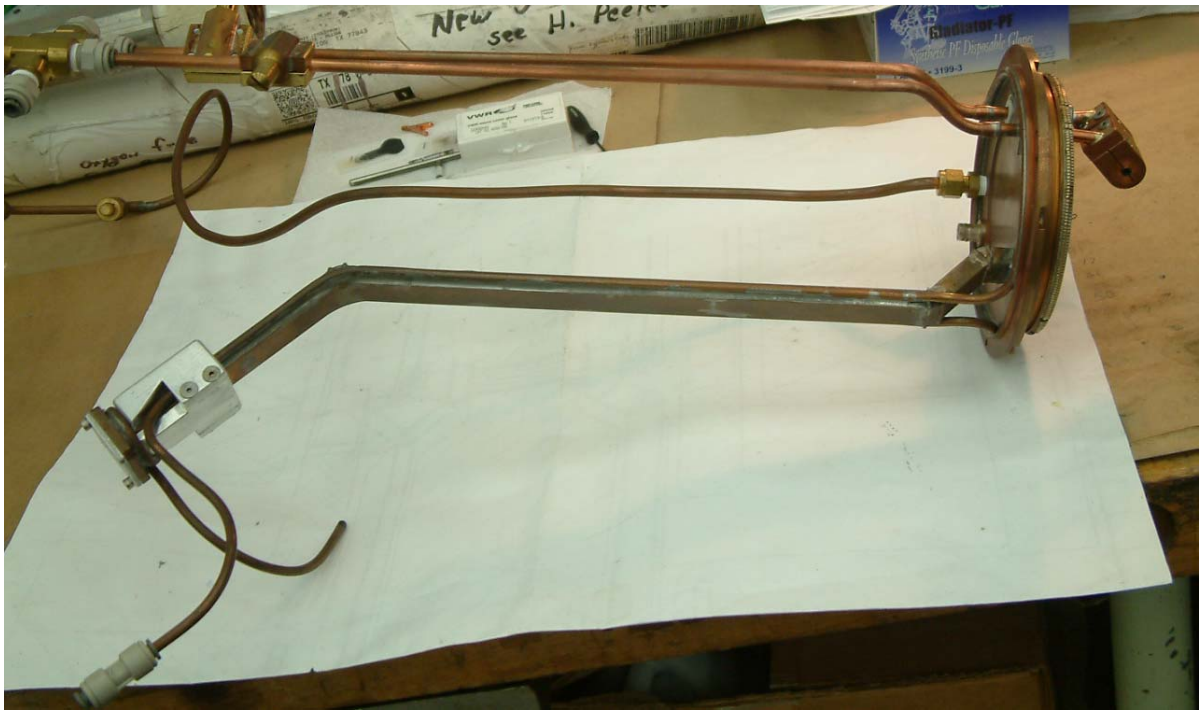

FIG. 1. The modified injection plate for ECR2. The high-temperature oven is at the top. The clamps containing the crucible are at the right.

The micro-oven that is currently used on ECR1 cannot reach sufficient temperatures in order to produce vapors of elements such as titanium, so it was decided that the more capable, high-temperature oven at the LBNL 88" Cyclotron Laboratory would be a good guide [1]. This oven was designed to reach temperatures in excess of 2000º C for the VENUS 28GHz ECR ion source. As shown in figure1 the oven is powered by two, water-cooled, copper leads. Stainless steel squirt-tubes inside the leads direct the water flow onto two copper clamps that hold the oven crucible (Fig. 2). Current flowing through the crucible provides the heat.

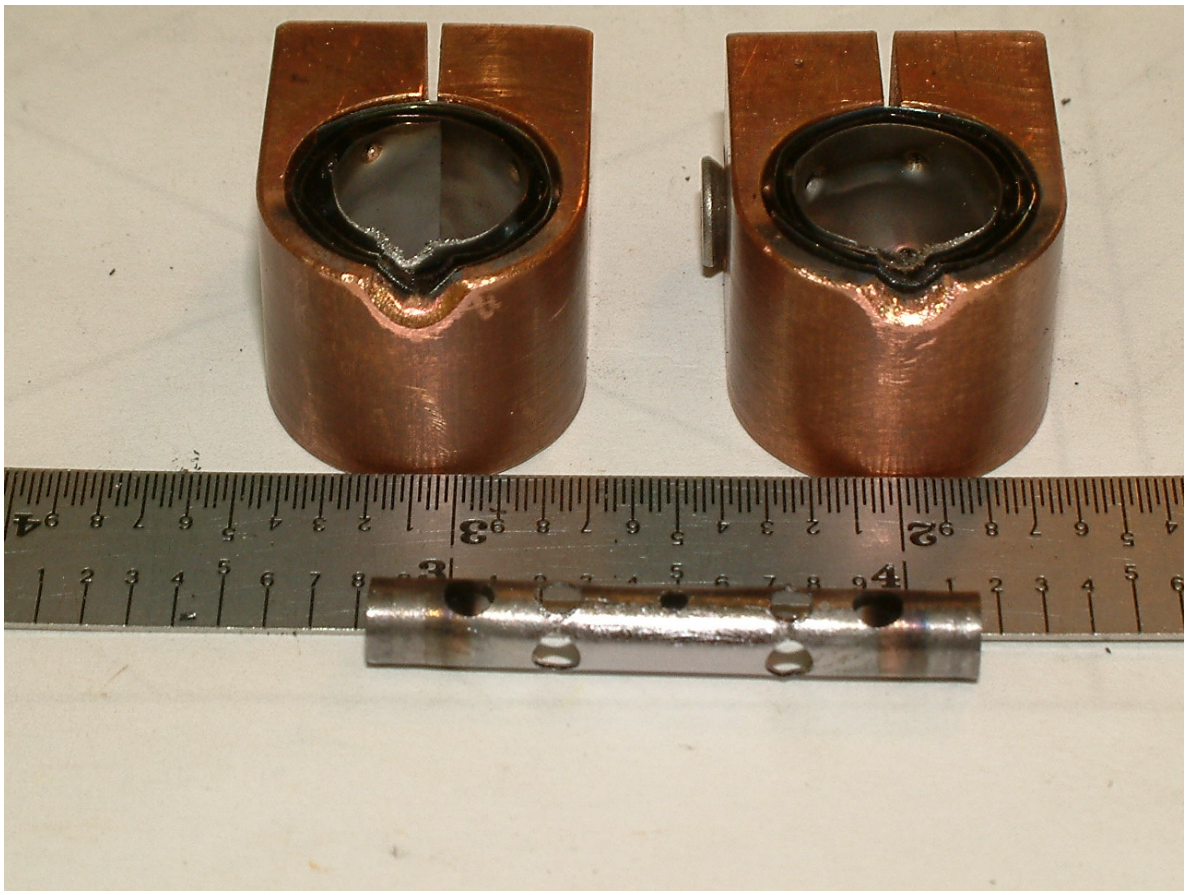

FIG. 2. The copper clamps and the detached, tantalum crucible.

A vacuum-chamber test stand was constructed to try out different crucible configurations. The crucible was fabricated from a 3/16” diameter, 0.0015” wall tantalum tube with tantalum plugs. After testing several configurations of the crucible, four 1/8” diameter holes were drilled into each end of the crucible outside of the plugs in an effort to concentrate the heat flow in the center. Vapor escapes from a 1/16” diameter hole drilled in the middle. Titanium was loaded into the crucible for a testing. Fig. 3 shows results from a successful test. A thin film of titanium was deposited onto a glass slide placed at the vapor outlet of the oven. Titanium was observed to be depositing when the current reached 110 amperes at 1.2 volts. The power supply was voltage controlled. As the oven heated up and evaporated more titanium, the power supply voltage was gradually raised to 1.4 volts in order to maintain a current of 100 amperes. The oven continued to produce vapor for a week. After these tests no evidence of heating the walls of the vacuum chamber was observed, a critical aspect in considering possible heat-damage to the permanent magnets in the ECR2 ion source.

The next step is to mount the oven onto ECR2 and observe its behavior in the production of beams of titanium and eventually in the production of beams requiring even higher vaporization temperatures.

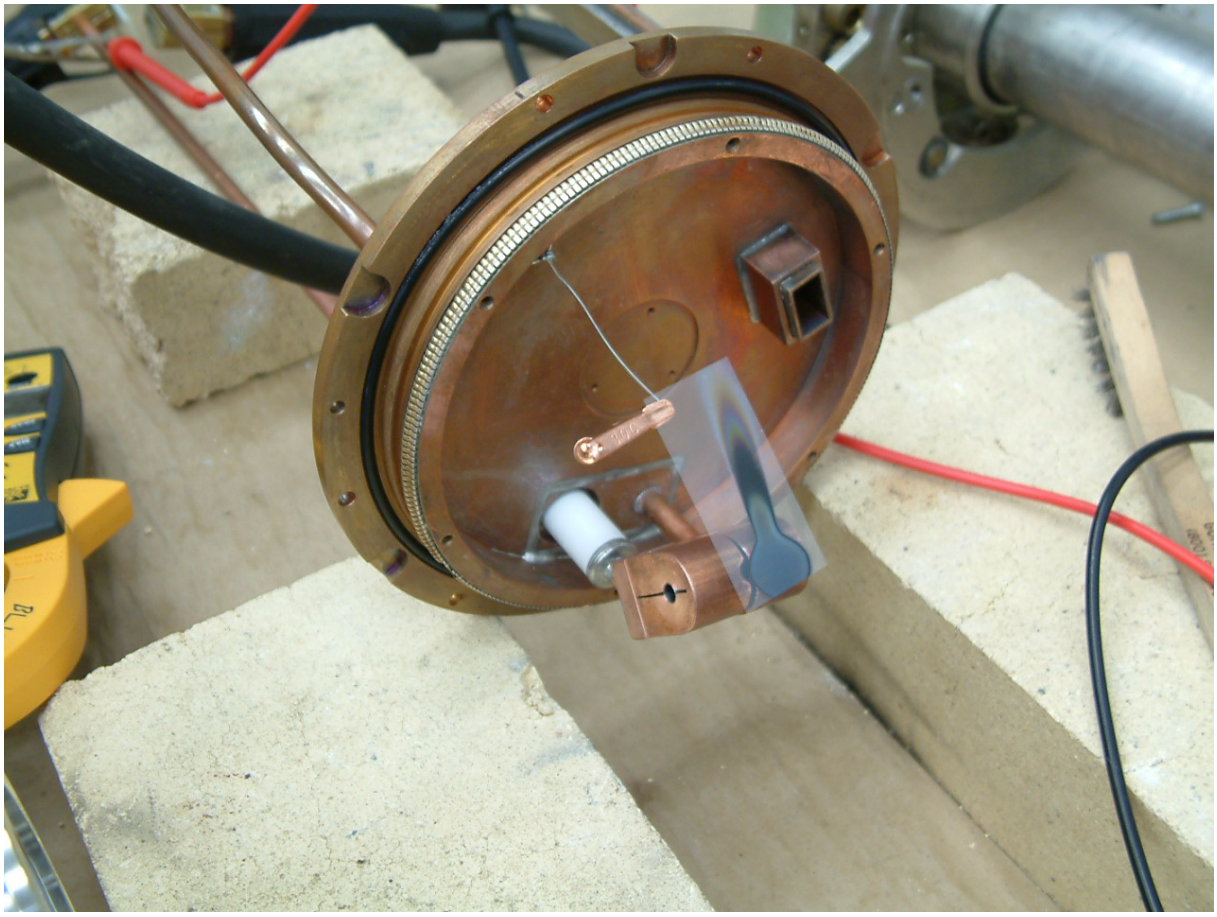

FIG. 3. Results of titanium test – titanium film on glass slide after one week.

[1] T. Loew, S. Abbott, M. Galloway, D. Leitner, C.M. Lyneis, Proceedings of the Particle Accelerator Conference (PAC07), Albuquerque, New Mexico, USA (2007) p. 1742.

Texas A&M cyclotron radiation effects facility
April 1, 2013 – March 31, 2014

H. L. Clark, J. Brinkley, L. Chen, G. Chubarian, V. Horvat, B. Hyman,
B. Roeder, and G. Tabacaru

The activity of the Radiation Effects Facility (REF) decreased over the previous reporting year. In this reporting period, the facility was used for 2,399 hours, which is a ~9% decrease over the 2,626 hours used in the 2012-2013 reporting period. However last year was the second highest usage year ever and nearly 800 hours were lost to unscheduled maintenance. Users of the facility (and hours used) over the past year were: NASA GSFC (261), Aeroflex (244.25), Sandia National Laboratory (155), SEAKR (147), International Rectifier (133.25), Honeywell (125.5), Intersil (115), NASA JPL (109.5), Microsemi (104), NAVSEA (90), BAE Systems (87), Hirex - France (74.5), Boeing Satellite Systems (70.5), Johns Hopkins APL (62.5), Intel Corp (57), Texas Instruments (47), TRAD - France (44), Northrop Grumman (39), Utah State University (32.5), InnoFlight (30), Air Force (29.5), Vanderbilt University (29.2), ICs LLC (24), University of Maryland (24), Southwest Research Institute (23), 3D Plus (16), Amtec (16), Fuji Electric Japan (16), INTA - Spain (16), Lockheed Martin (16), Maxwell (16), Peregrine (16), Silicon Space Technology (16), General Dynamics (15.5), SEMICOA (14), SunTronics (13), VPT Inc (12), ARQ - Spain (10.5), Ball Aerospace (8), JAXA - Japan (8), L-3 Communications (8), Montana State University (8), T2 Research (8) and Thales Alenia (8). New users included Utah State University, InnoFlight, INTA, ARQ and T2 Research.

Table I compares the facility usage by commercial and government customers. The ratio from

Table I. Radiation Effects Facility usage by commercial and government customers for this and previous reporting years.

Reporting Year	Total Hours	Commercial Hours (%)	Government Hours (%)
2013-2014	2,399	1,517 (63%)	882 (37%)
2012-2013	2,626	1,856 (71%)	770 (29%)
2011-2012	2,673	1,630 (61%)	1,043 (39%)
2010-2011	3,042	1,922 (63%)	1,121 (37%)
2009-2010	2,551	1,692 (66%)	859 (34%)
2008-2009	2,600	1,828 (70%)	772 (30%)
2007-2008	2,373	1,482 (62%)	891 (38%)
2006-2007	2,498	1,608 (64%)	890 (36%)
2005-2006	2,314	1,314 (57%)	1,000 (43%)
2004-2005	2,012	1,421 (71%)	591 (29%)
2003-2004	1,474	785 (53%)	689 (47%)
2002-2003	1,851	1,242 (67%)	609 (33%)
2001-2002	1,327	757 (57%)	570 (43%)
2000-2001	1,500	941 (63%)	559 (37%)
1999-2000	548	418 (76%)	131 (24%)
1998-1999	389	171 (44%)	218 (56%)
1997-1998	434	210 (48%)	224 (52%)
1996-1997	560	276 (49%)	284 (51%)
1995-1996	141	58 (41%)	83 (59%)

this reporting year (63% to 37%) is similar to the trend seen in previous reporting periods and commercial hours still dominate (see Fig. 1). Commercial hours decreased by 18% and government hours increased by 15% over hours from 2012-2013. 15 MeV/u ions were the most utilized and especially 15 MeV/u Au. A new beam of 24.8AMeV ^{107}Ag was added to SEELine users list. Much of the testing conducted at the facility continues to be for defense systems by both government and commercial agencies. It is expected that the facility will continue to be as active in future years. Almost 13% (193 hours) of the commercial hours were from foreign agencies from France, Japan and Spain.

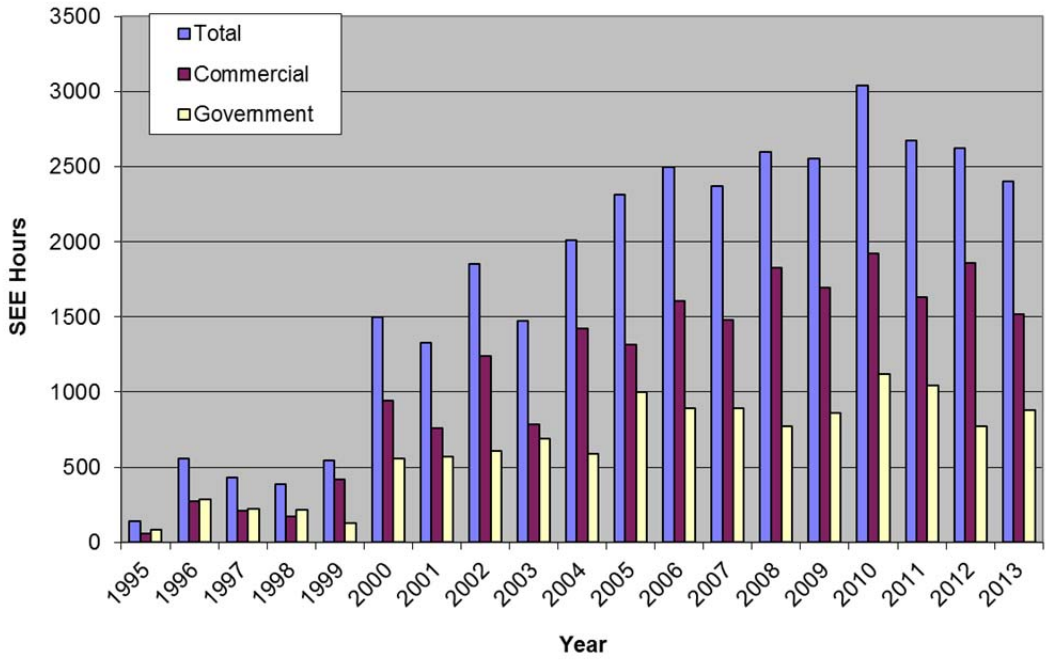

FIG. 1. Radiation Effects Facility usage by commercial and government customers for this and previous reporting years. The ratio from this reporting year (63% to 37%) is similar to the trends seen in previous reporting periods where commercial hours still dominate. About 13% (193 hours) of the commercial hours were from foreign agencies from France, Japan and Spain.

Cyclotron computing

R. Burch and K. Hagel

This past year we acquired a new block of networking address to allow for the continued growth of our networked devices. This block is non-routable, meaning these addresses cannot see or be seen outside the Institute network. These addresses allow us to free up routable address by using these non-routable addresses for printers, switches, UPS's, VME crates, scopes, etc. which do not require constant security updates, and in general, do not need to access sites outside the Institute.

To satisfy the constant increase of required disk space, we have added a 16 slot disk expansion unit and file server to serve the Institute computational servers. This increases our capacity and allows for further expansion. We have the capacity for 14 Terabytes of general lab expansion and 48 Terabytes of committed group capacity. The institute’s 47 computational servers (capable of running 644 jobs) are now served by 5 file servers. All files servers are networked via Gigabit network adapters to Gigabit switches which, in turn, feed the computational servers with 100 Megabit adapters.

New commodity base computers, such as the Raspberry-Pi, allow us to migrate a number of our administrative services to these low cost (~$70), low power (~6 Watt) units. We have taken advantage of this and migrated our two high powered (~400 Watt) Authentication, Authorization, and Accounting servers to three low powered Raspberry-Pi's with no issues of speed or capacity. We plan to pursue the migration of select administrative services, where advantageous, to such small form-factor fan-less PC's and Raspberry-Pi's so as to further reduce the cost, cooling, and power footprint of our administrative services.

Progress on the light ion guide project

G. Tabacaru, J. Arje, H. L. Clark, and D. P. May

The Light Ion Guide will produce radioactive ion beams [1] using the well-established technique of the helium-jet method. The primary beam impinging on a production target produces ionized, radioactive products that are stopped and trapped in helium gas. These ions are transported by the helium flow through an aperture where after a small acceleration they immediately encounter an RF-only sextupole ion guide that confines them further along its length allowing the helium to be pumped away before accelerating toward the Charge Breeding ECR Ion Source (CB-ECRIS). The CB-ECRIS will change the initial charge-state of the radioactive ions to higher charge states appropriate for reacceleration by the K500 cyclotron.

After proving the charge-breeding capabilities of CB-ECRIS [2] and determining parameters for the injection of the initial beam into CB-ECRIS, our efforts were directed to the coupling of the Light Ion Guide assembly with CB-ECRIS. The 1 meter long RF-only sextupole was installed, and a gas cell was built for the first on-line experiments. An extraction assembly after the RF-only sextupole was also mounted consisting of a plate with a 4 mm hole followed by a tube and an Einzel lens assembly. The tube was deemed necessary to further shape the electric field.

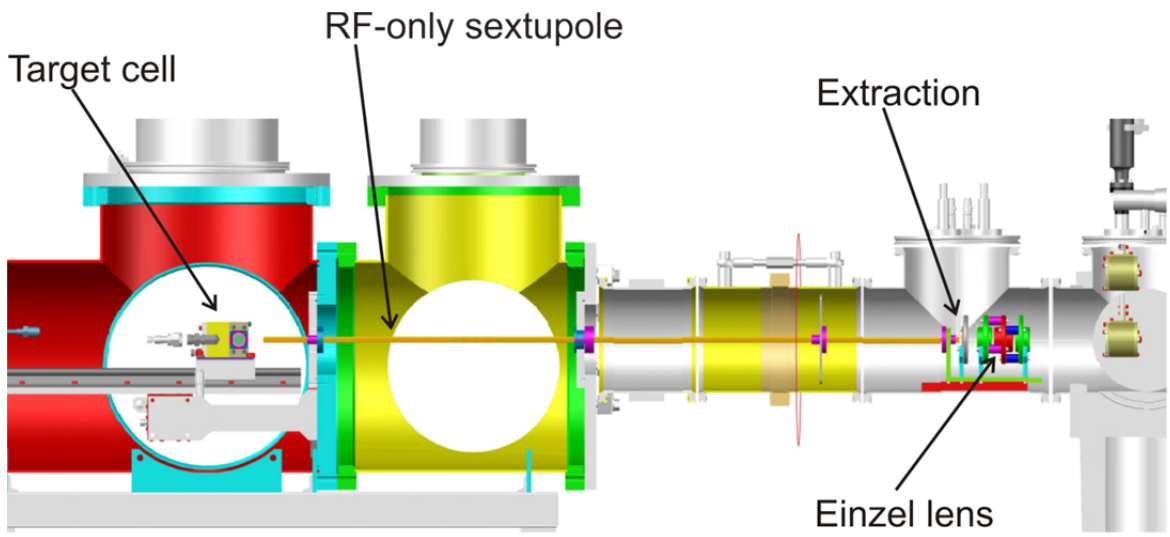

FIG. 1. View of the Light Ion Guide including the target chamber, the 1 meter long RF-only sextupole and the extraction part.

A series of experiments were performed with this configuration using a ^{228}Th radioactive source. We collected radioactivity as well as measured the current of ions coming from the target cell while also determining parameters for the operation of the Light Ion Guide. We found that once the CB-ECRIS was switched on, back-streaming beam from CB-ECRIS charged up the extraction part of the Light Ion Guide making difficult to transport any beam towards CB-ECRIS. Corrective measures were taken by replacing

unnecessary plastic parts with metallic parts, reducing the size of some plastic parts and reducing the exposure of the extraction parts to the back-streaming beam by placing shielding plates inside the beam pipe. Placing permanent magnets around the beam pipe also helped because the electrons coming from the back-streaming ion beam hitting Einzel lens components are deflected by the magnetic field and are thus prevented from depositing charge onto the plastic support parts.

The first on-line experiments were performed with a ^{16}O beam, a ^{12}C beam and an alpha beam at the energy of 6.3 MeV/A and with a proton beam at 15 MeV energy. In the first two experiments we were focused on optimizing the secondary beam transport conditions and reducing the charging effect at the operation of the CB-ECRIS. The first attempts to charge-breed stable beams were unsuccessful raising again questions about the initial beam injection into CB-ECRIS. The proton beam was used to produce ^{64}Ga via the $^{nat}Zn(p,n)^{64}Ga$ reaction. The ^{64}Ga production cross-section is about 170 mbarn at 14.1 MeV proton beam energy providing sufficient yield to verify the functioning of the target cell. Two exit holes were used for the target cell: 1 mm and 2 mm diameter. A small collection plate was installed directly in front of the target cell and positive or negative voltage was applied to it; positive voltage repels ions and negative voltage attracts ions to the plate. After 15 minutes of collection time, the plate was placed in front of a Germanium detector for a 30 minutes and the gamma line of 991 KeV was recorded to establish the percentage of the ions out of the total radioactivity collected. Table I summarizes the findings of these measurements and shows very high efficiency in the production of radioactive ^{64}Ga ions using the 2 mm hole.

Table I. Peak integral of ^{64}Ga 991 keV line and ion percentage production for 1 mm and 2 mm hole.

		991 KeV line – peak integral		
	I_p[nA]	Collection plate voltage -100 V	Collection plate voltage +100 V	Ion percentage
1 mm hole	7	106	58	45 %
	90	1100	781	29 %
	650	9213	8133	12 %
2 mm hole	65	2013	148	93 %
	500	14715	1434	90 %

The transport of the radioactive ions through the RF-only sextupole was not successful; however stable ion beams were transported. Our initial explanation is that the radioactive ions are quickly neutralized by the electrons coming from the primary beam interacting with the target cell windows. In the initial 80 mm distance, the radioactive ions are confined inside the RF-only sextupole but the rods are completely exposed and electrons will be attracted to the positively charged rods increasing the probability of the ions being neutralized. Most probably the stable ions suffer the same interaction, but their number being larger, we still can measure them. In the future, the solution to this problem will be the construction of a new RF-only sextupole with a better shielding and much higher acceptance.

[1] G. Tabacaru, D.P. May, and J. Arje, Proceedings of ECRIS2010, Grenoble, France http://accelconf.web.cern.ch/AccelConf/ECRIS2010/papers/proceed.pdf, MOPOT10

[2] G. Tabacaru, J. Arje, and D.P. May, *Progress in Research*, Cyclotron Instiute, Texas A&M University (2012-2013), p. IV-23; http://cyclotron.tamu.edu/2013%20Progress%20Report/4%20Superconducting%20Cyclotron,%20Instrumentation%20and%20RIB%20Upgrade/IV_2325_oper_progress%20on%20charge%20breeder.pdf

Computer controlled gas system for the H^- and ECR ion sources

L. Chen and H. L. Clark

We have developed a computer-controlled gas system for the ion sources at the Cyclotron Institute which will minimize the effort and error when changing gases. A prototype has been built and is currently ready for on-line testing with the H^- ion source. The prototype was designed specifically for the H^- ion source to control hydrogen and deuterium gases only but can be easily expanded to control multiple gases for the ECR ion sources. For convenience and portability, the gas bottles, computer, control equipment and gas valves are all assembled together on a single rack with wheels (Fig. 1). A rack-mounted Supermicro computer running Windows 7 acts as the main control server for the gas system. The software control program was built using LabVIEW 2012 and monitors hardware status and responds to user commands. For added convenience, a client software module was developed for any other computer on the network and will remotely control the gas system over Transmission Control Protocol (TCP) communication. Fig. 1 (right) shows the front panel of the client module which looks and operates exactly as the master control program. There is no limit to the number of clients that can be connected to the main server at the same time, and the main control server will broadcast any system changes to all clients that are connected. Additionally, the control system can be set to local control mode for quick on-site operation by a manual switch at the control rack. Then once switched back to remote control mode, the software control program will automatically update the system status and gain sole control of the system. An expanded gas control system for ECR2 will be developed after the on-line test of the prototype system for the H^- ion source has been completed.

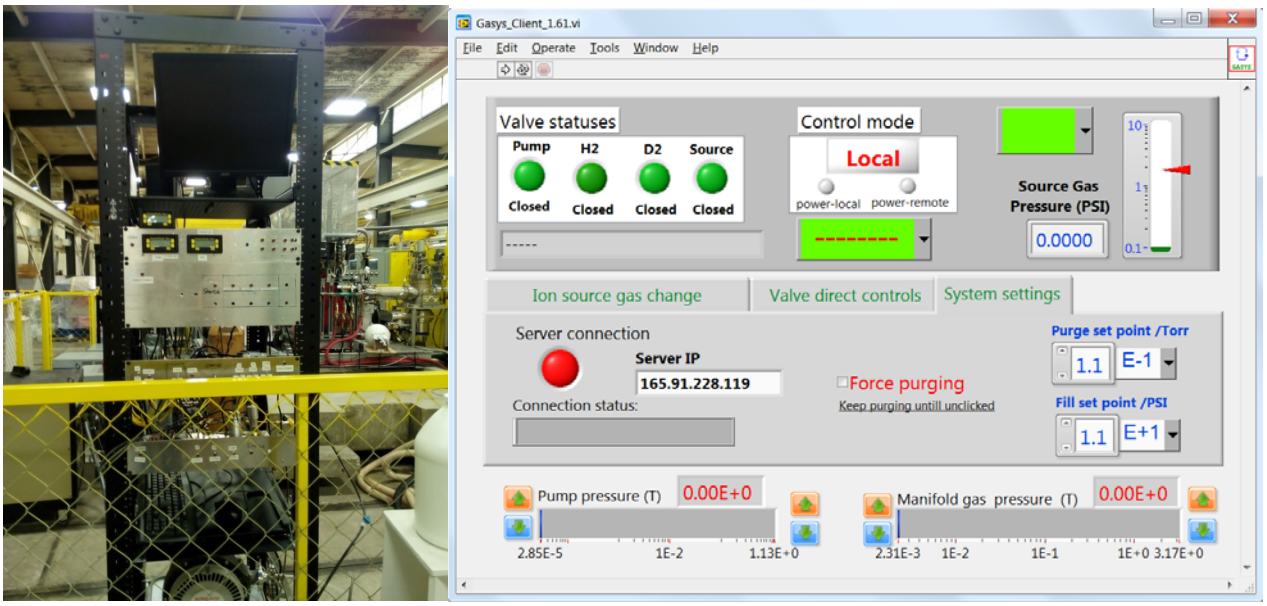

FIG. 1. Left – Front view of the prototype computer controlled gas system. Right – The control client front panel (user interface) of the gas control system.

Cyclotron Institute upgrade project

H. L. Clark, F. Abegglen, J. Arje, G. Chubaryan, G. Kim, D. P. May, B. Roeder, and G. Tabacaru

On January 3, 2005 the Cyclotron Institute Upgrade Project (CIUP) began with the approval of the CIUP management plan by the Department of Energy Nuclear Physics Office. The project will extend at least to the second quarter of calendar year 2015. When completed, the upgraded facility will provide high-quality re-accelerated secondary beams in a unique energy range in the world. Funding for the upgrade comes from several sources: the Department of Energy, matching support from TAMU, the Robert A. Welch Foundation and beam time sales for testing electronics components at the Cyclotron Institute.

The CIUP is divided into three major tasks: (1) Re-commission of the existing K150 (88") cyclotron and refurbish beam lines; (2) Construct light-ion and heavy-ion guides and produce 1+ radioactive ions; (3) Transport and charge boost radioactive ions and accelerate in the K500 cyclotron.

As detailed in the Management Plan, effort made during this year on Task 1 included,

- Development of the 13.7 MeV/u ^{40}Ar heavy-ion beam and
- Testing of the internal cryopanel for the K150 high vacuum system.

Progress was also made on Tasks 2 and 3. This included,

- Testing of the Light Ion Guide (LIG) gas cell,
- Completion of the Heavy Ion Guide transport system equipment. Below we report on a few of the accomplishments listed above.

I. K150 Cyclotron Development

In the past year, we provided 2,038 hours of beams for various experiments, notably four 25-35 MeV proton beams for the STAR/LIBERACE experiments and many 2-3 day duration, ^{12}C, ^{16}O, and proton beams for LIG development, and we also worked on developing an intense 12 MeV/u ^{40}Ar beam. But, problems with the deflector and the ion source have hindered our efforts. Also, we installed a large cryopanel, this will improve the cyclotron vacuum. And we briefly experimented with unbalancing the upper and lower TC01 trim coils to compensate for any magnetic differences due to different components in the upper and lower yoke holes. However as of yet we do not see any effect on our test beams. Several third harmonic beams were tuned, but the answer to why the third harmonics beams are so much less efficient has still eluded us. More evidence of the reality of the discrepancies between the CYDE magnetic maps and our actual cyclotron field was demonstrated when we tried Berkeley's solutions for two beams, 14 MeV/u $^{18}O^{6+}$ and 5 MeV/u $^{40}Ar^{9+}$. The Berkeley solutions, which are similar to the CYDE solutions, did not work for our cyclotron, and an additional +250A on TC12 for one beam and +230A on TC14 for the other beam were needed to bring the two beams out to the extraction radius. The 200-300A corrections are consistent with the discussion about the TOSCA modeling of the K150 cyclotron, described in the last year's Progress Report. The energy of the beams, especially the stripped extracted protons, is better understood thanks to STAR/LIBERACE group's determination of the proton beam energies. We now know that actual strip extracted beam energy is 94% of the nominal setup energy of

the cyclotron. Even with the deflector pushed out to its outer limits, it seems that we need to strip extract about 1" earlier than the usual deflector extracted beams in order to minimize beam losses on the parked deflector. With the knowledge about the proton beam energies, we have started to calibrate the 160 degree Analyzing Magnet. And so with that calibration, there is a general agreement between the nominal beam energy from the cyclotron and the resulting Analyzing Magnet setting in transporting that beam to the experimental areas. Fig. 1 shows all the beams from K150 up to April 2014.

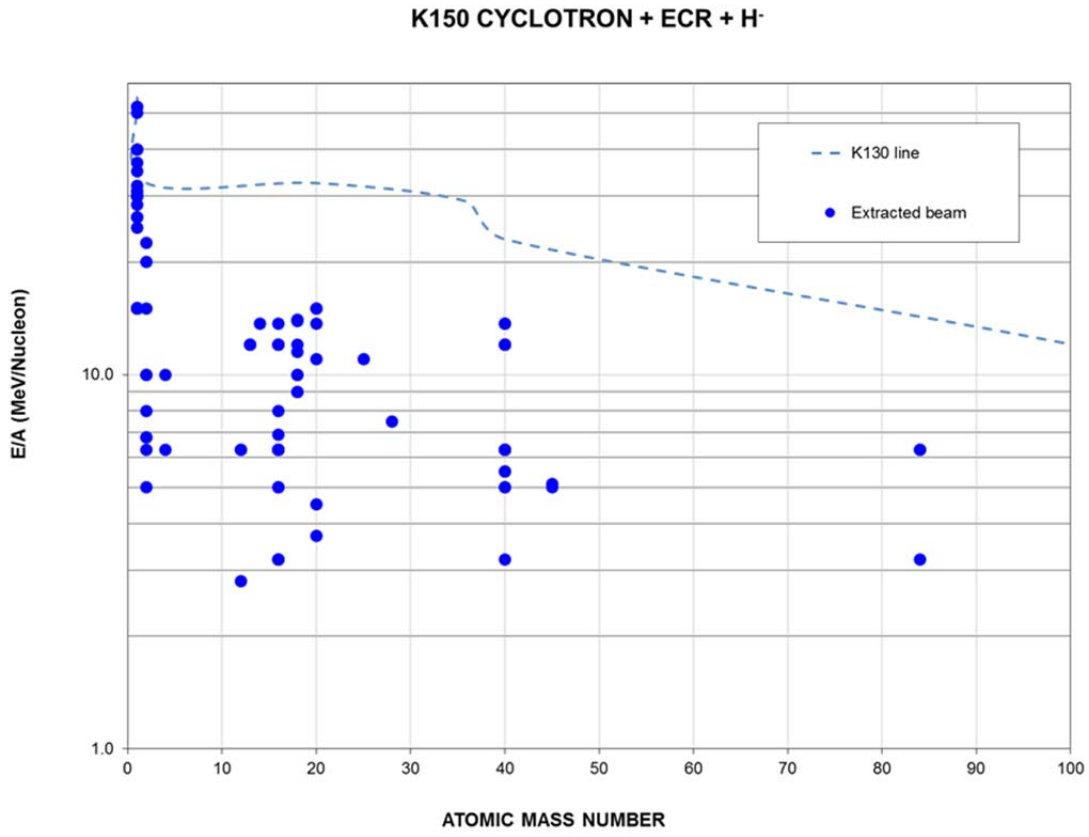

FIG. 1. Extracted beams from the K150 cyclotron with H- and ECR2 sources since May 2010.

II. Third Harmonics Beams

No third harmonic beam was used by any experiment in this time period. Not only do the third harmonic beams suffer from poor throughputs, about 1%, which is only one tenth of the first harmonic beams, they are also afflicted with instability problems (unstable beam intensity plus wandering beam energy). The instability not only makes it difficult to tune the beams, it also makes transporting the beams precisely to the experimental areas very difficult. This resulted in poor quality beams for the experiments. We have tuned out several third harmonic beams and tried to learn about the causes of the instability, but so far other than rather sensitive tunes of the various trim coils, which collectively may

cause the instability, we have not found the answer. We hope to scrutinize the beam current near the inflector exit and examine the beam losses at small cyclotron radii to learn more about the problems with the third harmonic beams. Because our usual beam probe travels only to 5" in radius from the cyclotron center, we are in the process of installing another probe to get close to the inflector.

III. ECR2 Ion Source

Several improvements were made to the ECR2 ion source in an attempt to improve the production of the ion beams of ^{40}Ar in high charge states (charge states 11^+ and higher). Prior to the improvements, a measurement of the ^{40}Ar beam production was conducted in July. At this time the source produced 77 μA of $^{40}Ar^{11+}$, 31.0 μA of $^{40}Ar^{12+}$, 8.5 μA of $^{40}Ar^{13+}$, and about 2.0 μA of $^{40}Ar^{14+}$. Following the July test, a few possibilities for improvement of the source were recorded. These improvements are described in the following paragraphs.

The first improvement was to attempt to make the temperature of the plasma chamber cooling water lower. It was noted that when the ion source was on with the maximum microwave power possible at the time that the temperature of the cooling water on the ion source plasma chamber increased to above 95°F. This increase in the plasma chamber cooling water temperature corresponded to an increase in the ion source vacuum to above $6x10^{-7}$ torr, and typical source vacuum was $7 – 8x10^{-7}$ torr. This relatively high vacuum inside the plasma chamber has been improved to $4x10^{-7}$ torr by using an external source of chilled water to chill the plasma chamber cooling water through a heat exchanger. After the installation of this additional cooling, the typical operating temperature of the ion source has been more stable at about 85°F.

The second improvement was to increase the maximum voltage for the ion source biased plate. Previously, the maximum possible voltage, as limited by the power supply, was -340 V. It was remarked that the biased plate was often at the highest possible voltage, so it was reasonable to think about trying higher voltages. To increase the voltage, a new power supply that could provide up to -600 V was purchased. It was found later that the optimum voltage on the bias plate for ^{40}Ar ion production was between -350 and -400 V.

The third improvement came from work of the staff on the 14.5 GHz klystron. In 2006, it had been recorded that high microwave power was needed to produce large amounts of ^{40}Ar beam. Several electronic problems were found with the klystron itself which were preventing the power from being increased further. The final improvements came when some small vacuum leaks in the ion source gas system were fixed and the inside of the plasma chamber itself was thoroughly cleaned.

After all of these improvements, a further test of the ECR2 ion source was conducted in September. With the optimized settings of the ion source, ECR2 produced 133 μA of $^{40}Ar^{11+}$, 86.0 μA of $^{40}Ar^{12+}$, 46.0 μA of $^{40}Ar^{13+}$, 19.5 μA of $^{40}Ar^{14+}$ and 1.3 μA of $^{40}Ar^{16+}$. These results have been roughly reproduced on two subsequent tests that occurred after this initial test, in particular, for the $^{40}Ar^{13+}$. However, further improvement is needed if the goal of about 100 μA of $^{40}Ar^{13+}$ out of the ion source is to be reached.

Further improvement of the ion source output may be possible if the source vacuum can be improved by cooling the plasma chamber even more than it is currently being cooled and attempting to

further optimize the settings for the ion source (magnetic field, microwave power, gas flow, etc.). One possible setting that we are currently investigating is the frequency of the second microwave (TWTA). Previously, this frequency had been 11.33 GHz, but the possibility that a higher frequency might improve the production of the ion beams of the higher ^{40}Ar charge states is currently being investigated.

IV. 12 MeV/u $^{40}Ar^{13+}$ Beam Development

Last year, we were able to accelerate and extract 13.7 MeV/u $^{40}Ar^{14+}$, getting 11 pnA on FC02. We needed 88 kV on the deflector. To increase the beam intensity we dropped the charge state by one, but in order to manage the deflector voltage we lowered the beam energy to 12 MeV/u. The expected deflector voltage is about 85 kV, whereas for the 13.7 MeV/u $^{40}Ar^{13+}$ it would have been 95-97 kV. We did extract 12 MeV/u $^{40}Ar^{16+}$ with 70 kV on the deflector, and then 12 MeV/u $^{16}O^{6+}$ with 75 kV. We conditioned the deflector up to 81 and 80 kV on two separate occasions to extract 14 MeV/u $^{18}O^{7+}$ and 15 MeV/u $^{20}Ne^{9+}$ beams, but we could not push it any higher, and the 12 MeV/u $^{40}Ar^{13+}$ beam was not extracted. However, we did work on beam tuning for the maximum beam transmission out to the extraction radius, getting up to about 14% of the injected beam current. As our goal is at least 10% throughput (from ILC02 to FC02 transmission efficiency), then with a 70% extraction efficiency, not an unreasonable number, this can be achieved. Given that the Berkeley's AECR-U, similar to our ECR2, achieved 9 puA of Ar^{13+}, it seems possible to extract 0.9 puA of 12 MeV/u $^{40}Ar^{13+}$ from the cyclotron.

V. Cryopanel Installation

A large cryopanel was designed, built, and installed in June of 2013, for the K150 cyclotron, see Fig. 2. It has two separate channels for LN2 and LHe cooling. The cryopanel was cooled with LN2 and beam tested with 6.3 MeV/u $^{40}Ar^{11+}$. The graph in Fig. 3 compares the intensity of the beam measured at various radii through the cyclotron without and with the cryopanel cooled. The intensity of the beam measured at ILC02 (after ECR2) was ~42 μA. The measured vacuum of the cyclotron only improved from 1.3×10^{-6} torr to 1.2×10^{-6} torr; however the ion gauge reads the vacuum at the outer edge of the cyclotron and the cryopanel is positioned well inside the cyclotron. With the cryopanel cooled to 74°K, the improvement in intensity was found to be ~21% on average throughout the cyclotron and ~25% at extraction. It was hoped that the effect of improving the beam intensity at the center region would have been greater, as this is the region where losses due to charge exchange from poor vacuum are the greatest. It was also hoped that the improvement in the vacuum would have increased the overall intensity by factors of 2 or greater.

FIG. 2. Top – Cryopanel for the K150 cyclotron. Bottom – Installed cryopanel in the K150 cyclotron. The cryopanel is stood off from the trim coil cover with three feet, one is very short near the center of the cyclotron, and two others are at outer radii.

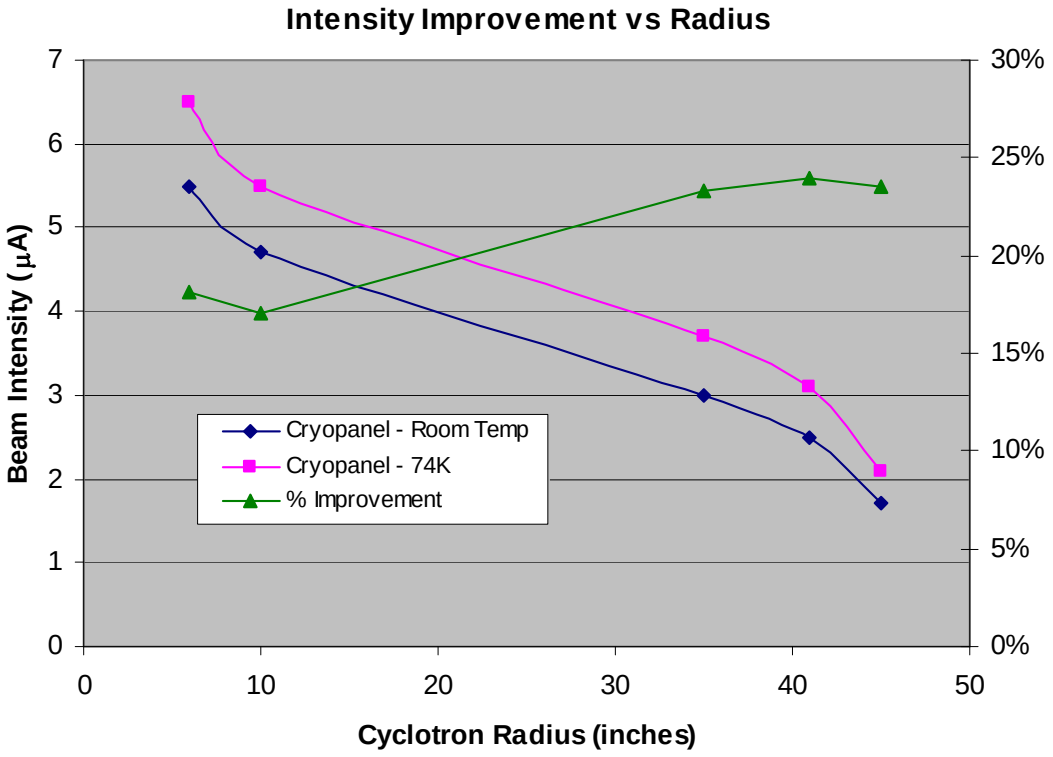

FIG. 3. The intensity of the beam measured at various radii through the cyclotron without and with the cryopanel cooled. With the cryopanel cooled to 74°K, the improvement in intensity was found to be ~25% at extraction.

VI. Light Ion Guide

A tremendous amount of effort has been made on understanding the production and transport of beam induced 1+ ions from the gas cell. The steps below describe the work that has been performed over the reporting period:

Three gas cells with various production targets were fabricated and one was installed in the LIG chamber. The purpose for fabricating multiple gas cells is to allow safe changes of the production targets and entrance / exit windows which in turn will reduce exposure time considerably.

The first experiment with the LIG was performed, using beams of 6.3 MeV/u ^{16}O with no production target. The purpose of the experiment was to test the functionality of the complex systems including the vacuum system, power supplies, safety interlocks and coordination of research and technical staff. With the beam passing through the gas cell, molecular ions of mass of 59 and 73 (impurities in the gas cell) were ionized and transported from the gas cell to the CB-ECR ion source.

The next experiment was made with beams of 6.3 MeV/u ^{12}C and nickel as the production target. By this process, Ni 1+ ions were made by sputtering the target with the ^{12}C beam. Unfortunately, no Ni ions were measured exiting the gas cell. We also tried introducing Kr gas in an attempt to measure

ionized Kr. However the yield of Kr ions was found to be extremely low and all attempts to increase the intensity were not successful.

The next experiment was made with beams of 6.3 MeV/u ^{4}He on ^{27}Al target in order to create ^{30}P (beta + radioactive, T1/2 = 2.5 min) as radioactive product. The reaction cross section of the process ^{27}Al(^{4}He,n)^{30}P is approximately 260 mb at 10.53 MeV with the recoil energy ranging between 0.5 MeV to 2.6 MeV. The LIG gas cell is designed to work with very low energy recoil products. Proton or ^{4}He beams will work to catch, thermalize and allow the extraction of radioactive products. Due to the lack of a diagnostic system (detector) after the 1 meter long SPIG, we could check only the production of stable beam at that position. However the correlation between the stable beam production and radioactivity production exists such that the higher the stable beam production is, the higher the radioactive yield it is. To check the radioactive products yield, the analysis magnet following the CB-ECR ion source was set to measure mass 30 in a 1+ charge state. A Germanium detector was installed on the CBECR ion source vertical injection line in order to measure the radioactive yields of the collected products. Unfortunately, no radioactive products were measured.

The unsuccessful experiment with ^{27}Al(^{4}He,n)^{30}P reaction led us to believe that the energy of the recoil products may be too high to exist the gas cell. Therefore we tried using a 15 MeV proton beam on a Ni target to produce ^{58}Cu. The cross section of the reaction ^{58}Ni(p,n)^{58}Cu is about 50 mb. For this reaction, the recoil product energy is lower than from ^{27}Al(^{4}He,n)^{30}P therefore the efficiency of gas cell should be higher. Unfortunately once again, no radioactive products were found regardless of a steady stable beam current coming out of the gas cell.

Since the lack of radioactivity exiting the gas cell from the production targets was not understood, tests with the open ^{228}Th radioactive source were performed once again. With the source placed in the gas cell (but with no beam going through the gas cell) good production of the daughter products was measured exiting the gas cell and transported through the CB-ECR ion source. However, when the beam was passed through the gas cell at high intensity, no daughter products were measured coming from the gas cell. Only when the beam was reduced to low intensity (~40 nA) were the daughter products measured exiting the gas cell.

Using the information learned with the open ^{228}Th radioactive source with respect to beam intensity, we once again tried an experiment with a 15 MeV proton beam on a ^{nat}Zn target to produce radioactive 1+ ions of ^{64,66,68}Ga. With the beam intensity kept low at ~40 nA, radioactive products were measured exiting the gas cell and were transport through the CB-ECR ion source.

After the radioactive beam production from the gas cell was demonstrated, the production efficiency effect was investigated. Two sizes (1mm and 2mm diameter) were tried as exit holes for the target gas cell. Collection plates were installed directly after the exit holes. After 15 minutes of collection, the plates were placed in front of a Germanium detector for 30 minutes and the gamma line of 991 KeV was collected to determine the production amounts. Table I summarizes the measurements and shows very high efficiency in the production of radioactive ^{64}Ga atoms from the 2 mm hole.

Table 1. Peak integrals of the ^{64}Ga keV line and the corresponding production percentages from 1 and 2 mm exit holes.

Hole Dia. (mm)	Beam Intensity (nA)	991 keV line – Peak integral	Atom Percentage
1	650	9,213	12 %
2	500	14,715	90 %

Despite the positive result of production from the gas cell, the transport of the radioactive ions through the RF sextupole was not successful perhaps caused by neutralizing effects from the primary beam. A new RF sextupole with a better shielding and a larger acceptance has been designed and is shown in Fig. 4.

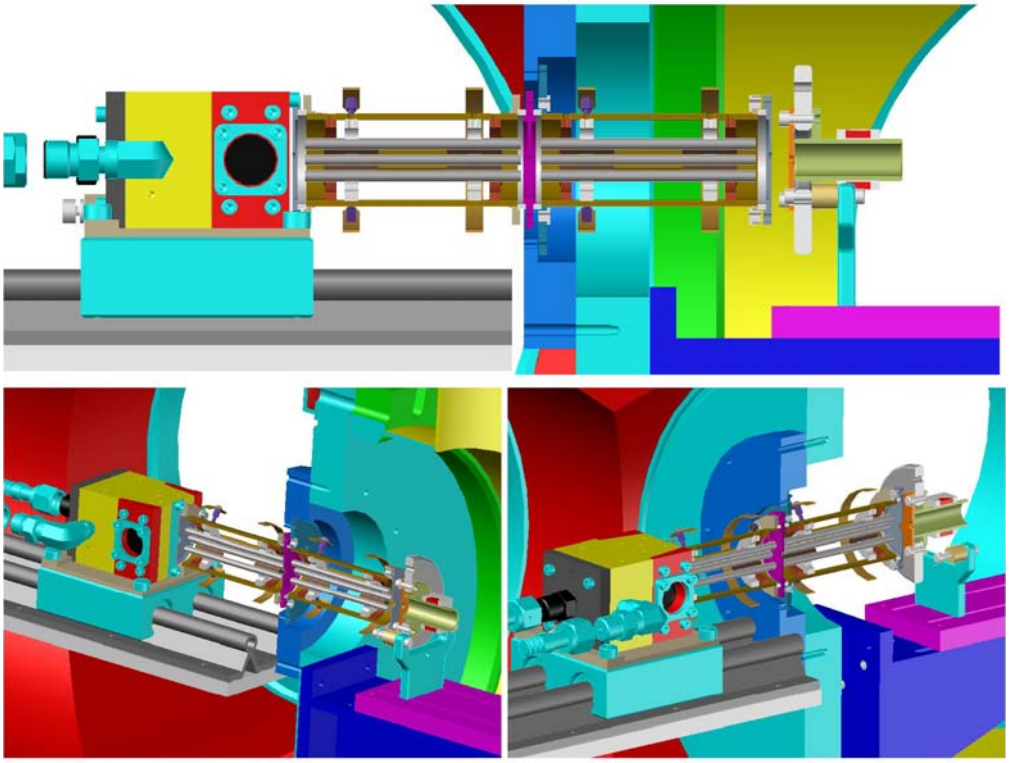

FIG. 4. The design for the new LIG RF sextupole.

VII. Heavy Ion Guide

The vacuum box for the gas catcher and the support stand have been finished and installed in the ion guide cave, see Fig. 5. The gas catcher has been installed inside the vacuum box.

FIG. 5. The support stand with the vacuum box shown installed in the heavy ion guide cave. The gas catcher is shown installed inside the vacuum box.

Restoration of beta-decay events that have occurred during the detection system's dead time

V. Horvat and J. C. Hardy

Dead time of the apparatus used for particle detection affects every measurement of nuclear half-life, while its nature and extent may not be exactly known. Consequently, the data obtained in such measurements yield results that may depend on some educated estimates of the dead-time effects. These effects increase when the product of the dead time per event and the event rate expected in the absence of dead time (*i.e.* the ideal rate) increases, in which case the errors in the estimates have a greater effect on the accuracy of the measured half-lives. Therefore, there is a need for a proven standard method of measurement and analysis that would provide the best accuracy and precision of the results for a given number of measured events.

Such a method has been developed recently [1]. It requires a measurement of the time of each particle-detection event, which can easily be accomplished using a suitable time-to-digital converter (TDC) [1]. The key element in the analysis is the imposition of a known, sufficiently large extending dead time to the measured sequence of events in order to produce a set of surviving events for which the effects of the actual dead time are completely obliterated by the effects of the imposed dead time. As a result, the dead time following each surviving event and the live time preceding each surviving event are known exactly, which provides for an exact statistical analysis of the time intervals between consecutive surviving events. We validated this method by using simulated data for the beta-decay of ^{26m}Al (at half-life $T_{1/2}$ = 6.3452 s [2]), with an assumed constant background event-rate of B = 1 s^{-1} and an initial decay rate, A, ranging from 100 s^{-1} to 100,000 s^{-1}. The imposed extending dead-time per event, τ_e, ranged from 2 μs to 512 μs, so that $A\tau_e$ ranged from $2'10^{-4}$ to as high as 51.2.

However, it turns out that the time it takes to analyze the data using this method for a given total number of events increases drastically as the event rate decreases. This is mainly because in this case the number of events per sample decreases, so that an increasingly larger number of samples must be analyzed. While the latter leads only to the need for increased computing power and memory size, the former presents an additional problem: As the average number of events per sample decreases and becomes too small, the distribution of the maximum-likelihood values of the fitting-function parameters obtained in the analysis of each sample broadens to the point at which it becomes affected by the physical restrictions of the problem, such as the requirement that all parameters have positive values. This leads to an increased systematic error and a biased result. Unfortunately, systematically ignoring the affected samples has the same kind of an effect.

A traditional solution to this problem would be to (a) produce a decay spectrum (*i.e.*, a time histogram) of the surviving events for each sample, (b) correct the number of events in each channel of each decay spectrum for dead-time effects, and (c) combine channel-wise the resulting dead-time-corrected (dead-time-free) decay spectra into a single decay spectrum for an analysis to determine the nuclear half-life. While parts (a) and (c) of this procedure are straightforward, part (b) may only seem straightforward because the live- and dead-times associated with each surviving event are assumed to be

known exactly. To the best of our knowledge, none of the existing published methods that could be applied here was proven to be unbiased, numerically problem-free, and applicable to the cases involving low event rates and large dead-time corrections. Thus, this problem is far from being trivial.

For the method in which the dead-time-corrected number of events in a given channel is obtained by dividing the observed number of events in that channel with the total channel live time and multiplying the result with the channel duration, the extent of the problem is illustrated in Fig. 1a, which is based a data set with approximately one million events simulated at a constant ideal event rate $\rho=10s^{-1}$, and partitioned into one thousand samples, each having 100 channels spanning the duration of 100 s. The imposed extendable dead time per event τ_e was varied from 0 to 120 ms. Evidently, the dead-time-corrected number of events divided by the actual number of events in the absence of dead time is increasingly greater than the expected value of 1 as the dead time increases, reaching the value of as high as 1.22 at τ_e = 100 ms. A similar behavior is expected in the case of constant τ_e and changing ρ, since for the given data set the effect depends on the observed event rate, which in turn depends on $\rho\tau_e$. It should be noted, though, that the same method of dead-time correction yields the expected (and desired) result, as

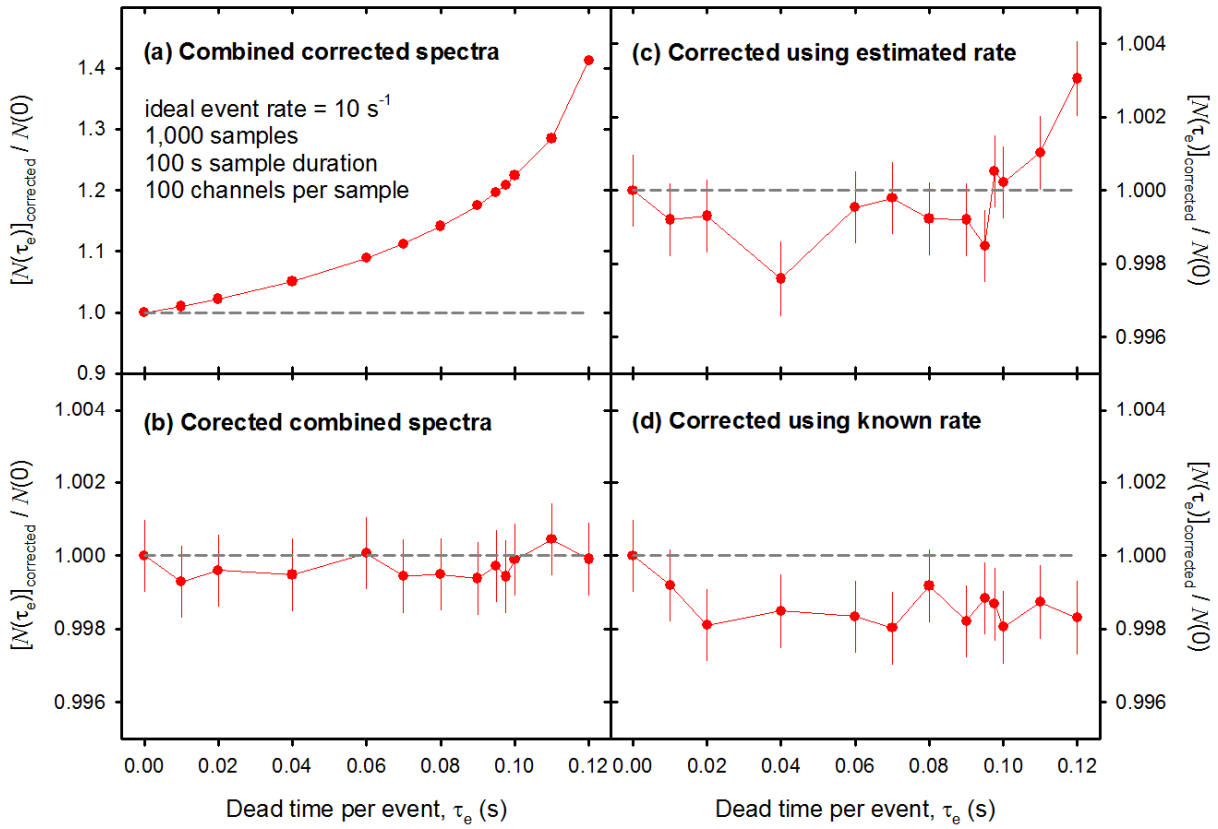

FIG. 1. Total dead-time-corrected number of events $[N(\tau_e)]_{corrected}$ divided by the total number of events in the absence of dead time $N(0)$ for a simulated data set described in the legend. (a) Live-time-fraction correction was applied to one channel of one sample at a time. (b) Live-time-fraction correction was applied to one channel at a time after all samples had been combined. (c) Simulated dead-time correction was applied to one channel of one sample at a time, using the ideal event rate estimated from the sum of three consecutive live-time intervals. (d) Simulated dead-time correction was applied to one channel of one sample at a time based on the ideal event rate actually used in the simulations.

shown in Fig. 1b, if part (c) of the procedure is applied before part (b). This shows that, for a given total number of events, the bias of this method increases as the observed (effective) event rate decreases. Unfortunately, the decay spectra obtained from each sample can be combined first and the combination dead-time corrected next only if the ideal event rate function is the same for all samples, which cannot be guaranteed in the real measurements of nuclear decay.

Therefore, a new approach to the problem is proposed here, in which (*i*) the events lost due to dead time are replaced by a statistically equivalent set of events and inserted appropriately into the sequence of surviving events, thus producing a statistically correct dead-time-free sequence of events. This would be followed by (*ii*) producing a decay spectrum of these events for each sample and (*iii*) combining channel-wise these decay spectra into a single decay spectrum for analysis. While parts (*ii*) and (*iii*) of this new procedure are straightforward, part (*i*) has yet to be developed. The key requirement is that the dead-time correction must be based solely on the known live-time and dead-time intervals associated with the surviving events, and specifically, without any advanced knowledge of the ideal rate or its time-dependence.

Given that the number of events lost due to the imposed extending dead time per event τ_e depends directly only on the duration of the dead-time interval following each surviving event (which is known exactly if τ_e is sufficiently large) and the ideal rate at the time of each surviving event (which is not known *a priori*), the latter quantity must be estimated based on the known live times preceding each surviving event. This is possible because, at a given ideal event rate ρ, the distribution of these live times is identical to the distribution dp_1/dt of the times between consecutive events in the absence of dead time, and is given by

$$dp_1/dx_1 = \exp(-x_1) \, , \tag{1}$$

where

$$x_1 = \rho t \, . \tag{2}$$

However, even though the mean value of x_1 equals 1, $1/t$ is not a good statistical estimate of ρ because the most probable value of dp_1/dx_1 is zero, which means that it is very likely to encounter a live time interval so small that its reciprocal value exceeds that of the actual ideal rate by many orders of magnitude. On the other hand, if n consecutive live times are combined, the distribution of their sum t_n is given by

$$dp_n/dx_n = (x_n)^{n-1} \exp(-x_n) / n! \, , \tag{3}$$

where $x_n = \rho t_n$. This distribution peaks at the value of $(x_n)_{peak} = n - 1$ and (for $n > 1$) it tends to zero both for extremely small and extremely large values of x_n, thus making $(n - 1)/ t_n$ a good statistical estimate of ρ.

The distribution of p_n gets narrower as n increases, in which case the estimates of ρ improve. However, a large value of n is not practical when ρ is expected to change significantly between the beginning and the end of the time interval x_n. On the other hand, when this is not the case, the live-time

intervals to be combined can be sampled using patterns that do not necessarily involve consecutive values.

To illustrate the new method of dead-time correction proposed here, we set $n = 3$ and use consecutive live-time values. Specifically, we populate the dead-time interval $(t_D)_i$ that follows the surviving event i (for all available values of i) with simulated events, assuming the ideal event rate of $1 / [(t_L)_i + (t_L)_{i+1} + (t_L)_{i+2}]$, where $(t_L)_i$, $(t_L)_{i+1}$, and $(t_L)_{i+2}$ are, respectively, the live-time intervals preceding the surviving events i, i+1, and i+2. The result is shown in Figure 1c. For comparison, we repeat the same procedure using the ideal event rate used in the simulation and show the result in Figure 1d. Apparently, the bias of the new method of dead-time correction, if any, is commensurate with the expected statistical fluctuations, at least for $\rho\tau_e < 1.1$, and the method works much better than the traditional method based on the channel-by-channel correction, one sample at a time.

[1] V. Horvat and J.C. Hardy, Nucl. Instrum. Methods Phys. Res. **A713**, 19 (2013).
[2] J.C. Hardy and I.S. Towner, Phys. Rev. C **79**, 055502 (2009).

Automatic degrader changer

M. Bencomo and J. C. Hardy

The purpose of this project was to design, build and install a remote-controlled degrader changer for the tape transport system. The changer allows a more efficient use of beam time by reducing the time it takes for the experimenter to adjust the degrader thickness at the beginning of an experimental run. The changer consists of two thin wheels (0.0625 in) with radius 2.50 and 3.85 in. with 4 (previously 3) and 8 slots, respectively, for different degrader thicknesses. These wheels can be rotated to different positions by two independent stepper motors using Arduino UNO [1] microcontrollers interfaced with Processing software [2].

Previously, we reported [3] a final design based on the spatial restrictions of the experimental set up as well as a working set of codes for the microcontrollers and the graphical user interface (GUI). As of today, only one change was made to the 2.5 in. radius wheel, adding an extra slot for a degrader combination of aluminized mylar tape and a 0.25 mil thick aluminum foil. This change was also made to the GUI. Another change made to the GUI was the addition of functions to retain the position of the wheels (Fig. 1) even after the computer controlling it has been turned off, allowing more control over the wheels as well as providing a manual overwrite.

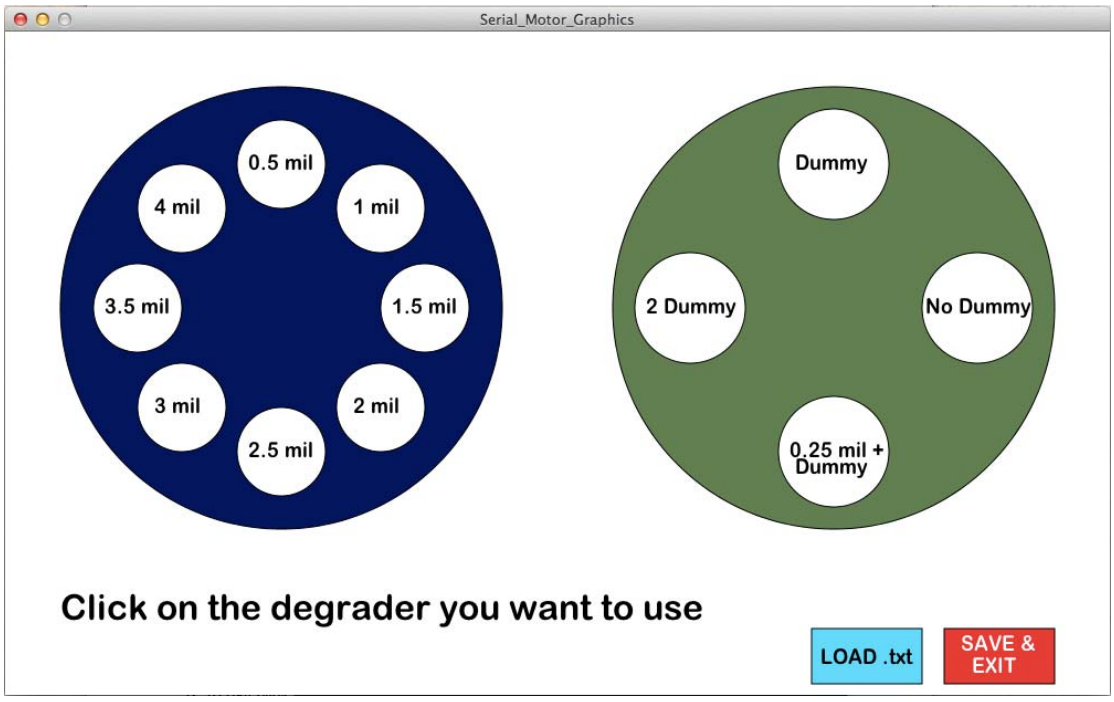

FIG. 1. Current GUI.

The extra slot added allows us to determine the beam implantation profile near the edges of the aluminized mylar tape. This profile is an important step in the experimental process to determine how the isotope of interest is being implanted as well as other impurities that may be stopped somewhere in the tape. Fig. 2 shows the implantation profile for a ^{42}Ti beam as a function of degrader thickness. It can be

seen in this particular profile that as the thickness of the degraders is increased more impurities get implanted and less ^{42}Ti is seen. The red points represent the measured values, while the blue, green and yellow lines represent the implantation of ^{42}Ti, ^{40}Sc and ^{38}Ca, which all had been identified at the focal plane of MARS.

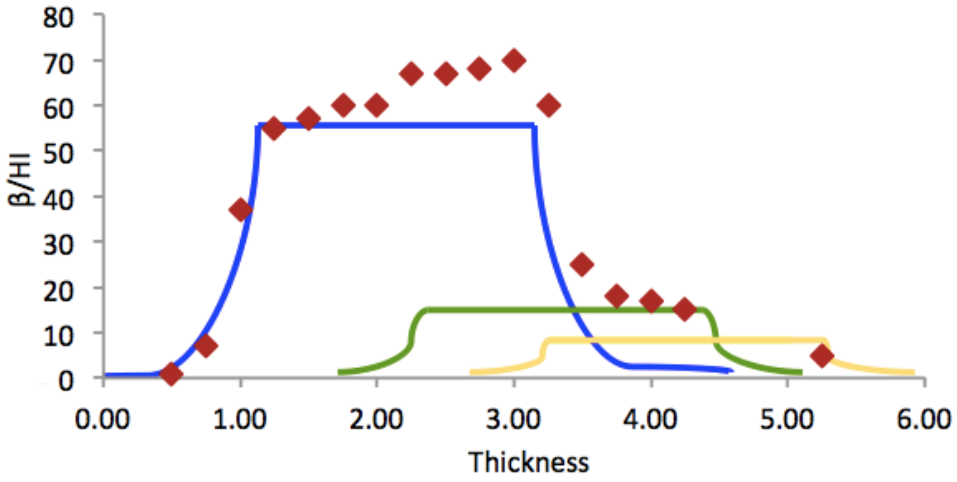

FIG. 2. Implantation profile for ^{42}Ti.

Currently, the automatic degrader changer has been built and installed. Tests have been made and improvements to design and GUI implemented. The degrader changer is fully functional and has already been used during experiments as shown by the data above. No further changes have been discussed or planned for the near future regarding this project as of now.

[1] http://arduino.cc
[2] http://processing.org
[3] M. Bencomo and J.C. Hardy *et al.*, *Progress in Research*, Cyclotron Institute, Texas A&M University (2012-2013), p. IV-31

Beam diagnostic stations for the TAMUTRAP beamlines

R. S. Behling, B. Fenker, M. Mehlman, D. Melconian, and P. D. Shidling

The goal of the upcoming TAMUTRAP facility is to measure the beta-neutrino correlation parameter of $T = 2$ superallowed beta-delayed proton emitters by observing the shape of the distribution of the resulting proton energy spectrum. The low energy radioactive ion beam (RIB) necessary for this experiment will be extracted from the T-REX gas catcher and transported through a multi-RFQ (Radio Frequency Quadrupole) Paul Trap cooler/buncher to the TAMUTRAP Penning trap facility. As development of the TAMUTRAP experiment continues, it will become important to determine the beam profile and position and to obtain an idea of the transverse emittance of the ion beam at various stages in the beam line. To this end, a beam diagnostics station based on a wedge-shaped micro-channel plate (MCP) detector with a phosphor screen for obtaining position information has been designed, and is currently in testing. Planned locations for these stations are shown in Fig. 1.

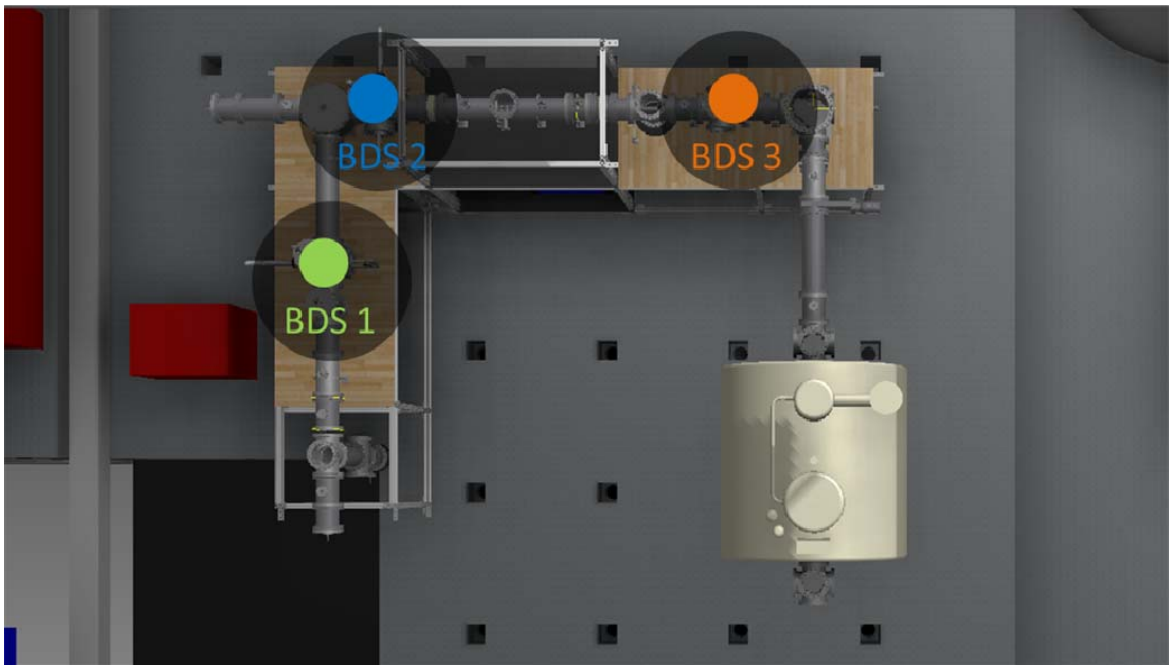

FIG. 1. Planned locations for the Beam Diagnostic Stations (BDS).

A Beam Imaging Solutions BOS-40-IW MCP detector (see Fig. 2) makes up the heart of the diagnostic station, and can provide a timing signal from the included metal anode or position information via the phosphor screen. This position information is recorded by a UEye camera for analysis. Transverse emittance measurements are planned to be performed by using this detector in conjunction with a pepper pot mask (right side of Fig. 2) placed upstream in the path of the beam. By calculating the separation of the resulting spots in the pattern on the phosphor and comparing these to the known pattern on the mask, the emittance can be deduced. Software has been written to perform these calculations in

LabView, and is currently being finalized. Additionally, longitudinal emittance will be calculated via timing information from the metalized anode of the MCP. A Faraday cup is also included in the beam diagnostic station for simple efficiency measurements and higher current tests. The entire system has been fabricated, and should be operational and fully tested within the upcoming months

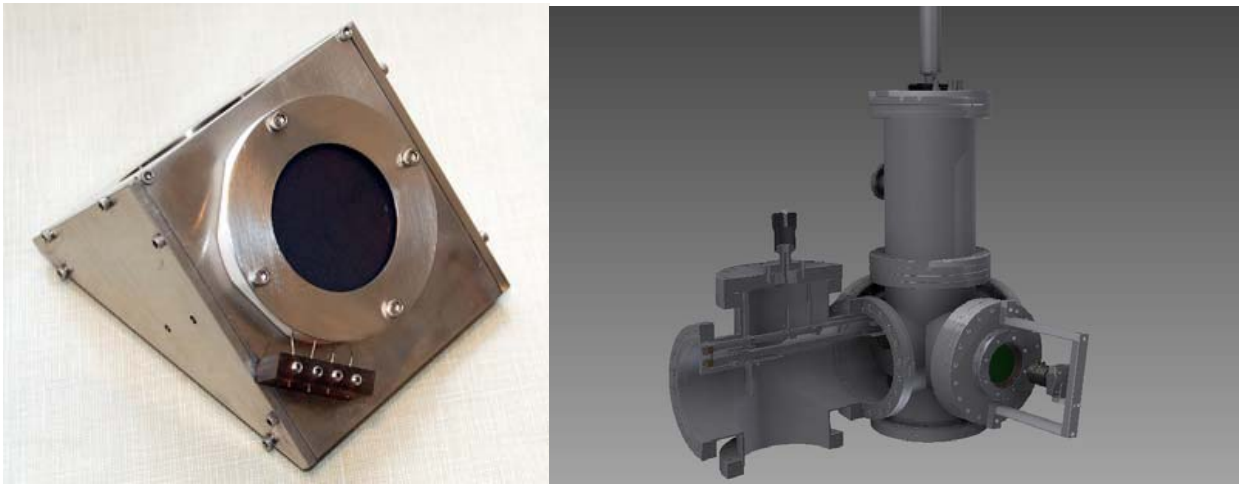

FIG. 2. The Beam Imaging Solutions BOS-40-IW multi-channel plate detector (left) and design of the beam profile and emittance measurement diagnostic station (right).

Transport efficiency of injection optics and RFQ of the TAMUTRAP facility

R. S. Behling, B. Fenker, M. Mehlman, D. Melconian, and P. D. Shidling

Significant progress has been made toward the commissioning of the TAMUTRAP facility over the past year. Different sections of beam line were tested using an in-house-designed ion gun employing potassium and sodium ion sources. As reported in our previous report [1], a low energy beam of 10 keV was successfully decelerated to several tens of eV using custom injection optics. The beam was then transported through the RFQ with and without the presence of a Helium buffer gas, and was extracted using a custom extraction optics. The total transmission efficiency of this beam line consisting of injection optics, RFQ, and extraction optics was around 3%. In order to determine the cause of this low transmission efficiency several offline tests were performed on the constituent sections.

Efficiency of Injection Optics

A modified three element lens is employed as the injection optics to focus the decelerating ions and inject them into the RFQ. This lens is formed by placing an electrode with a circular aperture between a region of low electric potential and a region of high electric potential (Fig. 1). A SIMION simulation predicted the efficiency of injection optics to be close to 100%.

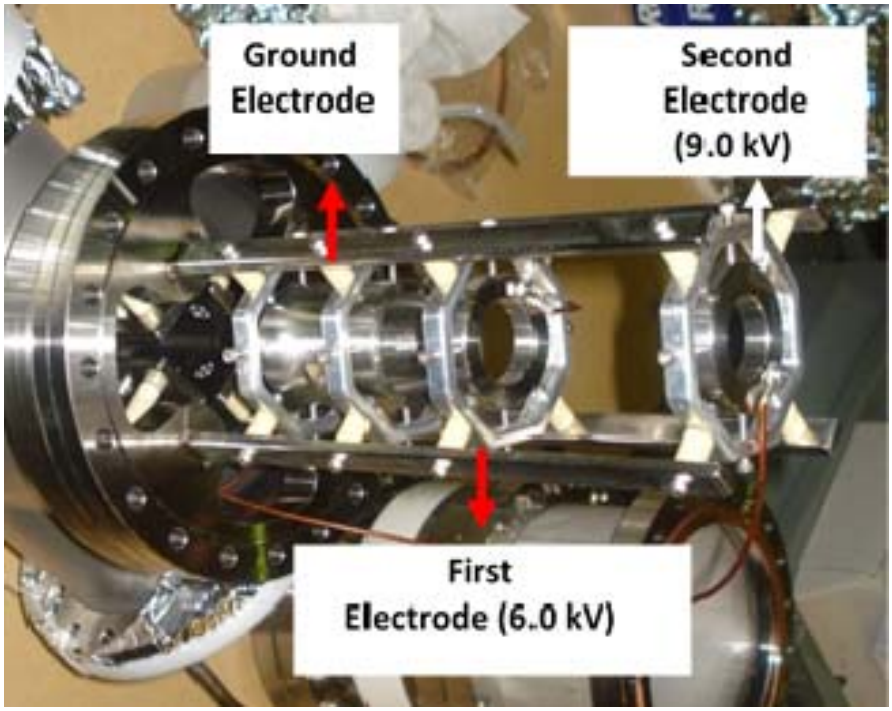

FIG. 1. Injection optics for the TAMUTRAP RFQ.

For testing, the injection optics was decoupled from the RFQ and extraction optics, and a Faraday cup was placed in the location of the RFQ preceded by a diaphragm of 6 mm. Two offline tests were performed by placing the Faraday cup at two different distances from the diaphragm. In the first test, the distance between the Faraday cup and the diaphragm reflected the position of the 1st segment of the RFQ. In the second test, the distance between the Faraday cup and the diaphragm reflected the position of the 3rd segment. The efficiency of the injection optics was determined by measuring the current before (F-cup-01) and after (F-Cup-02) the injection optics. The efficiency of the injection optics at 100 eV beam energy was around 45% when the Faraday cup was at the position of the 1st segment, and around 30% when the Faraday cup was at the position of the 3rd segment. This poor efficiency in the case of the low energy beam was suspected to be the result of two main causes: an insufficient beam line mechanical support structure due to which the beam pipes and the electrodes were not acceptably aligned with each other, and poor ion beam emittance from the ion gun. An improved mechanical support was designed to support the beam pipes (Fig. 2) and to aid in alignment. Collimators of 1 mm diameter were used in conjunction with an optical transit to align the inner electrodes with each other and with respect to the beam pipe. Adjustable PEEK screws were used to hold and adjust the injection optics electrodes as necessary. The improvement in the beam alignment with new support structure is shown in Fig. 2.

After installing this new mechanical support, the injection optics was once again tested by placing

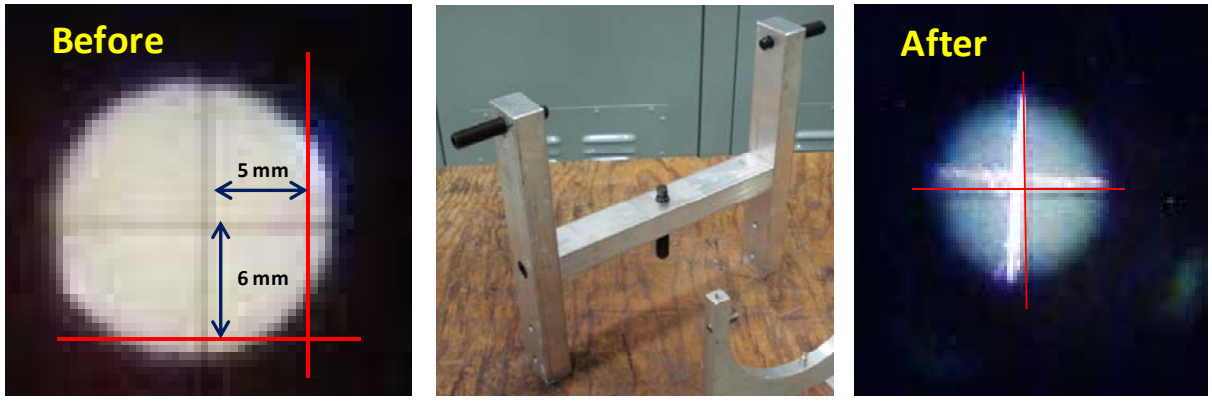

FIG. 2. Beamline mechanical support (middle) and images through the optical transport demonstrating the improved alignment.

a Faraday cup (F-cup-02) in place of the RFQ. The distance between the Faraday cup and the diaphragm was set to the position of the 3rd segment of the RFQ. The observed efficiency was two times better compared to the previously measured efficiency at 100 eV. Next, we studied the efficiency of the injection optics as a function of beam energy (Fig. 3) entering RFQ. The efficiency was found to be greater than 80% for beam energies greater than 75 eV, and dropped substantially when the beam energy was less than 30 eV. A likely cause for this low efficiency at 30 eV beam energy is large emittance of the beam exiting the ion gun. We believe improving the emittance of the ion gun to a more realistic value will increase the efficiency to as high as 90% at 30 eV beam energy.

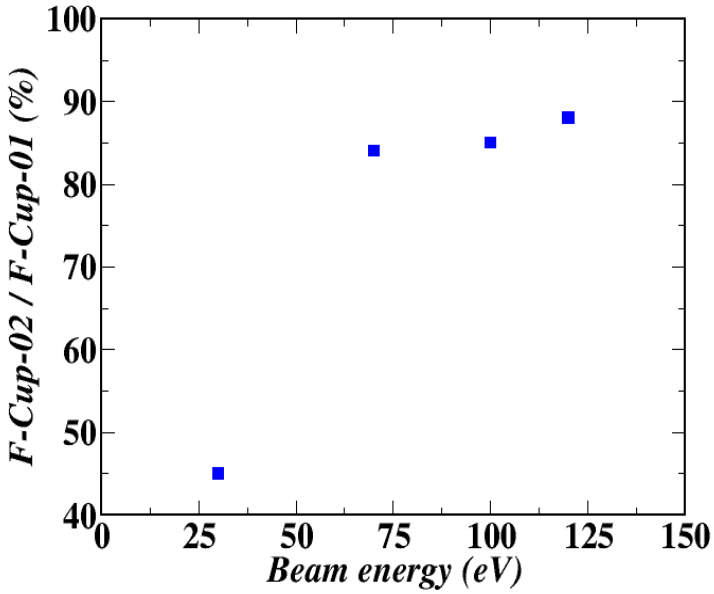

FIG. 3. Efficiency of the injection optics as a function of the beam energy entering the RFQ.

Transport Efficiency

Following these tests, the injection optics was coupled to the RFQ and extraction optics. Two Faraday cups were installed, one before the injection optics and the other at the exit of the extraction optics. The RFQ is 80 cm long with r_0 = 6mm.. In order to apply the longitudinal potential the structure was segmented into twenty eight pieces. The segments in the injection and trapping regions were made shorter than those in the center of the trap in order to give more control over the electric field in these regions. The RFQ was operated in continuous mode and was optimized by scanning the frequency and RF voltage applied to the segments (see Fig. 4). The maximum transmitted current was observed at 1.2 MHz. At each frequency the RF voltage was scanned by changing the power of the power amplifier. The peak-to-peak RF voltage at 1.2 MHz was around 123 V, yielding a total transport efficiency for these three elements of around 13% which was four times more compared to the previous value. It is predicted that the transmission efficiency of the RFQ alone was raised to 20-25% in continuous mode as a result of the improved alignment.

Despite this improvement, the efficiency is still lower than desired, mainly due to the unacceptable beam emittance coming from the ion gun and mechanical misalignment within the RFQ structure itself. As discussed, the electronics for the RFQ are working as expected, yielding up to 160 V peak-to-peak at frequencies between 0.5-1.5 MHz, and will be carried over to the improved mechanical structure. An improved designed is planned and is currently under development.

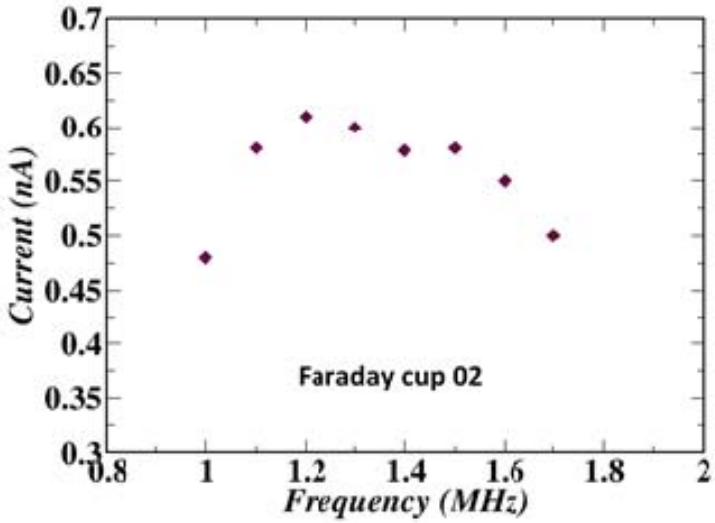

FIG. 4. Current observed at the exit of extraction optics as a function of frequency.

[1] R.S. Behling *et al.*, *Progress in Research*, Cyclotron Institute, Texas A&M University, (2012-2013), p IV-46.

Upgrades and status of the ^{37}K β-asymmetry experiment

R. S. Behling, B. Fenker, M. Mehlman, D. Melconian, and P. D. Shidling

The TRINAT collaboration performed a successful experiment to measure the beta-asymmetry parameter in ^{37}K in December of 2012. While progress in the analysis of this data is described in a separate report, we have also upgraded the apparatus in preparation for a run in May-June of 2014 with the goal of achieving an overall uncertainty of less than 0.5% in the beta-asymmetry. These upgrades include the installation of a forced-air cooling system for the silicon-strip detectors, stabilized LED gain monitoring of the photomultiplier tubes, and the installation and development of a new, larger set of micro-channel plates (MCPs) including a delay-line anode for position information.

The primary detection system in our apparatus is a pair of beta-telescopes placed along the nuclear polarization axis. We measure the beta-asymmetry by comparing the count rate in the detector parallel to the nuclear spin with that of the detector anti-parallel to the nuclear spin. Each beta-telescope consists of a thin silicon-strip detector backed by a plastic scintillator. The scintillator measures the full energy of the positron while the silicon detector helps to veto the gamma background and measure the positron's position. During the 2012 run, each of our double sided silicon-strip detectors (DSSSD) showed a leakage current about eight times the normal value. This large leakage current can decrease the pulse height and therefore increase the energy threshold of the detector. We attribute the leakage current to inductive heating of the detector and its surroundings by eddy currents induced in the vacuum chamber by the oscillating magnetic field that is necessary to produce the alternating-current MOT (AC-MOT). To keep the DSSSD nearer to room temperature, we have installed a gas system to cool the detectors by forced convection. Tests of this system demonstrate that it successfully cools the detectors enough that they maintain an acceptable leakage current.

The light output from the plastic scintillators described above are read out by a photomultiplier tube (PMT). It is well known that the gain of PMTs drift over time due to variations in temperature and count rate. In order to monitor these drifts over the roughly three week duration of our experiment, we have built a stable three-tiered gain-monitoring system. The gain of the PMTs are monitored by periodically injecting into them an LED pulse of constant brightness. Assuming a perfectly constant LED brightness, any variations in output charge are then attributable to drifts in the gain of the PMT. Since the brightness of standard LEDs are known to vary over time by a few percent, we use an optical fiber to split a constant fraction of the light output to a photodiode (PD) which gives an independent reading of the brightness. The PD's output signal is then used to drive an active gain-stabilization feedback loop designed by Y. Holler [1]. As a final precaution, we house the PD in a temperature stabilized box in order to minimize gain drifts in this detector. The temperature and LED stabilization units have been tested to work satisfactorily and the PMT's gain monitoring will be installed before the upcoming May-June run.

In addition to the detector systems described above, we use two sets of micro-channel plate (MCP) detectors to provide additional information about the decays. One of these detectors collects atomic shake-off electrons (SOEs) produced immediately following the positron-decay as a result of the

sudden change in nuclear charge. The SOEs are focused onto the MCP by a constant electric field. The observation of one or more SOEs is critical for tagging events that have decayed from within the trap where the atoms are highly polarized. In 2012, we observed rate fluctuations in phase with the oscillating (1 kHz) magnetic field of the AC-MOT, implying that some SOEs were being deflected beyond the edge of the 20 mm radius MCP.

Over the past year, we have replaced this MCP with a larger (40 mm radius) one and added a delay-line anode to provide position sensitivity. The larger MCP will allow us to collect more shake-off electrons and increase our rate of positron-electron coincidences that we use for our asymmetry measurement. The position sensitivity will be useful in two ways. First, measuring the position distribution of the SOEs as a function of magnetic field strength provides a unique opportunity to measure the energy distribution of SOEs from 5-30 eV (the lowest energy data currently available in the literature is 150 eV) [2]. Although this is not our main experimental program, a dedicated measurement has been approved by TRIUMF. Secondly, the newly added position sensitivity will provide redundant information about the trap's position and size. Our standard technique is to periodically photoionize a small fraction of the trapped atom and sweep the positive ion to one set of MCPs and the shake-off electron to the set of MCPs described above. Previously the transverse position was only measured by the MCP stack detecting the photoion. In the current setup, the photoelectron position will also be recorded and used to redundantly measure the trap position. The larger MCP and delay-line anode have been commissioned in an offline test chamber and are ready for use in the upcoming run.

In addition to the upgrades described here, our collaborators at TRIUMF have made significant improvements to the trapping, polarizing, and vacuum systems. With these improvements in place, we are schedule to take data at TRIUMF from May 22-25 and June 6-13. During this time we will collect data for a less than 0.5% measurement of the beta-asymmetry parameter.

[1] Y. Holler, J. Koch, and A. Naini, Nucl. Instrum. Methods **204**, 485 (1983).
[2] J. Behr, "*Low-energy atomic electrons emitted in positron decay*," TRIUMF EEC Submission, 2014

Compilation of beams produced with MARS

E. Simmons, R. E. Tribble, and RET group members past & present

The goal of this compilation was to make readily available all information gained over the years for each beam our group developed with the Momentum Achromat Recoil Spectrometer (MARS) line at Texas A & M University [1]. Starting with some of the first beams separated in 1992, all the way to the present, this survey includes all information that was ***recorded*** in our group's log books or was easily and accurately calculable. As of March 2014 this includes a total of 200 MARS experiments with about 40 different primary beams, each often looking at more than one secondary beam. The categories listed in Table I were filled in to the greatest degree possible, offering valuable information that can be used to plan future experiments.

Table I. List of MARS beam parameters recorded in the beam compilation spreadsheet.

- Experiment Label (ex. RUN1110A)
- Log Book Number & Page Number
- Experiment Start Date
- Group/Organization
- General Purpose
- D3 Degree of Elevation
- Cyclotron Used (K500 or K150)
- Primary Beam
- Particle, Charge State & Energy (MeV/u)
- Primary Target
  - Solid
    - Material, Thickness & Location
  - Gas
    - Type, Temp. (K) & Pressure (atm)
  - Window Material & Thickness (mil)
    - Entrance & Exit
- Degarders
  - Material, Thickness & Location
- Magnet Settings (Amperes & Polarity)
  - K5MB22AY
  - MARSBLD1
  - Q1
  - Q2
  - D1 - D2
  - D1 trim
  - Q3
  - S1
  - ExB Velocity Filter
    - B-Field
    - E-Field Upper & Lower Dial Settings
  - D3
  - S2
  - Q4
  - Q5
- All Slit Settings (cm)
  - Right After Primary Target
  - Coffin (Controls Momentum Spread)
  - Right After Coffin
  - Very End of Beam Line
- FC Location & Configuration
- Si Detectors Used for Production (DE-E)
  - Thickness (micron), Bias (V) & Leakage Current (uA)
- Secondary Targets
  - Material, Thickness & Location
- Secondary Beam Particle
  - Production Mechanism
  - Q-value (MeV)
  - Energy at End of MARS (MeV/u)
  - Calculated Bp Using D1-D2 (T m)
- Final Tuning File Name
- Numbers for Production Calculations
  - Number of Secondary Particles
  - Faraday Cup Count (in k)
  - Beam Current in the Coffin (nA)
- Best Production Results
  - Events per nC
  - Particles Per Second
- Secondary Energy Spread (%)
- Secondary Momentum Spread (%)
- Attenuation of Primary Beam
- Purity of Secondary Beam (%)

The information listed for the secondary beam regarding its Q-value and energy at the end of MARS was obtained from the program MARSINATOR [2] and the Bρ value was calculated with the current settings for D1-D2 and a spread sheet used by our group for that sole purpose [3]. All equations used are also written out for easy reference. A list of all relevant publications for the beams recorded in this compilation is also included, as well as general comments regarding the individual experiments. It is hoped that this list will be kept current and accessible to everyone wanting to use the MARS beam line. The latest version is currently located on the MARS TAMU-cyclotron website, specifically at http://cyclotron.tamu.edu/mars.html.

[1] R.E. Tribble, R.H. Burch and C.A. Gagliardi, Nucl. Instrum. Methods Phys. Res. **A285**, 441 (1989).
[2] A. Azhari, MARSINATOR Program
[3] L. Trache, Excel Spread Sheet

Detector developments for SAMURAI silicon tracker

A. Saastamoinen, M. McCleskey, B. T. Roeder, R. E. Tribble, L. G. Sobotka,[1] and C. Rasco[2]

[1] *Washington University, St. Louis, Missouri*

[2] *Louisiana State University, New Orleans, Louisiana*

We have continued characterizing the detectors and electronics for the SAMURAI Si project. Based on the results of our earlier in-beam tests at HIMAC facility [1], we have acquired new TTT2-500 double-sided silicon strip detectors (DSSSD). The new detectors are 500 μm thick, increasing the effective thickness by ~67% compared to the old 300 μm. To verify the performance of these new TTT2-500 detectors, and to see if increased thickness helps with proton detection, we have measured the responses of both 300 and 500 μm thick versions with 50 MeV protons from K150 cyclotron here at the Cyclotron Institute.

For these tests we used the present revision of the HINP16C chips. Both detectors were calibrated with a 4 species alpha source (^{148}Gd, ^{239}Pu, ^{241}Am, ^{244}Cm). The responses for 50 MeV protons were measured with the detector rotated at 8 degrees (to avoid channeling) and also at 30 degrees rotation to see that the energy deposit changed accordingly with the increased effective thickness. In both cases, behind the TTT2 detector was a 1 cm thick CsI detector with 32 elements coupled to standard NIM electronics to provide an independent trigger for the acquisition. In this experiment we also ran the TABS acquisition system by using the Cyclotron Institute DAQ software (CycApps) for the very first time. This allowed more convenient online monitoring than the NSCL DAQ that we have used previously.

Based on the source calibration, the 50 MeV proton energy deposit was observed to be close to the expected value in each case, as seen in Fig 1. The discrepancies are most likely due to the fact that the detector dead layer (Al contact + the implantation layer in Si) is only an estimate based on the Micron

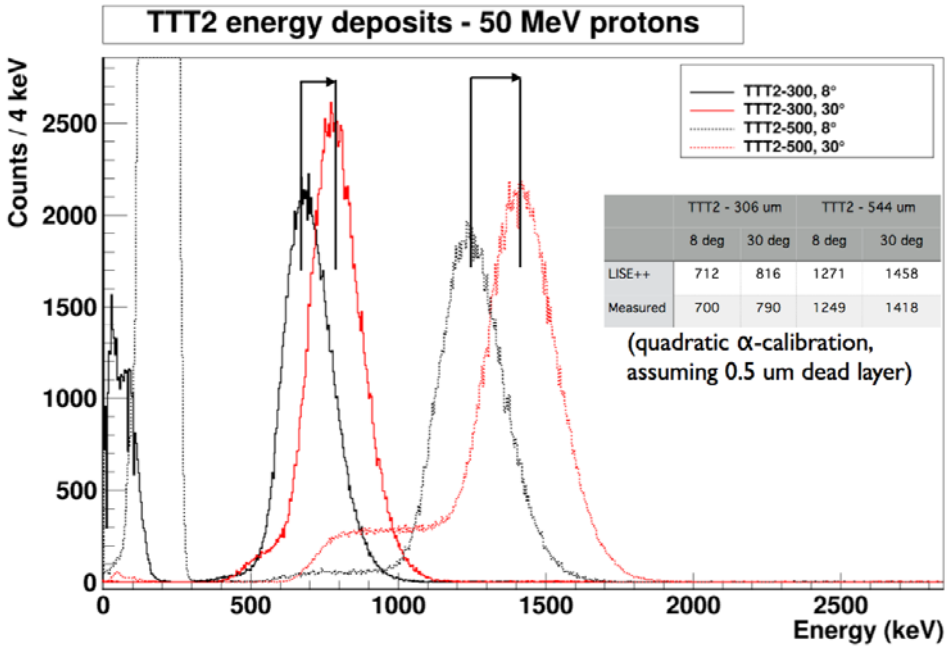

FIG. 1. Responses of TTT2-300 and 500 type detectors to the 50 MeV proton beam.

Semiconductor Ltd. specifications and for the fact that the lowest calibration energy is at 3.2 MeV, while the proton energy deposits are about 1.5 MeV. It is worth noting that while there is an offset in the energy compared to that expected (from LISE++ calculation), the energy deposit changes as expected when the effective thickness of the detector is increased in both cases.

The system was triggered with the CsI array, but also the triggering from the HINP16C chips was tested as shown in Fig. 2. We found that the electronics noise level was rather low, about 200 keV at worst. However, this may not be quite exact as it is known that the linearity of the present revision of the HINP16C chip is not very good below 0.5 MeV. The WU group will study the linearity in offline tests to provide a better estimate for the observed noise level. Based on this test it is likely that we saw proton responses in the test last year at HIMAC, but that the thresholds were too high in most channels giving poor efficiency. This gives a rather good foundation for testing the next evolution of the HINP chip to be produced later this year.

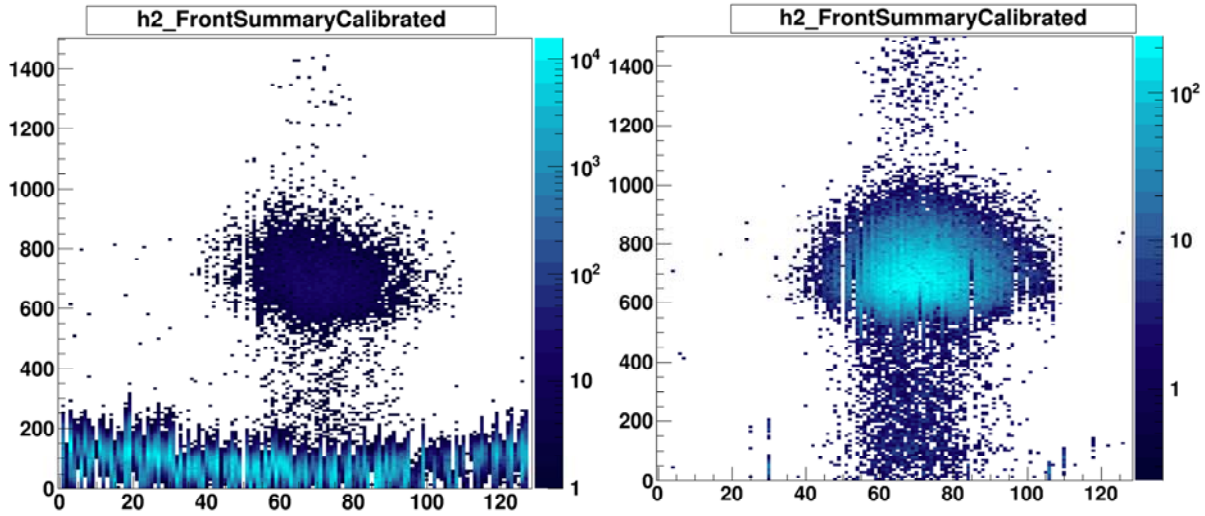

FIG. 2. Effect of triggering thresholds to the detection efficiency by individual strips (x-axis). Energy scale (y-axis) is in keV. Left side: Low thresholds (trigger mostly from noise) TTT/CsI = 12.5k/131k. Right side: Higher thresholds, cutting away noisy channels (trigger rate few Hz w/o beam), TTT/CsI = 21.9k/21.6k. In both cases the DAQ was triggered by the CsI array behind the Si detector and the thresholds of Si were adjusted as described.

[1] A. Saastamoinen *et al.*, *Progress in Research*, Cyclotron Institute, Texas A&M University (2012-2013), p. IV-55.

Development of a new MARS simulation in LISE++

B. T. Roeder and O. B. Tarasov[1]

[1]*National Superconducting Cyclotron Laboratory, Michigan State University, East Lansing, Michigan,*

LISE++ [1] is a program that has been developed since the 1980s to simulate the operation of fragment separators used to produce radioactive beams with various reaction mechanisms. While it was initially developed to simulate the LISE spectrometer [2] at GANIL, it has since been expanded and now contains configuration files for existing fragment and recoil separators such as the A1900 and the S800 at the NSCL-MSU, LISE3 at GANIL, FRS and SuperFRS at GSI, BigRIPS and RIPS at RIKEN. Given the versatility of this program, it seemed reasonable to develop a configuration file for the Momentum Achromat Recoil Separator, or MARS [3], that has been in operation here at the Cyclotron Institute at Texas A&M University, and producing radioactive beams, since 1991.

Previously, one of the problems with the LISE++ program was that it did not support individual quadrupole and sextupole elements in the spectrometer configuration. This prevented a straightforward simulation of the MARS spectrometer because it was not possible to compare old spectrometer calculations made with the TRANSPORT program [4] directly with the predictions of LISE++. Beginning with LISE++ version 9.5 (available in 2013), "extended" configurations which allowed the inclusion and calculation of matrices for quadrupoles and sextupoles in the spectrometer became available in the program. The ability to include quadrupoles and sextupoles, as well as an improvement to the calculation of the optical matrix of the compensating dipole in LISE++, has led to the new MARS configuration in LISE++.

In addition to the new configuration file, some measurements of the magnetic fields of the MARS quadrupoles were also conducted. In these measurements, four of the five MARS quadrupoles were measured for electric current vs. magnetic field with existing NMR probes. It is assumed that these NMR probes measured the magnetic fields at the pole tip of the quadrupoles, which is what is required for the quadrupole optical matrix calculation in both LISE++ and TRANSPORT. The results of these measurements for MARS quadrupoles Q1-Q4 and an estimation of the field vs. current for Q5, have been included in the new LISE++ configuration file for MARS. In this way, a direct comparison between the LISE++ simulation and the optimized settings for the dipoles and quadrupoles for a given radioactive beam in MARS can be made. Measurements of the field vs. current of quadrupole Q5 and the sextupole magnets are planned for later this year, provided the equipment needed to make these measurements is available.

The new "extended" MARS configuration in LISE++, including the quadrupoles, sextupoles, velocity filter, compensating dipole and slits, is shown in Fig. 1. This new configuration has been available for the user of LISE++ beginning with version 9.8.56 of the code. An example file with the new configuration can be found in the included files of the program in the directory "*LISE/files/examples/TAMU/TAMU-MARS_extended_35K.lpp*". This file gives a simulation of the p(^{36}Ar,^{35}K)2n reaction in MARS, which was recently produced in MARS and is reported this year as one of the new beams produced with MARS [5]. A comparison between the simulated ΔE vs. Y-position

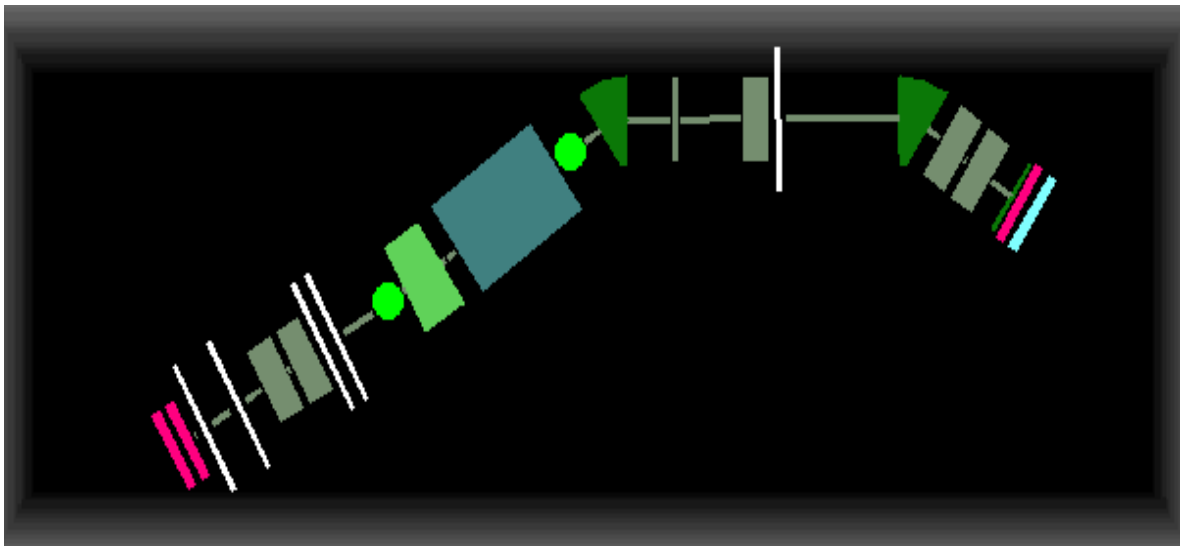

FIG. 1. A diagram of the new "TAMU-MARS_extended" configuration in the LISE++ simulation program.

spectrum obtained with this file and the actual ΔE vs. Y-position spectrum from the p(^{36}Ar,^{35}K)2n test experiment is shown in Fig. 2. The simulation predicts much more ^{34}Ar relative to the ^{32}Cl and ^{35}K than was seen in the experiment, but the simulated beam spot sizes on the detector and the mass dispersion are similar to what was obtained in the experiment.

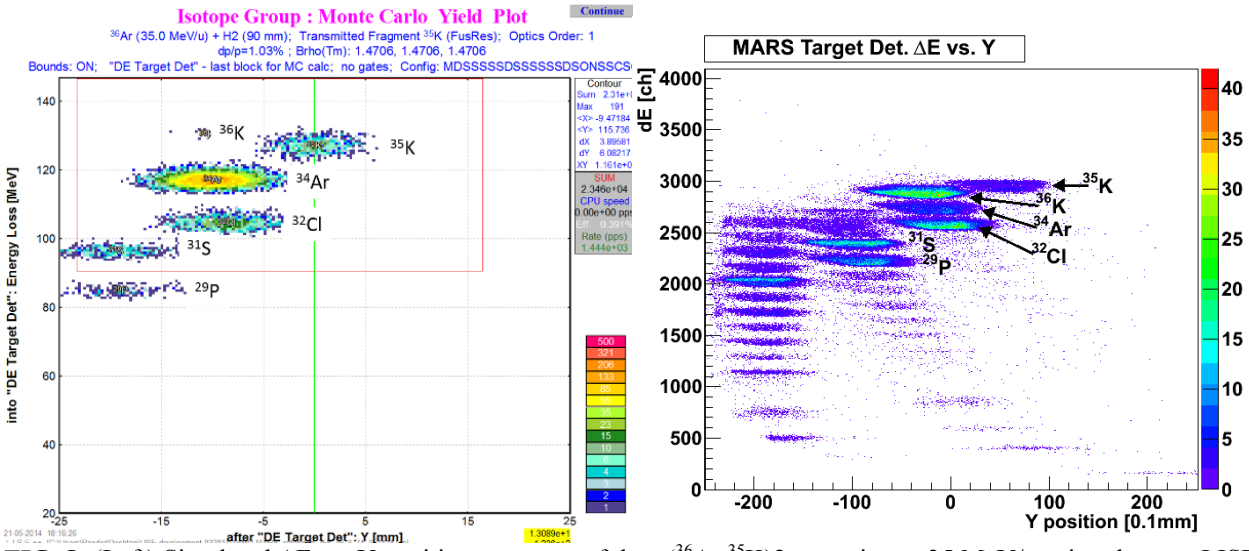

FIG. 2. (Left) Simulated ΔE vs. Y-position spectrum of the p(^{36}Ar,^{35}K)2n reaction at 35 MeV/u using the new LISE++ "TAMU-MARS_extended" configuration. (Right) MARS target detector spectrum for the ΔE vs. Y-position recorded during the production test experiment for the p(^{36}Ar,^{35}K)2n reaction at 35 MeV/u.

With this simulation of MARS in the LISE++ program, new experiments can be planned in advance as the user will have a better idea about the production rate and purity of their radioactive beam prior to their experiment. In addition, new methods of tuning the MARS optics can be studied in an effort

to improve the transmission. Finally, some possible future upgrades to the MARS beamline can be investigated.

[1] O.B. Tarasov and D. Bazin, Nucl. Instrum. Methods Phys. Res. **B266,** 4657 (2008).
[2] R. Anne *et al.*, Nucl. Instrum. Methods Phys. Res. **A257**, 215 (1987).
[3] R.E. Tribble, R.H. Burch, and C.A. Gagliardi, Nucl. Instrum. Methods Phys. Res. **A285**, 441 (1989).
[4] K.L. Brown, The ion optical program TRANSPORT, Technical Report 91, SLAC, (1979).
[5] B.T. Roeder *et al.*, *Progress in Research*, Cyclotron Institute, Texas A&M University (2013-2014), p. I-48.

Development of AstroBox2 detector

A. Saastamoinen, B. T. Roeder, A. Spiridon, R. E. Tribble, E. Pollaco,[1] L. Trache,[2] and G. Pascovici[2]

[1] *IRFU, CEA Saclay, Gif-sur-Yvette, France*

[2] *National Institute of Physics and Nuclear Engineering, Bucharest-Magurele, Romania*

In past years we have done several studies of beta-delayed proton emitters of astrophysical interest by implantation technique [1-5]. It was realized rather soon that shrinking the physical detection volume of elements in Si detector did not reduce the beta-background enough to create background free spectrum in the typical energy range of astrophysically interesting decays (E_p ~ few hundred keV). To further reduce the beta-background a novel detector, AstroBox, based on Micro Pattern Gas Amplifier Detector (MPGAD) was developed [6].

We are now building an upgraded version, AstroBox2. The major change to the earlier version will be the change of geometry of the MPGAD pad structure. The earlier cylindrical symmetry of the pads has been replaced by a set of rectangular pads that are arranged into a geometry along the beam axis to improve implantation control. The geometry of the pads is demonstrated in Fig. 1 showing a sample of the PCB onto which the detectors will be mounted. Total amount of active elements is 29. The readout electronics will be changed to accommodate the requirements of higher number of channels. We are planning to use mesytec MPR-16 preamplifiers coupled to MSCF-16 shapers which include also timing filter amplifiers and constant fraction discriminators for timing.

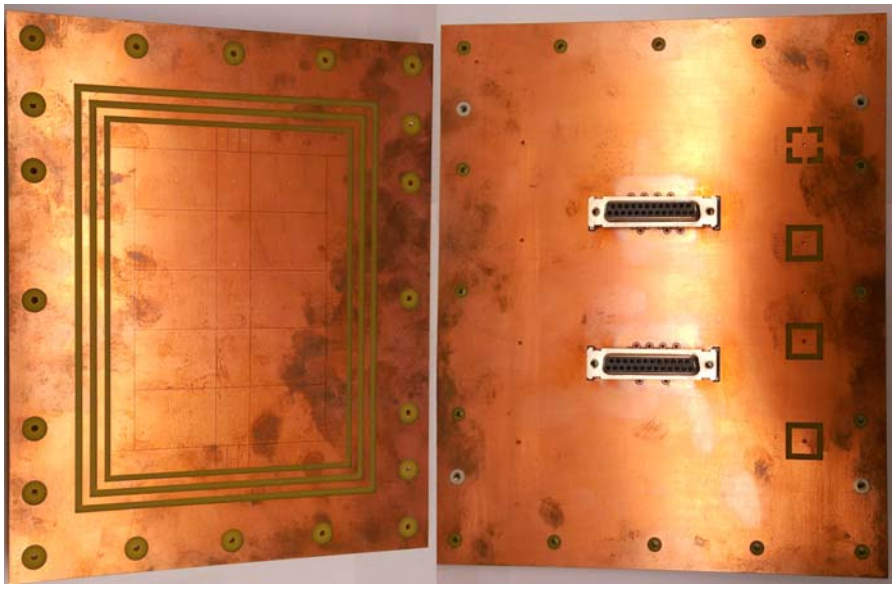

FIG. 1. A sample PCB of AstroBox2 detector. On left is the top side onto which the active elements are housed. On right is the bottom side which will face the vacuum chamber flange. The dSUB25 connectors for the signals and the high-voltage connections (the four squares) will be in air, eliminating the need for feed-throughs and cabling inside the gas volume.

The detector will be housed in a vacuum chamber illustrated in Fig. 2. The detector PCB will be mounted directly into one of the flanges, eliminating signal cabling from the gas volume. Furthermore the

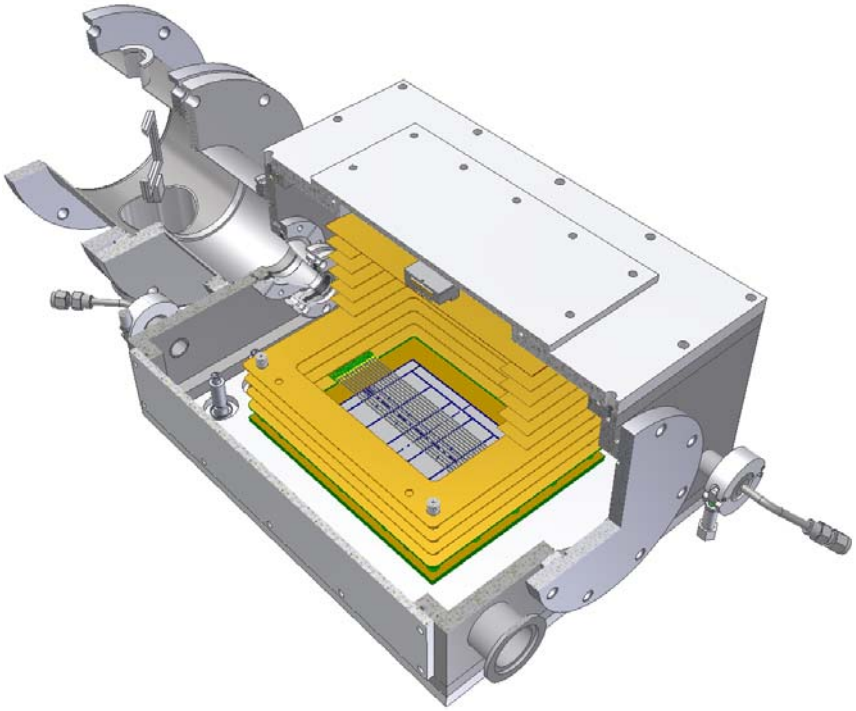

FIG. 2. Mechanical design of the AstroBox2 detector. The chamber is connected to the existing degrader chamber.

gas inlet and outlet are moved to opposite sides of the chamber to ensure more efficient circulation of the gas. For checking the detector functionality in online conditions, a holder and covering system for an alpha source is on top of the cathode. The window separating beam line vacuum and detection gas volume can be mounted either into the chamber wall or brought closer to the field cage. This will reduce straggling when stopping low energy (~10 MeV/u) beams. The side flanges are made thinner to improve gamma detection efficiency. Optionally these can be changed to dedicated flanges with cups that bring Ge detectors even closer (though the minimum distance will still be limited due to the safety gap between the field cage and the chamber wall).

The detector components are currently under construction and the detector will be assembled and tested during the summer and fall of 2014.

[1] A. Saastamoinen *et al.*, Phys. Rev. C **83**, 044808 (2011).

[2] L. Trache *et al.*, PoS (NIC X), 163 (2008)

[3] A. Saastamoinen *et al.*, AIP Conf. Proc. **1409**, 71 (2011).

[4] J. Wallace *et al.*, Phys. Lett. B **712**, 59 (2012).

[5] M. McCleskey *et al.*, Nucl. Instrum. Methods Phys. Res. **A700**, 124 (2013).

[6] E. Pollaco *et al.*, Nucl. Instrum. Methods Phys. Res. **A723**, 102 (2013).

Update on the upgrade of the Oxford detector – part 1

A. Spiridon, R. Chyzh, M. Dag, E. McCleskey, M. McCleskey, B. T. Roeder, A. Saastamoinen, R. E. Tribble, L. Trache, E. Pollacco,[1] and G. Pascovici[2]

[1]*IRFU, CEA Saclay, Gif-sur-Yvette, France*

[2]*Institut fuer Kernphysik der Universitaet zu Koeln, D-50937 Koeln, Germany*

Two years ago, we started work on upgrading the Oxford detector – one of the two focal plane detectors of the Multipole-Dipole-Spectrometer (MDM). In the nuclear astrophysics group, this setup has been used primarily to study scattering and transfer reactions involving nuclei with A≤26. However at higher masses than that, we found that we are having significant difficulties in particle identification due to the insufficient resolution of both the dE and E signals.

The upgrade being developed is intended to improve the detection of both of these signals. In the Oxford detector, energy loss comes from the ionization of isobutane by secondary beam particles and it is measured with three aluminum anode plates (for details see Ref. [1]). Currently, only the first two plates are connected and give us a signal with a reasonable energy resolution. The third plate gives a signal too noisy to be of any use. We proposed to improve the latter by introducing Micromegas [2]. The design of these detectors is similar to a gridded ionization chamber and provides gains of ~ 10^4, as well as very good resolution (see Ref. [3] for more information on the upgrade).

Over the last year, we finished the design of the new detection pads and ordered them from the manufacturer. They are expected to be completed in May 2014. We are also working on modifying the current chamber in order to have the necessary electrical feedthroughs for processing the additional signals. We have ordered most of the necessary cables and connectors and expect to have them by mid-May.

We are aiming to be ready to do initial testing – to characterize the Micromegas – in June 2014. Depending on the results of this, we may be able to use the modified Oxford detector in an experiment planned for September 2014.

For information on improving the residual energy signal, see part 2 of this paper in the same annual report.

[1] D.H. Youngblood *et al.*, Nucl. Instrum. Methods Phys. Res. **A361**, 359 (1995); M. McCleskey, Ph.D Thesis, Texas A&M University (2011).

[2] Y. Giomataris *et al.*, Nucl. Instrum. Methods Phys. Res. **A376**, 29 (1996).

[3] A. Spiridon *et al.*, *Progress in Research*, Cyclotron Institute, Texas A&M University (2012- 2013), p. IV-50.

Upgrade for the Oxford detector - part 2

R. Chyzh, A. Spiridon, V. Z. Goldberg, M. Dag, M. McCleskey, and R. E. Tribble

The Oxford [1] detector is the detector that is placed in the focal plane of the MDM (Multipole Dipole Multipole) [2] and is used for identification of the particles and their respective trajectories. One of the important parts of the Oxford detector is a scintillator which completely stops the particles and allows us to measure a signal that is proportional to the residual energy of the particles after they pass the gas chamber of the detector. Given the rather poor resolution of the scintillator, it was decided to replace it with silicon detector plates. This option should allow a much more accurate measurement of the residual energy of the particles (the energy resolution of a silicon detector is roughly 10 times better than the energy resolution of a scintillator).

Detailed drawings were made for the Si-detectors which are going to be used as a substitute for the scintillator. The schematic of a module that consists of two silicon plates is shown in Fig. 1.

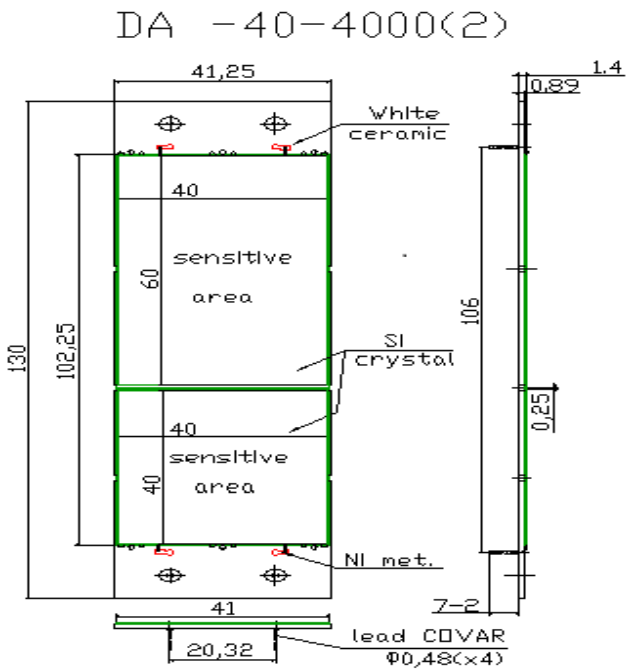

FIG. 1. The schematic of a module that consists of two silicon plates.

The two silicon plates are sitting on a ceramic platform. The thickness of the silicon is roughly 400 μm. This thickness is enough to stop a beam of ^{40}Ca with energy 24 MeV/u. The resistivity is estimated to be about 3-5 kOhm*cm, and requires a bias voltage of 50-70 V. For covering all the area in the focal plane of the Oxford detector (8.1cm x 33.6 cm), we need 8 modules. However due to possible longevity issues we will order at least 12 modules. At the moment we are finalizing the sizes of the

modules as well as the way they are going to be mounted to the flange in the backside of the Oxford detector.

We expect to complete the order by the end of the summer 2014.

[1] J.S. Winfield, D.M. Pringle, W.N. Catford, D.G. Lewis, N.A. Jelley, and K.W. Allen, Nucl. Instrum., Methods Phys. Res. **A251**, 297 (1986).

[2] D.M. Pringle, W.N. Catford, J.S. Winfield, D.G. Lewis, N.A. Jelley, K.W. Allen, and J.H. Coupland, Nucl. Instrum. Methods Phys. Res. **A245**, 230 (1986).

Preparation of Gd and Cd targets at Texas A&M University

T. A. Werke, D. A. Mayorov, M. M. Frey, and C. M. Folden III

Accelerator-based experiments in the Heavy Elements Group have required the preparation of thin targets of lanthanide elements. Targets of $^{156,157,158,160}Gd_2O_3$ and ^{nat}CdO were prepared in the last year using the Molecular Plating (MP) technique [1,2]. The Gd_2O_3 samples were prepared by dissolving ~1 mg of Gd_2O_3 in 2 M HNO_3 and evaporating to dryness under Ar gas. Each sample was then reconstituted with 5-10 μL of 0.1 M HNO_3 and 10-12 mL of anhydrous isopropanol. The CdO samples were prepared via the same method except the starting material was ^{nat}Cd metal instead of the oxide. The body of the electroplating cell is made from PEEK [3]. A Pt disk was used as the anode, and a 2 μm Ti foil served as the cathode and the backing onto which the material was plated.

The deposition voltage was 600-700 V with a current density of ~2 mA/cm^2. Deposition times ranged from 30-60 min. After deposition, the targets were baked in air at 200 °C for 30-60 min to convert the material to the oxide. The resulting targets had thicknesses between 225-655 μg/cm^2 as determined by weighing. The plating efficiencies were between 50-100%. Gd_2O_3 targets were characterized using secondary ion mass spectrometry (SIMS) to determine isotopic enrichment. Results are summarized in Table I.

Table I. Deposition conditions and enrichments for various metal oxide targets.

Isotope	Voltage (V)	Time (min)	Thickness (μg/cm^2)	Isotopic Enrichment
$^{156}Gd_2O_3$	700	100	479	Not measured
$^{157}Gd_2O_3$	700	45	365	88.5 %
$^{158}Gd_2O_3$	700	40	655	91.8 %
$^{160}Gd_2O_3$	600	43	523	91.5 %
^{nat}CdO	700	30	363	N/A

Future beam experiments will use a rotating target wheel to allow for use of higher beam currents [4]. An electrochemical cell based on the designs of Haba *et al.* [5] has been constructed to make targets for the rotating wheel, and first results are reported here. A schematic of the cell is shown in Fig. 1. One arc-shaped target of $^{nat}Gd_2O_3$ has been fabricated as a proof-of-principle. The ^{nat}Gd sample was prepared as described above with enough isopropanol added to ensure the plating solution covered the entire arc.

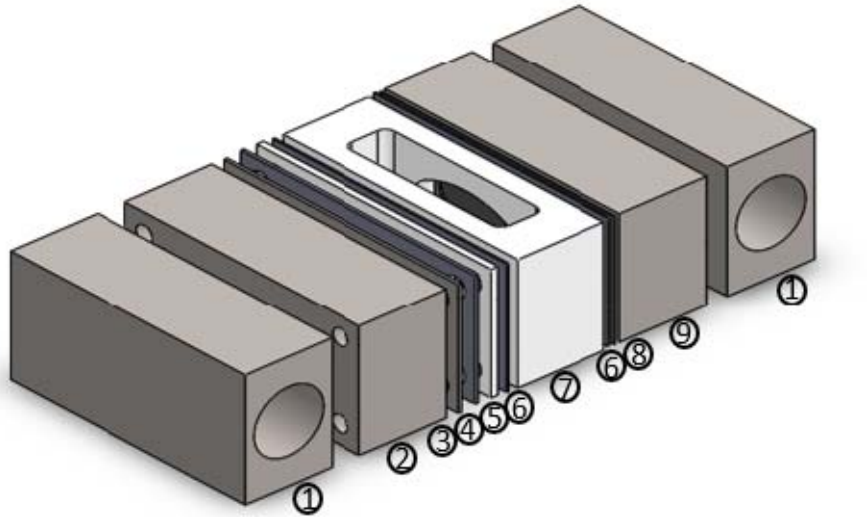

FIG. 1. Deposition cell for arc-shaped targets. (1) Ti Cooling Blocks, (2) Ti cathode, (3) Ti target frame, (4) 1.0 mm silicone seal, (5) 2.0 mm PEEK cover, (6) 0.6 mm silicon seal, (7) PEEK body, (8) 47 μm thick Pd anode, (9) Ti block.

The deposition was done for 60 min at 700 V. The resulting target is shown in Fig. 2. The thickness was 438 μg/cm^2 and the plating efficiency was 95%.

FIG. 2. Arc-shaped 438 μg/cm^2 $^{nat}Gd_2O_3$ target on 2 μm Ti backing.

[1] W. Parker and R. Falk, Nucl. Instrum. Methods **16**, 355 (1962).

[2] W. Parker *et al.*, Nucl. Instrum. Methods **26**, 61 (1964).

[3] D. Mayorov *et al.*, *Progress in Research*, Cyclotron Institute, Texas A&M University (2012-2013), p. II-7

[4] D. Mayorov *et al.*, *Progress in Research*, Cyclotron Institute, Texas A&M University (2013-2014), p. IV-50.

[5] H. Haba *et al.*, TASCA05 Workshop, http://www-win.gsi.de/tasca05/

Commissioning of a rotating wheel target for use in heavy element studies

D. A. Mayorov, L. D. Fields, and C. M. Folden III

To withstand the heat load of high intensity beams needed for production of heavy and superheavy elements, a specialized rotating wheel target system was developed [1]. The assembly was designed by Ferrotec Corporation and is shown in Figs. 1*a* and 1*b*. The assembly is mounted on an ISO200 flange, with a ferrofluidic seal dividing the in-air motor from the vacuum components it drives. The target wheel consists of three banana-shaped segments, each with an area of 4.7 cm^2. To avoid activating the target frame spokes, and reduce scattered beam background, a signal from an optical fiber probe tracking the target position triggers beam pulsing. A custom power supply panel was fabricated to power the Ethernet-based servo driver and motor.

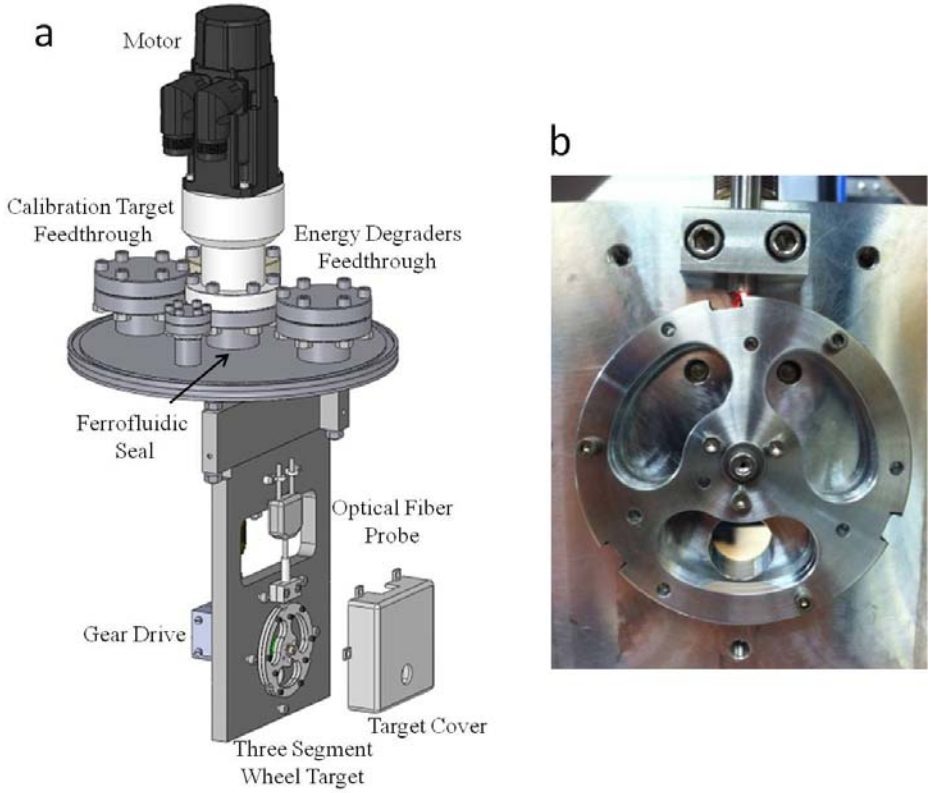

FIG. 1. (a) CAD drawing of rotating target wheel assembly, courtesy of Ferrotec Corp. (b) Image of the target wheel, with fiber optic probe positioned above and emitting a red light. The three notches serve as position markers to trigger beam pulsing.

The performance of the cyclotron and assembly to pulsing triggers was tested in an online experiment with a 15 MeV/u $^{20}Ne^{4+}$ beam (~500-1000 ions/s) delivered by the K500 cyclotron to the in-air station of the SEE-line cave. A ruggedized silicon detector, with an active area of 2.98 cm^2, was positioned behind the rotating wheel to record beam implantation events passing through the target

position. Using a NIM gate generator, the experimental set-up was first tested by varying pulsing time between 0.5 – 50 ms, accomplished by shifting the dee B phase angle by 13.2^{o}. It was determined that the K500 cyclotron is capable of pulsing the beam at frequencies of up to 250 Hz. Fig. 2a shows results for a 10 ms on / 10 ms off pulse time. Events beyond 20 ms are from missed beam-off triggers due to the substantial dead-time created by the high signal event rate; normal event rates in element production experiments are much lower.

The performance of the beam pulse trigger detected by the optical fiber probe was tested next. The target wheel was rotated at frequencies between 500 – 1700 rpm, in increments of ~250 rpm. Fig. 2b shows the result of that test for 1000 rpm. The fiber optic trigger is received as soon as the notch is seen by the optical fiber probe. The actual beam-off trigger is delayed just until the spoke between the target wedges enters the path of the beam. After another delay, a beam-on trigger follows. Both delays were calculated based on the wheel geometry and rotational frequency.

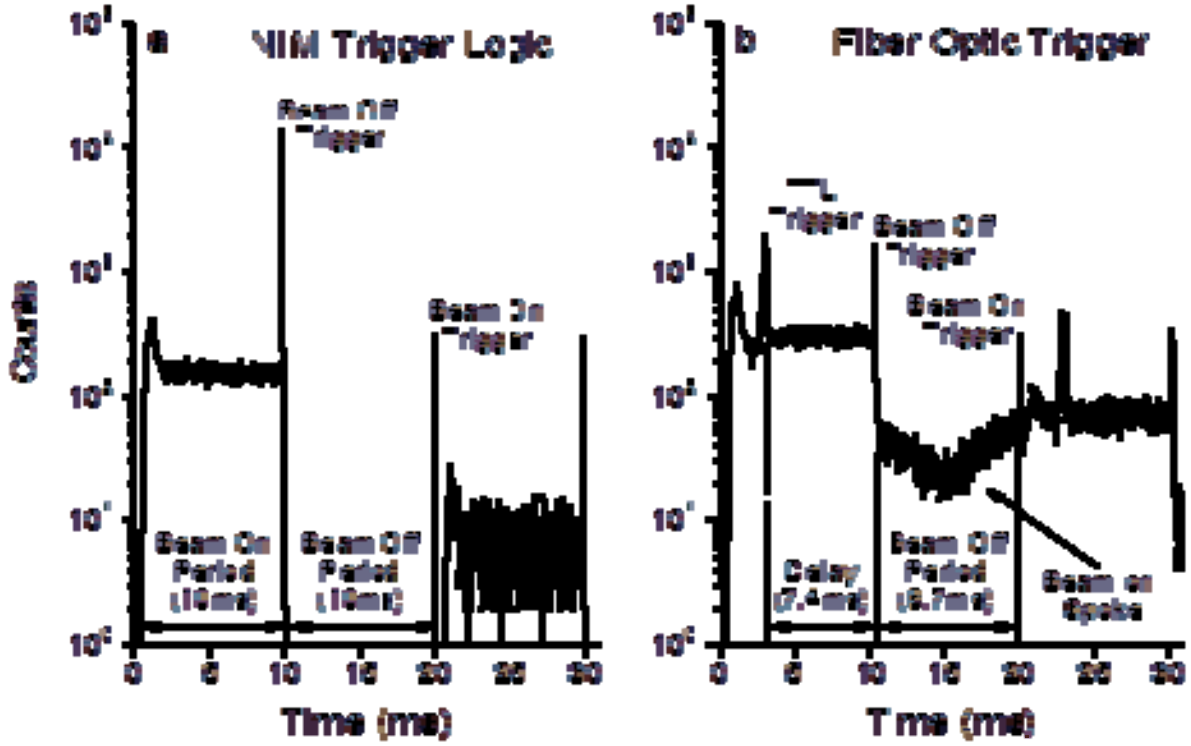

FIG. 2. (a) Beam implantation events with a 10 ms pulsing time triggered by a NIM gate generator. (b) Wheel target rotating at 1000 rpm. Beam-off triggers originate from notches on the wheel target (TTL trigger, see Figure 1b above). The time between the notch register and when the wheel spoke covers the beam path is the delay. The valley feature in the beam-off period is due to skipped beam-off triggers as discussed in the main text.

The performance of the system was overall satisfactory, with one drawback. The efficiency of the optical probe trigger was ~85%, suggesting a fault with either the analog (optical) input or digital (TTL pulse) output of the TTL signal generator. The presence of events in the beam-off window in Figure 2b is the result of this effect and the dip is from reduced event rate due to the spoke eclipsing the detector as it passed across the target position. Once this problem is addressed, the target wheel assembly should be

ready for use in heavy element production experiments. Preparation of specialized targets for use with the assembly is discussed in a separate contribution to this report [2].

[1] M.E. Bennett *et al.*, J. Radioanal. Nucl. Chem. **299**, 1107 (2013).
[2] T.A. Werke *et al.*, *Progress in Research*, Cyclotron Institute, Texas A&M University (2013-2014), p. IV-48.

Characterization of a gas stopper for heavy element chemistry studies

M. C. Alfonso, E. E. Tereshatov, D. A. Mayorov, T. A. Werke, and C. M. Folden III

The chemical and physical properties of the heaviest elements are of particular interest because relativistic effects increase as Z^2 (proton number). Transactinides (Z>103), elements where this effect is expected to be the largest, do not exist naturally and are produced via a fusion-evaporation reaction. The product of this reaction must be degraded down to sub-eV energies for a chemical study to be possible. Previous experiments have used a combination of degraders and a gas cell, also known as a Recoil Transfer Chamber (RTC), to degrade and transport the fusion-evaporation reaction product to the appropriate chemistry set-up. Here at Texas A&M University, a RTC has been fabricated (see Fig. 1); the design of the device is described in detail in [1]. A laminar gas flow and a series of electrodes that create a potential gradient guide the ions through the extraction nozzle to the aerosol chamber for transportation to a future chemistry experiment.

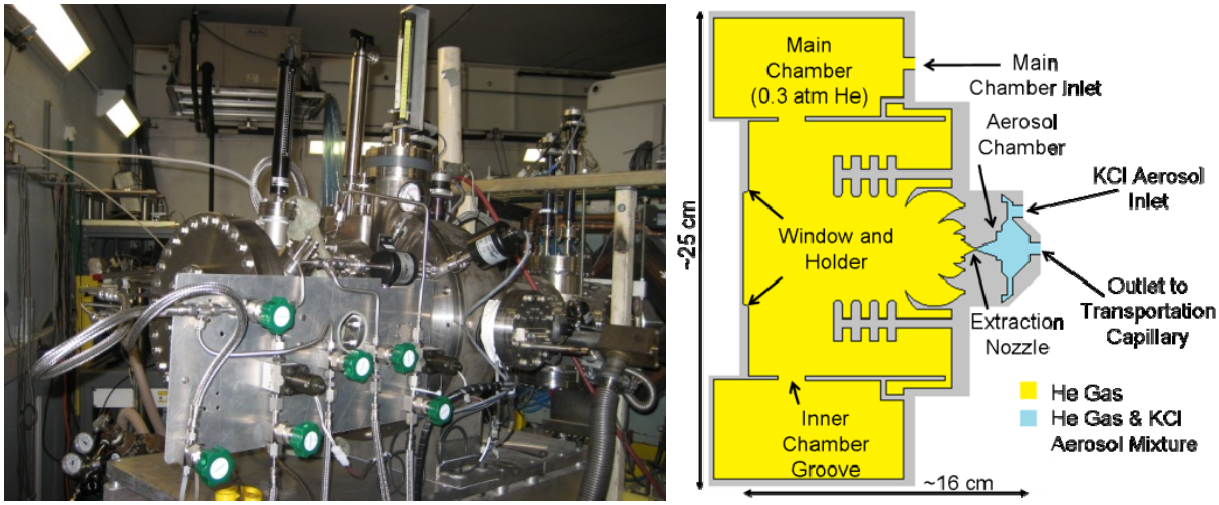

FIG. 1. Left: RTC attached to the end of the Momentum Achromat Recoil Spectrometer (MARS) beamline. Right: Schematic of the Texas A&M gas stopper.

The RTC was commissioned online using a high cross section fusion evaporation reaction, ^{118}Sn(^{40}Ar, 6n)^{152}Er, and preliminary results are presented here. A two-detector system was used to determine the extraction efficiency of the RTC; a detector was located directly after the RTC window and the extraction nozzle. Previous online experiments (see [2]) measured a peak extraction efficiency of approximately 40% with gas flow only (flow rate: 1.5-2.5 L/min). During an online experiment in March 2014, the potential gradient across the electrode system was optimized while the gas flow rate was held constant at 2.5 L/min. It was discovered that about a 22 V gradient across the entire device had the optimum extraction efficiency.

The angle of the rotating degrader upstream of the RTC window was then varied to better characterize the RTC extraction. The effective thickness of the rotating degrader increases with its angle, moving the stopped ^{152}Er distribution closer to the RTC window. Results for the extraction efficiency as

a function of degrader thickness are shown in Fig. 2. The RTC was run under two different modes during these measurements. One mode used only gas flow to transport the ions through the extraction nozzle, referred to as "gas flow only". The other mode used both gas flow and the optimum potential gradient across the electrode system to transport the ions through the extraction nozzle, referred to as "gas flow and electric field". The maximum measured extraction efficiencies are approximately 20% (gas flow only) and 35% (gas flow and electric field) (Fig. 2a). When the total degrader thickness was greater than 9 μm Mylar, ^{152}Er starts to "range-out" before reaching the end of the RTC window, and extraction efficiencies were corrected accordingly (Fig. 2b). The maximum "range-out" corrected extraction efficiencies are approximately 24% (gas flow only) and 43% (gas flow and electric field). The data suggest that ions thermalized too far into the device are defocused by the electric field, since extraction efficiency decreases with the addition of electric field at a degrader thickness less than 9 μm of Mylar. The difference in the centroid of the "gas flow only" results versus "gas flow and electric field" results implies that the gas flow works more effectively when the ions stop further into the RTC while the electric field works more effectively when the ions stop closer to the RTC window. Furthermore the broadening of the "gas flow and electric field" results, when corrected for "range-out", is evidence that the electric field can compensate when the ions stop too close to the window for the gas flow to be most effective.

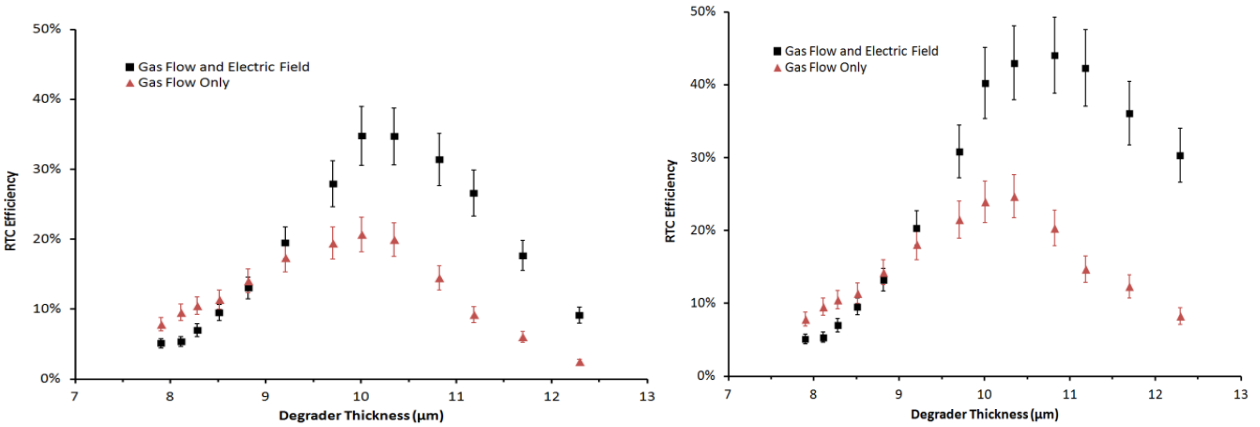

FIG. 2. Left: Extraction efficiency of the RTC as a function of the degrader thickness. Right: Extraction efficiency of the RTC as a function of the degrader thickness corrected for ions that "range-out" in the degraders. See main text for detailed discussion.

The transportation time of the device was determined to be 8.6 ± 1.0 s (gas flow only) and 6.9 ± 0.6 s (gas flow and electric field only), which is significant since the half life of ^{152}Er is 10.3 s. The extraction efficiencies corrected for decay loss were determined to be (44 ± 6)% (gas flow only) and (70 ± 9)% (gas flow and electric field). These extraction efficiencies are comparable to devices used worldwide [3-6]. Our device also has the advantage of a small emittance of the products exiting the extraction nozzle, and since this extraction efficiency can be achieved without the use of aerosols, a wider range of chemical systems can be studied using this RTC.

[1] M.C. Alfonso and C.M. Folden III, *Progress in Research*, Cyclotron Institute, Texas A&M University (2011-2012), p.II-46; http://cyclotron.tamu.edu/2012%20Progress%20Report/2%20Heavy%20Ion%20Reactions/II_46-51_development%20of%20a%20gas%20stopper.pdf.

[2] M.C. Alfonso *et al.*, *Progress in Research*, Cyclotron Institute, Texas A&M University (2012-2013), p.II-6; http://cyclotron.tamu.edu/2013%20Progress%20Report/2%20Heavy%20Ion%20Reactions/II_6_characterization%20of%20a%20gas%20stopper.pdf

[3] G. Savard *et al.*, Nucl. Instrum. Methods Phys. Res. **B204**, 582 (2003).

[4] M. Wada *et al.*, Nucl. Instrum. Methods Phys. Res. **B204**, 570 (2003).

[5] U.W. Kirbach *et al.*, Nucl. Instrum. Methods Phys. Res. **A484**, 587 (2002).

[6] L. Weissman *et al.*, Nucl. Phys. **A746**, 655c (2004).

Decay detector calibration and signal timing with oxford gas detector

J. Button, Y. Xu, Y. -W. Lui, and D. H. Youngblood

Introduction

The measurement of the GMR in unstable nuclei will be done using inverse kinematics, with a 40 MeV per nucleon beam of the unstable nucleus incident on a ^{6}Li target. Nuclei excited to the GMR region are particle unstable, and will decay by p, α or n decay shortly after excitation [1]. To reconstruct the event it is necessary to measure the energy and angle of the decay particle and of the residual heavy ion. In many lighter nuclei a few nucleons off stability, and in light proton rich nuclei, the neutron threshold is above the region of interest. There are 3 bodies in the final state (recoiling ^{6}Li, decay particle, and residual heavy ion). The recoiling ^{6}Li have low energy and for the most part will not get out of the target. Thus in order to experimentally determine the kinematics, we must measure at least three of the four quantities: decay particle energy and angle, and residual nucleus energy and angle. Thus a ΔE-ΔE-E decay detector composed of plastic scintillator arrays has been built and tested to measure the energy and angle of the light decay particle. The heavy ion will be measured using the Oxford detector in the MDM spectrometer. We have shown the viability of calibrating the decay detector components using the EDSE model for scintillator light output [2]. A hole in the decay detector with a horizontal and vertical opening of 4° allows the residual heavy-ion to enter the MDM spectrometer, which has a horizontal and vertical angular acceptance of ±2^{o}. The heavy-ions energy and angle will be determined with the focal plane detector. The decay detector can measure decay particles within an angular range of 4° to 45° with respect to the beam direction.

In November 2013 run we used a 30 MeV proton beam on a 12C target to obtain an energy loss calibration for the decay detector. Also, we used a 12 MeV/u beam of 16O on 12C target looking at α particles in the decay detector and 12C ions in the gas detector to determine the timing between signals from the gas detector at the back of the MDM spectrometer and the decay detector which is in the target chamber.

Decay Detector Calibration

We have tested the decay detector with a beam of 30 MeV protons scattered from a ^{12}C target. From the elastic scattering and inelastic scattering exciting the 2^{+} (4.4 MeV) and 3^{-} (9.6 MeV) levels of ^{12}C, we were able to find a good set of EDSE fit parameters (ρ_q, A, F) [3] which are intrinsic to the type of plastic scintillator used in all three layers of the detector. The last parameter, the normalization constant C, differs between all the strips and varies slightly according to the attenuation behavior along the length of each strip. Therefore, it is necessary to find the normalization constant C for ΔE1, ΔE2, and E of all segments of the decay detector. Fig. 1 shows the behavior of C for one of the vertical strips for signals coincident with each horizontal strip. It also shows the change in this behavior from experiment to experiment. Fig. 2 shows a comparison of the expected light output calculated from the EDSE model with the measure light output.

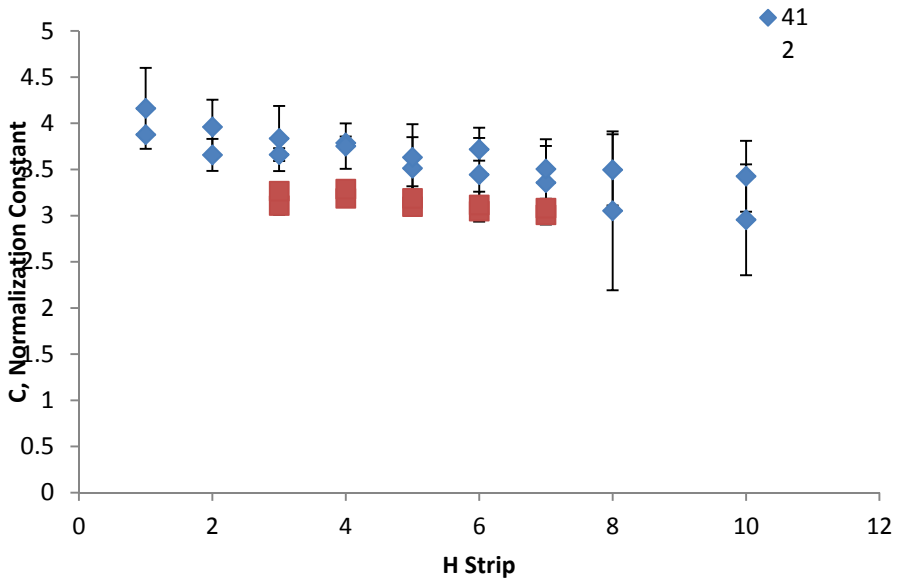

FIG. 1. Normalization constant for pixels on the V11 strip in coincidence with different horizontal strips (H Strip) for experiments done in April 2012 (412) and January 2013 (113).

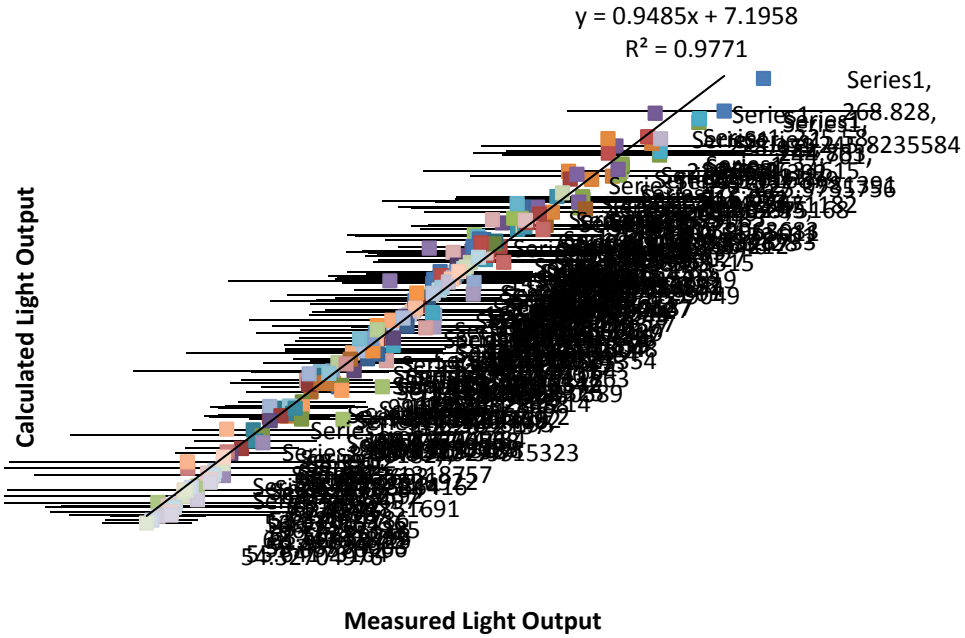

FIG. 2. Example of measured and calculated light outputs for all pixels along vertical strips due to incident protons. A linear fit shows that the measured and calculated light outputs are in good agreement. The parameters obtained by chi-square fits have the values ρ_q = 663.1 MeV/nm, F = .990, and A = 4.6×10^{-6}.

A full calibration before each production run will use proton and alpha energies near the top and bottom of the required range, such as 20 and 60 MeV for protons and 60 and 100 MeV for alphas.

Timing between Coincident Events

Using a 12 MeV/u beam of ^{16}O on a ^{12}C target, we wanted to establish a working method for identifying coincident events due to some proton or alpha decay in both the decay detector and the gas detector.

In the electronics setup, we use the ΔE2 layer as a trigger for the decay detector. And for the gas detector, the plastic scintillator in back is used as a trigger (Fig. 3). The time of flight of the heavy ion through the MDM spectrometer is approximately 250 nanoseconds.

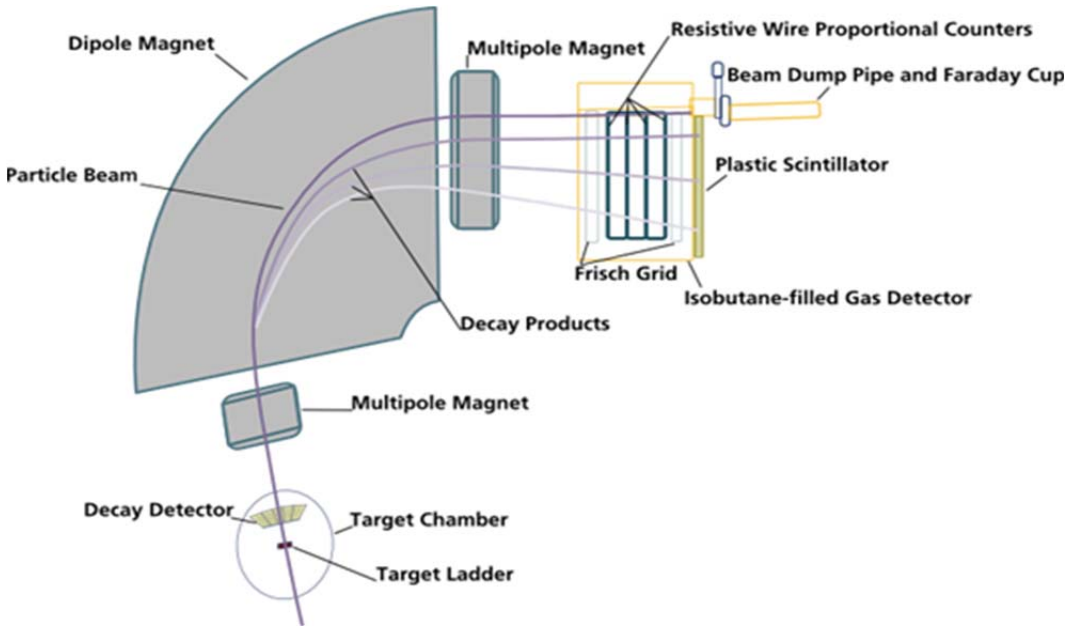

FIG. 3. Diagram of the experimental layout. The deltaE2 layer of the decay detector in the target chamber is used as a trigger to gate events from the decay detector and gas detector.

Starting with the trigger from the decay detector and stopping with the trigger from the gas detector, the time difference between the two triggers is measured by a Time-to-Amplitude Convertor (TAC) and is shown in Fig. 4. Peaks of equal height seemed to be spaced evenly at roughly 50 ns and to be coincident with the cyclotron RF. The primary peak at 300 ns corresponds with the calculated delay between the two triggers and is interpreted to be the true coincident events. To illustrate this, the two-dimensional E vs. ΔE spectrum (Fig. 5) from the gas detector is shown for all gated events (blue) and events coincident with the primary peak around 300 ns from the TAC spectrum (red).

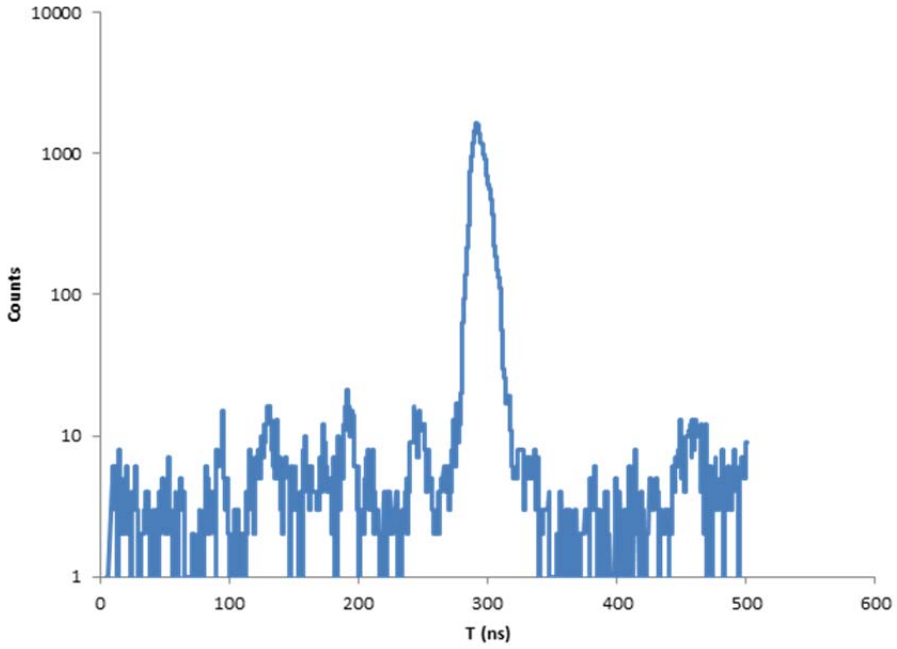

FIG. 4. TAC spectrum for timing between signals from the decay detector and the gas detector. The ΔE2 layer from the decay detector starts the TAC, and the plastic scintillator at the back of the gas detector stops it.

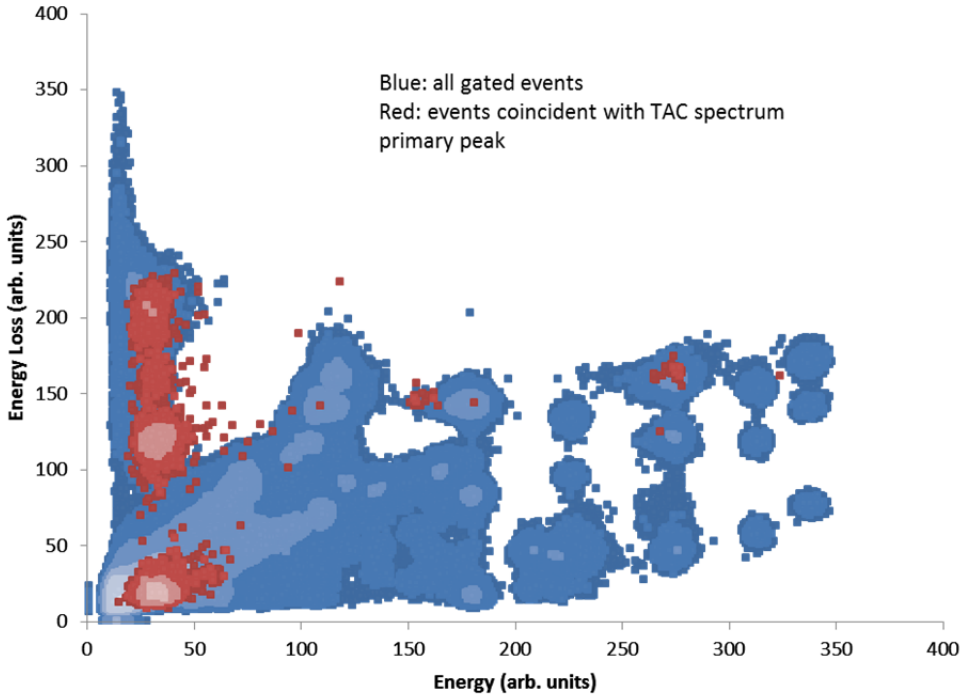

FIG. 5. Energy vs. Energy Loss signal from Oxford gas detector for all gated events (blue) and events coincident with primary peak from the TAC spectrum (red).

[1] Y. Toba, Y.-W. Lui, D.H. Youngblood, U. Garg, P. Grabmayr, K. Knöpfle, H. Riedesel, and G. Wagner, Phys. Rev. C **41**, 1417 (1990).
[2] J. Button, M.S. Thesis, Texas A&M University, 2013.
[3] K. Michaelian, A. Menchaca-Rocha, and E. Belmont-Moreno, Nucl. Instrum. Methods Phys. Res. **A356**, 297 (1995).

Construction of active target detector for experiments with rare isotope beams

G. V. Rogachev, E. Koshchiy, and E. Pollacco[1]
[1]*IRFU, CEA Saclay, Gif-Sur-Yvette, France*

Over the last 20-30 years experiments with rare isotope beams (RIBs) developed from being exotic undertakings in select few laboratories into the main stream of nuclear science. RIBs provide a pathway to venture far beyond the constrains typically encountered in the experiments with stable beams. RIBs open up an opportunity to study very exotic nuclei using relatively simple and well understood reactions, such as elastic and inelastic scattering, one/two nucleon transfer, Coulomb excitation, etc. They allow to measure the key reaction rates that are relevant for explosive processes in astrophysics with radioactive nuclei. All these benefits come at a price. Typical intensity of RIBs is many orders of magnitude lower than intensity of stable beams. Therefore, efficiency of experimental setup becomes determining factor for RIBs experiments. One of the most efficient experimental approach that can be used with RIBs is active target detector. These detectors can be designed to have almost 4π solid angle coverage, and they naturally allow to use thick target without loss of energy resolution. Thick target also allows to measure reaction excitation functions without need to change the beam energy. The versatility of these devises for RIBs experiments has been recognized and many nuclear physics laboratories around the world are in the process of constructing and using these devices (TACTIC at U of York/TRIUMF [1], MAYA at GANIL/TRIUMF [2], AT-TPC at NSCL [3], ACTAR at GANIL/GSI [4], ANASEN at FSU/LSU/NSCL [5,6], and others). While the concept is similar for all active target detectors (the target material is spatially extended and "active" to allow for tracking of the reaction products), the specific implementation may be very different depending on the energy range, type and quality of RIBs characteristic for the particular facility.

We started design and construction of a general purpose active target detector (Texas Active Target, TexAT) for experiments with rare isotope beams produced by either MARS separator or the new reaccelerated beams facility at the Cyclotron Institute. TexAT will be used for wide variety of experiments to detect the charged products of nuclear reactions with rare isotope beams. Resonance elastic and inelastic scattering of protons and α-particles, (α,p) and (p,α) reactions, nucleon-transfer reactions, such as (d,p), (d,3He), (p,d), (p,t), (4He,t) and decay spectroscopy studies are the examples of the experiments that can be performed with TexAT.

The initial step is a construction of two prototype active target detectors that consist of Time Projection Chambers for tracking of the recoils and the segmented silicon detectors backed by CsI(Tl) scintillators for measuring total energy of the recoils and providing a trigger. The silicon part is identical for both prototypes. The prototype active target detectors (TexAT-P1 and TexAT-P2) are needed for testing and development on a smaller scale technologies that will be used for the TexAT. The prototype detectors will also be used for conducting experiments with rare isotope beams at the Cyclotron Institute before the completion of TexAT.

The TexAT-P1 (Fig. 1) is the early implementation of active target approach at the Cyclotron Institute. The conventional technologies are used for the Time Projection Chamber of TexAT-P1. The

readout is performed by an array of position sensitive proportional counter wires located 6 cm below the reaction plane. The ionization electrons from the tracks of the recoils are projected onto the plane of readout wires by a set of field electrodes that are arranged to create a uniform electric field (the top "cathode" electrode is shown transparent). The trigger is provided by the hit in the silicon array. All major components of the TexAT-P1 have been procured or already assembled. The first experimental campaign with TexAT-P1 is planned for summer of 2014.

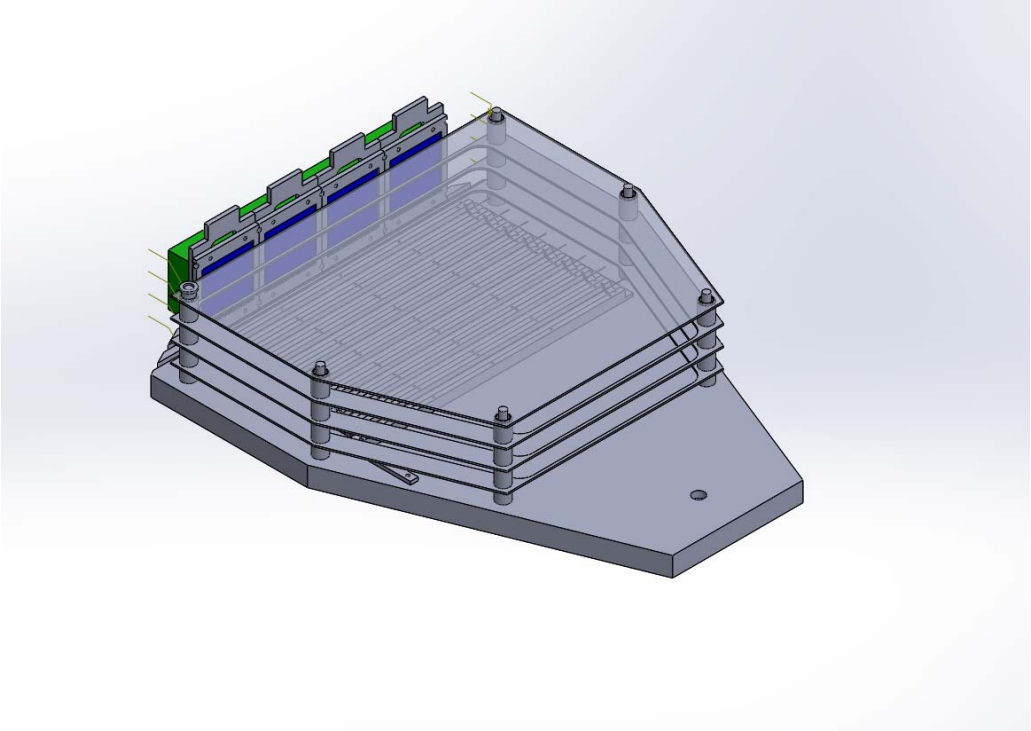

FIG. 1. Prototype of active target detector TexAT-P1.

The TexAT-P2 (Fig. 2) shares the silicon (shown in blue on both figures) and CsI(Tl) (shown in green) array with TexAT-P1 but will use different technology for the Time Projection Chamber (TPC). The wires will be replaced with the Micromegas [7] plate with 1024 independent channels (shown in red and yellow). This will improve tracking resolution and will enhance the performance of the prototype detector significantly, which will make the detector far more versatile. However, the number of readout channels required for this modification make it prohibitively expensive to use conventional electronics. Arrangements were made to procure a novel GET technology electronics [8] for the TexAT-P2. The components of GET electronics are the following. The AGET chips (64 independent channels each) provide preamplifier, shaper, TFA and CFD for each channel. They are placed on AsAd 2.1 PC boards that can accommodate 4 AGETs and provide the basic interface. Each AsAd board accommodates 256 channels. The CoBo card provides higher level interface between the AsAd and the MUTANT cards. The MUTANT card is used to produce a complex, hit pattern based trigger. The complete system of 1024 channels has a price tag of ~$80,000, compared to ~$1,000,000 for 1024 channels of conventional

electronics. The channel density of microMegas plate will not be uniform, with highest density (768 channels) reserved for the beam axis area (shown in yellow in Fig. 2). Important advantage of the TexAT-P2 over the TexAT-P1 is a much higher data throughput and a possibility to organize complex, hit pattern specific trigger that could be independent of the silicon array hit. All components of the GET electronics have been procured. Delivery time varies, but we expect the complete system to be operational by the end of 2014 - beginning of 2015.

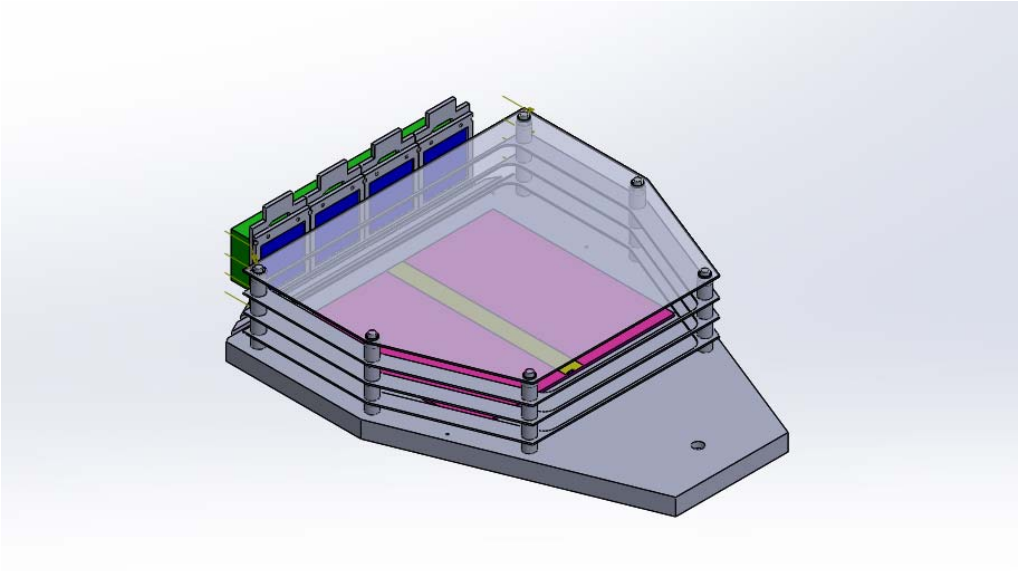

FIG. 2. Prototype of active target detector TexAT-P2.

[1] G. Ruprecht *et al.*, Europ. Phys. J. **A27**, 315 (2006).

[2] C.E. Demonchy *et al.*, Nucl. Instrum. Methods Phys. Res. **A583**, 341 (2007).

[3] D. Suzuki *et al.*, Nucl. Instrum. Methods Phys. Res. **A691**, 39 (2012).

[4] http://pro.ganil-spiral2.eu/spiral2/instrumentation/actar-tpc

[5] M. Matos *et al.*, Proc. of the 14th Int. Symp. On Capture Gamma-Ray Spectroscopy and Related Topics, Guelph, Ontario, Canada, August 2011 (World Scientific, Singapore, 2013), p. 481.

[6] G. Rogachev *et al.*, Prog. Of the 22nd Int. Conference on Application of Accelerators in Research and Industry (CAARI 2012), TMU-NP09-3.

[7] Y. Giomataris *et al.*, Nucl. Instrum. Methods Phys. Res. **A376**, 29 (1996).

[8] L. Pollacco *et al.*, Phys. Procedia, **37**, 1799 (2012).

FAUST upgrade for experimental proton-proton correlation functions

L. Heilborn, A. B. McIntosh, M. Youngs, K. Hagel, L. Bakhtiari, P. J. Cammarata, M. Chapman, J. Mabiala, L. W. May, A. Zarrella, and S. J. Yennello

The proton-proton correlation function has been predicted to be sensitive to the asymmetry energy of nuclear matter [1]. We plan to measure proton-proton correlation functions for reactions of 45 MeV/A ^{40}Ca, ^{40}Ar+^{58}Ni, ^{58}Fe at the Texas A&M Cyclotron Institute. The data will then be compared to Constrained Molecular Dynamics (CoMD) [2] results, for the purpose of investigating the impact of the asymmetry energy term of the equation-of-state on the shape and size of the correlation function. The FAUST (Forward Array Using Silicon Technology) array [3] of sixty-eight 2x2cm 300 μm thick Si backed by CsI(Tl)-photodiode detectors, arranged to geometrically accept the particles originating from the quasiprojectile (QP), or excited source resulting from the nuclear reaction, will be used for this experiment. The upgrade to enhance data collection for this purpose is described here.

A precise knowledge of the point of detection of the particles is essential when measuring a correlation function for a reaction, so improved angular resolution is of paramount importance [4]. In order to increase the angular resolution of charged-particle detection, the FAUST array is being upgraded using Dual-Axis Dual-Lateral (DADL) Si detectors [5]. The DADLs have uniform resistance across the front and back of the detectors and employ charge-splitting to determine the position of the detected light charged particles to within 200 μm.

Fig. 1 schematically shows the equipotential lines on the surface of a DADL detector. The uniform potential created by the reverse bias allows the holes or electrons to be collected on the opposite sides of the detector. Due to the resistive surface across each face of the detector, the holes on the back of the detector split proportionally to the two back signals, while the electrons are charge split proportionally

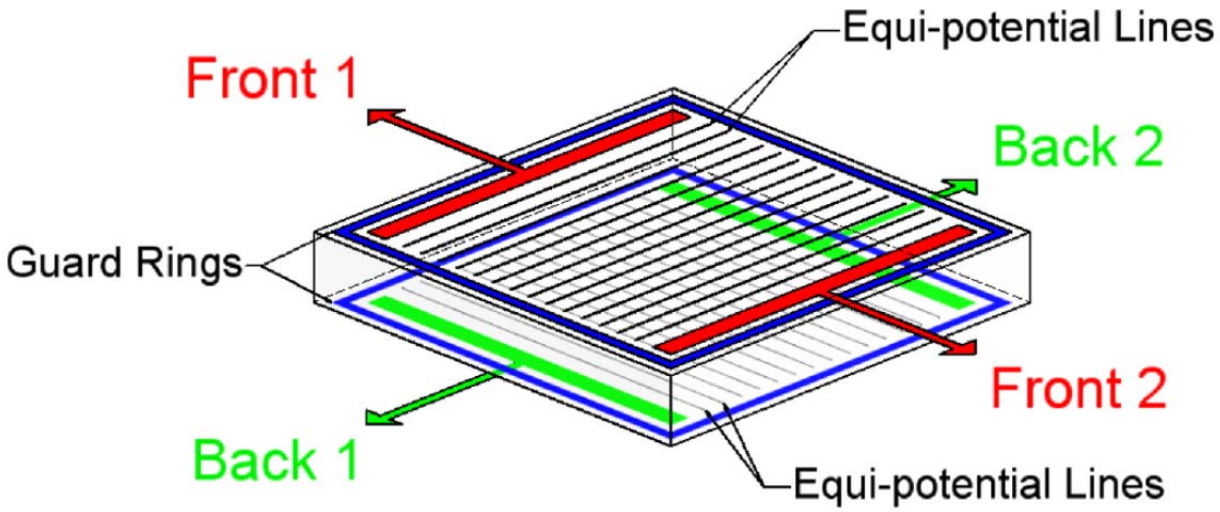

FIG. 1. Schematic of DADL, showing the equipotential lines on the uniformly resistive surface, which allows position to be determined by charge splitting [5].

to the two front signals. These four signals allow the relative x and y position of the detected fragment to be determined. Guard rings ensure a uniform potential across the entire surface of the detector [5].

In the first stage of the upgrade, the original silicon detectors of two of the five rings of FAUST have been replaced with position-sensitive DADLs. Particle identification and position information have been obtained using these 24 Si-CsI(Tl) telescopes, with newly developed software and electronics. Reactions of 15 MeV/A ^{4}He+^{64}Ni, ^{197}Au and ^{40}Ar+^{64}Ni, ^{197}Au were run, to see the results of elastically scattered α particles and light charged particle production, respectively, in the detectors. Protons and light charged particles produced in the reactions were measured in FAUST, with the help of the high-gain CSAs (charge sensitive amplifier), developed by RIS Corporation. The charge-splitting across the surface of the detector can result in a very small signal, which demands high-gain preamps. The total energy deposited in the Si wafer is determined by adding the two sides (Front 1 + Front 2 or Back 1 + Back 2). The separation of the LCPs is shown in a E-dE plot, derived from Si and CsI(Tl) signals, Fig. 2.

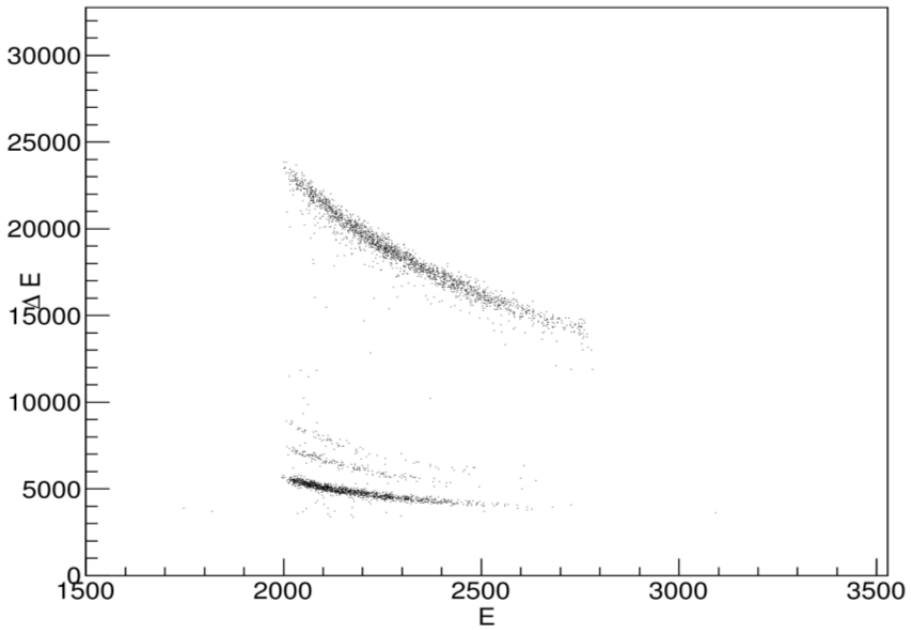

FIG. 2. Rough E-dE plot, shown here in ADC channel numbers from one of the detectors in Ring C for the reaction of 15 MeV/A α+ ^{197}Au, demonstrating the excellent p-d-t delineation using the new silicons and electronics from the FAUST upgrade.

The additional signals on each Si-CsI(Tl) telescope will result in an 150% increase in the number of channels processed, so Application-Specific Integrated Circuit (ASIC) Heavy Ion Nuclear Physics (HINP) chip electronics are used to deal with the increased number of signals. The necessary software and chipboards to accommodate this increase in signals have also been tested on-line during the recent test experiment. The biasing scheme has been scaled-up to accommodate 35% of the total array, and the

rest of the cabling and electronics will be designed in an analogous manner. The resultant position spectra for the DADLs installed can be seen in Fig. 3.

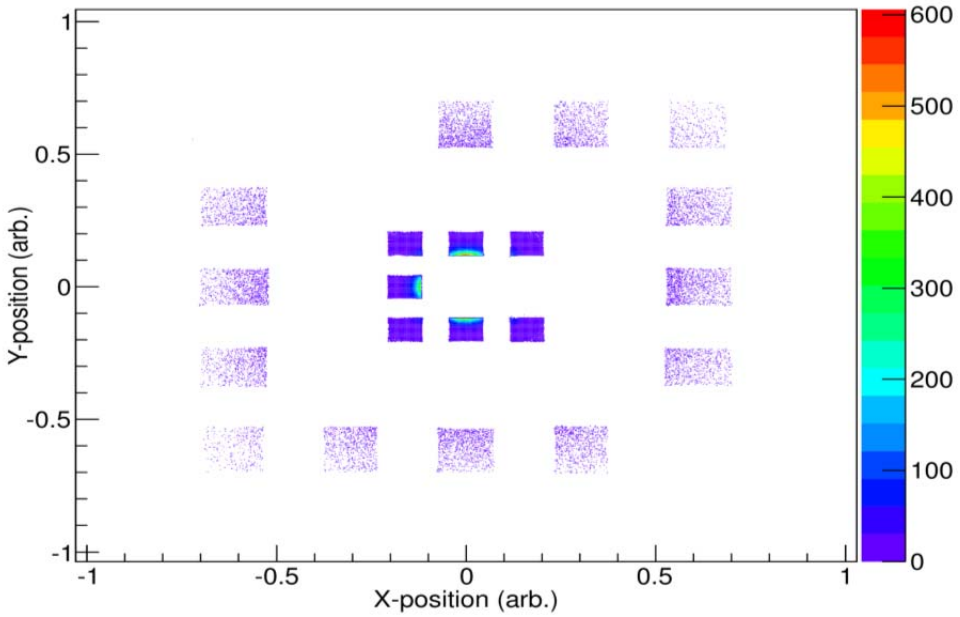

FIG. 3. Position spectra of detectors in rings A and C. The beam profile can be seen as the "hot spots" in Ring A (Innermost squares).

In addition to high positional accuracy of a detected particle, the relative alignment from one detector to another must be known. In order to calibrate relative detector position, a mask of 0.040" tungsten was designed and produced (design shown in Fig. 4). Slits of 0.010" were angled through the

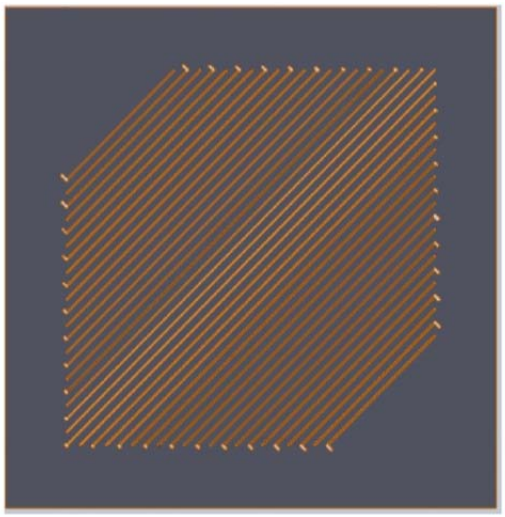

FIG. 4. SolidWorks drawing of mask, designed to position-calibrate all of the detectors in the FAUST array.

mask, in order to allow α particles from a well-collimated source or elastically scattered off of a gold target to reach each ring of FAUST. To prevent the large beam spot from scattering elastic alpha particles effectively around the slits in the mask, an aluminum collimator was used to reduce the beam spot to 1 mm. The square cut through the center (see Fig. 5) allows the beam to pass through, reducing beam

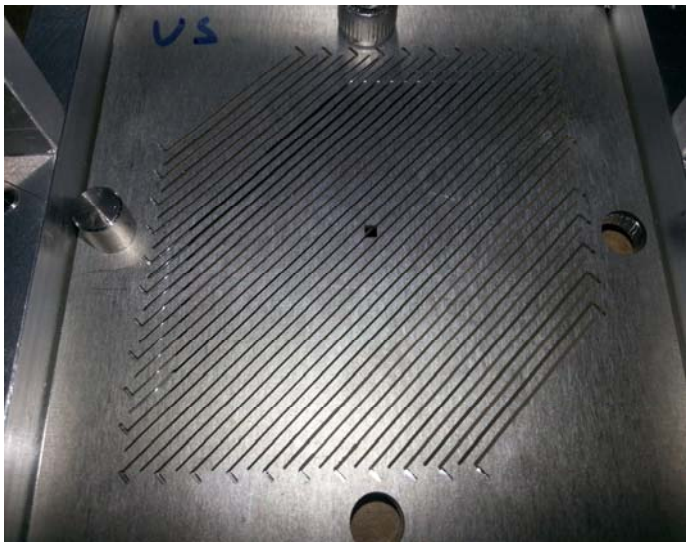

FIG. 5. Mask as machined by sinker and wire EDM at Reliable EDM. Square hole in the center allows the beam to pass through the mask, and deposit into a Faraday Cup after the FAUST array**.**

particle reactions with the tungsten mask. By gating on the collimated alpha particles elastically scattered from a gold target, the resultant pattern is shown in Fig. 6. The stripes from the mask can also be seen on the face of the detectors using a 228Th source, as shown in Fig. 7.

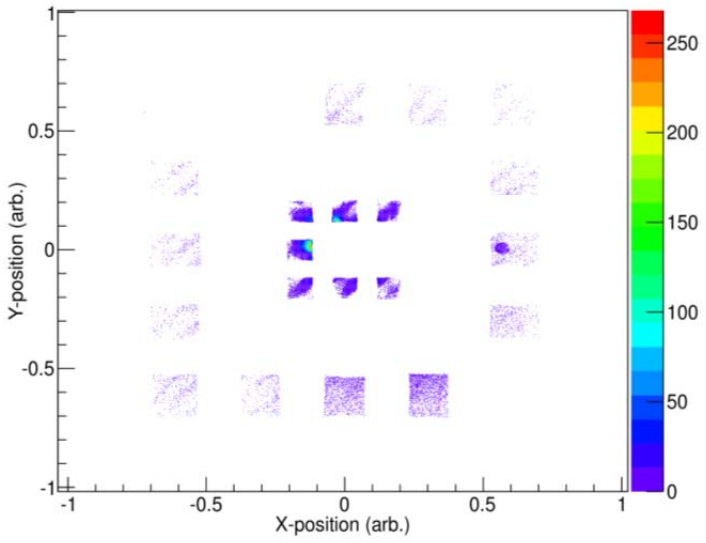

FIG. 6. Position spectra of elastically-scattered collimated 15 MeV/A α beam on the detectors in rings A and C, on ^{nat}Au target, through the W mask.

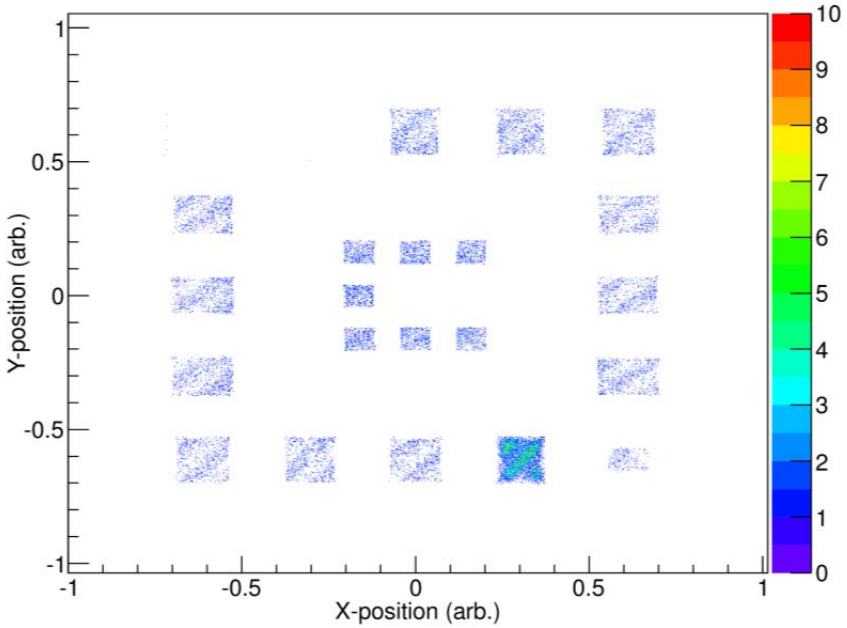

FIG. 7. Position spectra of highest-energy α from ^{228}Th on detectors in rings A and C, through the W mask.

Based on the successful test runs with the upgraded Si detectors, excellent PID and position resolution are expected to be achieved. The actual experiment with the completely upgraded array will allow the correlation function to be extracted from the 45 MeV/A ^{40}Ca, ^{40}Ar+^{58}Ni, ^{58}Fe reactions with different density-dependencies of the asymmetry energy in CoMD and iBUU simulations of the same reactions. For comparison between experimental data and results from simulations (CoMD and iBUU), a software filter of the geometric and energy acceptance of the FAUST array will be used event-by-event. The same data analysis performed upon the experimental results can then be compared to the simulations.

[1] L.W. Chen, V. Greco, C.M. Ko, and B.A. Li, Phys. Rev. Lett. **90**, 162701 (2003).

[2] M. Papa, G. Giuliani, and A. Bonasera, J. Comp. Phys. **208**, 403 (2005), ISSN 0021-9991, http://www. sciencedirect.com/science/article/pii/S0021999105000847.

[3] F. Gimeno-Nogues *et al.*, Nucl. Instrum. Methods Phys. Res. **A399**, 94 (1997), ISSN 0168-9002, http://www.sciencedirect.com/science/article/ pii/S0168900297009236.

[4] G. Verde *et al.*, Eur. Phys. J. A **30**, 81 (2006).

[5] S. Soisson *et al.*, Nucl. Instrum. Methods Phys. Res. **A613**, 240 (2010).

Design, fabrication and upgrades to the SPiRIT TPC target mechanism

A. B. McIntosh, C. Richers, M. Youngs, and S. J. Yennello

The SPiRIT TPC is a newly constructed Time Projection Chamber to be used to place constraints on the symmetry energy at high density. The symmetry energy impacts nucleosynthesis, properties of neutron stars, and mechanisms of heavy ion collisions. After two decades of active research, headway on the low-density behavior has been made; the behavior at high density is still largely unconstrained. Through measurements of charged pions and light charged particles produced in collisions of exotic tin isotopes at and above 200MeV/nucleon, the SPiRIT TPC (SAMURAI PIon Reconstruction and Ion Tracker, to be installed in the SAMURAI dipole magnet at RIKEN) can add constraints to the high density behavior of the symmetry energy and constrain the neutron and proton effective masses through yield ratios as well as directed flow of the light particles.

The SPiRIT TPC (formerly referred to as the SAMURAI TPC) was designed at TAMU, with significant contributions from Michigan State University. Fabrication at both institutions over the previous three years is now largely complete. Coupled with efforts at MSU and RIKEN on the electronics, the TPC has recorded tracks of cosmic rays passing through the detector.

The target mechanism for the TPC was subsequently designed and fabricated at TAMU. The requirements, listed below, largely overlap with the TPC overall:

- Made entirely of non-magnetic materials
- Avoid materials that could poison the detector gas of the TPC (such as silicone and halogen-containing compounds)
- Provide a wide range of motion to maximize the number of target positions
- Maximum target diameter of 3cm to accommodate exotic beams at RIKEN
- Allow the target ladder itself to hold a high voltage due to proximity to field cage, while maximizing the distance of the non-biased portion of the assembly from the field cage to avoid discharging
- Avoid blocking the UV laser beams used for position calibration
- External control of the target ladder, even when in a high magnetic field
- Position readout of the target ladder

Fig. 1 shows the 3D design of the assembly in Autodesk Inventor. The target ladder frames (yellow) are held to the target ladder (black). These parts are isolated electrically from the rest of the mechanism with insulating standoffs so that high voltage can be applied. The ladder is attached to a carriage (tan and green assembly) that can slide along one axis of motion, with low-friction plastic bearings sliding along two parallel ceramic-coated rails (dark gray). The lead screw (yellow) and bronze nut are used to transfer rotary motion to translational motion of the carriage and ladder. The rotary motion need to turn the lead screw is transferred via a series of brass miter gears, a telescoping U-Joint, and a hermetic rotary feed-thru from Kurt J. Lesker. The wire used to connect the ladder to the high voltage supply cable was coiled to accommodate the motion of the ladder and minimize sagging of the wire. The position of the ladder is determined using a specialty 500mm linear potentiometer made by ETI Systems.

Low DC voltage is applied to the two ends, and a sliding contact attached to the moving carriage allows a voltage measurement to provide position information.

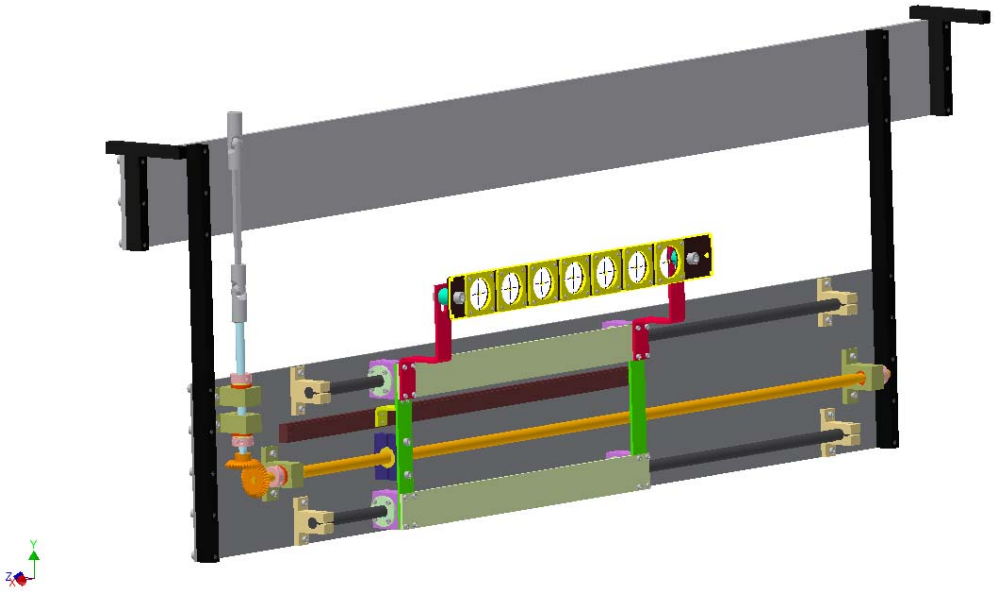

FIG. 1. Target Mechanism for SPiRIT TPC drawn in Autodesk Inventor.

The target mechanism was fabricated at TAMU. Potentially magnetic materials were tested for response to a 0.1T magnetic field produced by the TAMU K500 cyclotron main magnet (fringe field). Assembly and testing revealed quickly that it drives as designed and works well. Alignment can be accomplished by the following procedure: assemble all the parts, leaving the screws slightly loose. Slide the carriage back and forth, tightening the screws one by one while continuing to slide the carriage. Mild binding of the action can occur near one extreme of the range of motion due to the lead screw not being perfectly centered, but this only forfeits an inch of motion if properly aligned, and is not a significant problem. In air, high voltage was applied to the target ladder; up to 9kV applied before discharging to the air, which is a factor of four greater than is required. Discharge to other parts of the assembly did not occur.

The target mechanism assembly was mated with the SPiRIT TPC. Fig. 2 shows a photograph of the successful mating. The ladder can be assembled at the entrance window without damage to the field cage of the TPC. The ladder can be driven back and forth with minimal vibration in proximity to the field cage, and the coiled high-voltage wire does not present a discharge problem.

The external drive train of the target mechanism is designed and will be fabricated at TAMU. Figure 3 shows the 3D design of this assembly. It makes use of simple aluminum rods and custom right-angle enclosed gearboxes from W.M. Berg that use only brass and aluminum components. This will be assembled and tested at RIKEN in the summer of 2014.

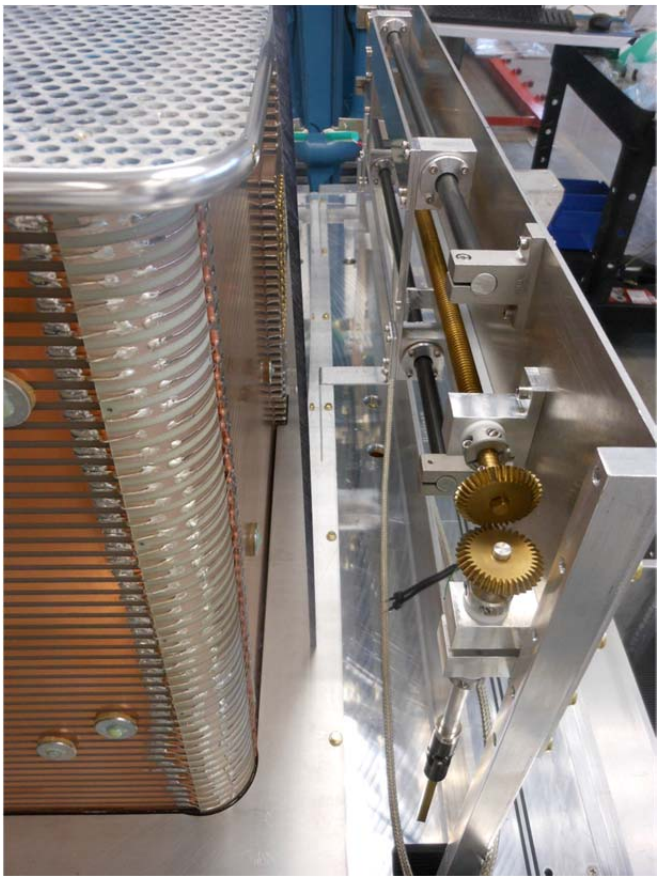

FIG. 2. Photograph of the SPiRIT Target Mechanism installed on the top plate of the SPiRIT TPC adjacent to the field cage.

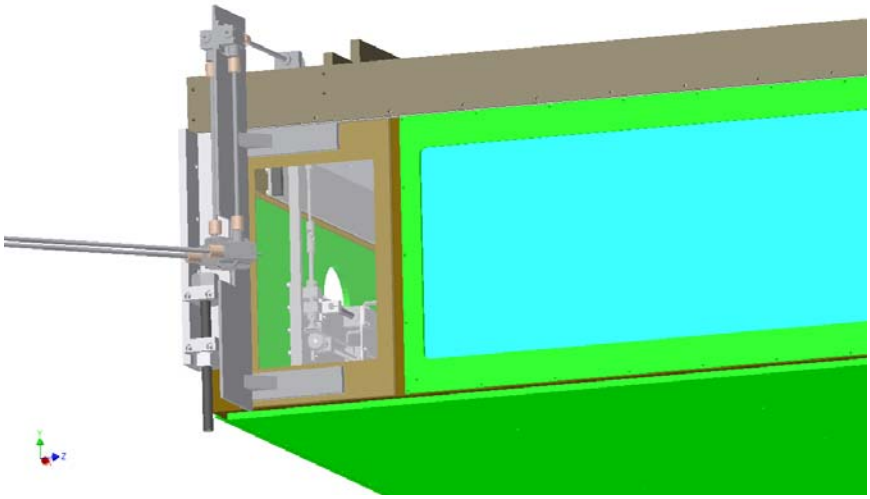

FIG. 3. Target Mechanism Extension drawn in Autodesk Inventor. The extension transfers the rotary motion from just outside the TPC to a location upstream that can be more easily accessed during an experiment.

Simple simulations have been performed to address whether the design can be modified to increase the acceptance of the TPC for mid-rapidity pions. A flat energy distribution up to 300MeV pion energy was sampled, with direction isotropic into 4π. The beam spot on target was assumed to be 2cm in diameter. The target was positioned at its current location with respect to the field cage entrance window; pions not passing through this window were rejected. The results of this simulation are shown in the left two panels of Figure 4, where the transverse momentum, p_t, is plotted as a function of rapidity in the lab frame (top) and the center of momentum frame (bottom). In the lab frame, particles going forward of roughly 45 degrees are accepted. This is due to the size of the entrance window and the proximity of the target. The curve in the line is due to the nature of the relation between rapidity and p_t for relativistic particles. The abrupt drop in intensity at high energy is merely due to the choice of 300MeV as the maximum energy in the Monte Carlo simulation. In the center of momentum frame (lower left), this same data shows that only pions with very low p_t will be measureable at mid-rapidity due to the geometry. To measure high p_t pions, one needs to select pions with a rapidity of at least 0.2 to 0.3. Since mid-rapidity pions with high p_t are predicted to be the most sensitive to the forces in the high-density region of the collision and thus to the symmetry energy, it may be beneficial to move the target closer to the entrance window to increase the geometric coverage of the pions. Theoretically, it should be possible to move the target by 0.632" from its current distance of 1.248" from the window. If this can be realized, we would increase our coverage significantly, as shown by the distributions in the right panels of Fig. 4. The slope

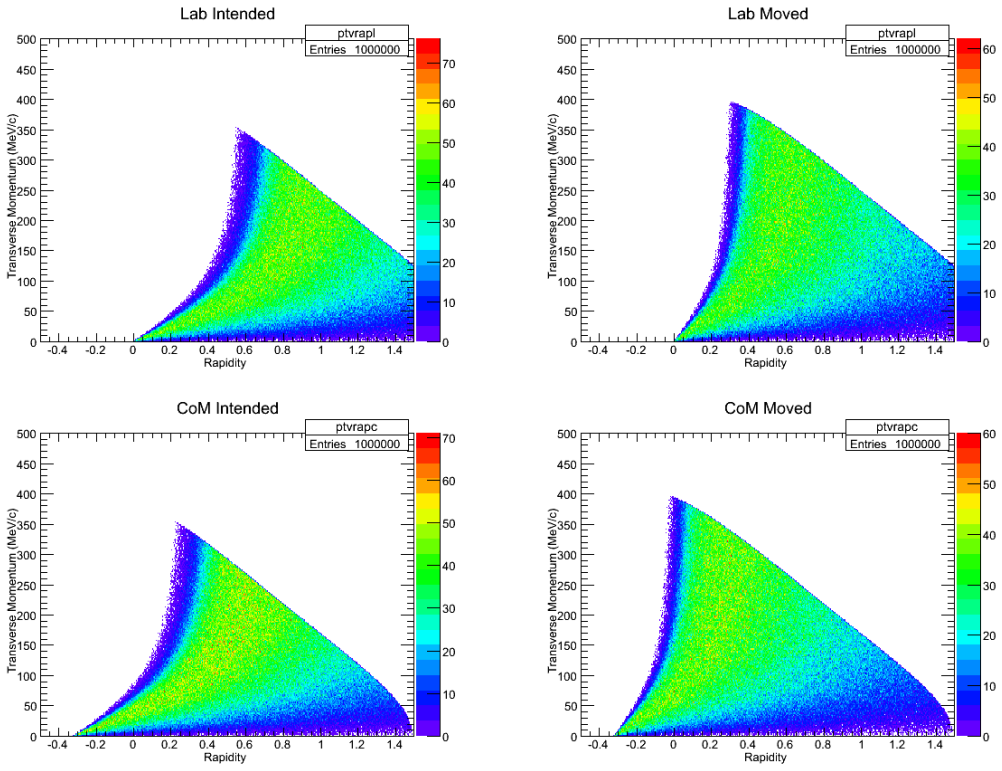

FIG. 4. Simple simulation of the phase space acceptance for pions accepted by the SPiRIT TPC for the current target position (left panels) and at the closest theoretically possible position (right) in the lab frame (top panels) and in the center of momentum frame (bottom panels).

of the cut-off from the angular acceptance is much steeper, and at mid-rapidity, there is significant yield out to high p_t, and high-statistics can be obtained from 0.0-0.2 in rapidity. An improvement to the target mechanism to allow the target to be positioned closer to the entrance window seems prudent. Possible solutions to hold the target closer to the window are being explored, including the possibility of adding a second axis of motion to the target mechanism.

The SPiRIT TPC will be installed in the SAMURAI magnet in the summer of 2014, including the insertion, lifting and alignment of the TPC, and the testing of the target mechanism. Concurrent with much of this work will be testing of the electronics and software development. This is in preparation for experiments expected to commence at SAMURAI in 2015.

Suitability study of the quadrupole triplet spectrometer (QTS) for selecting complete fusion residues in heavy ion collisions

A. B. McIntosh, L. Heilborn, M. Youngs, L. A. Bakhtiari, P. J. Cammarata, M. Chapman, K. Hagel, J. Mabiala, L. W. May, A. Zarrella, and S. J. Yennello

We have previously reported on observations of an asymmetry dependence of nuclear temperatures [1, 2, 3]. The experimental data used is a rich data set, but was not designed with this particular analysis in mind. There are two aspects of this measurement that one would like to improve. First and most important is the measurement of the free neutron multiplicity, which is the largest uncertainty in the measurement. Second, the reconstruction of quasi-projectile (QP) sources and the very strict selection on these sources allow only a very small fraction of the events into the analysis, increasing statistical error. Thus we propose to conduct an experiment that does not suffer these drawbacks, and will be poised to confirm or repudiate the temperature dependence of the caloric curve.

We intend to measure complete fusion of ^{64,70}Zn+^{12}C@15,25,35MeV/u. Light charged particles (LCPs) will be measured with the FAUST array, upgraded with the position-sensitive DADL [4, 5] detectors. To tag the events as fusion events, the heavy fusion residue would be measured via time-of-filght (TOF) and total energy. GEMINI and CoMD simulations have been performed [6] to investigate the suitability of the FAUST/QTS detector suite; the suite appears well suited to the measurement.

Previously, a Quadrupole Triplet has been re-commissioned as a focusing element for heavy reaction products at TAMU [7] for the reactions Xe,Sn+Ni@15MeV/u. The timing detectors in the device (PPACs) are expected to have more difficulty triggering on the small signals from lighter beams, and so plastic scintillators with photomultiplier tubes were added to the detector suite. The performance of the triplet was investigated with beams of ^{84}Kr@15,24.8MeV/u and ^{40}Ar@15,24.8MeV/u impinging on carbon targets; data of these beams as well as helium beams on nickel and gold targets was also obtained for testing the DADL upgrade of FAUST [8].

The QTS was able to focus all of these beams onto the downstream timing and energy detectors. The left panel of Fig. 1 shows the position of the elastically scattered (and stripped) beam as measured in the downstream PPAC for ^{84}Kr+^{12}C@24.8MeV/u after being focused by the QTS. By scaling the QTS power supply currents down to 80% of those used to focus the beam, the majority of the beam is defocussed. Impressively, a second set of ions can be focused by settings in the vicinity of 80%. This is illustrated in the right panel of Fig. 1. Here the outer ring corresponds largely to elastically scattered beam, while the inner spot corresponds to products with a lower BRho, such as the fusion residues of interest.

The PPACs were able to produce timing signals above the noise for the krypton beams at 15 and 24.8MeV/u, but not for the argon beams. Without significant improvement in the level of noise, this would not work for 35MeV/u Zn beams either. Though this should be possible, the use of the plastic scintillators seems best to more easily realize accurate timing signals. However, the use of PPACs for position information is still easily possible.

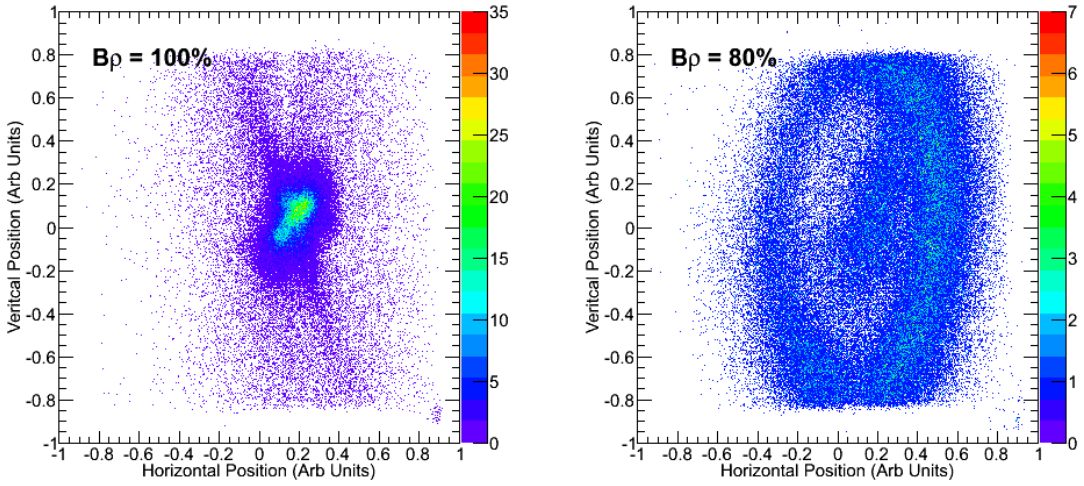

FIG. 1. Focus of heavy ions through the quadrupole triplet for reactions of ^{84}Kr@24.8MeV/u + C-nat. The left panel corresponds to the magnetic rigidity of the beam and the right panel to 80% of the rigidity of the beam. Similar focusing of beam and residues is observed in PPAC2 also for ^{84}Kr@15MeV/u and ^{40}Ar@15 and 24.8MeV/u.

The separation of products by the energy (y-axis) and TOF (x-axis, running backward) is shown in Fig. 2 for ^{84}Kr+^{12}C@5MeV/u. The upper peak corresponds to elastically scattered beam. Interestingly,

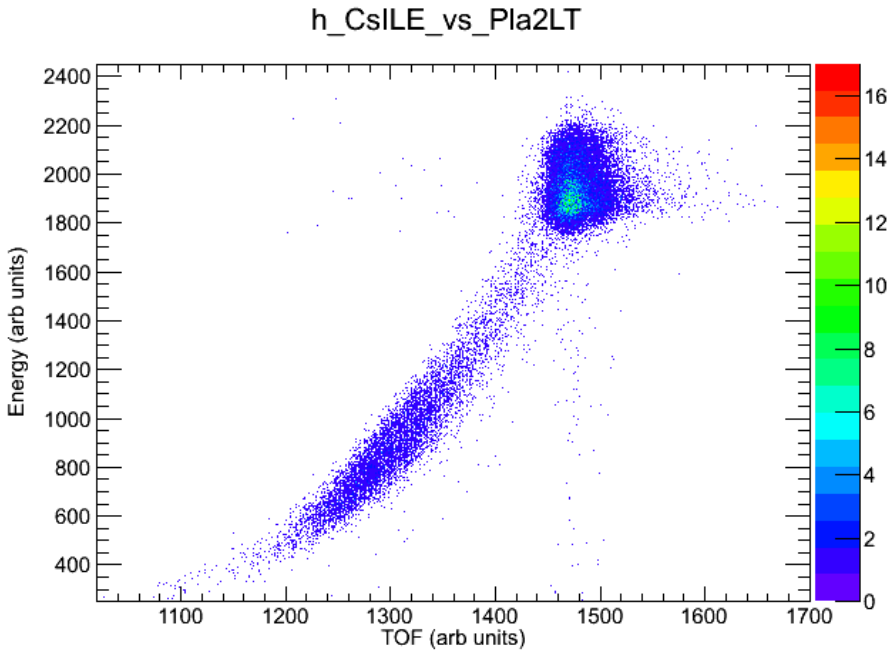

FIG. 2. Energy vs time-of-flight through the QTS for heavy products of ^{84}Kr@15MeV/u + C-nat. The magnetic field in the QTS is at 80% of what is necessary to focus the beam. The Energy is that measured in CsIL, and the TOF is started by Pla2L and stopped by PPAC1. The upper peak corresponds to beam particles and can be focused at BRho setting 100%. The lower band can be focused around 80% of the BRho of the beam as in Fig. 1.

the upper peak corresponds to particles that can be focused with a BRho of 100% (the beam), and to particles seen in the outer ring (as in Fig. 1, right panel), while the lower band corresponds to particles that can be focused with a BRho of 80% (is in Fig. 1 right panel). The band sweeping to lower energy and longer time may have two origins. This band is where the fusion residues would be located, but it is also possible that slit-scattered particles [9, 10] would lie in this band.

For subsequent experiments, both the QTS and rings A and C of FAUST were used. Though both arrays were working well independently, in any single given run, a very small number of coincidences were observed between FAUST and the QTS. There are several possible causes for the lack of coincidences. There may be a problem in the relative timing between the two electronic subsystems, which causes signals from the same physical event to be recorded in two separate data events. Another possible cause of the very low coincidence rate is a low live time of the data acquisition system. Still another possibility is that the probability for measuring these coincidences is low due to a combination of the acceptance angle of the triplet and the transport efficiency through the triplet. This needs to be investigated in detail.

These experiments have provided data that is useful as a guide to tuning the QTS to focus a desired BRho. The current settings required to focus each of the four beams (84Kr and 40Ar, each at 15 and 24.8MeV/u) were recorded. As shown in Fig. 3, the current required in each magnet increases linearly with the BRho of the (stripped) beam. A significant negative intercept exists for each magnet, suggesting a region of non-linear response at low current. Based on this data, we are able to say with confidence what power supplies will be necessary to focus beams of 70Zn@35MeV/u (BRho=2.04Tm). The supplies for Q26 and Q27 are adequate, while the supply for Q28 reaches a maximum current of 250A if wired in parallel, or 109A if wired in series. To focus particles with BRho=2.04Tm, 307A is required for Q28 if wired in parallel, or 54A if wired in series. Wiring in series is preferable, to minimize asymmetries in the magnetic field generated.

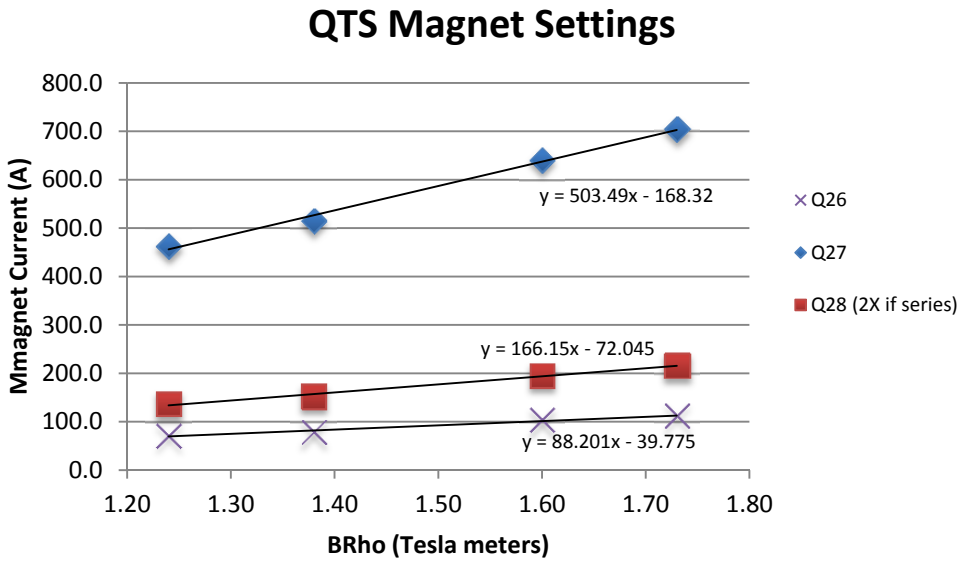

FIG. 3. Measured current setting for the QTS for four beams: 40Ar @ 15MeV/u (1.24Tm), 84Kr @ 15MeV/u (1.38Tm), 40Ar @ 24.8MeV/u (1.60Tm), and 84Kr @ 24.8MeV/u (1.73Tm). Q26, Q27 and Q28 refer to the three quadrupole magnets of the QTS. The magnetic field increases linearly with current; there is a large negative offset for all three magnets.

In summary, the QTS is capable of focusing quite well particles in the BRho region of interest for measuring complete fusion of Zn+C, though an upgraded power supply is required. The fusion residues likely can be well separated from the elastically scattered beam by the E-TOF technique. The main obstacles to be overcome are the low coincidence rate between FAUST and the QTS, and the large background of what may be slit-scattered particles in the region of the fusion residues.

[1] A.B. McIntosh *et al.*, Eur. Phys. J. A **50**, 35 (2014)

[2] A.B. McIntosh *et al.*, Phys. Rev. C **87**, 03467 (2013)

[3] A.B. McIntosh *et al.*, Phys. Lett. B **79**, 337 (2013).

[4] F. Gimeno-Nogues, Nucl. Instrum. Methods Phys. Res. **A399**, 94 (1997)

[5] S.N. Soisson *et al.*, Nucl. Instrum. Methods Phys. Res. **A613**, 240 (2010).

[6] A.B. McIntosh, FAUST/QTS Proposal, Internal Communication, TAMU-CI.

[7] P. Cammarata *et al.*, *Progress in Research*, Cyclotron Institute, Texas A&M University (2013-2014), p.IV-81.

[8] L.A. Heilborn *et al.*, *Progress in Research*, Cyclotron Institute, Texas A&M University (2013-2014), p.IV-64.

[9] E.D. Courant, Rev. Sci. Inst. **22**, 003 (1951).

[10] E.J. Burge and D.A. Smith, Rev. Sci. Inst. **33**, 37 (1962)

Pionic fusion at TAMU

A. Zarrella, A. Bonasera, P. Cammarata, L. Heilborn, J. Mabiala, L. W. May,
A. B. McIntosh, M. Youngs, and S. J. Yennello

Pionic fusion is the process by which two nuclei amalgamate during a collision and then cool by the exclusive emission of a pion. The resulting compound nucleus is left in or near its ground state [1]. The process requires that nearly all of the available kinetic and potential energy in the colliding system be concentrated into just a few degrees of freedom - the rest mass and kinetic energy of the emitted pion. Furthermore, the energy of the emitted pion is limited by the number of available final states of the fusion residue [2]. The combination of limited available energy and the extreme coherence required in the process ensures that the pionic fusion channel is greatly suppressed. Indeed, the measured pionic fusion cross sections range from hundreds of nanobarns for the lightest systems (He + He) to hundreds of picobarns as one moves to larger systems (A_{tot} = 6 - 24) [2-12].

Over this past year, forward progress has been made toward measuring cross sections of pionic fusion reactions using the Momentum Achromat Recoil Spectrometer (MARS) to measure pionic fusion residues. In August of 2013 a test experiment was conducted which aimed to identify pionic fusion reactions in the ^{12}C + ^{12}C reaction. GEANT4 simulations have been studied in an effort to identify a suitable "phoswich" (phosphor sandwich) detector construction for detecting and resolving charged pions. A phoswich is a charged particle detector made of a combination of scintillators with differing pulse shape characteristics which are optically coupled together and to a common photomultiplier tube. The parts for these phoswich detectors are fabricated and are being used in a test experiment starting May 23rd of this year.

The goal of the test run in August 2013 was to reproduce the ^{12}C + ^{12}C at 274.2 MeV measurements of Horn *et al.* [2] as a proof of concept for the detection of pionic fusion events using MARS. During the course of the experiment, MARS was tuned to look for both ^{24}Mg (π^0 emission channel) and ^{24}Na (π^+ emission channel) pionic fusion residues. Sixteen hours of data collection looking for ^{24}Na resulted in 5 counts inside the region of interest. A similar search for ^{24}Mg yielded no residues of interest. During this experiment, the beam intensity at the target location could not be measured and, as a result, it was impossible to perform a meaningful background measurement. Consequently, it cannot be determined whether the 5 counts of ^{24}Na are the result of pionic fusion reactions or background contamination. Moving forward, the decision has been made to switch to ^{4}He + ^{12}C pionic fusion reactions using a 220 MeV ^{4}He beam as these reactions have higher theoretical cross sections than those for the ^{12}C + ^{12}C system and the beam intensity from the K500 cyclotron will likely be higher for ^{4}He than for ^{12}C.

In addition to detecting the pionic fusion residues using MARS, the emitted charged pions from pionic fusion events will be detected using a phoswich detector array located in the MARS production chamber. A simulated phoswich unit has been built using GEANT4 in order to determine whether or not such a detector could be used to identify low energy charged pions. Fig. 1 shows a "fast vs. slow," dE-E plot produced by the GEANT phoswich. In most cases the pions (red points) are sufficiently separated

from the charged baryon (black points) and gamma interactions (green points). The neutron contamination (blue points), however, may pose a problem as they can be found throughout the pion response region. By requiring coincidence between the phoswich detectors and pionic fusion residues, the neutron contamination should be significantly reduced. The phoswich detector waveforms will also be recorded for pion-like events using a flash ADC. Analysis of these waveforms should also help to eliminate neutron contamination from charged pion events as the charged pions will deposit energy in both components of the phoswich while the neutrons will only deposit energy in one component, most likely the much thicker slow component. These two cases result in very different pulse shapes.

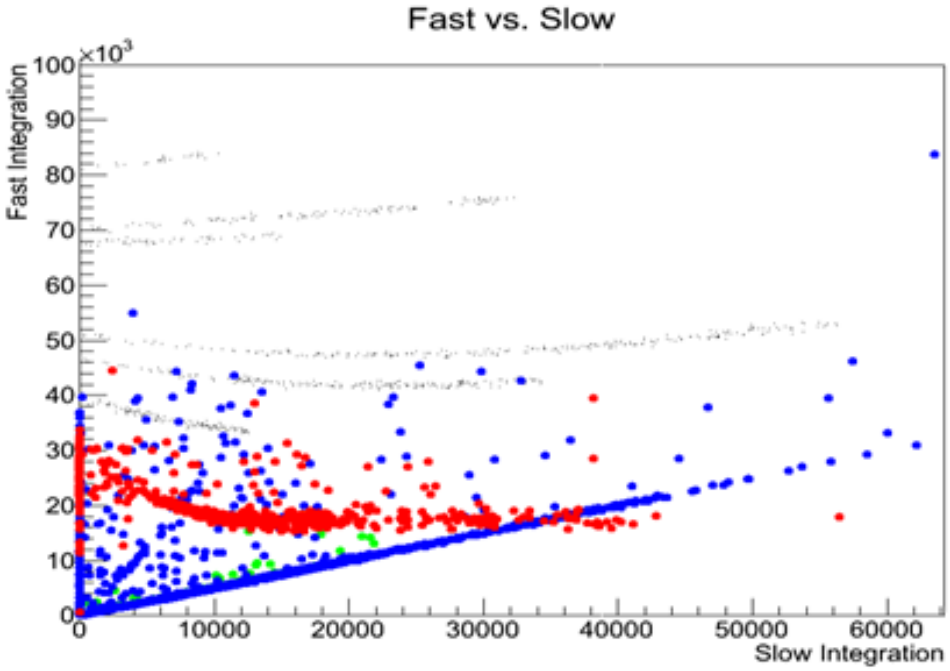

FIG. 1. A simulated "fast vs. slow" charge integration plot for different particle types interacting with a phoswich detector built using GEANT4. Pion hits (red points) are simulated along with charged baryon (black points), gamma (green points) and neutron (blue points) hits.

The MARS target chamber will be upgraded in order to accommodate the pion detector array. A cube feedthrough flange is being added in order to provide space for the many signal feedthroughs that will be necessary for the operation of the detectors. Existing flanges will also be outfitted with new feedthroughs. A test experiment will begin on May 23rd which will aim to measure the MARS transport efficiencies of the ^{16}O and ^{16}N residues of interest in the ^{4}He + ^{12}C pionic fusion reactions. Two phoswich detectors will be present in the production chamber for this test experiment in order to ensure sufficient detection efficiency of light charged particles. Construction of the phoswich array will begin after a successful test of the phoswich units in a beam experiment.

[1] P. Braun-Munzinger and J. Stachel. Ann. Rev. Nucl. Part. Sci. **37**, 97 (1987).

[2] D. Horn *et al*., Phys. Rev. Lett. **77**, 2408 (1996).
[3] Y. Le Bornec *et al*., Phys. Rev. Lett. **47**, 1870 (1981).
[4] L. Joulaeizadeh *et al.*, Phys. Lett. B **694**, 310 (2011).
[5] W. Schott *et al*., Phys. Rev. C **34**, 1406 (1986).
[6] M. Andersson *et al.*, Nucl. Phys. **A779**, 47 (2006).
[7] M. Andersson *et al.*, Phys. Lett. B **481**, 165 (2000).
[8] M. Andersson *et al.*, Phys. Scr. **T104**, 96 (2003).
[9] L. Bimbot *et al.*, Phys. Rev. C **30**, 739 (1984).
[10] L. Bimbot *et al.*, Phys. Lett. B **114**, 311 (1982).
[11] J. Homolka *et al.*, Phys. Rev. C **38**, 2686 (1988).
[12] N. Willis *et al.*, Phys. Lett. B **136**, 334 (1984).

Development and initial commissioning of the FAUST-QTS experimental beam line

P. Cammarata, A. B. McIntosh, M. B. Chapman, G. A. Souliotis, L. Bakthiari, S. Behling, G. Bonasera, L. A. Heilborn, K. Hagel, Z. Kohley, J. Mabiala, L. W. May, A. Raphelt, M. D. Youngs, A. Zarrella, and S. J. Yennello

The nuclear Equation-of-State (EoS) describes the thermodynamic properties from nuclei to neutron stars spanning a wide range of densities, temperatures and neutron-proton asymmetries [1–5]. Thus, the understanding of the EoS is important to understanding not only the reaction dynamics of heavy-ion collisions but also for describing astrophysical processes such as the formation of neutron stars and the dynamical collapse of supernovae [6–9] in addition to nuclear physics problems including understanding the structure of rare, exotic nuclei[10, 11]. Constraining the density dependence of the asymmetry energy (E_{sym}) [12–15], which describes how the EoS depends on the nucleon asymmetry of nuclear matter, $\frac{N-Z}{N+Z}$,can be probed via a number of sensitive observables. Many of these observables can been seen from heavy-ion collisions [13, 16–24], neutron skin thicknesses measurements [10, 25–28], and astrophysical measurements [1–5, 15, 29–31]. The observables from heavy-ion collisions change not only as a function of beam energy but also as a function of impact parameter, time evolution of the reacting system and the resulting products.

The scope of the initial commissioning phase of this campaign is focused on examining the dynamical break-up of the projectile- and target-like fragments from heavy-ion collisions. Specifically, we are interested in investigating the reaction mechanism competition involved to produce heavy ($Z \geq 3$) 3- or 4-body breaking of the reacting system at low-intermediate energy (~15 MeV/nucleon). In this specific case, it has been proposed that the isospin content, alignment and velocity distributions of the excited primary fragments, shape deformations of the heaviest fragments, and observables (multiplicity, isospin content, angular alignment, etc) associated with the emission of fragments from the low-density neck region produced in mid-peripheral heavy ion collisions represent observables sensitive to the EoS [20, 32–37]. This particular experiment attempts to measure a significant fraction of the observables from both the heavy, projectile-like fragments (PLFs) near the beam axis as well as the emitted intermediate mass fragments (IMFs) and light charged particles (LCPs) at lower intermediate energies, together, for a more complete picture of a majority of the charged particles in the event. In particular we are interested in measuring the heavy residues both near the beam axis in a Quadrupole Triplet Spectrometer (QTS), as well as in the Forward Array Using Silicon Technology[42] (FAUST). This is combined with measuring lighter particles (IMFs and LCPs) in the FAUST array that should provide for better characterization of the event. Data collected for the purposes of this experiment were from reactions of 15 MeV/nucleon ^{136}Xe,^{124}Sn+^{64}Ni and ^{124}Xe+^{58}Ni using the K500 Super-conducting cyclotron at Texas A&M University. Table I tabulates the reaction systems and their isospin asymmetry.

Table I. System to system isospin asymmetry

System	$\delta = \frac{N-Z}{A}$
^{136}Xe + ^{64}Ni	0.1800
^{124}Sn + ^{64}Ni	0.1702
^{124}Xe + ^{58}Ni	0.0989

The FAUST array has been coupled to the QTS which was previously used for RIB/facility upgrade experiments with BIGSOL[41, 43–46]. The new arrangement (Figs. 1 and 2) combines the FAUST array and the QTS for Time- of-Flight (ToF) mass measurements of heavy fragments in FAUST and the QTS for heavy PLFs/EVRs as well as ΔE-E measurements for isotopic resolution of LCPs/Light IMFs (Z≤10) and Z identification of heavier IMFs (up to the beam in some cases). The ToF mass identification in FAUST is achieved via newly designed integrated charge sensitive,

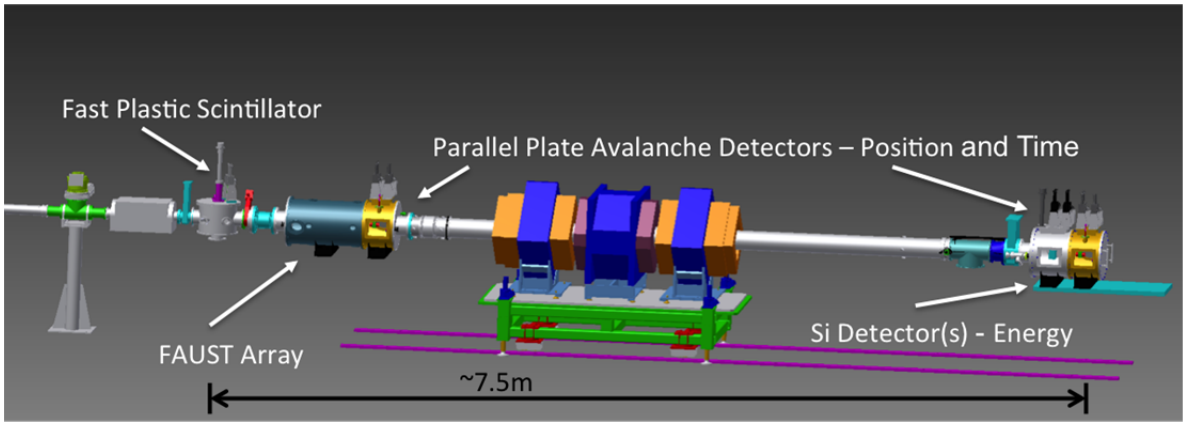

FIG. 1. Rendered CAD schematic of the FAUST-QTS beam line. The projectile is transported from the left to the right. The projectile generates a timing signal in the Fast Plastic used for both timing in FAUST and measuring beam intensity. After reacting with the target, IMFs, LCPs and PLFs are measured by a range of techniques in FAUST. The QTS has been coupled to FAUST to measure, through a narrow angular and $\beta\rho$ acceptance, the time-of-flight and energy of PLFs that escape through the throat of FAUST. This is accomplished through timing between the PPACs and energy resolved by the silicon detectors at the end of the spectrometer.

timing pickoff (CS/TPO) preamplifier upgrade to FAUST combined with a thin film, fast plastic time-zero detector up-stream of FAUST. The ToF mass measurements in the QTS were made using Parallel Plate Avalache Counters (PPACs)[47] for accurate time of flight coupled with a Si semiconductor detector at θ=0◦ at the back of the FAUST-QTS line. In forward focused intermediate energy nuclear reactions, this arrangement allows for large efficiency collection of the resultant PLF as well as emitted LCPs and IMFs.

FIG. 2. Actual picture of the FAUST-QTS line assembled and vacuum tight ready to be populated with detectors and cabled to data acquisition electronics. Picture taken in April 2013.

I. SIMULATIONS

Both Deep Inelastic Transport (DIT) [48] and Constrained Molecular Dynamics [49] models were use to generate PLFs in the range of interest. The results from DIT were statistically cooled by GEMINI [50] where as the CoMD was allowed to dynamically cool out to t=3000fm/c. The results of both were then analyzed through RAYTRACE [51] to approximate the efficiency and the resulting distributions at the Si detector after the QTS. Additionally, COSY-Infinity [52] was utilized to take into account possible 3rd order (or greater) effects, final approximation of magnetic current settings required, and visualization of the $\beta\rho$ dependent flight pattern through the QTS.

Simulations using COSY-Inifinity were examined to explore the effects of higher order aberrations on the lab-frame coordinate distribution of the particles of interest at the QTS Si detector. Higher order effects on the focusing of the particles of interest were observed to be dramatic for small changes (±5%) in $\beta\rho$. Based on these simulations we found that defocusing the last magnet in the QTS by 10%, allowed for a lower degree of aberration at the focal point. This effect was expected due to the asymmetric flight path length in the current configuration. Final current and magnetic field settings were determined empirically while tuning the primary beam on phosphorescent viewers and initial transport of particles of interest through the PPACs which allowed us to look at the lab-frame distribution of reaction

products in real time. The predictions by COSY-Infinity were consistent within error of the electrical current fluctuations of the magnet power supplies. The resultant flight path of a representative PLF emitted at $\theta = 1^{\circ}$ and $\beta\rho = 1.48$Tm through FAUST-QTS is shown in Fig. 3 as the red line. We can see for small changes of ±5% in $\beta\rho$, represented by the other differently colored lines, that significant efforts in particle focusing and collimation are required to reliably transport only the particles of interest to the focal plane. This, combined with coincidence measurements in FAUST and small angular and $\beta\rho$ acceptance of the QTS, provides for the ability to more efficiently filter and trigger on PLFs of interest while decreasing the number of scattered beam particles.

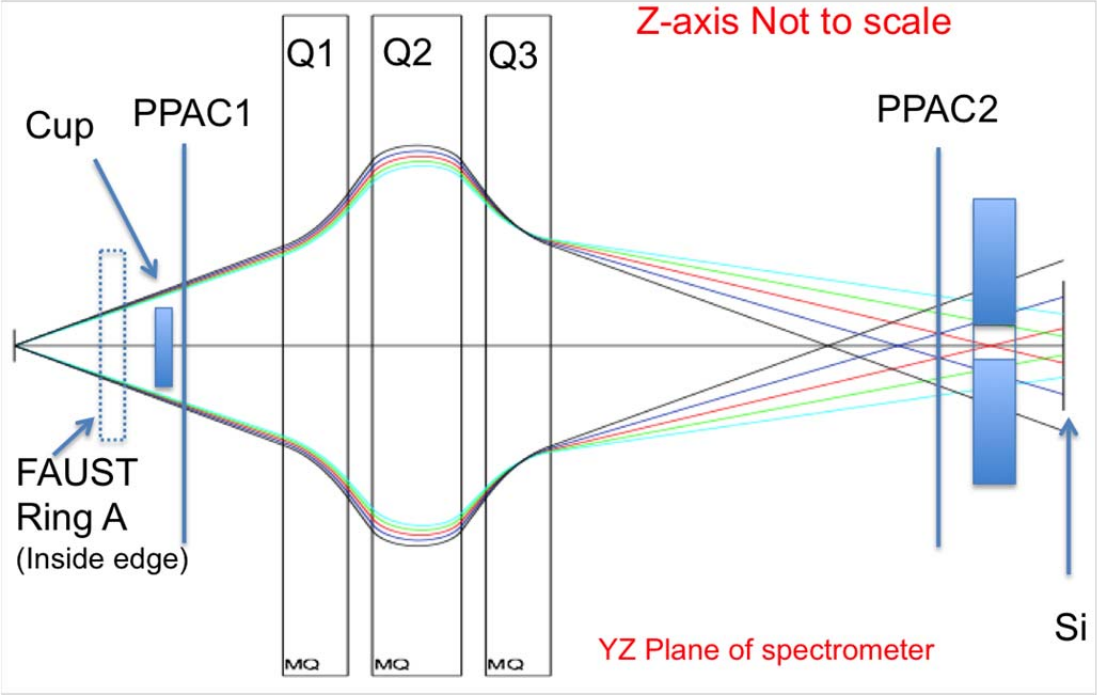

FIG. 3. Visualization of COSY-Inifity transport of the PLF emitted at $\theta = 1^{\circ}$ and $\beta\rho = 1.48$Tm through FAUST-QTS. Each color represents a shift of ± 5% increments in $\beta\rho$ where the red line is the PLF of interest (0%), +5%(black), +10% (blue), -5% (green) and -10% (light blue) deviation in $\beta\rho$. Efficient use of collimation and detector positioning, in conjunction with dynamics simulation fed transport approximations, allow for experimental filtering and triggering more effeciently on PLFs of interest while decreasing the number of scattered beam particles. Since the $\beta\rho$ of the PLF is near to that of the beam-like projectile scatter, attenuation of the beam-like scattered particles is accomplished through collimation and accurate de-focusing in combination with coincidence discrimination as provided by emitted particles detected in FAUST.

II. EXPERIMENTAL RESULTS

In keeping with the stated physics goal of the commissioning experiment, we have detected and reconstructed the hot, quasi-projectile like fragments resulting from a ternary breakup of the reaction system. Specifically, the breakup of the reaction system into three particles with Z≥3 is of interest to the community with respect to observing mechanism competition and the possible influence of the asymmetry energy in lower intermediate energy heavy-ion collisions. In this scenario, the projectile and target interacting and separating into a hot quasi-projectile and quasi- target. Because of detector thresholds and geometry, we are only able to detect the ternary breakup of the reaction system where the quasi-projectile (QP) breaks into a PLF and IMF. We then approximate the composition and energy of the quasi-target via momentum and mass conservation by assuming that all other particles are contained or are emitted from the quasi-target. This event selection requires that we are able to identify an IMF in FAUST in coincidence with another particle of Z≥3 in either FAUST or the QTS. The event-by-event multiplicity = 2 for particles of Z≥3 represents a small number of, not only, events with a particles of Z≥3, as seen in Fig. 4, but also represents less than 1% of the total number of events detected. Beam-like

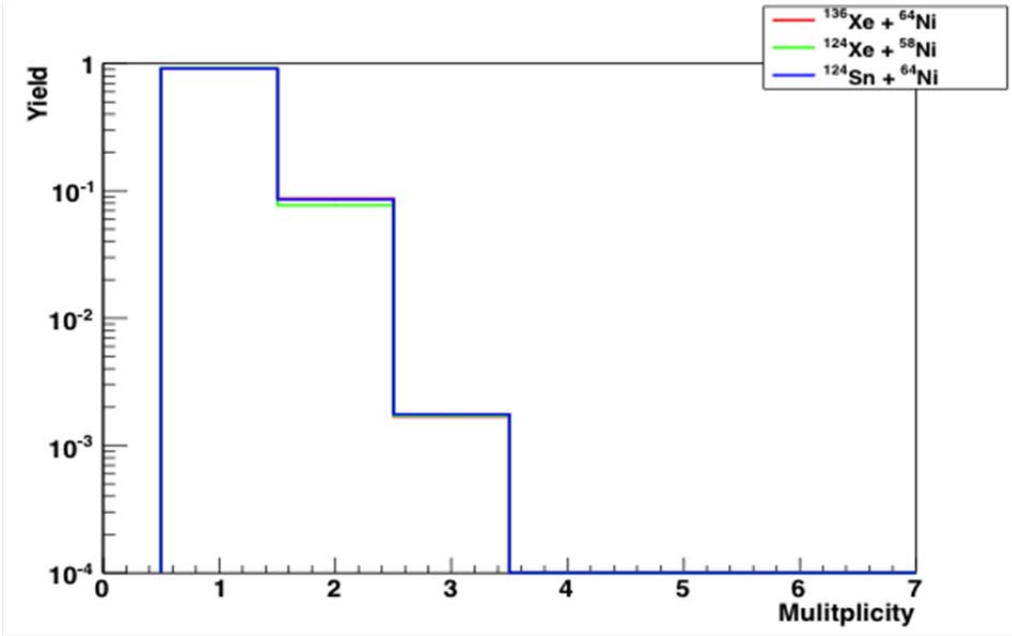

FIG. 4. Event multiplicity for particles with Z≥3. Events of interest are multiplicity = 2 because of FAUST-QTS is not able to detect target like particles. Because of this the target like particles are approximated by momentum and mass conservation and thus not explicity included in this multiplicity distribution.

particles identified in coincidence with the initial FAUST identified particle are removed from the data. Additionally, the reconstructed QP must have an energy $E_{QP} > 25\% \cdot E_{beam}$. For the events that pass this criterion, a large number of these events are forward focused with a majority of the detected PLFs detected in the QTS (low perpendicular velocity in the lab frame) and all of the IMFs detected in FAUST (swath at higher values of perpendicular velocity) as shown in Fig. 5.

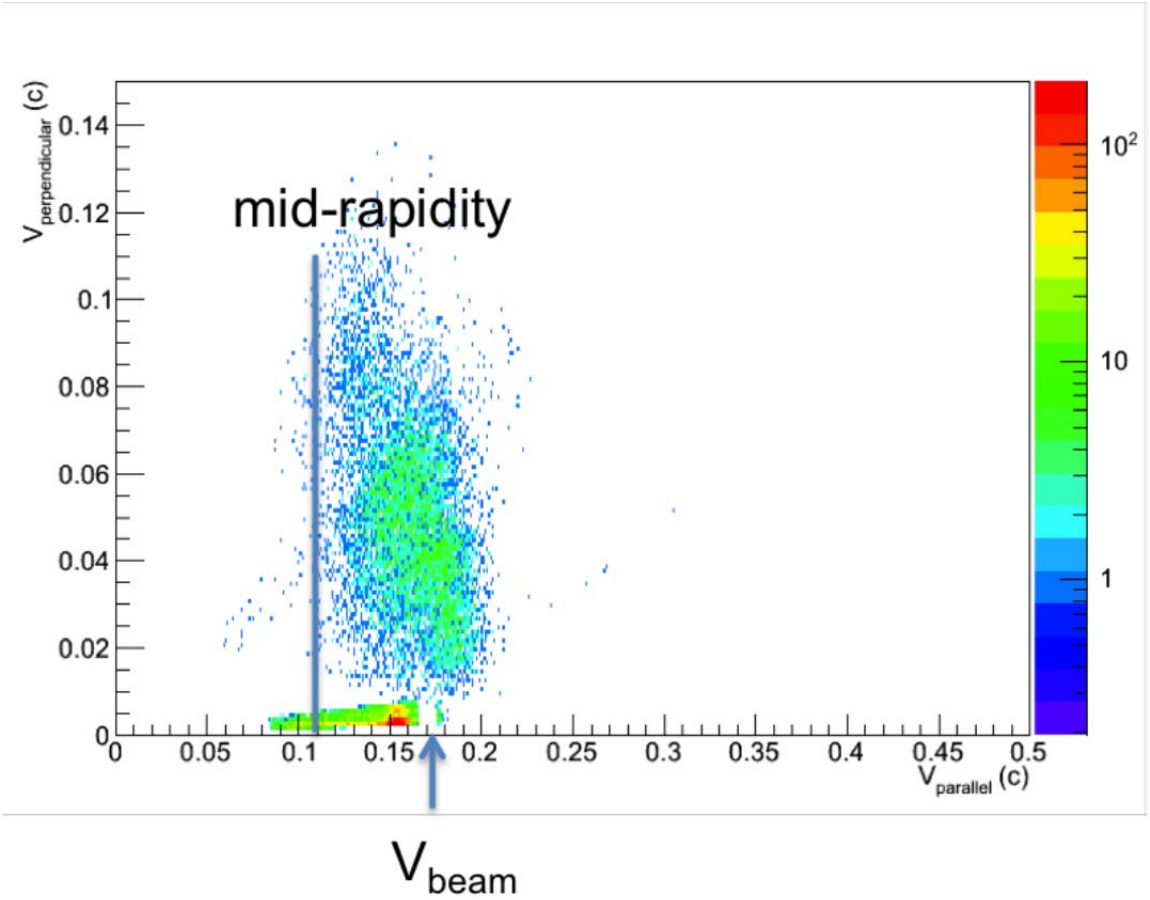

FIG. 5. $V_{perpendicular}$ vs $V_{parallel}$ for events with a multiplicity = 2 for particles with Z≥ meeting the criterion stated in the text.

[1] T. Klähn, D. Blaschke, S. Typel, E.N.E. van Dalen, A. Faessler, C. Fuchs, T. Gaitanos, H. Grigorian, A. Ho, E.E. Kolomeitsev *et al.*, Phys. Rev. C **74**, 035802 (2006).

[2] P. Danielewicz, R. Lacey, and W.G. Lynch, Science **298**, 1592 (2002).

[3] A. Steiner, M. Prakash, J. Lattimer, and P. Ellis, Phys. Rep. **411**, 325 (2005).

[4] A.W. Steiner, J.M. Lattimer, and E.F. Brown, Astrophys. J. **722**, 33 (2010).

[5] J.M. Lattimer and M. Prakash, Science **304**, 536 (2004).

[6] W. Hix, O. Messer, A. Mezzacappa, M. Liebendörfer, J. Sampaio, K. Langanke, D. Dean, and G. Martínez-Pinedo, Phys. Rev. Lett. **91**, 201102 (2003).

[7] C.J. Horowitz and J. Piekarewicz, Phys. Rev. Lett. **86**, 5647 (2001).

[8] S. Gandolfi, J. Phys. Conf. Ser. **420**, 012150 (2013).

[9] A. Bauswein, T.W. Baumgarte, and H.-T. Janka, Phys. Rev. Lett. **111**, 131101 (2013).

[10] B.A. Brown, Phys. Rev. Lett. **85**, 5296 (2000).

[11] R. Furnstahl, Nucl. Phys. **A706**, 85 (2002).

[12] P. Möller, W.D. Myers, H. Sagawa, and S. Yoshida, Phys. Rev. Lett. **108**, 052501 (2012).

[13] M.B. Tsang, J.R. Stone, F. Camera, P. Danielewicz, S. Gandolfi, K. Hebeler, C.J. Horowitz, J. Lee, W.G. Lynch, Z. Kohley *et al.*, Phys. Rev. C **86**, 015803 (2012).
[14] I. Tews, T. Krüger, K. Hebeler, and A. Schwenk, Phys. Rev. Lett. **110**, 032504 (2013).
[15] A.W. Steiner, J.M. Lattimer, and E.F. Brown, Astrophys. J. Lett. **765**, L5 (2013).
[16] M.B. Tsang, T.X. Liu, L. Shi, P. Danielewicz, C.K. Gelbke, X.D. Liu, W.G. Lynch, W.P. Tan, G. Verde, A. Wagner *et al.*, Phys. Rev. Lett. **92**, 062701 (2004).
[17] M.B. Tsang, Y. Zhang, P. Danielewicz, M. Famiano, Z. Li, W.G. Lynch, and A.W. Steiner, Phys. Rev. Lett. **102**, 122701 (2009).
[18] Z. Kohley, M. Colonna, A. Bonasera, L.W. May, S. Wuenschel, M. Di Toro, S. Galanopoulos, K. Hagel, M. Mehlman, W.B. Smith *et al.*, Phys. Rev. C **85**, 064605 (2012).
[19] Z. Kohley, G. Christian, T. Baumann, P.A. DeYoung, J.E. Finck, N. Frank, M. Jones, J.K. Smith, J. Snyder, A. Spyrou *et al.*, Phys. Rev. C **88**, 041601 (2013).
[20] V. Baran, M. Colonna, M. Di Toro, V. Greco, M. Zielinska-Pfabe, and H. Wolter, Nucl. Phys. **A703**, 603 (2002).
[21] E. Geraci, M. Bruno, M. D'Agostino, E. DeFilippo, A. Pagano, G. Vannini, M. Alderighi, A. Anzalone, L. Auditore, V. Baran *et al.*, Nucl. Phys. **A732**, 173 (2004).
[22] M.A. Famiano, T. Liu, W.G. Lynch, M. Mocko, A.M. Rogers, M.B. Tsang, M.S. Wallace, R.J. Charity, S. Komarov, D.G. Sarantites *et al.*, Phys. Rev. Lett. **97**, 052701 (2006).
[23] D. Shetty, S.J. Yennello, A. Botvina, G. Souliotis, M. Jandel, E. Bell, A. Keksis, S. Soisson, B. Stein, and J. Iglio, Phys. Rev. C **70**, 011601 (2004).
[24] G.-C. Yong, B.-A. Li, L.-W. Chen, and W. Zuo, Phys. Rev. C **73**, 034603 (2006).
[25] P.A. Souder, R. Holmes, C.-M. Jen, L. Zana, Z. Ahmed, A. Rakhman, and E. Cisbani *et al.*, PAC38 (2010).
[26] X. Roca-Maza, M. Centelles, X. Vinas, and M. Warda, Phys. Rev. Lett. **106**, 252501 (2011).
[27] S. Ban, C.J. Horowitz, and R. Michaels, J. Phys. G **39**, 015104 (2012).
[28] W. Horiuchi, Y. Suzuki, and T. Inakura, Phys. Rev. C **89**, 011601 (2014).
[29] P.B. Demorest, T. Pennucci, S.M. Ransom, M.S.E. Roberts, and J.W.T. Hessels, Nature **467**, 1081 (2010).
[30] K. Hebeler, J.M. Lattimer, C.J. Pethick, and A. Schwenk, Astrophys. J. **773**, 11 (2013).
[31] M. Prakash, Proc. Sci. 8th Int. Work. Crit. Point Onset Deconfinement (2013).
[32] R. Lionti, V. Baran, M. Colonna, and M. Di Toro, Phys. Lett. B **625**, 33 (2005).
[33] M. Colonna, J. Phys. Conf. Ser. **168**, 012006 (2009).
[34] V. Baran, M. Colonna, and M. Di Toro, Nucl. Phys. **A730**, 329 (2004).
[35] C. Rizzo, V. Baran, M. Colonna, A. Corsi, and M. Di Toro, Phys. Rev. C **83**, 014604 (2011).
[36] M. Di Toro, V. Baran, M. Colonna, G. Ferini, T. Gaitanos, V. Greco, J. Rizzo, and H. Wolter, Nucl. Phys. **A787**, 585 (2007).
[37] L. Shvedov, M. Colonna, and M. Di Toro, Phys. Rev. C **81**, 054605 (2010).
[38] H. Savajols and VAMOS Collaboration, Nucl. Phys. **A654**, 1027 (1999).
[39] J. Pouthas, B. Borderie, and R. Dayras, Nucl. Instrum. Methods Phys. Res. **A357**, 418 (1995).
[40] R.E. Tribble, R. Burch, and C. Gagliardi, Nucl. Instrum. Methods Phys. Res. **A285**, 441 (1989).

[41] G. Souliotis, D. Shetty, A. Keksis, E. Bell, M. Jandel, M. Veselsky, and S.J. Yennello, Phys. Rev. C **73**, 024606 (2006).
[42] F. Gimeno-Nogues, D. Rowland, E. Ramakrishnan, S. Ferro, S. Vasal, R. Gutierrez, R. Olsen, Y.-W. Lui, R. Laforest, H. Johnston *et al.*, Nucl. Instrum. Methods Phys. Res. **A399**, 94 (1997).
[43] G.A. Souliotis, A.S. Botvina, D.V. Shetty, A.L. Keksis, M. Jandel, M. Veselsky, and S.J. Yennello, Phys. Rev. C **75**, 011601 (2007).
[44] G.A. Souliotis, A.L. Keksis, B. Stein, M. Veselsky, M. Jandel, D. Shetty, S. Soisson, S. Wuenschel, and S.J. Yennello, Nucl. Instrum. Methods Phys. Res. **B261**, 1094 (2007).
[45] M. Barbui, S. Pesente, G. Nebbia, D. Fabris, M. Lunardon, S. Moretto, G. Viesti, M. Cinausero, G. Prete, V. Rizzi *et al.*, Nucl. Instrum. Methods Phys. Res. **B265**, 605 (2007).
[46] G.A. Souliotis, B. Stein, M. Veselsky, S. Galanopoulos, A. Keksis, Z. Kohley, D. Shetty, S. Soisson, S. Wuenschel, and S.J. Yennello, Nucl. Instrum. Methods Phys. Res. **B266**, 4692 (2008).
[47] D. Swan, J. Yurkon, and D. Morrissey, Nucl. Instrum. Methods Phys. Res. **A348**, 314 (1994).
[48] L. Tassan-Got and C. Stephan, Nucl. Phys. **A524**, 121 (1991).
[49] M. Papa, G. Giuliani, and A. Bonasera, J. Comput. Phys. **208**, 403 (2005).
[50] R. Charity, ICTP-IAEA Adv. Work. Model Codes (2008).
[51] S. Kowalski and H. Enge, Nucl. Instrum. Methods Phys. Res. **A258**, 407 (1987).
[52] K. Makino and M. Berz, Nucl. Instrum. Methods Phys. Res. **A558**, 346 (2006).

Remote control and monitoring system for the FAUST-QTS beam line

M. B. Chapman, P. Cammarata, S. Behling, and S. J. Yennello

Using Arduinos to Remotely Control and Monitor Stepper Motors and Solenoid Actuators

The construction of the new FAUST-QTS beam line has been completed with its inaugural experiment already concluded. One unique aspect of the new beam line is the inclusion of a stepper motor and solenoid actuator control system. The system allows for remote access to control systems inside the cave such as the target ladder position, Faraday cup alignment, and PPAC selection as shown in Fig. 1. Preset positions for the stepper motors can be set and recalled without the need for realignment. This saves wasted beam time by facilitating adjustments to the targets, detectors, and collimators without needing to enter the cave. The system consists of a computer with a USB hub branching off into the different Arduinos [1]. Arduinos are small open source micro controllers chosen for this application because of their low cost and ease of use. These Arduinos act as control and monitoring nodes for either a stepper motor or a solenoid actuator. They report the motors' and actuators' positions back to the computer, while also providing the power to drive them. A Python [2] script displays the information and allows the user to change settings through an intuitive graphical user interface (GUI).

There are two different types of nodes: stepper controller and solenoid controller. Each stepper

FIG. 1. Two stepper motors and two solenoids on top of the FAUST chamber in cave 2B.

controller consists of an Arduino with a motor shield attached that allows the Arduino to move the stepper motor with power provided by a DC power supply. Each solenoid controller is made up of an Arduino that provides a 5V DC signal to a relay board to toggle 120V AC to the solenoid (see Fig. 2). A 5V filter board was needed to prevent current feedback, generated when the solenoid is toggled, from causing the Arduino to lock up. A software reset was also implemented that can restart the Arduino if it does freeze. The GUI was developed utilizing Python with the Tkinter [3] graphics library, and PySerial [4] communications library. The interface allows for remote monitoring and motor movement with savable pre-sets for stepper motor positions. The system has been in use for over a month of beam time.

FIG. 2. A close up of the Arduino inside of the control box.

[1] Arduino, Arduino Micro Controller (https://arduino.cc)
[2] M. Lutz and D. Ascher, O'Reilly and Associates (1999)
[3] Tkinter, https://wiki.python.org/moin/TkInter (https://wiki.python.org)
[4] PySerial, http://pyserial.sourceforge.net/ (http://pyserial.sourceforge.net/)

Improved particle identification with the FAUST array

M. B. Chapman, P. Cammarata, S. Behling, and S. J. Yennello

One current method for particle identification with the FAUST [1] array utilizes a ΔE-E technique for isotopic particle identification. A new method is proposed to separate the detection of Light Charged Particles (LCPs) and lighter Intermediate Mass Fragments (IMFs) from the heavier IMFs. This will be accomplished by using Pulse Shape Discrimination [2] on the CsI photodiode signal to identify LCPs and light IMF, while gaining the Si for detecting heavier IMFs via ΔE-E analysis. The analog signal from the photodiode will be digitized with a flash Analog to Digital Converter (ADC). This technique can be further enhanced with the inclusion of a machine learning algorithm to train the computer to identify the isotopes based on rise time and full pulse shape analog input. The machine learning algorithm will be based on a dimensional reduction package [3] written in the statistical programming language R [4]. One major hurdle in implementing such a technique is the need to model both the detector and electronic response accurately. This is desired both to determine the time resolution required to digitize the CsI signal as well as for input data to train the machine learning algorithm. It is important to note that the algorithm can also be trained with experimental data.

A Geant4 model of the entire detector array has been created and simulations are ongoing utilizing the Eos supercomputer at the Texas A&M Super Computing Facility [5]. Fig. 1 is a ΔE-E plot created with data captured from the completed Geant4 simulation. Fig. 2 is an image of FAUST capture from inside Geant4. The electronics simulation is a work in progress. Collaboration is under way with the pre-amp manufacturer [6] to model the electronics' response utilizing the Simulation Program with Integrated Circuit Emphasis(SPICE) [7]. The simulation will be executed from a virtual machine with a root script to manage the simulated input data and the electronics output signals.

Two FAUST style Si-CsI telescope detectors have been built. They will be used for a control experiment for comparison with the simulation. The electronics for the planned experiment are still being finalized. A dual flash ADC method might prove to be the best way to digitize the analog pulse from the pre-amp, but the complexity makes it more difficult. The advantage of using two flash ADCs is the ability to capture the picosecond resolution rise time while also capture the microsecond fall time. If the simulation data can be shown to be reliable then the same experimental data will be used for development of the machine learning algorithm.

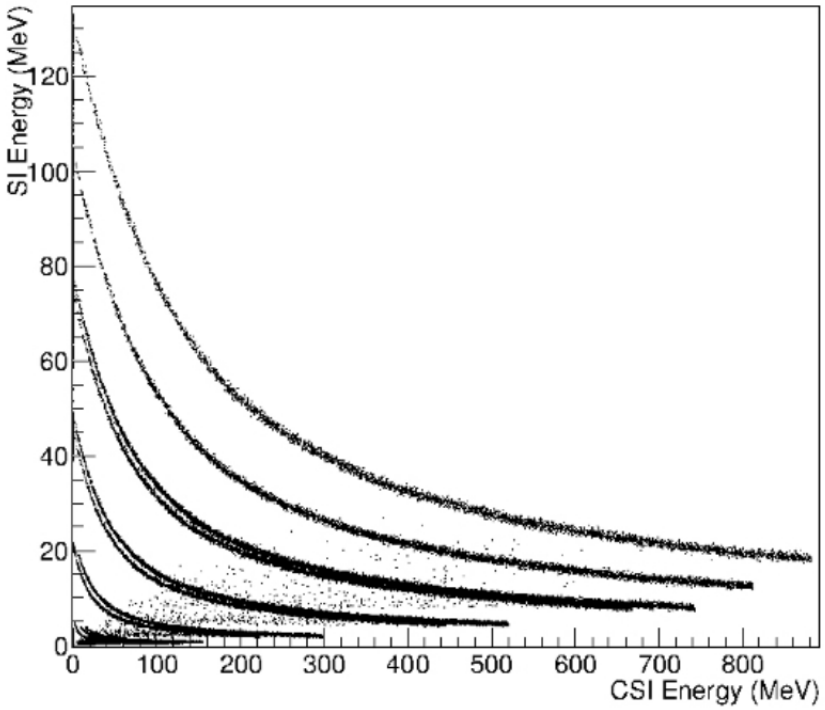

FIG. 1. A simulated ΔE-E plot from a typical ring A FAUST detector.

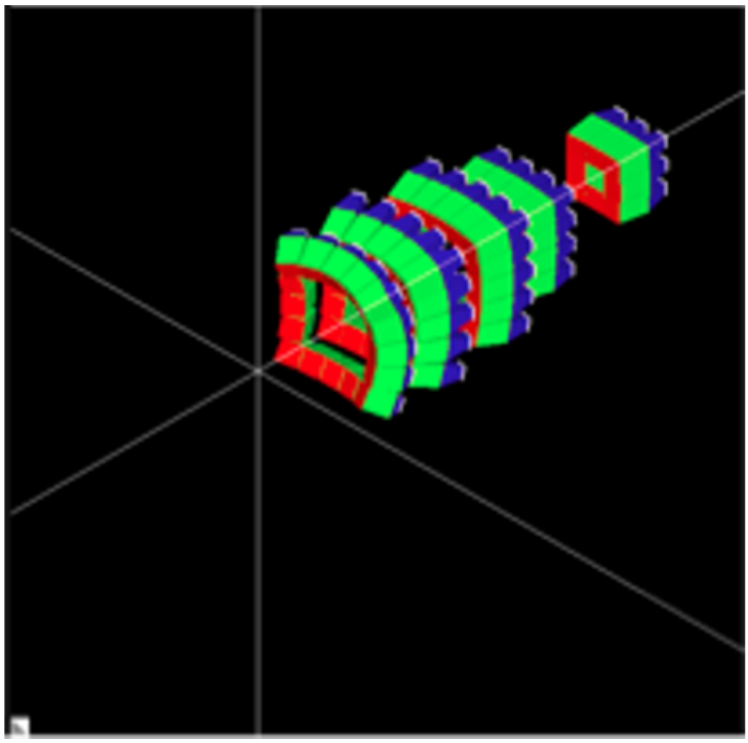

FIG. 2. The FAUST detector array modeled inside Geant4.

Special Acknowledgements

I would like to thank Larry May for his mathematics help with the 3D geometry required for the simulation. I would also like to thank Andrew Zarrella for his help in verifying some of the physics used in the Geant4 simulation and his help with the construction of the Si-CsI telescope.

[1] F. Gimeno-Nogues *et al.*, Nucl. Instrum. Methods Phys. Res. **A309**, 94 (1997).
[2] R. Laforest *et al.*, *Progress in Research*, Cyclotron Institute, Texas A&M University (1997-1998), p. II-1
[3] S. Weisberg, J. Statistical Software **7**, 1 (2002).
[4] *R: A Language and Environment for Statistical Computing* (R Foundation for Statistical Computing, Vienna, Austria, 2013)
[5] T.A.S. Faculty, Eos an IBM iDataplex Cluster (http://sc.tamu.edu/)
[6] D. Todd, RIS Corp (http://www.ris-corp.com/)
[7] SPICE, Simulation Program with Integrated Circuit Emphasis; (http://bwrcs.eecs.berkele.edu/Classes/IcBook/SPICE)

SECTION V

PUBLICATIONS

PAPERS PUBLISHED
April 1, 2013 – March 31, 2014

Unexpected characteristics of the isoscalar monopole resonance in the $A \approx 90$ region: Implications for nuclear incompressibility, D.H. Youngblood, Y.-W. Lui, Krishichayan, J. Button, M.R. Anders, M. L. Gorelik, M.H. Urin, and S. Shlomo**,** Phys. Rev. C **88**, 021301(R) (2013).

Astrophysical reaction rate for $^{17}F(p,\gamma)^{18}Ne$ from the transfer reaction $^{13}C(^{17}O,^{18}O)^{12}C$, T. Al-Abdullah, F. Carstoiu, X. Chen, H.L. Clark, C.A. Gagliardi, Y.-W. Lui, A. Mukhamedzhanov, G. Tabacaru, Y. Tokimoto, L. Trache, R.E. Tribble, and Y. Zhai, Phys. Rev. C **89**, 025809 (2014).

AstroBox: a novel detection system for very low-energy protons from β-delayed proton decay, E. Pollacco, L. Trache, E. Simmons, A. Spiridon, M. McCleskey, B.T. Roeder, A. Saastamoinen, R.E. Tribble, G. Pascovici, M. Kebbiri, J.P. Mols, and M. Raillot, Nucl. Instrum. Methods Phys. Res. **A723**, 102 (2013).

Digital beta counting for high-precision nuclear beta-decay lifetime measurements: Tested on ^{26m}Al, L. Chen, J.C. Hardy, M. Bencomo, V. Horvath, V.E. Iacob, N. Nica, and H.I. Park, Nucl. Instrum. Methods Phys. Res. **A728**, 81 (2013).

CKM unitarity normalization tests, present and future, (invited review article) J.C. Hardy and I.S. Towner, Annalen der Physik **525**, 443 (2013).

$\mathcal{Ft}$ values measured to ±0.1% for superallowed beta transitions: Metrology at sub-second time scales, J.C. Hardy, V.E. Iacob, H.I. Park, L. Chen, N. Nica, V. Horvat, R.E. Tribble and I.S. Towner, Appl. Rad. and Isot. **87**, 297 (2014).

Precise test of internal-conversion theory: Transitions measured in five nuclei spanning $50 \leq Z \leq 78$, J.C. Hardy, N. Nica, V.E. Iacob, S. Miller, M. Maguire, and M.B. Trzhaskovskaya, Appl. Rad. and Isot. **87**, 87 (2014).

Precise measurement of α_K for the 65.7-keV $M4$ transition in ^{119}Sn: Extended test of internal-conversion theory, N. Nica, J.C. Hardy, V.E. Iacob, M. Bencomo, V. Horvat, H.I. Park, M. Maguire, S. Miller, and M.B. Trzhaskovskaya, Phys. Rev. C **89**, 014303 (2014).

The β decay of ^{38}Ca: Sensitive test of isospin symmetry-breaking corrections from mirror superallowed $0^+ \rightarrow 0^+$ transitions, H.I. Park, J.C. Hardy, V.E. Iacob, M. Bencomo, L. Chen, V. Horvat, N. Nica, B.T. Roeder, E. Simmons, R.E. Tribble, and I.S. Towner, Phys. Rev. Lett. **112**, 102502 (2014).

Measurement of V_{ud} with $0^+ \rightarrow 0^+$ nuclear beta decays, J.C. Hardy and I.S. Towner, 11th International Conference on the Intersections of Particle and Nuclear Physics, AIP Conference Proceedings **1560**, 109 (2013).

Monitoring detachment and diffusion of metallic species in polycarbonate, M. Bencomo, M. Castro-Colin, J.A. López, and E. Ramirez-Homs, IX International Symposium on Radiation Physics, AIP Conference Proceedings **1544**, 19 (2013).

Nuclear data sheets for A = 148, N. Nica, Nuclear Data Sheets **117**, 1 (2014).

Transverse momentum of ionized atoms and diatomic molecules acquired in collisions with fast highly charged heavy ions, V. Horvat and R.L. Watson, Phys. Rev. A **88**, 022703 (2013).

Photoneutron cross sections for Mo isotopes: A step toward a unified understanding of (*γ*,*n*) and (*n*,*γ*) reactions, H. Utsunomiya, S. Goriely, T. Kondo, C. Iwamoto, H. Akimune, T. Yamagata, H. Toyokawa, H. Harada, F. Kitatani, Y.-W. Lui, A.C. Larsen, M. Guttormsen, P.E. Koehler, S. Hilaire, S. Péru, M. Martini, and A.J. Koning**,** Phys. Rev. C **88**, 015805 (2013).

Total absorption study of the β decay of ^{102,104,105}Tc, D. Jordan, A. Algora, J.L. Ta, B. Rubio, J. Agramunt, A.B. Perez-Cerdan, F. Molina, L. Caballero, E. Nacher, A. Krasznahorkay, M.D. Hunyadi, J. Gulyas, A. Vitez, M. Csatlos, L. Csige, J. Äystö, H. Penttilä, I.D. Moore, T. Eronen, A. Jokinen, A. Nieminen, J. Hakala, P. Karvonen, A. Kankainen, A. Saastamoinen, J. Rissanen, T. Kessler, C. Weber, J. Ronkainen, S. Rahaman, V. Elomaa, U. Hager, S. Rinta-Antila, T. Sonoda, K. Burkard, W. Huller, L. Batist, W. Gelletly, A.L. Nichols, T. Yoshida, A.A. Sonzogni, K. Peräjärvi, A. Petrovici, K.W. Schmid, and A. Faessler, Phys. Rev. C **87**, 044318 (2013).

Relative proton and γ widths of astrophysically important states in ^{30}S studied in the β-delayed decay of ^{31}Ar, G.T. Koldste, B. Blank, M.J.G. Borge, J.A. Briz, M. Carmona-Gallardo, L.M. Fraile, H.O.U. Fynbo, J. Giovinazzo, J.G. Johansen, A. Jokinen, B. Jonson, T. Kurturkian-Nieto, J.H. Kusk, T. Nilsson, A. Perea, V. Pesudo, E. Picado, K. Riisager, A. Saastamoinen, O. Tengblad, J.-C. Thomas, and J. Van de Walle, Phys. Rev. C **87**, 055808 (2013).

Towards commissioning the new IGISOL-4 facility, I.D. Moore, T. Eronen, D. Gorelov, J. Hakala, A. Jokinen, A. Kankainen, V.S. Kolhinen, J. Koponen, H. Penttilä, I. Pohjalainen, M. Reponen, J. Rissanen, A. Saastamoinen, S. Rinta-Antila, V. Sonnenschein, and J. Äystö, Nucl. Instrum. Methods Phys. Res. **B317**, 208 (2013).

Light element quantification by lithium elastic scattering, F.E. Portillo, J.A. Liendo, A.C. Gonzalez, D.D. Caussyn, N.R. Fletcher, O.A. Momotyuk, B.T. Roeder, I. Wiedenhoever, K.W. Kemper, P. Barber, and L. Sajo-Bohus, Nucl. Instrum. Methods Phys. Res. **B305**, 16 (2013).

Proton decay of excited states in ^{12}N and ^{13}O and the astrophysical ^{11}C(p,γ)^{12}N reaction rate, L.G. Sobotka, W.W. Buhro, R.J. Charity, J.M. Elson, M.F. Jager, J. Manfredi, M.H. Mahzoon, A.M. Mukhamedzhanov, V. Eremenko, M. McCleskey, R.G. Pizzone, B.T. Roeder, A. Spiridon, E. Simmons, L. Trache, M. Kurokawa, and P. Navratil, Phys. Rev. C **87**, 054329 (2013).

Implantation-decay station for low-energy β-delayed proton measurements, M. McCleskey, L. Trache, A. Saastamoinen, A. Banu, E. Simmons, B. Roeder, G. Tabacaru, R.E. Tribble, T. Davinson, P.J. Woods, and J. Aysto, Nucl. Instrum. Methods Phys. Res. **A700**, 124 (2013).

High-statistics measurement of the β-delayed α spectrum of ^{20}Na, K.L. Laursen, O.S. Kirsebom, H.O.U. Fynbo, A. Jokinen, M. Madurga, K. Riisager, A. Saastamoinen, O. Tengblad, and J. Äystö, Eur. Phys. J. A **49**, 79 (2013).

Measurement of characteristic prompt gamma rays emitted from oxygen and carbon in tissue-equivalent samples during proton beam irradiation, J.C. Polf, R. Panthi, D.S. Mackin, M. McCleskey, A. Saastamoinen, B.T. Roeder, and S. Beddar, Phys. Med. Biol. **58**, 5821 (2013).

Recommissioning of JYFLTRAP at the new IGISOL-4 facility, V.S. Kolhinen, T. Eronen, D. Gorelov, J. Hakala, A. Jokinen, K. Jokiranta, A. Kankainen, M. Koikkalainen, J. Koponen, H. Kulmala, M. Lantz, A. Mattera, I.D. Moore, H. Penttilä, T. Pikkarainen, I. Pohjlainen, M. Reponen, S. Rinta-Antila, J. Rissanen, C. Rodríguez Triguero, K. Rytkönen, A. Saastamoinen, A. Solders, V. Sonnenschein, and J. Äystö, Nucl. Instrum. Methods Phys. Res. **B317**, 506 (2013).

TRINAT: Measuring β-decay correlations with laser-trapped atoms, J.A. Behr *et al.*, ISAC and ARIEL: The TRIUMF Radioactive Beam Facilities and the Scientific Program, Hyperfine Interact. **225**, 115 (2014).

Isospin-symmetry-breaking effects in nuclear β decay, D. Melconian, 11th Conference on the Intersections of Particle and Nuclear Physics, AIP Conference Proceedings **1560**, 604 (2013).

The Francium facility at TRIUMF, S. Aubin *et al.*, 22nd Conference on Applications of Accelerators in Research and Industry, AIP Conference Proceedings **1525**, 530 (2013).

Atomic parity non-conservation: The Francium anapole project of the FrPNC collaboration at TRIUMF, S. Aubin *et al.*, 5th International Symposium on Symmetries in Subatomic Physics, Hyperfine Interac. **214**, 163 (2013).

Structure of ^{8}B from elastic and inelastic ^{7}Be+p scattering, J.P. Mitchell, G.V. Rogachev, E.D. Johnson, L.T. Baby, K.W. Kemper, A.M. Moro, P. Peplowski, A.S. Volya, and I. Wiedenhver, Phys. Rev. C **87**, 054617 (2013).

How much cooler would it be with some more neutrons? Exploring the asymmetry dependence of the nuclear caloric curve and the liquid-gas phase transition, A.B. McIntosh, J. Mabiala, A. Bonasera, P. Cammarata, K. Hagel, Z. Kohley, L. Heilborn, L.W. May, P. Marini, A. Raphelt, G.A. Souliotis, S. Wuenschel, A. Zarrella, H. Zheng, and S.J. Yennello, Eur. Phys. J. A **50**, 35 (2014).

Heavy-ion collisions: Direct and indirect probes of the density and temperature dependence of Esym, Z. Kohley and S.J. Yennello, Eur. Phys. J. A **50**, 31 (2014)

Quantum suppression of fluctuations and temperatures of reconstructed A~30 quasi-projectiles, B.C. Stein, A. Bonasera, G.A. Souliotis, H. Zheng, P.J. Cammarata, A.J. Echeverria, L. Heilborn, A.L. Keksis, Z. Kohley, J. Mabiala, P. Marini, L.W. May, A.B. McIntosh, C. Richers, D.V. Shetty, S.N. Soisson, R. Tripathi, S. Wuenschel, and S.J. Yennello, J. Phys. G **41**, 025108 (2014).

Critical scaling of two-component systems from quantum fluctuations, J. Mabiala, A. Bonasera, H. Zheng, A.B. Mcintosh, Z. Kohley, P. Cammarata, K. Hagel, L. Heilborn, L.W. May, A. Raphelt, G.A. Souliotis, A. Zarrella, and S.J. Yennello, Int. J. Mod. Phys. E **22**, 1350090 (2013)

Density determinations in heavy ion collisions, G. Röpke, S. Shlomo, A. Bonasera, J.B. Natowitz, S.J. Yennello, A.B. McIntosh, J. Mabiala, L. Qin, S. Kowalski, K. Hagel, M. Barbui, K. Schmidt, G. Giulani, H. Zheng, and S. Wuenschel, Phys. Rev. C **88**, 024609 (2013)

Experimental determination of the quasi-projectile mass with measured neutrons, P. Marini, A. Zarrella, A. Bonasera, G. Bonasera, P. Cammarata, L. Heilborn, Z. Kohley, J. Mabiala, L.W. May, A.B. McIntosh, A. Raphelt, G.A. Souliotis, and S.J. Yennello, Nucl Instrum. Methods Phys. Res. **A707**, 80 (2013).

Novel determination of density, temperature, and symmetry energy for nuclear multifragmentation through primary fragment-yield reconstruction, W. Lin, X. Liu, M.R.D. Rodrigues, S. Kowalski, R. Wada, M. Huang, S. Zhang, Z. Chen, J. Wang, G.Q. Xiao, R. Han, Z. Jin, J. Liu, F. Shi, T. Keutgen, K. Hagel, M. Barbui, C. Bottosso, A. Bonasera, J.B. Natowitz, E.J. Kim, T. Materna, L. Qin, P.K. Sahu, K.J. Schmidt, S. Wuenschel, and H. Zheng, Phys. Rev. C **89**, 021601 (2014).

Experimental search for super and hyper heavy nuclei at Cyclotron Institute Texas A&M University, Z. Majka, M. Barbui, F. Becchetti, G. Chubaryan, M. Cinausero, D. Fabris, G. Giuliani, H. Griffin, K. Hagel, J. Kallungkathariyil, E.-J. Kim, S. Kowalski, P. Lasko, M. Lunardon, T. Materna, S. Moretto, R. Murthy, J.B. Natowitz, G. Nebbia, and T. O'Donnel, Acta Physica Polonica B **45**, 279 (2014).

Exploring the alpha cluster structure of nuclei using the thick target inverse kinematics technique for multiple alpha decays, M. Barbui, K. Hagel, V.Z. Goldberg, J.B. Natowitz, H. Zheng, G. Giuliani, G.G. Rapisarda, S. Wuenschel, and X. Liu, Eur. Phys. J. Web of Conferences **66**, 03005 (2014).

The equation of state and symmetry energy of low density nuclear matter, K. Hagel, J.B. Natowitz and G. Röpke, Eur. Phys. J. A **50**, 39 (2014).

Experimental reconstruction of excitation energies of primary hot isotopes in heavy ion collisions near the Fermi energy, M.R.D. Rodrigues, W. Lin, X. Liu, M. Huang, S. Zhang, Z. Chen, J. Wang, R. Wada, S. Kowalski, T. Keutgen, K. Hagel, M. Barbui, C. Bottosso, A. Bonasera, J.B. Natowitz, T. Materna, L. Qin, P.K. Sahu, and K.J. Schmidt, Phys. Rev. C **88**, 034605 (2013).

Experimental study of fusion neutron and proton yields produced by petawatt-laser-irradiated D_2-^{3}He or CD_4-^{3}He clustering gases, W. Bang, M. Barbui, A. Bonasera, H.J. Quevedo, G. Dyer, A.C. Bernstein, K. Hagel, K. Schmidt, E. Gaul, M.E. Donovan, F. Consoli, R. De Angelis, P. Andreoli, M. Barbarino, S. Kimura, M. Mazzocco, J.B. Natowitz, and T. Ditmire, Phys. Rev. E **88**, 033108 (2013).

Temperature measurements of fusion plasmas produced by petawatt-laser--irradiated D_2- ^{3}He or CD_4- ^{3}He clustering gases, W. Bang, M. Barbui, A. Bonasera, G. Dyer, H.J. Quevedo, K. Hagel, K. Schmidt, F. Consoli, R. De Angelis, P. Andreoli, E. Gaul, A.C. Bernstein, M. Donovan, M. Barbarino, S. Kimura, M. Mazzocco, J. Sura, J.B. Natowitz, and T. Ditmire, Phy. Rev. Lett. **111**, 055002 (2013).

Measurement of the plasma astrophysical S factor for the ^{3}He (d, p)^{4}He reaction in exploding molecular clusters, M. Barbui *et al.*, Phys. Rev. Lett. **111**, 082502 (2013).

Average neutron detection efficiency for DEMON detectors, S. Zhang, W. Lin, M.R.D. Rodrigues *et al.*, Nucl. Instrum. Methods Phys. Res. **A709**, 68 (2013).

Suppression of the centrifugal barrier effects in the off-energy-shell neutron + ^{17}O interaction, M. Gulino, C. Spitaleri, X.D. Tang, G.L. Guardo, L. Lamia, S. Cherubini, B. Bucher, V. Burjan, M. Couder, P. Davies, R. de Boer, X. Fang, V.Z. Goldberg, Z. Hons, V. Kroha, L. Lamm, M. La Cognata, C. Li, C. Ma, J. Mrazek, A.M. Mukhamedzhanov, M. Notani, S. O'Brien, R.G. Pizzone, G.G. Rapisarda, D. Roberson, M.L. Sergi, W. Tan, I.J. Thompson, and M. Wiescher, Phys. Rev. C **87**, 012801 (2013).

Structure of light nuclei in resonance scattering experiments, G.V. Rogachev, M. Avila, L.T. Baby, J. Blackmon, V.Z. Goldberg, E.D. Johnson, M. Matos, K. Macon, J.P. Mitchell, L. Linhardt, A. Kuchera, E. Koshchiy, K. Kemper, D. Santiago-Gonzales, A. Volya, and I. Wiedenhoever, AIP Conf. Proc. **1524**, 58 (2013).

Clustering in A=10 nuclei, G.V. Rogachev, L. Baby, J. Belarge, J.C. Blackmon, V.Z. Goldberg, E.D.

Johnson, E. Koshchiy, A.N. Kuchera, L. Linhardt, K. Macon, M. Matos, D. Santiago-Gonzalez, and I. Wiedenhöver, J. Phys. **436**, 012041(2013).

Test of modern theoretical approaches using modern experimental methods, V.Z. Goldberg, G.V. Rogachev, and R.E. Tribble, Acta Phys. Polo. B. **45** 309 (2014).

Application of the Trojan Horse method to study neutron induced reactions: the ^{17}O (n, α) ^{14}C reaction, M. Gulino, C. Spitaleri, X.D. Tang, G.L. Guardo, L. Lamia, S. Cherubini, B. Bucher, V. Burjan, M. Couder, P. Davies, R. de Boer, X. Fang, V.Z. Goldberg, Z. Hons, V. Kroha, L. Lamm, and M. La Cognata, Eur. Phys. J. Web of Conferences **66**, 07008 (2014).

New determination of the ^{2}H(d,p)^{3}H and ^{2}H(d,n)^{3}He and reaction rates at astrophysical energies, A. Tumino, R. Spartá, C. Spitaleri, A.M. Mukhamedzhanov, S. Typel, R.G. Pizzone, E. Tognelli , S. Degl'Innocenti, V. Burjan, V. Kroha, Z. Hons, M. La Cognata, L. Lamia, J. Mrazek, S. Piskor, P.G. Prada Moroni, G.G. Rapisarda, S. Romano, and M.L. Sergi, Astrophys. J. **785**, 96 (2014).

On the measurement of the ^{13}C(*α*, *n*)^{16}O *S*-factor at negative energies and its influence on the *s*-process, M. La Cognata, C. Spitaleri, O. Trippella, G.G. Kiss, G.V. Rogachev, A.M. Mukhamedzhanov, M. Avila, G.L. Guardo, E. Koshchiy, A. Kuchera, L. Lamia, S.M.R. Puglia, S. Romano, D. Santiago, and R. Spartà, Astrophys. J. **777**, 143 (2013).

Anomalous asymptotics of radial overlap functions for bound systems of three or more particle, L.D. Blokhintsev, A.M. Mukhamedzhanov, and R. Yarmukhamedov, Eur. Phys. J. A **49**, 108 (2013).

Quantitative sum rule analysis of low-temperature spectral functions, N.P.M. Holt, P.M. Hohler, and R. Rapp, Phys. Rev. D **87**, 076010 (2013).

Dilepton spectroscopy of QCD matter at collider energies, R. Rapp, Adv. High Energy Phys. 2013, 148253 (2013).

Relativistic Langevin dynamics in expanding media, M. He, H. Van Hees, P.B. Gossiaux, R.J. Fries, and R. Rapp, Phys. Rev. E **88**, 032138 (2013).

The πρ could contribution to the ω width in nuclear matter, D. Cabrera and R. Rapp, Phys. Lett. B **729**, 67 (2014).

Dilepton emission in high-energy heavy-ion collisions with viscous hydrodynamics, G. Vujanovic, C. Young, B. Schenke, R. Rapp, S. Jeon, and C. Gale, Phys. Rev. C **89**, 034904 (2014).

In-medium quarkonia at SPS, RHIC and LHC, X. Zhao, A. Emerick, and R. Rapp, Nucl. Phys. **A904**, 611c (2013).

Dilepton production in high-energy heavy-ion collisions with 3+1D viscous hydrodynamics, G. Vujanovic, C. Young, B. Schenke, S. Jeon, R. Rapp, and C. Gale, Nucl. Phys. **A904**, 557c (2013).

Dilepton production in heavy-ion collisions, R. Rapp, Proceedings of Science **CPOD 2013**, 9 (2013).

Nonperturbative heavy-flavor transport at RHIC and LHC, M. He, R.J. Fries and R. Rapp, Nucl. Phys. **A910**, 409 (2013).

The many facets of the (non-relativistic) Nuclear Equation of State, G. Giuliani, H. Zheng, and A. Bonasera, Prog. Part. Nucl. Phys. **76**, 116 (2014).

Coulomb corrections to the extraction of the density and temperature in non-relativistic heavy ion collisions, H. Zheng, G. Giuliani, and A. Bonasera, J. Phys. G **41**, 055109 (2014).

Diagnostics improvement in the ABC facility and preliminary tests on laser interaction with light-atom clusters and p+ ^{11}B targets, F. Consoli *et al.,* Nucl. Instrum. Methods Phys. Res. **A720**, 149 (2013).

Density and temperature of fermions and bosons from quantum fluctuations, H. Zheng, G. Giuliani, and A. Bonasera, Nucl. Sci. Techniques **24**, 050512 (2013).

Coulomb corrections to density and temperature of bosons in heavy ion collisions, H. Zheng, G. Giuliani, and A. Bonasera , Phys. Rev. C **88**, 024607 (2013).

Gamow peak approximation near strong resonances, S. Kimura and A. Bonasera, Phys. Rev. C **87**, 058801 (2013).

Effects of initial state fluctuations on jet quenching, H.Z. Zhang, T. Song, and C.M. Ko, Phys. Rev. C **87**, 054902 (2013).

Energy dependence of pion in-medium effects on π^-/π^+ ratio in heavy ion collisions, J. Xu, L.W. Chen, C.M. Ko, B.A. Li, and Y.G. Ma, Phys. Rev. C **87**, 06701 (2013).

Quarkonia production in heavy ion collisions, C.M. Ko, K.C. Han, and T. Song, Nucl. Phys. **A910-911**, 474 (2013).

Exotic hadrons and hadron-hadron interactions in heavy-ion collisions, A. Ohnishi, S. Cho, T. Furumoto, T. Hyodo, D. Jido, C.M. Ko, K. Morita, S.H. Lee, M. Nielsen, T. Sekihara, S. Yasui, and K. Yazaki, Nucl. Phys. **A914**, 377 (2013).

Mean-field effects on matter and antimatter elliptic flows, C.M. Ko, L.W. Chen, V. Greco, F. Li, Z. W. Lin, S. Plumari, T. Song, and J. Xu, Nucl. Sci. Tech. **24**, 050525 (2013).

ψ' production and B decay in heavy ion collisions at LHC, B. Chen, Y. Liu, K. Zhou, and P.Z. Huang, Phys. Lett. B **726**, 725 (2013).

Shear viscosity of neutron-rich nucleonic matter near liquid-gas phase transition, J. Xu, L.W. Chen, C.M. Ko, B.A. Li, and Y.G. Ma, Phys. Lett. B **727**, 244-248 (2013).

Gluon dissociation of J/ψ beyond the dipole approximation, Y.P. Liu, C.M. Ko, and T. Song, Phys. Rev. C **88**, 064902 (2013).

Hot medium effects on J/ψ production in p+Pb collisions at $s^{1/2}_{NN}$ = 5.02 TeV", Y.P. Liu, C.M. Ko, and T. Song, Phys. Lett. B **728**, 437 (2013).

Elliptic flow splitting as a probe of the QCD phase structure at finite baryon chemical potential, J. Xu, T. Song, C.M. Ko, and F. Li, Phys. Rev. Lett. **112**, 012301 (2014).

Probing isospin- and momentum-dependent nuclear effective interactions in neutron-rich matter, L.W. Chen, C.M. Ko, B.A. Li, C. Xu, and J. Xu, Euro. Phys. J. A **50**, 29 (2014).

Elliptic flow difference between particles and antiparticles and the EOS of baryon-rich matter, C.M. Ko, L.W. Chen, V. Greco, F. Li, Z.W. Lin, S. Plumari, T. Song, and J. Xu, Proceedings of XXXI Max Born Symposium and HIC for FAIR Workshop on Critical Behavior in Hot and Dense Matter, Wroclaw, Poland (June 2013), edited by D. Blaschke and L. Turko, Acta Phys. Polo. B Proc. Suppl., **7**, 183 (2013).

Rapidity profile of the initial energy density in heavy-ion collisions, S. Ozonder and Rainer J. Fries, Phys. Rev. C **89**, 034902 (2014).

Jet-tagged back-scattering photons for quark gluon plasma tomography, Rainer J. Fries, Somnath De, and Dinesh K. Srivastava, Nucl. Phys. **A904-905**, 569 (2013).

Initial conditions with flow from a McLerran Venugopalan model with transverse dynamics, Guangyao Chen and Rainer J. Fries, J. Phys. Conf. Ser. **446**, 012021 (2013).

Azimuthal asymmetries from jets quenched in fluctuating backgrounds, Ricardo Rodriguez-Pedraza and Rainer J. Fries, J. Phys. Conf. Ser. **446** 012003 (2013).

Proceedings of workshop for young scientists on the physics of ultrarelativistic nucleus-nucleus collisions (Hot Quarks 2012), Copamarina, Puerto Rico, October 2012, edited by Markus Bleicher, Rainer J. Fries *et al.*, J. Phys. Conf. Ser. **446** (2013)

Energy dependence of moments of net-proton multiplicity distributions at RHIC, L. Adamczyk *et al.* (STARCollaboration), Phys. Rev. Lett. **112**, 032302 (2014).

Neutral pion cross section and spin asymmetries at intermediate pseudorapidity in polarized proton collisions at √s = 200 GeV, L. Adamczyk *et al.* (STAR Collaboration), Phys. Rev. D **89**, 012001 (2014).

Transverse-energy distributions at midrapidity in p + p, d + Au, and Au + Au collisions at $\sqrt{s_{NN}}$ = 62.4 - 200 GeV and implications for particle-production models, S.S. Adler *et al.* (PHENIX Collaboration), Phys. Rev. C **89**, 044905 (2014).

Jet-hadron correlations in $\sqrt{s_{NN}}$ = 200 GeV Au + Au and p + p collisions, L. Adamczyk *et al.* (STAR Collaboration), Phys. Rev. Lett. **112**, 122301 (2014)**.**

Fluctuations of charge separation perpindicular to the event plane and local parity violation in $\sqrt{s_{NN}}$ = 200 GeV Au+Au collisions at the BNL Relativistic Heavy Ion Collider, L. Adamczyk *et al.* [STAR Collaboration], Phys. Rev. C **88**, 064911 (2013).

Freeze-out dynamics via charged kaon femtoscopy in $\sqrt{s_{NN}}$ = 200 GeV central Au+Au collisions, L. Adamczyk *et al.* (STAR Collaboration), Phys. Rev. C **88**, 034906 (2013).

Third harmonic flow of charged particles in Au+Au collisions at $\sqrt{s_{NN}}$ = 200 GeV, L. Adamczyk *et al.* (STAR Collaboration), Phys. Rev. C **88**, 014904 (2013).

Elliptic flow of identified hadrons in Au+Au collisions at $\sqrt{s_{NN}}$ = 7.7-62.4 GeV, L. Adamczyk *et al.* (STAR Collaboration), Phys. Rev. C **88**, 014902 (2013).

Medium modification of jet fragmentation in Au+Au collisions at $\sqrt{s_{NN}}$ = 200 GeV measured in direct photon-hadron correlations, S.S. Adler *et al.* (PHENIX Collaboration), Phys. Rev. Lett. **111**, 032301 (2013).

Measurement of J/psi azimuthal anisotropy in Au+Au collisions at $\sqrt{s_{NN}}$ = 200 GeV, L. Adamczyk *et al.* (STAR Collaboration), Phys. Rev. Lett. **111**, 052301 (2013).

Experimental studies of di-jets in Au + Au collisions using angular correlations with respect to back-to-back leading hadrons, L. Adamczyk *et al.* (STAR Collaboration), Phys. Rev. C **87**, 044903 (2013).

J/psi production at high transverse momenta in p+p and Au+Au collisions at $\sqrt{s_{NN}}$ = 200 GeV, L. Adamczyk *et al.* (STAR Collaboration), Phys. Lett. B **722**, 55 (2013).

Direct photon production in d+Au collisions at $\sqrt{s_{NN}}$ = 200 GeV, S.S. Adler *et al*. (PHENIX Collaboration), Phys. Rev. C **87**, 054907 (2013).

System-size dependence of transverse momentum correlations at RHIC, L. Adamczyk *et al.* (STAR Collaboration), Phys. Rev. C **87**, 064902 (2013).

Observation of an energy-dependent difference in elliptic flow between particles and anti-particles in relativistic heavy ion collisions, L. Adamczyk *et al.* (STAR Collaboration), Phys. Rev. Lett. **110**, 142301 (2013).

Isoscalar and isovector dipole strength distributions in nuclei and the Schiff moment, N. Auerbach., Ch. Stoyanov, M.R. Anders, and S. Shlomo, Phys. Rev. C **89**, 014335 (2014).

Modern energy density functional for nuclei and the equation of state of nuclear matter, S. Shlomo, Invited Review Article in *The Universe Evolution: Astrophysical and Nuclear Aspects*, Editors, L. Blokhintsev and I. Strakovsky, (Nova Science Publishers, 2013).

Modern energy density functional for nuclei and the equation of state of nuclear matter, S. Shlomo, Proceedings of the 4th International Conference on "Current Problems in Nuclear Physics and Atomic Energy," Kyiv, Ukraine, Part I, 72 (2013).

SECTION VI

APPENDIX

TALKS PRESENTED
April 1, 2013 – March 31, 2014

Honoring the achievements of Joseph B. Natowitz, **R.E. Tribble**, International Workshop on Dynamics and Thermodynamics, College Station, Texas (August 2013).

Asymptotic normalization coefficients as an indirect technique for nuclear astrophysics (and more), **R.E. Tribble**, **Invited Presentation**, Seventh European Summer School for Experimental Nuclear Astrophysics, Catania, Italy (September 2013).

Radioactive ion beams for nuclear science at Texas A&M University, **R.E. Tribble**, **Invited Talk**, First International African Symposium on Exotic Nuclei, Cape Town, South Africa (December 2013).

Pandemonium: early perspectives on delayed-neutron decay, **J.C. Hardy**, **Invited Talk**, North American Workshop on Beta-Delayed Neutron Emission, Oak Ridge, Tennessee (May 2013).

Precise test of internal-conversion theory: transitions measured in five nuclei spanning $50 \leq Z \leq 78$, **J.C. Hardy**, **Invited Talk**, 19th International Conference on Radionuclide Metrology and its Applications, Antwerp, Belgium (June 2013).

Ft values measured to ±0.1% for superallowed beta transitions: metrology at sub-second time scales, **J.C. Hardy**, **Invited Talk**, 19th International Conference on Radionuclide Metrology and its Applications, Antwerp, Belgium (June 2013).

Precise measurement of branching ratios in the β decay of ^{38}Ca, **H.I. Park**, J.C. Hardy, V.E. Iacob, M. Bencomo, L. Chen, V. Horvat, N. Nica, E. Simmons, B.T. Roeder and R.E. Tribble, APS Meeting, Denver, Colorado (April 2013).

Another interesting case of ICC measurement: the 88-keV M4 transition in ^{127}Te, **N. Nica,** Annual Meeting of the U.S. Nuclear Data Program, Brookhaven National Laboratory, Upton, New York (November 2013).

Study of giant monopole resonance: present and future, , **Y.-W. Lui**, **Colloquium**, College of Physics, Qingdao University, Qingdao, China (June 2013).

What should be expected from the resonance scattering experiments in the nearest future? **V.Z. Goldberg**, **Invited Seminar**, GSI Helmholtz Centre for Heavy Ion Research, Darmstadt, Germany (May 2013).

Experiments to test current ab initio calculations, **V.Z. Goldberg**, **Invited Talk**, Conference on Nuclear Physics: Presence and Future, Boppard, Germany (June 2013).

The progress in the experimental studies of α cluster states, **V.Z. Goldberg**, Lomonosov State University, Moscow, Russia (June 2013).

Test of modern theoretical approaches using modern experimental methods, **V.Z. Goldberg**, **Invited Talk**, 33rd Mazurian Lakes Conference on Physics "Frontiers in Nuclear Physics", Piaski, Poland, (September 2013).

What are the alpha cluster states and how can they be studied ? **V.Z. Goldberg**, **Invited Lecture**, at 7th Europinian School on Experimental Nuclear Astrophysics, Santa Tecla, Italy (September 2013).

Resonance studies of nuclei beyong nuclear stability and development of theory, **V.Z. Goldberg**, **Invited Seminar**, Shanghai Jiaotong University, Shanghai, China (March 2014).

Experiements with rare beams for tests of modern nuclear structure calculations, **V.Z. Goldberg**, **Invited Seminar**, China Atomic Energy Institute, Beijing, China (March 2014).

Clusters in atomic nuclei, **V.Z. Goldberg**, **Invited Seminar**, China Atomic Energy Institute, China Atomic Energy Institute, Beijing, China (March 2014).

Reaction rates for explosive nuclear synthesis, **A. Spiridon**, 11th Russbach School on Nuclear Astrophysics, Russbach, Austria (March 2014).

Investigation of the nuclear structure of ^{17}O at high excitation energy with five-particle transfer reactions **B. Roeder**, "REUNIÃO DO COMITÊ DE AVALIAÇÃO DE PROJETOS DE EXPERIÊNCIAS PARA O ACELERADOR PELLETRON (CAP)" ("Meeting of the Experiment Evaluation Committee for experiments at the Pelletron Accelerator") University of São Paulo, São Paulo, Brazil (October 2013).

Probing properties of the weak interaction using trapped atoms and ions, **D. Melconian**, **Invited Seminar**, University of Notre Dame Nuclear Physics Laboratory, South Bend, Indiana (February 2014).

Precision measurements of β-decay correlation parameters from trapped atoms and ions, **D. Melconian**, **Invited Seminar**, X Latin American Symposium on Nuclear Physics and Applications, Montevideo, Uruguay (December 2013).

Precision β-decay studies using trapped atoms and ions, **D. Melconian**, **Invited Seminar**, National Superconducting Laboratory, Michigan State University, East Lansing, Michigan (November 2013).

Fundamentally cool physics with trapped atoms and ions, **D. Melconian**, **Invited Colloquium**, Texas A&M University, College Station, Texas (October 2013).

Nuclear spin polarization of $^{37,41}K$ by optical pumping, **B. Fenker**, Texas Section of the APS Meeting, Brownsville, Texas (October 2013).

Report on the measurement of the beta asymmetry parameter, A_β, of ^{37}K, **R.S. Behling**, ISAC Science Forum, TRIUMF, Vancouver, British Colombia (December 2012).

Report on the current status of the TAMUTRAP facility, **P. Shidling**, APS Division of Nuclear Physics meeting, Newport News, Virginia (October 2013).

Gluon polarization and jet production in STAR, **C.A. Gagliardi** (for the STAR Collaboration), XXI Int. Workshop Deep Inelastic Scatt. (DIS 2013), Marseille, France (April 2013).

Inclusive jet production in longitudinally polarized pp collisions at STAR, **Z. Chang** (for the STAR Collaboration), APS Meeting Div. Nucl. Phys., Newport News, Virginia (October 2013).

Gluon polarization and jet production in STAR, **P. Djawotho** (for the STAR Collaboration), 25th Int. Nucl. Phys. Conf. (INPC 2013), Florence, Italy (June 2013).*Transverse single-spin asymmetry in STAR at*

forward rapidity, **M.M. Mondal** (for the STAR Collaboration), 5th Workshop APS GHP (GHP13), Denver, Colorado (April 2013).

Introductory experimental nuclear astrophysics, **G.V. Rogachev**, **Invited Lecture**, 7th European Summer School on Experimental Nuclear Astrophysics, Catania, Italy (September 2013).

Nuclear reactions, **G.V. Rogachev**, **Invited Lecture**, Exotic Beams Summer School (EBSS2013), Lawrence Berkeley National Laboratory, Berkeley, California (July 2013).

Clusterization and the symmetry energy in low density nuclear matter, **J.B. Natowitz, Invited Talk**, 3rd International Symposium on Nuclear Symmetry Energy, NSCL/FRIB, East Lansing, Michigan (July 2013).

Why nuclear science was and is still so interesting to me, **J.B. Natowitz, Invited Talk**, International Workshop on Nuclear Dynamics and Thermodynamics, Texas A&M University, College Station, Texas (August 2013).

Probing the nuclear equation of state at low density using near Fermi-energy heavy ion collisions, **J.B. Natowitz, Invited Talk**, The 27th Texas Symposium on Relativistic Astrophysics, Dallas, Texas (December 2013).

Using light charged particles from heavy-ion collisions to study the asymmetry dependence of the nuclear caloric curve, **S.J. Yennello, Invited Talk**, Gorden Research Conference in Nuclear Chemistry, New London, New Hampshire (June 2013).

Asymmetry dependence of the nuclear caloric curve, **S.J. Yennello, Invited Talk,** International Nuclear Physics Conference, Florence, Italy (June 2013).

Using heavy-ion collisions to study the asymmetry dependence of the nuclear caloric curve, **S.J. Yennello**, **Invited Talk**, American Chemical Society Meeting, Indianapolis, Indiana (August 2013).

How much cooler would it be with some more neutrons? The influence of neutron-proton asymmetery on nuclear temperature, **A.B. McIntosh**, XXVII Texas Symposium on Relativistic Astrophysics, Dallas, Texas (December 2013).

Experimental results on critical temperatures and densities from Quantum Fluctuations, **J. Mabiala**, International Workshop on Nuclear Dynamics and Thermodynamics (IWNDT), Texas A&M University, College Station, Texas **(**August, 2013).

Critical scaling of excited nuclear systems from quantum fluctuations, **J. Mabiala**, APS Meeting, Denver, Colorado (April 2013).

Critical behavior of nuclear systems from quantum fluctuations, **J. Mabiala**, **Invited Talk**, 3rd International Symposium on Nuclear Symmetry Energy (NuSYM13), East Lansing, Michigan (July 2013).

Asymmetry dependence of the nuclear caloric curve, **A.B. McIntosh**, **Invited Talk**, International Symposium on Nuclear Symmetry Energy (NuSYM13), East Lansing, Michigan (July 2013).

Studies of N/Z equilibration via heavy-residue isoscaling, **G. Souliotis**, **Invited Talk**, International Workshop on Nuclear Dynamics and Thermodynamics (IWNDT), Texas A&M University, College

Station, Texas **(**August, 2013).

The influence of neutron-proton asymmetry on nuclear temperature, **A.B. McIntosh**, **Invited Talk**, International Workshop on Nuclear Dynamics and Thermodynamics (IWNDT), College Station, Texas (August 2013).

Current trends in nuclear reactions, **A.B. McIntosh**, **Invited Talk**, Gorden Research Conference in Nuclear Chemistry, New London, New Hampshire (June 2013).

Symmetry energy effects on reaction break-up mechanisms near the Fermi energy using Xe,Sn+Ni systems at 15A MeV, **P. Cammarata**, Gorden Research Conference in Nuclear Chemistry, New London, New Hampshire (June 2013).

Searching for observables sensitive to the nuclear equation of state: looking for the needle in the haystack using heavy-ion collisions, **P. Cammarata**, Southwest Regional ACS Meeting, Waco, Texas (November 2013).

In-medium effects and low density nuclear matter, **K. Hagel**, International Nuclear Physics Conference (INPC), Florence, Italy (June, 2013).

Experimental determination of Mott points in nuclear matter, **K. Hagel**, International Workshop on Nuclear Dynamics and Thermodynamics (IWNDT), Texas A&M University, College Station, Texas **(**August, 2013).

Clusterization in nuclear matter, **K. Hagel**, NUFRA, Kemer (Antalya), Turkey (October 2013).

Clustering and low density nuclear matter, **K. Hagel**, IX Workshop on Particle Correlations and Femtoscopy (WPCF2013), Acireale, Italy (November 2013).

Measurement of the plasma astrophysical S factor for the ^{3}He(d, p)^{4}He reaction in exploding molecular clusters, **M. Barbui**, **Invited Seminar**, Oak Ridge National Laboratory, Oak Ridge, Tennessee (October 2013).

Laser applications to nuclear astrophysics, **M. Barbui**, **Invited Seminar**, 7th European Summer School on Experimental Nuclear Astrophysics, Santa Tecla (CT), Sicily, Italy (September 2013).

Exploring the alpha cluster structure of nuclei using the thick target inverse kinematics technique for multiple alpha decays, **M. Barbui**, International Workshop on Nuclear Dynamics and Thermodynamics (IWNDT), Texas A&M University, College Station, Texas **(**August, 2013).

Exploring the alpha cluster structure of nuclei using the thick target inverse kinematics technique for multiple alpha decays, **M. Barbui**, K. Hagel, V.Z. Goldberg, J.B. Natowitz, H. Zheng, G. Giuliani, G.G. Rapisarda, S. Wuenschel and X. Liu, International Nuclear Physics Conference (INPC), Florence, Italy (June 2013).

Deep inelastic multi-nucleon transfer for creation of super- and hyper-heavy elements:a survey experiment, **S. Wuenschel**, J.B. Natowitz, K. Hagel, M. Barbui, G. Giuliani, E.J. Kim, N. Blando, H. Zheng, S. Kowalski, K. Schmidt, Z. Majka, Z. Sosin, and A. Wieloch, The Glenn T. Seaborg Award for Nuclear Chemistry Symposium, ACS National Meeting, Dallas, Texas (March 2014).

Survival of shell-stabilized, spherical nuclei and prospects for discovery of the next new element, **Charles M. Folden III**, **Invited Talk**, 247th American Chemical Society National Meeting, Dallas, Texas (March 2014).

Heavy elements research at Texas A&M University, **Charles M. Folden III**, **Invited Talk**, American Chemical Society Western Regional Meeting, Santa Clara, California (October 2013).

Offline development of new chemical systems for the future study of Rf chemistry, **Marisa C. Alfonso**, 246th American Chemical Society National Meeting, Indianapolis, Indiana (September 10, 2013).

Excitation functions of ^{45}Sc induced reactions: towards superheavy elements synthesis, **Tyler A. Werke**, 246th American Chemical Society National Meeting, Indianapolis, Indiana (September 2013).

Survival of shell-stabilized (superheavy) spherical nuclei using projectiles with Z > 20, **Charles M. Folden III**, 246th American Chemical Society National Meeting, Indianapolis, Indiana (September 2013).

Influence of projectiles with Z > 20 on synthesis of heavy evaporation residues near ^{208}Pb, **Dmitriy A. Mayorov**, 246th American Chemical Society National Meeting, Indianapolis, Indiana (September 2013).

Heavy element research at Texas A&M University, **Charles M. Folden III**, **Invited Talk**, FRIB Community Meeting, East Lansing, Michigan (August 2013).

Prospects for discovery of the next new element in complete fusion reactions, **Charles M. Folden III**, International Workshop on Nuclear Dynamics and Thermodynamics, College Station, Texas (August 2013).
Influence of projectiles with Z > 20 on synthesis of heavy evaporation residues, **Dmitriy A. Mayorov**, International Workshop on Nuclear Dynamics and Thermodynamics, College Station, Texas (August 2013).

Excitation functions of ^{45}Sc-induced reactions: towards superheavy elements synthesis, **Tyler A. Werke**, International Workshop on Nuclear Dynamics and Thermodynamics, College Station, Texas (August 2013).

Experimental and computational assessment of unique trace elements and isotopes ratios in plutonium from depleted uranium irradiated in fast reactor blankets, **Charles M. Folden III**, with Sunil S. Chirayath, DNDO ARI Grantees Program Review, Leesburg, Virginia (August 2013).

Effects of odd-Z projectiles on fusion-evaporation cross sections, **Tyler A. Werke**, American Physical Society April Meeting, Denver, Colorado (April 2013).

Production of nuclides near the N = 126 shell using projectiles with Z > 20, **Charles M. Folden III**, American Physical Society April Meeting, Denver, Colorado (April 2013).

Study of B-meson reconstruction in STAR, **M. Cervantes**, **Invited Talk**, Muon Telescope Meeting Rice University, Houston, Texas (November 2013).

Recent results on event-by-event fluctuations from the RHIC beam-energy scan program at RHIC, **Nihar Sahoo**, **Invited Talk**, Winter Workshop on Nuclear Dynamics, Galveston, Texas (April 2013).
Advancing the theory of deuteron stripping reactions populating bound states and resonances and application for nuclear astrophysics, **A.M. Mukhamedzhanov**, Instituto de Estructura de la Materia, Madrid, Spain (April 2013).

Gravitational interaction of nucleons with mini black holes, **A.M. Mukhamedzhanov**, Instituto de Estructura de la Materia, Madrid, Spain (April 2013).

Advancing the theory of deuteron stripping reactions populating bound states and resonances and application for nuclear astrophysics, **A.M. Mukhamedzhanov**, **Seminar**, CERN, Isolde Group, Geneva, Switzerland, (May 2013).

Advancing the theory of deuteron stripping reactions populating bound states and resonances and application for nuclear astrophysics, **A.M. Mukhamedzhanov**, **Invited Talk**, 2nd International workshop Tandem/ALTO, Orsay/Paris, France (May 2013).

Advancing the theory of deuteron stripping reactions populating bound states and resonances and application for nuclear astrophysics, **A.M. Mukhamedzhanov**, Surrey University, Guilford, United Kingdom (May 2013).

Advancing the theory of deuteron stripping reactions populating bound states and resonances and application for nuclear astrophysics, **A.M. Mukhamedzhanov**, **Invited Talk**, Workshop on Quasi-Free Scattering with Radioactive Beams 13, Terceira, Azore Islands, Portugal (September 2013).

Indirect methods in nuclear astrophysics, **A.M. Mukhamedzhanov**, **Invited Lecture**, European School on Nuclear Astrophysics, Santa Tecla, Italy (September 2013).

Gravitational interaction of nucleons with mini black holes, **A.M. Mukhamedzhanov**, **Invited Lecture**, European School on Nuclear Astrophysics, Santa Tecla, Italy (September 2013).

Nuclear reactions as indirect methods in nuclear astrophysics, **A.M. Mukhamedzhanov**, **Invited Talk**, 27th Texas Symposium on Relativistic Astrophysics, Dallas, Texas (December 2013).

Connections between dilepton data and chiral symmetry restoration, **P. Hohler**, **Invited Talk**, Int. Workshop on "Electromagnetic Probes of Strongly Interacting Matter", ECT* Trento, Italy (May 2013).

Theory of thermal electromagnetic radiation, **R. Rapp**, **3 Invited Lectures**, JET Collaboration Summer School, Ohio State University, Columbus, Ohio (June 2013).

Thermal electromagnetic emission, **R. Rapp**, **Invited Talk**, Int. Workshop on "Future Trends in High-Energy Nuclear Collisions, Beijing, China (August 2013).

Light vector mesons in medium: from constraints to predictions, **R. Rapp**, **Invited Talk**, EMMI RRTF Symposium on "Electromagnetic Emissivity of Matter under Extreme Conditions", GSI, Darmstadt, Germany (October 2013).

Heavy-flavor transport in heavy-ion collisions, **R. Rapp**, **Invited Talk**, EMMI Workshop on "Heavy Flavor and QCD Phase Structure in Heavy-Ion Collisions", Lawrence Berkeley National Laboratory, Berkeley, California (November 2013).

Heavy flavor and deconfinement, **R. Rapp**, **Invited Talk**, Sapore Gravis Workshop, Nantes, France (December 2013).
Background on thermal photon rates in QCD matter, **R. Rapp**, EMMI Rapid Reaction Task Force on "Direct-Photon Flow Puzzle", GSI, Darmstadt, Germany (February 2014).

Quarkonia in the quark-gluon plasma, **R. Rapp**, **Invited Seminar**, Tsinghua University, Beijing, China (August 2013).

Dileptons and chiral symmetry restoration, **P. Hohler**, **Invited Seminar**, Rice University, Houston, Texas (March 2014).

From dileptons in heavy-ion collisions to chiral restoration at high temperature, **R. Rapp**, **Invited Seminar**, Duke University, Durham, North Carolina (March 2014).

Mass generation+melting with the strong force, **R. Rapp**, Cyclotron's REU program, Texas A&M University, College Station, Texas (June 2013).

Mass melting and deconfinement at a trillion degrees, **R. Rapp**, Graduate Student Research Seminar, Texas A&M University, College Station, Texas (September 2013).

Dileptons and chiral symmetry restoration, **P. Hohler**, Nuclear Theory Seminar, Texas A&M University, College Station, Texas (March 2014).

On physics and status of AMPT, **C.M. Ko**, **Invited Talk**, International Workshop on Particle Production in Proton-Proton Interactions and Beyond, Bad Liebenzell, Germany (April 2013).

Elliptic flow difference between particles and antiparticles and the EOS of baryon-rich matter, **C.M. Ko**, **Invited Talk**, XXXI Max Born Symposium and HIC for FAIR Workshop on Critical Behavior in Hot Dense QCD, Wroclawski, Poland (June 2013).

Hadronization via coalescence in the AMPT approach, **C.M. Ko**, **Invited Talk**, International Workshop on Transport Theory in Heavy Ion Collisions, Frankfurt, Germany (July 2013).

Elliptic flow as a probe of the QCD phase diagram at finite chemical potential, **C.M. Ko**, **Invited Talk**, 10^{th} International Workshop on QCD Phase Transition and Relativistic Heavy Ion Physics, Chengdu, Sichuan, China (August 2013).

Fluctuations and correlations in AMPT, **C.M. Ko**, **Invited Talk**, 2^{nd} Workshop on Initial Fluctuations and Final Correlations, Chengdu, Sichuan, China (August 2013).

Elliptic flow of baryon-rich matter, **C.M. Ko**, **Invited Talk**, The 9^{th} International Workshop on Relativistic Aspects of Nuclear Physics, Rio de Janeiro, Brazil (September 2013).

Mean-field effects in hot dense matter, **C.M. Ko**, **Invited Talk**, Tribute to Gerald E. Brown Conference, Stony Brook, New York (November 2013).

Elliptic flow as a probe of the properties of baryon-rich QGP, **C.M. Ko**, **Invited Talk**, International Workshop on New Frontiers in QCD, Kyoto, Japan (December 2013).

Particle production in heavy ion collisions, **C.M. Ko**, **Invited Talk**, International Workshop on Simulations of Low and Intermediate Energy Heavy Ion Collisions, Shanghai, China (January 2014).

Hot medium effects on J/ψ production in p+Pb collisions at sqrt(s)=5.02 TeV, **Y. Liu**, International Workshop on Heaavy Flavor and QCD Phase Structure in High-Energy Collisions, Berkeley, California (November 2013).

Progress report from TAMU on recombination, **K. Han**, **Invited Talk**, 2013 JET Collaboration Meeting, Columbus, Ohio (June 2013).

Quarkonia production in heavy ion collisions, **C.M. Ko**, Shangahai Institute of Applied Physics, Chinese Academy of Sciences, Shanghai, China (January 2014).

Gluon dissociation of charmonium beyond the dipole approximation, **Y. Liu**, Cyclotron Institute, Texas A&M University, College Station, Texas (April 2013).

Hot medium effects on J/psi production in p+Pb collisions at 5.02 TeV, **Y. Liu**, Cyclotron Institute, Texas A&M University, College Station, Texas (November 2013).

Recombination for JET shower MC: status and discussion, **Rainer J. Fries**, **Invited Talk**, JET NLO and Monte Carlo Meeting, Detroit, Michigan (August 2013).

Uncertainties in jet event generators due to hadronization scheme, other issues with energy loss on E-by-E hydro, and the extraction of transport coefficients, **Rainer J. Fries**, **Invited Talk**, RHIC Strategy Meeting, Detroit, Michigan (August 2013).

Flowing gluon fields: collective phenomena in classical QCD, **Rainer J. Fries**, **Invited Talk**, 15th Conference on Elastic and Diffractive Scattering (EDS Blois 2013), Saariselka, Finland (September 2013).

Flowing gluon fields: collective phenomena in classical QCD, **Rainer J. Fries**, **Invited Talk**, 9th Workshop on High P_T at LHC, Grenoble, France (September 2013).

Initial flow of gluon fields in heavy ion collisions, **Rainer J. Fries**, 6th International Conference on Hard and Electromagnetic Probes of High Energy Nuclear Collisions (Hard Probes 2013), Cape Town, South Africa (November 2013).

Flow and energy momentum tensor from classical gluon fields, **Rainer J. Fries**, New Frontiers in QCD (NFQCD 2013), Kyoto, Japan (December 2013).

High energy nuclear collisions: hard probes, heavy quarks, strong gluon fields, **Rainer J. Fries**, **Invited Colloquium**, Texas A&M University at Commerce, Commerce, Texas (September 2013).

Modern energy density functional for nuclei and the nuclear matter equation of state, **S. Shlomo**, **Invited Talk**, Ben-Gurion University, Beer Sheva, Israel (April 2013).

From outside users

Distribution of angular momentum transfers from (p,d) and (p,t) reactions in the high excitation energy continuum region of gadolinium nuclei, **T. Tarlow**, APS Meeting Div. Nucl. Phys., Newport News, Virginia (October 2013).

Stewardship science at the University of Richmond, **A. Simon**, The Stewardship Science Academic Alliance annual symposium, Washington DC (February 2014).

Magnetic moment measurements extending isotopic chains, **G.J. Kumbartzki** and N. Benczer-Koller, XX International School on Nuclear Physics, Neutron Physics, and Applications, Varna, Bulgaria (September 2013).

RESEARCH PERSONNEL AND ENGINEERING STAFF

April 1, 2013 - March 31, 2014

Faculty and Research Group Leaders

Aldo Bonasera, Senior Scientist
Charles M. Folden III, Assist. Prof. of Nuclear Chemistry
Rainer Fries, Assist. Professor of Physics
Carl A. Gagliardi, Professor of Physics
John C. Hardy, Professor of Physics
Che Ming Ko, Professor of Physics
Dan Melconian, Assist. Professor of Physics
Saskia Mioduszewski, Assist. Prof. of Physics
J. B. Natowitz, Professor of Chemistry, Bright Chair
Ralf Rapp Associate Professor of Physics
Grigory Rogachev, Professor of Physics – From 9/1/13
Shalom Shlomo, Senior Scientist
Robert E. Tribble, Professor of Physics (20%) – From 3/1/14
Sherry J. Yennello, Professor of Chemistry, Director – From 3/1/14
Dave H. Youngblood, Professor of Physics
Akram M. Zhanov, Senior Scientist

Research Staff

Juha Arje, Research Scientist- To 1/1/14
Marina Barbui, Assist. Research Scientist
Henry Clark, Accelerator Physicist (50%)
Grigor Chubaryan, Research Scientist
Vladilen Goldberg, Research Scientist
John C. Hagel, Research Scientist (50%)
Vladimir Horvat, Research Scientist (50%)
Victor Iacob, Research Scientist – From 11/1/13
Yevgen Koshchiy, Assist. Research Scientist – From 10/22/13
Yiu-Wing Lui, Research Scientist
Ninel Nica, Associate Research Scientist
Alan McIntosh, Assist. Res. Scientist – From 4/1/13
George Souliotis, Associate Research Scientist
Livius Trache, Research Scientist – To 1/1/14

Visiting Scientists

Yu-Gang Ma – From 2/26/14
Dan-Yang Pang – From 3/1/14
Ian Towner – From 6/24/13 To 8/31/14

Accelerator Physics and Radiation Line Staff

Joseph Brinkley, Research Associate
Lixin Chen, Research Associate
Henry Clark, Accelerator Physicist (50%)
Vladimir Horvat, Research Scientist (50%)
Bruce Hyman, Research Associate
George Kim, Accelerator Physicist
Don May, Accelerator Physicist
Brian Roeder, Accelerator Physicist
Gabriel Tabacaru, Accelerator Physicist

Computer Systems Staff

Robert Burch, Jr., Lead Microcomputer/LAN Administrator
John C. Hagel, Research Scientist (50%)

Engineering Staff

Robert Olsen, Senior Mechanical Engineer

Postdoctoral Research Associates

Taun K. Bhardwaj – From 4/1/13
Matthew Cervantes – From 1/1/13
Guangyao Chen – From 10/14/13
Pibero Djawotho – To 6/30/13
Vasily Eremenko – To 4/30/13
Gianluca Giuliani – To 10/1/13
Paul Hohler
Eun-Joo Kim – To 1/1/14
Yunpeng Liu
Ellen McCleskey - From 12/1/13
Matthew McCleskey – To 3/1/14
Alan McIntosh – To 3/31/13
Mirganka Mondal
Hyo-In Park
Antti Saastamoinen
Nihar Sahoo – From 12/16/13
Praveen Shidling
Ellen Simmons – From 12/1/13
Taesoo Song – To 8/31/13
Sara Wuenschel
Evgeny Tereshatov – From 1/10/14
Yi Xu

STUDENTS

April 1, 2013 - March 31, 2014

Graduate Students

Mason Anders
Marisa Alfonso
Joseph Atchison – From 2/1/14
Matteo Barbarino
Richard Spence Behling
Miguel Bencomo
Jonathan Button
Paul Cammarata
Zilong Chang
Matthew Cervantes – To 8/15/12
Roman Chyzh
Guangyao Chen – To 10/13/13
Murat Dag
Benjamin Fenker
Kyong Choi Han
Lauren Heilborn
Nathan Holt
Feng Li
Shuai Liu – From 8/1/13
Larry May
Demitri Mayarov
Michael Mehlman
Andrew Raphelt - To 8/12/13
Steven Rose – From 1/16/13
Issac Sarver – From 9/1/13
Ellen Simmons – To 11/30/13
Alexandra Spiridon
Sidharth Somanathan
Tyler Werke
Andrew Zarrella
Hua Zheng

Undergraduates and Student Technicians

Robert Bordovsky – From 9/9/13
Nicolas Blando
Lindsay Bryce
Matthew Chapman
Haley Demos – To 10/10/13
Leslie Galvan – To 9/1/13
Zachary Gastony
Hunter Gould – To 1/13/14
Brook Johnson – From 2/17/14
Hanyu Li – To 8/19/13
Magaret Moetteli – From 2/24/14

ORGANIZATIONAL CHART - CYCLOTRON INSTITUTE

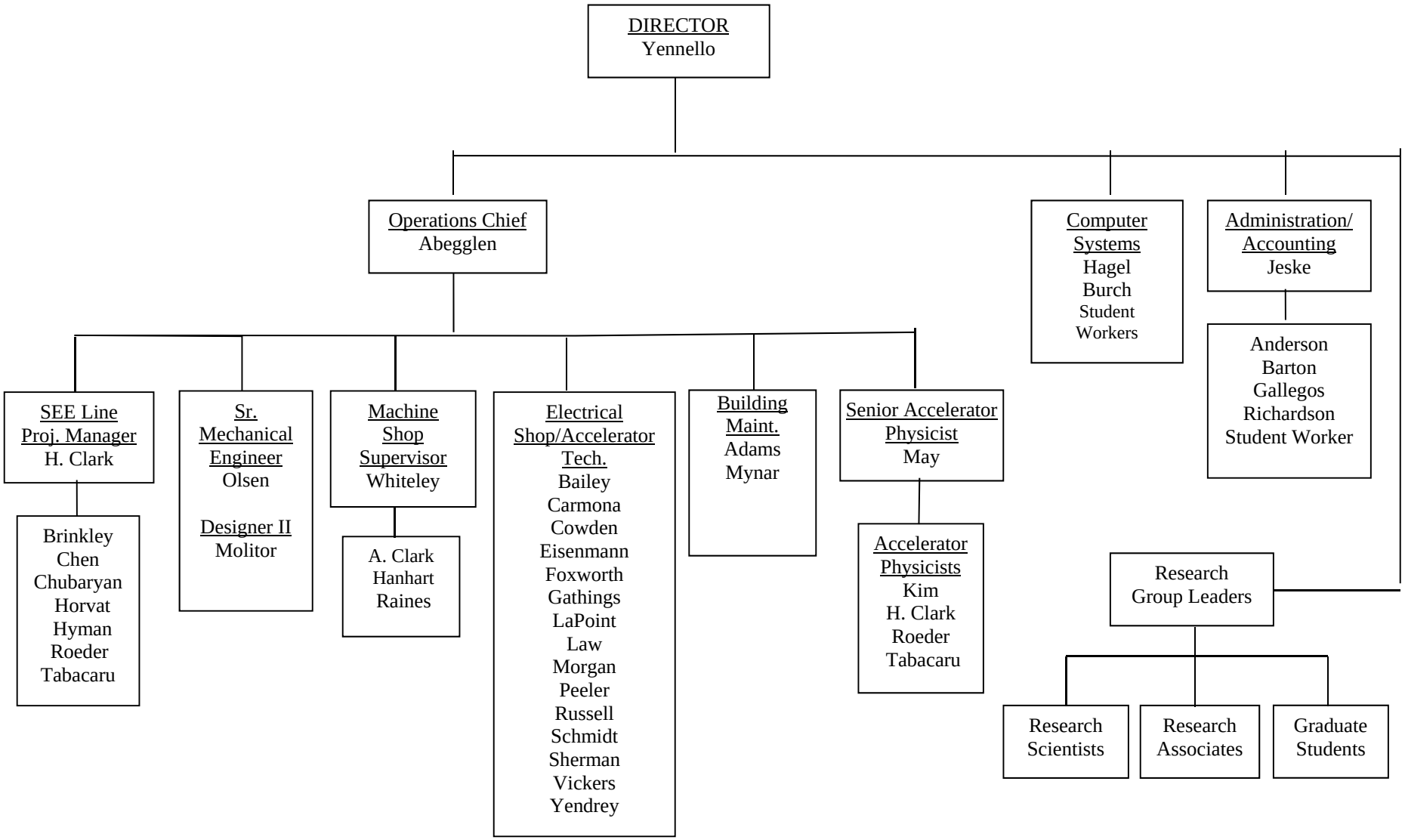

STUDENTS WHO RECEIVED GRADUATE DEGREES FROM THESIS WORK CONDUCTED AT THE CYCLOTRON INSTITUTE

April 1, 2013 – March 31, 2014

Name	Year	Thesis Title	Advisor	Present Position
Jonathan Button	2013	*Decay Detector for the Study of Gant Monopole Resonance in Unstable Nuclei*	D. H. Youngblood	Continue to Ph. D. degree
Guangyao Chen	2013	*Initial Conditions from Color Glass Condensate*	R. J. Fries	Post. Doc. at Cyclotron Institute, Texas A&M University
Ellen Nicole Simmons	2013	*The β-Delayed Proton and Gamma Decay of ^{27}P*	R. E. Tribble	Post. Doc. at Cyclotron Institute, Texas A&M University
Andrew Raphelt	2013	*Dependence of the Asymmetry Energy and Time in Dynamical Models using Isoscaling*	S. J. Yennello	Klein Collins High School, Spring, Texas

STUDENTS WHO RECEIVED GRADUATE DEGREES FROM NON-THESIS

April 1, 2013 – March 31, 2014

Name	Year	Advisor	Present Position
Yakup Boran	2013	D. Melconian	N/A
Benjamin Fenker	2013	D. Melconian	Continue to Ph. D. degree

INSTITUTE COLLOQUIA AND SEMINARS
April 1, 2013-March 31, 2014

2013

September 25	Prof. Wilton Catford, Department of Physics, University of Surrey, Guildford, United Kingdom	*TIARA Detector*
September 25	Prof. K. A. Gridnev, St. Petersburg State University, St. Petersburg, Russia	*Extreme Neutron Rich Sector of the Nuclear Chart: New Horizon*
September 26	Dr. Jiansong Wang, Institute of Modern Physics, Chinese Academy of Sciences, Lanzhou, China	*Elastic Scattering Studies at RIBLL*
September 26	Dr. Zhiqiang Chen, Institute of Modern Physics, Chinese Academy of Sciences, Lanzhou, China	*Accelerator Driven Systems Related Nuclear Data Research at IMP*
October 29	Prof. Peter Kuchment, Department of Mathematics, Texas A&M University,College Station, Texas	*Detection of Small Low Emission Sources*
November 19	Prof. Daniel Cebra, Department of Physics, Uinversity of California, Davis, Davis, California	*Exploring the Phase Diagram of QCD Matter*
December 6	Dr. Toshiki Maruyama, Advanced Science Research Center, Japan Atomic Energy Agency, Japan	*First-order Phase Transitions of Nuclear Matter and Inhomogeneous Structures of Mixed Phase*
December 11	Dr. Aliya Nurmukhanbetova, Nazarbayev University, Astana, Kazakhstan	*Nuclear Physics at Nazarbayev University in Astana, Kazakhstan*
December 11	Dr. Nessipbek Mynvayev, Nazarbayev University, Astana, Kazakhstan	*Nuclear Physics at Nazarbayev University in Astana, Kazakhstan*

2014

January 14	Dr. Ethan Uberseder, JINA/University of Notre Dame, South Bend, Indiana	*Hitting a Small Nail with a Very Big Hammer: Astrophysical Neutron Capture Cross Sections from Relativistic Coulomb Dissociation*

February 4	Dr. Shadi Bedoor, Department of Physics, Western Michigan University, Kalamazoo, Michigan	*Structural Evolution in the Neutron Rich-Nucleus ^{14}B*
March 4	Dr. Evgeniy Koshchiy, Cyclotron Institute, Texas A&M University, College Station, Texas	*Experiments with Array for Nuclear Astrophysics and Structure with Exotic Nuclei (ANASEN)*
March 18	Prof. Andreas Stolz, NSCL, Michigan State University, East Lansing, Michigan	*Diamond Detectors for Relativistic Heavy Ions*
March 25	Dr. N.D. Scielzo, Lawrence Livermore National Laboratory, Livermore, California	*Neutrino and Neutron Spectroscopy using Trapped Ions*